Design Strategies for Multicomponent Supramolecular Polymerization

A Thesis Submitted for the Degree of

Doctor of Philosophy

By

Aritra Sarkar

New Chemistry Unit

Jawaharlal Nehru Centre for Advanced Scientific Research

(A Deemed University)

Bangalore - 560064 (INDIA)

September 2020

Design Strategies for Multicomponent Supramolecular Polymerization

A Thesis Submitted for the Degree of

Doctor of Philosophy

By

Aritra Sarkar

UNDER THE SUPERVISION OF

Prof. Subi J. George

New Chemistry Unit

Jawaharlal Nehru Centre for Advanced Scientific Research

(A Deemed University)

Bangalore-560064 (INDIA)

September 2020

"The woods are lovely, dark and deep,

But I have promises to keep,

And miles to go before I sleep,

And miles to go before I sleep."

- *Robert Frost*

Dedicated to "Supramolecular Chemistry Laboratory"

DECLARATION

I hereby declare that the matter embodied in the thesis entitled **"*Design Strategies for Multicomponent Supramolecular Polymerization*"** is the result of investigations carried out by me at the New Chemistry Unit, Jawaharlal Nehru Centre for Advanced Scientific Research, Bangalore, India under the supervision of **Prof. Subi J. George** and that it has not been submitted elsewhere for the award of any degree or diploma.

       In Keeping with the general practice in reporting the scientific observations, due acknowledgement has been made whenever the work described is based on the findings of other fellow researchers. Any omission that might have occurred due to oversight or error is in judgement is regretted.

_____

Mr. Aritra Sarkar

(Ph. D Student)

Jawaharlal Nehru Centre for Advanced Scientific Research

Prof. Subi J. George
New Chemistry Unit
Jawaharlal Nehru Centre for Advanced
Scientific Research (JNCASR)
Bangalore-560064, India
Phone : +91 80 2208 2964
Fax: + 91 80 22082627
E-mail: george@jncasr.ac.in

Date

November 11, 2020

CERTIFICATE

I hereby certify that the matter embodied in this thesis entitled **"Design Strategies for Multicomponent Supramolecular Polymerization"** has been carried out by **Mr. Aritra Sarkar** at the New Chemistry Unit, Jawaharlal Nehru Centre for Advanced Scientific Research, Bangalore, India under my supervision and that it has not been submitted elsewhere for the award of any degree or diploma.

_____

Prof. Subi Jacob George

(Research Supervisor)

ACKNOWLEDGMENTS

PREFACE

This thesis presents the design strategies for synthesis of multicomponent supramolecular polymers. This describes the attempts to synthesize supramolecular copolymers in a controlled manner by manipulating various kinetic and thermodynamic pathways of supramolecular polymerization. The thesis is divided into Nine Chapters.

Chapter-1: presents the introduction which tries to summarize the importance of multicomponent polymers in nature and subsequent challenges and state of art efforts in achieving microstructure control in supramolecular assemblies.

Part A includes Chapters 2 to 7, wherein various thermodynamic and kinetic routes to synthesize multicomponent supramolecular polymerization are presented.

Chapter-2: The synthesis of supramolecular block copolymers (BCPs) constitutes a significant challenge due to the exchange dynamics of non-covalently bound monomers and hence requires fine microstructure control. This Chapter discusses, the cooperative supramolecular block copolymerization approach of fluorescent monomers in solution under thermodynamic control for the synthesis of axial organic heterostructures with light harvesting properties. The fluorescent nature of the core-substituted naphthalene diimide (cNDI) monomers enables a detailed spectroscopic probing during the supramolecular block copolymerization process to unravel a nucleation-growth mechanism, similar to that of chain copolymerization for covalent block copolymers. Structured illumination microscopy (SIM) imaging of BCP chains characterizes the segmented microstructure and also allows size distribution analysis to reveal the narrow polydispersity (polydispersity index (PDI) $\approx$ 1.1) for the individual block segments. Spectrally-resolved fluorescence microscopy on single block copolymerized organic heterostructures shows energy migration and light harvesting across the interfaces of linearly connected segments. Molecular dynamics and metadynamics simulations provide useful mechanistic insights into the free energy of interaction between the monomers as well as into monomer exchange mechanisms and dynamics, which have a crucial impact on determining the copolymer microstructure. Thus, comprehensive spectroscopic, microscopic, and computational analyses provide an unambiguous structural, dynamic, and functional characterization of the supramolecular BCPs.

Chapter-3: Supramolecular block copolymer under kinetic control analogous to classical chain growth living polymerization would be ideally suited for synthesis of supramolecular block copolymers with higher complexity, length and dispersity control. In Chapter 3, kinetically controlled synthesis of supramolecular block copolymer via two component seeded supramolecular polymerization is presented. Moreover, a two component sequence controlled supramolecular copolymerization by manipulating thermodynamic and kinetic routes in the pathway complexity of self-assembly of the constitutive monomers is also described. Extensive molecular dynamics simulations provided useful mechanistic insights into the monomer exchange rates and free energy of interactions between the monomers that dictate the self-assembly pathway and sequence. The fluorescent nature of core-substituted naphthalene diimide monomers have been further utilized to characterize the three sequences via structured illumination microscopy (SIM).

Chapter-4: An important scientific hurdle in supramolecular polymerization is the synthesis of well defined supramolecular block copolymer (BCP) with controlled structure and dispersity. In Chapter 4, a kinetically controlled seeded supramolecular block copolymerization between two different naphthalene diimide derivatives appended with cholesterol group via carbamate linkage is reported for the synthesis of monodisperse supramolecular BCPs with tunable block lengths. Structured illumination microscopy (SIM) imaging characterized the supramolecular BCPs and allowed the size distribution analysis to be performed for individual block segments.

Chapter-5: In this Chapter, the synthetic strategies reported in Chapters 3 and 4 is extended to the design of tricomponent supramolecular block copolymers via sequential addition of three different optically active but structurally similar core substituted naphthalene diimide monomers. Further presence of metastable state and kinetically controlled nucleation-elongation growth allowed the synthesis of three different sequences via sequential addition of the three different monomers. Fluorescent nature of core-substituted naphthalene diimide monomers have been further utilized to characterize the tricomponent supramolecular block copolymers via structured illumination microscopy (SIM).

Chapter-6: Chirality driven self-sorting is envisaged to be an efficient methodology for synthesis of multicomponent supramolecular polymers. In this Chapter, two fluorescent core-substituted naphthalene diimide based donor and acceptor molecules with minimal structural mismatch and comprising of strong self-recognizing chiral motif, is reported for the chirality to determine the narcissistic self-sorting and assembly process. As a consequence, stereoselective supramolecular polymerization with an unprecedented chirality control over energy transfer has been achieved.

Chapter-7: In this Chapter, a novel concept of diastereoselective supramolecular copolymerization is reported using supramolecular charge transfer (CT) copolymers via synergistic presence of chirality and CT interaction. The observed differences in macroscopic properties was further utilized to resolve the two CT assemblies using size exclusion chromatography analogous to classical resolution of enantiomeric helicenes via diastereomeric CT complexation with chiral acceptors.

Part B includes Chapters 8 and 9, which describes the pH-responsive supramolecular polymerization of peptide-appended NDI bolaamphiphiles.

Chapter-8: The pH-responsive nature of two self-assembled NDI-peptide amphiphile conjugates is described. This Chapter explains how subtle changes in the molecular design of π-stacked chromophore-peptide conjugates have a drastic impact on their equilibrium structure and ultimately functional properties.

Chapter-9: In this Chapter, transient supramolecular polymerization of peptide-appended NDI derivatives are reports by coupling the pH-dependent charge regulated disassembly to urease catalyzed conversion of urea into ammonia. The kinetic experiments under dissipative condition are indicative of a highly cooperative disassembly regulated by formation of a charged high energy metastable state. The fluorescent nature of the cNDI further enabled visualization of the active cooperative disassembly process using time dependent super-resolved structured illumination microscopy (SIM) imaging which shows the disassembly takes places at once throughout the polymer and is independent of polymer length.

TABLE OF CONTENTS

Chapter-1

An Introduction to Multicomponent Supramolecular Polymers

Chapter-2

Cooperative Supramolecular Block Copolymerization for the Synthesis of Functional Axial Organic Heterostructures

Chapter-3

Self-Sorted, Random and Block Supramolecular Copolymers via Sequence Controlled, Multicomponent Self-assembly

Chapter-4

Kinetically Controlled Synthesis of Supramolecular Block Copolymers with Narrow Dispersity and Tunable Block Lengths

Chapter-5

Tricomponent Supramolecular Block Copolymers via Sequential Seeded Polymerization

Chapter-6

Chirality Controlled Energy Transfer via Stereoselective Supramolecular Polymerization

Chapter-7

Charge-Transfer Resolution via Diastereoselective Supramolecular Polymerization

Chapter-8

Impact of NDI Core-Substitution on the pH-Responsive Nature of Peptide-Tethered Luminescent Supramolecular Polymers

Chapter-9

Charge-Regulated, Cooperative Disassembly of a Chemically Fuelled Transient Supramolecular Polymer

Chapter: 1

An Introduction to Multicomponent Supramolecular Polymers

Chapter: 1

An Introduction to Multicomponent Supramolecular Polymers

Abstract

Sequence controlled multicomponent polymers are ubiquitous in nature. DNA and RNA are some of the excellent examples of the same which regulate complex cellular functions and are in command of synthesizing functional protein and polypeptides. Inspired by nature, polymer chemists have adapted advanced polymerization techniques for the synthesis of the sequence defined covalent polymers. However, similar control for non-covalent analogues despite having significant progress in its synthetic strategies over the years is still lacking it. Here in this Chapter, a brief account of the recent efforts in this direction is presented and finally the aim of my thesis is discussed.

Multicomponent Supramolecular Polymers
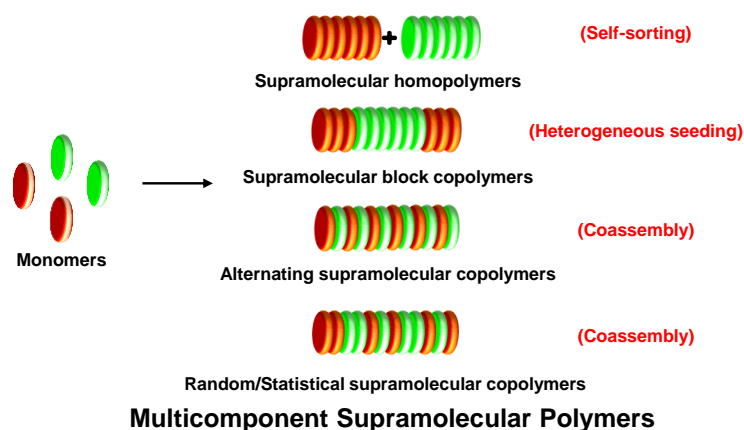
1.1. Biological Sequence Controlled Multicomponent Polymers:

Sequence controlled multicomponent polymerization is a ubiquitous phenomenon observed in nature.[1] For example, DNA, RNA, and polypeptides are naturally occurring sequence defined multicomponent biopolymers (Figure 1.1). Such precise positioning of different monomers units in biopolymers has a significant influence on polymer structures, properties, and functions. A key example could be natural transcription and translational process, which directs the synthesis of these biopolymers with precise tacticity, monomer sequences, and topology, e.g., nucleic acids, proteins, and polysaccharides. Next, these polymer chains form defined functional aggregates using intramolecular and intermolecular non-covalent associations such as folding into a protein structure (Figure 1.1d).[2] Altogether the defined sequence of the biopolymers regulates genetic replications and complex and adaptive evolutionary behaviours and functions.
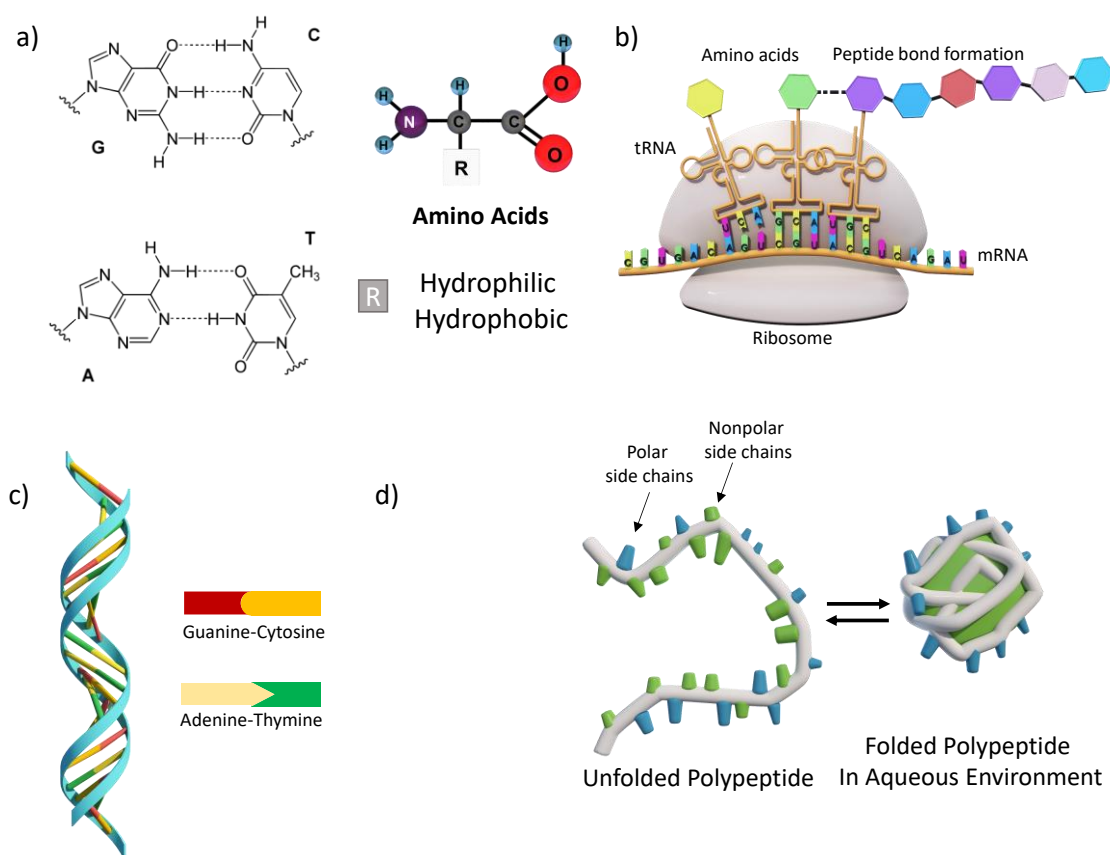
Figure 1.1. a) molecular structures of nucleobases adenine, thymine, guanine and cytosine and basic structure of amino acid, which nature uses for synthesis of sequence defined polymers. b) Cartoon representation of sequence defined polypeptide synthesis by nature using the genetic information transferred from DNA and RNA. c) Schematic illustration of DNA structures formed via specific hydrogen bonding between adenine-thymine and guanine-cytosine. d) The amino acid sequence of the synthesised polypeptide chain helps the protein to adopt its tertiary structures, which depends on precise positioning of hydrophilic and hydrophobic amino acids.

1.2. Synthetic Multicomponent Polymers:
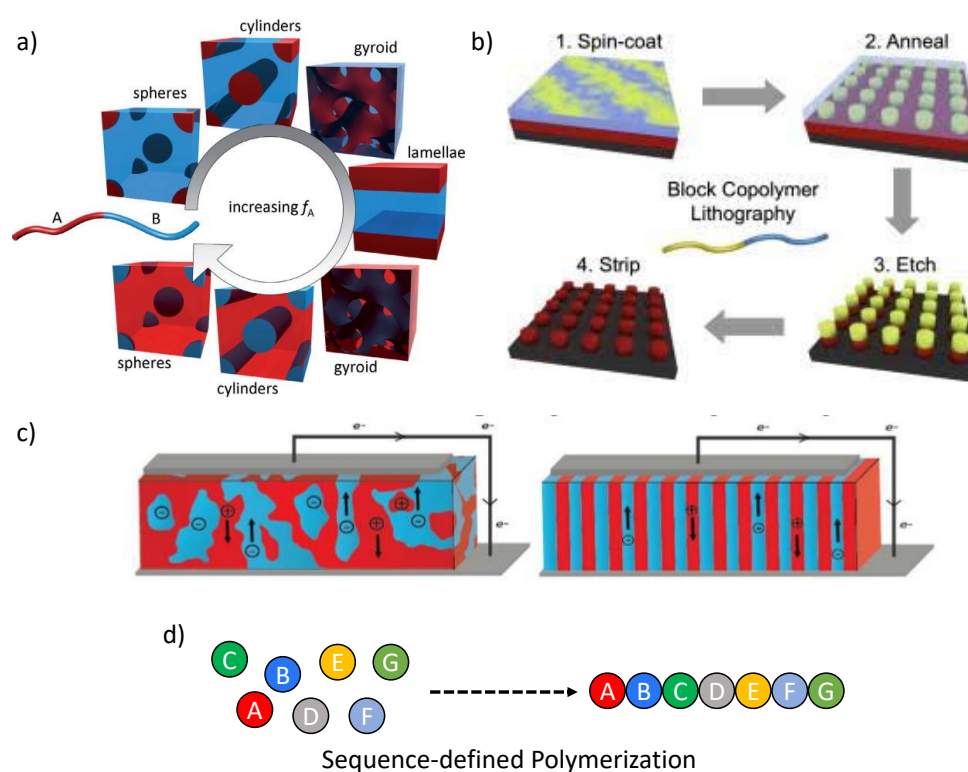
Figure 1.2. a) Various morphologies formed by the self-assembly of diblock copolymer (f_A represents fraction of one component A with respect to component B). Adapted by permission from Elsevier Publishers Ltd: Materials today, Copyright 2010 (Ref 7a). b) Schematic illustration of utilization of diblock copolymer self-assembly for lithography techniques. Adapted by permission from Elsevier Publishers Ltd: polymer, Copyright 2013 (Ref 8). c) Self-assembly of donor-acceptor diblock copolymer are utilized in organic photovoltaics for ordered arrangement of donor and acceptor component. Adapted by permission from Royal Society of Chemistry Publishers Ltd: Polymer Chemistry, Copyright 2018 (Ref 9a). d) Schematic illustration of sequence-defined covalent polymer synthesis, where n number of monomers can be arranged at precise positions.

Synthetic polymers are more diverse than biopolymers, thus increasing the possibility of a much broader range of chemical structures and functions. However, multicomponent synthetic polymers lack the precision and complexity of the sequence that biopolymers offer. Despite this lag, multicomponent synthetic polymer chemistry made significant developments over the last couple of decades, leading to monodisperse, complex structures.[3] Controlled living polymerization methods led to such remarkable development, which started taking shape during 1950s.[4] The subsequent development of other polymerization techniques such as solid-phase peptide synthesis and solid-phase iterative synthesis helped in the synthesis of synthetic polymers of higher sequence specificity.[5] One of the important outcomes of controlled polymerization techniques is the synthesis of block copolymers.[6] The inherent immiscibility of prepared blocky segments of block copolymer leads to self-organization into the plethora of

morphologies,[7] (Figure 1.2) which rapidly expanded its possible applications such as lithography,[8] and organic photovoltaics[6,7,9] with contributions from the fields of chemistry, physics and material science (Figures 1.2b and 1.2c). On the other hand, sequence-defined polymers, can be used to store monomer coded digital information thus finding applications in information technologies.[5]

1.3. Multicomponent Supramolecular Polymers:

The discovery of supramolecular polymers has broadened the scope for the synthesis of adaptive, dynamic, and evolutionary materials.[10] In such kinds of polymers, the monomeric units arrange itself using non-covalent interactions of various strengths.[11] Consequently, they are potential candidates for the realization of dynamic and adaptive out of equilibrium materials.[12] However, one of the grand challenges in the field of supramolecular polymers is the synthesis of well-defined copolymers.[13] For covalent copolymers, small changes in the copolymer composition and microstructure can have new emerging properties from them. Hence synthesis of well-defined supramolecular copolymer and sequence controlled supramolecular polymers are one of the challenges to be addressed. However, compared to the vast number of methods available for the synthesis of the covalent copolymers, only a few strategies are reported for the synthesis of well-defined supramolecular copolymers. The reason could be the kinetic lability of the non-covalent interactions,[14] absence of well-defined characterization techniques,[13c] lack of mechanistic understanding, and improper knowledge of interaction energies between the monomers. Thus, the supramolecular copolymerization, even with two components, is challenging. The outcomes could be either supramolecular homopolymers (self-sorted supramolecular polymers), alternating supramolecular polymers, or supramolecular block copolymers. In a recent review, Meijer and coworkers have defined and classified each type of copolymers by critically reflecting on its covalent counterpart, [15] In this Chapter we will discuss the current developments and challenges for the synthesis of self-sorted, alternating, and supramolecular block copolymers and how temporal control over supramolecular polymerization can provide a possible solution to this.

1.3.1. Energy Considerations for Multicomponent Supramolecular Polymers:

In supramolecular polymers, monomeric units are arranged by utilizing a variety of non-covalent interactions. Initially, supramolecular polymers were designed under thermodynamic control, where molecular information encoded within the monomer leads to spontaneous self-organization into desired materials. Hence during multicomponent supramolecular

polymerization, non-covalent interaction between the two monomers and the interaction energy between them will play a vital role in determining the microstructure.[15] While designing monomers for the two component (component 1 and component 2) supramolecular copolymer, we have to consider three primary interaction energies: ΔG_{1-1}, ΔG_{2-2}, and ΔG_{2-1} (Figure 1.3a). If the designed monomers have stronger homo-interaction energy than hetero-interaction energies, the possible outcome would be a self-sorted homopolymer (Figures 1.3b and 1.4a).
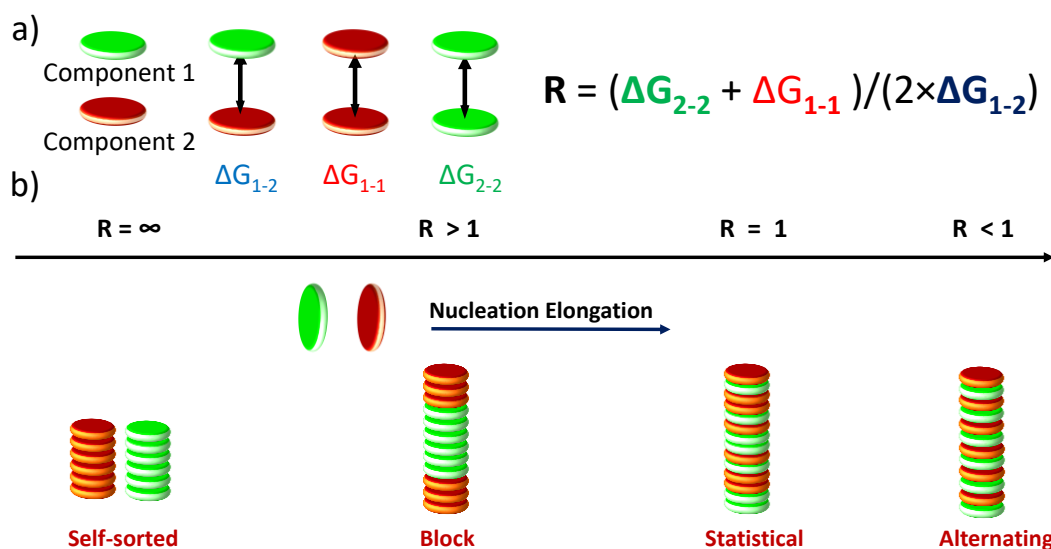
Figure 1.3. a) Schematic illustration of three basic type of interactions possible during a two component supramolecular polymerization and the equation for calculation of reactivity ratio (R). b) During two component nucleation elongation polymerization the possible microstructure of the copolymer will depend on the reactivity ratio between two monomers.

On the other hand, substantial hetero-interaction energy would be required to synthesize an alternating copolymer (Figure 1.4b). Thus, a balanced homo and hetero-interaction regime (slightly stronger homo-interaction energies than hetero-interaction energies) would develop a blocky supramolecular copolymer and will be a thermodynamically stable copolymer (Figure 1.4c). Another way to synthesize supramolecular block copolymer would require a living supramolecular polymerization between two monomers under kinetic control (Figure 1.5a). Here the polymerization efficiency between two monomers would also depend on the hetero-interaction energies. Stronger hetero-interaction energy would lead to more facile seeding between the two components under kinetic control. On the other hand, stronger homo-interaction energy over hetero-interaction energy may lead to failure of the seeding process under kinetic control leading to the formation of self-sorted homopolymers (Figure 1.5b). Self-sorted and supramolecular block copolymer synthesized considering interaction energies will

not be affected by the dynamics of supramolecular polymers. The stability of supramolecular block copolymers synthesized under kinetic control, on the other hand, would depend on
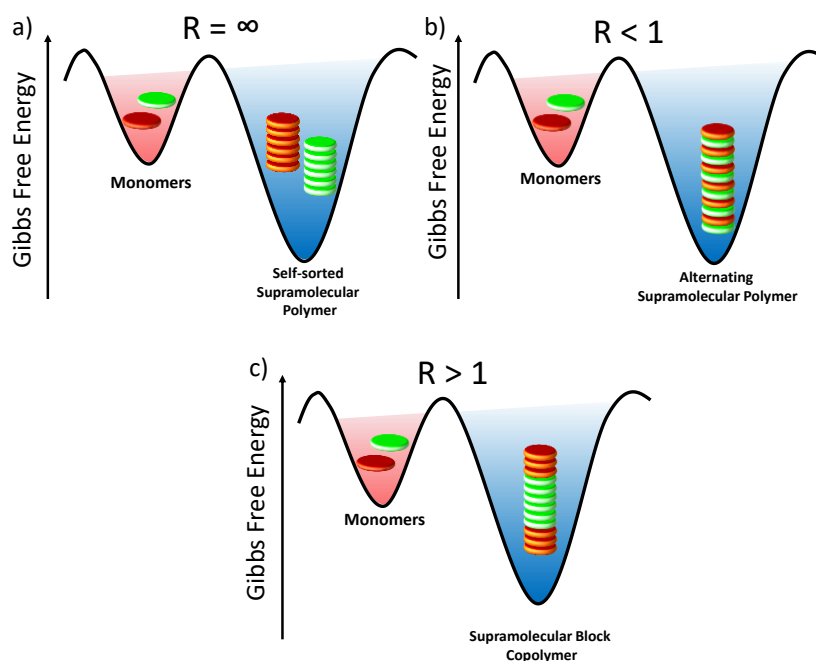
Figure 1.4. a) With a reactivity ratio of "∞" two monomers will always form self-sorted homopolymer which will be the thermodynamically most stable state. b) With a reactivity ratio of <1 (higher hetero-interaction energies than homo-interaction energies) two monomers will form alternating supramolecular copolymer which will be the thermodynamically most stable state. c) With a reactivity ratio of >1 (slightly higher homo-interaction energies than hetero-interaction energies) two monomers will form supramolecular block copolymer which will be the thermodynamically most stable state.
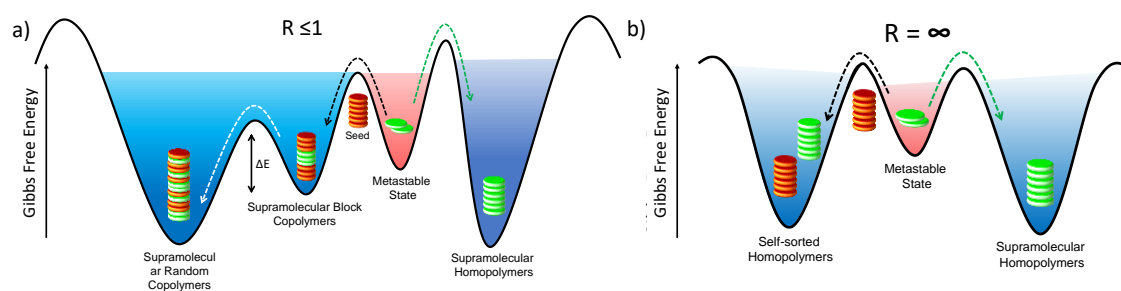
Figure 1.5. Synthesis of supramolecular block copolymer under kinetic control. a) During synthesis of supramolecular block copolymer, the hetero-interaction energies has to be higher than homo-interaction energies or comparable to each other (R≤1), so that a facile heterogeneous nucleation can take place. However, obtained block copolymer structure is a kinetically stable product and will be stabilized only when the dynamics of the system is low (ΔE>>RT). A high dynamic (ΔE<<RT) will eventually lead to randomization of the sequence to a random supramolecular copolymer. b) In contrary to that a high homo-interaction energy than hetero-interaction energies (R = ∞) will lead to an unsuccessful heterogeneous nucleation under kinetic control to result in self-sorted homopolymers.

monomer exchange dynamics (Figure 1.5a). High monomer exchange dynamics would eventually homogenize the two monomers transforming a supramolecular block copolymer into the random supramolecular copolymer. Thus, to stabilize the synthesized supramolecular block copolymers, we need to slow down the monomer exchanged dynamics. Recently several research groups have shown supramolecular polymers can be highly non-dynamic. Hence it would be possible to realize supramolecular block copolymers with such highly non-dynamic systems.

1.3.2. Self-Sorted Homopolymers:

Self-sorted homopolymers are analogous to covalent polymer blends of two or more polymers that provide new physical and chemical properties out of the polymer. However, contrary to the blended or alloyed copolymers, synthesis of the self-sorted supramolecular copolymer is challenging likely due to supramolecular self-assembly is dynamic and depends on mutual monomeric interactions.[16]
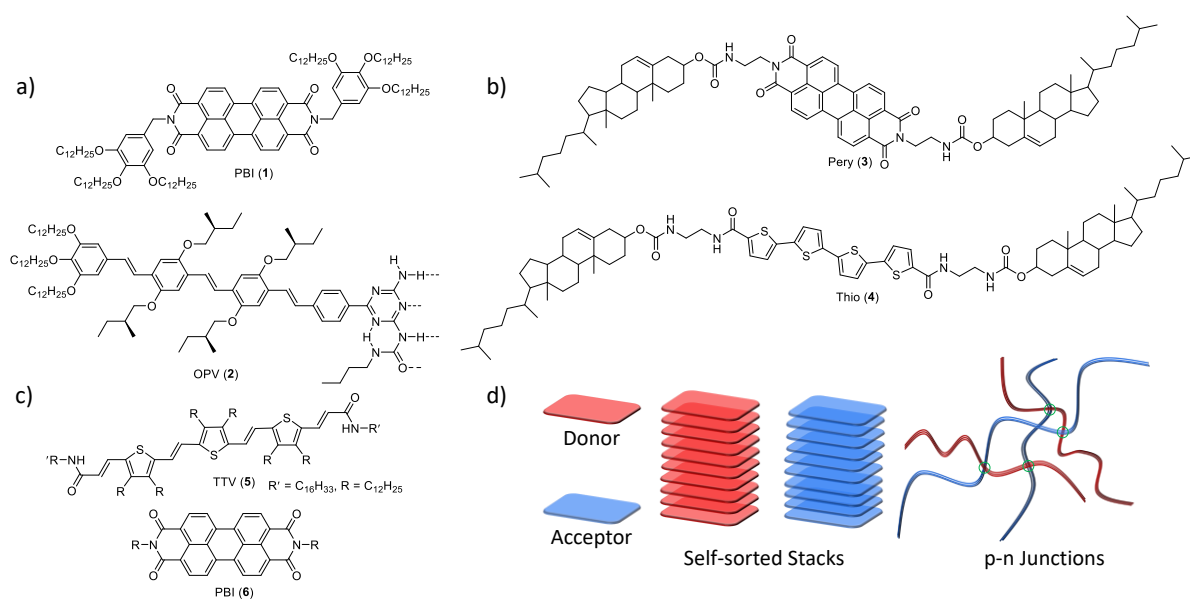
Figure 1.6. Molecular Structure of the structurally different donor and acceptor used by a) Meijer and coworkers, b) Shinkai and coworkers, and c) Ajayaghosh and coworkers for synthesis of orthogonal p-n junction and self-sorted homopolymers. d) Schematic illustration of the self-sorted stacks of donor and acceptor chromophores and formation of supramolecular p-n junction.

During self-assembly of small monomeric units, the material properties can be fully encoded into molecular building blocks. In this context, one of the design strategies could be self-assembling building blocks with a structural mismatch. Meijer and coworkers reported orthogonal self-assembly between perylene diimide and oligo (phenylene vinylene) (OPV) monomers (Figure 1.6a).[17] The molecular design consists of structurally different
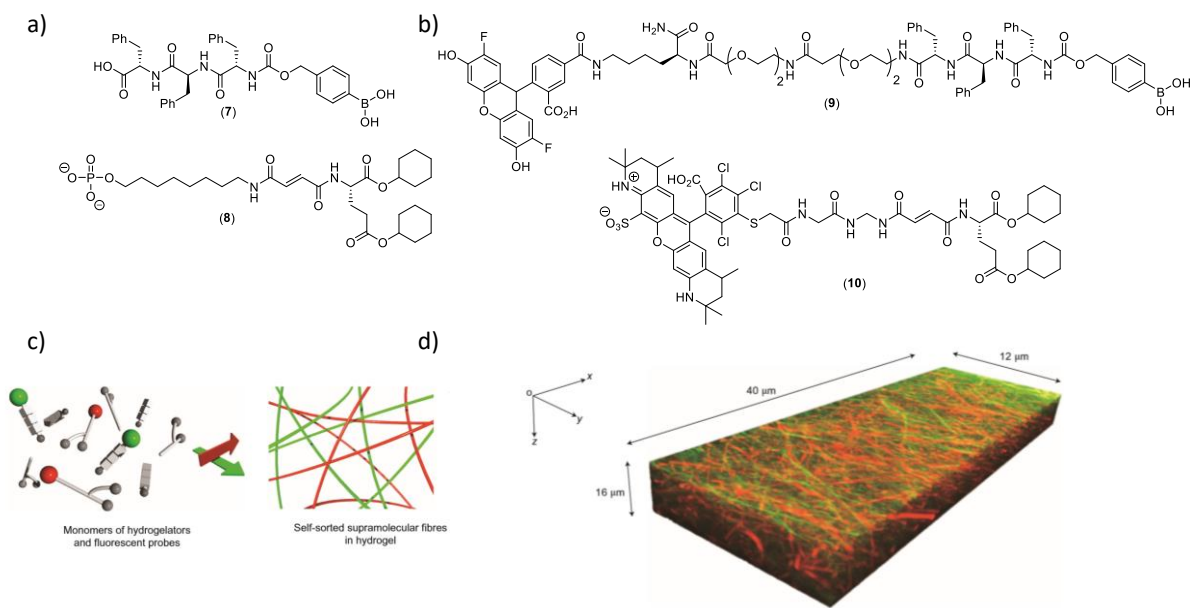
Figure 1.7. a) Molecular structure of the structurally different peptide-based monomer and lipid-based monomers used by Hamachi and coworkers for synthesis of self-sorted supramolecular polymers. b) Molecular structure of the fluorescent oregon Green-tethered peptide monomer and Alexa546-tethered lipid monomers utilized as a fluorescent tag for real-time visualization of the self-sorting process and for visualization of the self-sorted fibers. c) Cartoon representation of the formation of fluorescent self-sorted supramolecular polymers. Adapted by permission from springer nature Ltd: Nature Chemistry, Copyright 2016 (Ref 20). d) A three-dimensional confocal laser scanning microscope image of the fluorescent supramolecular polymers showing self-sorted network in the gel state. Adapted by permission from springer nature Ltd: Nature Chemistry, Copyright 2016 (Ref 20).

uridopyrimidone linked OPV and alkyl group tethered perylene bisimide derivatives, which prevails low hetero-interaction energies to drive the process to self-sorting. In similar approaches, Ajayaghosh and Shinkai independently studied self-sorted supramolecular homopolymers of p- and n-type of chromophores having structural and hydrogen bonding mismatch (Figures 1.6 and 1.6c).[18]

Although these molecular designs set the platform for synthesis of self-sorted supramolecular polymers, many of the analytical techniques generally used like spectroscopic (UV-Vis, CD, fluorescence), XRD, transmission electron microscopy, scanning electron microscopy were unable to give real-time insights into the phenomenon. In this regard, recent developments of super-resolution microscopy techniques are a significant step forward in analyzing multicomponent supramolecular polymerization.[19] Although electron microscopy techniques are powerful, but it require drying or freezing during sample preparation, which can mislead the morphological investigations. Moreover, the majority of the reported self-sorted supramolecular polymers have similar morphologies which cannot be distinguished using electron microscopy techniques. Super-resolved fluorescence microscopy techniques not only

allow us to investigate the supramolecular polymers without drying, but also allow us to distinguish chemical species with the usage of appropriate fluorescent probes. In such an attempt, Hamachi and coworkers designed self-sorted homopolymers based on lipid- and peptide-based monomers having a structural difference (Figure 1.7).[20] To characterize and distinguish the self-sorted polymer using stimulated emission depletion (STED) microscopy techniques, they have designed two fluorescent probes consisting of Oregon Green-tethered peptide monomer and Alexa546-tethered lipid monomer, which have hydrophobic cores identical to those of the corresponding monomers. Using these probes, they were able to label the two self-sorted gelators selectively, and the authors have shown the first example where directly imaged self-sorted fibers could be proved using STED microscopy. They have further impressively extended it to visualize the real-time evolution of the two self-sorted supramolecular homopolymers, which showed the non-synchronous formation of the two-fiber network and real-time visualization of a cooperative nucleation-elongation assembly.
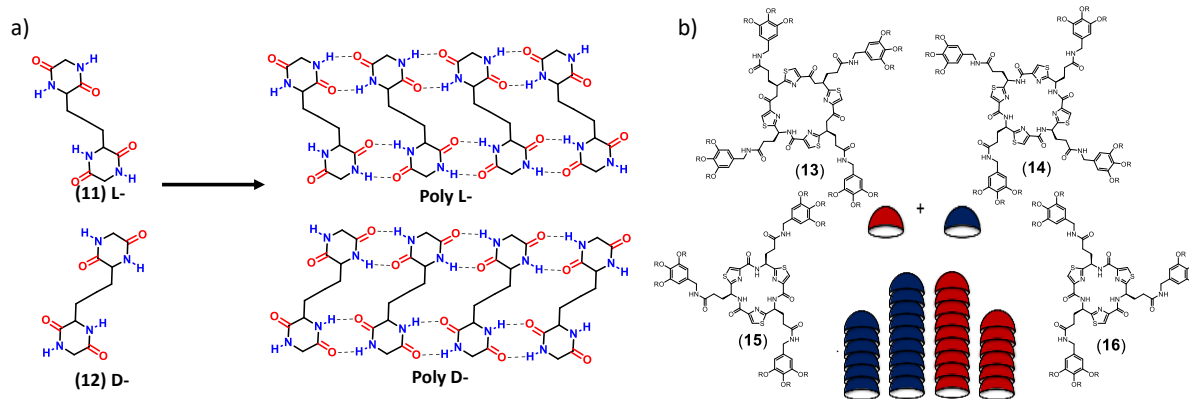
Figure 1.8. a) Chemical structures of "S"- (L-) and anti "S"- (D-) shaped cyclic dipeptide molecules and corresponding hydrogen bond assisted homochiral self-assembly. b) Chemical structures of the chiral bowl-shaped macrocycles and corresponding schematic illustration of these bowl-shaped macrocycles self-assembling into homochiral supramolecular polymers.

Another approach towards self-sorted homopolymer is stereoselective supramolecular polymerization between two chiral monomers,[21] which is analogous to the chiral resolution experiment accomplished by Pasteur. Compared to the spontaneous resolution in crystals,[22] chiral self-sorting in solution is also essential for the creation of chiral nanostructures. Aida and coworkers have shown chiral "S"- shaped cyclic peptide molecules undergo chirality driven self-sorting and stereoselective supramolecular polymerization (Figure 1.8a).[23] In this case, mutual intermolecular hydrogen bonding interactions between two enantiomers drive the self-sorting process. Thus, due to mismatch, the "S"- shape (**11**) and anti "S"- shape (**12**)
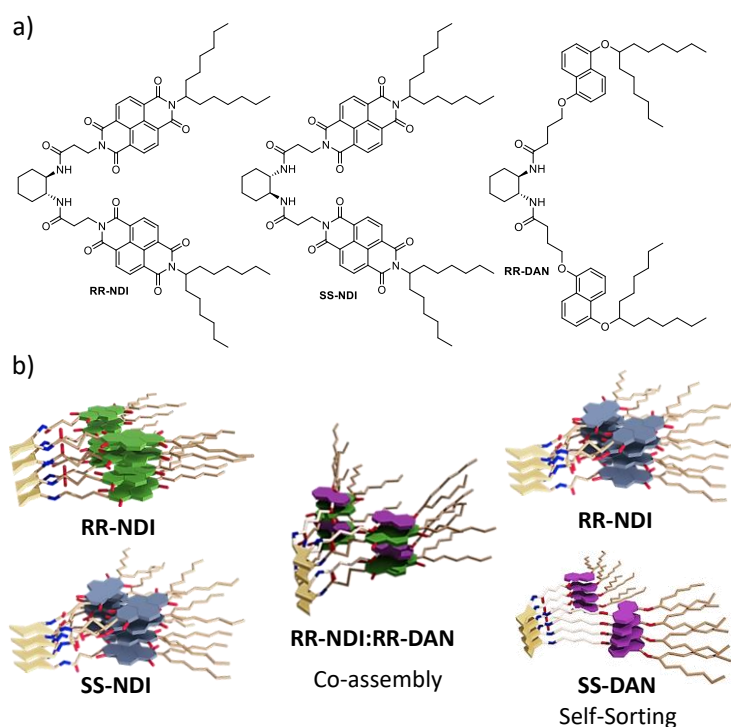
Figure 1.9. a) Chemical structure of the bis chromophoric donor **RR-/SS-NDI** and bis chromophoric donor **RR-DAN** used for chirality driven self-sorting between **RR-NDI:SS-NDI** and chirality driven orthogonal assembly between **SS-NDI:RR-DAN** and CT assembly formation between **RR-NDI:RR-DAN**. b) Cartoon representation of the stereoselective supramolecular polymerization between **RR-NDI:SS-NDI** and subsequently application of stereoselective supramolecular polymerization in arranging donor and acceptor components. Adapted by permission from John Wiley and Sons: Angewandte Chemie International Edition, Copyright 2015 (Ref 24).

conformation result in steric hindrance responsible for their chiral self-sorting occurs. Similarly, they have employed structural asymmetry in a bowl-shaped macrocycle for the construction of stereoselective supramolecular polymers (Figure 1.8b).[23b]

Our group has applied the chirality driven self-sorting process to the multichromophoric system and has shown its potential on arranging bischromophoric naphthalene diimide acceptor and dialkoxy naphthalene donor system (Figure 1.9).[24] We have shown that the same chirality of donor and acceptor component arranges itself as alternating charge-transfer supramolecular polymer, and the opposite chirality arranges them as orthogonal donor-acceptor stacks.

Without having enough knowledge of interaction energies between two monomers designing a self-sorting system based on structural mismatch and chirality is challenging, thus limiting the potential of self-sorted systems with diverse functionalities. A robust approach would be a chemically programmed assembly of monomers, where precise kinetic control over fiber will lead to a self-sorted network even with structurally similar monomers. Much more

complex structures can be built by such predictable "molecular triggered" self-sorted homopolymers. Examples of such a programmed self-sorted system are rare, and one important point to note that such a system with less structural mismatch requires a highly non-dynamic system that prevents homogenization of the self-sorted homopolymers. In such a category, Adams and coworkers have reported pH-controlled self-sorting of monomers in water (Figure 1.10).[25] The molecular design consists of peptide-based hydrogelators having different hydrophobicity, which implements a different pK_a for the two molecules. For a slow change in pH, which would help in achieving kinetic control over self-assembly of two monomers, they have exploited hydrolysis of glucono-d-lactone (GdL) to gluconic acid (Figures 1.10a and 1.10b). Coupling of slow pH change with known pK_a of the two gelators allows the predictable formation of self-assembly and formation of self-sorted supramolecular polymers. As the pH decreases slowly, a monomer having a higher pK_a starts assembling first and buffers the system before it reaches the pK_a of the second monomer, which leads to self-sorted fibers. Such pH-based systems offer several advantages. The apparent pk_a of the molecules correlates well with the overall hydrophobicity of the molecules, which could be designed as required by tuning the molecular structure. Hence this could be expanded to more complex and optically and electronically active molecules. Indeed, they have further extended this approach to peptide-based multichromophoric systems (Figure 1.10c).[26] As a molecular design, they have synthesized a peptide-based multichromophoric hydrogelator system having different donor and acceptor units. On extending similar concepts (kinetically controlled slow pH change) to such donor-acceptor systems, the authors have controlled the extent of energy transfer using programmed self-sorting. Whereas a rapid quenching using HCl leads to a random coassembly and facilitates the energy transfer process. Hence by choice of the trigger, the multicomponent self-assembly can be designed. Also, the authors have cleverly applied the strategy to synthesize self-sorted homopolymers p- and n-type of chromophores like reported by Shinkai and Meijer group,[26a] which are having good photoconductivity.
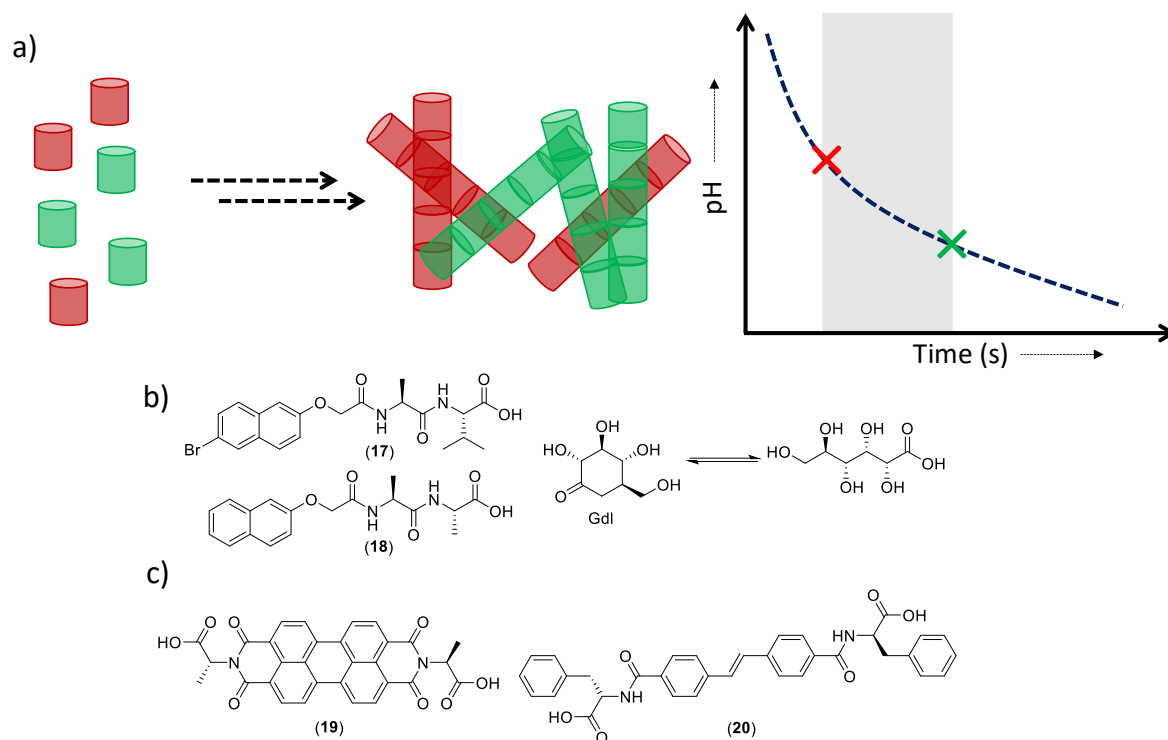
Figure 1.10. a) Schematic illustration of the programmed self-sorting between pH-responsive gelators having different pK_a. Red component having a higher pK_a will assembled first followed by self-assembly of the second component which will lead to a self-sorted homopolymers. b) Molecular Structures of the pH-responsive gelators molecules used by Adams and coworkers for synthesis of self-sorted homopolymers. Reaction scheme of hydrolysis of gluconolactone (gdl) in bsic pH into gluconic acid which will lead to a slow change in pH and thus leading to a sequential assembly of the two gelators. c) Molecular structure of the pH-responsive electronically active π-conjugated molecules used by Adams and coworkers for synthesis of supramolecular p-n junction.

One of the intriguing features of natural polymers is their ability to evolve and adapt to their environment. In a living system, biopolymers like DNA and RNA spontaneously form orthogonal supramolecular assembly, and their formation and collapse are entirely regulated using biological stimuli.[27] Hence the self-sorted supramolecular homopolymers should comprise features that respond to independently controlled external stimuli. Therefore, in the subsequent reports, Adams and Hamachi groups independently presented self-sorted homopolymers responsible to redox, enzyme, and light stimuli (Figure 1.10). To represent the concept, Adams and coworkers designed a photo-responsive stilbene-based monomer and have studied its orthogonal self-assembly with a peptide-based monomer using a slow pH change of gluconolactone as mentioned earlier (Figure 1.10).[28] After successfully synthesizing the self-sorted supramolecular homopolymer, they have demonstrated the photo-responsiveness of the stilbene moiety. Performed rheological data actively implemented a decrease in gel strength and selective removal of one of the homopolymers on light irradiation. This concept was further

utilized to achieve a spatial photopatterning using a photomask. Smith and coworkers also studied similar photo-responsive self-sorted homopolymer (Figure 1.11). Hamachi and coworkers have demonstrated stimuli-responsiveness in self-sorted supramolecular polymers comprising of a lipid- and a peptide-based molecule (Figure 1.12).[29] They have rendered the two monomer redox- and enzyme-responsive by tagging a nitro benzyl group to the peptide monomer and a phosphate group to the lipid-based monomer, respectively. After ensuring the self-sorted and orthogonal assembly of the two monomers, the authors have tested the orthogonal stimuli-responsive disruption of the assembled homopolymers. By combining spectroscopic and microscopic techniques, they could prove the orthogonal nature of the two stimuli as well as selective removal of one of the self-sorted homopolymers. The design of such multicomponent intelligent materials would open the path for regenerative medicine, adaptive and responsive smart materials. However, such examples are limited in the literature.
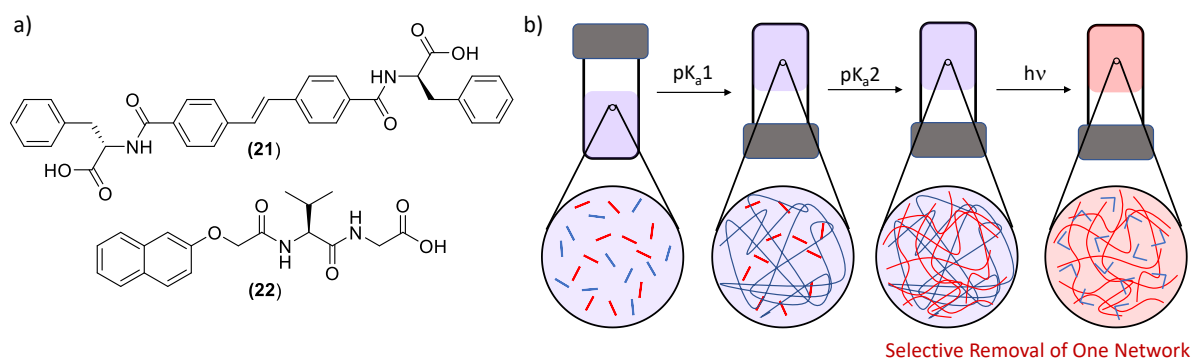
Figure 1.11. a) Molecular structure of the pH-responsive and photo-responsive monomer **21** and pH-responsive monomer **22** used by Adams and coworkers for synthesis of stimuli-responsive orthogonal self-assembled network. b) Schematic illustration of the sequential assembly of molecule **21** and **22** leading to a self-sorted network which on irradiation with light triggers selective disassembly of one of the homopolymer.
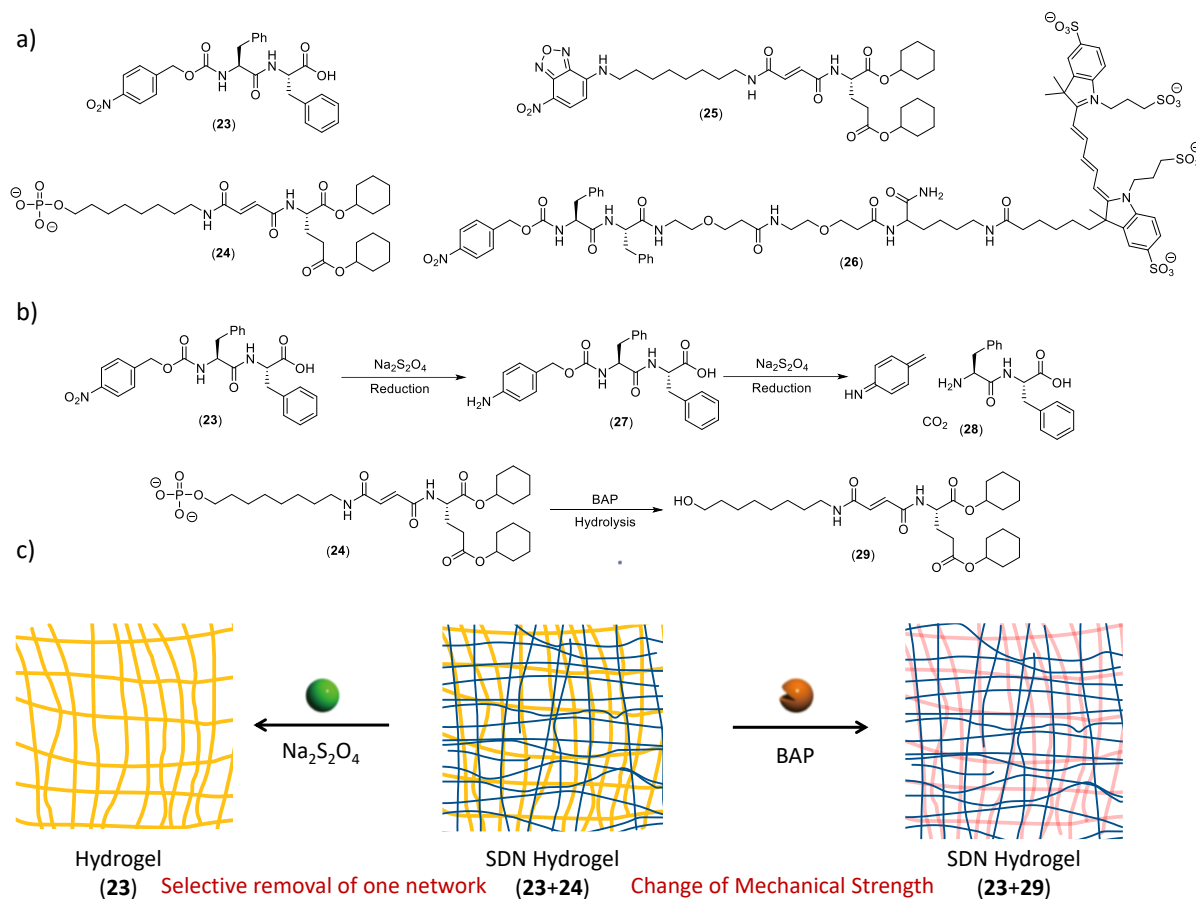
Figure 1.12. a) Molecular structure of the redox-responsive monomer (**23**) and enzyme-responsive monomer (**24**) and fluorescent probes (**25**, **26**) used by Hamachi and coworkers for synthesis of stimuli-responsive self-sorted homopolymers and for visualization of the self-sorted homopolymers. b) Chemical reaction between molecule **23** and $Na_2S_2O_4$ leads to reduction of the nitro group which results in degradation of self-assembling monomers. Chemical reaction between **24** and enzyme BAP leads to cleavage of phosphate group, which results in increased mechanical strength of the self-assembled gel of monomer **29**. c) Schematic illustration of the orthogonal stimuli-responsiveness of the self-sorted homopolymers.

1.3.3. Alternating Supramolecular Copolymers:

A significantly stronger hetero-interaction energy than the homo-interaction between two monomers will arrange them in an alternative manner. One vital point to notice is that although advanced covalent polymerization techniques can readily synthesize complex block copolymers, synthesis of an alternating copolymer is still a challenge in the covalent polymerization field, and there are only a handful of examples known today.

Coming back to multicomponent self-assembly to enhance the affinity between two different monomers, we can use either electronically complementary monomers or charge complementary monomers. Our group and Xi Zhang group have demonstrated the former approach in charge-transfer interaction promoted supramolecular copolymerization
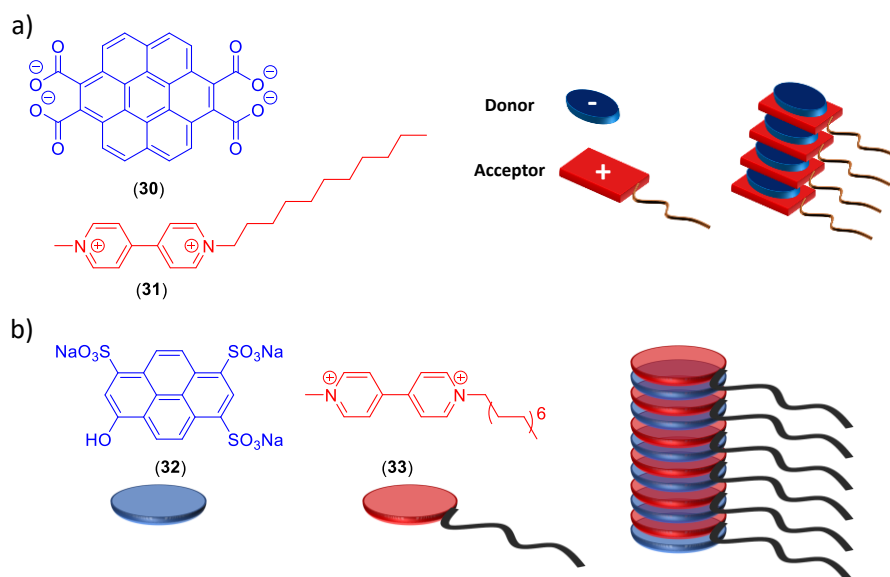
Figure 1.13. Molecular structures of the donor (**30** and **32**) and acceptor chromophores (**31** and **33**) used by a) George and Coworkers and b) Zhang and coworkers for the synthesis of alternating CT copolymers. Corresponding schematic representation demonstrating an alternating arrangement of the donor and acceptor chromophores.

between electron-deficient and electron-rich monomers (Figure 1.13).[30] Since CT interaction alone is not strong enough to synthesize an extended supramolecular polymer due to the lack of directional interactions, often additional non-bonding interactions like hydrogen bonding, amphiphilic designs, or host-guest interaction inside a cyclic guest molecule are utilized to synthesize extended supramolecular polymers.

More recently, Besenius and coworkers have come up with an excellent design strategy based on charge complementary interaction between positive and negatively charged dendritic peptide amphiphiles (Figure 1.14).[31] Monomers based on β-sheet forming oligopeptides forms an alternating supramolecular copolymer via electrostatic interaction. Apart from the two fundamental design strategies, other examples of alternating supramolecular copolymers are coassembly between cyclohexane tricarboxamide functionalized linear and bulky chain monomers. The bulky monomer, due to interchain repulsion, is unable to form stable homopolymers. However, upon coassembly with less bulky monomer organizes the stacks in an alternating fashion, which was confirmed using NMR spectroscopy.
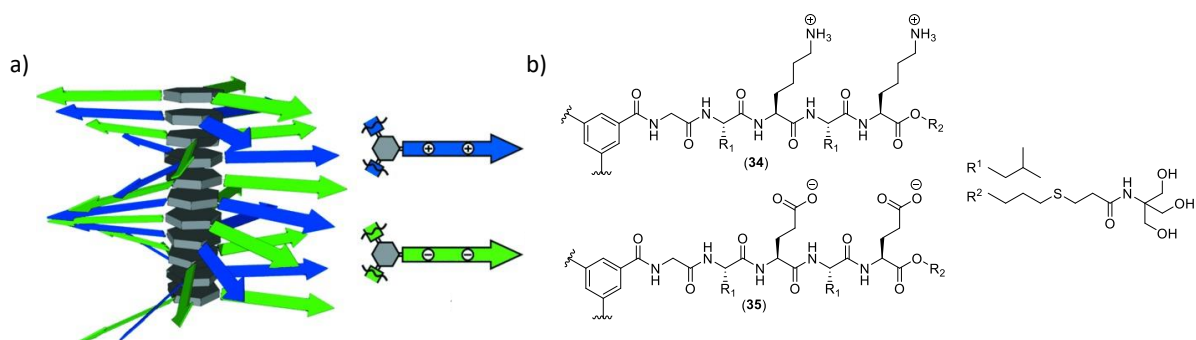
Figure 1.14. a) Schematic representation of the alternating copolymer formed between charge complementary peptide dendron monomers. Adapted by permission from John Wiley and Sons: Angewandte Chemie International Edition, Copyright 2013 (Ref 31). b) Molecular structure of the positively and negatively charged monomers use by Besenius and coworkers for synthesis of alternating copolymer.

CT alternating copolymers due to the complimentary electronic nature can act as conducting nanowires. Hence, our group has investigated nanofibers based on an alternating copolymer of donor-acceptor chromophores in the prospect of conducting nanowires.[32] Field-effect transistors fabricated using CT nanofibers as channel elements functioned as a good conductor. Alternating copolymers reported by Besenius and coworkers will be excellent materials to investigate the energy transport properties between the optically active donor and acceptor chromophores.

However, the synthesis of monodisperse alternating supramolecular polymers is substantially challenging. Unlike single component systems, the multicomponent system requires concurrent control over the growth process of both monomers. Recently our group has demonstrated the controlled synthesis of CT copolymers using either redox properties of supramolecular CT complexes or via reaction mediated generation of CT amphiphiles to acquire control over the nucleation and elongation process.[34] Next, one of the addressable challenges would be the controlled synthesis of supramolecular copolymers based on complementary electronic interaction.

1.3.4. Supramolecular Block copolymers:

By definition, if a supramolecular copolymer contains large homopolymeric domains of different monomers, it will be termed as a supramolecular block copolymers. However, compared to the multitude of methods available for the synthesis of covalent polymers,
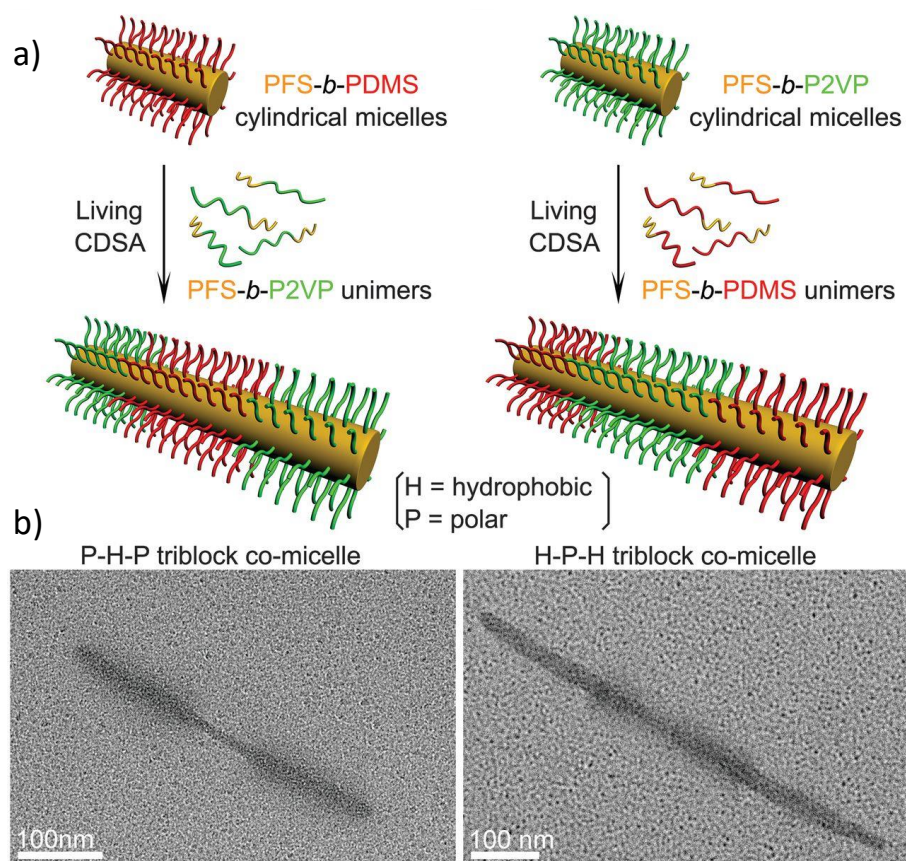
Figure 1.15. a) Schematic representation of synthesis of triblock copolymers via crystallization driven self-assembly of polyferrocenyl-X (X = PDMS, P2VP block copolymers). b) TEM image of synthesized block copolymers. Adapted by permission from The American Association for Advancement of Science: Science, Copyright 2015 (Ref 35e).

supramolecular block copolymer synthesis is rather challenging. Some of the causes to be mentioned are high kinetic lability of non-covalent bonds, inter- and intra-chain monomer exchange dynamics, which tends to homogenize the monomer composition based on their interaction energies (*vide infra*). Along with that, a lack of characterization techniques makes supramolecular copolymer microstructure determination even more challenging. One of the earlier breakthroughs in synthesizing supramolecular block copolymer came from the group of Manners and coworkers (Figure 1.15).[35] They have exploited polymeric self-assembly of covalent block copolymers. Their molecular design consists of one of the block segments as a crystallizable polymer, which rapidly forms rod-like micelles for a broad range of block ratios compared to the narrow cylindrical micelle building range of normal diblock copolymers. In a pioneering work, they have demonstrated an active living growth from the micelles chain ends

a)

b)
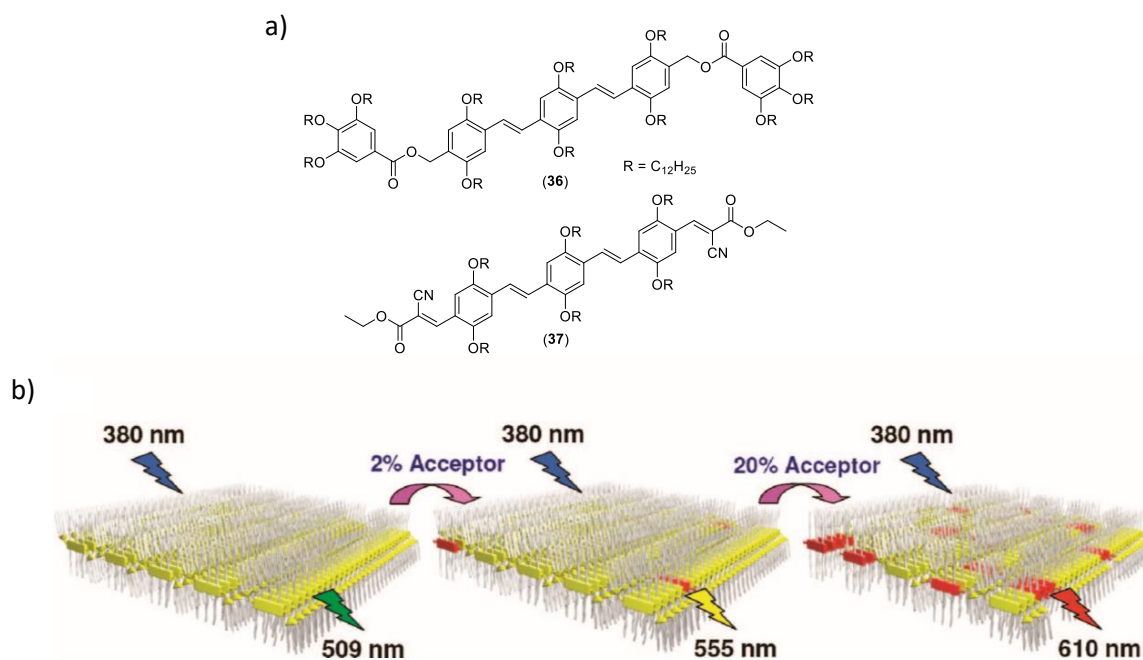
Figure 1.16. a) Chemical structure of the oligophenylene vinylene donor and acceptor used by Ajayaghosh and coworkers for synthesis of light harvesting assemblies. b) Schematic illustration of segregation of acceptor on increasing percentage of acceptor on the donor-acceptor co-assembly. Adapted by permission from The American Chemical Society: Journal of American Chemical Society, Copyright 2006 (Ref 36).

via crystallization driven self-assembly of polyferrocenyl isopryne block copolymer (unimer). In a step further, they have utilized the active chain ends of the micelles to add other PFS based diblock copolymer to synthesize triblock co micelles. Absence of unimer dissociation and micelles fusion over a month indicated the high kinetic stability of the resultant structures and thus facilitating the synthesis of higher complex sequences. These include non-centrosymmetric A-B-C triblock copolymer, unsymmetrical A-B diblock copolymer, penta block micelles, branched micelles copolymers and 2D block copolymers.

In comparison to the self-assembly of such large macromolecular monomers, where dynamics and kinetic lability is a less dominant factor, thermodynamic and kinetic stability over copolymers of small molecules is a grand challenge to be addressed. Some early molecular systems in this regard could be supramolecular copolymer reported by Ajayaghosh and coworkers.[36] During their investigations on energy transfer between two different oligophenylene derivatives, they have observed an increase in acceptor percentage possible phase segregation takes place within the fiber which leads to aggregate to aggregate energy transfer. According to the concept proposed by Meijer and coworkers, the balanced homo- against hetero-interaction energies (reactivity ratio) must have organized the coassembly in a

blocky fashion. However, they have not characterized the possible microstructures of the supramolecular polymer in detail (Figure 1.16).

One of the significant breakthroughs in this direction is the coassembly between electron-rich and electron-deficient hexabenzo coronene derivatives reported by Aida and coworkers.[37] In a typical copolymerization protocol, HBC_1 was allowed to self-assemble as nanotubes, and the terminal bipyridine groups were coordinated with Cu^{2+} ions, which provided enhanced thermal stability of HBC_1 nanotubes. Hence on cooling a high temperature solution of monomeric HBC_2 and self-assembled HBC_1, resulted in coassembly and formation of a linear heterojunction due to mutual electronic interaction (Figure 1.17). The authors have characterized the block copolymer using scanning electron microscopy (SEM) images, which showed the presence of bright and dark segments and elemental mapping, which depicted dispersed copper signature over bright segments and dispersed carbon signature over all of the nanotubes.
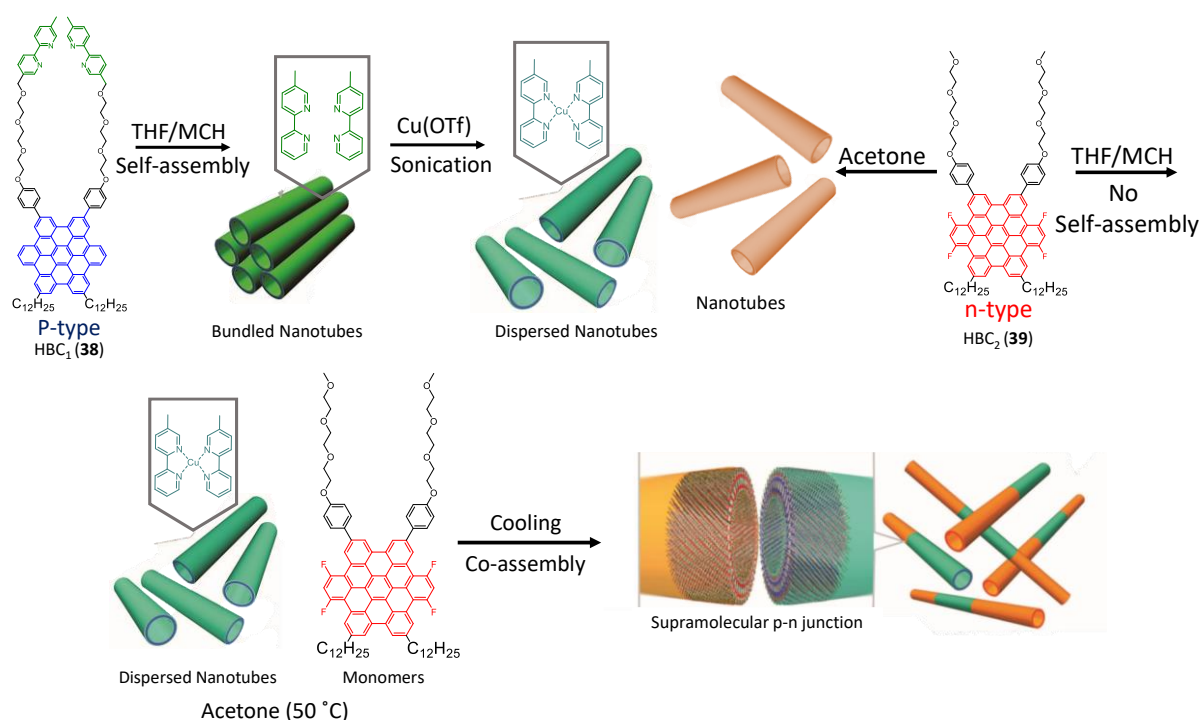
Figure 1.17. a) Molecular structure and schematic representation of synthesis of supramolecular axial p-n junction by Aida and coworkers between HBC_1 and HBC_2. Adapted by permission from The American Association for Advancement of Science: Science, Copyright 2011 (Ref 37).

Although, the seminal work reported by Aida showed the path for the synthesis of seed-induced multicomponent polymerization for block structures, the establishment of copolymerization techniques with different monomers in the same solvent remains a challenge for the synthesis of sophisticated and controlled block structures. One of the learning lessons

could be obtained from covalent copolymerization, where synthetic polymer chemists accurately controlled the copolymer microstructure by tuning the reactivity ratios of the monomers in combination with advanced polymerization methods.[38] Meijer and coworkers produced a supramolecular multiblock copolymer via cooling a monomeric solution of tripyridylamine tricarboxamide and triphenylamine tricarboxamide.[39] Detailed investigations revealed heterogeneous nucleation under thermodynamic control as the initiator for the copolymerization, and the block composition is closely related to the homo- against hetero-free energy of interactions (reactivity ratio), which organizes the chromophores in a blocky fashion (Figure 1.18). They have utilized combined spectroscopic, super-resolution microscopic techniques, and theoretical models to identify the multiblock structures. One crucial point to notice is that the strategy reported by Meijer and coworkers produced thermodynamically stable supramolecular block copolymers in comparison to the postulated kinetically stable supramolecular block copolymers. The proposed approach by Meijer and coworkers are analogous to the classical chain-growth block copolymer reported utilizing the difference in reactivity ratio between two monomers.
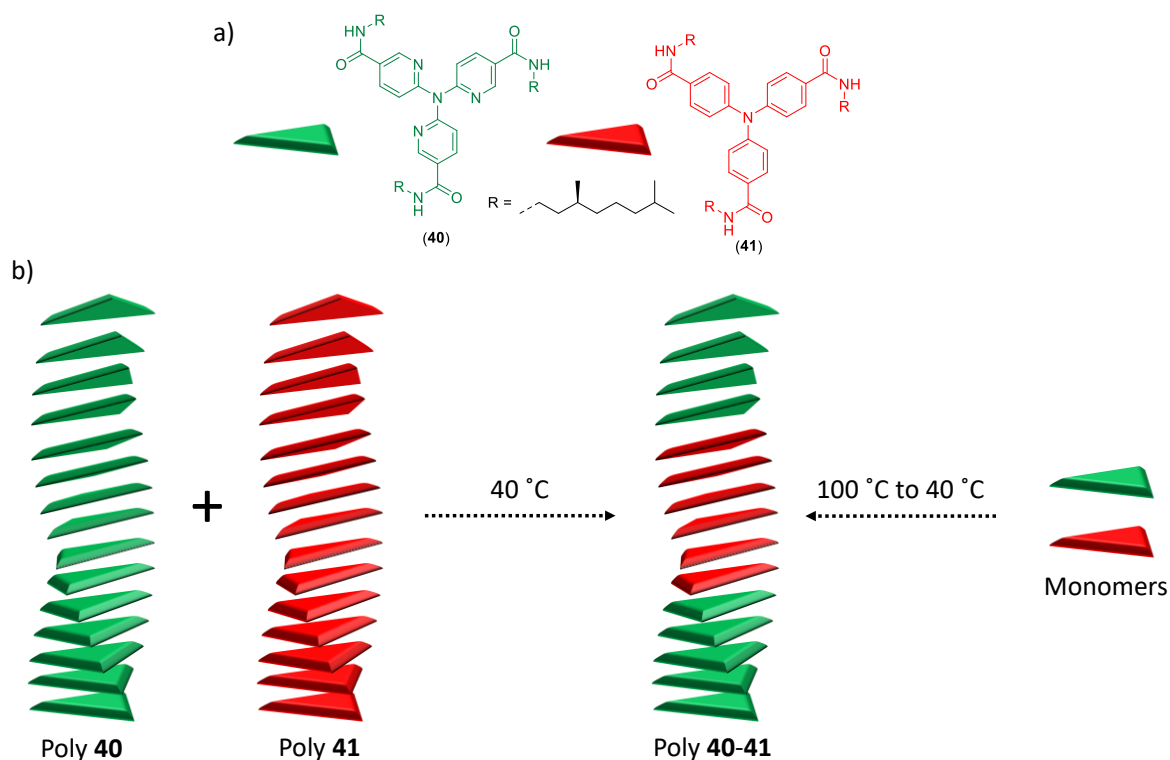
Figure 1.18. a) Molecular Structure of **40** and **41** used by Meijer and coworkers for synthesis of supramolecular block copolymer under thermodynamic control. b) Mixing of poly **40** and **41** or monomer **40** and **41** leads to synthesis of supramolecular block copolymer due to favorable reactivity ratio.

However, supramolecular polymerization under thermodynamic control leads to an uncontrolled nucleation step, thus generating polydisperse supramolecular polymers.[11a] The most sought-after choice to produce supramolecular BCPs with controlled block size and small dispersity would be seed- or initiator-induced living supramolecular polymerization. As mentioned in the introduction, the discovery of living covalent polymerization techniques led to groundbreaking developments of covalent polymer science and enabled the synthesis of a plethora of bock copolymers. Hence considerable efforts have been given to understand the mechanistic aspects of supramolecular polymerization. Subsequently, findings like pathway complexity in supramolecular polymerization,[40] and consequent kinetically controlled supramolecular polymerization provided access to novel out of equilibrium supramolecular polymerization and living supramolecular polymerization techniques. These designed living polymerization techniques helped in the synthesis of supramolecular polymers of controlled shape and size.[41] The next challenge would be to pursue living supramolecular polymerization between two optically and electronically different monomers leading to block supramolecular polymers endowing sophisticated structural and functional properties. However, the rational design of the monomeric building block for the synthesis of block copolymers via living supramolecular polymerization is highly challenging. Detailed investigations by Takeuchi and Sugiyashu group have implied the presence of metastable state delicately depends on molecular structures.[42] Again Sugiyashu group and later Würthner group have pointed out the importance of structural similarity of the two monomers in the synthesis of block supramolecular copolymer using living polymerization techniques.[43] A slight change of alkyl chain length or change in the stacking mode of chromophores could strongly interfere with the seeding process. Hence, after the pioneering work by Sugiyashu and coworkers on developing living supramolecular polymerization techniques using the pathway complexity of zinc porphyrin monomers,[41] they have attempted to synthesize supramolecular block copolymer between zinc and copper porphyrin monomers using living polymerization techniques. However, this attempt was not a great success, due to distortion and a change in the packing of the copper coordinated monomer. This reflects the importance of the reactivity ratio between the two monomers. Lower hetero-interaction energies between the two monomers is an important parameter that determines the efficiency of the seeding process between two different monomers. To address the issue, and to increase the affinity between two monomers, they have designed zinc and copper porphyrin monomers with four hydrogen bonding sites.[44] Nevertheless, unlike their previous system, the current system does not have a metastable state, which ruled out the possibility of living supramolecular polymerization under kinetic control.

Hence the authors have performed a living supramolecular polymerization between the two monomers based on a solvent mixing protocol, which is analogous to the crystallization driven self-assembly approach (Figure 1.19). The authors have demonstrated seed-induced supramolecular block copolymerization by using assembled copper porphyrin as seeds, and the monomers of zinc porphyrin in toluene were mixed to initiate seeded growth.
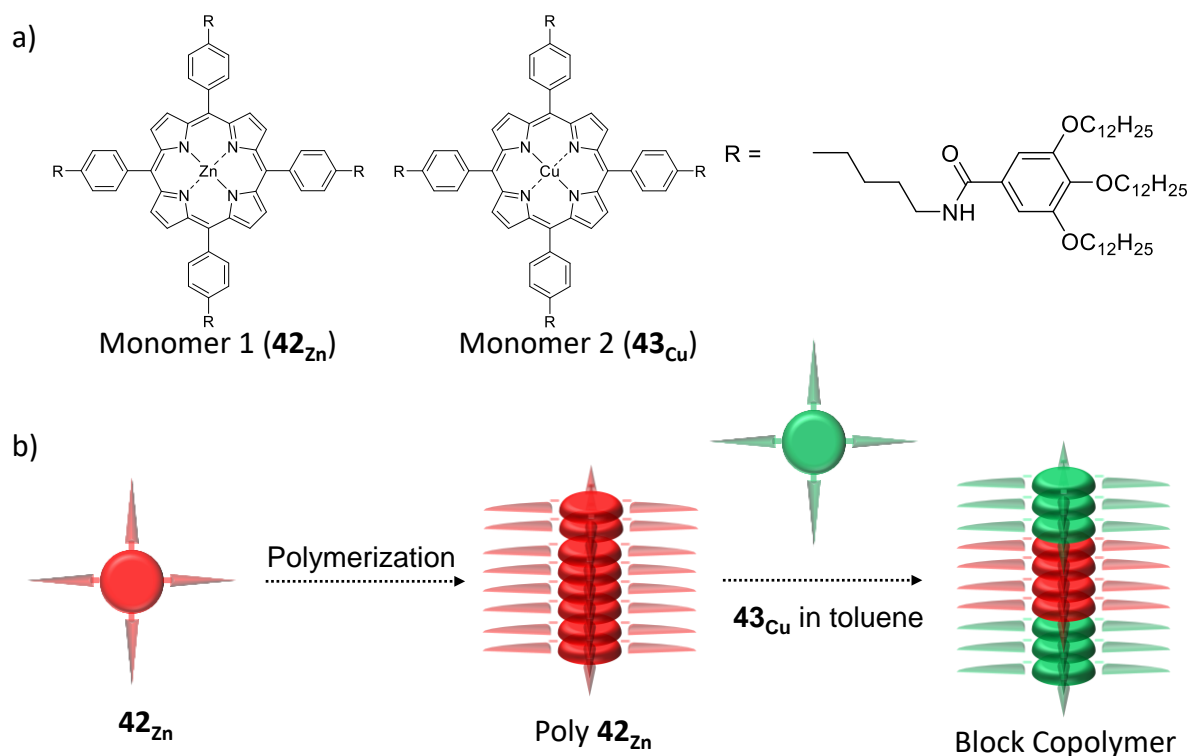
Figure 1.19. a) Molecular structures of **42$_{zn}$** and **43$_{Cu}$** used by Sugiyashu and coworkers for the synthesis of supramolecular block copolymers. b) Schematic illustration of synthesis of supramolecular block copolymers between porphyrin monomers using solvent mixing protocol.

The controlled degree of polymerization obtained (PDI = 1.2) provided evidence for the two component seeded supramolecular polymerization. Unlike previous examples, here, the faster kinetics of seeded growth than independent nucleation step facilitates the block copolymers formation. Although the authors were unable to visualize the segmented block structures, indirect proof of block structure derived from increased kinetic stability of the inner zinc porphyrin segments towards depolymerizing agents, an effect which could be attributed to compartmentalization effect in the blocky structure.

However, the establishment of multicomponent systems to carry out seeded supramolecular polymerization analogous to the conventional multicomponent living chain-growth polymerization remained a challenge for the synthesis of sophisticated multiblock structures with tailored functionality. A significant contribution to this challenge came from

Würthner and coworkers.[45] Earlier they have extensively investigated pathway complexity and living supramolecular polymerization of amide appended perylene bisimide derivatives. Their findings revealed an intramolecular hydrogen bonding based stabilization of monomeric species to introduce kinetic control over molecular self-assembly pathways
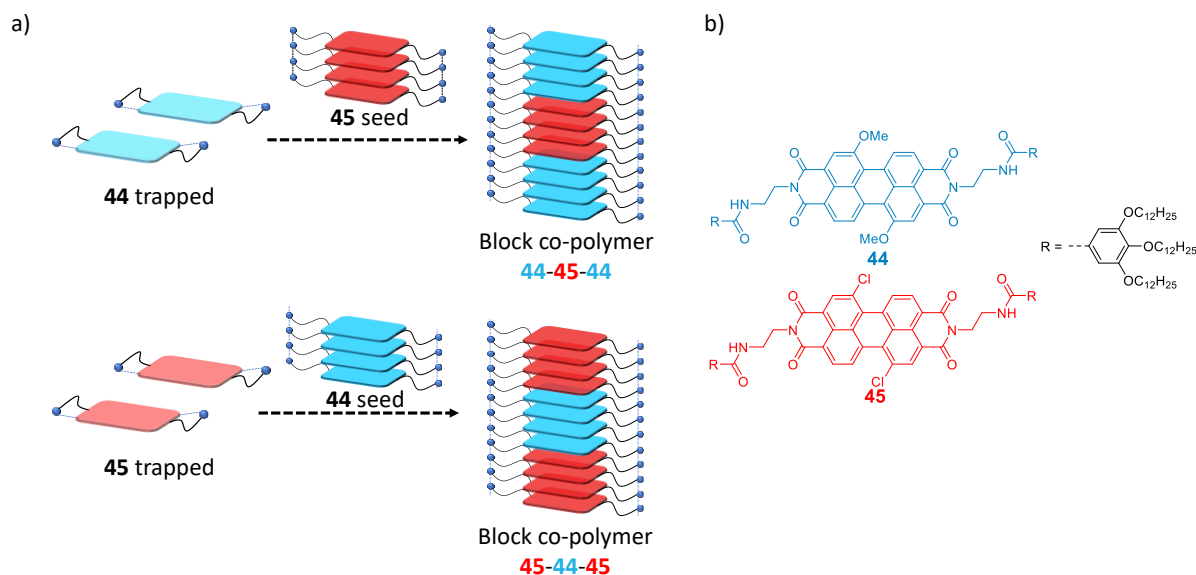
Figure 1.20. a) Schematic representation and b) molecular structure for the synthesis of supramolecular block copolymers between core-substituted perylene bisimide monomers using seeded supramolecular polymerization.

and controlled aggregate growth. Later, they have extended this design strategy to core-substituted perylene bisimide derivatives having different optical properties depending on core-substitution (Figure 1.20). Hence the authors have explored the possibility of synthesizing block supramolecular copolymers using living supramolecular polymerization between perylene diimide derivatives having various bay substitutions. The authors have demonstrated copolymerization and seeded assembly between two different kinetically trapped PBI derivatives, which leads to the formation of supramolecular block copolymers by chain-growth process from the introduced seed termini as confirmed by UV-Vis spectroscopy. The synthesized block copolymer segments were distinguishable in AFM, which depicted two specific block segments with a helical pitch of 10 and 5 nm. The method demonstrated by Würthner and coworkers is similar the conventional covalent block copolymer synthesis using sophisticated living polymerization methods. In this respect, the study carried out by Würthner and coworkers clearly illustrates the limitation of the current strategy for the integration of supramolecular block copolymers. Only molecules having almost identical intermolecular interaction sites and high/moderate hetero-interactions energies can be combined to synthesize supramolecular block copolymers

1.4. Conclusion:

In this Chapter, we have highlighted the synthetic strategies developed very recently, towards controlled multicomponent supramolecular polymerization. Despite having significant developments over the last decade, the extension of molecular self-assembly towards multicomponent supramolecular polymerization still remains as an open challenge. Particularly, a rationalized approach based on monomer-monomer interaction to develop controlled multicomponent self-assembly is required. The newly emerged challenge in this field is the synthesis of the supramolecular block copolymer, which has been recently attempted in a limited number of examples. Required structural similarity between chosen monomers for the synthesis of the supramolecular copolymer is the severe limitation, compared to the wide variety of monomers available for conventional living polymerization. One of the solutions could be to look for chromophores having small structural differences and a wide range of spectral and electronic properties. The distinct optical properties of these chromophores would be advantageous for spectroscopic and microscopic probing of the coassembly process. Core-substituted naphthalene dimides (cNDI) constitute an important class of molecules where we can tune the HOMO-LUMO energy gap by varying the core substitution to cover the entire visible spectral range.[46] Hence it will be instrumental in characterizing the multicomponent structures. In this Thesis, we have attempted to develop various synthesis strategies utilizing cNDI as a chromophore for controlled multicomponent supramolecular polymerization. We have further depicted that optical properties of the cNDI can be used to both characterize the multicomponent self-assembly as well to gain new emergent optical properties by the synthesis of controlled multicomponent self-assembly.

1.5. References:

[1] Berg, J. M.; Tymoczko, J. L.; Stryer, L. *Biochemistry*; *sixth edn.*; W. H. Freeman: New York, **2006**.

[2] Anfinsen, C. B. *Science* **1973**, *181*, 223.

[3] Lutz, J. F.; Lehn, J. M.; Meijer, E. W.; Matyjaszewski, K. *Nat. Rev. Mater.* **2016**, *1*, 16024-16038.

[4] a) Szwarc, M. *Nature* **1956**, *178*, 1168-1169. a) Matyjaszewski, K.; Xia, J. *Chem. Rev.* **2001**, *101*, 2921-2990.

[5] a) Merrifield, R. B. *J. Am. Chem. Soc.* **1963**, *85*, 2149-2154. b) Lutz, J. F.; Ouchi, M.; Liu, D. R.; Sawamoto, M. *Science* **2013**, *341*, 628.

[6] a) Bates, F. S.; Hillmyer, M. A.; Lodge, T. P.; Bates, C. M.; Delaney, K. T.; Fredrickson, G. H. *Science* **2012**, *336*, 434-440. b) Schacher, F. H.; Rupar, P. A.; Manners, I. *Angew. Chem., Int. Ed.* **2012**, *51*, 7898-7921.

[7] a) Botiz, I.; Darling, S. B. *Materials today* **2010**, *13*, 42-51. b) Bates, F. S. *Science* **1991**, *251*, 898-905.

[8] Nunns, A.; Gwyther, J.; Manners, I. *Polymer* **2013**, *54*, 1269-1284.

[9] a) Mitchell, V. D.; Jones D. J. *Polym. Chem.,* **2018**, *9*, 795-814. b) Günes, S.; Neugebauer, H.; Sariciftci, N. S. *Chem. Rev.* **2007**, *107*, 1324-1338. c) Thompson, B. C.; Fréchet, J. M. *Angew Chem., Int. Ed.* **2008**, *47*, 58-77.

[10] a) Aida, T.; Meijer, E. W.; Stupp, S. I. *Science* **2012**, *335*, 813-817. b) Jain, A.; George, S. J. *Mater. Today,* **2015**, *18*, 206-214. c) Teunissen, A. J. P.; van der Haas, R. J. C.; Vekemans, J. A. J. M.; Palmans, A. R. A.; Meijer, E. W. *Bull. Chem. Soc. Jpn.* **2016**, *89*, 308-314. d) Goor, O. J. G. M.; Hendrikse, S. I. S.; Dankers, P. Y. W.; Meijer, E. W. *Chem. Soc. Rev.* **2017**, *46*, 6621-6637.

[11] a) De Greef, T. F. A.; Smulders, M. M. J.; Wolffs, M.; Schenning, A. P. H. J.; Sijbesma, R. P.; Meijer, E. W. *Chem. Rev.* **2009**, *109*, 5687-5754. b) Yang, L.; Tan, X.; Wang, Z.; Zhang, X. *Chem. Rev.* **2015**, *115*, 7196-7239.

[12] a) van Rossum, S. A. P.; Solsona, M. T.; J. H. van Esch, J. H.; Eelkema, R.; Boekhoven, J. *Chem. Soc. Rev.* **2017**, *46*, 5519-5535. b) Sorrenti, A.; Iglesias, J. L.; Markvoort, A. J.; de Greef, T. F. A.; Hermans, T. M. *Chem. Soc. Rev.* **2017**, *46*, 5476-5490.

[13] a) de Greef, T. F. A.; Meijer, E. W. *Nature* **2008**, *453*, 171-173. b) Besenius, P. *Polymer Chemistry* **2017**, *55*, 34-78. c) Wehner, M.; Würthner, F. *Nat. Rev. Chem.* **2020**, *4*, 38-53.

[14] a) Albertazzi, L.; Zwaag, D. v. d.; Leenders, C. M. A.; Fitzner, R.; Hofstad, R. W. v. d.; Meijer, E. W. *Science* **2014**, *344*, 491-495. b) Lou1, X.; Lafleur1, R. P. M.; Leenders, C. M. A.; Schoenmakers, S. M. C.; Matsumoto, N. M.; Baker, M. B.; van Dongen, J. L. J.; Palmans, A. R.A.; Meijer, E. W. *Nat. Commun.* **2017**, *8*, 15420.

[15] Adelizzi, B.; Van Zee, N. J.; De Windt, L. N.; Palmans, A. R.; Meijer, E. W. *J. Am. Chem. Soc.* **2019**, *141*, 6110-6121.

[16] a) Safont-Sempere, M. M.; G. Fernández, Würthner, F. *Chem. Rev.* **2011**, *111*, 5784-5814. b) Buerklea, L. E.; Rowan, S. J. *Chem. Soc. Rev.* **2012**, *41*, 6089-6102.

[17] Herrikhuyzen, J. v.; Syamakumari, A.; Schenning, A. P. H. J.; Meijer, E. W. *J. Am. Chem. Soc.* **2004**, *126*, 10021-10027.

[18] a) Prasanthkumar, S.; Ghosh, S.; Nair, V. C.; Saeki, A.; Seki, S.; Ajayaghosh, A. *Angew. Chem., Int. Ed.* **2015**, *54*, 946-950. b) Sandeep, A.; Praveen, V. K.; Kartha, K. K.;

Karunakaranab, V.; Ajayaghosh, A. *Chem. Sci.* **2016**, *7*, 4460. c) Sugiyasu, K.; Kawano, S.; Fujita, N.; Shinkai, S. *Chem. Mater.* **2008**, *20*, 2863-2865.

[19] a) Kubota, R.; Nakamura, K.; Torigoe, S.; Hamachi, I. *ChemistryOpen* **2020**, *9*, 67-79. b) Pujals, S.; Feiner- Gracia, N.; Delcanale, P.; Voets, I.; Albertazzi, L. *Nat. Rev. Chem.* **2019**, *3*, 68-84.

[20] Onogi, S.; Shigemitsu, H.; Yoshii, T.; Tanida, T.; Ikeda, M.; Kubota, R.; Hamachi, I. *Nat. Chem.* **2016**, *8*, 743-752.

[21] a) Garcìa, L. P.; Amabilino, D. B. *Chem. Soc. Rev.* **2007**, *36*, 941-967. b) Jędrzejewska, H.; Szumna, A. *Chem. Rev.* **2017**, *117*, 4863-4899. c) Yashima, E.; Ousaka, N.; Taura, D.; Shimomura, K.; Ikai, T.; Maeda, K. *Chem. Rev.* **2016**, *116*, 13752-13990.

[22] Pasteur, L. *Ann. Chim. Phys.* **1853**, *38*, 437.

[23] a) Ishida, Y.; Aida, T. *J. Am. Chem. Soc.* **2002**, *124*, 14017-14019. b) Sato, K.; Itoh, Y.; Aida, T. *Chem. Sci.,* **2014**, *5*, 136-140.

[24] a) Narayan, B.; Bejagam, K. K.; Balasubramanian, S.; George, S. J. *Angew. Chem., Int. Ed.* **2015**, *54*, 13245-13249. b) Sarkar, A.; Dhiman, S.; Chalishazar, A.; George, S. J. *Angew. Chem., Int. Ed.* **2017**, *56*, 13767-13771.

[25] Morris, K. L.; Chen, L.; Raeburn. J.; Sellick, O. R.; Cotanda, P.; Paul, A.; Griffiths, P. C.; King, S. M.; O'Reilly, R. K.; Serpell, L. C.; Adams, D. J. *Nat. Commun.* **2013**, *4*, 1-6.

[26] a) Cross, E. R.; Sproules, S.; Schweins, R.; Draper, E. R.; Adams, D. J. *J. Am. Chem. Soc.* **2018**, *140*, 8667-8670. b) Ardoña, H. A. M.; Draper, E. R.; Citossi, F.; Wallace, M.; Serpell, L. C.; Adams, D. J.; Tovar, J. D. *J. Am. Chem. Soc.* **2017**, *139*, 8685-8692.

[27] Vignaud, T.; Blanchoin, L.; Théry, M. *Trends Cell Biol.* **2012**, *22*, 671-682.

[28] a) Draper, E. R.; Eden, E. G. B.; McDonald T. O.; Adams, D. J. *Nat. Chem.* **2015**, *7*, 848-852. b) Draper, E. R.; Adams, D. J. *Chem. Commun.* **2016**, *52*, 8196.

[29] Shigemitsu, H.; Fujisaku, T.; Tanaka, W.; Kubota, R.; Minami, S.; Urayama, K.; Hamachi, I. *Nat. Nanotech.* **2018**, *13*, 165-172.

[30] a) Zhang, X.; Wang, C. *Chem. Soc. Rev.* **2011**, *40*, 94-101. b) Wang, C.; Guo, Y.; Wang, Y.; Xu, H.; Wang, R.; Zhang, X. *Angew. Chem., Int. Ed.* **2009**, *48*, 8962-896. c) Kumar, M.; Rao, K. V.; George, S. J. *Phys. Chem. Chem. Phys.* **2014**, *16*, 1300-1313. d) Rao, K. V.; Jayaramulu, K.; Maji, T. K.; George, S. J. *Angew. Chem., Int. Ed.* **2010**, *49*, 4218-4222.

[31] a) Frisch, H.; Unsleber, J. P.; Lgdeker, D.; Peterlechner, M.; Brunklaus, G.; Waller, M.; Besenius, P. *Angew. Chem., Int. Ed.* **2013**, *52*, 10097-10101. b) Frisch, H.; Fritz, E.; Stricker, F.; Schmüser, L.; Spitzer, D.; Weidner, T.; Ravoo, B. J.; Besenius, P. *Angew. Chem., Int. Ed.* **2016**, *55*, 7242-7246.

[32] Sagade, A. A.; Rao, K. V.; Mogera, U.; George, S. J.; Datta, A.; Kulkarni, G. U. *Adv. Mater.,* **2013**, *25*, 559.

[33] Sarkar, A.; Kölsch, J.; Berač, C. M.; Venugopal, A.; Sasmal, R.; Otter, R.; Besenius, P.; George, S. J. *ChemistryOpen* **2020**, *9*, 346-350.

[34] Jain, A.; Dhiman, S.; Dhayani, A.; Vemula, P. K.; George, S. J. *Nat. Commun.* **2019**, *10*, 450.

[35] a) Wang, X.; Guerin, G.; Wang, H.; Wang, Y.; Manners, I.; Winnik, M. *Science* **2007**, *317*, 644-648. b) Gilroy, J. B.; Gädt, T.; Whittell, G. R.; Chabanne, L.; Mitchels, J. M.; Richardson, R. M.; Winnik, M. A.; Manners, I. *Nat. Chem.* **2010**, *2*, 566-570. c) Finnegan, J. R.; Lunn, D. J.; Gould, O. E. C.; Hudson, Z. M.; Whittell, G. R.; Winnik, M. A.; Manners, I. *J. Am. Chem. Soc.* **2014**, *136*, 13835-13844. d) Qiu, H.; Gao, Y.; An Du, V.; Harniman, R.; Winnik, M. A.; Manners, I. *J. Am. Chem. Soc.* **2015**, *137*, 2375-2385. e) Qiu, H.; Hudson, Z. M.; Winnik, M. A.; Manners, I. *Science* **2015**, *347*, 1329-1332.

[36] Ajayaghosh, A.; Vijayakumar, C.; Praveen, V. K.; Babu, S. S.; Varghese, R. *J. Am. Chem. Soc.* **2006**, *128*, 7174-7175.

[37] Zhang, W.; Jin, W.; Fukushima, T; Saeki, A.; Seki, S.; Aida, T. *Science* **2011**, *334*, 340-343.

[38] a) Coates, G. W. *Chem. Rev.* **2000**, *100*, 1223-1252. b) Ouchi, M.; Nakano, M.; Nakanishi, T.; Sawamoto, M. *Angew. Chem., Int. Ed.* **2016**, *55*, 14584-14589.

[39] Adelizzi, B.; Aloi, A.; Markvoort, A. J.; Ten Eikelder, H. M.; Voets, I. K.; Palmans, A. R.; Meijer, E. W. *J. Am. Chem. Soc.* **2018**, *140*, 7168-7175.

[40] a) Korevaar, P. A.; de Greef, T. F. A.; Meijer, E. W. *Chem. Mater.* **2014**, *26*, 576-586. b) Korevaar, P. A.; George, S. J.; Markvoort, A. J.; Smulders, M. M.; Hilbers, P. A.; Schenning, A. P.; de Greef, T. F. A.; Meijer, E. W. *Nature* **2012**, *481*, 492-496.

[41] a) Fukui, T.; Kawai, S.; Fujinuma, S.; Matsushita, Y.; Yasuda, T.; Sakurai, T.; Seki, S.; Takeuchi, M.; Sugiyasu, K. *Nat. Chem.* **2017**, *9*, 493-499. b) Ogi, S.; Sugiyasu, K.; Manna, S.; Samitsu, S.; Takeuchi, M. *Nat. Chem.* **2014**, *6*, 188-195. c) Ogi, S.; Stepanenko, V.; Sugiyasu, K.; Takeuchi, M.; Würthner, F. *J. Am. Chem. Soc.* **2015**, *137*, 3300-3307. d) Ogi, S.; Stepanenko, V.; Thein, J.; Würthner, F. *J. Am. Chem. Soc.* **2016**, *138*, 670-678. e) Endo, M.; Fukui, T.; Jung, S. H.; Yagai, S.; Takeuchi, M.; Sugiyasu, K. *J. Am. Chem. Soc.* **2016**, *138*, 14347-14353.

[42] a) Ogi, S.; Fukui, T.; Jue, M. L.; Takeuchi, M.; Sugiyasu, K. *Angew. Chem., Int. Ed.* **2014**, *53*, 14363-14367. b) Fukui, T.; Takeuchi, M.; Sugiyasu, K. *Scientific Reports* **2017**, *7*, 2425.

[43] Wagner, W.; Wehner, M.; Stepanenko, V.; Würthner, F. *CCS Chem.* **2019**, *1*, 598-613.

[44] Jung, S. H.; Bochicchio, D.; Pavan, G. M.; Takeuchi, M.; Sugiyasu, K. *J. Am. Chem. Soc.* **2018**, *140*, 10570-10577.

[45] Wagner, W.; Wehner, M.; Stepanenko, V.; Würthner, F. *J. Am. Chem. Soc.* **2019**, *141*, 12044-12054.

[46] Sakai, N.; Mareda, J.; Vauthey, E.; Matile, S. *Chem. Commun.* **2010**, *46*, 4225-4237.

Chapter: 2

Cooperative Supramolecular Block Copolymerization for the Synthesis of Functional Axial Organic Heterostructures

Chapter: 2

Cooperative Supramolecular Block Copolymerization for the Synthesis of Functional Axial Organic Heterostructures

Abstract

Synthesis of a supramolecular block copolymers (BCPs) constitutes a significant challenge due to the exchange dynamics of non-covalently bound monomers and hence demand a fine microstructure control. Further, temporal stability of segmented microstructure is a prerequisite to explore the applications of functional supramolecular BCPs. Herein, we report a cooperative supramolecular block copolymerization of fluorescent monomers in solution under thermodynamic control, for the synthesis of unprecedented light harvesting axial organic heterostructures. Fluorescent nature of the core-substituted naphthalene diimide (cNDI) monomers enables a detailed spectroscopic probing during the supramolecular block copolymerization process to unravel a nucleation growth mechanism. Structured illumination microscopy (SIM) imaging of BCP chains characterizes the segmented microstructure for the individual block segments. Spatially- and spectrally-resolved fluorescence microscopy on single block copolymerized organic heterostructures shows efficient energy migration and light harvesting across the interfaces of linearly connected segments. Molecular dynamics and metadynamics simulations unveils useful mechanistic insights into the free energy of interaction between the monomers which have a crucial impact on determining the copolymer microstructure.
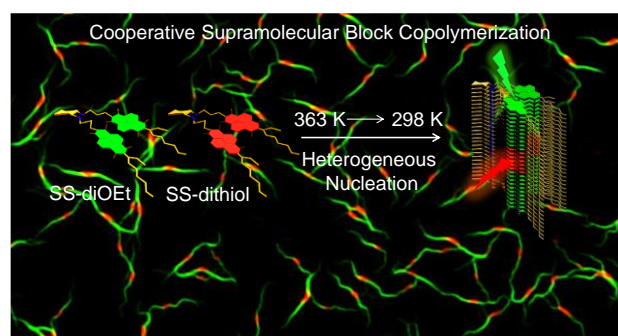
2.1. Introduction:

The field of supramolecular polymers has evolved as one of the most important research topic over the last two decades for the realization of ordered, nano-structured materials with adaptive and reversible functions.[1] Synthesis of supramolecular copolymers,[2] having multiple monomeric components, with microstructural control is considered as the ensuing level of complexity to be addressed for the design of next generation functional supramolecular materials such as organic heterostructures with nanoscale axial heterojunctions or nanostructures with reconfigurable monomer sequence for efficient functional output.[3] Although, several synthetic strategies are available to tailor the monomer sequence in covalent copolymers[4], the microstructure control in supramolecular copolymers has been mostly limited to alternate[5], statistical[2a,6] and periodic arrangements[7] of monomers due to the labile nature of its constituent monomers held by non-covalent interactions. On the other hand, supramolecular block copolymers (BCPs)[1b,2a,b] with segmented microstructure containing long sequences of individual monomers would be the most functionally appealing architecture and has been a holy grail for supramolecular chemists due to the monomer dynamics and difficulty in characterizing such structures.[2a]

In a pioneering work, Manners and coworkers have demonstrated supramolecular BCP structures from self-assembled cylindrical micelles of kinetically inert, poly(ferrocenyldimethylsilane) (PFS)-core containing block copolymers, using a crystallization-driven self-assembly (CDSA) approach.[8] This living crystallization methodology allowed the uniform epitaxial growth on kinetically stable seeds, by the sequential addition of soluble macromolecular monomers to construct a plethora of block copolymer architectures.[9] However, supramolecular copolymerization of unimolecular small monomers has been a grand challenge due to the fast exchange of monomers during non-covalent synthesis and are seldom reported. In an early attempt, Aida and coworkers have demonstrated the seeded growth of hexabenzocoronene (HBC) derived amphiphilic monomers on kinetically stable stacks of electronically complementary HBC monomers to accomplish supramolecular triblock nanostructures.[10] Similarly, Sugiyasu and coworkers have achieved supramolecular BCPs via seeded growth of porphyrin monomers using the solvent-mixing protocol,[11] in a procedure analogous to the CSDA for polymeric micelles.[8,9] To introduce an additional kinetic control for the synthesis of well-defined segmented microstructures, Würthner and coworkers have demonstrated a seed-induced living supramolecular polymerization (LSP)[2b,12,13] approach for the BCP synthesis of core-substituted

perylenediimide monomers.[14] Well-defined triblock supramolecular polymer architectures were made under kinetic control by introducing kinetically trapped states of one of the monomer to the seeds of another. In a similar kinetically controlled approach, we have recently reported supramolecular BCPs of fluorescent core-substituted naphthalene diimide (cNDI)[15] monomers via heterogeneous nucleation triggered seeded supramolecular polymerization.[16] Seeded LSP process under kinetic control, is analogous to the well-established living polymerization techniques[17] for the synthesis covalent BCPs[4] and hence has the potential for better structural control if the monomer exchange dynamics can be retarded.

Another synthetic approach to realize the covalent block copolymers is via chain-growth copolymerization by modulating the reactivity ratio of the constituting monomers,[2a,18] although dispersity control is compromised to a certain extent compared to the living polymerization strategies. An equivalent non-covalent synthetic method would be a cooperative or nucleation growth supramolecular copolymerization under thermodynamic conditions.[1a,19] However, thermodynamically controlled cooperative supramolecular copolymerization often resulted in statistical,[6] periodic or gradient[20] microstructures rather than the desired block organization of the monomers, due to the lack of fine tuning in the free energy of hetero- versus homo-monomeric interactions which determines the reactivity ratio.[2a] In a unique manifestation of supramolecular block copolymerization under thermodynamic control, recently Meijer and coworkers obtained supramolecular BCPs[21] by utilizing a balanced mismatch penalty and cooperativity difference between the two triarylamine based monomers and the segmented structure has been unambiguously characterized with spectroscopic and super-resolution microscopic techniques.[22] We envision that this synthetic strategy for supramolecular BCPs would result in stable segmented microstructures[2a] and hence are ideally suited for exploring various applications.

We envisage that supramolecular block copolymerization of organic chromophoric monomers with complementary optical or electronic properties would provide an attractive bottom-up strategy for the synthesis of organic axial heterostructures with designed interfaces and anisotropic energy or electron transport properties potentially useful in photovoltaics, energy conversion, and supramolecular electronics.[3,23] Although inorganic axial heterostructures with two dissimilar semiconducting components are well exploited,[24] the synthesis of analogous organic heterostructures with linear heterojunctions has been a substantial challenge. In a seminal work, Aida and coworkers have shown enhanced energy transport across the linear p-n heterojunctions of HBC derived supramolecular BCPs.[10a]

Although Manners and coworkers have elegantly shown an efficient exciton transport through semi-conducting cores[25] and color tunable fluorescent multi-block nanostructures,[26] in their segmented supramolecular block micelles, the transport properties through the linear heterojunctions are not yet investigated. This scenario encouraged us to explore the energy-transport properties along the axial heterostructures at the nanoscale, by the synthesis of supramolecular BCPs of π-conjugated monomers with dissimilar optical properties.

In this Chapter, we report for the first time the thermodynamically controlled, solution phase synthesis of supramolecular BCPs of fluorescent cNDI donor and acceptor monomers, with optical complementarity, to facilitate an energy transfer process along the resulting organic heterostructures. Detailed spectroscopic probing and extensive molecular dynamics simulations unveil a nucleation growth mechanism for this supramolecular block-copolymerization process, controlled by the free energy of monomer-monomer interactions (reactivity ratio) between the monomers. Structured illumination microscopy (SIM) imaging further provides an unambiguous characterization of the segmented microstructure of these supramolecular blocky copolymers with the narrow size distribution of the individual segments. We further demonstrate that the degree of polymerization and the block lengths in these supramolecular block structures can be altered by modulating the monomer exchange dynamics with different annealing temperatures. Finally, spatially- and spectrally-resolved fluorescence microscopy studies on single supramolecular BCP with donor-acceptor-donor segmented microstructure, reveal an unprecedented energy migration and light harvesting across the nanoscale axial heterojunctions.

2.2. Molecular Design:
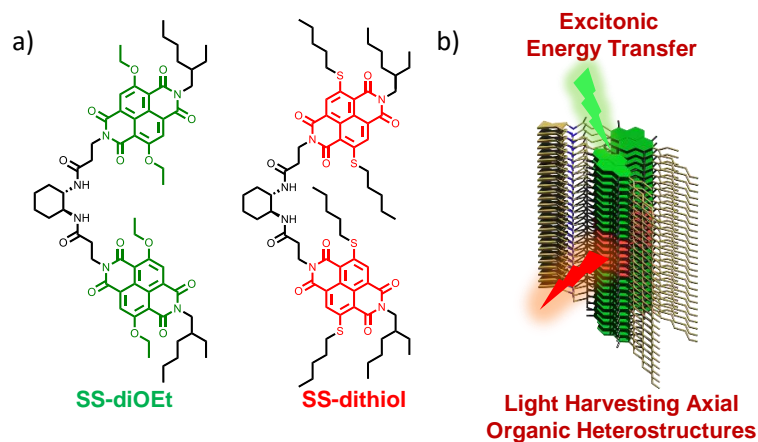
Figure 2.1. a) Molecular structures of **SS-diOEt** and **SS-dithiol** used in in the present study for fabricating the organic heterostructures. b) Schematic representation of light harvesting axial organic heterostructures (supramolecular block copolymers) obtained using the coassembly of **SS-diOEt** and **SS-dithiol** monomers.

Supramolecular block copolymerization in solution under thermodynamic control requires two structurally similar monomers with a cooperative, nucleation-elongation growth mechanism of homopolymerization.[19,21] In order to minimize the structural mismatch between the monomers, we have used cNDI derivatives as the monomers, since its HOMO-LUMO energy levels and the resultant optoelectronic properties can be modulated by the simple core-substitution with heteroatoms having varying donor strengths.[15] In the present study, we have used ethoxy (-OEt) and pentane thiol (-SC_5H_{11}) cNDI derivatives (Figure 2.1a), which would render green and red fluorescent monomers, respectively that helps to characterize the resultant supramolecular polymer via spectroscopic probing and fluorescence microscopic visualization. Further, we envisage that the Förster Resonance Energy Transfer (FRET) between green and red monomers can be used to impart functional characteristics to resulting BCPs as light harvesting axial organic heterostructures (Figure 2.1b).

Further to facilitate a hydrogen-bonded cooperative supramolecular polymerization, we have attached the cNDI π-conjugated derivatives to chiral *trans*-1,2-bis(amido)-cyclohexane motif and the resultant bischromophoric derivatives (**SS-dithiol** and **SS-diOEt**) are expected to grow by following a nucleation-elongation mechanism (Figure 2.1a).[27] In addition, the chiral diaminocyclohexane cores are known to induce chirality during the self-assembly process to aid the chiroptical probing of the supramolecular copolymerization process.

SS-dithiol and **SS-diOEt** monomer was synthesized following the synthetic Schemes 2.1 to 2.5 in supporting information. All the molecules have been characterized by ^{1}H NMR, mass spectrometry, and elemental CHNS analysis.

2.3. Results and Discussion:

2.3.1. Self-assembly Studies:

We have first investigated the mechanistic aspects of the supramolecular homopolymerization of **SS-diOEt** and **SS-dithiol** monomers. Both the monomers remains in its monomeric state in 1,1',2,2'-tetrachloroethane (TCE) solvent as evident from the sharp n-π* transition at 533 nm and π-π* transitions at 372 nm and 354 nm for **SS-dithiol** (Figure 2.2) and sharp n-π* transition at 472 nm along with π-π* transitions at 344 nm and 361 nm for **SS-diOEt** (Figure 2.5). Weak circular dichroism (CD) signal originating from the intrachromophoric interactions and unchanged ratio of the intensity of vibronic transition at 373 nm and 354 nm of π-π* absorption band with concentration,[27b] further supports the absence of intermolecular interactions in TCE for both monomers (Figures 2.2 and 2.5). Supramolecular homopolymerization of these monomers was performed in methylcyclohexane (MCH)/TCE solvent mixtures (TCE/MCH,
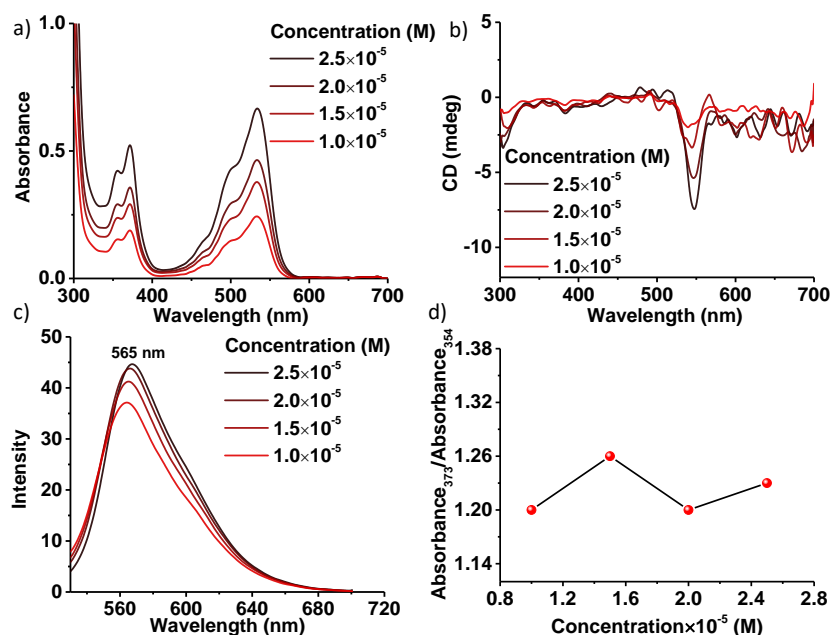
Figure 2.2 a) Concentration-dependent absorption spectra of **SS-dithiol** in TCE showing no shift in π-π* and n-π* bands and no change in intensity ratio between π-π* vibronic transitions. This points towards absence of any intermolecular interaction. Corresponding concentration-dependent b) CD spectra and c) emission spectra (λ_{ex} = 530 nm). d) Plot of ratio of intensity of vibronic transition at 373 nm and 354 nm of π-π* absorption band showing no reversal of intensity between vibronic transitions depicting absence of any intermolecular interaction and self-assembly in TCE. (l = 10 mm).
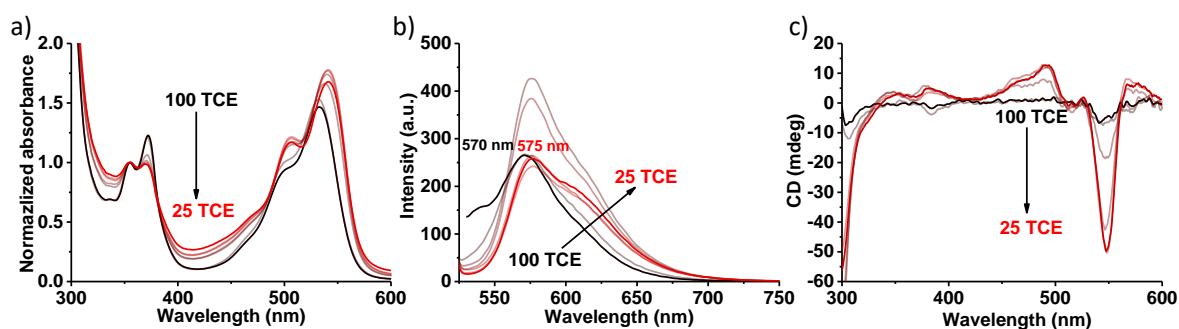
Figure 2.3. Solvent composition-dependent self-assembly studies of **SS-dithiol** in TCE/MCH solvent mixture. Composition-dependent a) normalized absorption spectra, b) emission spectra (λ_{ex} = 530 nm) and c) CD spectra of **SS-dithiol** shows appearance of CD signal upon increasing the percentage of MCH into TCE. Respective changes points towards self-assembly of the molecule into TCE, MCH solvent mixture. The changes get saturated at 25/75 (v/v) solvent mixture. ([**SS-dithiol**] = 2.5×10⁻⁵ M, l = 10 mm).

40/60 (v/v) to TCE/MCH, 25/75 (v/v)) and was probed by various spectroscopic changes that are very sensitive to interchromophoric interactions. Samples were prepared by annealing the solutions of respective monomers in appropriate solvent mixtures to 363 K followed by cooling to 298 K. Absorption spectra of **SS-dithiol** showed broadening and red shift of the n-π* transition to 540 nm along with the reversal of vibronic intensities of π-π* transition at 372
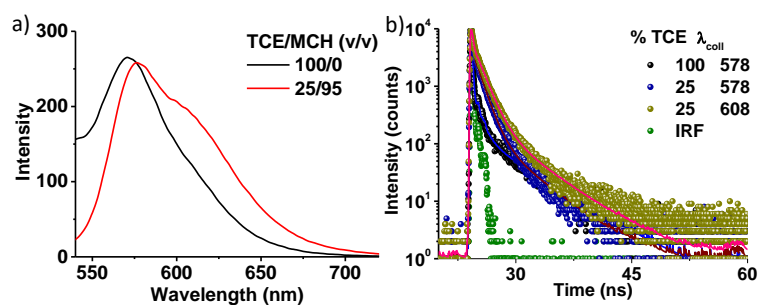
Figure 2.4. a) Emission spectra of **SS-dithiol** in monomeric and homopolymeric state depicting appearance of red shifted emission band on self-assembly. b) Lifetime decay profile of monomeric **SS-dithiol** in TCE (λ_{ex} = 532 nm) and its comparison with **SS-dithiol** homopolymers in TCE/MCH, 25/75 (v/v) solvent mixture (λ_{ex} = 532 nm) showing an increase in the sharp decay component and decrease in lifetime due to efficient excitonic migration in self-assembled nanostructures. ([**SS-dithiol**] = 2.5×10^{-5} M, TCE/MCH solvent mixture, l = 10 mm).

TCE/MCH (v/v)	λ_{coll} (nm)	t_1 (ns)	t_2 (ns)	t_3 (ns)
100/0	578	0.93 (8.75 %)	5.21 (12.81 %)	0.03 (78.44 %)
25/75	578	0.99 (54.21 %)	0.08 (36.05 %)	4.07 (9.73 %)
25/75	608	0.12 (24.31 %)	1.16 (63.21 %)	4.50 (12.48 %)

Table 2.1. Comparison of the lifetime data in tabulated format for homopolymeric and monomeric state of **SS-dithiol**.

nm and 354 nm with increasing percentages of MCH in TCE (TCE/MCH, 40/60 (v/v) to TCE/MCH, 25/75 (v/v)*, Figure 2.3). These changes account for the increased interchromophoric interactions due to hydrogen bonding promoted π-stacking of monomers. Similarly, **SS-diOEt** also exhibited a bathochromic shift of n-π* transition to 470 nm and reversal of vibronic intensities of π-π* transitions (Figure 2.5). Increased interchromophoric interactions on self-assembly further resulted in the appearance of a strong CD signal with maxima at 548 nm for **SS-dithiol** and 484 nm for **SS-diOEt** (Figures 2.3 and 2.5). Further investigation revealed the CD signal of **SS-diOEt** is contaminated with linear dichroism (LD).[21] Both **SS-dithiol** and **SS-diOEt** monomers showed a bathochromic shift in emission maxima upon self-assembly, indicating a J-type slipped organization of chromophores which is also supported by the time-resolved fluorescence decay experiments (Figures 2.3, 2.4 and 2.5).
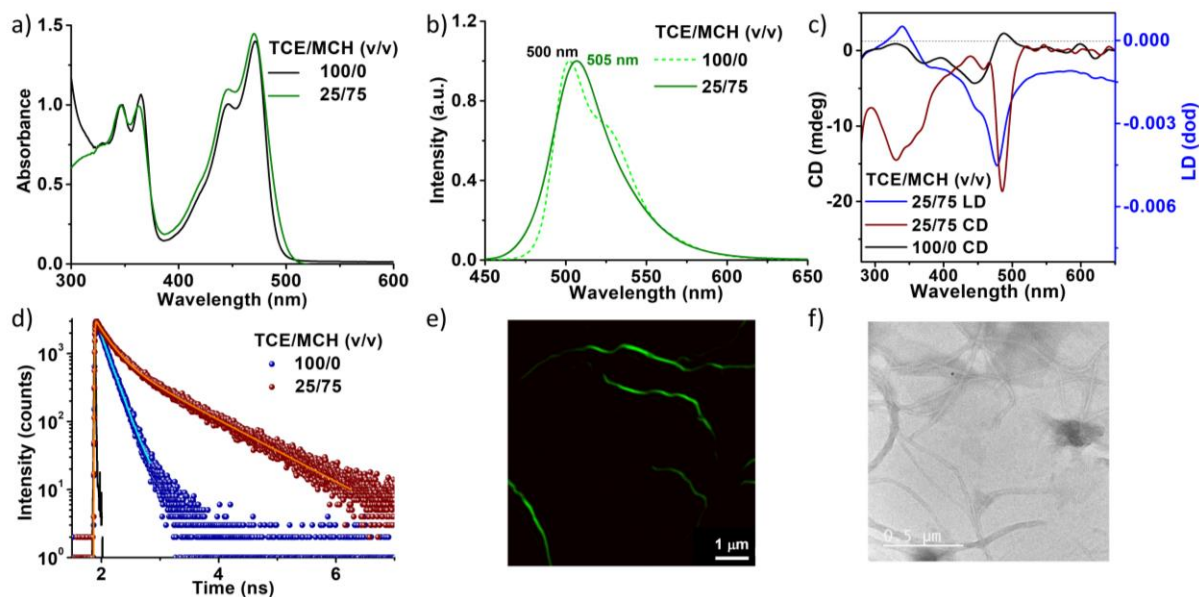
Figure 2.5. Supramolecular homopolymerization of **SS-diOEt**. a) Normalized absorption and b) normalized emission spectra (λ_{ex} = 430 nm) of **SS-diOEt** in TCE and in TCE/MCH, 25/75 (v/v) solvent mixture. c) Corresponding CD and LD spectra of **SS-diOEt** in TCE and in TCE/MCH, 25/75 (v/v) solvent mixture. CD spectra of **SS-diOEt** homopolymer is contaminated with linear dichroism (LD). d) Lifetime decay profile (λ_{ex} = 442 nm and λ_{coll} = 530 nm) of **SS-diOEt** in TCE and TCE/MCH, 25/75 (v/v). e) SIM microscopy image of **SS-diOEt** homopolymers in green channel (λ_{ex} = 488 nm, λ_{coll} = 495-575 nm) showing presence of green-emitting long 1D supramolecular polymers. f) TEM image of self-assembled **SS-diOEt** showing 1D supramolecular polymers. ([**SS-diOEt**] = 2.5×10^{-5} M, TCE/MCH, 25/75 (v/v) solvent mixture, l = 10 mm).

TCE/MCH (v/v)	λ_{coll} (nm)	t_1 (ns)	t_2 (ns)
100/0	530	1.78 (100 %)	
25/75	565	2.37 (36.98 %)	9.56 (63.02 %)

Table 2.2. Lifetime data of **SS-diOEt** in monomeric state in TCE and self-assembled state in TCE/MCH, 25/75 (v/v). ([**SS-diOEt**] = 2.5×10^{-5} M, λ_{ex} = 442 nm).
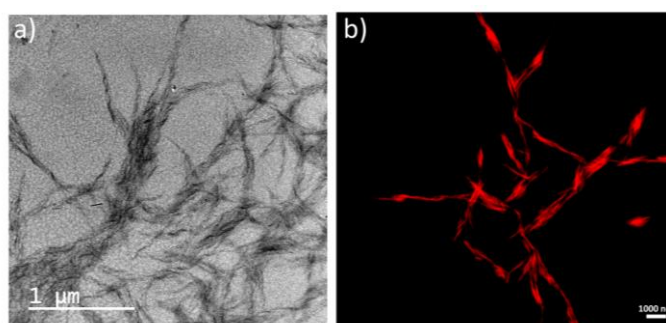
Figure 2.6. a) TEM and b) SIM microscopy image (red channel, λ_{ex} = 561 nm, λ_{coll} = 570-650 nm) of **SS-dithiol** supramolecular homopolymers. (TCE/MCH, 25/75 (v/v), [**SS-dithiol**] = 2.5×10^{-5} M).

The green (λ_{max} = 505 nm) and red (λ_{max} = 575nm) emission of the **SS-diOEt** and **SS-dithiol** aggregates (Figures 2.3b and 2.5b), respectively enabled its visualization through structured illumination microscopy (SIM), as green- and red-emitting supramolecular polymers (Figures 2.5e and 2.6). Distinct absorption and emission spectral features of stacked **SS-diOEt** and **SS-dithiol** monomers facilitate the independent probing of monomers during the supramolecular copolymerization process and the orthogonal visualization using SIM microscopy. Whereas **SS-dithiol** gets excited at both green (λ_{ex} = 488 nm) and red channels (λ_{ex} = 561 nm), **SS-diOEt** selectively gets excited at the green channel, facilitating the visualization of supramolecular copolymers with different microstructure (Figure 2.7). On heating the homopolymers of **SS-dithiol** and **SS-diOEt** to 363 K, the CD signal decreases along with a hypsochromic shift in the absorption and emission spectra (Figures 2.8 and 2.9), suggesting the disassembly to monomers.
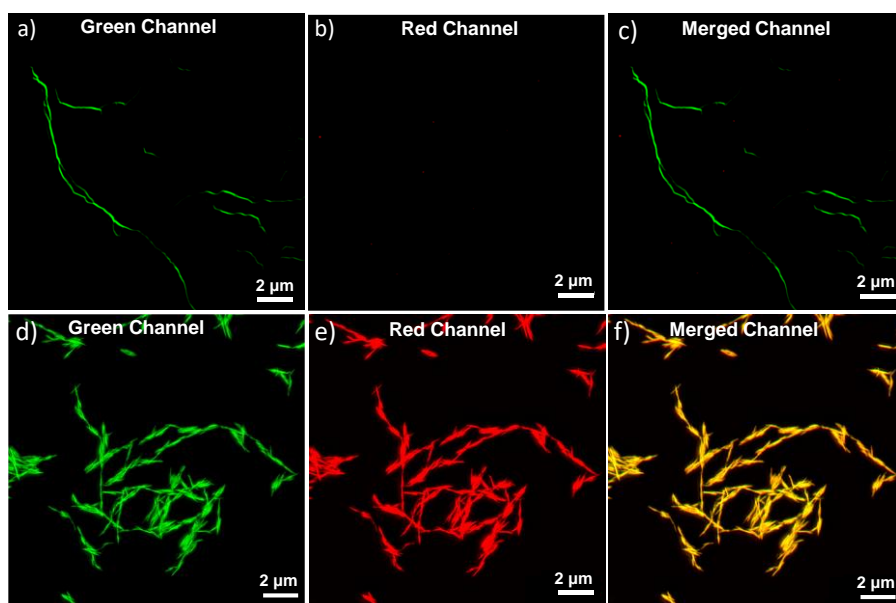
Figure 2.7. SIM microscopy images of **SS-dithiol** and **SS-diOEt** homopolymers in green (λ_{ex} = 488 nm, λ_{coll} = 495-575 nm) and red (λ_{ex} = 561 nm, λ_{coll} = 570-650 nm) channel for orthogonal imaging of the two components. a) and d) shows the images collected at green channel for **SS-diOEt** and **SS-dithiol** homopolymers, respectively. Both **SS-dithiol** and **SS-diOEt** homopolymers gets excited at green channel. b) and e) shows the images collected at red channel for homopolymers of **SS-diOEt** and **SS-dithiol**, respectively. Since **SS-diOEt** does not get excited at red channel we don't observe any homopolymers in red channel for **SS-diOEt**. Whereas **SS-dithiol** gets excited at red channel and provides a red-emitting **SS-dithiol** homopolymer. c) and f) represents the merged image of green and red channel showing a yellow-emitting homopolymer for **SS-dithiol** and a green-emitting homopolymer for **SS-diOEt**. (TCE/MCH, 25/75 (v/v), [**SS-dithiol**] = [**SS-diOEt**] = 2.5×10⁻⁵ M, l = 10 mm).
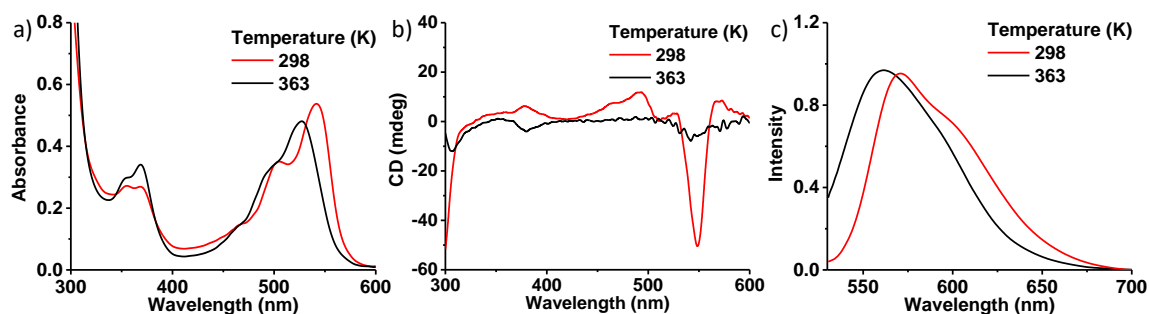
Figure 2.8. Temperature-dependent a) absorption, b) CD, and c) normalized emission spectra (λ_{ex} = 530 nm) of **SS-dithiol** homopolymers. ([**SS-dithiol**] = 2.5×10^{-5} M, TCE/MCH, 25/75 (v/v), l = 10 mm).
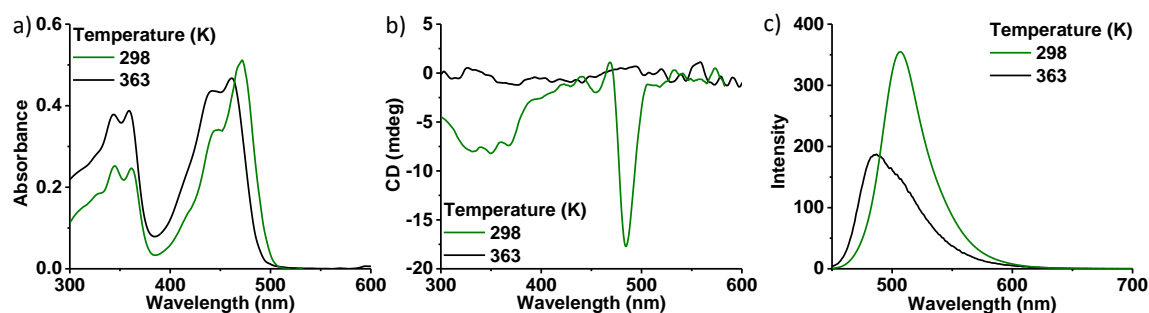
Figure 2.9. Temperature-dependent a) absorption, b) CD, and c) emission spectra (λ_{ex} = 430 nm) of supramolecular homopolymers of **SS-diOEt**. (TCE/MCH, 25/75 (v/v), [**SS-diOEt**] = 2.5×10^{-5} M, l = 10 mm).

2.3.2. Mechanistic Investigations:

To investigate the self-assembly mechanism of the supramolecular homopolymerization process, respective monomeric solutions at high temperature (363 K) were cooled slowly with a ramping rate of 1 K/min and the degree of aggregation (α) was monitored at corresponding aggregation spectral features. The cooling curve obtained by monitoring the CD signal at 548 nm for the **SS-dithiol** monomers ([**SS-dithiol**] = 2.5×10^{-5} M, TCE/MCH, 25/75 (v/v)) showed a non-linear curve, which could be fitted to a nucleation-elongation model with an elongation temperature (T_e) of 323 K (Figure 2.10 and Table 2.3).[28] On the other hand, **SS-diOEt** monomers in the same solvent composition (2.5×10^{-5} M, TCE/MCH, 25/75 (v/v)) while cooling (cooling rate = 1K /min) from its monomeric solution at high temperature to 298 K gets trapped in a metastable state (Figure 2.11a). However, the metastable state gradually gets converted into a thermodynamically stable supramolecular polymer as evident from the time-dependent absorption changes at 370 nm (Figures 2.11b and 2.11c). The heating curve obtained by probing the absorbance changes at 480 nm for thermodynamically stable self-assembled **SS-diOEt** depicted the presence of large hysteresis between the heating and cooling curve which confirms **SS-diOEt** self-assembly is under kinetic control. Since the CD signal of **SS-diOEt** is contaminated with linear dichroism (LD), the corresponding changes in absorption

were probed to follow the self-assembly. Interestingly, the obtained kinetic data could be well fitted with an autocatalytic Watzky and Finke[29] model suggesting the presence of nucleation-elongation growth mechanism, for **SS-diOEt** monomers (Figure 2.11b and Table 2.4). Thus, both **SS-dithiol** and **SS-diOEt** monomers undergo nucleation-elongation homopolymerization under thermodynamic and kinetic control, respectively.
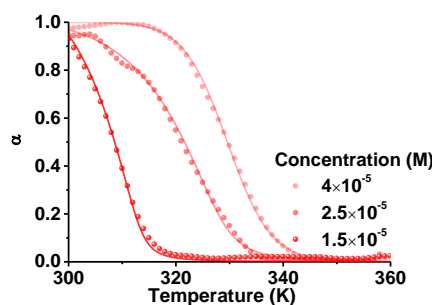
Figure 2.10. Temperature-dependent degree of aggregation (α) of **SS-dithiol** monomers obtained by probing the absorption changes at 550 nm with 1 K/min cooling rate shows that **SS-dithiol** follows a nucleation-elongation growth mechanism. The elongation temperature (T_e) increases on increase in concentration of **SS-dithiol**. (TCE/MCH, 25/75 (v/v), $l = 10$ mm).

Concentration (M)	ΔH_e (kJ/mol)	ΔS_e (kJ/molK)	ΔH_{nuc} (kJ/mol)	T_e (K)
4×10^{-5}	-60.27 ± 1.37	-0.09 ± 0.004	-13.03 ± 0.43	334.51 ± 0.29
2.5×10^{-5}	-120.62 ± 1.24	-0.28 ± 0.01	-10.26 ± 0.47	323.50 ± 0.22
1.5×10^{-5}	-120.98 ± 2.76	-0.29 ± 0.008	-8.64 ± 0.32	313.75 ± 0.17

Table 2.3 Thermodynamic parameters (ΔH_e = enthalpy of elongation, ΔS_e = entropy of elongation, ΔH_{nuc} = enthalpy of nucleation) obtained from fitting the cooling curve of **SS-dithiol** with a nucleation-elongation model. (TCE/MCH, 25/75 (v/v)).
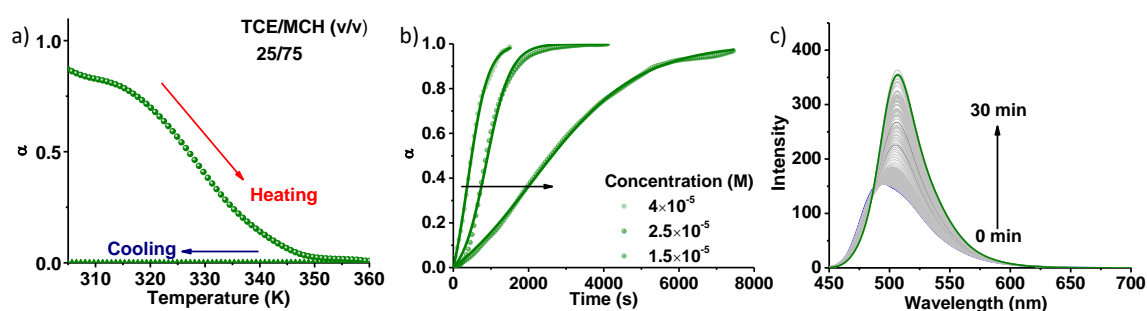
Figure 2.11. a) Temperature-dependent degree of aggregation (α) for **SS-diOEt** obtained by probing the absorbance changes at 480 nm with 1 K/min cooling rate and heating rate shows presence of a hysteresis between heating and cooling curve. b) Time-dependent absorption changes monitored at 370 nm for metastable **SS-diOEt**, depicts conversion of a metastable state into thermodynamically stable aggregated state with nucleation-elongation growth. c) Time-dependent evolution of emission spectra ($\lambda_{ex} = 430$ nm) of metastable **SS-diOEt** into thermodynamically stable self-assembled state. ([**SS-diOEt**] = 2.5×10^{-5} M, TCE/MCH, 25/75 (v/v), $l = 10$ mm).

Concentration (M)	k_{nu} (s^{-1})	k_e (M^{-1}s^{-1})
4×10^{-5}	$(7.28 \times 10^{-4}) \pm (4.05 \times 10^{-6})$	74.44 ± 0.42
2.5×10^{-5}	$(1.92 \times 10^{-4}) \pm (1.61 \times 10^{-6})$	116.44 ± 0.50
1.5×10^{-5}	$(1.29 \times 10^{-4}) \pm (1.95 \times 10^{-7})$	39.15 ± 0.06

Table 2.4. List of kinetic parameters obtained from fitting the time-dependent absorbance changes of **SS-diOEt** with a Watzky-Finke[29] model of nucleation-elongation mechanism. (TCE/MCH, 25/75 (v/v)).

2.3.3. Fibers Stability and Monomer Exchange Dynamics of SS-dithiol and SS-diOEt from Molecular Simulations:

In silico investigations based on high-resolution (atomistic or fine coarse-grained) molecular models are important to complement and rationalize the experimental findings, offering a detailed insight into the structural and dynamic behavior of supramolecular polymers.[30] In particular, recently it was demonstrated that the combination of metadynamics simulations and fine coarse-grained molecular models allow to investigate the mechanisms and relative kinetics of rare monomer exchange events that occur within and in/out of the dynamic supramolecular polymers.[31] We exploited a similar approach here to explore the relative stabilities, and intrinsic dynamics of the supramolecular homopolymers of **SS-dithiol** and **SS-diOEt** studied herein. We first built all atom (AA) models for both **SS-dithiol** and **SS-diOEt** monomers (Figure 2.12a). We then used these as a reference to develop coarse-grained (CG) models for the same monomers (Figure 2.12b). As recently done for similar self-assembling monomers,[16] the CG models for the **SS-dithiol** and **SS-diOEt** monomers were developed based on the MARTINI CG force field[32] and have been further refined in order to reproduce the correct behavior of the monomers in the solvent (cyclohexane) seen in the AA models and the monomer-monomer interactions.[30b] Using these CG models, we studied the dimerization free-energies associated with the **SS-diOEt/SS-diOEt**, **SS-dithiol/SS-diOEt**, and **SS-dithiol/SS-dithiol** interaction in cyclohexane (Figure 2.12c: green (**SS-diOEt**)-green (**SS-diOEt**), green (**SS-diOEt**)-red (**SS-dithiol**) and red (**SS-dithiol**)-red (**SS-dithiol**) dimerization ΔG values, respectively) employing Well-tempered Metadynamics (WT-MetaD)[33] simulations. The ΔG data obtained from the WT-MetaD simulations showed that the most stable interaction is the one given by **SS-diOEt** homodimer, followed by the **SS-dithiol/SS-diOEt** heterodimer and the **SS-dithiol** homodimer. This information is useful to understand the extent to which different monomers are likely to mix during the supramolecular copolymerization process in solution.
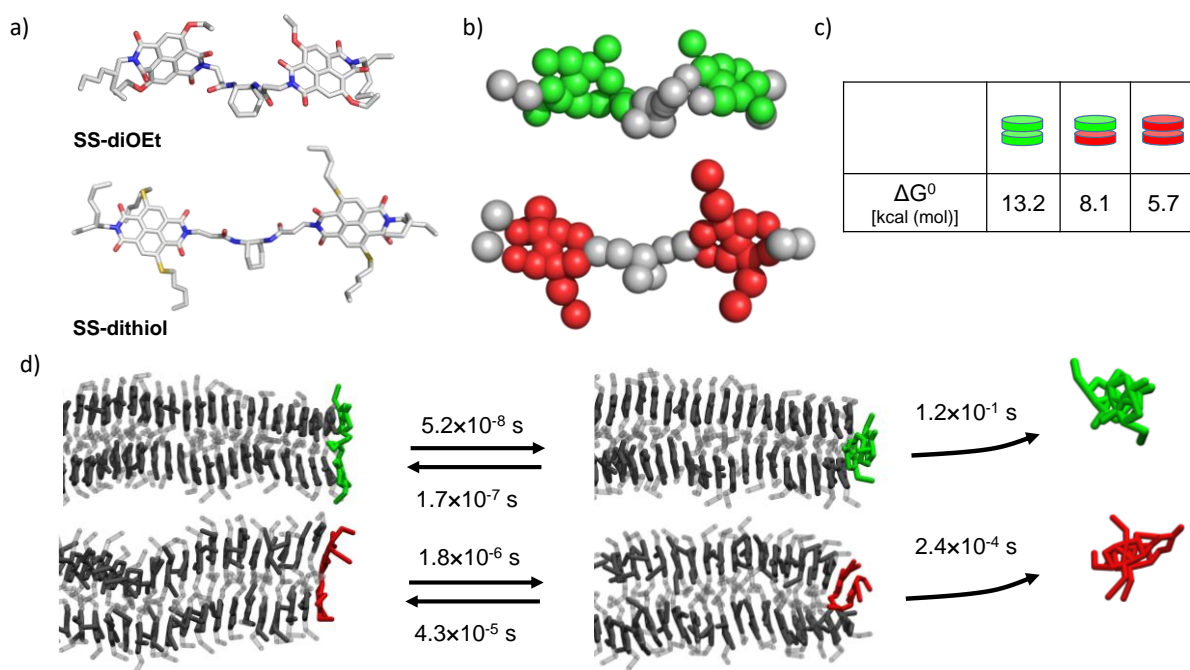
Figure 2.12. Molecular modeling of monomer exchange in the fibers. a) All-atom (AA) models of **SS-diOEt** and **SS-dithiol** (hydrogen atoms not shown for clarity). b) Coarse-grained (CG) models for both the monomers. c) Dimerization/binding free energies for the **SS-diOEt/SS-diOEt**, **SS-diOEt/SS-dithiol**, and **SS-dithiol/SS-dithiol** interactions. d) Schematic representation and characteristic timescales (t_{CG}) for the exchange steps involved in the process of monomer exchange from the fiber tips in both **SS-diOEt** (top) and **SS-dithiol** (bottom). Monomer exchange steps: (i) the monomer on the tip, starting from an open/stacked state (left), closes in "sandwich conformation" (middle), and (ii) from such closed conformation exchanges with the solution (right).

As a next step, we built two CG models of preformed supramolecular polymers (one for **SS-dithiol** and one for **SS-diOEt**) composed of 40 initially extended stacked monomers (Figure 2.12d). These CG stack models have been solvated, equilibrated, and relaxed in explicit CG cyclohexane solvent molecules by running 1 µs classical CG molecular dynamics (MD) simulations at the temperature of 300 K and pressure of 1 atm (see experimental section). To explore the event of monomer exchange from the fibers' tips, we have performed multiple infrequent WT-MetaD simulations by activating/biasing the unbinding of the first monomer from the tip of the stacks and the release of the monomers into the cyclohexane solvent. We could observe that in both stacks the exchange event is characterized by two different steps: (1) the monomer at the stack tip closes-up in a "sandwich" conformation and (2) from such closed state, the monomer can get released to the solvent (see experimental section).[31] We ran multiple infrequent WT-MetaD simulations exploring step 1 (back and forth closing and opening of the tip monomer) and step 2 (exchange of a closed monomer with the solution). The transition/exchange times obtained from these WT-MetaD runs allowed us to reconstruct the
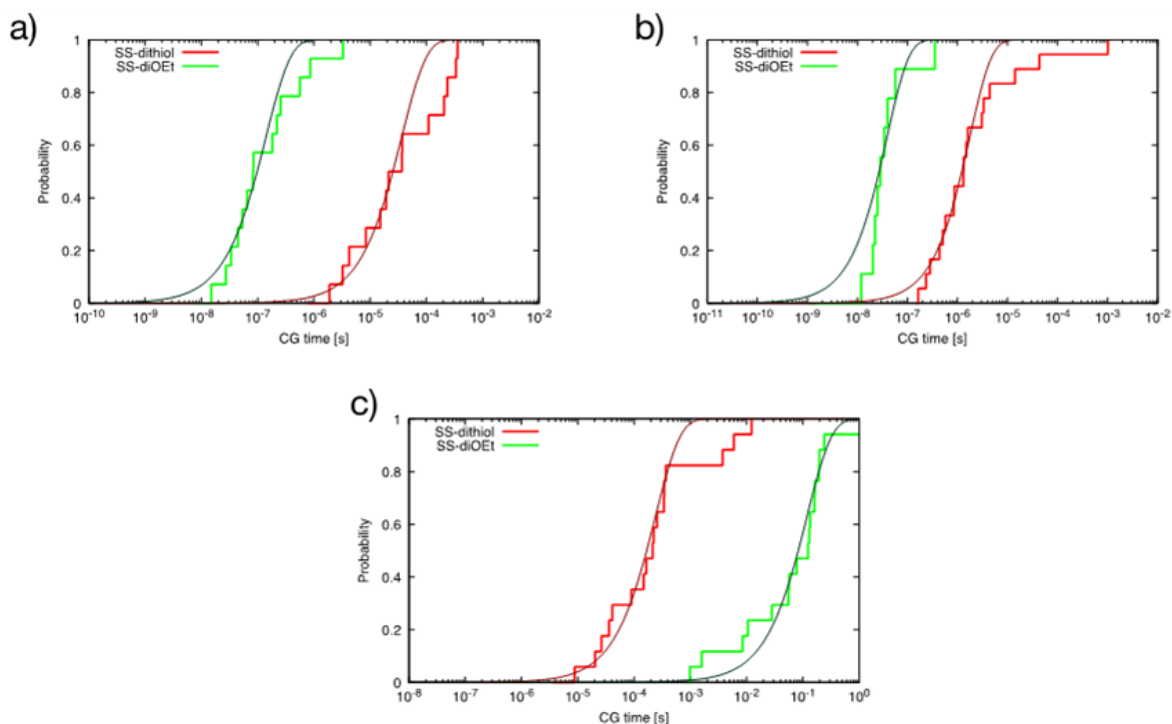
Figure 2.13. Transition times extracted from the infrequent MetaD simulations. The plots report the empirical and theoretical distributions of the transition times for **SS-dithiol** (red) and **SS-diOEt** (green) for the events of a) tip opening, b) tip closing and c) monomer exchange from the head of the fibers to the cyclohexane solvent. For tip opening we have a $\tau_{\text{SS-dithiol}}=4.3\cdot10^{-5}$ s with a p-value=0.226, and $\tau_{\text{SS-diOEt}}=1.6\cdot10^{-7}$ s with a p-value=0.555. For tip closing we have a $\tau_{\text{SS-dithiol}}=4.3\cdot10^{-6}$ s with a p-value=0.705, and $\tau_{\text{SS-diOEt}}=5.2\cdot10^{-8}$ s with a p-value=0.385. For monomer exchange we have $\tau_{\text{SS-dithiol}}=2.4\cdot10^{-4}$ s with a p-value=0.589, and $\tau_{\text{SS-diOEt}}=1.2\cdot10^{-1}$ s with a p-value=0.460
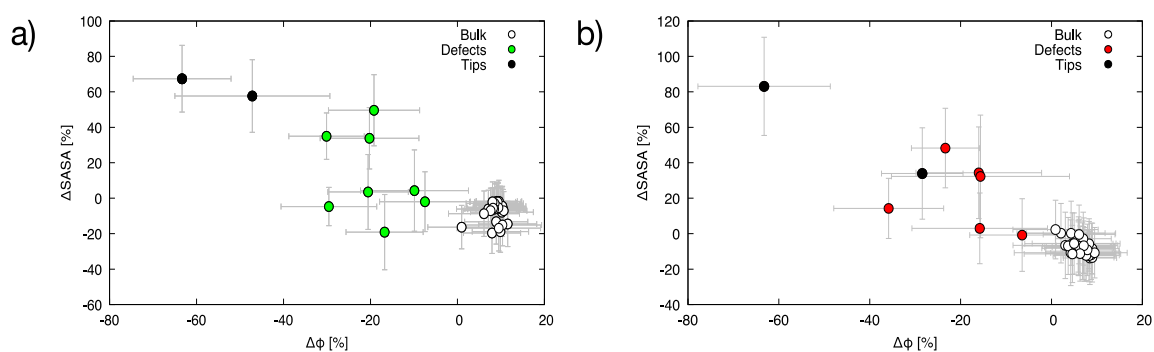
Figure 2.14. Defects analysis in the a) **SS-diOEt** and b) **SS-dithiol** stacks. Here we show the Solvent Accessible Surface Area (SASA, *y* axis) and the order parameter given by the coordination number between the monomer cores (*x* axis) for all the monomers in the fibers expressed in terms of variations respect to the monomer average values in the fibers. The analysis allows to divide the monomers in these fibers in three groups: bulk (ordered) monomers (white points), tips (black points) and defects (in red in **SS-dithiol** and in green in **SS-diOEt**). [31,16] It is evident the larger number of defects in the **SS-diOEt** fiber compared to the **SS-dithiol** fiber.

unbiased kinetics for the steps involved in the monomer exchange and to estimate their characteristic timescales (Figure 2.12d). The statistics obtained from these WT-MetaD simulations fit well with the Poissonian exchange distributions expected for rare events, proving the appropriateness of the adopted method (Figure 2.13).[31]

From exchange distributions, we calculated the characteristic exchange timescales (*i.e.* the average residence times of the monomers on the stack tips) for the two systems (Figure 2.12d). Although these exchange timescales are extracted from CG models and are therefore qualitative, these are nonetheless useful to compare the dynamics and monomer exchange from the tips of the two stacks (step 2). In particular, this event is found to be slower (less likely) in **SS-diOEt** ($t_{CG} \sim 1.2 \times 10^{-1}$ s) than in **SS-dithiol** ($t_{CG} \sim 2.4 \times 10^{-4}$ s). Conversely, the closing/opening of monomers at the tip of the stacks (exchange step 1) seems to be faster in the **SS-diOEt** (closing/opening timescales, t_{close}/t_{open}, in the order of $\sim 10^{-8}/10^{-7}$ s) than in the **SS-dithiol** (t_{close}/t_{open} in the order of $\sim 10^{-6}/10^{-5}$ s). The slower monomer exchange kinetics of **SS-diOEt** with the solvent is in line with the higher **SS-diOEt-SS-diOEt** interaction energies reported in Figure 2.12c. In general, in these stacks the closure into the "sandwich" conformation of the monomers at the chain-end appears to be faster than the opening, suggesting that, statistically, the tips of these stacks are intrinsically more disordered compared to the perfectly organized monomers expected in the bulk. In fact, monomers closure along the fibers introduces defects inside these stacks, while such defects are known to be important for the exchange of monomers and the overall dynamics of the assembly.[31,30b,34] A more in-depth analysis of MD simulations of these stacks indicated that at the equilibrium, both assemblies possess stacking defects at the tips as well as in their interior. Analyzing the extent of solvent exposure of monomers in these stacks and the extent of ordered regions indicate that the **SS-diOEt** assembly tends to form more defects along its length with respect to the **SS-dithiol** (Figure 2.14). This is interesting, as such defects may constitute hot spots from where the monomers can exchange in/out of the stacks and eventually leading to the mixing of monomers and assemblies during the supramolecular copolymerization process.[4b,31,34] Thus, based on this analysis the **SS-diOEt** assemblies appear overall more disordered than **SS-dithiol** ones. The relatively slow dynamics and static nature of **SS-diOEt** fibers as seen in the simulations, originating from the strong monomer-monomer interaction energies in these assemblies (Figure 2.12c), and their higher tendency to disorder (compared to **SS-dithiol**) is in agreement with the experimental observation of the entrapment of these monomers into a local minimum metastable state (disordered) in the free energy landscape during its temperature-dependent supramolecular homopolymerization process. On the other hand, the faster dynamics of **SS-**

dithiol assemblies may enable them to reach the thermodynamic equilibrium during the self-assembly process as seen in the experiments in a more facile way compared to **SS-diOEt**.

2.3.4. Supramolecular Block Copolymerization under Thermodynamic Control:
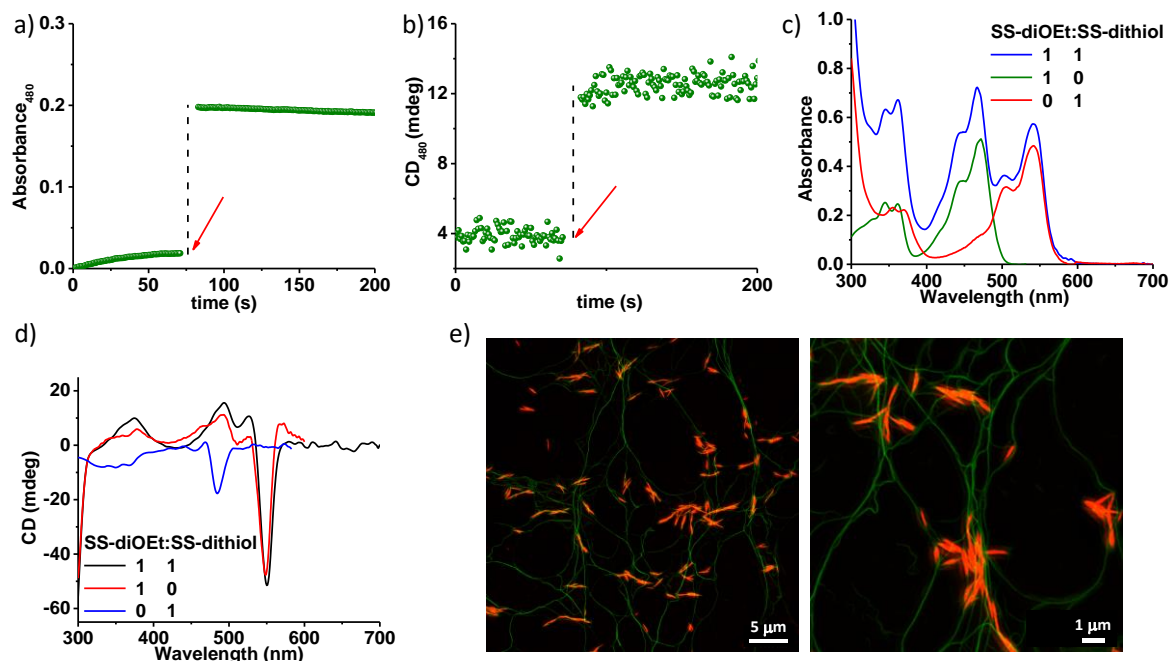
Figure 2.15. Time-dependent a) absorbance and b) CD changes monitored at 480 nm upon addition of 1 equivalent of self-assembled **SS-dithiol** as a seed into the metastable state of **SS-diOEt** showing absence of seeded nature under kinetic conditions. c) Absorption and d) CD spectra of the solution after addition of the seed. e) SIM microscopy images after completion of polymerization process of **SS-diOEt** (1 day) showing no supramolecular block copolymer formation. ([**SS-diOEt**] = [**SS-dithiol**] = 2.5×10^{-5} M, TCE/MCH, 25/75 (v/v), l = 10 mm).

Having investigated the mechanistic aspects of supramolecular homopolymerization of both **SS-dithiol** and **SS-diOEt**, we next attempted the supramolecular block copolymerization process to construct the axial organic heterostructures. Since **SS-dithiol** forms stable supramolecular homopolymers under thermodynamic conditions and **SS-diOEt** forms a kinetically controlled metastable phase as dormant monomeric state prior to time-dependent supramolecular homopolymerization process, first we attempted the heterogeneous seeded supramolecular polymerization under kinetic control to construct multicomponent block topology.[15] However, the introduction of **SS-dithiol** seeds into the metastable state of **SS-diOEt** does not trigger an immediate growth of later, which ruled out the possibility of heterogeneous nucleation process of the monomers under kinetic control (Figure 2.15). This observation was quite surprising. We can rationalize this in light of the results from the simulations. In fact, we speculate that this could be due to the slower dynamics (at room

temperature) of **SS-diOEt** monomers and their higher free energy of monomer-monomer interactions compared to that of hetero-monomeric interactions (Figure 2.12c). This would make **SS-diOEt** monomers that exchange out of the assembly into the solution more prone to re-assemble with other **SS-diOEt** monomers rather than to stack onto **SS-dithiol** assemblies. At the same time, it is also possible that the intrinsic presence of defects at the tips of **SS-dithiol** and **SS-diOEt** stacks, originating from monomers in sandwiched conformation might also prevent the heterogeneous nucleation during the seeding experiments under kinetic control.
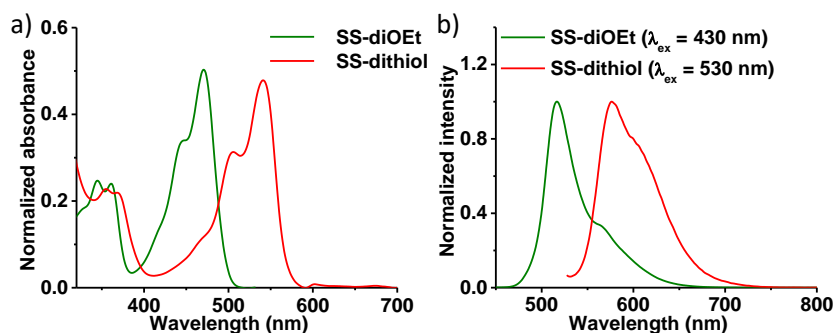
Figure 2.16. Combined a) absorption and b) normalized emission spectra of supramolecular homopolymers of **SS-diOEt** (λ_{ex} = 430 nm) and **SS-dithiol** (λ_{ex} = 530 nm), depicting separate absorption and emission maxima as a result of different core-substitution. (TCE/MCH, 25/75 (v/v), [**SS-dithiol**] = [**SS-diOEt**] = 2.5×10^{-5} M, l = 10 mm).

We envision that supramolecular copolymerization of the monomers under thermodynamic control[16,17], analogous to the classical chain copolymerization, would be another strategy to achieve block microstructure. Furthermore, the reactivity ratio (R) of 1.17 that can be calculated from the interaction free-energies of Figure 2.12c (as R = ($\Delta G_{\text{SS-diOEt-SS-diOEt}}$+$\Delta G_{\text{SS-dithiol-SS-dithiol}}$)/$2 \times \Delta G_{\text{SS-diOEt-SS-dithiol}}$) obtained from the CG simulations suggests the possibility of the blocky organization during a cooperative supramolecular copolymerization analogous to the chain copolymerization in covalent polymeric systems. Since **SS-dithiol** is having a red shifted and overlapping absorption spectral features with that of the **SS-diOEt**, the growth of **SS-diOEt**, monomers cannot be selectively monitored using the absorbance changes during the coassembly process (Figure 2.16a). Furthermore, CD spectral features of **SS-diOEt** cannot be used to probe its growth, as it is contaminated with LD. Hence, we have utilized the distinct
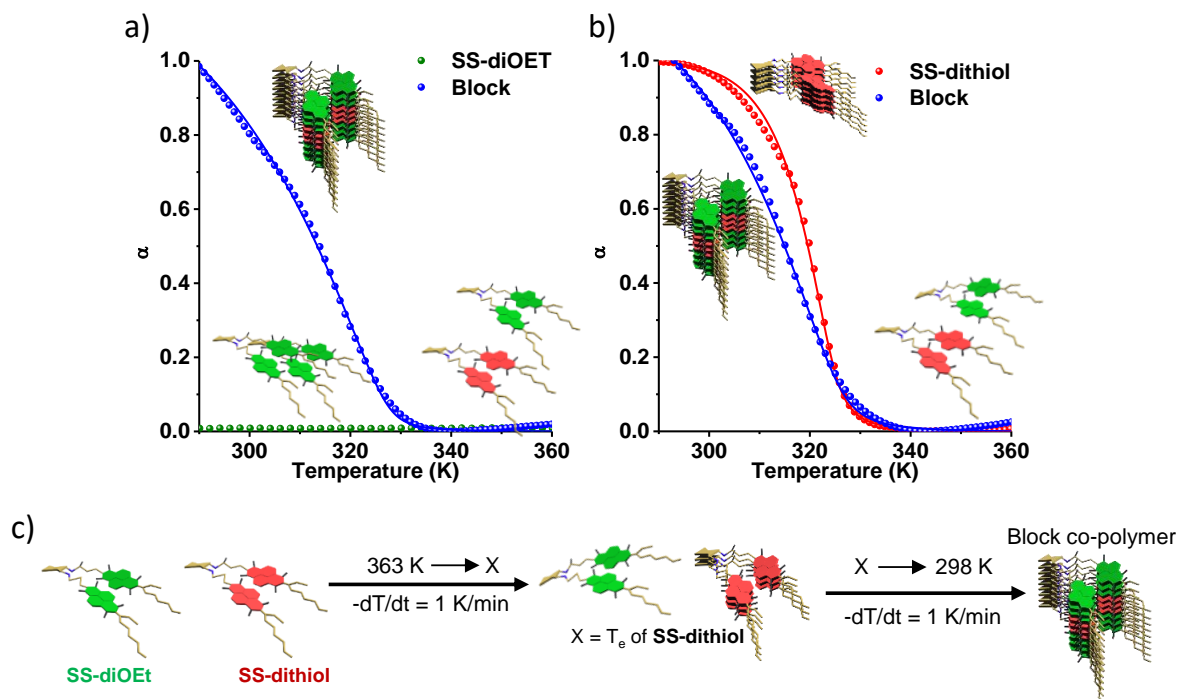
Figure 2.17. Temperature-dependent degree of aggregation (α) (1 K/min cooling rate) obtained by probing the emission changes at a) 490 nm for **SS-diOEt** (λ_{ex} = 430 nm) and b) 570 nm for **SS-dithiol** (λ_{ex} = 530 nm) shows **SS-diOEt** and **SS-dithiol** elongates at the same temperature confirming the coassembly process. The nucleation temperature of the mixture in the two graphs matches with that of pure **SS-dithiol**. c) Schematic illustration of the heterogeneous nucleation and supramolecular block copolymerization process under thermodynamic control. "X" represents the T_e of **SS-dithiol** at a particular concentration which triggers the heterogeneous nucleation of **SS-diOEt** in **SS-dithiol** seeds. ([**SS-diOEt**] = [**SS-dithiol**] = 2.5×10⁻⁵ M, TCE/MCH, 25/75 (v/v), l = 10 mm).

green (λ_{max} = 505 nm) and red (λ_{max} = 575 nm) emission of **SS-diOEt** and **SS-dithiol** monomers, respectively which could also be selectively excited, to probe the growth process (Figure 2.16b). In a typical supramolecular copolymerization process under thermodynamic conditions, a 1:1 mixture (c = 2.5×10⁻⁵ M) of **SS-diOEt** and **SS-dithiol** in TCE/MCH, 25/75 (v/v) solvent mixture was heated to 363 K and cooled under thermodynamic control at a rate of 1 K/min. Temperature-dependent emission changes of a 1:1 mixture of **SS-dithiol** and **SS-diOEt** obtained via selective excitation (λ_{ex} = 430 nm for **SS-diOEt** and 530 nm for **SS-dithiol**) and monitoring at 490 nm and 570 nm for **SS-dithiol** and **SS-diOEt**, respectively indicated the coassembly between the two components. Temperature-dependent emission changes of **SS-dithiol** showed a two step non-linear changes, which could be fitted to a cooperative nucleation-elongation model. Interestingly, the elongation temperature of 325 K of the 1:1 monomeric mixture matches well with that of **SS-dithiol** homopolymer at the same concentration (T_e = 325 K, c = 2.5×10⁻⁵ M) (Figures 2.17b, 2.18a, 2.18b, Tables 2.5 and 2.6).
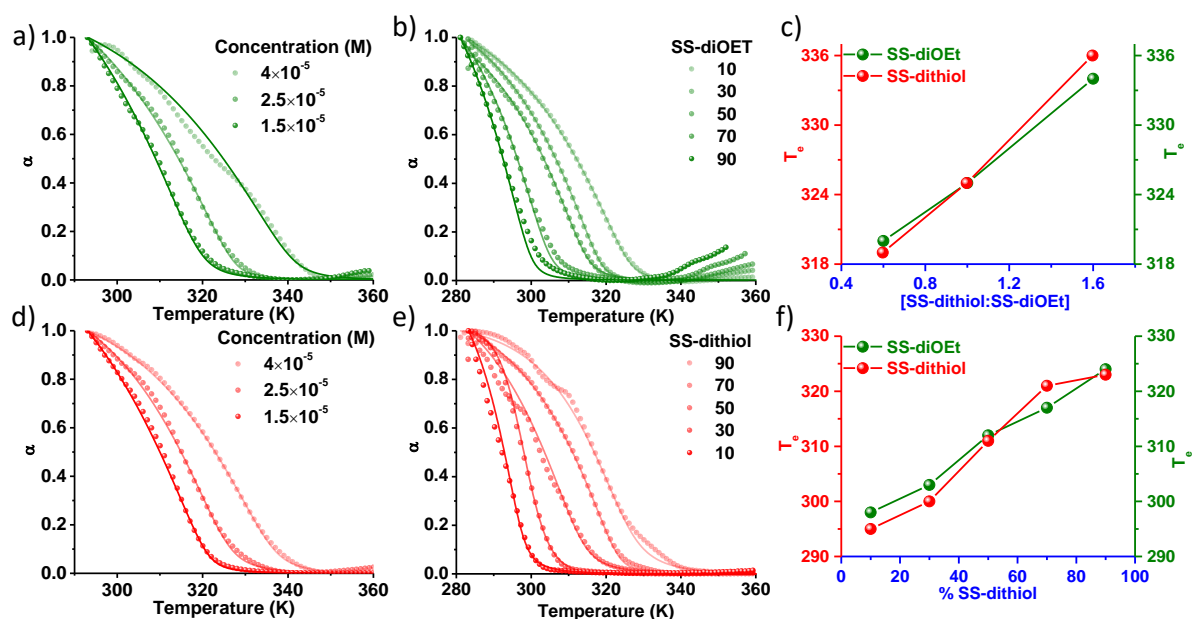
Figure 2.18. Coassembly mechanism of a mixture of **SS-diOEt** and **SS-dithiol** and heterogeneous nucleation under thermodynamic control. Temperature-dependent degree of aggregation (α) was obtained by probing the emission changes at 490 nm for **SS-diOEt** (green colored curves) (λ_{ex} = 430 nm) and 570 nm for **SS-dithiol** (red colored curves) (λ_{ex} = 530 nm) with 1 K/min cooling rate. a) and d) On changing **SS-dithiol** concentration with a fixed **SS-diOEt** concentration, the **SS-diOEt** elongation temperature decreases with decrease in **SS-dithiol** concentration confirming the coassembly of the two molecules. c) Plot of elongation temperature (T_e) of the coassembled solution against variable **SS-dithiol** concentration while keeping **SS-diOEt** concentration constant. b), e) Decrease in T_e during heterogeneous nucleation of coassembled solution of **SS-diOEt** and **SS-dithiol** keeping the total concentration constant showing formation of nuclei of **SS-dithiol** first followed by growth of both molecules on the existing seed. f) Plot of elongation temperature (T_e) against different **SS-dithiol**:**SS-diOEt** molar ratio with a fixed total concentration at 3×10^{-5} M. ([**SS-diOEt**] = [**SS-dithiol**] = 2.5×10^{-5} M, TCE/MCH, 25/75 (v/v), l = 10 mm).

SS-dithiol	SS-diOEt	ΔH_e (kJ/mol)	ΔS_e (kJ/molK)	ΔH_{nuc} (kJ/mol)	T_e (K)
4×10^{-5} M	2.5×10^{-5} M	-27.68±0.90	-0.00±0.002	-15.47±0.41	328.77±0.35
2.5×10^{-5} M	2.5×10^{-5} M	-32.11±0.0012	-0.01±0.001	-20.35±0.30	325.83±0.11
1.5×10^{-5} M	2.5×10^{-5} M	-33.61±0.52	-0.01±0.001	-16.68±0.22	320.64±0.128

Table 2.5. Thermodynamic parameters obtained by fitting the cooling curve of Figure 2.18a with nucleation-elongation model. (TCE/MCH, 25/75 (v/v)).

More importantly, the selective probing of the **SS-diOEt** emission during coassembly, also followed a nucleation-elongation mechanism with identical T_e (325 K) as that of **SS-dithiol**,

SS-dithiol	SS-diOEt	ΔH_e (kJ/mol)	ΔS_e (kJ/molK)	ΔH_{nuc} (kJ/mol)	T_e (K)
4×10^{-5} M	2.5×10^{-5} M	-38.47 ± 0.26	-0.02 ± 0.0008	-16.79 ± 0.14	334.97 ± 0.08
2.5×10^{-5} M	2.5×10^{-5} M	-45.11 ± 0.64	-0.05 ± 0.002	-14.40 ± 0.20	325.65 ± 0.13
1.5×10^{-5} M	2.5×10^{-5} M	-32.61 ± 0.56	-0.009 ± 0.001	-20.57 ± 0.38	319.62 ± 0.13

Table 2.6. Thermodynamic parameters obtained by fitting the cooling curve of Figure 2.18d with nucleation-elongation model (TCE/MCH, 25/75 (v/v)).

Concentration (M)	% SS-dithiol	% SS-diOEt	ΔH_e (kJ/mol)	ΔS_e (kJ/molK)	ΔH_{nuc} (kJ/mol)	T_e (K)
3×10^{-5}	90	10	-61.42 ± 0.95	-0.10 ± 0.003	-10.20 ± 0.21	323 ± 0.18
3×10^{-5}	70	30	-43.87 ± 0.33	-0.04 ± 0.001	-17.22 ± 0.15	321.52 ± 0.06
3×10^{-5}	50	50	-44.52 ± 1.34	-0.05 ± 0.004	-13.35 ± 0.34	311.43 ± 0.20
3×10^{-5}	30	70	-229.97 ± 0.88	-0.68 ± 0.002	-0.45 ± 0.007	301.53 ± 0.18
3×10^{-5}	10	90	-80.19 ± 3.87	-0.18 ± 0.01	-11.16 ± 0.43	296.12 ± 0.15

Table 2.7. Thermodynamic parameters obtained by fitting the cooling curve of Figure 2.18b with nucleation-elongation model. (TCE/MCH, 25/75 (v/v)).

Concentration (M)	% SS-dithiol	% SS-diOEt	ΔH_e (kJ/mol)	ΔS_e (kJ/molK)	ΔH_{nuc} (kJ/mol)	T_e (K)
3×10^{-5}	90	10	-35.45 ± 0.26	-0.02 ± 0.0008	-18.78 ± 0.15	324 ± 0.06
3×10^{-5}	70	30	-38.68 ± 0.74	-0.03 ± 0.002	-18.90 ± 0.39	317 ± 0.14
3×10^{-5}	50	50	-41.93 ± 1.84	-0.04 ± 0.005	-15.92 ± 0.62	313 ± 0.29
3×10^{-5}	30	70	-46.47 ± 2.29	-0.06 ± 0.007	-14.70 ± 0.61	303 ± 0.27
3×10^{-5}	10	90	-44.27 ± 2.37	-0.06 ± 0.008	-15.86 ± 0.77	298 ± 0.29

Table 2.8. Thermodynamic parameters obtained by fitting the cooling curve of Figure 2.18e with nucleation-elongation model (TCE/MCH, 25/75 (v/v)).

despite the fact, the **SS-diOEt** homopolymer at the same concentration gets trapped into a metastable state under similar conditions. This provides a clear indication of heterogeneous nucleation and supramolecular copolymerization process of **SS-dithiol** and **SS-diOEt** monomers (Figure 2.17b, Tables 2.5 and 2.6). Supramolecular copolymerization of **SS-diOEt** and **SS-dithiol** mixtures with constant **SS-diOEt** (c = 2.5×10^{-5} M) and varying **SS-dithiol** (1.5×10^{-5} to 4×10^{-5} M) concentrations, showed a decrease in T_e of the supramolecular copolymer with a decrease in **SS-dithiol** concentration (Figures 2.18a, 2.18b and 2.18c). Further, on variation of monomer ratio (**SS-dithiol:SS-diOEt** from 9:1 to 1:9) by keeping the total concentration constant (3×10^{-5} M) (Figures 2.18d, 2.18e and 2.18f), showed a linear decrease in T_e proportional with the decrease in the **SS-dithiol** concentration. These observations clearly indicate the heterogeneous nucleation of **SS-diOEt** on **SS-dithiol** nuclei rather than a cooperative alternating copolymerization of a heterodimer. Absorption spectra of the copolymerized solution matched well with individual homopolymer spectra (Figure 2.19a),
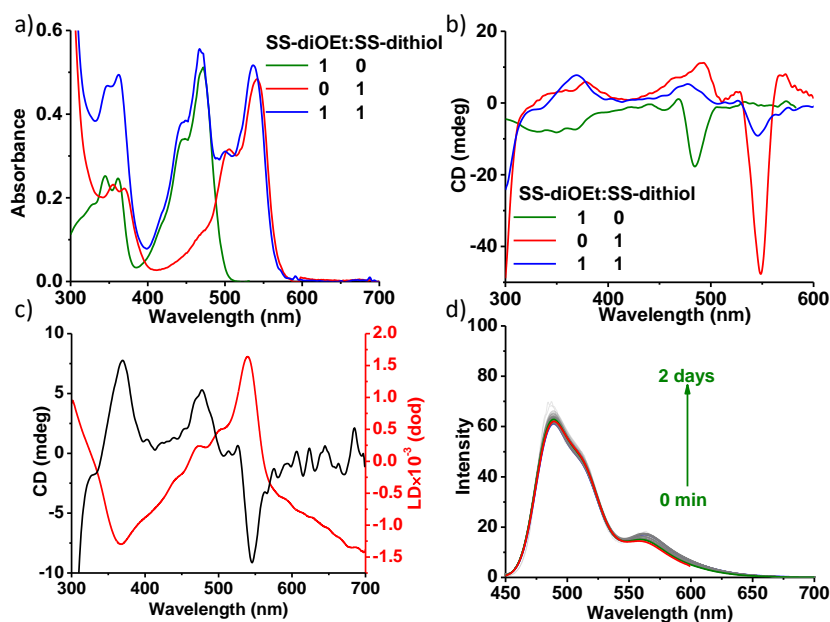
Figure 2.19. a) Absorption, b) CD spectra of the coassembled solution of **SS-diOEt** and **SS-dithiol**. c) Corresponding LD spectra overlaid with the CD spectra of the coassembled solution of **SS-diOEt** and **SS-dithiol**. d) Time-dependent emission changes (λ_{ex} = 430 nm) of copolymerized solution showing its stability over time. ([**SS-diOEt**] = [**SS-dithiol**] = 2.5×10^{-5} M, TCE/MCH, 25/75 (v/v), l = 10 mm).
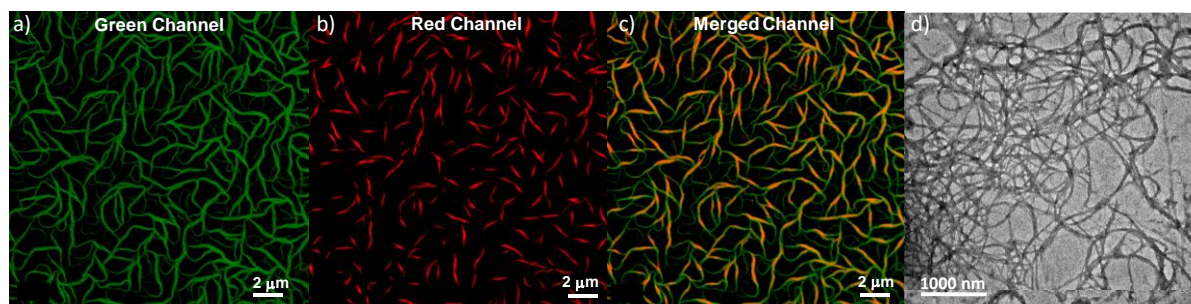
Figure 2.20. SIM microscopy of the coassembled solution of **SS-diOEt** and **SS-dithiol** showing presence of supramolecular multi BCP when collected at a) green channel (λ_{ex} = 488 nm, λ_{coll} = 495-575 nm), b) red channel (λ_{ex} = 561 nm, λ_{coll} = 570-650 nm) and c) merged channel. d) Corresponding TEM image showing presence of supramolecular polymers. ([**SS-diOEt**] = [**SS-dithiol**] = 2.5×10^{-5} M, TCE/MCH, 25/75 (v/v), l = 10 mm).

however, CD spectra of the copolymerized solution was contaminated with LD (Figures 2.19b and 2.19c). Time-dependent emission changes showed the stability of the copolymer over two days (Figure 2.19d).

Recently we have shown that SIM imaging is very useful for the visualization of multicomponent supramolecular fibers with improved resolution, compared to standard diffraction-limited microscopy imaging.[26] Further SIM imaging could be performed using the inherent emission of monomeric components, which avoids the structural modification of monomers often required to improve the resolution of fluorescence imaging. Thus,

visualization of the coassembled solution using SIM microscopy (upon selective excitation and probing through different emission channels) revealed blocky supramolecular polymers with alternating red and green segments of stacked **SS-diOEt** and **SS-dithiol** monomers (Figure 2.20). Since **SS-dithiol** also gets excited at the green channel due to its broad absorption, we observe a continuous green-emitting chain in the green channel due to the contribution from both monomers. However, the low quantum yield of **SS-dithiol** in comparison to **SS-diOEt** resulted in low green intensity in its segments compared to the highly intense green emission from the **SS-diOEt** blocks (Figure 2.21). This is more evident in the green intensity profile, which showed a variation depending on the nature of segments. However, visualizing through the red channel and corresponding intensity profiles selectively probed the red segments. Complementary nature of red and green intensity profiles from the merged channel unequivocally proved the presence of the alternate segmental organization. Blocky organization of the components in the supramolecular copolymer rather than an alternating monomer sequence originates from the lower hetero-free energy gain ($\Delta G_{\text{SS-diOEt-SS-dithiol}}$) compared to the total homo-free energy gain ($\Delta G_{\text{SS-diOEt-SS-diOEt}}$, $\Delta G_{\text{SS-dithiol-SS-dithiol}}$), as reported by Meijer and coworkers (*vide supra*).[16] Solution phase energy transfer studies between **SS-diOEt** and **SS-dithiol** segments indicated a quenching in donor emission with the enhancement of acceptor emission at 570 nm indicating close proximity between donor and acceptor segments (Figure 2.22).
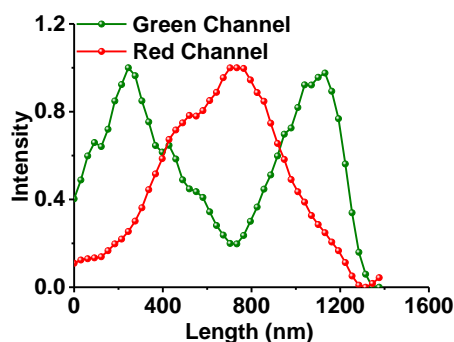
Figure 2.21. Corresponding intensity profile of the fibers in green, and red channel illustrating that the green and red emission does not overlay with each other.
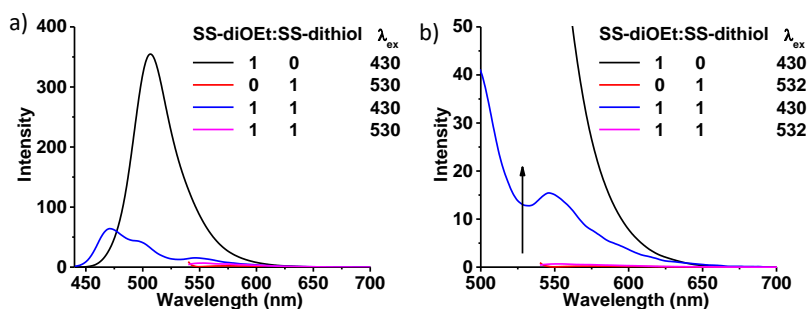
Figure 2.22. Energy transfer studies between coassembled solution of **SS-diOEt** and **SS-dithiol**. a) Emission spectra of coassembled solution and its comparison with pure **SS-diOEt** (donor) and **SS-dithiol** (acceptor) of same concentration, showing quenching of **SS-diOEt** emission due to energy transfer. b) Zoomed in region corresponding to acceptor emission showing enhancement in acceptor emission. ([**SS-diOEt**] = [**SS-dithiol**] = 2.5×10^{-5} M, TCE/MCH, 25/75 (v/v), l = 10 mm).

SS-diOEt	SS-dithiol	λ_{coll} (nm)	t_1 (ns)	t_2 (ns)	t_3 (ns)
1	0	515	1.01 (29.36 %)	2.54 (64.84 %)	11.24 (5.80 %)
1	1	515	0.9 (17.45 %)	1.91 (62.67 %)	6.91 (19.88 %)

Table 2.9. Lifetime data of the block copolymer solution when collected at donor emission (λ_{ex} = 442 nm) and comparison with pure donor. ([**SS-diOEt**] = [**SS-dithiol**] = 2.5×10^{-5} M, TCE/MCH, 25/75 (v/v), l = 10 mm).
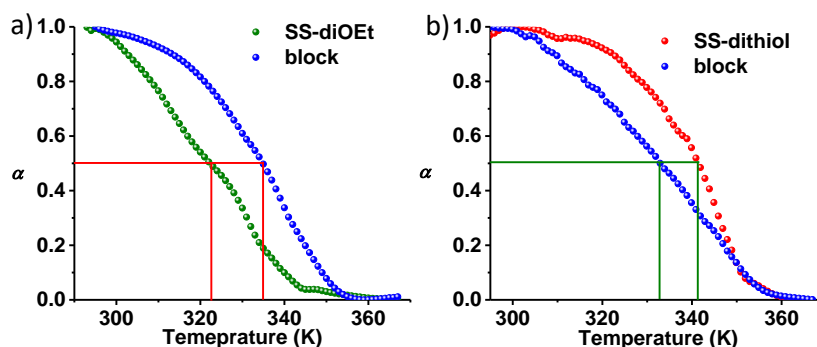
Figure 2.23. Heating curves of the block copolymer solution (1:1) obtained via monitoring temperature-dependent selective excitation and emission changes (1 K/min heating rate) describes the increase in stability of the **SS-diOEt** component and a decrease in stability of the **SS-dithiol** component. a) Corresponds to heating curve of pure **SS-diOEt** homopolymer and **SS-diOEt** in block copolymer (λ_{ex} = 430 nm and λ_{coll} = 490 nm). b) Corresponds to heating curve of pure **SS-dithiol** homopolymer and **SS-dithiol** in block copolymers (λ_{ex} = 530 nm and λ_{coll} = 570 nm). ([**SS-diOEt**] = [**SS-dithiol**] = 2.5×10^{-5} M, TCE/MCH, 25/75 (v/v), l = 10 mm).

	430 nm	530 nm
SS-diOEt	322 K	
SS-dithiol		341 K
Block copolymer	335 K	334 K

Table 2.10. Melting temperature of **SS-diOEt** and **SS-dithiol** in block copolymer and its comparison with individual pure homopolymer showing an increase in stability for **SS-diOEt** and decrease in stability for **SS-dithiol**. ([**SS-diOEt**] = [**SS-dithiol**] = 2.5×10^{-5} M, TCE/MCH, 25/75 (v/v), l = 10 mm).

Melting temperature (T$_m$) obtained from the heating curve of the supramolecular block copolymer (heating rate = 1 K/min) shows an increase in stability of **SS-diOEt** segment from 322 K to 335 K and a decrease in stability of **SS-dithiol** segment from 341 K to 334 K, compared to the corresponding pure components at similar concentrations (Figure 2.23 and Table 2.10). This further rule out any narcissistically self-sorted arrangement between **SS-diOEt** and **SS-dithiol** stacks which would have resulted in similar stability for both individual stacks and the mixture.

2.3.5. Dynamicity Controlled Tuning of Block Length and Complexity:
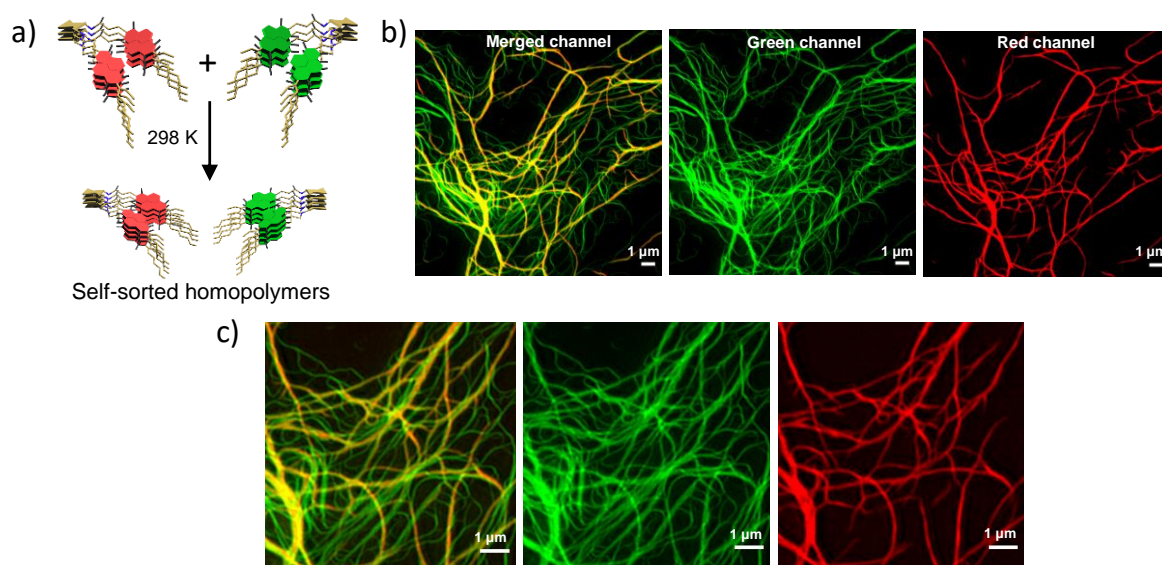
Figure 2.24. a) Schematic illustration and b) SIM image of post synthetically mixed **SS-diOEt** and **SS-dithiol** homopolymers showing self-sorted arrangement of **SS-diOEt** and **SS-dithiol** stacks. c) Zoomed in SIM image of self-sorted **SS-diOEt** and **SS-dithiol** stacks. ([**SS-diOEt**] = [**SS-dithiol**] = 2.5×10^{-5} M, TCE/MCH, 25/75 (v/v), l =10 mm).

Mixing of the supramolecular homopolymers of **SS-diOEt** and **SS-dithiol** (c =2.5×10^{-5} M, TCE/MCH, 25/75 (v/v)) at room temperature results in narcissistically self-sorted green and red chains as evident from SIM microscopic images and unchanged absorption and CD spectral features (Figures 2.24 and 2.25). We have observed a decrease in **SS-diOEt** emission intensity

which could be due to energy transfer between the closely entangled network of **SS-diOEt** and **SS-dithiol**. The self-sorted supramolecular stacks remain intact with time at room temperature, as evident from the spectroscopic and microscopic studies performed after two days, suggesting that these systems are less dynamic at room temperature (Figure 2.26). This observation is again consistent with the CG MetaD simulations, which revealed a slow monomer exchange dynamic, especially in the **SS-diOEt** stacks compared to similar stacks reported in the literature,[26] which is also due to the monomer conformational transitions associated with the exchange process. As mentioned before, the considerable interaction energy between the monomers of **SS-diOEt** may prevent the monomer from reshuffling between the two stacks at room temperature. However, heating curves of **SS-diOEt** and **SS-dithiol** homopolymers at similar concentrations (c = 2.5×10^{-5} M) showed differential stability, with higher melting temperature (T_m) for **SS-dithiol** (T_m= 342 K) stacks compared to the assemblies of **SS-diOEt** (T_m = 328 K) (Figure 2.27 and Table 2.11). The lower stability of **SS-diOEt** supramolecular homopolymers seen in the experiments can be attributed to the intrinsically more disordered nature (in terms of the internal organization of the monomers) in this case. In fact, detailed analysis of the internal ordering of these fibers inferred from the MD simulations evidenced the presence of defects along the stacks,[24c,25] while these are more present in **SS-diOEt** than in **SS-dithiol** (*vide supra*).
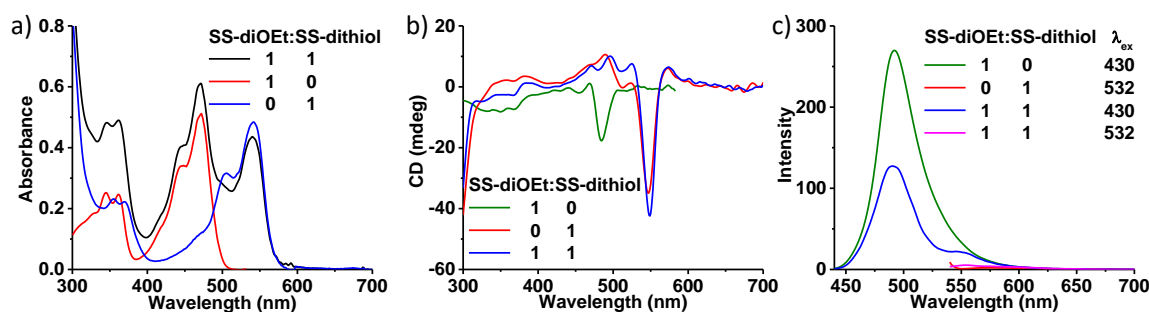
Figure 2.25. a) Absorption, b) CD, and c) emission spectra (λ_{ex} = 430 nm) of narcissistically self-sorted polymers of **SS-diOEt** and **SS-dithiol** obtained by mixing individually prepared homopolymers of **SS-diOEt** and **SS-dithiol**. ([**SS-diOEt**] = [**SS-dithiol**] = 2.5×10^{-5} M, TCE/MCH, 25/75 (v/v), l = 10 mm).
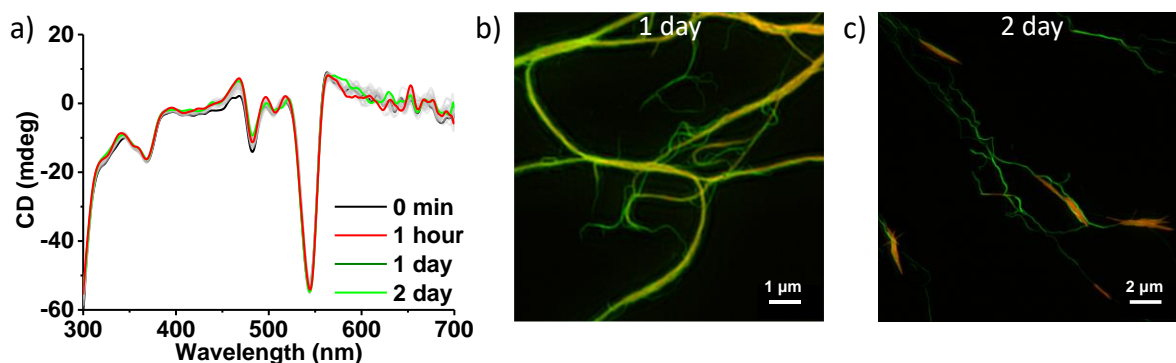
Figure 2.26. a) Time-dependent CD spectra of self-sorted stacks of **SS-diOEt** and **SS-dithiol** obtained by mixing individually prepared **SS-diOEt** and **SS-dithiol** homopolymers. SIM microscopy images of self-sorted polymers after b) 1 day and c) 2 day. (TCE/MCH, 25/75 (v/v)).
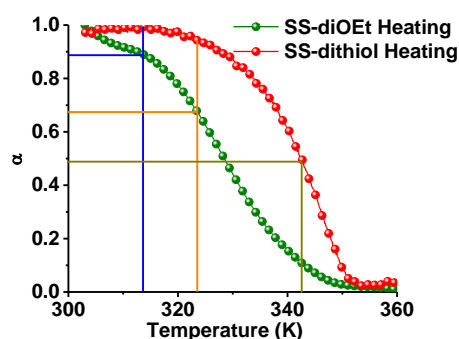
Figure 2.27. Heating curve of same concentration of **SS-diOEt** and **SS-dithiol** homopolymers showing their different amount of melting at different temperature and their different stability. ([**SS-diOEt**] = [**SS-dithiol**] = 2.5×10^{-5} M, TCE/MCH, 25/75 (v/v), l = 10 mm, obtained by probing the temperature-dependent absorbance changes at 480 for **SS-diOEt** and 550 nm for **SS-dithiol**).

	Melting % at 323K	Melting % at 343 K
SS-diOEt	22 %	90 %
SS-dithiol	5 %	53 %

Table 2.11. Tabulated melting percentages of **SS-diOEt** and **SS-dithiol** homopolymers at different temperatures obtained from the heating curve of Figure 2.27.

We have annealed the mixture of homopolymers at two temperatures (323 K and 353 K) in an attempt to investigate the effect of monomer exchange dynamics in the reorganization of structure and also to modulate the length distribution of the blocks. Thus, we sought of increasing the temperature of the system to increase the monomer exchange dynamics (Figure 2.28a). Further, we anticipated that the difference in the extent of melting of two homopolymers at a higher temperature, would lead to differential exchange dynamics for the two segments, and hence cooling down from high temperatures would affect the length distribution of the blocky segments in the resulting supramolecular copolymers. Interestingly on cooling the self-

58

sorted solution of the homopolymers from (heating and cooling rate = 1 K/min) 323 K and 353 K to room temperature leads to the formation of isolated supramolecular block copolymer chains as evident from the SIM images (Figures 2.28b and 2.28c). A large number of isolated chains in the SIM image allowed us to perform an unprecedented statistical analysis on dynamic supramolecular block copolymers to extract the degree of polymerization, block lengths, and dispersity similar to studies performed on polymeric blocky cylindrical micelles. Figure 2.28d shows the contour length distributions (CLD) of the degree of polymerization (top panel) and lengths of both block segments (middle and bottom), of the supramolecular block copolymers obtained from the analysis of "100 discrete" chains from SIM images. CLD analyses showed that the supramolecular block copolymers formed by the annealing showed excellent dispersity and length control as evident from the weight average length (L_w), number average length, (L_n) and the polydispersity index (PDI). The overall length of the supramolecular block copolymer chains obtained by annealing from 323K was calculated to be 2090 nm (L_n) and 2322 nm (L_w) with a PDI of 1.11. On the other hand, stacks obtained by annealing from 343 K showed an increase in the degree of polymerization (DP) as evident from the L_n and L_w of 5075 nm and 5393 nm, respectively with a PDI of 1.06 (Table 2.12). Thus, it is evident that the annealing process increases both the fraction of monomers in solution and the monomer exchange dynamics, thus favoring a high degree of polymerization while cooling down. A similar trend was also observed in the length distribution of both green and red block segments. L_n and L_w values for green blocks (**SS-diOEt)** in the supramolecular block
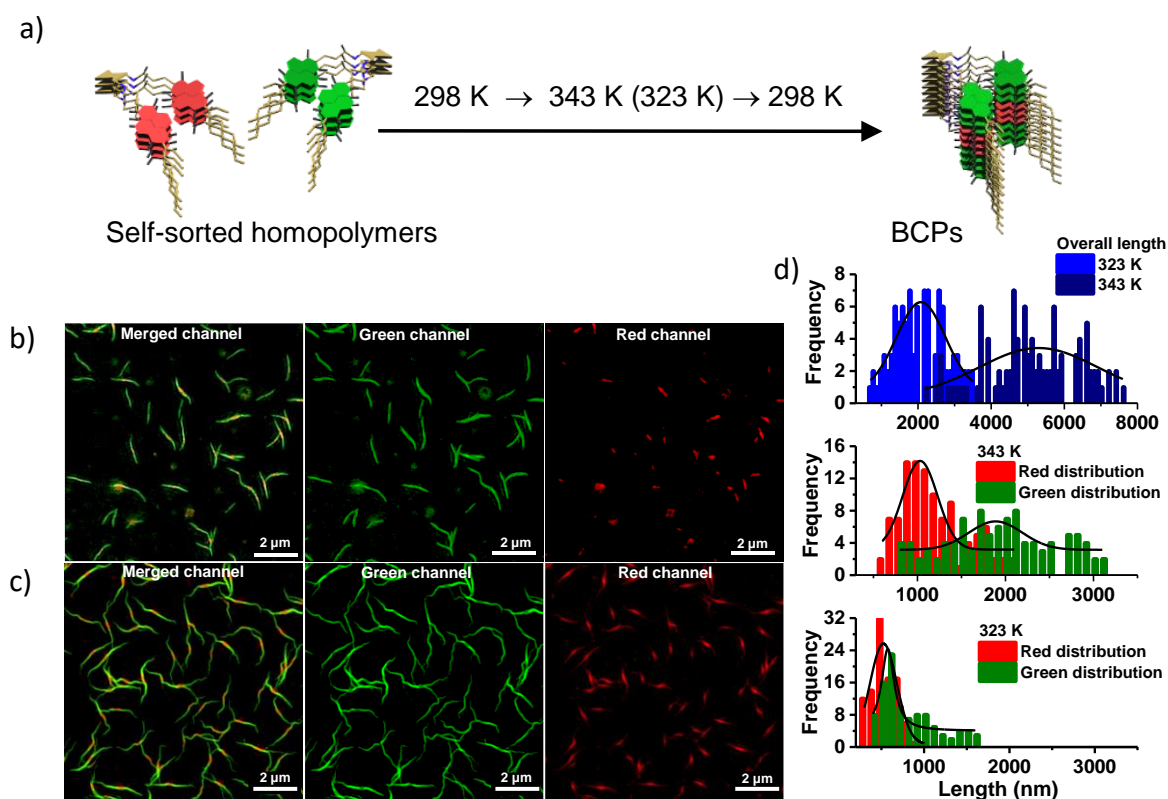
Figure 2.28. Distribution analyses of triblock microstructures. a) Schematic illustration of the annealing induced reorganization of self-sorted homopolymers to BCPs by slow cooling form 343 K and 323 K. SIM microscopy images of block copolymers in green, red and merged channel obtained via annealing from b) 323 K and c) 343 K (heating rate = cooling rate = 1 K/min). d) Contour length distribution analyses showing the average lengths of the BCPs (above) and both green and red blocks, upon the annealing process from 323 K and 343 K to 298 K. In each case, 100 individual BCP chains were counted to construct the distribution. ([**SS-diOEt**] = [**SS-dithiol**] = 2.5×10^{-5} M, TCE/MCH, 25/75 (v/v), l = 10 mm, (green channel: λ_{ex} = 488 nm, λ_{coll} = 495-575 nm), (red channel: λ_{ex} = 561 nm, λ_{coll} = 570-650 nm)).

Annealing Temperature	L_n (nm)	L_w (nm)	PDI
323 K	2090	2322	1.11
343 K	5075	5393	1.06

Table 2.12. Calculated number average length distribution (L_n), weight average length distribution (L_w) and polydispersity index (PDI) of overall block supramolecular copolymer at 323 K and 343 K.

Annealing Temperature	L_n (nm)	L_w (nm)	PDI
323 K	540	581	1.07
343 K	1195	1306	1.09

Table 2.13. Calculated number average length distribution (L_n), weight average length distribution (L_w) and polydispersity index (PDI) of red component in block supramolecular copolymer at 323 K and 343 K.

Annealing Temperature	L_n (nm)	L_w (nm)	PDI
323 K	800	935	1.16
343 K	1919	2115	1.10

Table 2.14. Calculated number average length distribution (L_n), weight average length distribution (L_w) and polydispersity index (PDI) of green component in block supramolecular copolymer at 323 K and 343 K.

copolymer annealed from 323 K, was calculated to be 800 nm and 935 nm (PDI~ 1.16), respectively whereas the red blocks (**SS-dithiol**) exhibited L_n and L_w values of 540 nm and 581 nm (PDI~1.07) (Figure 2.28d, Tables 2.13 and 2.14). However, in supramolecular block copolymers annealed from 343 K, the length of both blocks were increased leading to the increase in the overall length of the multicomponent stacks as observed (Green: $L_n =$ 1915 nm, $L_w =$ 2115 nm, PDI = 1.10; Red: $L_n =$ 1195 nm, $L_w =$ 1306 nm, PDI = 1.09) (Table 2.13, and 2.14).

It is worth noting that both the number and weight average lengths of the green (**SS-diOEt**) blocks are always higher than that of the red blocks (**SS-dithiol**) in the supramolecular block copolymers. We envisage that this could be due to the significantly higher interactions between the monomers of **SS-diOEt** compared to that of **SS-dithiol** monomers. This is similar to the chain copolymerization process of covalent systems, where higher reactivity of one of the monomers leads to a larger block length of the particular monomer. The length distribution analysis could not be measured for the extended supramolecular blocky copolymers obtained via the cooperative growth from the monomeric state at 363 K due to the entangled network of green and red segments. Interestingly, the topology of the supramolecular block copolymer synthesized by annealing the self-sorted homopolymers from 343 K and 323 K are found to be a green-red-green triblock structure with a narrow dispersity. This observation is in support of the spectroscopic studies which showed that nucleation of **SS-dithiol** monomers with higher T_e and subsequent heterogeneous seeded growth of the **SS-diOEt** monomers in a cooperative manner triggers the supramolecular block copolymerization.

2.3.6. Directional Energy Harvesting in Axial Organic Supramolecular Block Copolymer:
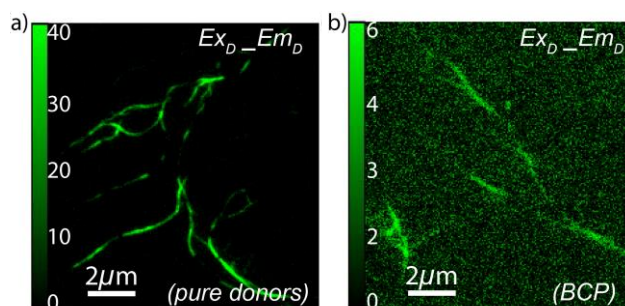
Figure 2.29. Average fluorescence intensity images in D-channel of a) pure donors, and b) donor in BC fibril, under identical experimental conditions.

As there is a considerable amount of overlap between the emission spectrum of **SS-diOEt** (energy donor (D)) and the absorption spectrum of **SS-dithiol** (energy acceptor (A)) monomers organized in the supramolecular block copolymers, we anticipated efficient energy migration along the pi-stacked chromophores organized along the fibers. Indeed, the bulk solution phase emission spectrum of these supramolecular donor-acceptor block copolymers, when excited the donor monomers (λ_{ex} = 430 nm), showed a quenching of donor emission (510 nm) with a concomitant two fold enhancement of the acceptor emission intensity (560 nm) when compared with the direct excitation of the acceptor. Such amplification in acceptor emission along with the quenching of the donor emission indicates the possibility of excitation migration and energy transfer between the donor-acceptor block segments.

The donors and the acceptors have arranged themselves in a segmented fashion within a single supramolecular block copolymer, where the acceptor segment resides at the middle and donor towards both ends (Figures 2.28b and 2.28c). This topology with alternatively stacked chromophoric segments (with either electronic or optical complementary monomers) of 300-500 nm length can be called as organic axial heterostructures with a linear donor-acceptor interface or junctions, reminiscent of a well-studied class of inorganic axial heterostructures.[2,3,4] This type of segmented arrangement of chromophores encouraged us to look into the energy transfer within a single D-A-D axial heterostructure. We wanted to investigate whether upon the excitation of donor molecules, is there any directional transfer of energy into the acceptor part or not?

To investigate the possibility of energy transfer, we performed spatially- and spectrally-resolved fluorescence microscopy of individual block copolymerized heterostructures. First, we identified single BC fibrils via direct excitation of the donor and acceptor blocks, with the
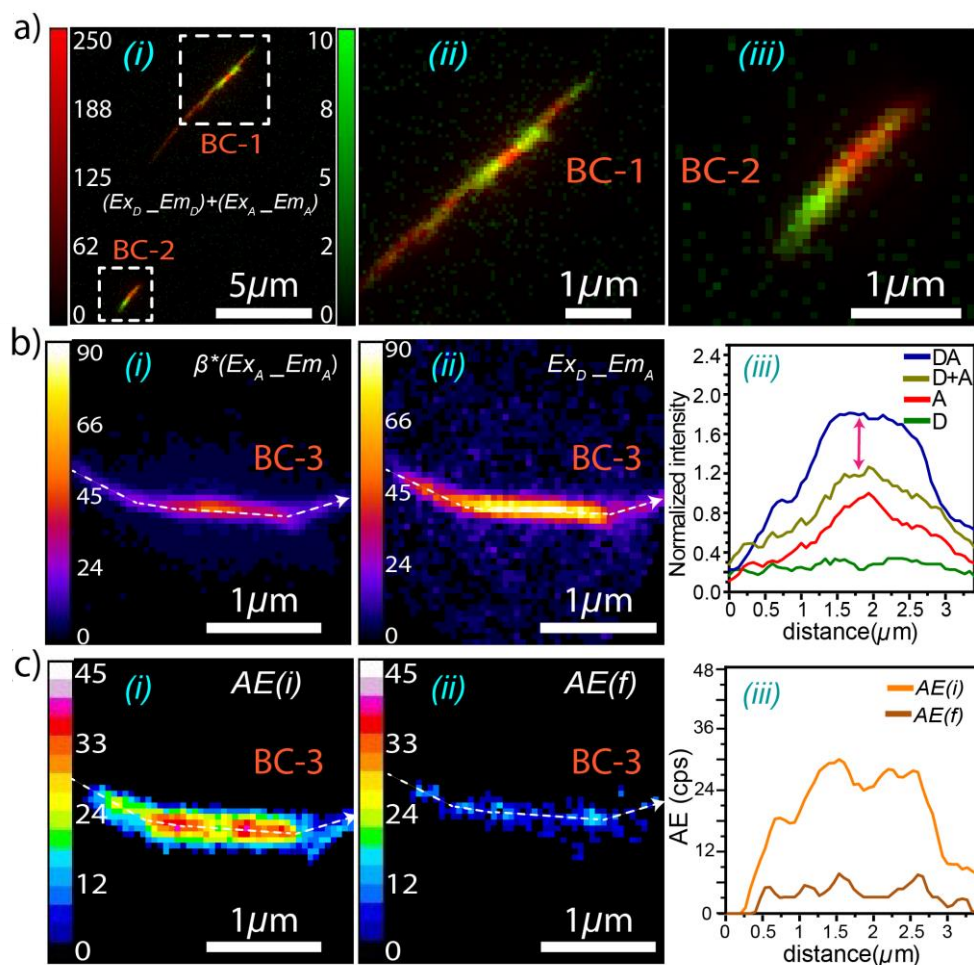
Figure 2.30. Spatially- and spectrally-resolved fluorescence images of individual supramolecular block copolymers (BC). Pseudo-colour colocalized average fluorescence image of BC fibrils is in a(i), and corresponding two representative fibrils BC-1 and BC-2 are in a(ii) and a(iii). The fluorescence image b(i) is the expected emission of only acceptors (Em_A) via direct excitation with 405 nm (Ex_D), and the sensitized emission of ac-ceptors from the same BC fibril is b(ii). The corresponding normalized intensity line profiles (along white dashed arrow) (b(iii)), showing the relative A-channel emission (Em_A) via 405 nm excitation (Ex_D) of individual donor and acceptor ([D], [A]), their cumulative intensity ([D+A]), and sensitized emission due to energy transfer [DA]. Intensities are normalized with the acceptor emission intensity [A]. The spatially-resolved acceptor intensity enhancement (AIE) of BC-3 at pre- and post-acceptor photo-bleaching are in c(i) and c(ii), respectively, and the corresponding line profiles are in c(iii).

collection of respective emissions in two energetically separated (D and A) detection channels. Careful superposition of these two images of the same area allowed us to generate an energy-mapped pseudo color colocalized image that provides quantitative information on the spatial variation in the intensity of donors (colored green) and acceptors (colored red). In such energy-mapped color images (Figure 2.30a(i)), several spatially segregated single BC fibrils with donor and acceptor blocks can be readily visualized. Two representative BC fibrils, BC-1, and BC-2 are shown in Figure 2.30a (ii and iii), which clearly depict the alternating segment distribution of donor and acceptor blocks within each BC fibril. It is interesting to note that, we always find that the donor segments within the BC fibrils have extremely feeble fluorescence when excited directly. This is in stark contrast to donor-only fibrils, where the emission is (typically) at least an order of magnitude higher when imaged under identical conditions (Figure 2.29). This dramatic quenching of emission intensity of donors provides indirect evidence of excitation energy migration from the donor blocks to adjacent acceptor blocks within the BC fibrils. To thoroughly investigate energy transfer (or excitation energy migration) between donor and acceptor blocks, we performed dual-excitation sensitized emission imaging of individual BC heterostructures.[30] This was achieved by imaging of the acceptor emission (545-635 nm) for a single fibril (BC-3) via separately exciting the acceptors (532 nm) and the donors (405 nm). First, we obtained a fluorescence intensity image of BC-3 via direct excitation of the acceptors, which was then factorized by the relative change in the extinction coefficients of the acceptor at the two excitation wavelengths ($\epsilon_{405}/\epsilon_{532}$). This operation yields the emission intensity of the acceptors due to their direct excitation at the donor excitation wavelength (Figure 2.30b(i)). As the contribution of the donor emission in the acceptor channel was nominal (verified using pure donor blocks was excited using 405 nm, Figure 2.31), Figure 2.30b(i) effectively portrays the maximum expected emission intensity over the entire BC fibril in the absence of any energy transfer. However, upon selective excitation of the donors in the single BC fibrils, we find significantly enhanced emission in the acceptor segment (Figure 2.30b(ii)), attributed to the sensitized emission of the acceptors (via donors). Such enhancement of the acceptor emission, as portrayed in the spatial distribution of intensities over BC-3 (Figure 2.30b(iii)), serves as a strong indicator of excitation energy transfer from flacking donor blocks to adjacent acceptor blocks in each BC fibril.
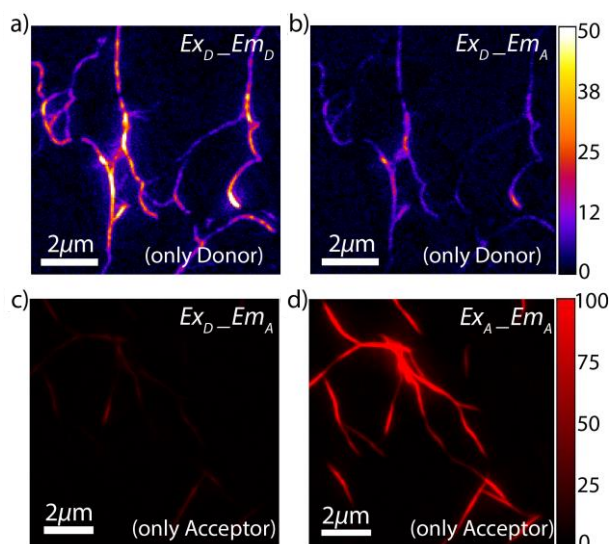
Figure 2.31. Average fluorescence intensity images of same area of only donor sample (**SS-diOEt**) via donor wavelength excitation, emission collected in a) D-channel and b) A-channel. Average fluorescence intensity images with emission in A-channel of same area of only acceptor sample (**SS-dithiol**) via excitation at c) donor wavelength and d) acceptor wavelength.
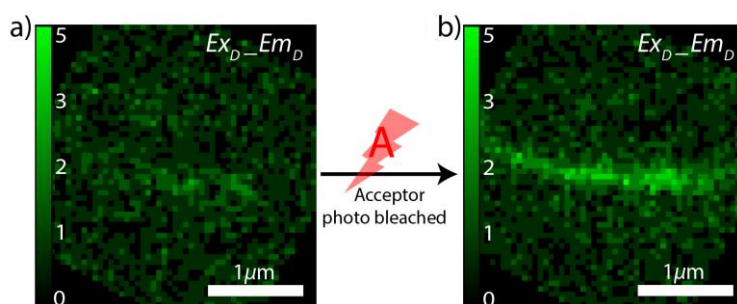
Figure 2.32. Average fluorescence intensity images of donors in D-channel of BC-3 with a) pre photo-bleaching, and b) post photo-bleaching of acceptor molecules.
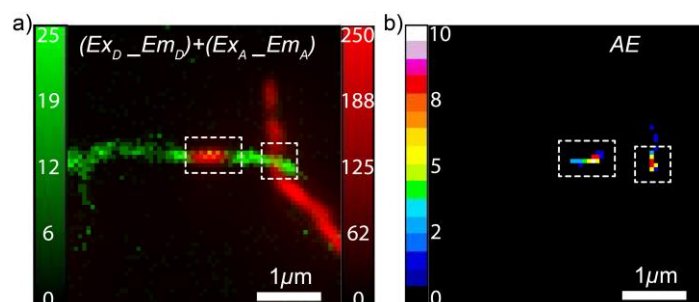
Figure 2.33. Pseudo colour colocalized image in a) of another area, and corresponding *AE* (acceptor intensity enhancement) image in b).
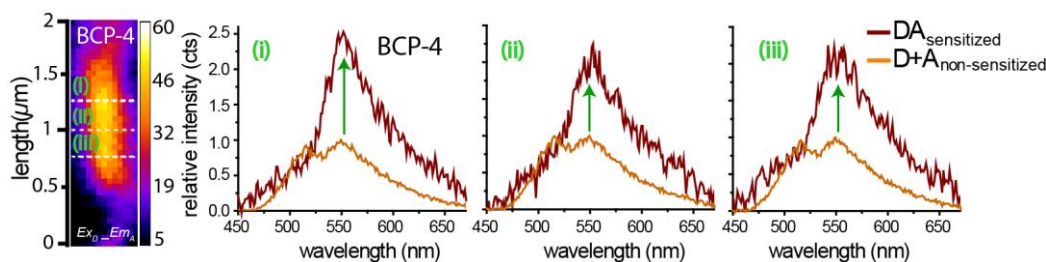
Figure 2.34. Spatially-resolved spectra at three different positions (marked with white dashed rectangles) of an individual BC fibril (BC-4). $DA_{sensitized}$ and $D+A_{non-sensitized}$ refer to the emission spectra due to sensitization and without sensitization.

The sensitized fluorescence image of BC-3 (Figure 2.30c(i)) depicts the acceptor intensity enhancement (AE) due to energy transfer from donors. Interestingly, we find substantial spatial non-uniformity in the AE for a single BC fibril; for instance, the central region of BC-3 has considerably lower sensitized emission owing to the absence of the donors within in the acceptor segment as compared to that in the interface regions where both donors and acceptors are present. Further, we checked with narcissistically self-sorted donor and acceptor supramolecular stacks and observed AE only at regions where both fibrils are in contact due to the close proximity of donors and acceptors (Figure 2.33). To corroborate whether the observed enhancement of acceptor emission (Figure 2.30c(i)) indeed owes to excitation migration from the donor segments,[32] we selectively photo-bleached the acceptors of BC-3 using intense 532 nm laser excitation such that the donor molecules remain unaffected. We find that upon progressive irreversible photo-bleaching of acceptors, there is a concurrent enhancement in the emission of donors (Figure 2.32), owing to the unavailability of enough acceptors to transfer their excitation energy. As a consequence of the obstruction in this process, the sensitized emission image of BC-3 after photo-degradation of the acceptors (Figure 2.30c(ii)) shows nominal AE. It is relevant to mention that spatially-resolved fluorescence spectroscopy measurements on single BC heterostructures (Figure 2.34) further validate the above dual-excitation sensitized emission imaging results, which provides support to the hypothesis of energy migration from one block/segment to another.

2.4. Conclusion:

In conclusion, we have explored the cooperative supramolecular block copolymerization of optically distinct core-substituted naphthalenediimde (cNDI) monomers with slightly different substituents at the core for the synthesis of light harvesting organic heterostructure. The characteristic and distinct optical properties of core-substituted NDI derivatives, which are sensitive to intermolecular interactions aided the spectroscopic probing of the microstructure

during thermodynamically driven supramolecular copolymerization. Distinct green and red fluorescence of the **SS-diOEt** and **SS-dithiol** stacked monomers, respectively facilitated the structural characterization of multi-block microstructure of these supramolecular BCPs via the visualization through SIM. Further, the effective fluorescence imaging allowed a unique size distribution analysis of individual blocks which showed a narrow polydispersity with a PDI of 1.1. The free energy data for the **SS-dithiol** and **SS-diOEt** intermixing and the comprehension of the exchange mechanisms in these BCPs obtained from the CG simulations helped us in rationalizing the experimental results. Finally, spatially- and spectrally- resolved FRET based microscopy studies on single BCP chains, showed directional light harvesting along the axial heterojunctions, thus demonstrating its remarkable potential as functional organic heterostructures.

Supramolecular block copolymerization from monomeric state of components presented here follows a nucleation growth mechanism and hence reminiscent of classical chain-growth copolymerization of covalent polymers, where blocky organization monomers is determined by its reactivity ratio. We envisage that this synthetic strategy can be generalized for the synthesis of a variety of axial organic heterostructures with stable segmented microstructure for diverse optoelectronic applications and catalysis.

2.5. Experimental Section (Spectroscopy and Microscopy):

General Methods:

Materials: All chemicals were purchased from the commercial sources and were used as such without any further purification. Spectroscopic grade solvents were used for all spectroscopic measurements.

NMR Measurements: NMR spectra were recorded with a Bruker AVANCE 400 (400 MHz) Fourier transform NMR spectrometer with chemical shifts reported in parts per million (ppm) with respect to TMS. Splitting patterns are designated as s, singlet; d, doublet; bs, broad singlet; m, multiplet; t, triplet.

Matrix-Assisted Laser Desorption Ionization (MALDI): MALDI was performed on a Bruker daltonics Autoflex Speed MALDI TOF System (GT0263G201) spectrometer using trans-2-[3-(4-tert-Butylphenyl)-2-methyl-2-propenylidene] malononitrile (DCTB) and α-Cyano-4-hydroxy-cinnamic acid (CCA) as the matrix.

Optical Measurements: UV-Visible absorption spectra were recorded on a Perkin Elmer Lambda 900 UV-Vis-NIR Spectrometer and emission spectra were recorded on Perkin Elmer LS 55 Luminescence Spectrometer. Fluorescence spectra of solutions were recorded with 430

nm and 530 nm excitation wavelength. 10 mm × 10 mm quartz cuvettes were used for measurements. Circular Dichroism measurements were performed on a JASCO J-815 spectrometer where the sensitivity, time constant, and scan rate were chosen appropriately. Corresponding temperature-dependent measurements were performed with a CDF – 426S/15 Peltier-type temperature controll.

Fitting of Cooling Curves: Nucleation-elongation model was fitted using MatlabR2008b software.

Fluorescence Lifetime Measurements: Time-resolved decay experiments were recorded on a Horiba Delta Flex Time-Correlated Single Photon Counting (TCSPC) instrument. A 442 nm nano-LED and 532 nm nano-LED with a pulse repetition rate of 1 MHz was used as the light source. The instrument response function (IRF) was collected by using a scatterer (Ludox AS40 colloidal silica, Sigma Aldrich). For both 442 nm LED and 532 nm nano-LED light source, the instrumental full width at half maximum including detector response was 0.2 ns. The excited state decay of the sample was collected by fixing the emission wavelength. The decay was fitted to appropriate best fit multiexponential decay using IBH software (DAS6).

Transmission Electron Microscopy (TEM): TEM measurements were performed on JEOL JEM 3010 operated at 300 kV. Samples were prepared by placing a drop of solution on carbon coated copper grids followed by drying at room temperature. The images were recorded with an operating voltage of 300 kV.

Structured Illumination Microscopy (SIM): Optical setup for imaging in Structured Illumination Microscopy (SIM) method: The fluorescence images of supramolecular polymers were acquired using an inverted Zeiss ELYRA PS1 microscope in structured illumination mode. Two lasers channel I - 488 nm (200 mW) (Green channel) and channel II - 561 nm (200 mW) (Red channel) have been used for excitation of **SS-diOEt** and **SS-dithiol** fluorophores. 10% laser power from the objective top was used for structured illumination imaging. Imaging was performed using a Zeiss oil–immersion objective (Plan–apochromat 63x/1.40 Oil DIC M27, numerical aperture (NA) 1.40 oil). Fluorescence light was spectrally filtered with emission filters for channel I - MBS–488+EF BP 495–575/LP 750 for laser line 488 nm and for channel II - MBS– 561+EF BP 570–650/LP 750 for laser line 561 nm and and imaged using a PCO edge sCMOS camera (quantum yield >70%). Structured illumination images were processed using structured illumination analysis package for Zen software (Zeiss). Additional software have been used for colour adjustment (ImageJ). The channels were merged to investigate the spatial correlation between green- and red-emitting fibers.

Polydispersity Index (PDI) Calculation From SIM Images: SIM images were recorded for block copolymers via merging channel I and channel II. Then 100 fibres were selected from different regions of the grid and analysed using ImageJ software package developed by US. National Institute of Health to calculate the length of green stacks, red stacks and the overall length of the block copolymer. The average length and PDI were calculated using following equations 1-3 equations. Where, Ni is the number of fibres chosen for analysis and Li is the length of fibres for the sample.

$$\text{Number average length, } L_n = \sum_{i=1}^{n} \frac{N_i L_i}{N_i} \tag{1}$$

$$\text{Weight average length, } L_w = \sum_{i=1}^{n} \frac{N_i L_i^2}{N_i L_i} \tag{2}$$

$$\text{Polydispersity index, } PDI = \frac{L_w}{L_n} \tag{3}$$

2.6. Synthetic Schemes and Procedures:
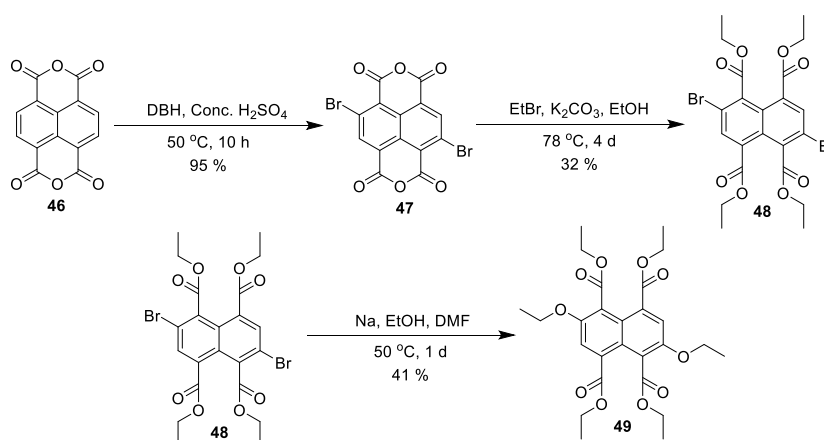
Scheme 2.1. Synthesis of molecules **47** to **49**.
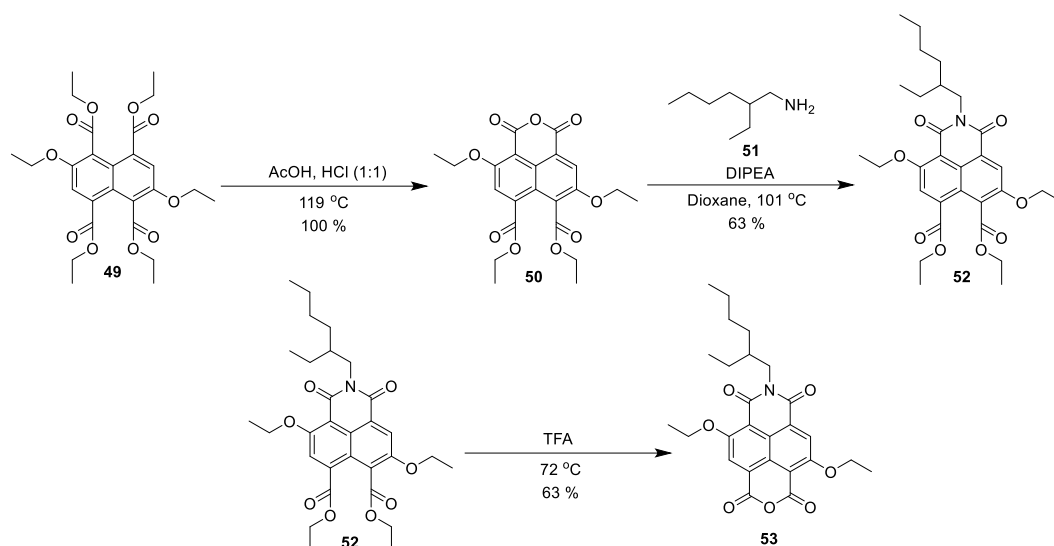
Scheme 2.2. Synthesis of molecules **50** to **53**.
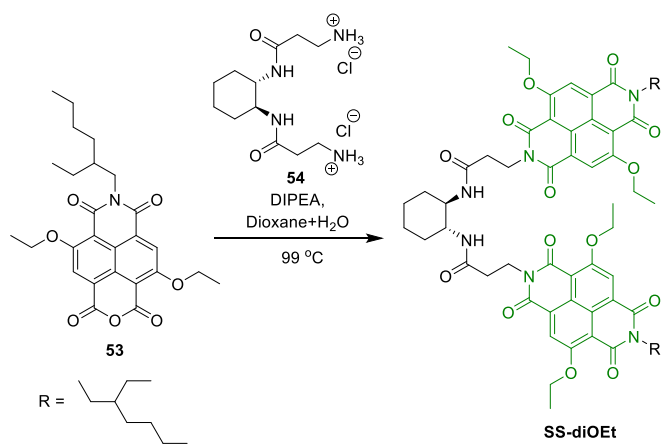
Scheme 2.3. Synthesis of **SS-diOEt**.
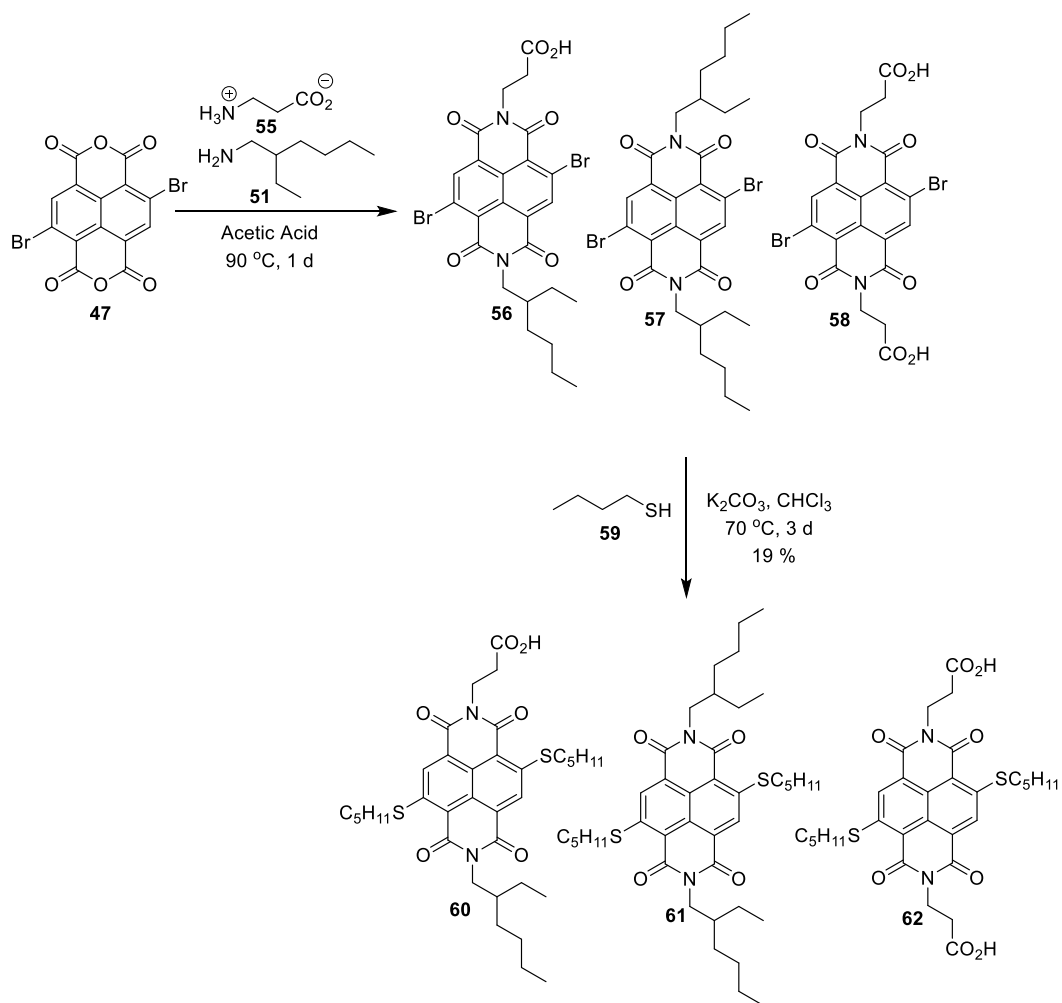
Scheme 2.4. Synthetic route to molecule **60**.
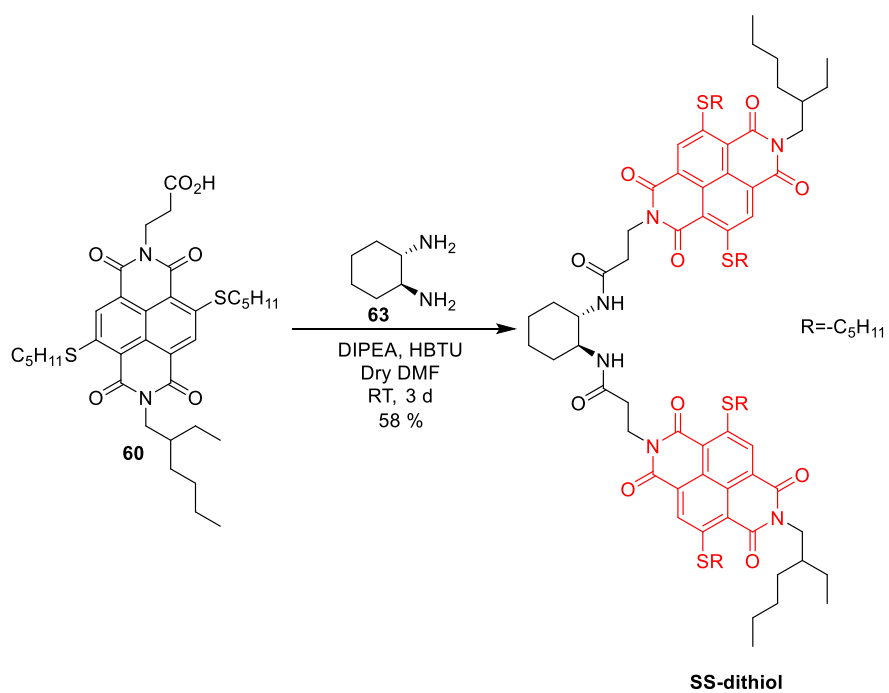
Scheme 2.5. Synthetic route to molecule **SS-dithiol**.

SS-dithiol and **SS-diOEt** was synthesized using the synthetic route depicted in Scheme 2.1 to Scheme 2.5. Molecule **54** was synthesized following earlier reported procedure.[27a]

Synthesis of 47: Commercially available naphthalene dianhydride (**46**) (6 g, 22.39 mmol) was taken in a single necked 250 mL round bottom flask and 50 mL of concentrated sulphuric acid added at 0 °C. The mixture was stirred over ice to dissolve **46**. Then, DBH (1,3-Dibromo-5,5-dimethylhydantoin) (8 g, 27.97 mmol) was added to the reaction mixture in 4 portions over an hour at 0-25 °C. The reaction was allowed to proceed at 50 °C for 10 hours and the progress of reaction was monitored using ^{1}H NMR in DMSO-d_6. The reaction mixture was poured into crushed ice to precipitate **47** as a yellow solid. The product was filtered and washed with methanol. The product was air dried overnight to afford **47** in 95 % yield. ^{1}H NMR: (400 MHz, DMSO-d_6, ppm): δ = 8.78 (s, 2H); ^{13}C NMR: (100 MHz, DMSO-d_6, ppm): δ = 157.9, 156.4, 137.5, 129.4, 127.4, 124.2, 123.4.

Synthesis of 48: 47 (8.37 g, 19.65 mmol) was taken in a 250 mL round bottom flask with ethyl bromide (117.76 g, 1080 mmol) and potassium carbonate (16.29 g, 117.9 mmol). 80 mL of ethanol was added to this and the reaction was refluxed at 78 °C for 4 days. The color of the reaction mixture changed from yellow to white during the course of the reaction. At the completion of the reaction, the reaction mixture was worked up with ethyl acetate and water. The organic layer was collected and evaporated under vacuum to dryness. The crude mixture was purified with column chromatography using 10-40 % ethyl acetate in hexane to obtain product of **48** as a white crystalline powder in 32 % yield. ^{1}H NMR: (400 MHz, CDCl$_3$, ppm): δ = 8.07 (s, 2H), 4.35-4.45 (m, 8H), 1.40-1.45 (m, 12H); ^{13}C NMR: (100 MHz, CDCl3 ppm): δ = 166.72, 166.55, 134.89, 134.68, 133.08, 128.85, 121.65, 62.71, 62.63, 14.40, 14.19; HRMS (ESI, positive mode) m/z: calculated for $C_{22}H_{22}Br_2O_8$: 573.9661, found: 590.0021 [M+NH$_4$]$^+$.

Synthesis of 49: Sodium (8 g, 347.83 mmol) was cut, rolled into strips and taken into a three necked 250 mL round bottom flask. Under nitrogen atmosphere, dry ethanol (150 ml) was injected in increments of 30 ml, over ice, till the sodium was fully dissolved, to give a cloudy white viscous suspension of freshly prepared sodium ethoxide. Separately, a suspension of **48** (8.44 g, 14.69 mmol) in 30 mL of 1:1 ethanol: dry DMF was prepared and introduced into the reaction mixture drop wise. The color of the reaction mixture deepens as the reaction proceeds. Following this, the reaction mixture was allowed to stir for 24 hours at 50 °C. Upon consumption of 3, the reaction mixture was worked up with CH$_2$Cl$_2$, and 1 N HCl. The organic layer was evaporated under vacuum. The crude was purified using 0-20 % ethyl acetate: hexane solvent gradient during column chromatography. The pure product was obtained as yellow powder in 41 % yield. ^{1}H NMR: (400 MHz, CDCl$_3$, ppm): δ = 7.65 (s, 2H), 4.35 (q, 8H, J = 8

Hz), 4.20 (q, 4H, J = 6.8 Hz), 1.25-1.57 (m, 18 H); ^{13}C NMR: (100 MHz, CDCl$_3$, ppm): δ = 168.03, 167.04, 153.56, 133.30, 125.23, 120.64, 119.61, 66.36, 62.00, 61.49, 15.13, 14.32, 14.30; HRMS (ESI, positive mode) m/z: calculated for C$_{26}$H$_{32}$O$_{10}$: 504.1995, found: 527.1880 [M+Na]$^+$.

Synthesis of 50: 300 mg of **49** was taken in a single necked RB and in it 10 mL of acetic acid and 2 mL of HCl was added and refluxed at 119 ˚C. The progress of the reaction was monitored by TLC and after complete consumption of starting material the excess acetic acid was evaporated and the crude was extracted using ethyl acetate water mixture. The organic layer was collected and dried over sodium sulphate to get the pure product in 97 % yield. ^{1}H NMR: (400 MHz, CDCl$_3$, ppm): 8.36 (s, 1H), 7.70 (s, 1H), 4.51-4.36 (m, 6H), 4.29 (q, 2H), 1.61 (t, 3H), 1.52-1.38 (m, 9H); ^{13}C NMR: (100 MHz, CDCl$_3$, ppm): δ = 166.7, 166.1, 160.7, 160.4, 155.7, 154.2, 137.5, 128.0, 124.3, 121.7, 121.0, 120.3, 118.6, 104.7, 66.3, 66.0, 62.5, 61.8, 14.6, 14.0; HRMS (ESI, positive mode) m/z: calculated for C$_{22}$H$_{22}$O$_9$: 430.1264, found: 431.1265 [M+H]$^+$.

Synthesis of 52: 200 mg of **50** was taken in a single neck RB and in it 20 mL of dioxane, 90 mg of **51** and 90 mg of N,N-Diisopropylethylamine (DIPEA) was added and refluxed at 101 ˚C. The progress of the reaction was monitored by NMR. After completion of the reaction the excess dioxane was evaporated under reduced pressure and the crude mixture was extracted using chloroform and 1 (N) HCl. The organic layer was collected and evaporated to dryness to get the crude product which was further purified using column chromatography with a gradient ranging from 50 % ethyl acetate in hexane to 80 % ethyl acetate in hexane to get product as a brown liquid in 35 % yield. ^{1}H NMR: (400 MHz, CDCl$_3$, ppm): 8.42 (s, 1H), 7.72 (s, 1H), 4.38-4.48 (m, 8H), 4.30 (q, 2H), 4.05-4.16 (q, 2H), 1.90-2.0 (m, 1H), 1.59-1.65 (m, 4H), 1.32-1.45 (m, 14), 0.7-0.8 (m, 6H); ^{13}C NMR: (100 MHz, CDCl$_3$, ppm): δ = 167.65, 167.01, 163.77, 162.11, 159.89, 154.75, 136.55, 127.66, 126.57, 124.99, 123.24, 122.41, 119.96, 119.96, 109.82, 66.50, 66.28, 62.61, 61.98, 44.63, 38.00, 31.08, 29.01, 24.45, 23.42, 15.21, 15.15, 14.44, 14.41, 14.39, 11.02; HRMS (ESI, positive mode) m/z: calculated for C$_{30}$H$_{39}$NO$_8$: 541.2676, Found: 542.2731 [M+H]$^+$.

Synthesis of 53: 60 mg of **52** was taken in a single neck RB and in it trifluoroacetic acid (TFA) was added and refluxed at 72 ˚C. The progress of the reaction was monitored by thin layer chromatography and after complete consumption of starting materials the excess TFA was evaporated and the reaction mixture was extracted using chloroform water. The organic layer was collected and evaporated to get the crude product which was further purified using column chromatography with a gradient ranging from chloroform to 2 % methanol in chloroform to

get a yellow solid in 86 % yield. ^{1}H NMR: (400 MHz, CDCl$_3$, ppm): 8.48 (s, 1H), 8.44 (s, 1H), 4.49-4.56 (m, 4H), 4.06-4.16 (m, 2H), 1.91-2.08 (q, 3H), 1.65 (t, 6H), 1.31-1.44 (m, 15H), 0.85-0.94 (m, 6H); ^{13}C NMR: (100 MHz, CDCl$_3$, ppm): δ = 162.75, 161.66, 161.29, 160.26, 160.22, 155.61, 139.62, 128.93, 126.15, 124.02, 123.83, 123.57, 121.89, 120.02, 114.40, 112.11, 107.11, 67.00, 66.98, 45.00, 38.11, 34.16, 32.27, 31.96, 31.03, 30.04, 29.97, 29.86, 29.70, 29.51, 29.31, 28.95, 24.36, 23.43, 23.03, 15.07, 15.02, 14.44, 14.41, 10.96. HRMS (ESI, positive mode) m/z: calculated for C$_{26}$H$_{29}$NO$_7$: 467.1944, Found: 468.1998 [M+H]$^+$.

Synthesis of SS-diOEt: 100 mg of compound **53** was taken in a single necked RB and in it 32 mg of **54** and 12 mg of DIPEA dissolved in 20 mL of dioxane and 20 mL of water was added and refluxed at 99 ˚C. The progress of the reaction was monitored by NMR and after completion of the reaction excess dioxane was evaporated and the reaction mixture was extracted using 1 (N) HCl and chloroform solution. The organic was collected and evaporated to dryness. The crude mixture was purified via column chromatography with a gradient ranging from chloroform to 1 % methanol in chloroform followed by using SX-3 bio beads in chloroform. The pure product was obtained as yellow powder in 18 % yield. ^{1}H NMR: (400 MHz, CDCl$_3$, ppm): δ = 8.39 (d, 4H), 6.75 (d, 2H), 4.48 (m, 12H), 4.09 (t, 4H), 3.58 (m, 2H), 2.69 (t, 4H), 2.05-2.08 (m, 2H), 1.94-1.95 (m, 2H), 1.62-1.67 (m, 12 H), 1.19-1.39 (m, 22 H) 0.8-0.94 (m, 12 H); ^{13}C NMR: (150 MHz, DMSO-d$_6$, ppm): δ = 179.14, 171.25, 162.68, 162.30, 161.29, 161.24, 161.10, 159.86, 127.34, 126.70, 126.63, 123.53, 123.47, 119.82, 119.43, 66.30, 66.17, 53.24, 44.47, 42.951, 37.71, 36.62, 30.66, 30.56, 29.72, 29.68, 29.34, 28.62, 23.17, 23.08, 14.85, 14.08, 10.62; HRMS (APCI, positive mode) m/z: calculated for C$_{64}$H$_{79}$N$_6$O$_{14}$: 1154.5654, found: 1155.5652 [M+H]$^+$; MALDI-TOF (CCA matrix, positive mode): m/z calculated for C$_{64}$H$_{78}$N$_6$O$_{14}$: 1154.5576, found: 1155.776 [M+H]$^+$.

Synthesis of 56: 1 g of **47** (2.34 mmol) was taken in a round bottom flask (RB) and 0.91 g (7.04 mmol) of 2-ethylhexan-1-amine (**51**) and 0.627 g (7.04 mmol) of 3-ammoniopropanoate (**55**) dissolved in 90 ml of acetic acid was added slowly into it. The reaction mixture was then refluxed at 363 K for 1 day. After 1 day the reaction mixture was cooled to room temperature and 100 ml water was poured into it to precipitate out the products. Obtained precipitate was filtered and subsequently washed with methanol to remove the excess water and acetic acid. The precipitate was dried under vacuum and obtained as a mixture of product **56**, **57** and **58**. Due to the insolubility of the products, no purification was done and the crude mixture was directly used for the subsequent reaction.

Synthesis of 60: 500 mg of the crude mixture containing **56**, **57** and **58** was taken in a RB flask and 1.71 g of pentane-1-thiol (**59**), 2.28 g of K$_2$CO$_3$ and 50 mL of chloroform was added in it.

The reaction mixture was refluxed at 323 K for 3 days. After 3 days the excess pentane thiol was evaporated under reduced pressure and the resultant crude mixture was extracted using chloroform and 1 N HCl solution. The organic layer was collected and evaporated to get the crude product which was further purified via column chromatography using a solvent gradient ranging from pure chloroform to 15 % methanol in chloroform to get 300 mg of the pure product as a red powder. Combined yield of step 1 and 2 (Scheme 2.4): 19 %; ^{1}H NMR: (400 MHz, CDCl$_3$, ppm): δ = 8.67 (S, 2H, H^{Ar}), 4.54 (t, J = 7.2 Hz, 2H, CH$_2^{\beta\text{-alanine}}$), 4.17 (m, 2H, CH$_2^{\text{ethylhexaylamine}}$), 3.21 (q, J = 8 Hz, 4H, SCH$_2$), 2.81-2.88 (m, 2H, CH$_2^{\beta\text{-alanine}}$), 1.84-1.98 (m, 8H, CH$_2^{\text{ethylhexaylamine}}$, CH$_2^{\text{pentanethiol}}$), 1.61-1.54 (m, 4H, CH$_2^{\text{pentanethiol}}$), 1.25-1.47 (m, 10H, CH$_2^{\text{ethylhexaylamine}}$, CH$_2^{\text{pentanethiol}}$), 0.87-0.95 (m, 12H, CH$_3^{\text{ethylhexaylamine}}$, CH$_3^{\text{pentanethiol}}$); ^{13}C NMR: (100 MHz, CDCl$_3$, ppm): δ = 163.89, 163.50, 163.01, 162.65, 149.46, 149.10, 128.69.60, 128.61, 125.24, 124.15, 123.61, 119.64, 118.99, 45.22, 38.14, 36.71, 32.68, 32.63, 31.67, 31.63, 31.04, 28.95, 27.96, 27.89, 24.37, 23.45, 22.67, 14.40, 14.24, 10.96; HRMS (ESI, positive mode) m/z: calculated for C$_{35}$H$_{46}$N$_2$O$_6$S$_2$: 654.2797, found for **60**: 655.2747 [M+H]$^+$.

Synthesis of SS-dithiol: 60 mg (0.091 mmol) of **60**, 16 mg (0.124 mmol) of 2-(1H-benzotriazol-1-yl)-1,1,3,3-tetramethyluronium Hexafluorophosphate Benzotriazole Tetramethyl Uronium (HBTU) and 39 mg (0.104 mmol) of N,N-Diisopropylethylamine (DIPEA) were taken in a two necked 50 ml RB and 5 mL of DMF was added into it at room temperature and stirred for 30 minutes under nitrogen atmosphere. After 30 minutes, 5 mg (0.041 mmol) of (SS)-*trans*-1,2-bis(amido)-cyclohexane (**63**) dissolved in 5 ml of DMF was drop wise added into the reaction mixture. The reaction was stirred at room temperature for 3 days. Progress of the reaction was monitored using TLC too ensure complete consumption of amine. After completion of the reaction the excess DMF was evaporated under reduced pressure and it was extracted using saturated K$_2$CO$_3$ and chloroform solution. The organic layer was collected and further extracted with chloroform and water. The final organic layer was evaporated under reduced pressure and a column chromatography was performed with a solvent gradient ranging from pure chloroform to 2 % methanol chloroform to get 35 mg of the product as a red powder. Yield: 58 %. ^{1}H NMR: (400 MHz, CDCl$_3$, ppm): δ = 8.46 (d, 2H, H^{Ar}), 6.73 (brs, 2H, H^{NH}), 4.51 (t, J = 6.4 Hz, 2H, CH$_2^{\beta\text{-alanine}}$), 4.12 (t, J = 6.4 Hz, 2H, CH$_2^{\text{ethylhexaylamine}}$), 3.60 (t, J = 10 Hz, 2H, CH$_2^{\text{Cyclohexane}}$), 3.07 (t, J = 8 Hz, 8H, SCH$_2$), 2.88-2.71 (m, 4H, CH$_2^{\text{pentanethiol}}$), 1.93-2.08 (m, 4H, CH$_2^{\text{Cyclohexane}}$), 1.69-1.88 (m, 10H, CH$_2^{\text{ethylhexaylamine}}$, CH$_2^{\text{pentanethiol}}$, CH$_2^{\text{Cyclohexane}}$), 1.25-1.44 (m, 42H, CH$_2^{\text{ethylhexaylamine}}$, CH$_2^{\text{pentanethiol}}$), 0.85-0.97 (m, 24H, CH$_3^{\text{ethylhexaylamine}}$, CH$_3^{\text{pentanethiol}}$); Elemental analysis calculated for: C$_{76}$H$_{102}$N$_6$O$_{10}$S$_4$: C 65.26, H 6.40, N 6.65, S 8.24, found: C 65.21, H 6.80, N

6.94, S 8.56; MALDI-TOF (DCTB matrix, positive mode): m/z: calculated for $C_{35}H_{46}N_2O_6S_2$: 1387.91, found for **SS-dithiol**: 1409.68 $[M+Na]^+$. ^{13}C NMR could not be recorded due to insolubility of **SS-dithiol** in common deuterated solvents at high concentration and precipitation over time.

2.7. Experimental Procedures:

Protocol I: Sample Preparation Protocol for Individual Self-assembly Study: A high concentration stock solution of **SS-diOEt** and **SS-dithiol** was prepared in TCE (1,1,2,2-Tetrachloroethane) (c = 5×10^{-3} M) and then appropriate volume was injected into a mixture of TCE and MCH (Methylcyclohexane) to adjust the final concentration and solvent composition to the required percentages (TCE/MCH, 25/75 (v/v) for self-assembled solutions).

For example, 12.5 μL of 5×10^{-3} M stock of **SS-diOEt** is added to a premixed solution of 612.5 μL of TCE and in 1875 μL of methylcyclohexane (MCH) to prepare the final self-assembling solution of 2.5×10^{-5} M, TCE/MCH, 25/75 (v/v) with total 2500 μL sample volueme.

Protocol II: Sample Preparation Protocol for Self-assembly Study of the Mixture: Self-assembled solution containing a mixture of **SS-dithiol** and **SS-diOEt** was prepared by injecting the stock solution in TCE (c = 5×10^{-3} M) into TCE and MCH solvent mixture to adjust the solvent composition to 25/75 (v/v) and concentration of **SS-dithiol** and **SS-diOEt** to 2.5×10^{-5} M and then the required experiments are performed.

Protocol III: Sample Preparation Protocol for Annealing Experiments at Different Temperature: To prepare the as mixed self-sorted solution, self-assembled solution of **SS-diOEt** and **SS-dithiol** were taken at high concentration (c = 5×10^{-5} M) and equal volumes were mixed to get a final concentration of **SS-dithiol** and **SS-diOEt** to 2.5×10^{-5} M. This self-sorted solution was then heated to the respective anneling temperature with a heating rate of 1 K/min and cooled to 298 K with a cooling rate of 1 K/min to get the block copolymers.

2.8. Experimental Section (Spatially- and Spectrally-Resolved FRET Microscopy-Based Techniques on Block Copolymers):

2.8.1. Experimental Procedures:

2.8.1.1. Wide-field Fluorescence Microscopy and Data Analyses:

A home built inverted wide-field optical fluorescence microscope (Nikon TE2000U) was used for the energy-mapped fluorescence imaging and spectroscopy of the supramolecular block copolymers (BCP) and homopolymers. The details of the setup were provided elsewhere.[38] A 405 nm and a 532 nm DPSS lasers (LASERGLOW) were used to illuminate a (25x25) μm^2

area of the spin-cast sample via an oil-immersion objective lens (1.49 NA, 60X, Nikon, Apo TIRF). The emissions were collected by the same objective lens and passed through the appropriate dichroic mirror(s) and band pass filter(s). Finally, the samples were imaged using an air cooled CCD (DVC 1412AM) at 300 ms integration time. It should be emphasized that identical excitation power (~4 Wcm^{-2} as measured before the objective lens) was maintained for both the lasers throughout the fluorescence imaging. To find the distribution of **SS-diOEt** (donors) and **SS-dithiol** (acceptors) within a single BC fibril, the donors and acceptors were excited with 405 nm and 532 nm, respectively; and their corresponding emission from the same area was collected by two energetically separated channels, 492-536 nm for donors (D-channel) and 545-635 nm for acceptor (A-channel) band pass filters denoted by green and red colour, respectively. The pseudo-colour co-localized image was generated by the quantitative superposition of both these images via careful pixel-by-pixel matching. The image analysis and spectral plots were done with ImageJ (NIH) and Origin (2018) software, respectively.

For spatially-resolved spectroscopy, individual supramolecular BC fibril was excited at higher power (~10 W/cm^2) and the spectral images were recorded using a combination of slit and transmission grating (70 grooves/mm) placed before an air-cooled sCMOS camera (Hamamatsu C13440, integration time 1sec). The calibration of pixel to wavelength conversion was done with the help of several laser lines. All the experiments were done at 295K temperature in ambient humidity (relative humidity, RH~55%). To evade the misinterpretation in the energy transfer calculation due to the photo-bleaching of donor molecules, always the measurement was first performed with 532 nm excitation followed by 405 nm.

2.8.2. Method Section:

2.8.2.1. Calculation of Acceptor Intensity Enhancement (AE) using FRET microscopy

Ideally, energy transfer is the sensitized emission of acceptor in the presence of donor via donor excitation. However, all excited donors may not participate in energy transfer and will emit by themselves, but their emission can bleed (*bleed-through*) into A-channel. In addition, the acceptor can also be excited directly at the donor excitation wavelength (*cross-talk*) and contribute to the A-channel emission. So, the resulting enhanced emission has also non-sensitized components (*bleed-through* and *cross-talk*), which need to be corrected further, to get the apparent enhancement in acceptor intensity. For that, the correction factors were calculated from the control experiments on pure (unmixed) donor and acceptor samples.

In order to do that, only donor sample (**SS-diOEt**) was imaged both in D-channel as well as in A-channel via donor excitation (405 nm). The ratio of decrease of donor emission intensity in A-channel (Em_A) to D-channel (Em_A), via donor wavelength excitation (Ex_D),

$(\frac{Ex_D\_Em_A}{Ex_D\_Em_D})$ is termed as **α** factor. The dual channels emission of only donors via donor wavelength excitation is shown in. Similarly, only acceptor sample (**SS-dithiol**) was excited with 405 nm (Ex_D) and 532 nm (Ex_A) and corresponding emissions were collected in A-channel (Em_A). So, the ratio of decrease of acceptor emission intensity with 405 nm excitation to that of 532 nm excitation ($\frac{Ex_D\_Em_A}{Ex_A\_Em_A}$) is termed as. As the quantum efficiency of acceptor is a common factor both emissions, **β** factor can also be written as ratio of their extinction coefficients at two different excitations ($\frac{\varepsilon_D}{\varepsilon_A}$). Correspond to fluorescence images of only acceptors in A-channel via both excitations. These two calculated factors were used further for the elimination of non-sensitized components from the BC fluorescence emission to get the *acceptor intensity enhancement* (*AE*) due to energy transfer.[39]

$$AE = (Ex_D\_Em_A) - \alpha(Ex_D\_Em_D) - \beta(Ex_A\_Em_A)$$

2.8.2.2. Acceptor Photobleaching:

For the selective photobleaching of acceptor molecules, a high power (~120 Wcm^{-2}) of 532 nm laser was used. The sample was continuously irradiated for 15 minutes, resulting the gradual bleaching of acceptors with faint emission. It also results in enhancement of D-channel emission.

2.8.2.3. Spatially-Resolved Fluorescence Spectroscopy:

When the BC sample is excited with donor wavelength (Ex_D), the donors and acceptors, which do not participate in energy transfer, get excited directly. Their spectral spillover to the acceptor emission region will also contribute to intensity enhancement. This false intensity contribution (without energy transfer) is depicted as *D+A$_{non\text{-}sensitized}$* (summation of D and A emission in A emission region without sensitization) in. However, the actual emission spectra have much-enhanced emission in the acceptor emission region and is shown as *DA$_{sensitized}$* (*DA* emission with energy transfer). To show relative intensity enhancement, the sensitized spectra is normalized with respect to non-sensitized spectra.

2.9. Experimental Section for Computational Details:

2.9.1. Development of the Molecular Models:

We built all atom (AA) models of monomers **SS-dithiol** and **SS-diOEt** using the General Amber Force Field (GAFF)[40]. We then used these AA models as a reference to parameterize and optimize coarse-grained (CG) models of the monomers. The CG models of **SS-dithiol** and **SS-diOEt** have been built based on the MARTINI force field [32] and then fine-tuned in order

to be consistent with the AA models for what pertains to the behavior of the individual monomers in cyclohexane solution and the strength of the monomer-monomer interactions in the solvent. First, we perfroemd all atom molecular dynamic simulations (AA-MD) of monomers **SS-dithiol** and **SS-diOEt** in explicit cyclohexane solvent, from which we calculated the radius of gyration (Rg) and the solvent accessible surface area (SASA) of the equilibrated monomers in solution. Following, we perfroemd CG-MD simulations of the same monomers as immerged in two simulation boxes filled with explicit cyclohexane (MARTINI SC1 beads).[32] We then refined the bonded parameters in the CG model in order to ensure that the bond, angle distributions, etc. were consistent between CG and AA models. We also compared the radii of gyration (Rg) of **SS-dithiol** and **SS-diOEt** monomers in cyclohexane to ensure a consistent behavior between AA and CG models for what pertained to the behavior of the monomers in solution. Complete parameters for the CG models of monomers **SS-dithiol** and **SS-diOEt** used in all simulations conducted herein are provided as supplementary material (GROMACS format ITP files).

2.9.2. Molecular Simulations:

All simulations have been performed with the GROMACS molecular dynamics suite version 2018.6[41], patched with the Plumed plugin version 2.5.[42] In all AA production runs, we used the md integrator with a time step of 2 fs. All simulations have been conducted at the temperature of 300 K and pressure of 1 atom using the v-rescale thermostat[43] with a time constant of 1 ps and the Parrinello-Rahman barostat[44] with a time constant of 1 ps. In all CG production simulations, we used the md integrator with a time step of 20 fs. Also the CG simulation were conducted at 300 K and 1 atm using the v-rescale thermostat[43] with a time constant of 1 ps and the Parrinello-Rahman barostat[43] with a time constant of 8 ps.

2.9.3. Modeling Internal Stability of the Fibers:

We constructed two pre-stacked fibers for CG molecule **SS-dithiol** and **SS-diOEt**, each composed of 40 initially extended monomers, which have been then pre-equilibrated in cyclohexane via CG-MD simulations. From both the conformations we performed 1 µs of unbiased CG-MD simulation, computing the Solvent Accessible Surface Area (SASA) and the core-core coordination number for every monomer. In the same spirit of the[31], we plotted their deviation from the average for every monomer, and highlighting their position in the fiber (as tips, defect, and bulk monomers). Such analysis highlights a larger presence of defects in the **SS-diOEt** fiber with respect to the **SS-dithiol** one.

2.9.4. Dimerization Energies:

We computed the dimerization free energy of the **SS-dithiol:SS-dithiol**, **SS-diOEt:SS-diOEt**, and **SS-diOEt:SS-dithiol** groups by means of WT-Metadynamics[33] (WT-MetaD) simulations. We set up the CG system with two pre-stacked monomers which are constrained in closed conformation (monomers interact only via one **SS-dithiol** or **SS-diOEt** group), and we ran 500 ns WT-MetaD runs using as collective variables (CVs) the number of contacts between the red or green cores which are initially in contact in the two monomers (CV1) and the minimum distance between the atoms of the two monomers (CV2), depositing a 1 kJ/mol gaussian bias with a width of 0.1 nm and 2 contacts every 10 ps, using a bias factor of 25. After reaching the WT-MetaD convergence, we reweighted the obtained FES using the Tiwary and Parrinello algorithm.[11]

2.9.5. Modeling the Rare Event of Monomer Exchange From the Fibers Tips:

After studying the equilibrium properties of the fiber, we wanted to explore the dynamics of monomer exchange in these supramolecular homopolymeric stacks. Preliminary CG-MD and CG-MetaD simulations demonstrated that the exchange of monomers from the tips of the stacks is not a single step event, but that in order to exchange, the open/stacked monomers have to close-up in sandwich conformation (step 1: open → close) and from such conformation can then exchange with the solution (step 2: closed → solvent). We studied the characteristic timescales involved in such rare molecular transition events occurring at the stack tip. These events occur on timescales that are way beyond the ones accessible via classical/unbiased MD simulations. Thus, we ran multiple infrequent WT-MetaD CG simulations activating the rare event of monomer exchange from the stack ends, similarly to what was previously done to study monomer exchange events in other supramolecular polymers.[31,14] In this way, we could explore the process of monomer opening/closing and monomer exchange from the tips of fibers **SS-dithiol** and **SS-diOEt** at a resolution of ~5 Å (resolution of our CG models) and reconstruct the original (native/unbiased) kinetics for those events. It is worth noting that the extracted exchange timescales are extracted from simplified CG models, and thus have a qualitative value (the dynamics and conformational sampling may be accelerated in CG simulations, and the conversion of time in CG simulations is not straightforward to convert into real-time). Nonetheless the extracted transition times can be safely compared between them and be used to compare the dynamics of the different systems studied herein.

We then ran 20 infrequent CG WT-MetaD simulations for each stack of **SS-dithiol** and **SS-diOEt** in all the 3 investigated phenomena. The characteristic timescales for the events were then calculated from the poissonian fit of the unbiased transition times distributions

obtained from the 25 infrequent WT-MetaD runs.[47] The unbiased transition time (t) can be calculated from each individual WT-MetaD run as:

$$t = t_{WT-MetaD}\langle e^{\beta(V(s(R),t))}\rangle_{WT-MetaD} \tag{1}$$

Where $V(s®,t)$ is the time-dependent bias provided for the transition during the run, the exponential (brackets) is averaged over the WT-MetaD run and β is kT^{-1}. The transition times (t) calculated from the WT-MetaD runs for were then used to build the transition probability distribution $P_{n\geq 1}$ (namely, the probability to observe at least one exchange event by time t):

$$P_{n\geq 1} = 1 - e^{\frac{-t}{\tau}} \tag{2}$$

where τ is the characteristic time for the rare events. Figure 2.13 shows the exchange times collected from the individual runs. These fit well with poissonian transition probability distributions $P_{n\geq 1}$, as expected for rare events (dark red and dark green), demonstrating that the approach is working properly.[47] From the green and red $P_{n\geq 1}$ curves it is possible to calculate the characteristic timescales (TAU: τ) for exchanging one monomer from the fiber's tip in both systems.

To model the 3 different processes, we used 3 different collective variables (CVs):

1. For the monomer opening, we considered 2 CVs – CV1: the distance between the two beads at both ends of the monomers, and CV2: the distance from the bead at the center of the core in the closed monomer and the bead at the center of the core in the fiber –, to identify precisely the correct opening of the monomer. We used a bias factor of 15, a gaussian height of 1.0 kJ mol^{-1}, a deposition stride of 1 gaussian every 5000 timestep with a sigma of 0.1 nm for both the distances. Simulations were terminated once the distance between the two core beads (our CV2) was smaller than 0.5 nm.

2. For the monomer closing, we considered one single CV: the distance between the two beads at both ends of the monomers. We used a bias factor of 15, a gaussian height of 1.0 kJ mol^{-1}, a deposition stride of 1 gaussian every 5000 timestep with a sigma of 0.1 nm. Simulations were terminated once the distance between the two beads at both ends were closer than 0.5 nm.

3. For the monomer exchange, we considered one single CV: the number of contacts between the core of the biased monomer's beads and the core of all the other monomers. We used a bias factor of 15, a gaussian height of 1.0 kJ mol^{-1}, a deposition stride of 1 gaussian every 5000 timestep with a sigma of 2. Simulations were terminated once the minimum distance between all the atoms of the biased monomer and any other monomer reached 1.5 nm.

2.10. References:

[1] a) De Greef, T. F. A.; Smulders, M. M. J.; Wolffs, M.; Schenning, A. P. H. J.; Sijbesma, R. P.; Meijer, E. W. *Chem. Rev.* **2009**, *109*, 5687-5754. b) de Greef, T. F. A.; Meijer, E. W. *Nature* **2008**, *453*, 171-173. c) Aida, T.; Meijer, E. W.; Stupp, S. I. *Science* **2012**, *335*, 813-817. d) Vantomme, G.; Meijer, E. W. *Science* **2019**, *363*, 1396-1397. e) Aida, T. *Adv. Mater.* **2019**, 1905445. f) Aida, T.; Meijer, E. W. *Isr. J. Chem.* **2020**, *60*, 33-47.

[2] a) Adelizzi, B.; Van Zee, N. J.; De Windt, L. N.; Palmans, A. R.; Meijer, E. W. *J. Am. Chem. Soc.* **2019**, *141*, 6110-6121. b) Wehner, M.; Würthner, F. *Nat. Rev. Chem.* **2020**, *4*, 38-53. c) Besenius, Pol. *Polymer Chemistry* **2017**, *55*, 34-78.

[3] a) Jain, A.; George, S. J. *Mater. Today,* **2015**, *18*, 206-214. b) Jain, A.; George, S. J. *Nat. Nanotech.* **2016**, *11*, 843-844.

[4] a) Lutz, J. F.; Ouchi, M.; Liu, D. R.; Sawamoto, M. *Science* **2013**, *341*, 634-636. b) Bates, F. S.; Hillmyer, M. A.; Lodge, T. P.; Bates, C. M.; Delaney, K. T.; Fredrickson, G. H. *Science* **2012**, *336*, 434-440. c) Schacher, F. H.; Rupar, P. A.; Manners, I. *Angew. Chem., Int. Ed.* **2012**, *51*, 7898-7921.

[5] a) Frisch, H.; Unsleber, J. P.; Lgdeker, D.; Peterlechner, M.; Brunklaus, G.; Waller, M.; Besenius, P. *Angew. Chem., Int. Ed.* **2013**, *52*, 10097-10101. b) Frisch, H.; Fritz, E.; Stricker, F.; Schmüser, L.; Spitzer, D.; Weidner, T.; Ravoo, B. J.; Besenius, P. *Angew. Chem., Int. Ed.* **2016**, *55*, 7242-7246. c) Zhang, X.; Wang, C. *Chem. Soc. Rev.* **2011**, *40*, 94-101. d) Wang, C.; Guo, Y.; Wang, Y.; Xu, H.; Wang, R.; Zhang, X. *Angew. Chem., Int. Ed.* **2009**, *48*, 8962-8965. e) Appel, E. A.; Biedermann, F.; Rauwald, U.; Jones, S. T.; Zayed, J. M.; Scherman, O. A. *J. Am. Chem. Soc.* **2010**, *132*, 14251-14260.

[6] a) Van Gestel, J.; Palmans, A. R. A.; Titulaer, B.; Vekemans, J. A. J. M.; Meijer, E. W. *J. Am. Chem. Soc.* **2005**, *127*, 5490-5494. b) Smulders, M. M. J.; Schenning, A. P. H. J.; Meijer, E. W. *J. Am. Chem. Soc.* **2008**, *130*, 606-611. c) Jin, W.; Fukushima, T.; Niki, M.; Kosaka, A.; Ishii, N.; Aida, T. *Proc. Natl. Acad. Sci.* **2005**, *102*, 10801-10806. d) Helmich, F.; Smulders, M. M. J.; Lee, C. C.; Schenning, A. P. H. J.; Meijer, E. W. *J. Am. Chem. Soc.* **2011**, *133*, 12238-

12246. e) Kim, T.; Mori, T.; Aida, T.; Miyajima, D. *Chem. Sci.* **2016**, *7*, 6689-6694. f) Ajayaghosh, A.; Varghese, R.; George, S. J.; Vijayakumar, C. *Angew. Chem., Int. Ed.* **2006**, *45*, 1141-1144. g) García, F.; Sánchez, L. *J. Am. Chem. Soc.* **2012**, *134*, 734-742. h) Smulders, M. M. J.; Stals, P. J. M.; Mes, T.; Paffen, T. F. E.; Schenning, A. P. H. J.; Palmans, A. R. A.; Meijer, E. W. *J. Am. Chem. Soc.* **2010**, *132*, 620-626. i) Coelho, J. P.; Matern, J.; Albuquerque, R. Q.; Fernández, G. *Chem. Eur. J.* **2019**, *25*, 8960-8964.

[7] a) Yagai, S.; Hamamura, S.; Wang, H.; Stepanenko, V.; Seki, T.; Unoike, K.; Kikkawa, Y.; Karatsu, T.; Kitamura, A.; Würthner, F. *Org. Biomol. Chem.* **2009**, *7*, 3926-3929. b) Görl, D.; Zhang, X.; Stepanenko, V.; Würthner, F. *Nat. Commun.* **2015**, *6*, 7009.

[8] a) Wang, X.; Guerin, G.; Wang, H.; Wang, Y.; Manners, I.; Winnik, M. *Science* **2007**, *317*, 644-648. b) Gilroy, J. B.; Gädt, T.; Whittell, G. R.; Chabanne, L.; Mitchels, J. M.; Richardson, R. M.; Winnik, M. A.; Manners, I. *Nat. Chem.* **2010**, *2*, 566-570. c) Hailes, R. L. N.; Oliver, A. M.; Gwyther, J.; Whittell, G. R.; Manners, I. *Chem. Soc. Rev.,* **2016**, *45*, 5358-5407.

[9] a) Gädt, T.; Ieong, N. S.; Cambridge, G.; Winnik, M. A.; Manners, I. *Nat. Mater.* **2009**, *8*, 144. b) Hudson, Z. M.; Boott, C. E.; Robinson, M. E.; Rupar, P. A.; Winnik, M. A.; Manners, I. *Nat. Chem.* **2014**, *6*, 893-898. c) He, X.; Hsiao, M.-S.; Boott, C. E.; Harniman, R. L.; Nazemi, A.; Li, X.; Winnik, M. A.; Manners, I. *Nat. Mater.* **2017**, *16*, 481-488. d) Qiu, H.; Gao, Y.; Boott, C. E.; Gould, O. E. C.; Harniman, R. L.; Miles, M. J.; Webb, S. E. D.; Winnik, M. A.; Manners, I. *Science* **2016**, *352*, 697-701. e) J. R. Finnegan, D. J. Lunn, O. E. C. Gould, Z. M. Hudson, G. R. Whittell, M. A. Winnik, Manners, I. *J. Am. Chem. Soc.* **2014**, *136*, 13835-13844. f) Qiu, H.; Gao, Y.; An Du, V.; Harniman, R.; Winnik, M. A.; Manners, I. *J. Am. Chem. Soc.* **2015**, *137*, 2375-2385. g) Nazemi, A.; He, X.; MacFarlane, L. R.; Harniman, R. L.; Hsiao, M.-S.; Winnik, M. A.; Faul, C. F. J.; Manners, I. *J. Am. Chem. Soc.* **2017**, *139*, 4409-4417.

[10] a) Zhang, W.; Jin, W.; Fukushima, T.; Saeki, A.; Seki, S.; Aida, T. *Science* **2011**, *334*, 340-343. b) Zhang, W.; Jin, W.; Fukushima, T.; Mori, T.; Aida, T. *J. Am. Chem. Soc.* **2015**, *137*, 13792-13795.

[11] Jung, S.H.; Bochicchio, D.; Pavan, G.M.; Takeuchi, M.; Sugiyasu, K. *J. Am. Chem. Soc.* **2018**, *140*, 10570-10577.

[12] a) Fukui, T.; Kawai, S.; Fujinuma, S.; Matsushita, Y.; Yasuda, T.; Sakurai, T.; Seki, S.; Takeuchi, M.; Sugiyasu, K. *Nat. Chem.* **2017**, *9*, 493-499. b) Ogi, S.; Sugiyasu, K.; Manna, S.; Samitsu, S.; Takeuchi, M. *Nat. Chem.* **2014**, *6*, 188-195. c) Ogi, S.; Stepanenko, V.; Sugiyasu, K.; Takeuchi, M.; Würthner, F. *J. Am. Chem. Soc.* **2015**, *137*, 3300-3307. d) Dhiman, S.; George, S. J. *Bull. Chem. Soc. Jpn.* **2018**, *91*, 687-699. e) Matern, J.; Dorca, Y.; Sánchez, L.; Fernández, G. *Angew. Chem., Int. Ed.* **2019**, *58*, 16730-16740. f) van der Zwaag, D.; De Greef,

T. F. A.; Meijer, E. W. *Angew. Chem., Int. Ed.* **2015**, *54*, 8334-8336. g) Mukhopadhyay, R. D.; Ajayaghosh, A. *Science* **2015**, *349*, 241-242. h) Würthner, F. *Nat. Chem.* **2014**, *6*, 171-173.

[13] a) Mishra, A.; Korlepara, D. B.; Kumar, M.; Jain, A.; Jonnalagadda, N.; Bejagam, K. K.; Balasubramanian, S.; George, S. J. *Nat. Commun.* **2018**, *9*, 1295. b) Jain, A.; Dhiman, S.; Dhayani, A.; Vemula, P. K.; George, S. J. *Nat. Commun.* **2019**, *10*, 450. c) Ogi, S.; Stepanenko, V.; Thein, J.; Würthner, F. *J. Am. Chem. Soc.* **2016**, *138*, 670-678. d) Ogi, S.; Matsumoto, K.; Yamaguchi, S. *Angew. Chem., Int. Ed.* **2018**, *57*, 2339-2343. e) Greciano, E. E.; Matarranz, B.; Sánchez, L. *Angew. Chem., Int. Ed.* **2018**, *57*, 4697-4701. f) Endo, M.; Fukui, T.; Jung, S. H.; Yagai, S.; Takeuchi, M.; Sugiyasu, K. *J. Am. Chem. Soc.* **2016**, *138*, 14347-14353. g) Langenstroer, A.; Kartha, K. K.; Dorca, Y.; Droste, J.; Stepanenko, V.; Albuquerque, R. Q.; Hansen, M. R.; Sánchez, L.; Fernández, G. *J. Am. Chem. Soc.* **2019**, *141*, 5192-5200. h) Wilkins, C. J.; He, X.; Symons, H. E.; Harniman, R. L.; Faul, C. F. J.; Manners, I. *Chem. Eur. J.* **2018**, *24*, 15556-15565. i) Robinson, M. E.; Lunn, D. J.; Nazemi, A.; Whittell, G. R.; De Cola, L.; Manners, I. *Chem. Commun.* **2015**, *51*, 15921-15924. j) Aliprandi, A.; Mauro, M.; Cola, L. D. *Nat. Chem.* **2016**, *8*, 10-15

[14] a) Wagner, W.; Wehner, M.; Stepanenko, V.; Würthner, F. *J. Am. Chem. Soc.* **2019**, *141*, 12044-12054. b) Wagner, W.; Wehner, M.; Stepanenko, V.; Würthner, F. *CCS Chem.* **2019**, *1*, 598-613.

[15] a) Sakai, N.; Mareda, J.; Vauthey, E.; Matile, S. *Chem., Commun.* **2010**, *46*, 4225-4237. b) Sarkar, A.; Kölsch, J. C.; Berač, C. M.; Venugopal, A.; Sasmal, R.; Otter, R.; Besenius, P.; George, S. J. *ChemistryOpen* **2020**, *9*, 346-350.

[16] Sarkar, A.; Sasmal, R.; Empereur-mot, C.; Bochicchio, D.; Kompella, S. V. K.; Sharma, K.; Dhiman, S.; Sundaram, B.; Agasti, S. S.; Pavan, G. M.; George, S. J. *J. Am. Chem. Soc.* **2020**, *142*, 7606-7617.

[17] a) Lutz, J. F.; Lehn, J-M.; Meijer, E. W.; Matyjaszewski, K. *Nat. Rev. Mater.* **2016**, *1*, 16024-16038. b) Szwarc, M. *Nature* **1956**, *178*, 1168-1169. c) Matyjaszewski, K.; Xia, J. *Chem. Rev.* **2001**, *101*, 2921-2990.

[18] Odian, G. G. Principle of Polymerization, *Third Ed.*; Wiley, Ed.; **1991**.

[19] a) Kulkarni, C.; Balasubramanian, S.; George, S. J. *ChemPhysChem* **2013**, *14*, 661-673. b) Jonkheijm, P.; van der Schoot, P.; Schenning, A. P. H. J.; Meijer, E. W. *Science* **2006**, *313*, 80-83. c) Kulkarni, C.; Bejagam, K. K.; Senanayak, P. S.; Narayan, K. S.; Balasubramanian, S.; George, S. J. *J. Am. Chem. Soc.* **2015**, *137*, 3924-3932.

[20] Kitamoto, Y.; Pan, Z.; Prabhu, D. D.; Isobe, A.; Ohba, T.; Shimizu, N.; Takagi, H.; Haruki, R.; Adachi, S. I.; Yagai, S. *Nat. Commun.* **2019**, *10*, 4578.

[21] Adelizzi, B.; Aloi, A.; Markvoort, A. J.; Ten Eikelder, H. M.; Voets, I. K.; Palmans, A. R.; Meijer, E. W. *J. Am. Chem. Soc.* **2018**, *140*, 7168-7175.

[22] Adelizzi, B.; Aloi, A.; Van Zee, N. J.; Palmans, A. R. A.; Meijer, E. W.; Voets, I. K. *ACS Nano* **2018**, *12*, 4431-4439. b) Kubota, R.; Nakamura, K.; Torigoe, S.; Hamachi, I. *ChemistryOpen* **2020**, *9*, 67-79. c) Albertazzi, L.; Zwaag, D. v. d.; Leenders, C. M. A.; Fitzner, R.; van der Hofstad, R. W.; Meijer, E. W. *Science* **2014**, *344*, 491-495.

[23] Schenning, A. P. H. J.; Meijer, E. W. *Chem. Commun.* **2005**, *26*, 3245-3258.

[24] a) Yang, C.; Barrelet, C.J.; Capasso, F.; Lieber, C. M. *Nano Letters* **2006**, *6*, 2929-2934. b) Tian, B.; Zheng, X.; Kempa, T.J.; Fang, Y.; Yu, N.; Yu, G.; Huang, J.; Lieber, C. M. *Nature* **2007**, *449*, 885-889. c) Costi R.; Saunders E. A.; Elmalem E.; Salant A.; Banin, U. *Nano Letters* **2008**, *8*, 637-641.

[25] Jin, X.; Price, M. B. Finnegan, J. R.; Boott, C. E.; Richter, J. M.; Rao, A.; Menke, S. M.; Friend, R. H.; Whittell, G. R.; Manners, I. *Science* **2018**, *360*, 897-900.

[26] Hudson, Z. M.; Lunn, D. J.; Winnik, M. A.; Manners, I. *Nat. Commun.* **2014**, *5*, 3372.

[27] a) Narayan, B.; Bejagam, K. K.; Balasubramanian, S.; George, S. J. *Angew. Chem., Int. Ed.* **2015**, *54*, 13245-13249. b) Sarkar, A.; Dhiman, S.; Chalishazar, A.; George, S. J. *Angew. Chem., Int. Ed.* **2017**, *56*, 13767-13771.

[28] a) H. M. M. ten Eikelder, A. J. Markvoort, T. F. A. de Greef, P. A. J. Hilbers, *J. Phys. Chem. B* **2012**, *116*, 5291-5301. b) Zhao, D.; Moore, J. S. *Org. Biomol. Chem.* **2003**, *1*, 3471-3491.

[29] Oosawa, F.; Asakura, S. *Academic Press Inc., New York*, **1975**.

[30] a) Bochicchio, D.; Pavan. G. M. *Adv. Phys. X* **2018**, *3*, 1436408. b) Bochicchio, D.; Pavan. G. M. *ACS Nano* **2017**, *11*, 1000-1011. c) Gasparotto, P.; Bochicchio, D.; Ceriotti, M.; Pavan, G. M. *J. Phys. Chem. B* **2020**, *124*, 589-599.

[31] Bochicchio, D., Salvalaglio, M., Pavan, G. M. *Nat. commun.* **2017**, *8*, 1-11.

[32] Marrink, S. J., Risselada, H. J., Yefimov, S., Tieleman, D. P., De Vries, A. H. *J. Phys. Chem. B*, **2007**, *111*, 7812-7824.

[33] Barducci, A., Bussi, G., & Parrinello, M. *Physical review letters*, **2008**, *100*, 020603.

[34] Bochicchio, D.; Kwangmettatam, S.; Kudernac, T.; Pavan. G. M. *ACS Nano* **2019**, *13*, 4322-4334

[35] Das, S.; Sharma, D. K.; Chakrabarty, S.; Chowdhury, A.; Sen Gupta, S. *Langmuir* **2015**, *31*, 3402-3412.

[36] Berney, C.; Danuser, G. *Biophys J.* **2003**, *84*, 3992-4010

[37] a) Haedler, A. T.; Kreger, K.; Issac, A.; Wittmann, B.; Kivala, M.; Hammer, N.; Köhler, J.; Schmidt, H.-W.; Hildner, R. *Nature* **2015**, *9*, 196-200. b) Wan, Y.; Stradomska, A.; Knoester, J.; Huang, L. *J. Am. Chem. Soc.* **2017**, *139*, 7287-7293. c) Brixner, T.; Hildner, R.; Köhler, J.; Lambert, C.; Würthner, F. *Adv. Energy Mater.* **2017**, 1700236.

[38] De, S.; Layek, A.; Raja, A.; Kadir, A.; Gokhale, M. R.; Bhattacharya, A.; Dhar, S.; Chowdhury, A. *Adv. Funct. Mater.* **2011**, *21*, 3828-3835.

[39] Sorkin, A.; McClure, M.; Huang, F.; Carter, R. *Curr. Biol.* **2000**, *10*, 1395-1398.

[40] Wang, J.; Wolf, R. M.; Caldwell, J. W.; Kollman, P. A.; Case, D. A. *J. Comput. Chem.* **2004**, *25*, 1157. ISO 690.

[41] Abraham, M. J.; Murtola, T.; Schulz, R.; Páll, S.; Smith, J. C.; Hess, B.; Lindahl, E. *SoftwareX* **2015**, *1-2*, 19-25.

[42] a) Tribello, G. A.; Bonomi, M.; Branduardi, D.; Camilloni, C.; Bussi, G. *Comput. Phys. Commun.* **2014**, *185*, 604-613. b) Bonomi, M.; Bussi, G.; Camilloni, C.; Tribello, G. A.; Banaś, P.; Barducci, A.; Bernetti, M.; Bolhuis, P. G.; Bottaro, S.; Branduardi, D.; Capelli, R.; Carloni, P.; Ceriotti, M.; Cesari, A.; Chen, H.; Chen, W.; Colizzi, F.; De, S.; De La Pierre, M.; Donadio, D.; Drobot, V.; Ensing, B.; Ferguson, A. L.; Filizola, M.; Fraser, J. S.; Fu, H.; Gasparotto, P.; Gervasio, F. L.; Giberti, F.; Gil-Ley, A.; Giorgino, T.; Heller, G. T.; Hocky, G. M.; Iannuzzi, M.; Invernizzi, M.; Jelfs, K. E.; Jussupow, A.; Kirilin, E.; Laio, A.; Limongelli, V.; LindorffLarsen, K.; Löhr, T.; Marinelli, F.; Martin-Samos, L.; Masetti, M.; Meyer, R.; Michaelides, A.; Molteni, C.; Morishita, T.; Nava, M.; Paissoni, C.; Papaleo, E.; Parrinello, M.; Pfaendtner, J.; Piaggi, P.; Piccini, G. M.; Pietropaolo, A.; Pietrucci, F.; Pipolo, S.; Provasi, D.; Quigley, D.; Raiteri, P.; Raniolo, S.; Rydzewski, J.; Salvalaglio, M.; Sosso, G. C.; Spiwok, V.; Šponer, J.; Swenson, D. W. H.; Tiwary, P.; Valsson, O.; Vendruscolo, M.; Voth, G. A.; White, A. *Nat. Methods* **2019**, *16*, 670-673.

[43] Bussi, G.; Donadio, D.; Parrinello, M. *J. Chem. Phys.* **2007**, *126*, 014101.

[44] a) Parrinello, M.; Rahman, A. *Phys. Rev. Lett.* **1980**, *45*, 1196. b) Parrinello, M.; Rahman, A. *J. Appl. Phys.* **1981**, *52*, 7182-7190.

[45] Tiwary P.; Parrinello. M. *J. Phys. Chem. B* **2015**, *119*, 736-742.

[46] a) Tiwary, P.; Parrinello, M. *Phys. Rev. Lett.* **2013**, *111*, 230602. b) Salvalaglio, M.; Tiwary, P.; Parrinello, M. *J. Chem. Theory Comput.* **2014**, *10*, 1420-1425

[47] Gasparotto, P.; Bochicchio, D.; Ceriotti, M.; Pavan, G. M. *J. Phys. Chem. B* **2020**, *124*, 589-599.

Chapter: 3

Self-Sorted, Random and Block Supramolecular Copolymers via Sequence Controlled, Multicomponent Self-assembly

Chapter: 3

Self-Sorted, Random and Block Supramolecular Copolymers via Sequence Controlled, Multicomponent Self-assembly

Abstract

Multicomponent supramolecular copolymerization promises to construct complex nanostructures with emergent properties. However, even with two monomeric components, various possible outcomes such as self-sorted supramolecular homopolymers, a random supramolecular copolymer or a complex supramolecular block copolymer can occur determined by their intermolecular interactions and monomer exchange dynamics and hence structural prediction is extremely challenging. Herein, we target this challenge and demonstrate unprecedented two component sequence controlled supramolecular copolymerization by manipulating thermodynamic and kinetic routes by exploiting pathway complexity of the molecules thereby mapping the complete energy landscape. Extensive molecular dynamics simulations provided useful mechanistic insights into the monomer exchange rates and free energy of interactions between the monomers to bias the assembly pathway and sequence. Fluorescent nature of core-substituted naphthalene diimide monomers has been further utilized to characterize the three sequences via structured illumination microscopy (SIM).

Sequence Controlled Supramolecular Polymerization
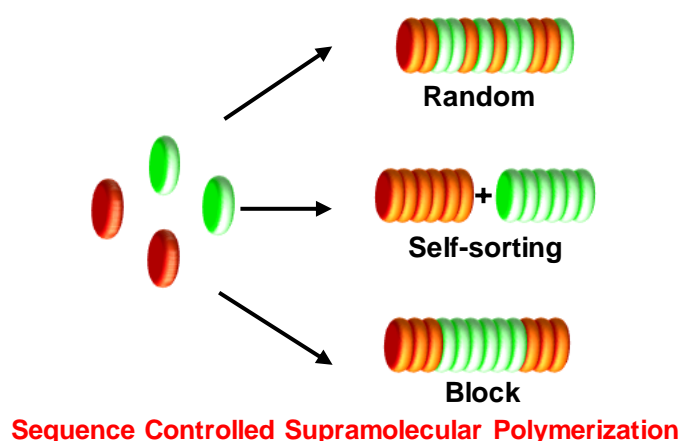
3.1. Introduction:

Sequence controlled polymerization is a vital phenomenon observed in natural systems. The genetic information is encoded by nucleobase sequences in DNA and protein's structure and function is determined by its amino acid sequence.[1] This sequence-control has been implemented in covalent polymers via elegant synthetic strategies resulting in emergent structural properties and multitude of applications.[2] On the other hand, supramolecular polymers, composed of dynamic non-covalent interactions between monomers, with predictive sequence would provide an opportunity to dynamically rearrange/reconfigure the composition similar to natural systems.[3] However, supramolecular polymerization with even two components is challenging and the sequence outcome could be either narcissistically self-sorted supramolecular homopolymers (AAA and BBB), a random (AABABB) supramolecular copolymer, alternate supramolecular copolymer (ABABAB) or complex supramolecular block copolymer (AABBAA) whose sequence is determined by the free energy of intermolecular (homo- AA, BB vs. hetero- AB) interactions, monomer structure and monomer exchange dynamics. In this study, we have demonstrated an unprecedented two component sequence controlled supramolecular copolymerization into the three unique sequences by exploiting the delicate balance between the kinetic and thermodynamic parameters of self-assembly. We further manipulate these parameters to illustrate dynamic reconfiguration of these sequences into one another.

Narcissistically self-sorted supramolecular polymers have been achieved by high homo-recognition (ΔG_{AA}, ΔG_{BB} > ΔG_{AB}) between monomers, designed with structural mismatch or low monomer exchange dynamics.[4-7] Adams and coworkers reported pH-programmed self-sorting of gelator monomers with different pKa.[5] On the other hand structural mismatch between donor and acceptor chromophores leading to orthogonal supramolecular homopolymers have been reported.[6] We have reported that chirality driven mismatch can also be used to construct self-sorted systems even with structurally similar monomers.[7] In contrast, alternating supramolecular copolymers require stronger hetero-recognition between monomers (AA, BB < AB) and has been preferentially attained by strong hetero-complementary interactions such as electrostatic and donor-acceptor charge-transfer interactions. Charge-transfer supramolecular polymers reported by our group, Zhang and others are excellent examples of alternating supramolecular polymers with electronically complementary donor and acceptor monomers.[8] Besenius and coworkers employed complementary electrostatic interactions from lysine and glutamic acid residues to obtain alternating arrangement at neutral

pH.[9] Scherman and coworkers has utilized strong charge-transfer ternary complexes with cucurbit[8]uril to manifest alternate host-guest supramolecular polymer.[10] These self-sorted or alternating supramolecular copolymers have been achieved mostly under thermodynamic conditions, where the interaction energies between the monomers determines the sequence.

However, supramolecular block copolymer arrangement has been a grand challenge in the field.[11] This is due to specific requirements such as structural similarity between monomers, low exchange dynamics and delicate balance between homo- and hetero-recognition between monomers. However, mechanistic understanding[12] and development of living supramolecular polymerization has aided in addressing this challenge.[11b,13,14] Meijer and coworkers have constructed supramolecular block copolymers under thermodynamic control with monomers exhibiting reactivity ratio difference analogous to the synthesis of block copolymers via chain-growth polymerization in covalent polymers.[15] In another approach, Yagai and coworkers have demonstrated coassembly between two monomers under thermodynamic control to result in a supramolecular copolymer, where the monomer composition varies gradually during the polymerization and along the polymer chain.[16] Supramolecular block copolymerization under kinetic control requires sequential addition of dormant monomers undergoing nucleation-elongation growth. However, this is challenging, as minor difference in structure alters the energy landscape significantly. Hence, Sugiyasu and Takeuchi's group[17] achieved block sequence by crystallization-driven self-assembly approach similar to Manners and coworkers elegantly established in block copolymer assemblies.[18] Aida and coworkers synthesized p-n junction via seeded assembly between electronically different chromophores.[19] Recently, Würthner and coworkers presented the synthesis of supramolecular copolymers of core-substituted perylene bisimide using kinetically control seeded supramolecular polymerization which is more closer to the conventional multicomponent living polymerization leading to block copolymers.[20]

So far, the narcissistically self-sorted homopolymer, supramolecular block copolymer and random supramolecular copolymer sequences have been synthesized separately owing to their orthogonal and unique requisites. Thus, achieving the three sequences from the same monomer pair and their dynamic reconfiguration is still elusive. In order to achieve precise sequence control, it is necessary to move through the complete energy landscape of self-assembly via thermodynamic and kinetic routes. To realize this, herein we introduce an unprecedented two component supramolecular polymerization with unique sequence control
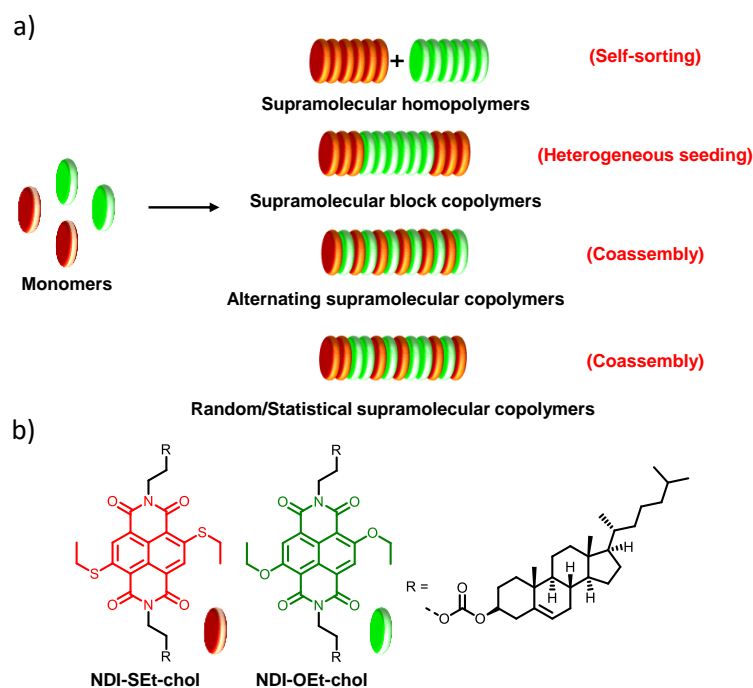
Scheme 3.1. Two component supramolecular polymerization. a) Schematic representation of two component supramolecular polymerization into self-sorted supramolecular homopolymers, heterogeneously seeded supramolecular block copolymers, coassembled supramolecular alternating or random supramolecular copolymers. b) Molecular structures of **NDI-SEt-chol** and **NDI-OEt-chol** used for the two component supramolecular polymerization.

to access self-sorted, alternate and block copolymer arrangement via pathway complexity (Scheme 3.1).[21]

3.2. Molecular Design:

To attempt this, we chose our previously studied molecular design based on carbonate cholesterol appended naphthalene diimide[22] which due to long-range dipole-dipole interactions followed a cooperative mechanism, necessary for seeded supramolecular polymerization. Secondly, to have minimum structural perturbation and to probe the polymerization process, we symmetrically disubstituted the naphthalene diimide core with ethane thiol (**NDI-SEt-chol**) and ethoxy (**NDI-OEt-chol**) groups to give red- and green-emissive dyes respectively (Scheme 1). These molecules have unique optoelectronic properties as well as different absorption and emission profiles aiding to the orthogonal probing of their self-assembly via spectroscopic and super-resolved florescence microscopy characterization (SIM).

3.3. Supramolecular Polymerization of NDI-SEt-chol and NDI-OEt-chol:
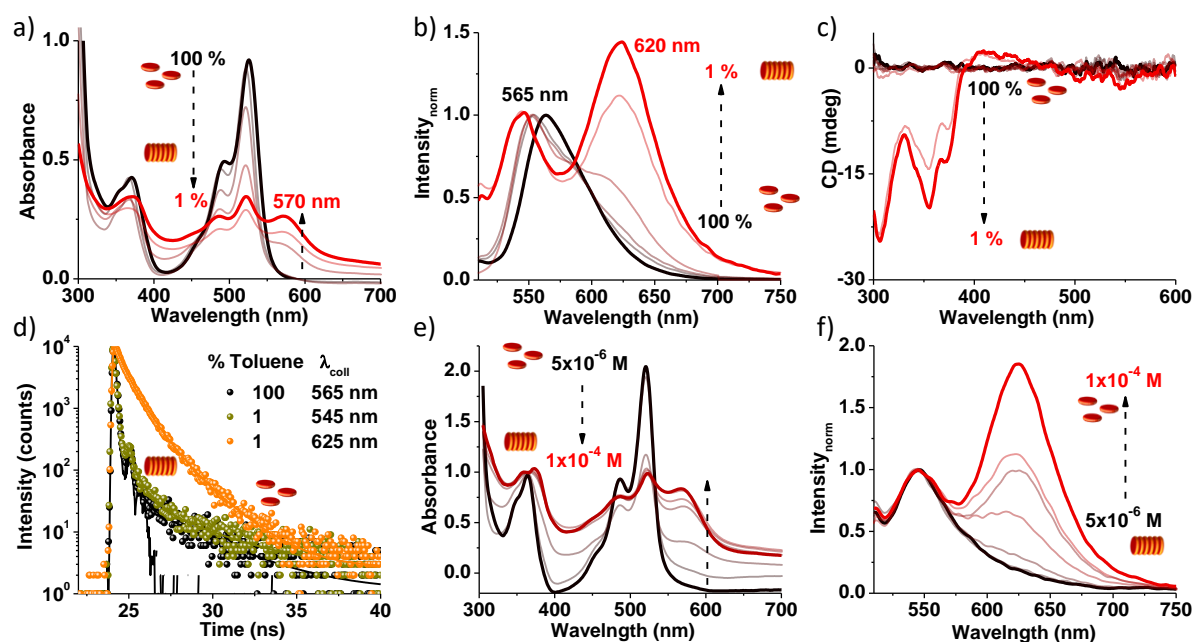
Figure 3.1. Self-assembly properties of **NDI-SEt-chol**. Composition-dependent a) absorption, b) normalized emission (λ_{ex} = 480 nm) and c) CD spectral changes with varying % of toluene/MCH solvent mixture. d) Lifetime decay profile (λ_{ex} = 480 nm) collected at 565 nm for molecularly dissolved state in toluene and at 625 nm and 545 nm for self-assembled state. Respective concentration-dependent e) absorption and f) normalized emission spectra (λ_{ex} = 480 nm) dictating gradual disassembly with decrease in concentration (toluene/MCH, 1/99 (v/v)). ([**NDI-SEt-chol**] = 5×10^{-5} M, l = 10 mm).

Toluene/MCH (v/v)	λ_{coll} (nm)	t_1 (ns)	t_2 (ns)	t_3 (ns)
100/0	565	0.3 (47.80 %)	3.25 (52.20 %)	
1/99	545	0.6 (34.10 %)	1.85 (57.29 %)	0.08 (8.62 %)
1/99	625	0.3 (19.98 %)	0.8 (62.49 %)	1.94 (17.53 %)

Table 3.1. Listed lifetime data for monomeric **NDI-SEt-chol** in toluene and self-assembled **NDI-SEt-chol** in toluene/MCH, 1/99 (v/v). ([**NDI-SEt-chol**] = 5×10^{-5} M).

Core-substituted NDI (cNDI) monomers **NDI-SEt-chol** and **NDI-OEt-chol** have distinct absorption (450-600 nm and 400-500 nm, respectively) and emission profiles (570-750 nm and 450-570 nm, respectively), which allowed the orthogonal probing of its self-assembly characteristics. Both **NDI-SEt-chol** and **NDI-OEt-chol** are soluble in toluene and the supramolecular polymerization of these monomers could be induced in the toluene-MCH solvent mixture (toluene/MCH, 1/99 (v/v) to toluene/MCH, 8/92 (v/v) for **NDI-SEt-chol** and toluene/MCH, 5/95 (v/v) to toluene/MCH, 40/60 (v/v) in for **NDI-OEt-chol**) and was probed spectroscopically. Solvent composition-dependent studies of molecule **NDI-SEt-chol** at $5 \times 10^{-}$

[5] M concentration depicted broadening of absorption spectra along with appearance of red shifted absorbance band at 590 nm on increasing the percentage of MCH in toluene (Figure 3.1a). Emission spectra also followed a bathochromic shift to 620 nm in comparison to monomeric emission at 570 nm in toluene (Figure 3.1b). Lifetime decay profile collected at aggregate emission band (620 nm) showed and enhanced lifetime in comparison to the lifetime collected at monomer emission band (565 nm) (Figures 3.1d and Table 3.1). These observations revealed an emissive J-type slipped organization of **NDI-SEt-chol** chromophore in the stacks. Similarly, molecule **NDI-OEt-chol** also showed spectroscopic signature of emissive a self-assembly below toluene/MCH, 30/70 (v/v). Absorption spectra of molecule **NDI-OEt-chol** at 5×10^{-5} M concentration also got broadened on increasing the percentage of MCH in toluene (Figure 3.2a). Changes in solvent composition revealed quenching of emission at 500 nm along with appearance of a broad emission at 630 nm (Figure 3.2c). Lifetime decay profile collected at 500 nm indicated a completely different and decreased lifetime (Figure 3.2d) in toluene/MCH, 5/95 (v/v) in comparison to lifetime collected at 500 nm in toluene. A different lifetime at 500 nm in toluene/MCH, 5/95 (v/v) compared to toluene suggests emission at 500 nm in toluene/MCH, 5/95 (v/v) comes from self-assembled species rather than from monomeric species. Also, lifetime decay profile collected at 630 nm showed presence of very high lifetime species which was assigned to an excimer emission from self-assembled **NDI-OEt-chol** (Figure 3.2d, Table 3.2). Self-assembly is further evident from appearance of CD signal at π-π* and n-π* absorption maxima in case of molecule **NDI-OEt-chol** below toluene/MCH, 30/70 (v/v) (Figure 3.2b). Similarly, molecule **NDI-SEt-chol** below toluene/MCH, 5/95 (v/v) consist of CD signal at π-π* absorption maxima implying formation of chiral self-assembly biased by the peripheral cholesterol groups (Figure 3.1c).[23] Concentration-dependent studies at toluene/MCH, 5/95 (v/v) resulted in disappearance of spectroscopic features of aggregate absorption, CD and emission spectra of **NDI-SEt-chol** and **NDI-OEt-chol**, which denoted intermolecular nature of self-assembled **NDI-SEt-chol** and **NDI-OEt-chol** (Figures 3.1e, 3.1f, 3.2e and 3.2f).
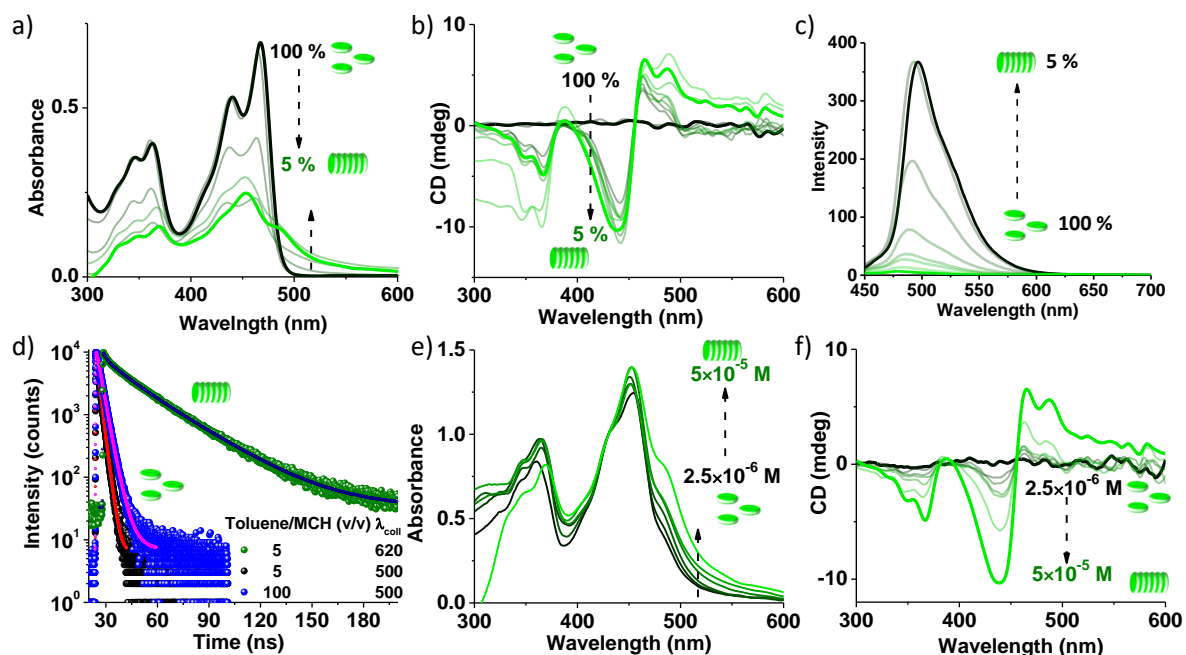
Figure 3.2. Self-assembly properties of **NDI-OEt-chol**. Composition-dependent a) absorption, b) CD and c) emission (λ_{ex} = 430 nm) spectral changes with varying % of toluene/MCH solvent mixture. d) Lifetime decay profile (λ_{ex} = 442 nm) collected at 500 nm and 620 nm. Respective concentration-dependent e) absorption, and f) CD spectra dictating gradual disassembly with decrease in concentration (Toluene/MCH, 5/95 (v/v)). ([**NDI-OEt-chol**] = 5×10^{-5} M, toluene/MCH, 5/95 (v/v), l = 10 mm).

Toluene/MCH (v/v)	λ_{coll} (nm)	t_1 (ns)	t_2 (ns)	t_3 (ns)
100/0	500	2.72 (92.88 %)	5.15 (7.12 %)	
5/99	500	1.55 (5.86 %)	2.59 (62.49 %)	0.04 (17.53 %)
5/99	620	10.55 (13.85 %)	25.28 (83.83 %)	1.27 (2.32 %)

Table 3.2. Listed lifetime data for monomeric **NDI-OEt-chol** in toluene and self-assembled **NDI-OEt-chol** in toluene/MCH, 5/95 (v/v). ([**NDI-OEt-chol**] = 5×10^{-5} M).

NDI-SEt-chol and **NDI-OEt-chol** formed red- (λ_{max} = 625 nm) and green-emissive (λ_{max} = 480 nm), one dimensional supramolecular polymers respectively as evident from the structured illumination microscopy (SIM) and transmission electron microscopy (TEM) images (Figure 3.3). The good spectral overlap between the absorption spectrum of **NDI-SEt-chol** and emission spectrum of **NDI-OEt-chol**, further enables the probing of the copolymerization process via Förster Resonance Energy Transfer (FRET) (Figure 3.4).
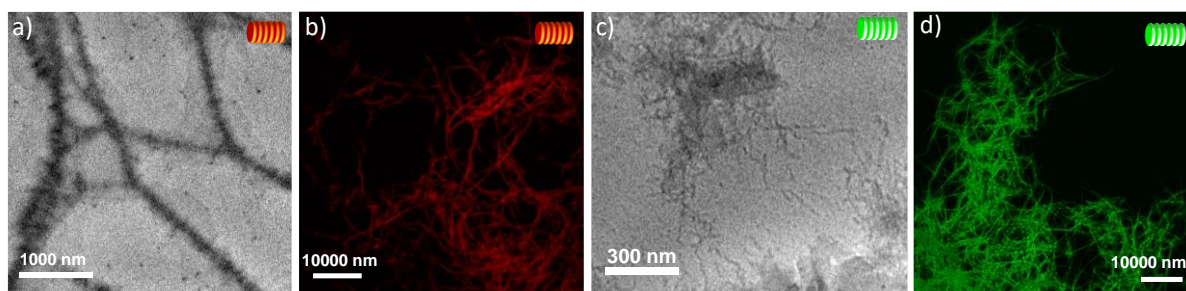
Figure 3.3. TEM image of the a) self-assembled **NDI-SEt-chol** and c) self-assembled **NDI-OEt-chol** showing 1D fiber morphology. SIM image of self-assembled b) **NDI-SEt-chol** (channel II) and d) self-assembled **NDI-OEt-chol** (channel I) showing red and green fluorescent fibers respectively. ([**NDI-SEt-chol**] = [**NDI-OEt-chol**] = 5×10^{-5} M, toluene/MCH, 5/95 (v/v), l = 10 mm, Channel II: λ_{ex} = 561 nm, λ_{coll} = 570-650 nm, Channel I: λ_{ex} = 488 nm, λ_{coll} = 495-575 nm).
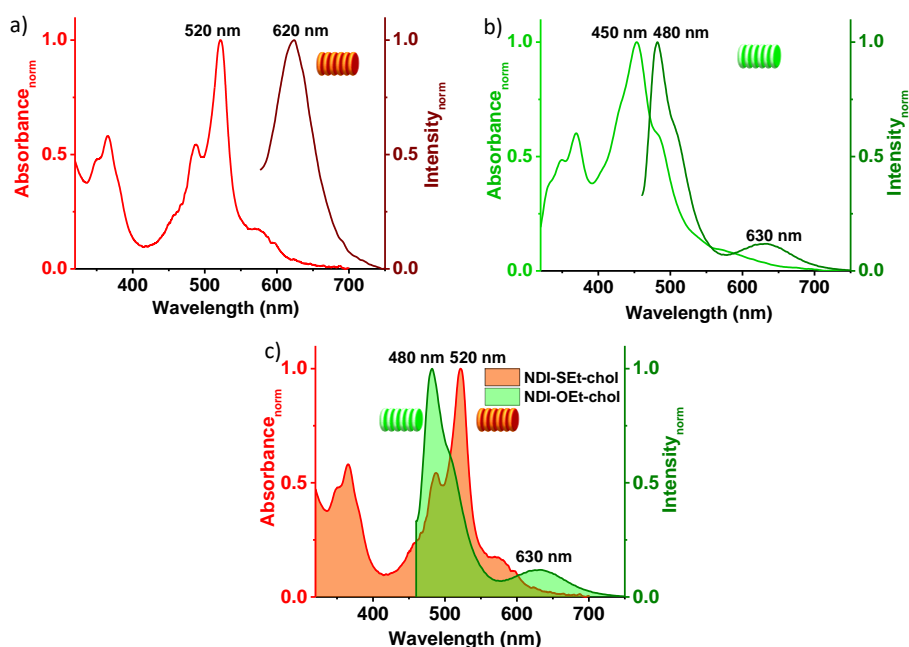
Figure 3.4. Spectral overlap between **NDI-SEt-chol** and **NDI-OEt-chol**. Overlap of absorption and emission spectra of a) **NDI-SEt-chol** (λ_{ex} = 480 nm) and b) **NDI-OEt-chol** (λ_{ex} = 442 nm). c) Absorption spectra of self-assembled **NDI-SEt-chol** and emission spectra of self-assembled **NDI-OEt-chol** showing sufficient overlap between them to act as a FRET pair. ([**NDI-SEt-chol**] = [**NDI-OEt-chol**] = 5×10^{-5} M, toluene/MCH, 5/95 (v/v)).

3.4. Pathway Complexity of NDI-SEt-chol and NDI-OEt-chol:

Temperature and time-dependent spectroscopic analyses of **NDI-SEt-chol** and **NDI-OEt-chol** in various toluene/MCH solvent mixture provided mechanistic insights into the supramolecular polymerization process and the free energy landscapes. Interestingly, temperature-dependent cooling curves of **NDI-SEt-chol** (363 K to 298 K) recorded at 1 K/min and monitored at 590 nm absorption band (toluene/MCH, 5/95 (v/v) and 5×10^{-5} M), depicted a two-state transition
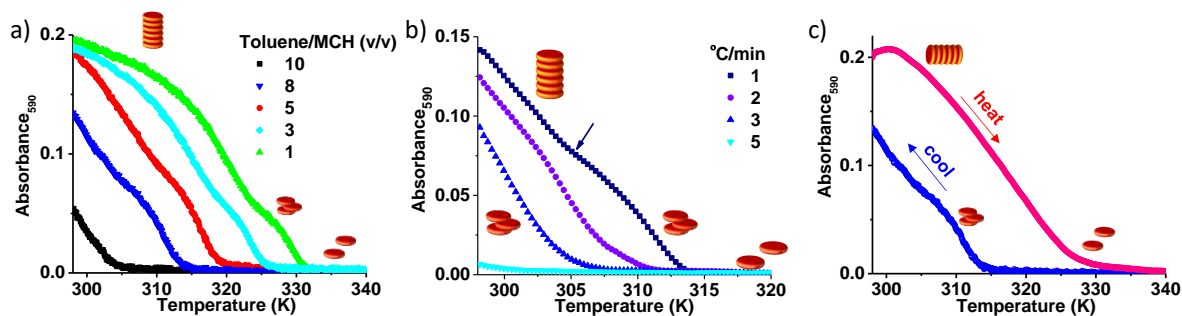
Figure 3.5. Pathway complexity in the self-assembly of **NDI-SEt-chol**. a) Solvent composition-dependent cooling curve of **NDI-SEt-chol** (obtained by monitoring the absorbance at 590 nm) depicting two-state transition of monomer → **State A** → **State B**. The difference between the two transition temperatures (corresponding to **State A** and **State B**) in the cooling curve increases with increase in toluene fraction, suggesting greater stabilization of metastable **State A** in higher toluene fractions i.e. low aggregating conditions (cooling rate = 1 K/min). b) Temperature-dependent absorbance changes at 590 nm with varying cooling rate. An increase in cooling rate leads to the preferential formation of kinetic trapped **State A** over thermodynamically stable **State B** (toluene/MCH, 8/92 (v/v), l = 10 mm). c) Self-assembly of **NDI-SEt-chol** is under kinetic control as represented by hysteresis between heating and cooling curves (cooling rate = heating rate = 1 K/min) monitored by the absorbance at 590 nm (toluene/MCH, 8/92 (v/v)). ([**NDI-SEt-chol**] = 5×10^{-5} M)

corresponding to a gradual conversion of monomer to an intermediate self-assembled **State A** finally to the self-assembled **State B**, corresponding to the supramolecular polymeric state (Figure 3.5a). **State A** was stabilized more in higher toluene percentages and lower concentration (toluene/MCH, 10/90 (v/v) and toluene/MCH, 8/92 (v/v)) and further, a fast cooling (≥ 5 K/min, ≥ toluene/MCH, 5/95 (v/v)) resulted in exclusive formation of **State A** (Figure 3.5b). Also, the presence of hysteresis between the cooling and heating profiles (Figure 3.5c) indicated **State A** to be a non-equilibrium metastable state *en route* to the thermodynamically stable **State B** of the supramolecular polymer.

To get further insight into the pathway selectivity in the self-organization of **NDI-SEt-chol** and the metastable **State A**, we further performed concentration and temperature-dependent spectroscopic studies and Molecular Dynamics (MD) simulations. The formation of **State A** resulted in insignificant changes in absorption and emission spectra compared to monomeric state and remains CD inactive, suggesting the formation of less-ordered small aggregates or a conformationally locked, metastable states for the monomers of **NDI-SEt-chol** prior to the nucleation process (Figures 3.6a, 3.6b, 3.6c and 3.6d). The transition to **State B** was accompanied with a significant broadening of the absorption spectrum and appearance of the new red shifted aggregate absorption band at 590 nm and the emission band at 625 nm implying the formation of an extended self-assembled structure with exciton-coupled π-stacked chromophores (Figures 3.6a, 3.6b, 3.6c and 3.6d). Gas phase quantum chemical calculations
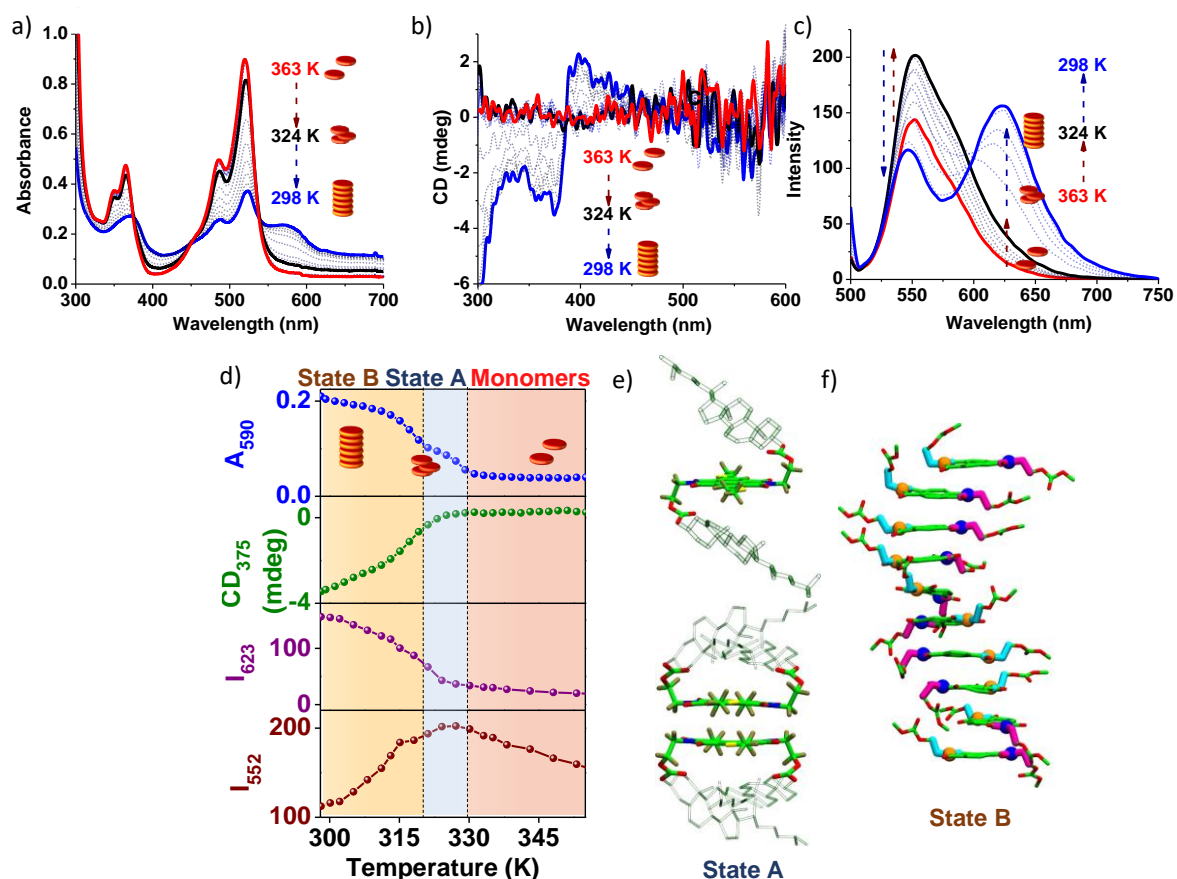
Figure 3.6. Characterization of metastable **State A** and thermodynamically stable **State B**. Temperature-dependent a) absorption, b) CD and c) emission spectra of **NDI-SEt-chol** (λ_{ex} = 480 nm). Red line belongs to molecularly dissolved state at high temperature. Black line represents **State A** and blue line represents final thermodynamically stable **State B** ([**NDI-SEt-chol**] = 5×10^{-5} M, toluene/MCH, 3/97 (v/v), cooling rate = 2 K/min). d) Comparison of absorbance at 590 nm, CD at 375 nm and emission changes (λ_{ex} = 480 nm) at 623 nm and 552 nm against temperature. Absorbance and emission at 552 nm show two-step transition. The pink regime indicates molecularly dissolved state, blue region shows the region where **State A** occurs and the orange region shows conversion to final thermodynamically stable **State B**. e) Side view of the metastable locked chair conformation (top) and side view of the locked dimer conformation (bottom) optimized at the PM6 // BLYP-D3/DZVP level of theory (**State A**) and f) snapshot of chair decamer obtained from MD simulations (**State B**). Cholesterol hydrogens are not shown for clarity. ([**NDI-SEt-chol**] = [**NDI-OEt-chol**] = 5×10^{-5} M, toluene/MCH, 3/97 (v/v)).

and all-atom molecular dynamic simulations with explicit solvation suggested the formation of locked monomers and dimers as **State A**, which convert to extended supramolecular polymers (**State B**) via conformational changes in the monomer structure (Figures 3.6e and 3.6f). Interestingly, self-assembled **State A** transformed to final **State B** with time and time-dependent absorbance changes monitored at 590 nm showed a non-linear, sigmoidal transformation with a lag phase and nucleation-elongation growth mechanism (Figure 3.7). An increasing percentage of toluene followed an enhancement in lag time due to more stabilization
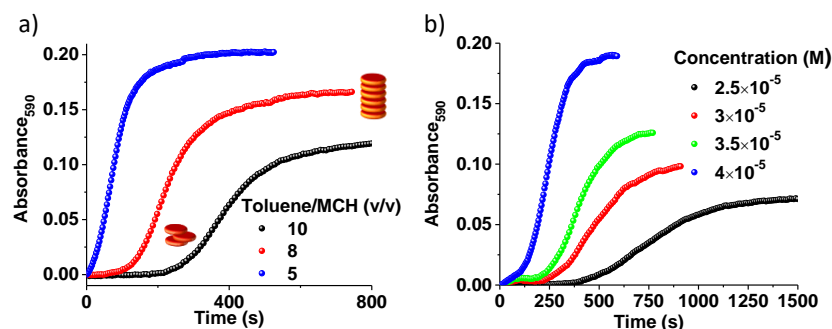
Figure 3.7. Time-dependent absorption changes at 590 nm of a fast cooled (5 K/min) solution of **NDI-SEt-chol** from 363 K to 298 K depicting self-assembly of **NDI-SEt-chol** into **State B** via sigmoidal nucleation-elongation kinetics. a) Composition-dependent kinetic data monitored using the absorbance changes at 590 nm. b) Concentration-dependent kinetics data monitored using the absorbance changes at 590 nm. ([**NDI-SEt-chol**] = 5×10^{-5} M, l = 10 mm, toluene/MCH, 5/95 (v/v)).
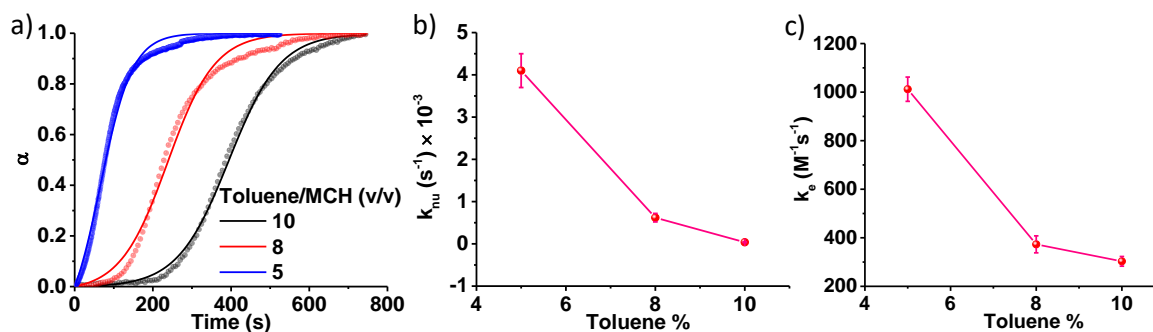
Figure 3.8. a) Fitting of time-dependent nucleation-elongation growth of molecule **NDI-SEt-chol** into Watzky and Finke model[24] to extract the k_{nu} (nucleation rate constant) and k_e (elongation rate constant). Kinetic parameters plotted against % of toluene shows an increase in both b) k_{nu} and c) k_e with decrease of toluene %. ([**NDI-SEt-chol**] = 5×10^{-5} M, toluene/MCH solvent mixture).
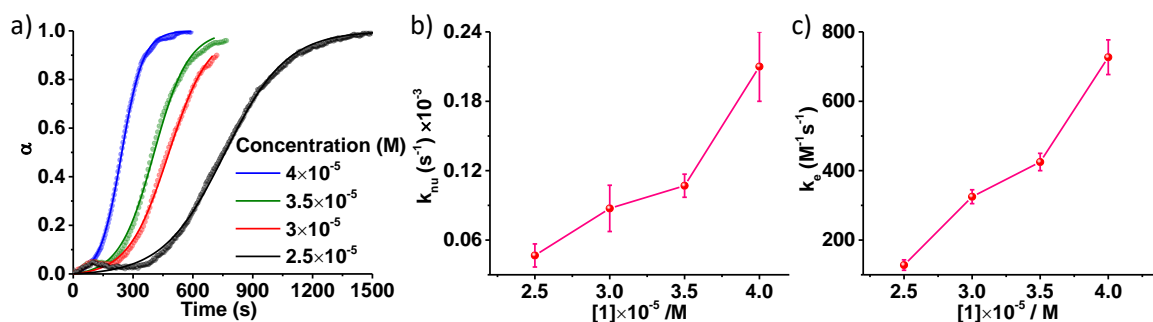
Figure 3.9. a) Fitting of time-dependent nucleation-elongation growth for molecule **NDI-SEt-chol** into Watzky and Finke model to extract the k_{nu} (nucleation rate constant) and k_e (elongation rate constant). Kinetic parameters plotted against concentration which shows an increase in both b) k_{nu} and c) k_e with increase in concentration of **NDI-SEt-chol.** (toluene/MCH, 5/95 (v/v)).

of **State A** at higher percentage of toluene (Figure 3.7). A decrease in lag time with an increase in the concentration of monomers designates an on-pathway formation of **State A**. The kinetic

data obtained could be well fitted with Watzky and Finke model[24] to extract k_{nu} (nucleation rate constant), k_e (elongation rate constant) where all the parameters showed a linear relationship against percentage of toluene and concentration (Figures 3.8 and 3.9).
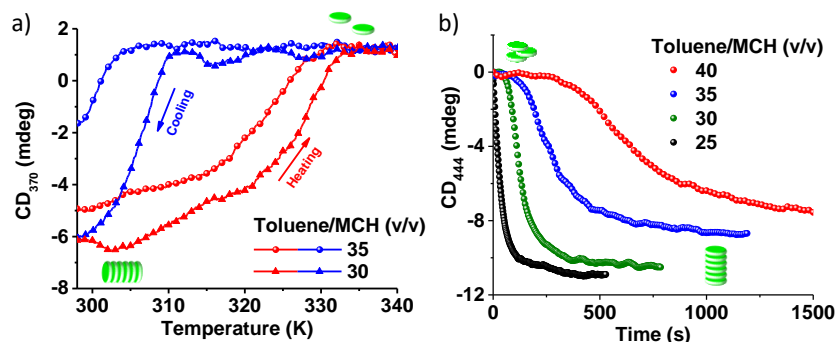
Figure 3.10. Pathway complexity in the self-assembly of **NDI-OEt-chol**. a) Self-assembly of **NDI-OEt-chol** under kinetic control as represented by hysteresis between heating and cooling curves (cooling rate = heating rate = 1 K/min) monitored with the CD intensity at 370 nm, for varying toluene/MCH solvent compositions. b) Time-dependent CD changes at 444 nm of fast cooled solution of **NDI-OEt-chol** from 363 K to 298 K via 5 K/min depicting self-assembly of **NDI-OEt-chol** into **State B** via sigmoidal nucleation-elongation kinetics. ([**NDI-OEt-chol**] = 5×10^{-5} M, l = 10 mm).
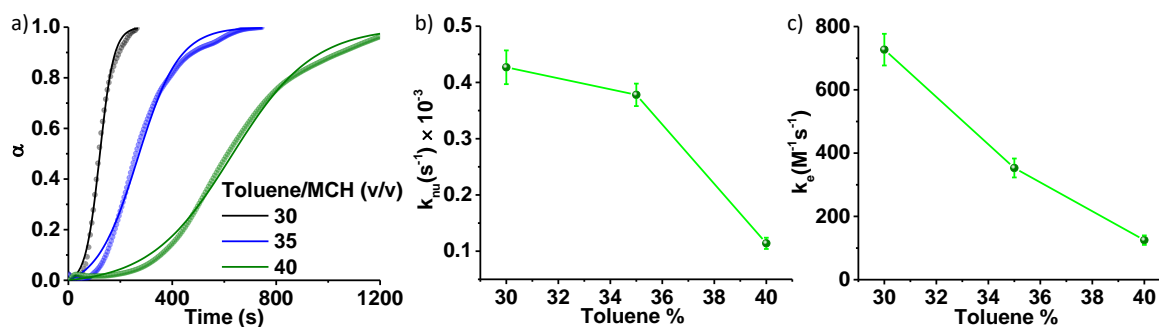
Figure 3.11. a) Fitting of time-dependent nucleation-elongation growth for molecule **NDI-OEt-chol** into Watzky and Finke model to extract the k_{nu} (nucleation rate constant) and k_e (elongation rate constant) for toluene/MCH, 30/70 (v/v), toluene/MCH, 35/65 (v/v) and toluene/MCH, 40/60 (v/v). Kinetic parameters plotted against % of toluene shows an increase in both b) k_{nu} and c) k_e with decrease of toluene %. ([**NDI-OEt-chol**] = 5×10^{-5} M).

Interestingly, molecule **NDI-OEt-chol** also having an on-pathway metastable state and shows a similar hysteresis and kinetically controlled nucleation-elongation growth at higher solvent percentages of good solvent, toluene (> toluene/MCH, 30/70 (v/v)) (Figures 3.10 and 3.11).

3.5. Fibers Stability and Monomer Exchange Kinetics of NDI-SEt-chol vs. NDI-OEt-chol:
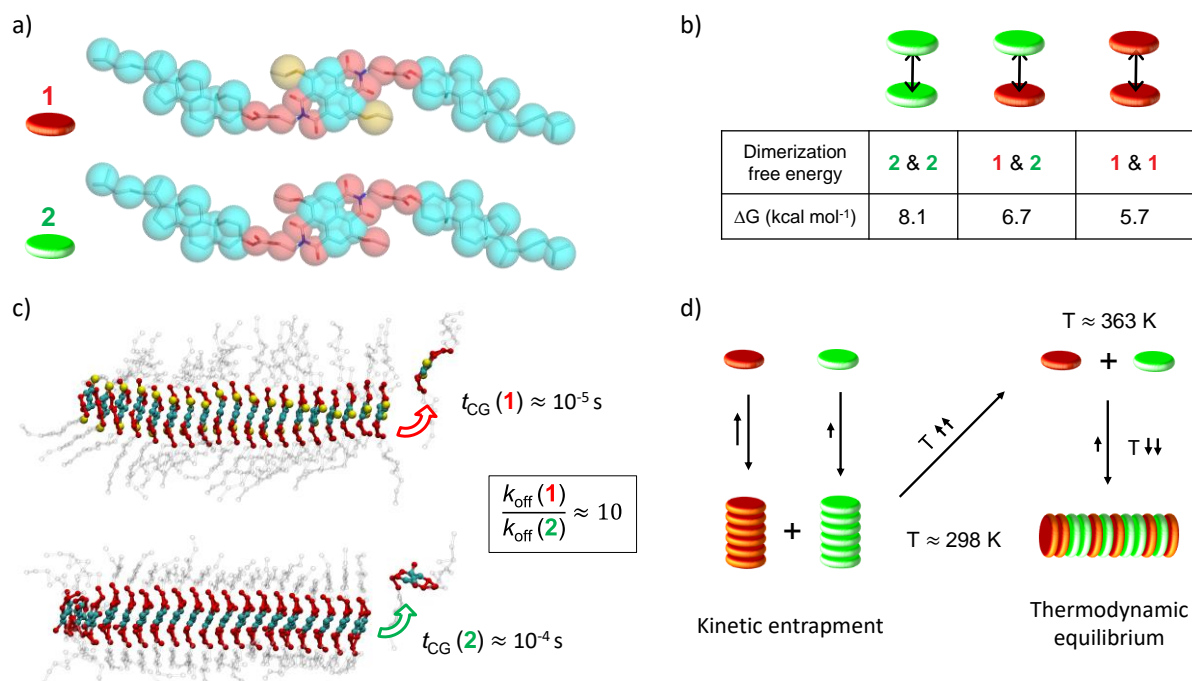
Figure 3.12. Coarse-grained molecular simulations of systems **NDI-SEt-chol** and **NDI-OEt-chol**. a) CG models of monomers **NDI-SEt-chol** and **NDI-OEt-chol** (resolution ~5Å). b) The dimerization free-energies, ΔG, obtained from WT-MetaD simulations allow to compare the strength of monomer-monomer interactions (**NDI-SEt-chol-NDI-SEt-chol** *vs.* **NDI-SEt-chol-NDI-OEt-chol** *vs.* **NDI-OEt-chol-NDI-OEt-chol**). c) Infrequent WT-MetaD simulations exploring the mechanism and kinetics of monomer exchange form the tips of fibers **NDI-SEt-chol** and **NDI-OEt-chol**. Monomer exchange is found to be ~10 times faster in fiber **NDI-SEt-chol** than in fiber **NDI-SEt-chol**. d) Model for the formation of narcissistically self-sorted homopolymers of **NDI-SEt-chol** and **NDI-OEt-chol** at room temperature (kinetically trapped state), while increasing the temperature to ~363 K moves the equilibrium toward the monomers, which then tend to self-assemble in a random fashion upon self-assembly at lower temperature (~298 K).

Molecular simulations are extremely useful to obtain a molecular level understanding of dynamic supramolecular polymers.[25,26,27] In particular, by combining fine coarse-grained (CG) models and enhanced sampling approaches it is possible to explore the monomer-monomer interactions, the monomer exchange kinetics and the relative stability of assemblies.[17,28] Hence we have built fine CG models for monomers **NDI-SEt-chol** and **NDI-OEt-chol** (with a resolution ~5Å), which are shown in Figure 3.12a. Using the same approach used recently for modeling similar supramolecular assemblies,[17,25-28] the CG models, which are based on the MARTINI CG force field,[29] have been then refined in order to be consistent with the behavior of the systems seen at the all-atom level (see experimental section). We used well-tempered metadynamics (WT-MetaD) simulations[30] to explore the stacking/de-stacking of monomers in

explicit cyclohexane solvent (equivalent to MCH at the level of resolution of the CG models used herein).[17] This allowed us to compare the free energy of binding between different monomers i.e., **NDI-SEt-chol**-**NDI-SEt-chol** vs. **NDI-SEt-chol**-**NDI-OEt-chol** vs. **NDI-OEt-chol**-**NDI-OEt-chol** (Figure 3.12b). The **NDI-OEt-chol**-**NDI-OEt-chol** interaction (8.1 kcal mol^{-1}) was found to be stronger than the mixed **NDI-SEt-chol**-**NDI-OEt-chol** interaction (6.7 kcal mol^{-1}) and of the **NDI-OEt-chol**-**NDI-OEt-chol** interaction (5.7 kcal mol^{-1}). Accordingly, fiber **NDI-SEt-chol** was found to be more dynamic than fiber **NDI-OEt-chol**. Starting from pre-equilibrated stacks containing 20 monomers of **NDI-SEt-chol** or **NDI-OEt-chol**, we used infrequent WT-MetaD simulations to activate and study the event of monomer exchange from the tips of the two fibers.[17,28] At this scale, the exchange of monomers out from the assemblies is a rare event, the kinetics of which can be reliably reconstructed from multiple biased WT-MetaD exchange runs.[17,28,31,32] These simulations provided characteristic exchange timescales (t_{CG}) in the order of ~10^{-4} s for fiber **NDI-OEt-chol** vs. ~10^{-5} s for fiber **NDI-SEt-chol** (Figure 3.12c). While these exchange timescales are obtained from approximated CG models and should be thus considered qualitatively, these still maintain a useful comparative value, indicating that the monomer exchange rate (k_{off}) is ~10 times faster in fiber **NDI-SEt-chol** than in fiber **NDI-OEt-chol**.

Altogether, these data allowed us to propose the scheme for the formation of block vs. random supramolecular polymers of **NDI-SEt-chol** and **NDI-OEt-chol** as shown in Figure 3.12d. At room temperature (298 K) monomer exchange in/out these fibers is rare and fibers **NDI-SEt-chol** and fibers **NDI-OEt-chol** remains in a self-sorted kinetically trapped state as long as the system is at 298 K. However, when temperature is increased to 363 K, the equilibrium moves toward the monomers and hence fibers **NDI-SEt-chol** and **NDI-OEt-chol** disassemble with time. From such a disassembled state, the mixing of monomers then become quite random, consistent with the rather similar **NDI-SEt-chol**-**NDI-SEt-chol** vs. **NDI-SEt-chol**-**NDI-OEt-chol** vs. **NDI-OEt-chol**-**NDI-OEt-chol** monomer-monomer interactions (Figure 3.12b). This has been supported by means of experiments and self-assembly simulations (*vide infra*).

3.6. Controlled Supramolecular Polymerization:

As discussed above, during a two component supramolecular polymerization, there are many possible outcomes: formation of supramolecular homopolymers (narcissistic self-sorting), supramolecular random copolymer, supramolecular alternating copolymer and supramolecular block copolymer (Scheme 3.1). Based on the essential requirements as mentioned above, we thought of using molecules **NDI-SEt-chol** and **NDI-OEt-chol** exhibiting kinetically controlled growth and low structural mismatch for a sequence controlled supramolecular polymerization. By exploiting, thermodynamic and kinetic routes of sample preparation and the molecular level insight obtained from MD simulations of monomer exchange dynamics and interaction energies, we envisage to obtain the three structurally distinct supramolecular polymers by utilizing the same molecules. We use extensive spectroscopic and microscopic probing and MD simulations to characterize these sequence controlled supramolecular assemblies.

3.6.1. Random Supramolecular Copolymers under Thermodynamic Control:

First, we investigated the temperature-dependent supramolecular copolymerization of an equimolar mixture of **NDI-SEt-chol** and **NDI-OEt-chol** monomers, by slowly cooling (1 K/min) from 363 K to 298 K. The growth process of both **NDI-SEt-chol** and **NDI-OEt-chol** can be selectively probed by monitoring their aggregation band at 590 nm and 490 nm, respectively. Homopolymerization of individual monomers (2.5×10^{-5} M) in toluene/MCH, 5/95 (v/v) solvent mixture, by cooling at a rate of 1 K/min, showed distinct self-assembling behavior. Monomer **NDI-SEt-chol** gets trapped in the metastable **State A**, whereas **NDI-OEt-chol** undergoes a cooperative supramolecular polymerization with an elongation temperature (T_e) of 332 ± 1 K (Figure 3.13a). Since at this solvent composition monomer **NDI-OEt-chol** does not show any lag phase and has a higher kinetic and thermodynamic stability, molecule **NDI-SEt-chol** was used as a seed and molecule **NDI-OEt-chol** was used as a metastable state (3.13b) (*vide infra*).

We envisage that, on supramolecular copolymerization, strong homo-recognition between monomers **NDI-SEt-chol** and **NDI-OEt-chol** would lead to self-sorted supramolecular homopolymers, while strong hetero-recognition between the monomers would be required to construct supramolecular alternating copolymers (Figure 3.14a). Temperature-
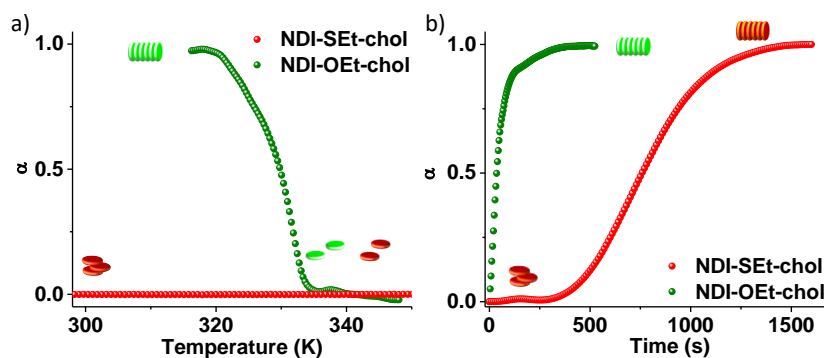
Figure 3.13. Kinetic and thermodynamic stability of **NDI-SEt-chol** and **NDI-OEt-chol** assemblies. a) Comparison of thermodynamic stability of self-assembled **NDI-SEt-chol** and **NDI-OEt-chol**. Cooling curve (1 K/min) for **NDI-SEt-chol** (obtained by following absorbance changes at 590 nm) shows no growth but the formation of metastable **State A**, whereas molecule **NDI-OEt-chol** (obtained by following absorbance changes at 490 nm) undergoes self-assembly with T_e (elongation temperature) = 333 K indicating its higher thermodynamic stability. b) Comparison of self-assembly kinetics of molecules **NDI-SEt-chol** and **NDI-OEt-chol** when cooled at a rate of 5 K/min. Whereas molecule **NDI-SEt-chol** shows a kinetics with sigmoidal growth at this solvent composition, molecule **NDI-OEt-chol** due to higher stability shows very fast kinetics. ([**NDI-SEt-chol**] = [**NDI-OEt-chol**] = 2.5×10^{-5} M, toluene/MCH, 5/95 (v/v)).

dependent supramolecular copolymerization of 1:1 mixture of **NDI-SEt-chol** and **NDI-OEt-chol** from 363 K to 298 K at 1 K/min showed cooperative growth of both **NDI-SEt-chol** and **NDI-OEt-chol** (when monitored exclusively at their individual aggregation bands) with the identical T_e of 332 ± 1 K matching well with the T_e of pure **NDI-OEt-chol** (Figure 3.14b) suggesting the coassembly of monomers. At a constant concentration of **NDI-OEt-chol**, the variation of concentration of **NDI-SEt-chol** did not result in any change in their elongation temperature (Figure 3.14c, and 3.14d). Further, the variation of monomer composition (1:2 ratio) while keeping the total concentration at 2.5×10^{-5} M showed a change in T_e proportionally with the concentration of **NDI-OEt-chol** (Figures 3.14e, and 3.14f) and matched well with the T_e of pure **NDI-OEt-chol** of similar concentrations. These observations hint towards the heterogeneous nucleation of monomers of **NDI-SEt-chol** triggered by **NDI-OEt-chol**, than the
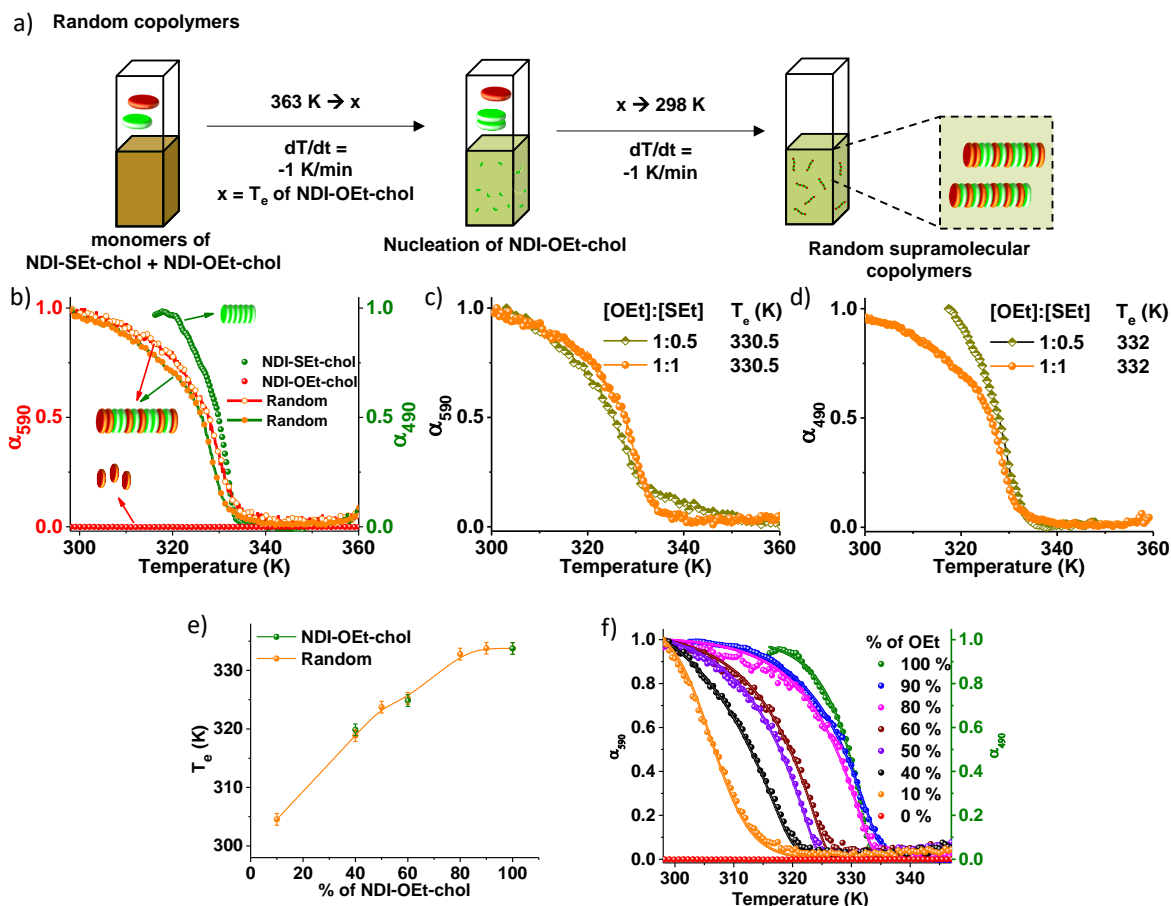
Figure 3.14. a) Schematic representation showing the preparation of random supramolecular copolymer under thermodynamic control. b) Cooling curves of homopolymers of **NDI-SEt-chol** and **NDI-OEt-chol** and the copolymer, showing heterogeneous nucleation under thermodynamic control, with nucleation and growth of **NDI-SEt-chol** on *in situ* formed nuclei of **NDI-OEt-chol**, when monitored at aggregated band of **NDI-SEt-chol** and **NDI-OEt-chol**. ([**NDI-SEt-chol**] = [**NDI-OEt-chol**] = 2.5×10⁻⁵ M). c), d)Temperature-dependent cooling curves of coassembled solution of **NDI-SEt-chol** and **NDI-OEt-chol** keeping the concentration of **NDI-OEt-chol** constant and with varying concentrations of **NDI-SEt-chol**, which shows a constant T_e when monitored c) at 590 nm (corresponds to aggregate band of **NDI-SEt-chol**) and d) at 490 nm (corresponds to aggregate band of **NDI-OEt-chol**) showing formation of nuclei of **NDI-OEt-chol**, followed by the growth of both **NDI-SEt-chol** and **NDI-OEt-chol** to form an random copolymer. ([**NDI-OEt-chol**] = 2.5×10⁻⁵ M). e) Plot of decrease in T_e during the thermodynamic supramolecular copolymerization of **NDI-SEt-chol** and **NDI-OEt-chol** for various molar ratios between **NDI-SEt-chol** and **NDI-OEt-chol**. The matching T_e of coassembled solution with that of pure stacks of **NDI-OEt-chol** (green dots), at respective concentrations confirms heterogeneous nucleation. f) Corresponding fitting of the cooling curves during the thermodynamic supramolecular copolymerization of **NDI-SEt-chol** and **NDI-OEt-chol** for various molar ratios between **NDI-SEt-chol** and **NDI-OEt-chol** using nucleation-elongation model. ([**NDI-SEt-chol**] + [**NDI-OEt-chol**] = 2.5×10⁻⁵ M, toluene/MCH, 5/95 (v/v), cooling rate = 1 K/min).
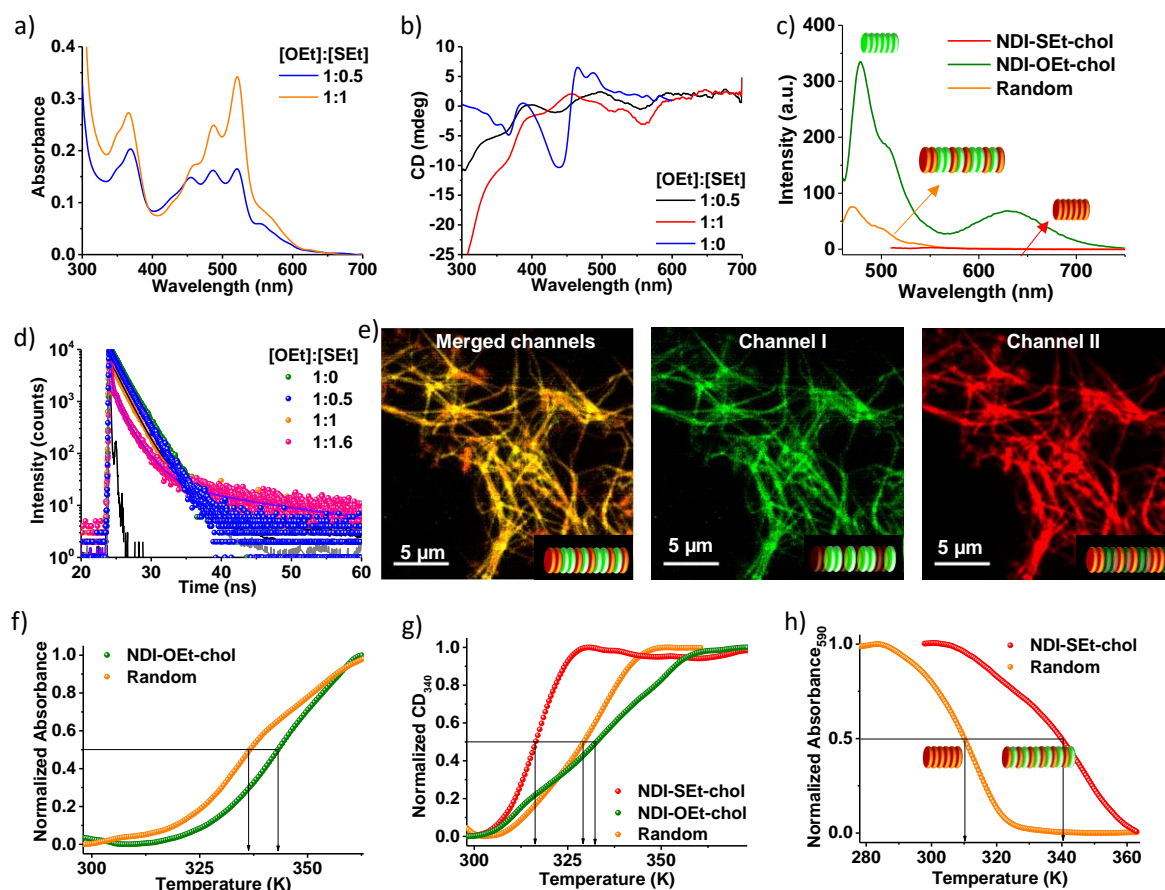
Figure 3.15. Characterization of random supramolecular copolymers at a varying concentration of **NDI-SEt-chol** and with constant concentration of **NDI-OEt-chol**. a) Absorption, b) CD and c) emission spectra (λ_{ex} = 442 nm) of the copolymerized solutions. Corresponding lifetime decay profiles collected d) at 480 nm (λ_{ex} = 442 nm) ([**NDI-OEt-chol**] = 2.5×10^{-5} M, toluene/MCH, 5/95 (v/v)). Quenched donor emission with the absence of excimer band depicting the formation of supramolecular random copolymers. e) SIM image displaying completely overlapping red and green emission from **NDI-SEt-chol** and **NDI-OEt-chol** respectively confirming the formation of supramolecular random copolymers. ([**NDI-SEt-chol**] = [**NDI-OEt-chol**] = 2.5×10^{-5} M, toluene/MCH, 5/95 (v/v)). f) Heating curve (1 K/min) monitored at 490 nm absorbance, shows a decrease in stability of random supramolecular copolymer in comparison to pure **NDI-OEt-chol** at same concentration. g) Heating curve obtained from monitoring CD changes at 340 nm reiterates the decrease and increase in the stability of random supramolecular copolymer in comparison to pure **NDI-OEt-chol** and pure **NDI-SEt-chol** at same concentration respectively. h) Heating curve monitored at 590 nm (absorbance) reiterates the increase in stability of component **NDI-SEt-chol** in random supramolecular copolymer in comparison to pure **NDI-SEt-chol** of same concentration. ([**NDI-SEt-chol**] = [**NDI-OEt-chol**] = 2.5×10^{-5} M, l = 10 mm, toluene/MCH, 5/95 (v/v), heating rate = 1 K/min, (Channel I: λ_{ex} = 488 nm, λ_{coll} = 495-575; Channel II: λ_{ex} = 561 nm, λ_{coll} = 570-650 nm)).

cooperative growth of a hetero-dimer, which would have resulted in maximum T_e at 1:1 monomer composition. However, the resultant solution showed a new CD spectrum different from individual components with no bisignation at the absorption maximum of **NDI-OEt-chol**, elucidating a random arrangement of monomers rather than blocky supramolecular

polymerization (Figures 3.15a and 3.15b). The absence of excimer emission of **NDI-SEt-chol** and significant fluorescence quenching of **NDI-OEt-chol** due to energy transfer depicts a negligible domain formation of **NDI-OEt-chol** (Figures 3.15c, 3.15d). Further, the heating curve of the random supramolecular copolymer showed significantly high stability with a melting temperature (T_m) of 340.2 K, which is 30 K higher than the homo supramolecular polymer of **NDI-SEt-chol** (Figures 3.15f, 3.15g 3.15h). Finally, the microscopic visualization of these supramolecular polymers showed no distinct red- and green-emissive fibers and a complete spatial overlap validates the formation of the random supramolecular copolymers (Figure 3.15e). We envisage that reactivity ratio (($\Delta G_{\text{NDI-SEt-chol-NDI-SEt-chol}}+\Delta G_{\text{NDI-OEt-chol-NDI-OEt-chol}}$)/$2\times\Delta G_{\text{NDI-SEt-chol-NDI-OEt-chol}}$) of monomers **NDI-SEt-chol** and **NDI-OEt-chol** is 1.02, where disassembled **NDI-SEt-chol** and **NDI-OEt-chol** tend to mix at the level of individual monomers or as small groups of **NDI-SEt-chol** and **NDI-OEt-chol**, leading to a random arrangement of monomers under thermodynamic conditions.[15] This is consistent with the rather similar **NDI-SEt-chol**-**NDI-SEt-chol** vs. **NDI-SEt-chol**-**NDI-OEt-chol** vs. **NDI-OEt-chol**-**NDI-OEt-chol** monomer-monomer interaction energies obtained from the simulations and with the mixing

[**OEt:SEt**]	t_1 (ns)	t_2 (ns)	t_3 (ns)	t_4 (ns)
1:0		0.59 (6.3 %)	1.83 (92.2 %)	6.16 (1.5 %)
1:0.5	0.010 (23.4 %)	0.8 (11.2 %)	1.85 (64.9 %)	8.81 (0.5 %)
1:1	0.016 (25.9 %)	0.7 (11.5 %)	1.85 (60.3 %)	14.83 (2.3 %)
1:1.6	0.024 (48.9 %)	0.7 (11.8 %)	2.01 (31.9 %)	18.25 (7.4 %)

Table 3.3. Lifetime data of randomly arranged **NDI-SEt-chol** and **NDI-OEt-chol** when collected at 480 nm. (λ_{ex} = 442 nm, [**NDI-OEt-chol**] = 2.5×10^{-5} M, toluene/MCH, 5/95 (v/v)).

Component	590 nm	430 nm	340 nm
NDI-SEt-chol	310 K		316 K
NDI-SEt-chol in random	340 K		
NDI-OEt-chol		336 K	333 K
NDI-OEt-chol in random		343 K	329.3 K

Table 3.4. Listed T_m and T_e respectively values for **NDI-SEt-chol** and **NDI-OEt-chol** in random arrangement at different wavelengths ([**NDI-SEt-chol**] = [**NDI-OEt-chol**] = 2.5×10^{-5} M, toluene/MCH, 5/95 (v/v)).

fashion that in such conditions is entropically more favourable (random mixing). This has been further confirmed by means of a coarse-grained molecular dynamics simulation (CG-MD) simulation where 75 + 75 initially disassembled **NDI-SEt-chol** and **NDI-OEt-chol** monomers

self-assemble spontaneously during 10 µs of CG-MD in explicit cyclohexane solvent (Figure 3.16a). During this simulations, **NDI-SEt-chol** and **NDI-OEt-chol** monomers mix in a quite random fashion to result in short segments and individual monomers as evident from Figure 3.16. Notably, the size of the **NDI-SEt-chol** and **NDI-OEt-chol** domains in the mixed stack is related, together with a favored random mixing, in consistent with the fact that **NDI-SEt-chol**-**NDI-SEt-chol** vs. **NDI-SEt-chol**-**NDI-OEt-chol** vs. **NDI-OEt-chol**-**NDI-OEt-chol** interactions, though very similar, are not perfectly identical. This is also supported by the analysis of the contacts between the centers of the monomer cores (core-core coordination) in the system during the CG-MD simulations (Figure 3.16b). In general, a number of contacts equal to 2 identifies a perfect supramolecular polymer, where each monomer has exactly 2 neighbors stably coordinated through their cores. A value of 1 in all curves would mean perfect alternated intermixing of cores. It is interesting to note that in the case where the simulations stat from 75 + 75 initially disassembled monomers, all three red, green and yellow lines tend to equilibrate close to 1, demonstrating the intermixing of small groups (i.e. dimers, trimers, etc.) of red or green is present in the self-assembled structure (in principle, a perfect mixing of alternated **NDI-SEt-chol** and **NDI-OEt-chol** monomers would be compatible with identical red-red, green-green and green-red interaction energies).These observations, shows a marked
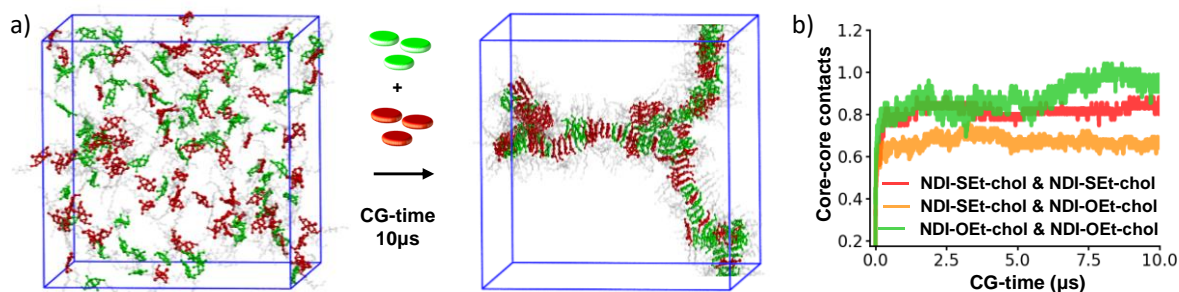
Figure 3.16. a) Self-assembly of **NDI-SEt-chol** and **NDI-OEt-chol** monomers (75 + 75) during 10 µs of CG-MD. During the run, the **NDI-SEt-chol** and **NDI-OEt-chol** monomers mix randomly together, in the form of short red and green segments and monomers suggesting the formation of random supramolecular copolymers. b) Number of contacts between the centers of the red (**NDI-SEt-chol**)-red (**NDI-SEt-chol**) (red curve), green (**NDI-OEt-chol**)-green (**NDI-OEt-chol**) (green curve) and green (**NDI-OEt-chol**)-red (**NDI-SEt-chol**) (yellow curve) monomer cores in the system during the CG-MD - similar contacts between the yellow (**NDI-SEt-chol**-**NDI-OEt-chol** contacts) vs. red (**NDI-SEt-chol**-**NDI-SEt-chol** contacts) and green (**NDI-OEt-chol**-**NDI-OEt-chol** contacts) lines identify intermixing between the monomers.

difference from a recent report by Meijer and coworkers, where prevailing homo- over hetero-recognition leads to the formation of supramolecular block copolymer under thermodynamic control.[11,15] Altogether our results strongly demonstrate that such different behavior between

supramolecular systems based on similar concepts is most likely the consequence of homo- vs. hetero- monomer-monomer interactions in the system. In fact, a perfect segregation in stable blocks starting from disassembled monomers would imply stronger homo- vs. hetero-monomer-monomer interactions in the system. However, since our current system shows a rather similar hetero- vs. homo-recognition under thermodynamic conditions, heterogeneous nucleation under kinetic control and at low monomer dynamics (at low temperature) appears to be the only way to obtain supramolecular block copolymers (*vide supra*).[20]

3.6.2. Kinetically Stable, Narcissistically Self-Sorted Supramolecular Homopolymers:
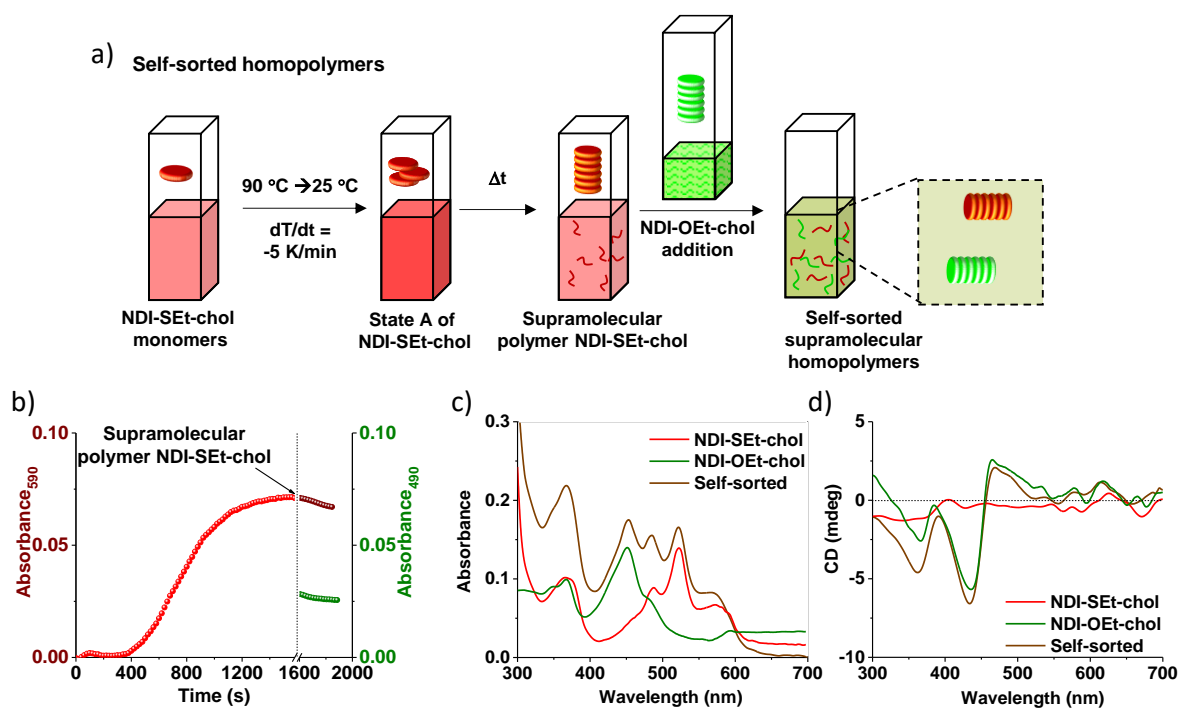
Figure 3.17. Synthesis of self-sorted supramolecular homopolymers of **NDI-SEt-chol** and **NDI-OEt-chol**. a) Schematic representation showing the preparation of the self-sorted homopolymers. b) Time-dependent absorbance changes monitored at the aggregate bands of **NDI-SEt-chol** (590 nm) and **NDI-OEt-chol** (490 nm). Addition of supramolecular polymer of **NDI-OEt-chol** to a kinetically grown supramolecular polymer of **NDI-SEt-chol** (after 1600 seconds), shows insignificant changes in the supramolecular organization of **NDI-SEt-chol** and **NDI-OEt-chol**. c) Absorption and d) CD spectra of the self-sorted assembly showing individual assembly signatures in the self-sorted arrangement. ([**NDI-SEt-chol**] = [**NDI-OEt-chol**] = 2.5×10^{-5} M, toluene/MCH, 5/95 (v/v), l = 10 mm).

Supramolecular random copolymerization under thermodynamic conditions prompted us to investigate the monomer exchange dynamics at room temperature and kinetic stability of the stacks by probing the spectroscopic properties of a mixture of homopolymers of **NDI-SEt-chol** and **NDI-OEt-chol**. To investigate this, an equimolar mixture of **NDI-SEt-chol** and **NDI-OEt-chol** stacks was synthesized by the post-synthetic mixing of the supramolecular homopolymers of **NDI-SEt-chol** and **NDI-OEt-chol**, made individually by the kinetically controlled nucleation growth (Figure 3.17a). Independent spectroscopic probing of the **NDI-SEt-chol** and **NDI-OEt-chol** monomers in the homopolymers, did not show any absorbance changes at 590 nm for **NDI-SEt-chol** and 490 nm for **NDI-OEt-chol**, hinting towards the absence of any structural reorganization upon mixing (Figure 3.17b). Further, the final absorption and CD of this mixture matches well with the summation of the two individual supramolecular polymers (Figures 3.17c and 3.17d), hinting to a self-sorted fibers. In addition, absence of energy transfer depicted by insignificant quenching of donor (**NDI-OEt-chol**) emission in the mixture characterizes that the homopolymers of **NDI-SEt-chol** and **NDI-OEt-chol** are spatially self-sorted (Figures 3.18a and 3.18b). The heating curves of self-sorted assemblies and individual homo stacks match well and show an identical melting temperature (T_m) of 313±1 K reiterating that the supramolecular homopolymers are spatially segregated (Figures 3.18c, 3.18d and 3.18e). Low exchange dynamics of the monomers at 298 K were further probed via energy transfer for three days, which did not show any change in the emission profile of the donor-acceptor mixture (Figures 3.18f and 3.18g). These kinetically stable, self-sorted supramolecular homopolymers were microscopically visualized by selective excitation of **NDI-SEt-chol** and **NDI-OEt-chol** (561 nm and 488 nm respectively) using SIM as spatially segregated green- and red-emissive supramolecular polymers (Figure 3.18h). This is again
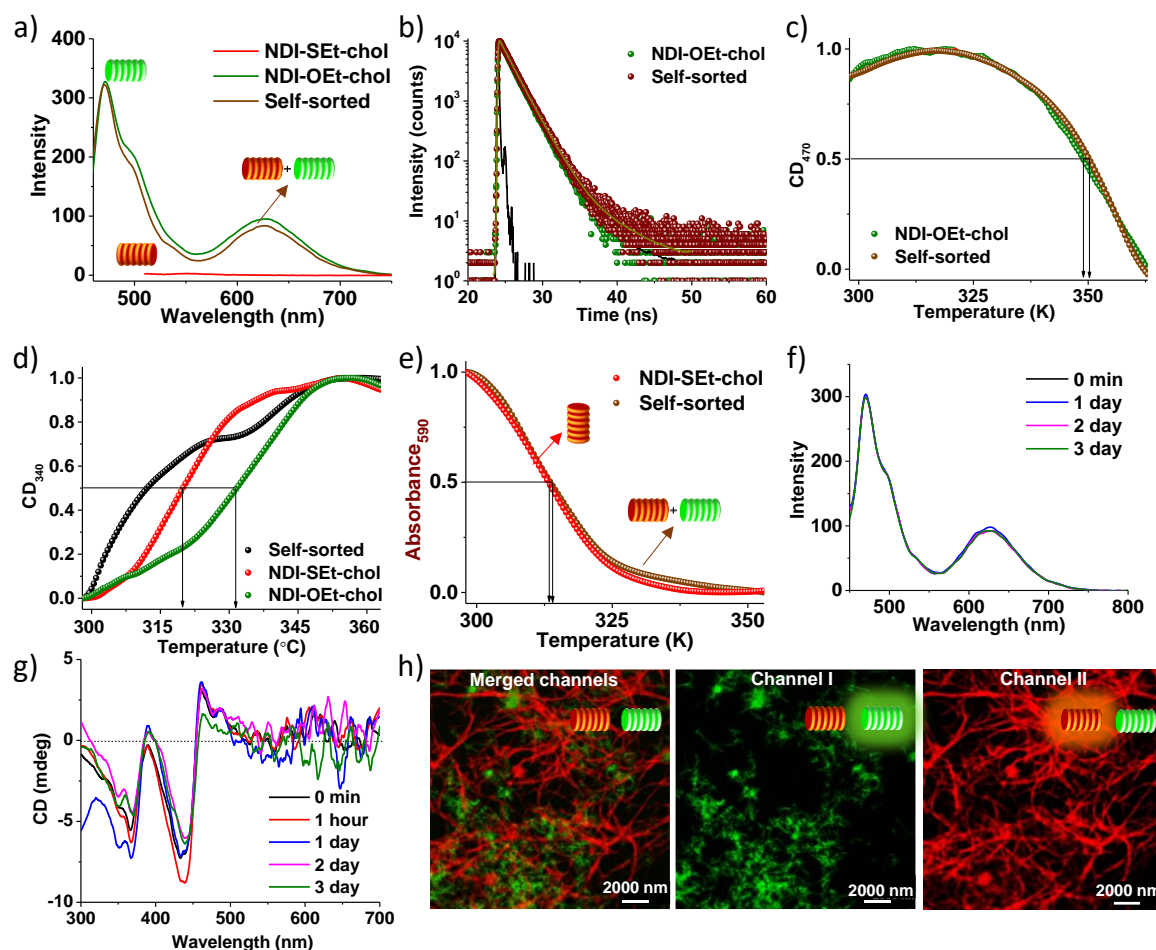
Figure 3.18. a) Emission spectra of self-sorted and homopolymers of **NDI-SEt-chol** and **NDI-OEt-chol** (λ_{ex} = 442 nm, l = 10 mm), showing negligible energy transfer in the self-sorted state as evident from the lack of quenching of both aggregate and excimer emission of the donor **NDI-OEt-chol** (λ_{ex} = 442 nm, l = 10 mm). b) Lifetime decay profile of molecule **NDI-OEt-chol** in the self-sorted arrangement and corresponding comparison with donor in absence of acceptor, (λ_{ex} = 442 nm, λ_{coll} = 480 nm) showing no energy transfer in self-sorted arrangement. c) Heating curve (1 K/min) monitored at 470 nm (absorbance), shows unaltered stability of self-sorted supramolecular copolymer in comparison to pure **NDI-OEt-chol** at same concentration. d) The heating curve obtained by monitoring CD changes at 340 nm containing contribution from both self-assembled **NDI-SEt-chol** and **NDI-OEt-chol** shows a two-step transition while heating. The inflection point in the heating curve takes place due to complete melting of self-assembled **NDI-SEt-chol** at that temperature in the self-sorted assembly. Further heating curve shows melting of component **NDI-SEt-chol** finishes before component **NDI-OEt-chol**. e) The heating curve (monitored with the absorbance at 590 nm) of the solution of self-sorted supramolecular polymers of **NDI-SEt-chol** and **NDI-OEt-chol** showing similar stability of **NDI-SEt-chol** compared to the pure supramolecular polymer of **NDI-SEt-chol** (heating rate = 1 K/min). Time-dependent f) emission spectra (λ_{ex} = 442 nm, l = 10 mm) and g) CD spectra of the self-sorted fibers, which does not show any changes with time suggesting the low dynamics of the monomers. h) Corresponding SIM images showing spatially segregated supramolecular polymers of **NDI-SEt-chol** and **NDI-OEt-chol** confirming the self-sorted arrangement. ([**NDI-SEt-chol**] = [**NDI-OEt-chol**] = 2.5×10^{-5} M, toluene/MCH, 5/95 (v/v), l = 10 mm, Channel I: λ_{ex} = 488 nm, λ_{coll} = 495-575; Channel II: λ_{ex} = 561 nm, λ_{coll} = 570-650 nm).

111

	t_1 (ns)	t_2 (ns)	t_3 (ns)
NDI-OEt-chol	0.59 (6.3 %)	1.83 (92.2 %)	6.16 (1.5 %)
Self-sorted	0.14 (4.7 %)	1.77 (92.9 %)	7.39 (2.4 %)

Table 3.5. Lifetime data of **NDI-OEt-chol** in self-sorted assembly and that of pure **NDI-OEt-chol** of same concentration (λ_{ex} = 442 nm, λ_{coll} = 480 nm). ([**NDI-SEt-chol**] = [**NDI-OEt-chol**] = 2.5×10⁻⁵ M, toluene/MCH, 5/95 (v/v)).

Component	590 nm	470 nm	340 nm
NDI-SEt-chol	313.2 K		319.8 K
NDI-SEt-chol in self-sorted	313.9 K		
NDI-OEt-chol		348.8 K	331.6 K
NDI-OEt-chol in self-sorted		349.9 K	

Table 3.6. Listed T_m and T_e values respectively for **NDI-SEt-chol** and **NDI-OEt-chol** in self-sorted arrangement at different wavelengths. ([**NDI-SEt-chol**] = [**NDI-OEt-chol**] = 2.5×10⁻⁵ M, toluene/MCH, 5/95 (v/v)).
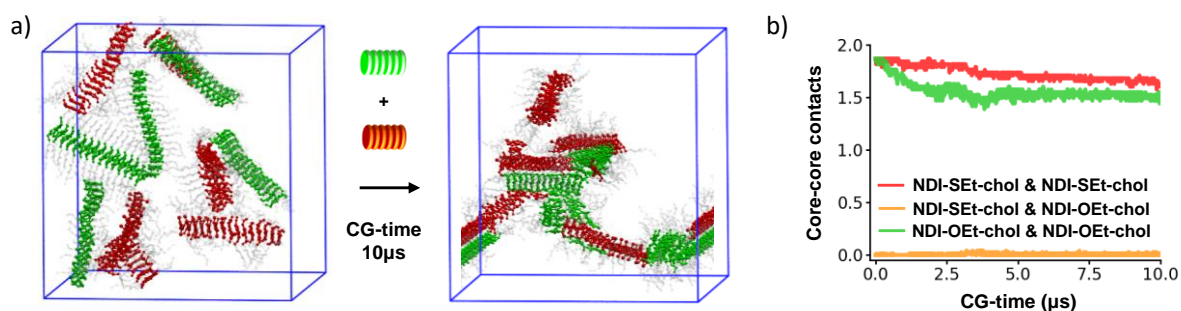
Figure 3.19. a) Self-assembly of 5 + 5 preformed stacks each containing 15 monomers of **NDI-SEt-chol** and **NDI-OEt-chol** during 10 µs of CG-MD. During the run, the **NDI-SEt-chol** and **NDI-OEt-chol** stacks interact and self-assemble, yet remaining quite stable. b) Number of contacts between the centers of the red (**NDI-SEt-chol**)-red (**NDI-SEt-chol**) (red curve), green (**NDI-OEt-chol**)-green (**NDI-OEt-chol**) (green curve) and green (**NDI-OEt-chol**)-red (**NDI-SEt-chol**) (yellow curve) monomer cores in the system during the CG-MD – the negligible yellow contacts identify negligible intermixing between the different monomers in the system.

consistent with the low monomer exchange dynamics seen for these assemblies from the simulations. This was also further supported by a CG-MD simulation where we inserted 5 + 5 preformed stacks of **NDI-SEt-chol** and **NDI-OEt-chol** monomers, respectively. During the run, the stacks were seen to interact in a stable way, but with very limited internal mixing (Figure 3.19a). The persistence of the **NDI-SEt-chol** and **NDI-OEt-chol** stacks is also evident in the number of contacts of red (**NDI-SEt-chol**) and green (**NDI-OEt-chol**) cores during the CG-MD (close to 2 and minimally changing during the simulation), which means that the fibers

are quite ordered and stable and negligible rearrangements in terms of monomer mixing occur in the stacks (Figure 3.19b).

3.6.3. Supramolecular Block copolymer under Kinetic Control:
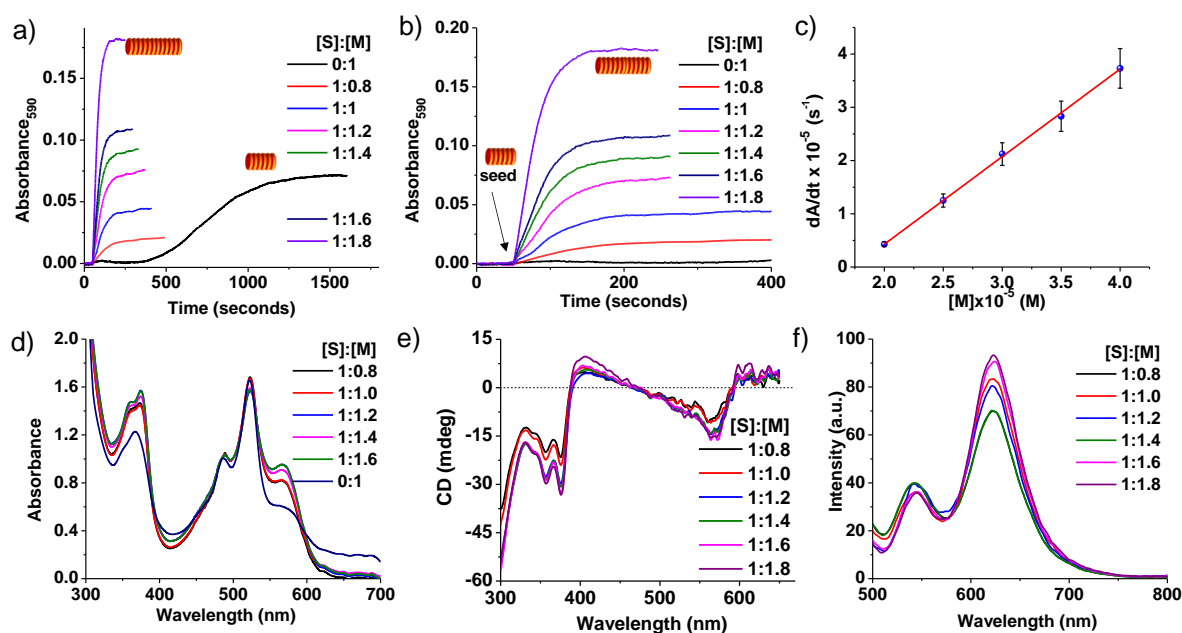
Figure 3.20. Homoseeding studies of supramolecular polymerization of molecule **NDI-SEt-chol** (Monomer (M)) initiated upon addition of its own seed (Seed (S)). a) Time-dependent absorbance changes at 590 nm (aggregate band of **NDI-SEt-chol**) along with the delayed growth of pure stacks of **NDI-SEt-chol** and b) corresponding zoomed in portion of the seeded growth, suggesting the seeded supramolecular polymerization of **NDI-SEt-chol** from metastable **State A** on addition of homoseed of **NDI-SEt-chol** ([S] = 2.5×10^{-5} M and [S]:[M] = 1:0.8, 1:1.0, 1:1.2, 1:1.4, 1:1.6, 1:1.8). c) The plot of polymerization rate obtained from absorbance changes at 590 nm shows a linear relationship with monomer concentration. This refers to the seeded nature of the process. The final d) absorption, e) CD and f) emission spectra (λ_{ex} = 442 nm) of the solutions after the seeded growth indicating self-assembled state. (toluene/MCH, 5/95 (v/v), l = 10 mm).

Random copolymerization of the monomers during the thermodynamic supramolecular copolymerization (vide supra), suggests that construction of two component supramolecular block copolymers requires a kinetically controlled living supramolecular polymerization process. Low monomer exchange dynamics at room temperature, kinetically realizable metastable monomer states, nucleation growth mechanism of self-assembly and tendency of hetero-recognition due to low monomer structural mismatch between **NDI-SEt-chol** and **NDI-OEt-chol**, as evident from the detailed probing of the kinetic and thermodynamic aspects (vide supra) of the monomers, are perfectly suited for the construction of block supramolecular structures via heterogeneous nucleation of the second monomer on the seeds or stacks of the first molecule. Molecule **NDI-SEt-chol** exhibits seeding characteristics as displayed by

immediate non-sigmoidal growth of metastable **State A** of **NDI-SEt-chol** upon the addition of pre-grown seeds of **NDI-SEt-chol** during the lag phase (Figure 3.20).[14]

Due to kinetically controlled nucleation growth of **NDI-SEt-chol** with a longer lag phase compared to **NDI-OEt-chol**, along with the higher kinetic and thermodynamic stability of **NDI-OEt-chol**, latter was introduced as a seed to the metastable monomers of **NDI-SEt-chol** to trigger the heterogeneous nucleation (Figure 3.21a). A self-assembled segment of monomers **NDI-OEt-chol** (seeds), was synthesized by sonicating a solution of kinetically grown **NDI-OEt-chol** (5×10^{-4} M) for 5 minutes (toluene/MCH, 5/95 (v/v)) as described in the experimental section and Figure 3.21b shows stability of the seeds on sonication where sonication does not lead to disassembly of the seeds. Further metastable state of **NDI-SEt-chol** (**State A**) was synthesized by the fast cooling (5 K/min) of its monomeric solution at 363 K in toluene/MCH, 5/95 (v/v). The addition of seeds of **NDI-OEt-chol** to **State A** of **NDI-SEt-chol** resulted in an instantaneous non-sigmoidal growth depicting heterogeneous nucleation and supramolecular copolymerization, which is evident from the changes in absorbance monitored selectively at 590 nm corresponding to the aggregate band of **NDI-SEt-chol** (Figures 3.21c and 3.21e). Variation of monomer to seed concentration showed consistent heterogeneous nucleation on the introduction of seed (Figures 3.21c and 3.21e). Increase of monomer concentration with a constant seed concentration showed a linear increase in polymerization rate without any lag phase (Figure 3.21d). In addition, the variation of seed concentration with constant monomer concentration showed a linear increase in polymerization rate with an increase of seed concentration (Figure 3.21f). These kinetic features refer to the seeded supramolecular polymerization between **NDI-SEt-chol** and **NDI-OEt-chol**.[20] We have ruled out the possibility of secondary nucleation as a side-reaction that competes with seeding to make triblock morphologies by plotting half time of the seeding kinetics against monomer concentration.[33] This was fitted using standard models available to exclude the possibility of any secondary nucleation (Figure 3.21g).

Absorption and CD spectra of the resultant coassembled solution show that individual aggregation characteristics of both molecules are retained (Figures 3.21h and 3.21i). Further, persistent excimer emission confirms the presence of homopolymeric domains of **NDI-OEt-**
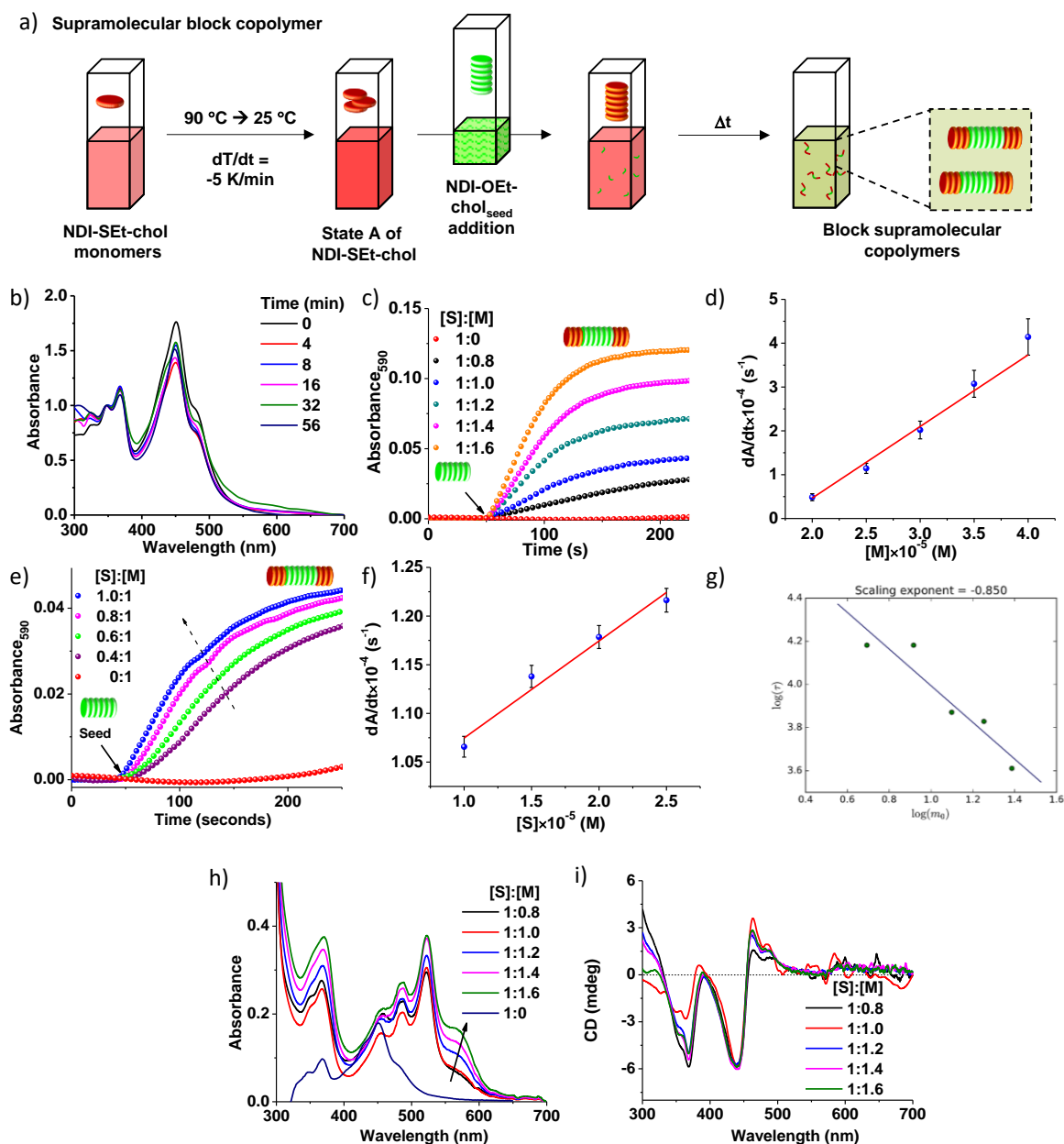
Figure 3.21. a) Schematic illustration presenting the synthesis of the supramolecular block copolymers. b) Absorption spectra of the seed of **NDI-OEt-chol** prepared by sonication with different sonication time does not show any disassembly ([**NDI-OEt-chol**] = 5×10^{-4} M, toluene/MCH, 5/95 (v/v)). c), e) Time course of the supramolecular polymerization of **State A** of **NDI-SEt-chol** (Monomer (M)) (obtained by monitoring absorbance changes at 590 nm) initiated by addition of seed (S) of **NDI-OEt-chol** under the condition of c) [S]:[M] = 1:0.8, 1:1.0, 1:1.2, 1:1.4, 1:1.6 at constant [S] = 2.5×10^{-5} M and e) [S]:[M] = 1:1, 0.8:1, 0.6:1, 0.4:1 at constant [M] = 2.5×10^{-5} M. d) and f) Plots of the rate of change in absorbance at 590 nm at saturation as a function of [M] and [S], respectively showing linear relationship. g) Plot of log half time against log (m_0) (m_0 = initial monomer concentration) obtained using the data from 3.21c and subsequent fitting of the curve to determine the scaling exponent. h) Final absorption and i) CD spectra of the solutions after the seeding experiments corresponding to Figure 3.21c. (toluene/MCH, 5/95 (v/v), l = 10 mm).
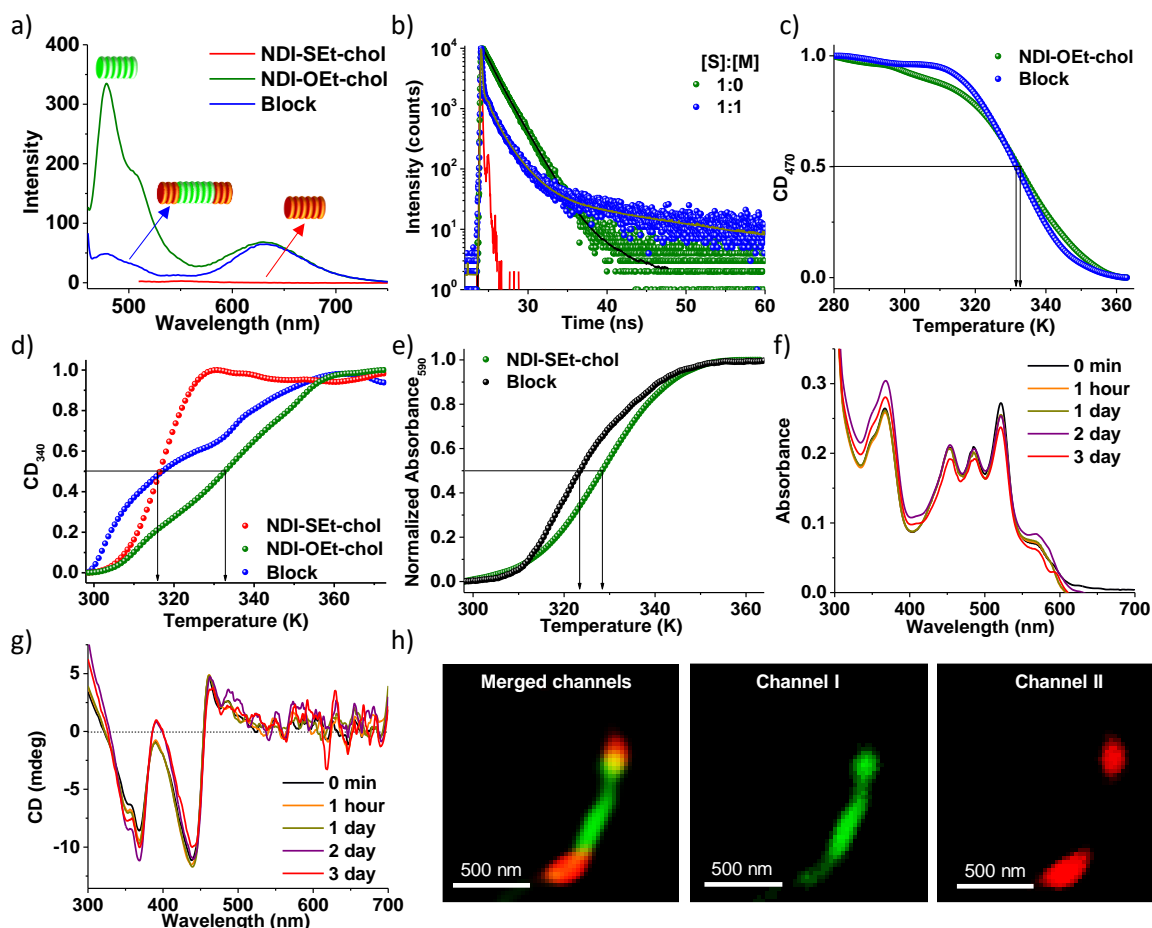
Figure 3.22. a) Emission spectra (λ_{ex} = 442 nm) displaying a significant donor emission quenching due to energy transfer from **NDI-OEt-chol** to **NDI-SEt-chol** illustrating an efficient interaction between supramolecular polymers of **NDI-SEt-chol** and **NDI-OEt-chol** and thus suggesting a block formation. b) Lifetime decay profile collected at 480 nm (λ_{ex} = 442 nm) showing decrease in lifetime of donor (**NDI-OEt-chol**). The heating curves obtained by monitoring CD changes c) at 470 nm (corresponding to CD signal of pure **NDI-OEt-chol**) which shows similar melting curve as that of pure self-assembled **NDI-OEt-chol**. d) Probing of CD changes at 340 nm (contains CD signal of both **NDI-SEt-chol** and **NDI-OEt-chol)** show two-step transition. The inflection point in the heating curve suggests a complete melting of **NDI-SEt-chol** from the supramolecular block copolymer. Further heating shows melting of component **NDI-SEt-chol** finishes before component **NDI-OEt-chol**. e) Absorbance changes at 590 nm (contains contribution from **NDI-SEt-chol** only), for the block structures shows lower stability of **NDI-SEt-chol** as compared to pure **NDI-SEt-chol** at same concentration. Time-dependent f) Absorption g) CD spectra showing no change up to 3 days suggesting low dynamics within the block. h) SIM images of channel I (green), channel II (red) and merged channel, showing the formation of the supramolecular block copolymer. ([**NDI-SEt-chol**] = [**NDI-OEt-chol**] = 2.5×10^{-5} M, toluene/MCH, 5/95 (v/v), heating rate = 1 K/min, Channel I: λ_{ex} = 488 nm, λ_{coll} = 495-575; Channel II: λ_{ex} = 561 nm, λ_{coll} = 570-650 nm).

chol in the resultant structure (Figure 3.22a). In addition, the self-assembled emission of **NDI-OEt-chol** at 480 nm is significantly quenched upon copolymerization, suggesting an efficient energy transfer to **NDI-SEt-chol**, which also hints towards the close proximity of the self-assembled domains of **NDI-SEt-chol** and **NDI-OEt-chol** (Figures 3.22a and 3.22b). All these

observations corroborate to the formation of a supramolecular block copolymer with an alternating sequence of self-assembled segments of **NDI-SEt-chol** and **NDI-OEt-chol**. The melting curves of the resultant coassembled stacks showed increased stability of **NDI-SEt-chol** and a negligible difference in the stability of **NDI-OEt-chol** illustrating a block structure (Figures 3.22c, 3.22d and 3.22e). Importantly, no significant changes were observed in the spectroscopic features of these block structures, even after 3 days illustrating its low dynamics and high kinetic stability (Figures 3.22f and 3.22g). The supramolecular block copolymers were visualized by merging green and red emission channels in SIM images showing a spatial correlation of green-emitting fibers terminating with two red-emitting segments (Figure 3.22h). Due to sonication of supramolecular polymers of **NDI-SEt-chol** to prepare seed, the sizes of final supramolecular block copolymers are smaller than that of random and self-sorted supramolecular polymers as seen before.

[**OEt**]:[**SEt**]	t_1 (ns)	t_2 (ns)	t_3 (ns)	t_4 (ns)
1:0		0.59 (6.3 %)	1.83 (92.2 %)	6.16 (1.5 %)
1:0.2	0.012 (35.9 %)	0.69 (2.1 %)	1.84 (59.9 %)	12.86 (2.1 %)
1:0.5	0.013 (64.6 %)	0.65 (2.3 %)	1.87 (29.5 %)	14.07 (57.5 %)
1:1	0.018 (53.0 %)	0.8 (10.4 %)	2.09 (27.6 %)	19.36 (9.0 %)
1:1.6	0.03 (52.5 %)	1.28 (21.8 %)	3.06 (13.9 %)	21.34 (11.8 %)

Table 3.7. Lifetime data of **NDI-SEt-chol** and **NDI-OEt-chol** in block copolymer when collected at 480 nm (λ_{ex} = 442 nm). ([**NDI-OEt-chol**] = 2.5×10^{-5} M, toluene/MCH, 5/95 (v/v)).

Component	590 nm	470 nm	340 nm	430 nm
NDI-SEt-chol	310±1 K		316±1 K	
NDI-SEt-chol in Block	307±1 K		307±1 K	308±1 K
NDI-OEt-chol		332±1 K	332±1 K	328±1 K
NDI-OEt-chol in Block		332±1 K	340±1 K	323±1 K

Table 3.8. Listed T_m and T_e values for **NDI-SEt-chol** and **NDI-OEt-chol** in block arrangement at different wavelengths. ([**NDI-SEt-chol**] = [**NDI-OEt-chol**] = 2.5×10^{-5} M, toluene/MCH, 5/95 (v/v)).

These experimental evidences were again supported with molecular simulations. We equilibrated by means of a 10 μs CG-MD simulation a CG system containing 75 initially dispersed monomers of **NDI-SEt-chol** in the presence of 5 preformed stacks of **NDI-OEt-chol**

(seeds) similar to a heterogeneous nucleation experiment. In this run, we could observe spontaneous self-assembly of red monomers (**NDI-SEt-chol**) using the green stacks (**NDI-OEt-chol**) as nucleation sites (Figure 3.23). Thus, the simulations show that the self-assembly of **NDI-SEt-chol** is seeded by the assemblies of **NDI-OEt-chol**, in consistent with the experiments. Also, at the same time, this CG-MD shows no appreciable internal rearrangements or dynamic equilibrium of the formed assemblies. The g(r) peaks, absent initially for the assemblies of **NDI-SEt-chol** (g(r)=0), increase at the end of the CG-MD. While the number of core-core contacts remains nearly constant (close to 2) for the green monomers, the red increases during the CG-MD, but the yellow contacts (indicating intermixing) is close to 0, indicating negligible intermixing of monomers (Figure 3.23b). This simulation confirms that the **NDI-SEt-chol** monomers indeed self-assemble onto the **NDI-SEt-chol** seeds, but no internal reshuffling of **NDI-SEt-chol** and **NDI-OEt-chol** monomers is evidenced in the generated assemblies in the timescale accessible by these simulations.
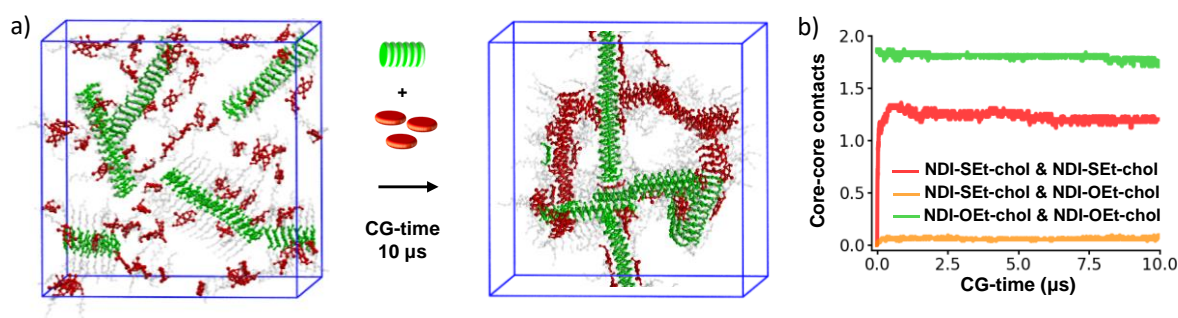
Figure 3.23. a) Self-assembly of 75 initially disassembled monomers in the presence of 5 preformed stacks each containing 15 monomers of **NDI-OEt-chol** (seeds) observed during 10 µs of CG-MD. During the run, the **NDI-SEt-chol** monomers self-assemble between them using the **NDI-OEt-chol** stacks as nucleation seeds. b) Number of contacts between the centers of the red (**NDI-SEt-chol**)-red (**NDI-SEt-chol**) (red curve), green (**NDI-OEt-chol**)-green (**NDI-OEt-chol**) (green curve) and green (**NDI-OEt-chol**)-red (**NDI-SEt-chol**) (yellow curve) monomer cores in the system during the CG-MD - the negligible **NDI-OEt-chol**-**NDI-SEt-chol** (yellow curve) contacts identify negligible intermixing between the different monomers in the system.

3.7. Conclusion:

In conclusion, through appropriate usage of kinetic and thermodynamic pathway complexity[21] of molecular self-assembly, we have accomplished an unprecedented sequence control in the supramolecular copolymerization of two core-substituted naphthalene diimide π-conjugated monomers to yield self-sorted, random and block supramolecular polymers. Further the characteristic and distinct optical properties of both cNDI monomers which are highly sensitive to the intermolecular interactions along with the induced circular dichroism form the peripheral chiral groups could be explored for the in situ spectroscopic probing of the monomer sequence

during the kinetically and thermodynamically driven supramolecular copolymerization process. Further, orthogonal, green and red fluorescence of the monomers **NDI-SEt-chol** and **NDI-OEt-chol** in the supramolecular copolymers provided a handle to probe the monomer exchange dynamics in the stacks and also helped to uniquely characterize these multicomponent structures by visualized under super-resolved structured illumination microscopy. Detailed molecular dynamic simulations provided mechanistic insights into the strength of the inter-monomeric interactions and provided insight into the relative rate of the monomer exchange dynamics in these assemblies, which was crucial for rationalizing the results from heterogenous nucleation experiments. Thermodynamic copolymerization of monomers **NDI-SEt-chol** and **NDI-OEt-chol** resulted in the random sequence of monomers, due to the comparable **NDI-SEt-chol**-**NDI-SEt-chol**, **NDI-OEt-chol**-**NDI-OEt-chol** and **NDI-SEt-chol**-**NDI-OEt-chol** interaction energies between the monomers. On the other hand, self-sorted homopolymers of **NDI-SEt-chol** and **NDI-OEt-chol** could be realized by exploiting low monomer exchange dynamics or high kinetic stability of these assemblies. Finally, the most challenging block supramolecular copolymers with domains of **NDI-SEt-chol** and **NDI-OEt-chol** have been synthetized by heterogenous seeded growth.

As mentioned above, the spectroscopic results of the sequence controlled supramolecular copolymerization was supported by SIM imaging of the resultant fibers. SIM is ideally suited for the current study as it can visualize the fibers with improved resolution, compared to a standard diffraction-limited microscopy imaging, using the inherent chromophore emission of their monomeric building blocks. While SIM provides an easy to implement a strategy to improve imaging resolution without any perturbation to the monomeric structures, it comes with the caveat of limited improvement in resolution (~120 nm). As a result, a detailed length distribution and yield analysis of the supramolecular block copolymers could not be performed. While other super-resolution imaging strategies can achieve better resolution, they require specialized fluorophores (in case of Stimulated Emission Depletion (STED) or Stochastic Optical Reconstruction Microscopy (STORM)[34,35] or dynamically binding probes (in case of interface point accumulation for imaging in nanoscale topography (PAINT)[36,37] to acquire better-resolved images. The integration of such specialized conditions can lead to significant changes in the mechanism and monomer exchange dynamics. Hence SIM was the best choice under these circumstances to visualize the resultant multicomponent fibers and further improvements on the imaging aspects are underway.

Although, sequence-controlled polymers in covalent polymers are defined as sequential positioning of monomers along the polymer backbone[2], here we have utilized the terminology

to define the microstructure of a two component supramolecular copolymerization. Synthesis of block-supramolecular structures through kinetically controlled heterogeneous nucleation strategy presented here is particularly interesting as it is reminiscent of the macroinitiator approach in classical living polymerization by the sequential addition of monomers. This strategy is expected to give pure blocks with a control on the length, compared to the thermodynamically driven cooperative supramolecular copolymerization based on the reactivity ratio of monomers. We plan to investigate the dispersity and length control of block segments in near future similar to what has been achieved in single component supramolecular polymers.[14,38] Further, supramolecular block copolymerization of optoelectronically active π-conjugated monomers as described here, would be the way forward to synthesize axial organic heterostructures with a pure donor-acceptor interface to extract interesting functions analogous to well-studied axial inorganic heterostructures. Moving towards higher complexity in terms of multicomponent systems and careful utilization of equilibrium and non-equilibrium states can render much wider regime of structural and functional states of supramolecular polymers.

3.8. Experimental Section (Spectroscopy and Microscopy):

General Methods:

Materials: All other chemicals were purchased from the commercial sources and were used as such without any further purification. Spectroscopic grade solvents were used for all spectroscopic measurements.

NMR Measurements: NMR spectra were recorded with a Bruker AVANCE 400 (400 MHz) Fourier transform NMR spectrometer and JEOL 600 MHZ NMR spectrometer with chemical shifts reported in parts per million (ppm) with respect to TMS. Splitting patterns are designated as s, singlet; d, doublet; bs, broad singlet; m, multiplet; t, triplet.

Matrix-Assisted Laser Desorption Ionization (MALDI): MALDI was performed on a Bruker daltonics Autoflex Speed MALDI TOF System (GT0263G201) spectrometer using trans-2-[3-(4-tert-Butylphenyl)-2-methyl-2-propenylidene] malononitrile (DCTB) as the matrix.

Optical Measurements: Electronic absorption spectra were recorded on a Perkin Elmer Lambda 900 UV-Vis-NIR Spectrometer and emission spectra were recorded on Perkin Elmer LS 55 Luminescence Spectrometer. UV-Vis and emission spectra were recorded in 10 mm path length cuvettes. Circular Dichroism measurements were performed on a JASCO J-815 spectrometer where the sensitivity, time constant, and scan rate were chosen appropriately.

Corresponding temperature-dependent measurements were performed with a CDF – 426S/15 Peltier-type temperature control.

Fitting of Cooling Curves: Nucleation-elongation model was fitted using MatlabR2008b software.

Fluorescence Lifetime Measurements: Time-resolved decay experiments were recorded on a Horiba Delta Flex Time-Correlated Single Photon Counting (TCSPC) instrument. A 442 nm nano-LED and 532 nm nano-LED with a pulse repetition rate of 1 MHz was used as the light source. The instrument response function (IRF) was collected by using a scatterer (Ludox AS40 colloidal silica, Sigma Aldrich). For both 442 nm LED and 532 nm nano-LED light source, the instrumental full width at half maximum including detector response was 0.2 ns. The excited state decay of the sample was collected by fixing the emission wavelength. The decay was fitted to appropriate best fit multiexponential decay using IBH software (DAS6).

Transmission Electron Microscopy (TEM): TEM measurements were performed on JEOL JEM 3010 operated at 300 kV. Samples were prepared by placing a drop of solution on carbon coated copper grids followed by drying at room temperature. The images were recorded with an operating voltage of 300 kV.

Structured Illumination Microscopy (SIM): Optical setup for imaging in Structured Illumination Microscopy (SIM) method: The fluorescence images of supramolecular polymers were acquired using an inverted Zeiss ELYRA PS1 microscope in structured illumination mode. Two lasers channel I - 488 nm (200 mW) (Green channel) and channel II - 561 nm (200 mW) (Red channel) have been used for respective excitation of **NDI-SEt-chol** and **NDI-OEt-chol** fluorophores. 10 % laser power from the objective top was used for structured illumination imaging. Imaging was performed using a Zeiss oil–immersion objective (Plan–apochromat 63x/1.40 Oil DIC M27, numerical aperture (NA) 1.40 oil). Fluorescence light was spectrally filtered with emission filters for channel I - MBS–488+EF BP 495–575/LP 750 for laser line 488 nm (green channel) and for channel II - MBS– 561+EF BP 570–650/LP 750 for laser line 561 nm (red channel) and and imaged using a PCO edge sCMOS camera (quantum yield > 70 %). Structured illumination images were processed using structured illumination analysis package for Zen software (Zeiss). Additional software have been used for colour adjustment (ImageJ). The channels were merged to investigate the spatial correlation between green and red-emitting fibers.

3.9. Synthetic Schemes and Procedures:

The synthesis of molecule **NDI-SEt-chol** and **NDI-OEt-chol** is shown in Scheme 3.2 to 3.3. Compound **47**, **64**, **48**, **49** was synthesized following earlier reported procedures.[7b,22]
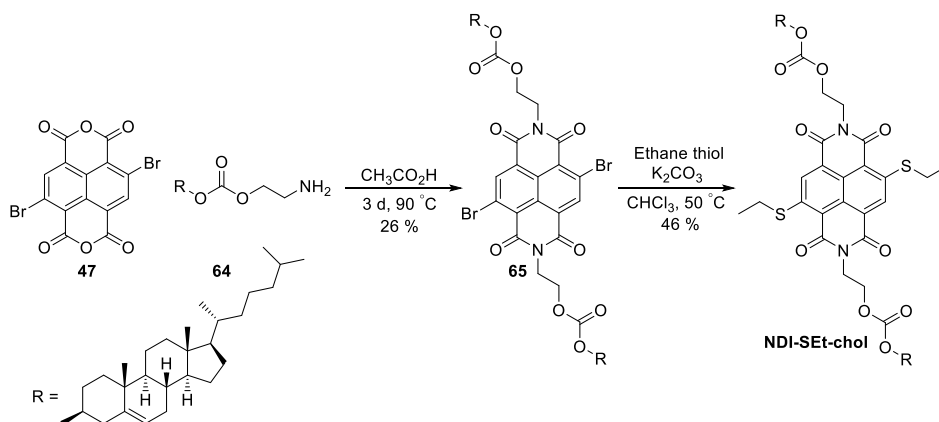
Scheme 3.2. Synthetic route to molecule **NDI-SEt-chol**.
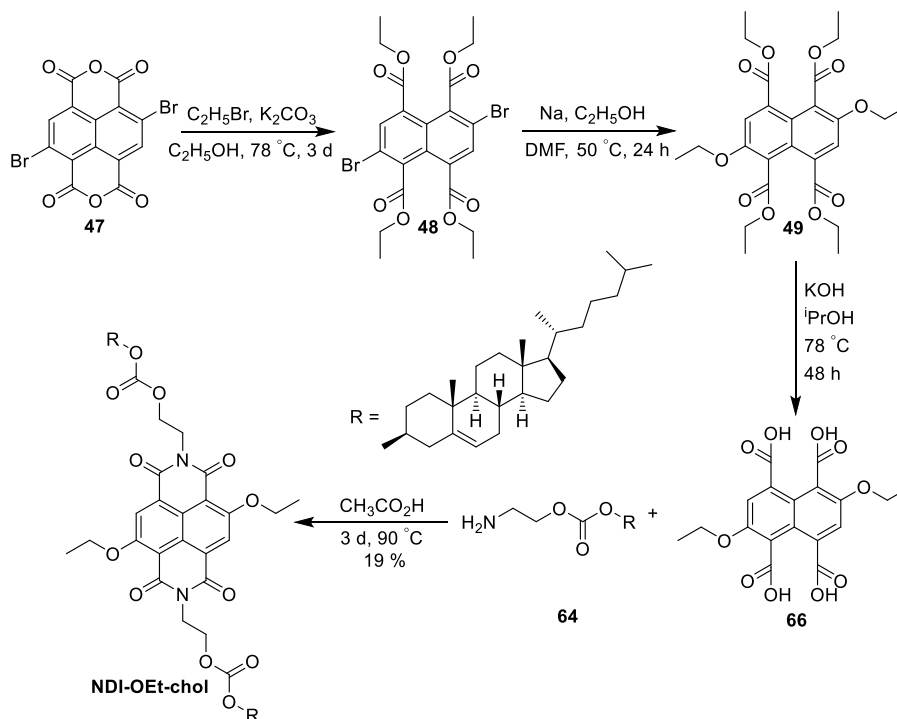
Scheme 3.3. Synthetic route to molecule **NDI-OEt-chol**.

Synthesis of 65: Compound **47** (0.24 g, 0.56 mmol) was weighed in a 100 mL single necked round bottom (RB) flask. Compound **64** (0.8 g, 1.68 mmol) was taken separately in a 50 mL round bottom flask and dissolved in acetic acid (15 mL). The resulting solution was added to compound **47** under continuous stirring and heated for 20 hours at 90 °C. Progress of the reaction was monitored by thin layered chromatography (TLC). A color change was observed from yellow to orange as the reaction proceeded. The resulting solution was poured into water

to get orange precipitate which was filtered, washed with methanol and air-dried overnight. The obtained compound was purified by flash column chromatography (silica gel 230-400 mesh) using 90 % chloroform in hexane to attain the pure product as a yellow solid. Yield = 26 %. ^{1}H NMR: (400 MHz, CDCl$_3$, ppm): δ = 8.98 (s, 2H), 5.33 (d, J = 4 Hz, 2H), 4.38-4.57 (m, 12H), 1.04-2.35 (m, 54H), 0.99 (s, 6H), 0.90 (d, J = 8 Hz, 6H), 0.87 (d, J =12 Hz, 6H), 0.85 (d, J = 8 Hz, 6H), 0.67 (s, 6H); ^{13}C NMR: (150 MHz, CDCl$_3$, ppm): δ = 160.94, 160.82, 154.44, 139.27, 139.21, 128.59, 127.89, 125.23, 124.05, 122.96, 78.24, 78.19, 64.28, 56.66, 49.95, 42.29, 39.50, 36.51, 22.81, 22.55, 19.26, 18.70, 11.84; MALDI-TOF (DCTB, negative mode): m/z calculated for C$_{74}$H$_{100}$Br$_2$N$_2$O$_{10}$: 1336.57, found: [M]$^{\cdot}$ = 1336.64 (Molecular ion peak is observed as radical ions due to the electron-deficient nature of naphthalene diimide cores).

Synthesis of NDI-SEt-chol: Compound **65** (0.2 g, 0.15 mmol) and K$_2$CO$_3$ (0.83 g, 6 mmol) were taken in a 100 mL three-necked round bottom flask, followed by the addition of chloroform (30 mL) and ethane thiol (5 mL, excess) to it. The reaction mixture was refluxed at 70 ˚C for two days. Progress of the reaction was monitored by TLC. Color of the reaction mixture was observed to change from orange to red as the reaction proceeds. Excess pentane thiol and chloroform were removed under reduced pressure and the resulting solid residue was washed with water followed by extraction with chloroform. The organic layer was separated and the solvent was evaporated under reduced pressure to get solid red powder. The obtained compound was purified by flash column chromatography (silica gel 230-400 mesh) using a gradient ranging from 0 to 1 % methanol in chloroform to get a red powder. Yield = 46 %. ^{1}H NMR: (400 MHz, CDCl$_3$, ppm): δ = 8.66 (s, 2H, H^{Ar}), 5.32 (bs, 2H, CH^{cholesterol}), 4.39-4.59 (m, 12H, CH$_2$, SCH$_2$, CH$_2$^{cholesterol}), 3.23 (q, J = 8 Hz, 4H, CH$_2$), 2.36-2.37 (bs, 4H, CH$_2$^{cholesterol}), 2.16 (s, 6H, CH$_2$^{cholesterol}, CH^{cholesterol}), 1.55-2.1 (m, 14 H, CH$_2$^{cholesterol},CH^{cholesterol}), 1.02-2.37 m, 30H, CH^{cholesterol}, CH$_2$^{cholesterol}), 0.99 (s, 12H, CH^{cholesterol}, CH$_2$^{cholesterol}), 0.91 (d, J = 8 Hz, 6H, CH$_3$^{cholesterol}), 0.87 (d, J = 12 Hz, 6H, CH$_3$^{cholesterol}), 0.85 (d, J = 8 Hz, 6H, CH$_3$^{cholesterol}), 0.67 (s, 6H, CH$_3$^{cholesterol}); ^{13}C NMR: (100 MHz, CDCl$_3$, ppm): δ = 163.29, 162.45, 154.43, 148.89, 139.39, 128.26, 125.07, 123.61, 122.90, 118.88, 78.07, 64.42, 56.71, 56.18, 50.00, 42.34, 39.74, 39.64, 39.54, 37.99, 36.84, 36.54, 36.21, 35.81, 31.92, 31.88, 28.24, 28.03, 27.64, 26.36, 24.30, 23.86, 22.82, 22.57, 21.06, 19.27, 18.73, 12.88, 11.88; MALDI-TOF (DCTB, negative mode): m/z calculated for C$_{78}$H$_{110}$N$_2$O$_{10}$S$_2$: 1298.76, found: [M]$^{\cdot}$ = 1298.82 (Molecular ion peak is observed as radical ions due to the electron-deficient nature of naphthalene diimide cores).

Synthesis of 66: 49 (1 g, 1.98 mmol) was taken in a round bottom flask and 200 mL of 1 M KOH in isopropanol solution was added to it and refluxed for 72 hours. After 72 hours, the

excess isopropanol was evaporated and the residue obtained was directly used for the next reaction.

Synthesis of NDI-OEt-chol: Compound **49** was taken in a 250 mL single necked round bottom flask. Compound **64** (1.88 g, 4 mmol) was taken in a separate 50 mL round bottom flask and dissolved in acetic acid (150 mL) and added to compound **49** under stirring and heated for 24 hours at 90 ˚C. Progress of the reaction was monitored by TLC. After completion of the reaction, the reaction mixture color changed from yellow to orange. The resulting solution was poured into water to get orange precipitate which was filtered, washed with methanol and air-dried overnight. The obtained compound was purified by flash column chromatography (silica gel 230-400 mesh) using a gradient ranging from 0 to 2 % methanol in chloroform. Yield = 19 %. ^{1}H NMR: (400 MHz, CDCl$_3$, ppm): δ = 8.47 (s, 2H, H^{Ar}), 5.30 (d, J = 8 Hz, 2H, CH^{cholesterol}), 4.40-4.58 (m, 16H, CH$_2$, SCH$_2$, CH$_2^{cholesterol}$), 2.65 (m, 4H, CH$_2^{cholesterol}$), 2.17 (s, 4H, CH$_2^{cholesterol}$), 1.8-2.1 (m, 12H, CH$_2^{cholesterol}$,CH^{cholesterol}), 1.83 (m, 8H, CH$_2^{cholesterol}$,CH^{cholesterol}), 1.1-1.5 (m, 30H), 1.0 (s, 6H, CH$_2^{cholesterol}$,CH^{cholesterol}).99 (s, 6H, CH$_2^{cholesterol}$), 0.91 (d, J = 8 Hz, 6H, CH$_2^{cholesterol}$), 0.87 (d, J = 12 Hz, 6H, CH$_2^{cholesterol}$), 0.85 (d, J = 8 Hz, 6H, CH$_2^{cholesterol}$), 0.67 (s, 6H, CH$_2^{cholesterol}$); ^{13}C NMR: (100 MHz, CDCl$_3$, ppm): δ = 162.53, 161.04, 160.13, 154.44, 139.38, 127.11, 123.71, 122.92, 119.80, 110.74, 78.00, 76.70, 66.33, 64.59, 56.71, 56.18, 50.01, 42.34, 39.74, 39.54, 39.34, 37.97,36.85, 36.55, 36.21, 35.80, 31.91, 31.87, 28.23, 28.02, 27.63, 24.29, 23.86, 22.82, 22.57, 21.06, 19.27, 18.73, 14.80, 11.87; MALDI-TOF (DCTB, negative mode): m/z calculated for C$_{78}$H$_{110}$N$_2$O$_{12}$: 1266.80, found: [M]$^{\dot{-}}$ = 1267.26 (Molecular ion peak is observed as radical ions due to the electron-deficient nature of naphthalene diimide cores).

3.10. Experimental Procedures:

All kinetics of self-assembly of **NDI-SEt-chol** and **NDI-OEt-chol** were monitored by absorption changes at 590 nm and 490 nm, respectively.

Protocol I: Preparation of kinetically grown supramolecular polymers of **NDI-SEt-chol** and **NDI-OEt-chol**: A stock solution of **NDI-SEt-chol** or **NDI-OEt-chol** was prepared in toluene. An appropriate volume of this stock is added to a toluene/MCH mixture to prepare the final self-assembling solution. The solution is then heated to 363 K and then cooled at a rate of 5 K/min to form metastable **State A** (in case of **NDI-SEt-chol**) and then left at 298 K to kinetically grow to **State B**.

Protocol II: Preparation of self-sorted homopolymers: A solution of 5x10^{-5} M **NDI-OEt-chol** is kinetically grown as in protocol I. Separately, a solution of 5×10^{-5} M **NDI-SEt-chol** is

kinetically grown as in protocol I. After the growth saturates, an appropriate volume of the solution of **NDI-OEt-chol** is added to prepare final concentration of [**NDI-SEt-chol**] = [**NDI-OEt-chol**] = 2.5×10^{-5} M.

Protocol III: Preparation of random supramolecular copolymer: A solution of [**NDI-SEt-chol**] = [**NDI-OEt-chol**] = 2.5×10^{-5} M is heated to 363 K and subsequently cooled to 298 K at a cooling rate of 1 K/min. **Protocol IV:** Preparation of supramolecular block copolymer: Seed solution is prepared by sonicating a solution of kinetically grown 5×10^{-4} M **NDI-OEt-chol** for 5 minutes. Separately, a required solution of **NDI-SEt-chol** is heated to 363 K and subsequently cooled to 298 K at cooling rate of 5 K/min to obtain metastable **State A**. The seed solution with of appropriate concentration/volume is injected at t = 40 sec within the lag phase. The kinetics is then monitored at 590 nm (aggregate band of **NDI-SEt-chol**).

3.11. Experimental Section for Computational Investigations:

Two key observations from our experiments were the lag phase, arising from the metastable **State A** and the copolymerization of **NDI-SEt-chol** and **NDI-OEt-chol**. In order to obtain molecular level insights into these two aspects, computational investigations using two different approaches were carried out. Gas phase quantum chemical calculations and all-atom molecular dynamics simulations were performed to identify metastable states and ground state geometries of short oligomers. Copolymerization and monomer exchange dynamics were studied employing coarse-grained molecular dynamics simulations.

3.11.1. Computational Investigations of Pathway Complexity:

3.11.1.1. Quantum Chemical Calculations:

Computational Details:

The initial structure of the monomer was constructed using GaussView 5.0.9.[39] Gas phase geometry optimizations using the semi-empirical PM6 method [40] were carried out using Gaussian09.[41] These calculations helped us to achieve good conformational and configurational sampling in a facile manner, thereby generating a variety of initial configurations for higher level optimizations conducted as per the details mentioned in the next paragraph.

Gas phase geometry optimizations employing Density Functional Theory (DFT) were performed using the QUICKSTEP[42] module in CP2K package.[42,43,44] The valence electrons were treated with a mixed basis set with an energy cutoff of 280 Ry. The short-range version of the double zeta single polarization basis set was used. The effect of core electrons on the nucleus was described using Geodecker-Teter-Hutter (GTH) pseudopotentials.[45] BLYP

exchange-correlation functional[46,47] was employed. van der Waals interactions were taken care through empirical DFT-D3 corrections.[48]

3.11.1.2. All-atom Molecular Dynamics (AA-MD) Simulations of "NDI-SEt-chol":
Computational Details:

Solute molecules (**NDI-SEt-chol**) were modeled using General Amber Force Field (GAFF)[49] with Restrained ElectroStatic Potential (RESP) charges.[50] To obtain these charges, a monomer of **1** in the growable boat conformation was geometry optimized in gas phase at HF/6-31G(d) level. The coordinate file of the optimized geometry was uploaded to the PyRED program[51] of the R.E.D. Server Development[52] for calculating ElectroStatic Potential (ESP) at the same level of theory and fitting it to obtain site charges. The force field topology and parameter files were obtained using AmberTools17[53] and AnteChamber Python Parser interfacE (ACPYPE).[54] OPLS-AA[55] and OPLS-UA[56] force fields were used for toluene and methylcyclohexane solvent molecules respectively. The solute-solvent cross interactions were handled employing GAFF mixing rules. Three-dimensional periodic boundary conditions were applied in all the simulations. Non-bonded interactions were treated with a cutoff distance of 12 Å. Long-range electrostatic interactions were evaluated using the Particle Mesh Ewald (PME)[57] method. The initial configurations for all the simulations were generated using Packmol-17.221.[58] All the AA-MD simulations were carried out using GROMACS-5.1.4 package,[59]. Leapfrog integrator with a time step of 0.5 fs was used to update the positions and velocities at each time step. The temperature was maintained at 298.15 K using the velocity-rescaling thermostat[60] with a coupling constant of 1 ps, and the pressure was maintained at 1 atm using Parrinello-Rahman barostat[61] with a coupling constant of 10 ps. Long-range corrections to energy and pressure were applied. The coordinates of the system were saved every 1 ps for further analysis, performed using VMD-1.9.2,[62] and TCL scripts written in-house.

3.11.2. Computational Investigations of Monomer Exchange Dynamics:

3.11.2.1. Development of the Molecular Models:

We built All Atom (AA) models of molecules **NDI-SEt-chol** and **NDI-OEt-chol** using the General Amber Force Field (GAFF)[49] and used these AA models as a reference to parametrize Coarse-Grained (CG) models of the molecules. The CG models for monomers **NDI-SEt-chol** and **NDI-OEt-chol** have been built based on the MARTINI force field[63] and then fine-tuned to be consistent with the AA models for what concerns the behavior of the individual monomers in solution and the strength of the monomer-monomer interactions in the solvent. First, we ran all atom molecular dynamic simulations (AA-MD) of monomer **NDI-SEt-chol** and **NDI-OEt-**

chol in explicit cyclohexane solvent, from which we calculated the radius of gyration (R_g) of the monomers. Then we used these AA models to estimate the monomer-monomer pairwise dimerization free energies between each combination of the monomers (i.e. **NDI-SET-chol**-**NDI-SEt-chol**, **NDI-OEt-chol**-**NDI-OEt-chol** and **NDI-OEt-chol**-**NDI-SEt-chol**) in cyclohexane at atomistic level using well-tempered metadynamics (WT-MetaD)[64] simulations. Given the complexity of the possible interaction modes of such complex monomers, and the fact that the cores are the unique difference between monomers **NDI-SEt-chol** and **NDI-OEt-chol** (the arms are identical), in this phase we focused on the monomer cores only, comparing the different ΔG of stacking of **NDI-SEt-chol**-**NDI-SEt-chol** *vs.* **NDI-SEt-chol**-**NDI-OEt-chol** *vs.* **NDI-OEt-chol**-**NDI-OEt-chol** cores. The **NDI-OEt-chol**-**NDI-OEt-chol** interaction (8.1 kcal mol^{-1}) was found stronger than the mixed **NDI-SEt-chol**-**NDI-OEt-chol** interaction (6.7 kcal mol^{-1}) and of the **NDI-SEt-chol**-**NDI-SEt-chol** interaction (5.7 kcal mol^{-1}). The CG models of monomers **NDI-SEt-chol** and **NDI-OEt-chol** were parametrized accordingly, by opportunely choosing the MARTINI CG beads to reproduce the AA R_g and dimerization ΔG. In particular, the MARTINI CG beads used in the models are SC1 for the aromatic rings, SC5 for alkyl chains, SP3 for ester and amide units, EO for ether units and C5 for sulfide groups. The unique difference between CG models of monomer **NDI-SEt-chol** and **NDI-OEt-chol** is the beads containing a sulfur vs. oxygen atom (C5 or EO beads, respectively). We performed CG WT-MetaD[64] simulations to obtain all pairwise dimerization free energies ΔG between the **NDI-SEt-chol**-**NDI-SEt-chol**, **NDI-OEt-chol**-**NDI-OEt-chol** and **NDI-SEt-chol**-**NDI-OEt-chol** CG cores. Then, similarly to what was previously done to model other supramolecular architectures,[65,66] we iteratively refined the non-bonded interactions between the CG beads until satisfactory agreement with the dimerization ΔG obtained from the AA simulations was reached. The parameters for the optimized models of CG cores **NDI-SEt-chol** and **NDI-OEt-chol** are reported below. Finally, we added the two side arms of monomers **NDI-SEt-chol** and **NDI-OEt-chol**, and we ran CG-MD simulations of the monomers in simulation boxes filled with explicit cyclohexane (MARTINI SC1 beads)[63]. We refined the bonded parameters to ensure that the bond, angle distributions, etc. were consistent between CG and AA models. We then also compared the radii of gyration (R_g) of **NDI-SEt-chol** and **NDI-OEt-chol** monomers in cyclohexane to ensure a consistent behavior between AA and CG models for what pertained behavior of the monomers in solution. Complete parameters for the CG models of molecules **NDI-SEt-chol** and **NDI-OEt-chol** used in all simulations conducted herein are provided as supplementary material (GROMACS format ITP).

3.11.2.2. Molecular Simulations:

All simulations have been performed with the GROMACS molecular dynamics suite[67] version 2018.4, patched with the Plumed plugin[68] version 2. In AA production runs, we used the md integrator with a time step of 2 fs, the v-rescale thermostat[60] with a time constant of 1 ps and the Berendsen barostat[69] with a time constant of 1 ps. In CG production runs, we used the md integrator with a time step of 20 fs, the v-rescale thermostat[60] with a time constant of 1 ps and the Berendsen barostat[69] with a time constant of 8 ps.

The three AA WT-MetaD simulations used to estimate dimerization free energies ΔG between the monomer cores were performed using two collective variables (CVs): i.e., (CV1) the distance between the two centers of mass of each core and (CV2) the angle between the planes vectors defined by each molecule's core (using the atoms in aromatic cycles) rescaled to yield values between 0 and 1, similarly to what was previously done to study another supramolecular fiber. [70] During 175 ns of WT-MetaD, the cores were seen to bind/unbind many times. In these simulations we used a bias factor of 10, a gaussian height of 2 kJ mol^{-1}, a deposition stride of 1 gaussian every 2000 timesteps. For CV1 we used a wall at 3.5 nm and a sigma of 0.06, with grid range from 0 to 5 and grid spacing of 0.006. For CV2 we used a sigma of 0.04, with grid range from 0 to 1 and grid spacing of 0.002. For the three CG WT-MetaD simulations we used bias factor of 15, a gaussian height of 1 kJ mol^{-1}, a deposition stride of 1 gaussian every 200 timesteps. Other parameters used for CVs were identical to the ones used in AA WT-MetaD simulations.

3.11.2.3. Modeling Monomer Exchange from Fibers Tips:

The exchange of monomers out from an assembly might be a rare event at a molecular scale (occurring on long timescales inaccessible to classical AA MD simulations). We used multiple infrequent WT-MetaD[71] CG simulations activating the rare event of monomer exchange from the fibers tips), similarly to what was previously done to study other supramolecular architectures. [65, 66, 68] In this way, we could explore the process of monomer exchange from the tips of fibers **NDI-SEt-chol** and **NDI-OEt-chol** at a resolution of ~5 Å (resolution of our CG models) and recalculate the original (native/unbiased) kinetics for the exchange event. While it is worth noting that the extracted exchange timescales are extracted from simplified CG models, and thus have little quanttative value (the dynamics and conformational sampling is sensibly accelerated in CG simulations, and the conversion of time in CG simulations is not straightforward to convert into real time), these nonetheless maintain an important comparative and qualitative value.

We constructed two pre-stacked fibers for CG molecule **NDI-SEt-chol** and **NDI-OEt-chol**, each composed of 20 monomers, which have been pre-equilibrated in cyclohexane. We then ran 25 infrequent CG WT-MetaD simulations for each fiber of **NDI-SEt-chol** and **NDI-OEt-chol** activating the exchange of a monomer from fibers' tips. The characteristic timescales for the monomer exchange events from the tips for fibers **NDI-SEt-chol** and **NDI-OEt-chol** were then calculated from the poissonian fit of the unbiased transition times distributions obtained from the 25 infrequent WT-MetaD runs.[70,71] The unbiased transition time (t) can be calculated from each individual WT-MetaD run as:

$$t = t_{WT-MetaD} \langle e^{\beta(V(s(\mathbf{R}),t))} \rangle_{WT-MetaD} \tag{1}$$

where $V(s(\mathbf{R}),t)$ is the time-dependent bias provided for the transition during the run, the exponential (brackets) is averaged over the WT-MetaD run and β is kT^{-1}. The transition times (t) calculated from the WT-MetaD runs for were then used to build the transition probability distribution $P_{n \geq 1}$ (namely, the probability to observe at least one exchange event by time t):

$$P_{n \geq 1} = 1 - e^{-\frac{t}{\tau}} \tag{2}$$

where τ is the characteristic time for the exchange events. shows the exchange times collected from the individual runs (grey segments). These fit well with poissonian transition probability distributions $P_{n \geq 1}$, as expected for rare events (red and green), demonstrating that the approach is working properly.[70,72] From the green and red $P_{n \geq 1}$ curves it is possible to calculate the characteristic timescales (TAU: τ) for exchanging one monomer from the fiber tip in both systems. We observe that while fiber **NDI-SEt-chol** exchanges monomers on a timescale of ~10 µs (10^{-5} s in CG time), the same event is ~10 times slower in system **NDI-OEt-chol** (10^{-4} s). This demonstrates that at a supramolecular level, in terms of monomer exchange from the fiber tip, system **NDI-OEt-chol** is ~10 times less dynamic and less prone to exchange monomers compared to system **NDI-SEt-chol**.

Furthermore, in order to demonstrate that these fibers indeed most probably exchange monomers from the tips, it was necessary to prove that exchanging monomers from the middle of fibers is a less favored, more unlikely event (thus, proving that exchanging monomers from the tip corresponds to the fastest exchange pathways for these fibers). To this end, we ran 25 infrequent WT-MetaD simulations activating the rare event of fibers breakage in the middle of 20-monomer model fibers (i.e., creating a defect from which monomers can exchange, as recently demonstrated for other fibers).[70] A qualitative analysis of 25 infrequent WT-MetaD

CG simulations activating fiber breaking/defect formation along the two fibers provided a free-energy barrier for the event as high as ~40 kJ mol^{-1} (9.5 kcal mol^{-1}) for both fibers. Given that exchanging from the tips requires to cross a lower free energy barrier (~25-27 kJ mol^{-1}), this makes monomer exchange from along the fibers a very rare event. This proves that these fibers indeed most likely exchange monomers from the tips, and that comparing the kinetics of exchange from the terminal points of the fibers is indeed a reliable way to compare between the fibers dynamics (i.e., this compares the fastest exchange pathway in both systems).

All infrequent WT-MetaD CG simulations used in this section were performed using a single collective variable (CV): the number of contacts between MARTINI CG beads of the molecules' cores. We used a bias factor of 12, a gaussian height of 0.5 kJ mol^{-1}, a deposition stride of 1 gaussian every 10000 timesteps, a sigma of 0.5 with grid range from 0 to 20 and grid spacing of 0.002. We also adapted the time step of the integrator to 15 fs to ensure simulations were stable. Simulations were terminated once the CV reached 0.

3.11.2.4. Self-assembly Simulations:

We performed additional CG-MD simulations to study self-assembly in the systems with a larger number of monomers to study the mixing of monomers **NDI-SEt-chol** and **NDI-OEt-chol** in the systems in different starting conditions. This allowed us to qualitatively compare at the molecular level, the monomer mixing and supramolecular dynamics in the systems and to compare experimental and computational results. We ran three CG-MD simulations of 10 μs of CG systems containing a total of 150 monomers in cyclohexane using three different starting configurations: (1) 75 free molecules of **NDI-SEt-chol** + 75 free molecules of **NDI-OEt-chol**, (2) 75 free molecules of **NDI-SEt-chol** + 5 pre-stacked fibers of 15 molecules of **NDI-OEt-chol** and (3) 5 pre-stacked fibers of 15 molecules of **NDI-SEt-chol** + 5 pre-stacked fibers of 15 molecules of **NDI-OEt-chol**. The simulation parameters were identical to those used in section 1 for CG simulations. Qualitatively, the results from these self-assembly simulations were found in good agreement with the experimental results. Videos of these 3 self-assembly simulations are provided as supplementary materials.

3.12. References:

[1] Berg, J. M.; Tymoczko, J. L.; Stryer, L. *Biochemistry*; 6th edn, W. H. Freeman: New York, **2006**.

[2] a) Lutz, J. F.; Ouchi, M.; Liu, D. R.; Sawamoto, M. *Science* **2013**, *341*, 1238149. b) Lutz, J. F.; Lehn, J-M.; Meijer, E. W.; Matyjaszewski, K. *Nat. Rev. Mater.* **2016**, *1*, 16024-16038.

[3] a) de Greef, T. F. A.; Meijer, E. W. *Nature* **2008**, *453*, 171-173. b) Draper, E.R.; Adams, D. J. *Chem. Soc. Rev.* **2018**, *47*, 3395-3405. c) Besenius, P. *Polymer Chemistry* **2017**, *55*, 34-78. d) Vantomme, G.; Meijer, E. W. *Science* **2019**, *363*, 1396-1397.

[4] a) Safont-Sempere, M. M.; Fernández, G.; Würthner, F. *Chem. Rev.* **2011**, *111*, 5784-5814. b) Shigemitsu, H.; Fujisaku, T.; Tanaka, W.; Kubota, R.; Minami, S.; Urayama, K.; Hamachi, I. *Nat. Nanotech.* **2018**, *13*, 165-172. c) Onogi, S.; Shigemitsu, H.; Yoshii, T.; Tanida, T.; Ikeda, M.; Kubota, R.; Hamachi, I. *Nat. Chem.* **2016**, *8*, 743-752.

[5] a) Morris, K. L.; Chen, L.; Raeburn. J.; Sellick, O. R.; Cotanda, P.; Paul, A.; Griffiths, P. C.; King, S.M.; O'Reilly, R. K.; Serpell, L. C.; Adams, D. J. *Nat. Commun.* **2013**, *4*, 1-6. b) Draper, E. R.; Eden, E. G. B.; McDonald T. O.; Adams, D. J. *Nat. Chem.* **2015**, *7*, 848-852. c) Cornwell, D. J.; Daubney, O. J.; Smith, D. K. *J. Am. Chem. Soc.* **2015**, *137*, 15486-15492.

[6] a) Prasanthkumar, S.; Ghosh, S.; Nair, V. C.; Saeki, A.; Seki, S.; Ajayaghosh, A. *Angew. Chem., Int. Ed.* **2015**, *54*, 946-950. b) Sandeep, A.; Praveen, V. K.; Kartha, K. K.; Karunakaranab, V.; Ajayaghosh, A. *Chem. Sci.* **2016**, *7*, 4460-4467. c) Herrikhuyzen, J. v.; Syamakumari, A.; Schenning, A. P. H. J.; Meijer, E. W. *J. Am. Chem. Soc* **2004**, *126*, 10021-10027.

[7] a) Narayan, B.; Bejagam, K. K.; Balasubramanian, S.; George, S. J. *Angew. Chem., Int. Ed.* **2015**, *54*, 13245-13249. b) Sarkar, A.; Dhiman, S.; Chalishazar, A.; George, S. J. *Angew. Chem., Int. Ed.* **2017**, *56*, 13767-13771.

[8] a) Zhang, X.; Wang, C. *Chem. Soc. Rev.* **2011**, *40*, 94-101. b) Wang, C.; Guo, Y.; Wang, Y.; Xu, H.; Wang, R.; Zhang, X. *Angew. Chem., Int. Ed.* **2009**, *48*, 8962-896. c) Kumar, M.; Rao, K. V.; George, S. J. *Phys. Chem. Chem. Phys.* **2014**, *16*, 1300-1313. d) Rao, K. V.; Jayaramulu, K.; Maji, T. K.; George, S. J. *Angew. Chem., Int. Ed.* **2010**, *49*, 4218-4222.

[9] a) Frisch, H.; Unsleber, J. P.; Lgdeker, D.; Peterlechner, M.; Brunklaus, G.; Waller, M.; Besenius, P. *Angew. Chem., Int. Ed.* **2013**, *52*, 10097-10101. b) Frisch, H.; Fritz, E.; Stricker, F.; Schmüser, L.; Spitzer, D.; Weidner, T.; Ravoo, B. J.; Besenius, P. *Angew. Chem., Int. Ed.* **2016**, *55*, 7242-7246.

[10] Appel, E. A.; Biedermann, F.; Rauwald, U.; Jones, S. T.; Zayed, J. M.; Scherman, O. A. *J. Am. Chem. Soc.* **2010**, *132*, 14251-14260.

[11] a) Adelizzi, B.; Van Zee, N. J.; De Windt, L. N.; Palmans, A. R.; Meijer, E. W. *J. Am. Chem. Soc.* **2019**, *141*, 6110-6121. b) Wehner, M.; Würthner, F. *Nat. Rev. Chem.* **2019**, *4*, 38-53. c) Jain, A.; George, S. J. *Mater. Today,* **2015**, *18*, 206-214.

[12] a) Jonkheijm, P.; van der Schoot, P.; Schenning, A. P. H. J.; Meijer, E. W. *Science* **2006**, *313*, 80-83. b) De Greef, T. F. A.; Smulders, M. M. J.; Wolffs, M.; Schenning, A. P. H. J.;

Sijbesma, R. P.; Meijer, E. W. *Chem. Rev.* **2009**, *109*, 5687-5754. c) Kulkarni, C.; Balasubramanian, S.; George, S. J. *ChemPhysChem* **2013**, *14*, 661-673.

[13] a) Dhiman, S.; George, S. J. *Bull. Chem. Soc. Jpn.* **2018**, *91*, 687-699. b) van der Zwaag, D.; De Greef, T. F. A.; Meijer, E. W. *Angew. Chem., Int. Ed.* **2015**, *54*, 8334-8336. c) Mukhopadhyay, R. D.; Ajayaghosh, A. *Science* **2015**, *349*, 241-242. d) Matern, J.; Dorca, Y.; Sánchez, L.; Fernández, G. *Angew. Chem., Int. Ed.* **2019**, *58*, 16730-16740.

[14] a) Fukui, T.; Kawai, S.; Fujinuma, S.; Matsushita, Y.; Yasuda, T.; Sakurai, T.; Seki, S.; Takeuchi, M.; Sugiyasu, K. *Nat. Chem.* **2017**, *9*, 493-499. b) Ogi, S.; Sugiyasu, K.; Manna, S.; Samitsu, S.; Takeuchi, M. *Nat. Chem.* **2014**, *6*, 188-195. c) Ogi, S.; Stepanenko, V.; Sugiyasu, K.; Takeuchi, M.; Würthner, F. *J. Am. Chem. Soc.* **2015**, *137*, 3300-3307. d) Ogi, S.; Stepanenko, V.; Thein, J.; Würthner, F. *J. Am. Chem. Soc.* **2016**, *138*, 670-678. e) Endo, M.; Fukui, T.; Jung, S. H.; Yagai, S.; Takeuchi, M.; Sugiyasu, K. *J. Am. Chem. Soc.* **2016**, *138*, 14347-14353. f) Kemper, B.; Zengerling, L.; Spitzer, D.; Otter, R.; Bauer, T.; Besenius, P. *J. Am. Chem. Soc.* **2018**, *140*, 534-537. g) Ogi, S.; Matsumoto, K.; Yamaguchi, S. *Angew. Chem., Int. Ed.* **2018**, *57*, 2339-2343. h) Greciano, E. E.; Matarranz, B.; Sánchez, L. *Angew. Chem., Int. Ed.* **2018**, *57*, 4697-4701. i) Robinson, M. E.; Lunn, D. J.; Nazemi, A.; Whittell, G. R.; De Cola, L.; Manners, I. *Chem. Commun.* **2015**, *51*, 15921-15924.

[15] Adelizzi, B.; Aloi, A.; Markvoort, A. J.; Ten Eikelder, H. M.; Voets, I. K.; Palmans, A. R.; Meijer, E. W. *J. Am. Chem. Soc.* **2018**, *140*, 7168-7175.

[16] Kitamoto, Y.; Pan, Z.; Prabhu, D. D.; Isobe, A.; Ohba, T.; Shimizu, N.; Takagi, H.; Haruki, R.; Adachi, S. I.; Yagai, S. *Nat. Commun.* **2019**, *10*, 4578.

[17] a) Jung, S. H.; Bochicchio, D.; Pavan, G. M.; Takeuchi, M.; Sugiyasu, K. *J. Am. Chem. Soc.* **2018**, *140*, 10570-10577.

[18] a) Wang, X.; Guerin, G.; Wang, H.; Wang, Y.; Manners, I.; Winnik, M. *Science* **2007**, *317*, 644-648. b) Gilroy, J. B.; Gädt, T.; Whittell, G. R.; Chabanne, L.; Mitchels, J. M.; Richardson, R. M.; Winnik, M. A.; Manners, I. *Nat. Chem.* **2010**, *2*, 566-570. c) Finnegan, J. R.; Lunn, D. J.; Gould, Z. M. Hudson, O. E. C.; Whittell, G. R.; Winnik, M. A.; Manners, I. *J. Am. Chem. Soc.* **2014,** *136,* 13835-13844. d) Schacher, F. H.; Rupar, P. A.; Manners. I. *Angew. Chem., Int. Ed.* **2012**, *51*, 7898-7921. e) Qiu, H.; Gao, Y.; An Du, V.; Harniman, R.; Winnik, M. A.; Manners, I. *J. Am. Chem. Soc.* **2015**, *137*, 2375-2385.

[19] Zhang, W.; Jin, W.; Fukushima, T; Saeki, A.; Seki, S.; Aida, T. *Science* **2011**, *334,* 340-343.

[20] a) Görl, D.; Zhang, X.; Stepanenko, V.; Würthner, F. *Nat. Commun.* **2015**, *6*, 7009. b) Wagner, W.; Wehner, M.; Stepanenko, V.; Würthner, F. *J. Am. Chem. Soc.* **2019**, *141*, 12044-12054.

[21] a) Korevaar, P. A.; de Greef, T. F. A.; Meijer, E. W. *Chem. Mater.* **2014**, *26*, 576-586. b) Korevaar, P. A.; George, S. J.; Markvoort, A. J.; Smulders, M. M.; Hilbers, P. A.; Schenning, A. P.; de Greef, T. F. A.; Meijer, E. W. *Nature* **2012**, *481*, 492-496. c) Langenstroer, A.; Kartha, K. K.; Dorca, Y.; Droste, J.; Stepanenko, V.; Albuquerque, R. Q.; Hansen, M. R.; Sánchez, L.; Fernández, G. *J. Am. Chem. Soc.* **2019**, *141*, 5192-5200.

[22] a) Kulkarni, C.; Bejagam, K. K.; Senanayak, P. S.; Narayan, K. S.; Balasubramanian, S.; George, S. J. *J. Am. Chem. Soc.* **2015**, *137*, 3924-3932. b) Kulkarni, C.; George, S. J. *Chem. Eur. J.* **2014**, *16*, 4537-4541.

[23] a) George, S. J.; Tomović, Ž.; Schenning, A. P. H. J.; Meijer, E. W. *Chem. Commun.* **2011**, *47*, 3451-3453. b) Cat, I. D.; Guo, Z.; George, S. J.; Meijer, E. W.; Schenning, A. P. H. J.; Feyter, S. D. *J. Am. Chem. Soc.* **2012**, *134*, 3171-3177.

[24] Oosawa, F.; Asakura, S. *Academic Press Inc., New York*, **1975**.

[25] Bochicchio, D.; Pavan. G. M. *Adv. Phys. X* **2018**, *3*, 1436408.

[26] Bochicchio, D.; Pavan. G. M. *ACS Nano* **2017**, *11*, 1000-1011.

[27] Gasparotto, P.; Bochicchio, D.; Ceriotti, M.; Pavan, G. M. *J. Phys. Chem. B* **2020**, *124*, 589-599.

[28] Bochicchio, D.; Salvalaglio, M.; Pavan, G. M. *Nat. Commun.* **2017**, *8*, 147

[29] Marrink, S. J.; Risselada, H. J.; Yefimov, S.; Tieleman, D. P.; de Vries, A. H. *J. Phys. Chem. B.* **2007**, *111*, 7812-7824.

[30] Barducci, A., Bussi, G.; Parrinello, M. *Phys. Rev. Lett.* **2008**, *100*, 020603.

[31] Tiwary, P.; Parrinello, M. *Phys. Rev. Lett.* **2013**, *111*, 230602.

[32] Salvalaglio, M.; Tiwary, P.; Parrinello, M. *J. Chem. Theory Comput.* **2014**, *10*, 1420-1425.

[33] a) Meisl, G.; Kirkegaard, J. B.; Arosio, P.; Michaels, T. C. T.; Vendruscolo, M.; Dobson, C. M.; Linse, S.; Knowles, T. P. J. *Nat. Protoc.* **2016**, *11*, 252-272. b) Iglesias, J. L.; Tassoni, A.; Adachi, T.; Stich, M.; Hermans, T. M. *Nat. Nanotech.* **2018**, *13*, 1021-1027.

[34] Vicidomini, G.; Bianchini, P.; Diaspro, A. *Nat. Methods* **2018**, *15*, 173-182.

[35] Albertazzi, L.; van der Zwaag, D.; Leenders, C. M. A.; Fitzner, R.; van der Hofstad, R. W.; Meijer, E. W. *Science* **2014**, *344*, 491-495.

[36] Adelizzi, B.; Aloi, A.; Van Zee, N. J.; Palmans, A. R. A.; Meijer, E. W.; Voets, I. K. *ACS Nano* **2018**, *12*, 4431-4439.

[37] Sasmal, R.; Saha, N. D.; Schueder, F.; Joshie, D.; Sheeba, V.; Jungmann, R.; Agasti. S. S. *Chem. Commun.,* **2019**, *55*, 14430-14433.

[38] a) Vázquez-González, V.; Mayoral, M. J.; Chamorro, R.; Hendrix, M. M. R. M.; Voets, I. K.; Gonzalez-Rodriguez, D. *J. Am. Chem. Soc.* **2019**, *141*, 16432-16438. b) Bousmail, D.; Chidchob, P.; Sleiman, H. F. *J. Am. Chem. Soc.* **2018**, *140*, 9518-9530.

[39] Dennington, R.; Keith, T.; Millam, J. *GaussView*, version 5.0.9; Semichem, Inc.: Shawnee Mission, KS, **2009**.

[40] Stewart, J. J. P. *J. Mol. Model.* **2007**, *13*, 1173-1213.

[41] Frisch, M. J.; Trucks, G. W.; Schlegel, H. B.; Scuseria, G. E.; Robb, M. A.; Cheeseman, J. R.; Scalmani, G.; Barone, V.; Mennucci, B.; Petersson, G. A.; Nakatsuji, H.; Caricato, M.; Li, X.; Hratchian, H. P.; Izmaylov, A. F.; Bloino, J.; Zheng, G.; Sonnenberg, J. L.; Hada, M.; Ehara, M.; Toyota, K.; Fukuda, R.; Hasegawa, J.; Ishida, M.; Nakajima, T.; Honda, Y.; Kitao, O.; Nakai, H.; Vreven, T.; Montgomery, Jr., J. A.; Peralta, J. E.; Ogliaro, F.; Bearpark, M.; Heyd, J. J.; Brothers, E.; Kudin, K. N.; Staroverov, V. N.; Kobayashi, R.; Normand, J.; Raghavachari, K.; Rendell, A.; Burant, J. C.; Iyengar, S. S.; Tomasi, J.; Cossi, M.; Rega, N.; Millam, N. J.; Klene, M.; Knox, J. E.; Cross, J. B.; Bakken, V.; Adamo, C.; Jaramillo, J.; Gomperts, R.; Stratmann, R. E.; Yazyev, O.; Austin, A. J.; Cammi, R.; Pomelli, C.; Ochterski, J. W.; Martin, R. L.; Morokuma, K.; Zakrzewski, V. G.; Voth, G. A.; Salvador, P.; Dannenberg, J. J.; Dapprich, S.; Daniels, A. D.; Farkas, Ö.; Foresman, J. B.; Ortiz, J. V.; Cioslowski, J.; Fox, D. J. *Gaussian 09*, revision B.01; Gaussian, Inc.: Wallingford, CT, **2009**.

[42] VandeVondele, J.; Krack, M.; Mohamed, F.; Parrinello, M.; Chassaing, T.; Hutter, J. *Comput. Phys. Commun.* **2005**, *167*, 103-128.

[43] Hutter, J.; Iannuzzi, M.; Schiffmann, F.; VandeVondele, J. CP2K: *WIREs Comput. Mol. Sci.* **2014**, *4*, 15-25.

[44] VandeVondele, J.; Hutter, J. *J. Chem. Phys.* **2007**, *127*, 114105.

[45] Goedecker, S.; Teter, M.; Hutter, J. *Phys. Rev. B: Condens. Matter Mater. Phys.* **1996**, *54*, 1703-1710.

[46] Becke, A. D. *J. Chem. Phys.* **1993**, *98*, 5648-5652.

[47] Lee, C.; Yang, W.; Parr, R. G. *Phys. Rev. B: Condens. Matter Mater. Phys.* **1988**, *37*, 785-789.

[48] Grimme, S.; Antony, J.; Ehrlich, S.; Krieg, H. A. *J. Chem. Phys.* **2010**, *132*, 154104.

[49] Wang, J.; Wolf, R. M.; Caldwell, J. W.; Kollman, P. A.; Case, D. A. *J. Comput. Chem.* **2004**, *25*, 1157-1174.

[50] Bayly, C. I.; Cieplak, P.; Cornell, W.; Kollman, P. A. A. *J. Chem. Phys.* **1993**, *97*, 10269-10280.

[51] Vanquelef, E.; Simon, S.; Marquant, G.; Garcia, E.; Klimerak, G.; Delepine, J. C.; Cieplak, P.; Dupradeau, F. Y. *Nucleic Acids Res.* **2011**, *39*, W511-W517.

[52] Wang, F.; Becker, J.-P.; Cieplak, P.; Dupradeau, F. Y. Université De Picardie - Jules Verne, Sanford Burnham Medical Research Institute, Nov. 2013. https://upjv.q4md-forcefieldtools.org/REDServer-Development/.

[53] Case, D.; Cerutti, D.; Cheatham, T.; Darden, T.; Duke, R.; Giese, T.; Gohlke, H.; Goetz, A.; Greene, D.; Homeyer, N.; Izadi, S.; Kovalenko, A.; Lee, T.; LeGrand, S.; Li, P.; Lin, C.; Liu, J.; Luchko, T.; Luo, R.; Mermelstein, D.; Merz, K. M.; Monard, G.; Nguyen, H.; Omelyan, I.; Onufriev, A.; Pan, F.; Qi, R.; Roe, D. R.; Roitberg, A.; Sagui, C.; Simmerling, C.; Botello-Smith, W.; Swails, J.; Walker, R.; Wang, J.; Wolf, R.; Wu, X.; Xiao, L.; York, D.; Kollman, P. *Amber 2017*; University of California: San Francisco, **2017**.

[54] Sousa da Silva, A. W.; Vranken, W. F. ACPYPE - AnteChamber PYthon Parser interfacE. *BMC Res. Notes* **2012**, *5*, 367-369.

[55] Jorgensen, W. L.; Maxwell, D. S.; Tirado-Rives, J. *J. Am. Chem. Soc.* **1996**, *118*, 11225-11236.

[56] Kaminski, G.; Friesner, R.; Tirado-Rives, J.; Jorgensen, W. *J. Phys. Chem. B* **2001**, *105*, 6474-6487.

[57] Essmann, U.; Perera, L.; Berkowitz, M. L.; Darden, T.; Lee, H.; Pedersen, L. G. *J. Chem. Phys.* **1995**, *103*, 8577-8593.

[58] Martínez, L.; Andrade, R.; Birgin, E. G.; Martínez, J. M. *J. Comput. Chem.* **2009**, *30*, 2157-2164.

[59] Abraham, M. J.; Murtola, T.; Schulz, R.; Páll, S.; Smith, J. C.; Hess, B.; Lindahl, E. *SoftwareX* **2015**, *1-2*, 19-25.

[60] Bussi, G.; Donadio, D.; Parrinello, M. *J. Chem. Phys.* **2007**, *126*, 014101-014107.

[61] Parrinello, M.; Rahman, A. *J. Appl. Phys.* **1981**, *52*, 7182-7190.

[62] Humphrey, W.; Dalke, A.; Schulten, K. *J. Mol. Graphics* **1996**, *14*, 33-38.

[63] Marrink, S. J.; Risselada, H. J.; Yefimov, S.; Tieleman, D. P.; De Vries, A. H. *J. Phys. Chem. B* **2007**, *111*, 7812-7824.

[64] Barducci, A.; Bussi, G.; Parrinello, M. *Phys. Rev. Lett.* **2008**, 100, 20603.

[65] Bochicchio, D.; Pavan, G. M. *ACS Nano* **2017**, *11*, 1000-1011.

[66] Casellas, N. M.; Pujals, S.; Bochicchio, D.; Pavan, G. M.; Torres, T.; Albertazzi, L.; García-Iglesias, M. *Chem. Commun.* **2018**, *54*, 4112-4115.

[67] Berendsen, H. J. C.; van der Spoel, D.; van Drunen, R. GROMACS: *Comput. Phys. Commun.* **1995**, *91*, 43-56.

[68] Tribello, G. A.; Bonomi, M.; Branduardi, D.; Camilloni, C.; Bussi, G. *Comput. Phys. Commun.* **2014**, *185*, 604-613.

[69] Berendsen, H. J. C.; Postma, J. P. M.; van Gunsteren, W. F.; DiNola, A.; Haak, J. R. *J. Chem. Phys.* **1984**, *81*, 3684-3690.

[70] Bochicchio, D.; Salvalaglio, M.; Pavan, G. M. *Nat. Commun.* **2017**, *8*, 147.

[71] Tiwary, P.; Parrinello, M. *Phys. Rev. Lett*. **2013**, *111*, 230602.

[72] Salvalaglio, M.; Tiwary, P.; Parrinello, M. *J. Chem. Theory Comput.* **2014**, *10*, 1420-1425.

Chapter: 4

Kinetically Controlled Synthesis of Supramolecular Block Copolymers with Narrow Dispersity and Tunable Block Lengths

Chapter: 4

Kinetically Controlled Synthesis of Supramolecular Block Copolymers with Narrow Dispersity and Tunable Block Lengths

Abstract

An important scientific hurdle in supramolecular polymerization is the synthesis of well-defined supramolecular block copolymers (BCP). Hence it has been adequately pursued either via thermodynamic copolymerization or via heterogeneous nucleation under kinetic control. However, the polydisperse structural outcome limits the fundamental development in the field. Herein we report a kinetically controlled seeded supramolecular block copolymerization between core-substituted naphthalene diimide (cNDI) derivatives for the synthesis of monodisperse supramolecular BCP with tunable block lengths. Structured illumination microscopy (SIM) imaging characterized the supramolecular BCPs and allowed the size distribution analysis to be performed for individual block segments. The strategy reported here should lead the way towards the synthesis of supramolecular BCP of higher complexity and controlled length.
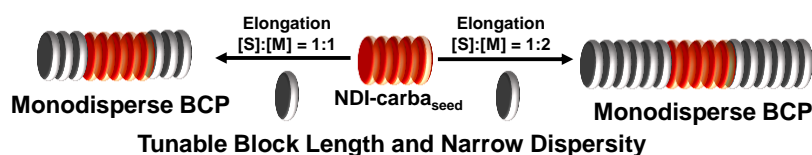
4.1. Introduction:

Supramolecular polymerization has emanated as an exciting field for the synthesis of ordered materials with adaptive and reversible functions.[1] The latest fascinating advancement in this field is the non-covalent synthesis of supramolecular BCPs.[2] In one of the attempts, Aida and coworkers have demonstrated seeded growth of hexabenzocoronene derived amphiphiles on electronically complementary kinetically stable seeds by temperature variation.[3] Sugiyasu and coworkers have demonstrated synthesis of supramolecular BCPs between porphyrin monomers using a solvent mixing protocol.[4] In a different approach, Meijer and coworkers have established supramolecular block copolymerization under thermodynamic control by modulating the free energy of interaction between monomers.[5]

We envisage supramolecular BCP synthesis via kinetic control analogous to living chain-growth polymerization are ideally suited for the controlled synthesis of supramolecular BCPs with controlled length and dispersity. In pioneering studies, Manners and coworkers have established a living crystallization driven self-assembly approach on poly ferrocenyl (PFS) polyisoprene BCPs micelles resulting in the formation of triblock co-micelles of narrow dispersity.[6] This living crystallization driven approach was further applied to crystallizable perylene diimide monomers and platinum-palladium complexes for the controlled synthesis of BCPs.[7] However, similar living supramolecular copolymerization with low molecular weight monomers driven by specific supramolecular interactions has been a significant challenge due to fast monomer exchange dynamics and are seldom reported. Recently Würthner and coworkers have reported seed induced LSP[8,9] approach between core-substituted perylene diimide monomers for the BCP synthesis.[10] Despite this progress, precise dimensional control and modulation of individual block length for supramolecular BCPs, which can significantly improve their functions, remains elusive due to lack of characterization methods and lower kinetic stability of the synthesized copolymers. Recently we have reported seeded supramolecular polymerization between optically different core-substituted naphthalene diimides (cNDI)[11] and have characterized the copolymers using super-resolved structured illumination microscopy (SIM) imaging (see also Chapter 2 and Chapter 3).[12] However, lower kinetic stability of the seeds and metastable species prohibited further modulation of individual block length and degree of polymerization. In this Chapter, we present kinetically controlled living supramolecular polymerization between optically different naphthalene diimide (NDI) molecules (Figure 4.1a), which exhibits pathway complexity and kinetically controlled nucleation-elongation mechanism via metastable species. Long lifetime and significant

stability of the metastable state and kinetically stable seeds prepared by sonication allowed us to investigate the seed induced synthesis of supramolecular BCP with a narrow dispersity. We further demonstrate that the degree of polymerization and block length can be altered by modulating the amount of monomer added in the kinetically stable seeds (Figure 4.1b).

4.2. Molecular Design:

The monomer design consists of carbamate cholesterol appended naphthalene diimides, which due to the presence of hydrogen bonding groups are expected to follow a cooperative supramolecular polymerization.[13] To perform the supramolecular copolymerization, ethanethiol-disubstituted cNDI (**NDI-carba-SEt**) and its unsubstituted NDI (**NDI-carba**) derivatives, with similar structural features are used as the monomers (Figure 4.1a). This molecular design allows the spectroscopic characterization of the supramolecular polymerization process through characteristic changes in the absorption and fluorescence changes of cNDI chromophores upon stacking and also through the induced circular dichroism (ICD) signals at the electronic transitions of cNDI chromophores upon self-assembly from the peripheral chiral cholesterol groups. Since, the monomer **NDI-carba** is not fluorescent, ethoxy-
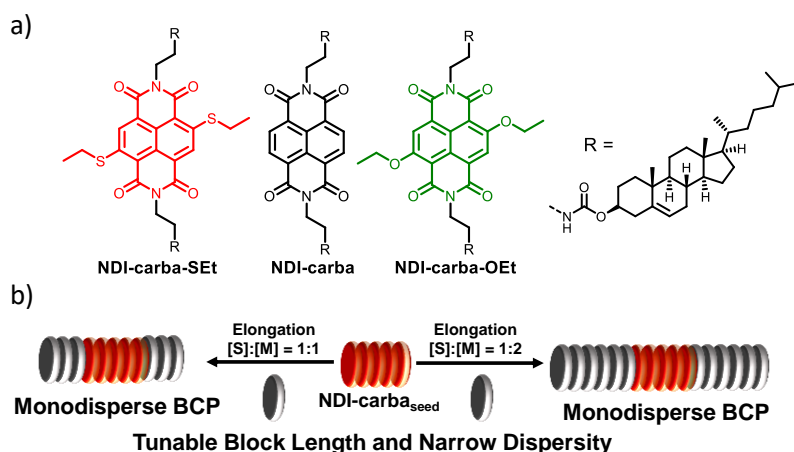
Figure 4.1. a) Molecular structures of the components **NDI-carba-SEt** and **NDI-carba** used in the present study for supramolecular BCP synthesis under kinetic control. b) Schematic illustration of heterogeneous seeding under kinetic control in presence of seed of **NDI-carba-SEt** for the synthesis of supramolecular BCP with tunable block length and narrow dispersity.

disubstituted cNDI (**NDI-carba-SEt**) (Figure 4.1a), is used as a fluorescent stain to visualize copolymer microstructure using SIM microscopy. All the molecules were synthesized and characterized by NMR spectroscopy and mass spectrometry (see experimental section).

4.3. Results and Discussion:

4.3.1. Self-assembly Studies:

We first investigated the optical properties of the monomers **NDI-carba-SEt** and **NDI-carba** in its monomeric and assembled states. Monomers **NDI-carba-SEt** and **NDI-carba** exist in its native monomeric state in 1,1',2,2; tetrachloroethane (TCE) (Figure 4.2). Supramolecular homopolymerization of **NDI-carba-SEt** and **NDI-carba**, was studied in TCE/methyl cyclohexane (MCH) solvent mixture (TCE/MCH, 1/99 (v/v) to TCE/MCH, 5/95 (v/v)).

Supramolecular homopolymers of **NDI-carba-SEt** and **NDI-carba** are characterized by its spectral features, characteristic of π-stacked NDI chromophores.[12] Both homopolymers in TCE/MCH, 5/95 (v/v), exhibited a hypochromic shift and broadening of π-π* absorption maximum with a characteristic change in the absorbance ratio of its vibronic bands compared to its monomers (A_{370}/A_{353} = 1.2 to 1 for molecule **NDI-carba-SEt** and A_{380}/A_{360} = 1.13 to 1.08 for molecule **NDI-carba** upon monomer to homopolymers transformation) (Figure 4.2a, and 4.2d). This is accompanied by the broadening and hypochromic shift of the n-π* absorption bands for monomer **NDI-carba-SEt** (Figures 4.2a and 4.2d). Homopolymers of **NDI-carba-SEt** and **NDI-carba** also exhibited an ICD signal at the electronic transitions as evident from the CD spectra (Figures 4.2b, and 4.2e), which is biased by the peripheral chiral
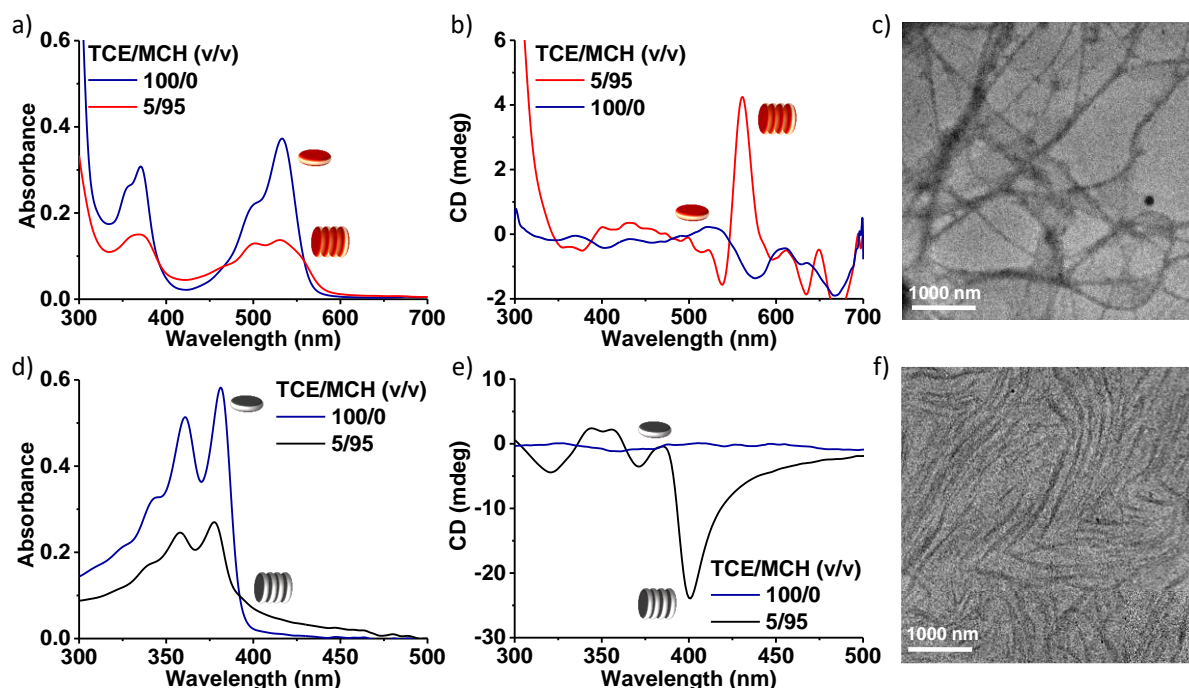
Figure 4.2. a), d) Absorption, b), e) CD spectra of molecules **NDI-carba-SEt** and **NDI-carba** in monomeric (TCE) and in homopolymeric state (TCE/MCH, 5/95 (v/v)). Corresponding TEM image of c) homopolymeric **NDI-carba-SEt** and f) homopolymeric **NDI-carba** (TCE/MCH, 5/95 (v/v)). ([**NDI-carba-Set**] = [**NDI-carba**] = 2.5×10^{-5} M, l = 10 mm).

cholesterol moieties. Homopolymers of **NDI-carba-SEt** and **NDI-carba** imaged through transmission electron microscopy (TEM) showed the formation of micrometer long one-dimensional (1D) fibers (Figures 4.2c and 4.2f). Since cNDI derivatives are well-studied for its emission characteristics, we further investigated fluorescence properties of monomers and homopolymers of **NDI-carba-SEt** and **NDI-carba**. Monomers of **NDI-carba-SEt** showed an emission band at 560 nm ($\lambda_{ex} = 490$ nm), which exhibited a bathochromic shift to 574 nm upon homopolymerization ($\lambda_{ex} = 490$ nm) (Figure 4.3a). Emissive J-type supramolecular organization of monomers in its homopolymers, is further confirmed with time-resolved fluorescence measurements (Figures 4.3b and 4.3c, Table 4.1). On the other hand, the fluorescence of homopolymers of **NDI-carba**, with weakly fluorescent, unsubstituted NDI monomers, is completely quenched (Figure 4.3d). Thus, we have prepared a structurally similar, green-emissive cNDI monomer **NDI-carba-OEt** ($\lambda_{ex} = 430$ nm and $\lambda_{max} = 490$ nm), with ethoxy-substitution, as a fluorescent tag (1 %) to visualize the homopolymers of **NDI-carba** (Figures 4.3e and 4.3f). The emissive J-aggregates of **NDI-carba-SEt** facilitated its visualization under the SIM microscope as red-emitting 1D supramolecular polymers (Figure 4.4b). Similarly, the homopolymerized solution of **NDI-carba** containing 1 % of **NDI-carba-OEt** as a fluorescent tag was visualized as green-emissive fibers under SIM fluorescence microscopy (Figure 4.4c). Moreover, the distinct absorption and emission profiles the monomers **NDI-carba-SEt** and **NDI-carba-OEt** (Figure 4.4) is an important factor for the orthogonal visualization of self-assembled monomers of **NDI-carba-SEt** and **NDI-carba** during multicomponent supramolecular copolymerization (*vide infra*).
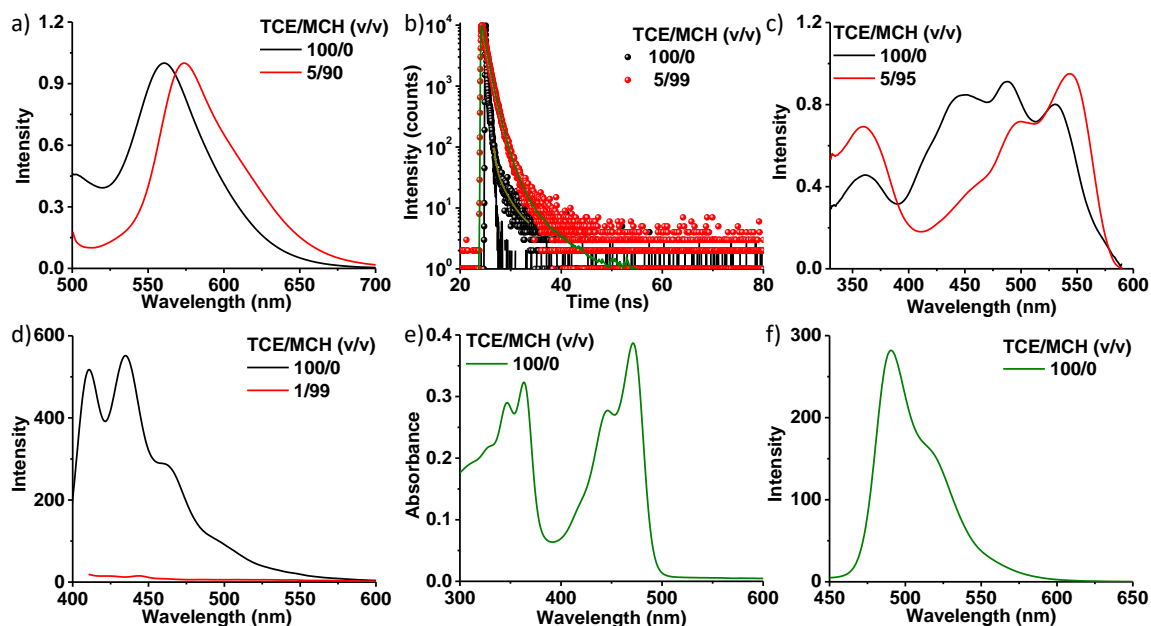
Figure 4.3. a) Normalized emission spectra (λ_{ex} = 490 nm), b) lifetime decay profile, c) excitation spectra (λ_{coll} = 600 nm) of monomeric **NDI-carba-SEt** in TCE and homopolymeric **NDI-carba-SEt** in TCE/MCH, 5/95 (v/v). d) Emission spectra (λ_{ex} = 370 nm) of monomeric **NDI-carba** in TCE and homopolymeric **NDI-carba** in TCE/MCH, 5/95 (v/v). e) Absorption spectrum and f) emission spectrum (λ_{ex} = 430 nm) of molecule **NDI-carba-OEt** in TCE. ([**NDI-carba-SEt**] = [**NDI-carba**] = [**NDI-carba-OEt**] = 2.5×10^{-5} M, l = 10 mm).

TCE/MCH (v/v)	λ_{coll} (nm)	t_1 (ns)	t_2 (ns)	t_3 (ns)
100/0	590	2.27 (76.48 %)	0.3 (23.52 %)	
5/95	590	1.49 (32.88 %)	5.35 (2.02 %)	0.7 (65.10 %)

Table 4.1. Lifetime data of monomeric **NDI-carba-SEt** in TCE and homopolymeric **NDI-carba-SEt** in TCE/MCH, 5/95 (v/v). ([**NDI-carba-SEt**] = 2.5×10^{-5} M).
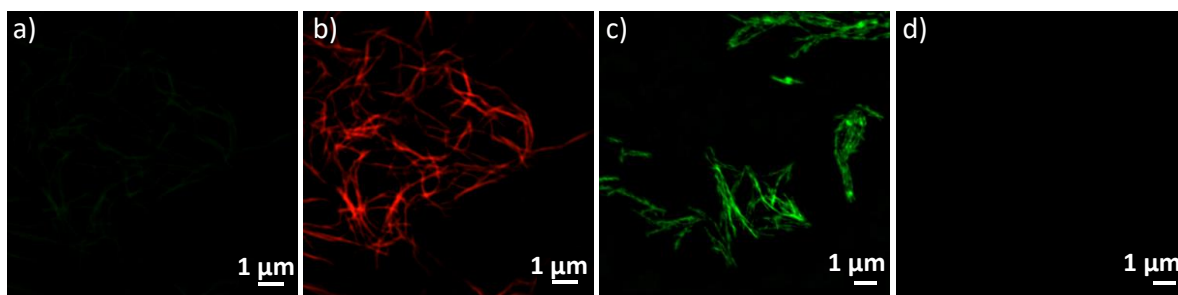
Figure 4.4. SIM images of homopolymers of **NDI-carba-SEt** in a) green channel and b) red channel. SIM images of homopolymers of **NDI-carba** mixed with 1 % of **NDI-carba-OEt** in c) green channel and d) red channel. (Channel I: λ_{ex} = 488 nm, λ_{coll} = 495-575 nm, channel II: λ_{ex} = 561 nm, λ_{coll} = 570-650 nm, TCE/MCH, 5/95 (v/v), [**NDI-carba-SEt**] = [**NDI-carba**] = 2.5×10^{-5} M).

4.3.2. Mechanistic Investigations:

Probing the kinetic profiles at the characteristic absorption features of the assembled NDI chromophores (563 nm for **NDI-carba-SEt** and 395 nm for **NDI-carba**), showed a sigmoidal growth of the supramolecular polymers with a lag phase when monomers of **NDI-carba-SEt** and **NDI-carba** in TCE were introduced into to MCH solvent (TCE/MCH, 1/99 (v/v) to TCE/MCH, 5/95 (v/v), 2.5×10^{-5} M, 298 K). The sigmoidal growth kinetics of both the monomers could be fitted to an autocatalytic nucleation-elongation model (Figures 4.5 and 4.6, Table 4.2) which confirms the operation of a nucleation-elongation growth mechanism during
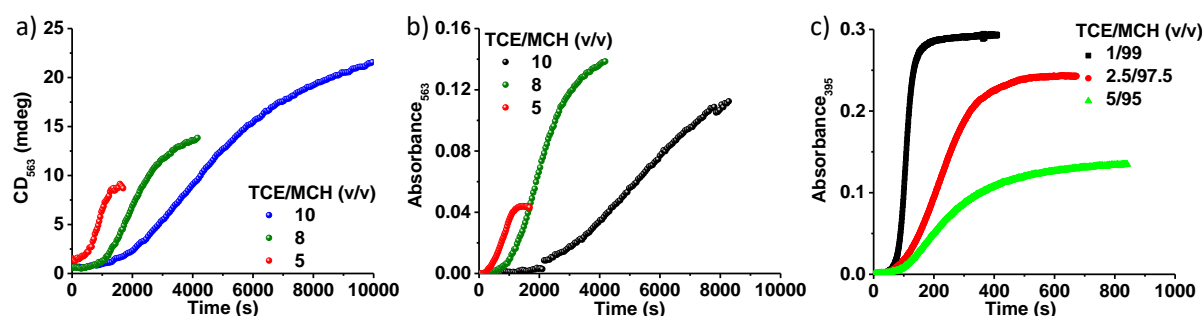
Figure 4.5. Time-dependent a) CD changes and b) absorbance changes at 563 nm during evolution of metastable state of **NDI-carba-SEt** into homopolymeric state at various percentages of TCE in MCH. c) Time-dependent absorbance changes monitored for **NDI-carba** at 365 nm during evolution of metastable state into homopolymeric state. ([**NDI-carba-SEt**] = [**NDI-carba**] = 2.5×10^{-5} M).
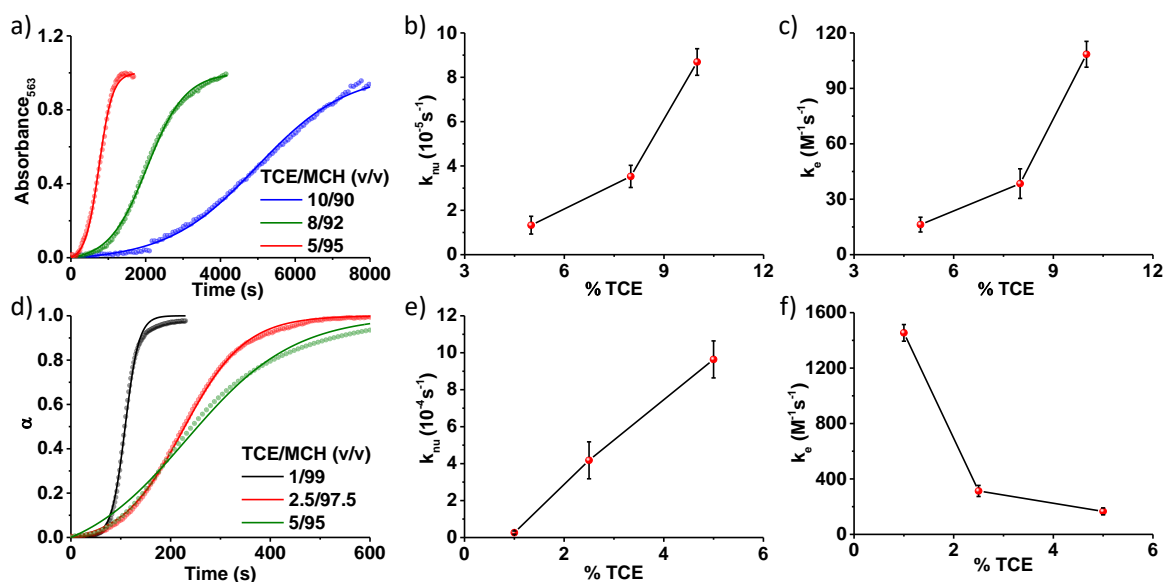
Figure 4.6. a) and d) Fitting of time-dependent absorbance changes of Figure 4.5 into Watzky-Finke model to extract the nucleation (k_{nu}) and elongation (k_e) rate constants for **NDI-carba-SEt** and **NDI-carba**, respectively. Plot of b), e) k_{nu} and c), f) k_e against percentage of TCE for **NDI-carba-SEt** and **NDI-carba**, respectively. ([**NDI-carba-SEt**] = [**NDI-carba**] = 2.5×10^{-5} M).

transformation of metastable state into homopolymeric state.[14] The transformation of metastable state into homopolymeric state is accelerated at higher percentage of TCE which is evident from the plot of k_{nu} and k_e against % of TCE.

NDI-carba-SEt	% TCE	k_{nu} (s^{-1}) × 10^{-5}	k_e (M^{-1}s^{-1})	NDI-carba	% TCE	k_{nu} (s^{-1}) × 10^{-5}	k_e (M^{-1}s^{-1})
	10	8.69	108.46		1	0.264	1454.19
	8	3.53	38.45		2.5	4.18	313.21
	5	1.33	16.28		5	9.64	166

Table 4.2. Listed values of k_{nu} and k_e obtained using the kinetic data of Figure 4.6.

Further the lag time increases (384 seconds to 1000 seconds for **NDI-carba-SEt** and 98 seconds to 1350 seconds for **NDI-carba**) with a decrease in concentration (2.5×10^{-5} M to 10^{-5} M) (Figure 4.7). These observations indicate the initial formation of on-pathway metastable state from the monomers, which evolves to supramolecular polymers in a cooperative manner with time.
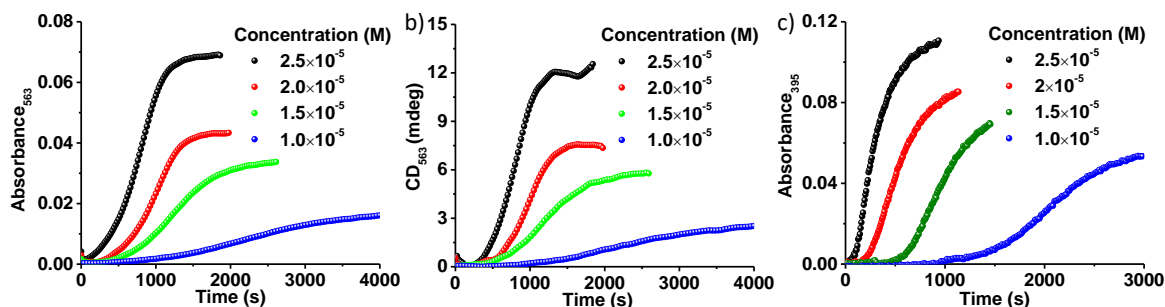
Figure 4.7. Concentration-dependent a) absorbance and b) CD changes monitored at 563 nm during conversion of metastable state of **NDI-carba-SEt** into homopolymeric state of **NDI-carba-SEt**. c) Concentration-dependent absorbance changes monitored at 395 nm during conversion of metastable state of **NDI-carba** into homopolymeric state. (TCE/MCH, 5/95 (v/v)).

Metastable state of **NDI-carba-SEt** showed a change in the ratio between vibronic bands of π-π^* absorption maximum (A_{370}/A_{353} 1.2 for monomers, 1 for homopolymers, and 1.05 for metastable state) and emission spectra depicted a broadening and appearance of weak emission band at a higher wavelength (585 nm, λ_{ex} = 490 nm) compared to the absorption and emission spectra of monomer in TCE (560 nm, λ_{ex} = 490 nm) (Figures 4.8a and 4.8b). Further excitation spectra collected at the emission maximum of metastable state showed the presence of a blue shifted excitation spectrum compared to the monomeric state (Figure 4.8c). Similarly, the metastable state of **NDI-carba** showed absorption spectra resembling that of a monomeric state and the metastable species was found to be CD inactive (Figure 4.9). The DLS spectra

recorded for metastable state of **NDI-carba-SEt** and **NDI-carba** depicted the presence of smaller size aggregates compared to the homopolymeric state (Figures 4.8 and 4.9). The different absorption and emission spectral features compared to monomeric species, indicate less-ordered small aggregates as metastable states prior to the nucleation and elongation event. This observation is in line with the various aggregated metastable states formed under kinetic conditions for similar hydrogen-bonded chromophoric monomers.[15]
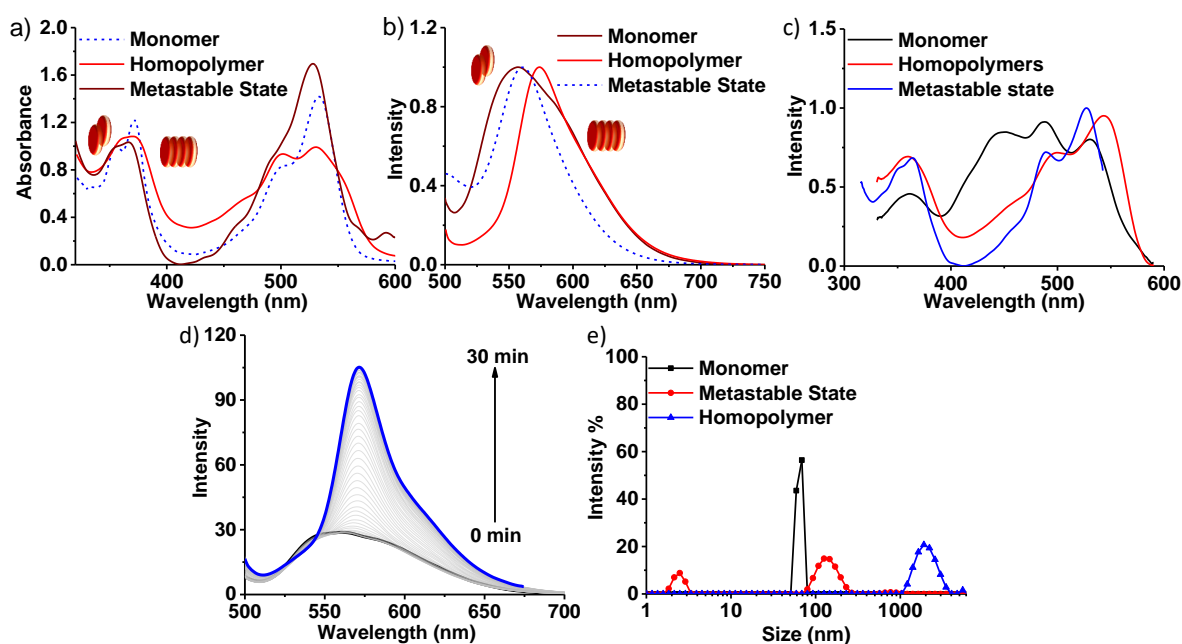
Figure 4.8. Spectroscopic investigation of metastable state of **NDI-carba-SEt**. a) Absorption and b) emission (λ_{ex} = 490 nm) spectrum of metastable state of molecule **NDI-carba-SEt** and its comparison with monomeric and homopolymeric state. c) Excitation spectra of metastable state (λ_{coll} = 590 nm), and its comparison with homopolymers (λ_{coll} = 600 nm) and monomers (λ_{coll} = 600 nm). d) Time-dependent emission spectra (λ_{ex} = 490 nm) during conversion of metastable state into homopolymeric state. e) DLS spectra of metastable state of **NDI-carba-SEt** and its comparison with homopolymeric and monomeric state. (TCE/MCH, 5/95 (v/v), [**NDI-carba-SEt**] = 2.5×10^{-5} M).
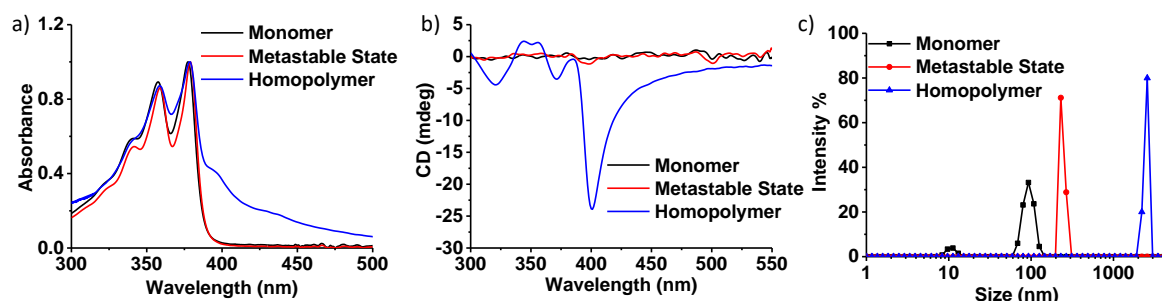
Figure 4.9. Spectroscopic investigation of metastable state of **NDI-carba**. a) Absorption and b) CD spectra spectrum of metastable state of molecule **NDI-carba** and its comparison with monomeric and homopolymeric state. c) DLS spectrum of metastable state of **NDI-carba** and its comparison with homopolymeric and monomeric state. (TCE/MCH, 5/95 (v/v), [**NDI-carba**] = 2.5×10^{-5} M).

4.3.3. Dispersity Control of Supramolecular Block Copolymers:

Kinetically realizable metastable states and nucleation-elongation growth mechanism with a lag phase during the supramolecular polymerization of **NDI-carba-SEt** and **NDI-carba** prompted us to investigate the kinetically controlled, seed induced supramolecular block copolymerization. In a typical experiment, seeds of one of the monomers are introduced to the metastable state of the other monomer to trigger the heterogeneous nucleation of the later. In the present study, monomers of **NDI-carba** is used as the feeding monomer due to its longer lag phase, whereas self-assembled **NDI-carba-SEt** is used as the seed. Thus, seeds of the homopolymers of **NDI-carba-SEt** with a narrow dispersity (L_n = 634 nm, L_w = 664 nm, PDI = 1.04±0.02) were prepared by the sonication of its homopolymers (10^{-5} M) for four hours at 298 K (Figure 4.10). Subsequent addition of **NDI-carba-SEt$_{seed}$** (10^{-5} M) to the metastable states of **NDI-carba** (10^{-5} M), triggered the spontaneous growth of the latter monomer without any lag phase, characteristic of a seeded growth (Figure 4.11a). This is evident from the decrease of t_{50} (time required for 50 % conversion) from 2000±60 seconds for an unseeded growth to 37±5 seconds for the seeded growth. The rate of growth of **NDI-carba** could be further accelerated by increasing the ratio of the seeds **NDI-carba-SEt**, indicating the formation of supramolecular BCPs via seeding (Figure 4.11a). Fitting of the kinetics of the seeded growth of **NDI-carba** to the model proposed by Zhao and Moore[14] showed a linear increase of kc* (c* is the concentration of added seed termini and k is the polymerization rate constant) (Figure 4.11b),
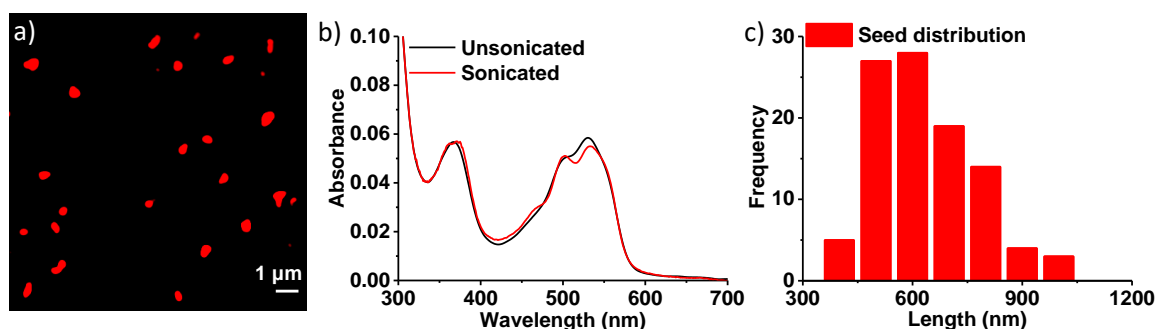
Figure 4.10. a) SIM microscopy images of prepared **NDI-carba-SEt$_{seed}$** solution after sonication of **NDI-carba-SEt** homopolymers for 4 hours in an ultrasonic bath visualized through channel II. b) Absorption spectra of **NDI-carba-SEt** homopolymers and its comparison with sonicated solution of **NDI-carba-SEt** homopolymer. c) Length distribution analysis of the seed solution prepared by sonicating **NDI-carba-SEt** homopolymers for 4 hours in an ultrasonic bath. (Channel II: λ_{ex} = 561 nm, λ_{coll} = 570-650 nm, [**NDI-carba-SEt**] = 10^{-5} M, TCE/MCH, 5/95 (v/v)).
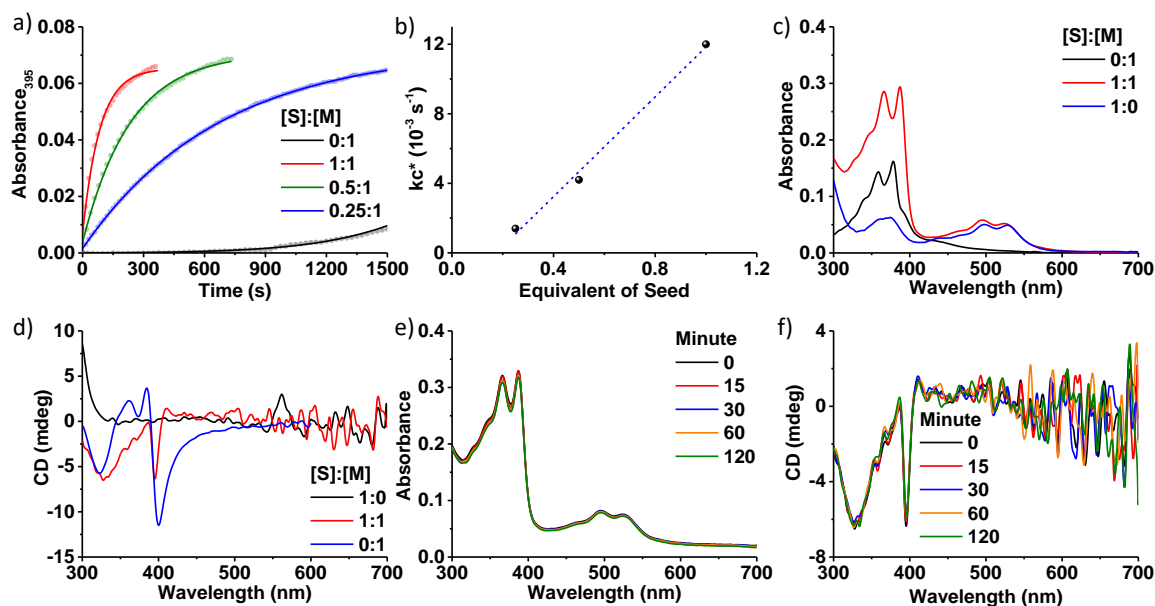
Figure 4.11. a) Time course of the supramolecular polymerization on addition **NDI-carba**$_{monomers}$ on various equivalent of **NDI-carba-SEt**$_{seed}$ ([**NDI-carba**] = 10^{-5} M). b) Plot of kc* value as a function of equivalent of **NDI-carba-SEt**$_{seed}$ showing a linear relationship. c) Absorption and d) CD spectrum of prepared supramolecular BCP and its comparison with individual homopolymers. Time-dependent e) absorption and f) CD spectra showing stability of the synthesized block copolymer with time. ([**NDI-carba-SEt**] = 10^{-5} M, TCE/MCH, 5/95 (v/v)).

with the **NDI-carba-SEt**$_{seed}$ concentration, reiterating the formation of supramolecular BCPs via heterogeneous nucleation. The resultant supramolecular BCPs could be visualized by the merging of the fluorescence imaging of the monomer **NDI-carba-SEt** and bright field imaging of the non-fluorescent component **NDI-carba**, which showed triblock chains with red-emitting segments in the middle and non-fluorescent segments at the termini (Figure 4.12). However, statistical analyses of BCPs from these images were difficult. As expected, of the absorption spectra of these supramolecular BCPs, individual aggregation characteristics of its components are retained (Figure 4.11c). Time-dependent absorption and CD spectra of the synthesized supramolecular BCP implied stability of the BCPs and low dynamics of the system (Figures 4.11e and 4.11f).
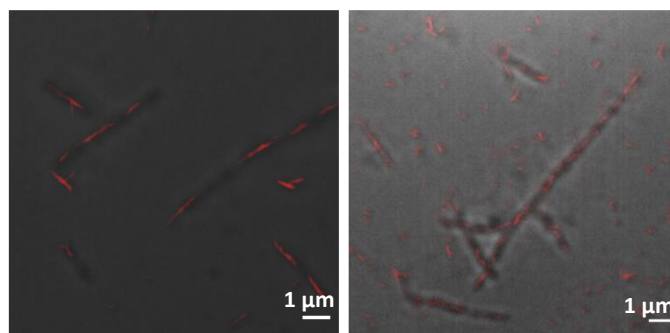
Figure 4.12. Visualization of the supramolecular BCP by merging SIM image collected at channel II (λ_{ex} = 561 nm, λ_{coll} = 570-650 nm) and bright field image.

In order to stain the non-fluorescent blocks of supramolecular BCPs and thus to perform its structural analyses, we have incorporated 1 % of fluorescent monomer **NDI-carba-OEt** to the monomer feed of **NDI-carba**, during the seeding process. Detailed spectroscopic investigation revealed similar seeding characteristics and monomer organization as observed before for pure monomers of **NDI-carba** suggesting that the introduction of a small amount of the fluorescent comonomers has only minimal effects on the structure of resultant BCPs (Figure 4.13). Visualization of the resultant solution after seeding, by merging green and red channel using SIM clearly showed the formation of supramolecular BCP structures with green-red-green segmented block topology, as expected from the growth of **NDI-carba** and **NDI-carba-OEt** ([**NDI-carba**]:[**NDI-carba-OEt**] = 100:1) onto the red **NDI-carba-SEt** seeds (Figure 4.14). A large number of isolated BCP chains further allowed us to perform the statistical analyses to determine the degree of polymerization and dispersity. Length distribution analysis performed on such 100 chains showed BCPs synthesized under kinetic control have excellent dispersity and length control as evident from the weight average length (L_w), number average length (L_n), and the polydispersity index (PDI). The overall length of the supramolecular BCPs
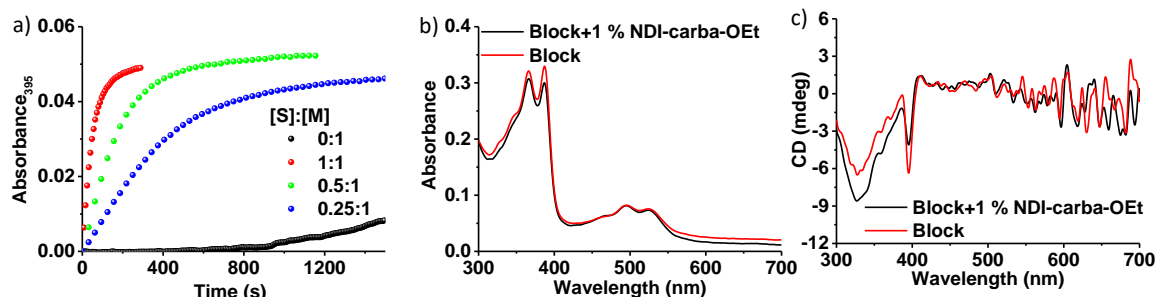
Figure 4.13. a) Time course of the supramolecular polymerization on addition of (**NDI-carba** + 1 % of **NDI-carba-OEt**) monomers onto the sonicated seed solution of **NDI-carba-SEt**. b) Absorption and c) CD spectra of the prepared supramolecular BCP in presence of 1 % of **NDI-carba-OEt** and its comparison with prepared block copolymers between **NDI-carba-SEt** and **NDI-carba**. ([**NDI-carba**] = 10^{-5} M, TCE/MCH, 5/95 (v/v)).

was found to be 1031 nm (L_n), 1078 nm (L_w) with a PDI of 1.04±0.04 (Table 4.3). The L_n and L_w of the green segments of the BCPs were found to be 410 and 437 nm with a low PDI of 1.06±0.03 (Table 4.3), whereas the red segments have a L_n and L_w of 668 and 700 nm (PDI = 1.04±0.02) (Table 4.3). It is important to note that the length and distribution of the red segments remain similar to that of the seeds used, suggesting the kinetic stability of the seeds. One of the advantages of seed-induced living supramolecular block copolymerization is tunable block lengths, by varying the monomer to seed ratio. In order to investigate this possibility, we have introduced (Figure 4.14a) higher concentration of monomer to the seeds of monomers **NDI-carba-SEt**, with a [**NDI-carba-SEt$_{Seed}$**]:[**NDI-carba$_{Monomer}$**] = 1:2 ratio

and in presence of the fluorescent comonomer **NDI-carba-OEt** ([**NDI-carba**]:[**NDI-carba-OEt**]=100:1). Statistical analyses performed on 100 isolated chains of resultant supramolecular BCPs, showed a length, L_n = 1382 nm (L_w = 1463 nm, PDI =1.05±0.03) (Table 4.3), of the chains which are higher compared to the [**NDI-carba-SEt$_{Seed}$**]:[**NDI-carba$_{Monomer}$**] = 1:1 ratio seeding experiments. Similarly, the L_n and L_w of the grown green blocks were calculated to be 582 nm and 627 nm (PDI = 1.07±0.04)
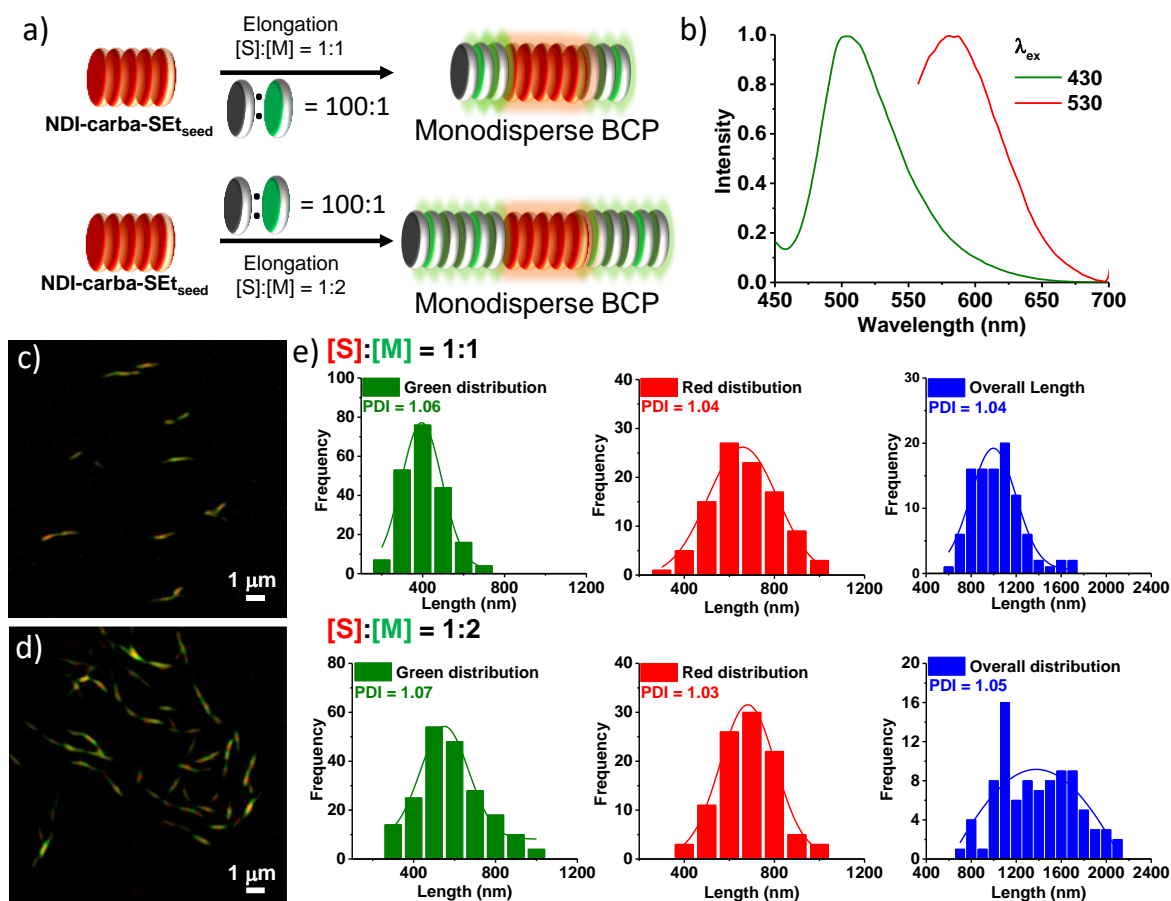
Figure 4.14. Visualization of the BCPs of **NDI-carba-SEt$_{seed}$** and **NDI-carba-OEt$_{monomer}$** containing 1 % of **NDI-carba-OEt** as a fluorescent stain. a) Schematic illustration of addition of different amount of **NDI-carba** monomer onto **NDI-carba-SEt** seed for modulation of block copolymer length. b) Emission spectra of the synthesized supramolecular block copolymer. SIM microscopy images of synthesized supramolecular BCPs of c) [S]:[M] = 1:1 and d) [S]:[M] = 1:2 in the merged channel (channel I + channel II). e) Length distribution analysis of synthesized supramolecular BCPs with [S]:[M] = 1:1 and [S]:[M] = 1:2 showing formation of monodisperse supramolecular polymers and an increase in length on increasing the monomer concentration. (Channel I: λ_{ex} = 488 nm, λ_{coll} = 495-575 nm, channel II: λ_{ex} = 561 nm, λ_{coll} = 570-650 nm, [**NDI-carba-SEt$_{seed}$**] = 10^{-5} M, TCE/MCH, 5/95 (v/v)).

[S]:[M]	Overall Length	L_n (nm)	L_w (nm)	PDI	Green Segment Length	L_n (nm)	L_w (nm)	PDI	Red Segment Length	L_n (nm)	L_w (nm)	PDI
1:1		1031	1078	1.04		410	437	1.06		668	700	1.04
1:2		1382	1463	1.05		582	627	1.07		684	707	1.03

Table 4.3. Calculated L_n, L_w and PDI of overall BCPs, green segment, and red segment of the BCPs at [S]:[M] ratio of 1:1 and 1:2. (Obtained using Figure 4.14e).

which is again higher than [**NDI-carba-SEt$_{Seed}$**]:[**NDI-carba$_{Monomer}$**] = 1:1 ratio seeding experiment (Table 4.3). However, the red block segments retained a constant length and polydispersity (Table 4.3), suggesting the living nature and controllable block lengths of the present system. On addition of higher concentration of **NDI-carba$_{monomers}$** onto **NDI-carba$_{seed}$** ([**NDI-carba-SEt$_{Seed}$**]:[**NDI-carba$_{monomer}$**] = 1:3) leads larger structures with connected multiblock segments of green and red component (Figure 4.15), which hampered the length distribution analyses over a wide range of concentration.
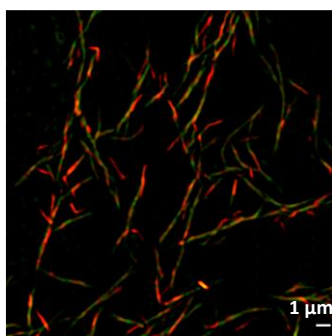
Figure 4.15. SIM microscopy images of synthesized supramolecular BCPs of **NDI-carba-SEt**$_{seed}$:**NDI-carba**$_{monomer}$ ratio of 1:3 in the merged channel (channel I + channel II). (Channel I: λ_{ex} = 488 nm, λ_{coll} = 495-575 nm; channel II: λ_{ex} = 561 nm, λ_{coll} = 570-650 nm, [**NDI-carba-SEt**] = 10^{-5} M, TCE/MCH, 5/95 (v/v)).

4.4. Conclusion:

In conclusion, we have explored the seeded supramolecular polymerization between optically different naphthalene diimide molecules (**NDI-carba-SEt** and **NDI-carba**) under kinetic control for the synthesis of monodisperse supramolecular BCPs and to tune the block copolymer length. The characteristic optical properties of NDI derivatives, which are sensitive to intermolecular interactions aided the spectroscopic probing of the supramolecular copolymerization. We have also introduced a green fluorescent component **NDI-carba-OEt**, which can be used as a fluorescent tag for the nonfluorescent component to facilitate the structural characterization of the polymers via SIM imaging. Further, the effective fluorescence imaging enabled a unique size distribution analysis of individual blocks which showed the

formation of of supramolecular BCPs of narrow polydispersity and tunable length by varying seed to monomer ratio.

4.5. Experimental section:

General Methods:

NMR Measurements: NMR spectra were recorded with a Bruker AVANCE 400 (400 MHz) Fourier transform NMR spectrometer and JEOL 600 MHz NMR spectrometer with chemical shifts reported in parts per million (ppm) with respect to TMS. Splitting patterns are designated as s, singlet; d, doublet; bs, broad singlet; m, multiplet; t, triplet; q, quartet; quin, quintet and br, broad.

Optical Measurements: Electronic absorption spectra were recorded on a Perkin Elmer Lambda 900 UV-Vis-NIR Spectrometer. Circular Dichroism (CD) spectra were recorded on a JASCO J-815 spectrometer where the sensitivity, time constant and scan rate were chosen appropriately. Emission spectra were recorded on Perkin Elmer LS 55 Luminescence Spectrometer. 10 mm × 10 mm quartz cuvettes were used for measurements at room temperature.

Transmission Electron Microscopy (TEM): TEM measurements were performed on a JEOL, JEM 3010 operated at 300 kV. Samples were prepared by placing a drop of the solution on carbon-coated copper grids followed by drying at room temperature. The images were recorded with an operating voltage of 300 kV.

Matrix-Assisted Laser Desorption Ionization (MALDI): MALDI was performed on a Bruker daltonics Autoflex Speed MALDI TOF System (GT0263G201) spectrometer using trans-2-[3-(4-tert-Butylphenyl)-2-methyl-2-propenylidene] malononitrile (DCTB) and α-Cyano-4-hydroxy-cinnamic acid (CCA) as the matrix.

Fluorescence Lifetime Measurements: Time-resolved decay experiments were recorded on a Horiba Delta Flex Time-Correlated Single Photon Counting (TCSPC) instrument. A 532 nm nano-LED with a pulse repetition rate of 1 MHz was used as the light source. The instrument response function (IRF) was collected by using a scatterer (Ludox AS40 colloidal silica, Sigma Aldrich). For 532 nm nano-LED light source, the instrumental full width at half maximum including detector response was 0.2 ns. The excited state decay of the sample was collected by fixing the emission wavelength. The decay was fitted to appropriate best fit multiexponential decay using IBH software (DAS6).

Structured Illumination Microscopy (SIM): Optical setup for imaging in Structured Illumination Microscopy (SIM) method: The fluorescence images of supramolecular polymers

were acquired using an inverted Zeiss 3 ELYRA PS1 microscope in structured illumination mode. Two lasers channel I - 488 nm (200 mW) (Green channel) and channel II - 561 nm (200 mW) (Red channel) have been used for respective excitation of **NDI-carba-SEt** and **NDI-carba-OEt** fluorophores. 10 % laser power from the objective top was used for structured illumination imaging. Imaging was performed using a Zeiss oil–immersion objective (Plan–apochromat 63x/1.40 Oil DIC M27, numerical aperture (NA) 1.40 oil). Fluorescence light was spectrally filtered with emission filters for channel I - MBS–488+EF BP 495–575/LP 750 for laser line 488 nm (green channel) and for channel II - MBS– 561+EF BP 570–650/LP 750 for laser line 561 nm (red channel) and and imaged using a PCO edge sCMOS camera (quantum yield > 70 %). Structured illumination images were processed using structured illumination analysis package for Zen software (Zeiss). Additional software have been used for colour adjustment (ImageJ). The channels were merged to investigate the spatial correlation between green- and red-emitting fibers.

4.6. Synthetic Schemes and Procedures:

Synthetic schemes for synthesis of molecule **NDI-carba-SEt**, **NDI-carba**, and **NDI-carba-OEt** is shown in Scheme 4.1, Scheme 4.2, Scheme 4.3.

Synthetic Schemes:
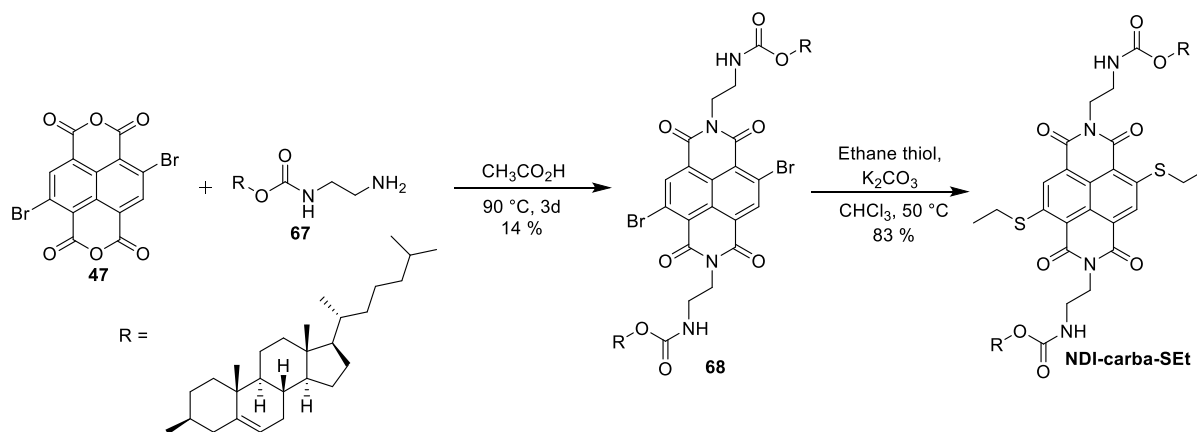
Scheme 4.1. Synthetic scheme for molecule **NDI-carba-SEt**.
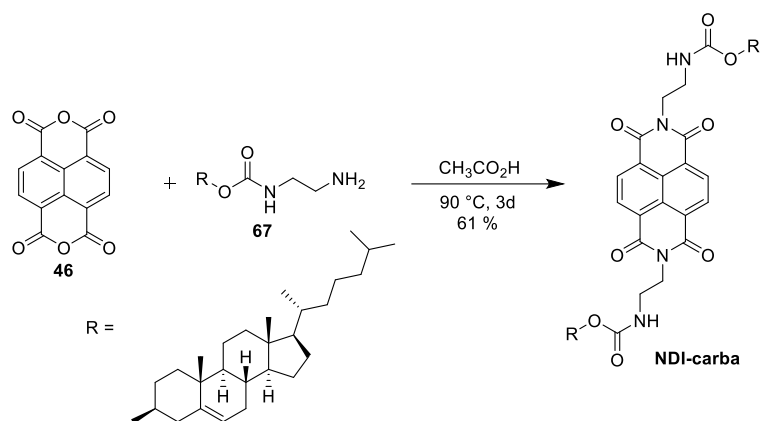
Scheme 4.2. Synthetic scheme for molecule **NDI-carba**.
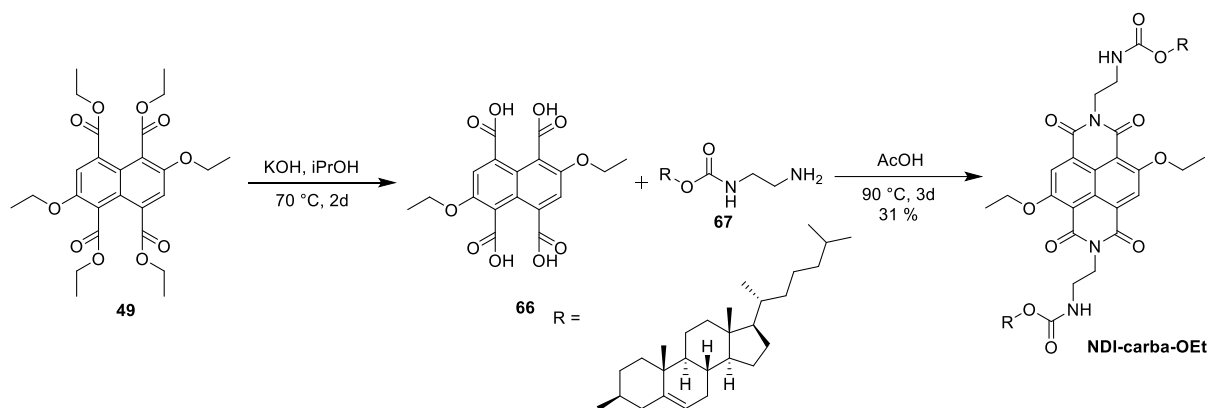
Scheme 4.3. Synthetic scheme for molecule **NDI-carba-OEt**.

Synthetic Procedure:

Molecules **47** and **67** were synthesized following previously reported procedures.[12,15]

Synthesis of 68: Compound **47** (461 mg, 1.082 mmol) was taken in a 100 mL round bottom (RB) flask and to it an acetic acid solution of **67** (1.535 g, 3.247 mmol) was added. The reaction mixture was heated at 90 °C for 20 hrs. The extent of the reaction was monitored by thin layer chromatography. After completion of the reaction cold water was added to it and an orange coloured precipitate was obtained. The precipitate was filtered and washed thoroughly with water and methanol followed by drying at room temperature. The crude product obtained was loaded in to 230-400 mesh silica gel and was purified using a gradient ranging from 1-2% MeOH/CHCl$_3$ to get the pure product as orange solid. The yield obtained was 14 %. ^{1}H NMR (600 MHz, CDCl$_3$, ppm): δ = 8.99 (s, 2H), 5.12 (s, 2H), 4.93 (d, J = 5.4 Hz, 2H), 4.40 (t, J = 6 Hz, 4H), 4.24 (s, br, 2H), 3.59 (m, 4H), 2.2-1.95 (m, 4H), 1.9-1.6 (m, 10H), 1.59-1.25 (m, 14H), 0.97-0.85 (m, 52H), 0.67 (d, J = 9 Hz, 6H). MALDI-TOF (DCTB, negative mode): m/z calculated for C$_{74}$H$_{104}$Br$_2$N$_4$O$_8$: 1335.61, found: [M]$^{\dot{}}$ = 1336.00 (Molecular ion peak is observed as radical ions due to the electron-deficient nature of naphthalene diimide cores). We could not record ^{13}C NMR of **68** due to low solubility in CDCl$_3$.

Synthesis of NDI-carba-SEt: Compound **68** (209 mg, 0.156 mmol) was taken in a 2 necked 100 mL round bottom flask. To it K_2CO_3 (216 mg, 1.565 mmol) and excess ethane thiol (3 mL) and 40 mL chloroform was added and refluxed at 50 °C for 2 days. The reaction was monitored by thin layer chromatography. After completion the reaction the excess ethane thiol and chloroform was evaporated under reduced pressure and loaded into silica gel (230-400 mesh) and purified using a gradient ranging from 0.1-0.5 % MeOH/CHCl3 to get a red coloured powder. The yield obtained was 83 %.^{1}H NMR (600 MHz, CDCl3, ppm): δ = 8.44 (s, 2H), 5.17 (s, 2H), 5.05 (s, 2H), 4.50 (d, J = 6.6 Hz, 4H), 4.35 (m, 6H), 3.58 (q, J = 4.2 Hz, 4H), 2.2-1.95 (m, 4H), 1.9-1.67 (m, 10H), 1.65 (t, J = 4.2 Hz, 6H), 1.59-1.0 (m, 15H), 0.96-0.85 (m, 51H), 0.66 (s, 6H); ^{13}C NMR (100 MHz, CDCl3, ppm) δ = 156.4, 139.75, 128.12, 122.37, 56.67, 56.16, 50.04, 49.93, 42.31, 39.72, 39.53, 38.39, 37.00, 36.57, 36.51, 36.20, 35.81, 31.87, 28.24, 28.02, 26.46, 24.29, 23.86, 22.82, 22.56, 21.02, 19.30, 18.72, 12.82, 11.87. MALDI-TOF (DCTB matrix, negative mode): m/z calculated for $C_{78}H_{112}S_2Br_2N_2O_8$ $[M]^+$ = 1297.80, found $[M]^{\cdot}$ = 1297.51 (Molecular ion peak is observed as radical ions due to the electron-deficient nature of naphthalene diimide cores).

Synthesis of NDI-carba: Compound **46** (500 mg, 1.86 mmol) and **67** (2.2 g, 4.66 mmol) were taken in 250 mL 2 necked round bottom flask fitted with refluxed condenser and a continuous N_2 flow. Then 75 mL dry DMF was added to the reaction mixture and heated at 130 °C for 15-20 min until the compound gets dissolved in to the DMF. The heating is continued for another 10 hours. The progress of the reaction was monitored by thin layer chromatography. After 12 hrs when the reaction is completed the reaction mixture is allowed to cool down to room temperature. A precipitate was observed at the bottom of the round bottom flask. MeOH was added into it to complete precipitation. The precipitate was filtered and washed thoroughly with MeOH and toluene mixture to remove the coloured portion of the precipitate. The white coloured precipitate obtained after washing with methanol and toluene was further washed with methanol to remove the excess of toluene. At last the white solid obtained was kept for drying overnight under vacuum oven. Then the compound was loaded into normal silica gel (100 mesh) for further purification using a gradient ranging from 1-2 % MeOH/CHCl3.The compound was obtained as white powder having yield = 61 %. ^{1}H NMR (600 MHz, CDCl3, ppm): δ = 8.75 (s, 4H), 5.07 (d, 2H), 4.39-4.28 (m, 6H), 3.59 (t, J = 7.8, 4H), 2.24-1.59 (m, 14H), 1.54-0.85 (m, 68H), 0.66 (s, 6H); ^{13}C NMR (150 MHz, CDCl3, ppm) δ = 163.40, 156.61, 139.97, 131.37, 126.79, 122.61, 74.63, 56.90, 56.38, 50.19, 42.54, 40.71, 39.95, 39.77, 38.58, 37.12, 36.75, 36.43, 36.04, 32.09, 28.47, 28.26, 28.20, 24.52, 24.09, 23.06, 22.80, 21.25, 19.54, 18.96, 12.09; MALDI-TOF (DCTB, negative mode): m/z calculated for $C_{74}H_{104}N_4O_8$: 1176.79,

found: $[M]^{\cdot} = 1176.92$ (Molecular ion peak is observed as radical ions due to the electron-deficient nature of naphthalene diimide cores).

Synthesis of 66: 49 (1 g, 1.98 mmol) was taken in a round bottom flask and 200 mL of 1 M KOH in isopropanol solution was added to it and refluxed for 72 hours. After 72 hours, the excess isopropanol was evaporated and the residue obtained was directly used for the next reaction without further purification.

Synthesis of NDI-carba-OEt: Compound **66** (711 mg, 1.812 mmol) was taken in a 250 mL round bottom flask and to it separately a prepared **67** solution in glacial acetic acid was added. The reaction mixture was heated at 90 °C for 20 hrs. The extent of reaction is monitored by thin layer chromatography. After completion of the reaction an excess of water was added to it to get a light orange coloured precipitate. The precipitate was filtered and washed thoroughly with methanol and kept overnight for drying under vacuum. The crude obtained was loaded in to 230-400 mesh silica gel for further purification. The yield obtained was 14 %. ^{1}H NMR (600 MHz, CDCl$_3$, ppm)**:** $\delta = 8.39$ (s, 2H), 5.19 (s, 2H), 5.16 (s, 2H), 4.49 (q, $J = 6.6$ Hz, 4H), 4.35 (m, 6H), 3.57 (m, 4H), 2.18-2.16 (m, 4H), 2.01-1.7 (m, 8H), 1.61 (t, $J = 6.6$ Hz, 6H), 1.55-1.01 (m, 20H), 0.97-0.86 (m, 48H), 0.67 (s, 6H); ^{13}C NMR (150 MHz, CDCl$_3$, ppm): $\delta = 162.68$, 161.27, 160.02, 156.33, 139.73, 126.98, 123.54, 122.38, 119.63, 110.42, 74.25, 66.35, 56.63, 56.11, 49.91, 42.28, 40.23, 40.13, 39.77, 39.68, 39.50, 38.38, 36.88, 36.49, 36.16, 35.79, 31.83, 29.69, 28.21, 28.00, 24.26, 23.83, 22.81, 22.54, 20.99, 19.28, 18.69, 14.78, 11.83; MALDI-TOF (DCTB matrix, negative mode)**:** m/z calculated for C$_{78}$H$_{112}$N$_2$O$_{10}$ [M]$^+$ = 1264.84, found [M]$^+$ = 1265.235 (Molecular ion peak is observed as radical ions due to the electron-deficient nature of naphthalene diimide cores).

4.6. Experimental Procedures:

Protocol of Sample Preparation:

Protocol I: Sample Preparation Protocol for NDI-carba-SEt and NDI-carba Homopolymers: A stock solution of **NDI-carba-SEt** or **NDI-carba** (c = 5×10^{-3} M) was prepared in TCE. An appropriate volume of this stock is added to a TCE/MCH mixture and the solution was incubated for 2 hours to synthesize the homopolymers.

For example, 12.5 μL of 5×10^{-3} M stock of **NDI-carba-SEt** is added to a premixed solution of 112.5 μL of toluene and in 2375 μL of methyl cyclohexane (MCH) to prepare the final self-assembling solution of 5×10^{-5} M, 5 % toluene/MCH with total 2500 μL sample volume.

Protocol II: Preparation of Supramolecular Block Copolymer: A Seed solution of **NDI-carba-SEt** was prepared by sonicating a hot solution (363 K) of **NDI-carba-SEt** homopolymers (of different concentration) for 2 hours in an ultrasonic bath maintained at 298 K. The monomeric solution of **NDI-carba** in TCE (5×10^{-3} M) was then added into the sonicated seed solution and kinetics of the process was monitored following absorbance changes at 395 nm.

4.7. References:

[1] a) De Greef, T. F. A.; Smulders, M. M. J.; Wolffs, M.; Schenning, A. P. H. J.; Sijbesma, R. P.; Meijer, E. W. *Chem. Rev.* **2009**, *109*, 5687-5754. b) de Greef, T. F. A.; Meijer, E. W. *Nature* **2008**, *453*, 171-173. c) Aida, T.; Meijer, E. W.; Stupp, S. I. *Science* **2012**, *335*, 813-817. d) Vantomme, G.; Meijer, E. W. *Science* **2019**, *363*, 1396-1397. e) Aida, T. *Adv. Mater.* **2019**, 1905445. f) Aida, T.; Meijer, E. W. *Isr. J. Chem.* **2020**, *60*, 33-47.

[2] a) Adelizzi, B.; Van Zee, N. J.; De Windt, L. N.; Palmans, A. R.; Meijer, E. W. *J. Am. Chem. Soc.* **2019**, *141*, 6110-6121. b) Wehner, M.; Würthner, F. *Nat. Rev. Chem.* **2020**, *4*, 38-53. c) Besenius, P. *Polymer Chemistry* **2017**, *55*, 34-78.

[3] a) Zhang, W.; Jin, W.; Fukushima, T.; Saeki, A.; Seki, S.; Aida, T. *Science* **2011**, *334*, 340-343. b) Zhang, W.; Jin, W.; Fukushima, T.; Mori, T.; Aida, T. *J. Am. Chem. Soc.* **2015**, *137*, 13792-13795.

[4] Jung, S. H.; Bochicchio, D.; Pavan, G. M.; Takeuchi, M.; Sugiyasu, K. *J. Am. Chem. Soc.* **2018**, *140*, 10570-10577.

[5] Adelizzi, B.; Aloi, A.; Markvoort, A. J.; Ten Eikelder, H. M.; Voets, I. K.; Palmans, A. R.; Meijer, E. W. *J. Am. Chem. Soc.* **2018**, *140*, 7168-7175.

[6] a) Wang, X.; Guerin, G.; Wang, H.; Wang, Y.; Manners, I.; Winnik, M. *Science* **2007**, *317*, 644-648. b) Gilroy, J. B.; Gädt, T.; Whittell, G. R.; Chabanne, L.; Mitchels, J. M.; Richardson, R. M.; Winnik, M. A.; Manners, I. *Nat. Chem.* **2010**, *2*, 566-570. c) Hailes, R. L. N.; Oliver, A. M.; Gwyther, J.; Whittell, G. R.; Manners, I. *Chem. Soc. Rev.* **2016**, *45*, 5358-5407.

[7] a) Wilkins, C. J.; He, X.; Symons, H. E.; Harniman, R. L.; Faul, C. F. J.; Manners, I. *Chem. Eur. J.* **2018**, *24*, 15556-15565. b) Wan, Q.; To, W.; Chang, X.; Che, C. M. *Chem* **2020**, *6*, 1-23.

[8] a) Fukui, T.; Kawai, S.; Fujinuma, S.; Matsushita, Y.; Yasuda, T.; Sakurai, T.; Seki, S.; Takeuchi, M.; Sugiyasu, K. *Nat. Chem.* **2017**, *9*, 493-499. b) Ogi, S.; Sugiyasu, K.; Manna, S.; Samitsu, S.; Takeuchi, M. *Nat. Chem.* **2014**, *6*, 188-195. c) Ogi, S.; Stepanenko, V.; Sugiyasu, K.; Takeuchi, M.; Würthner, F. *J. Am. Chem. Soc.* **2015**, *137*, 3300-3307. d) Dhiman, S.;

George, S. J. *Bull. Chem. Soc. Jpn.* **2018**, *91*, 687-699. e) Matern, J.; Dorca, Y.; Sánchez, L.; Fernández, G. *Angew. Chem., Int. Ed.* **2019**, *58*, 16730-16740. f) van der Zwaag, D.; De Greef, T. F. A.; Meijer, E. W. *Angew. Chem., Int. Ed.* **2015**, *54*, 8334-8336. g) Mukhopadhyay, R. D.; Ajayaghosh, A. *Science* **2015**, *349*, 241-242. h) Würthner, F. *Nat. Chem.* **2014**, *6*, 171-173.

[9] a) Mishra, A.; Korlepara, D. B.; Kumar, M.; Jain, A.; Jonnalagadda, N.; Bejagam, K. K.; Balasubramanian, S.; George, S. J. *Nat. Commun.* **2018**, *9*, 1295. b) Jain, A.; Dhiman, S.; Dhayani, A.; Vemula, P. K.; George, S. J. *Nat. Commun.* **2019**, *10*, 450. c) Ogi, S.; Stepanenko, V.; Thein, J.; Würthner, F. *J. Am. Chem. Soc.* **2016**, *138*, 670-678. d) Ogi, S.; Matsumoto, K.; Yamaguchi, S. *Angew. Chem., Int. Ed.* **2018**, *57*, 2339-2343. e) Greciano, E. E.; Matarranz, B.; Sánchez, L. *Angew. Chem., Int. Ed.* **2018**, *57*, 4697-4701. f) Endo, M.; Fukui, T.; Jung, S. H.; Yagai, S.; Takeuchi, M.; Sugiyasu, K. *J. Am. Chem. Soc.* **2016**, *138*, 14347-14353. g) Langenstroer, A.; Kartha, K. K.; Dorca, Y.; Droste, J.; Stepanenko, V.; Albuquerque, R. Q.; Hansen, M. R.; Sánchez, L.; Fernández, G. *J. Am. Chem. Soc.* **2019**, *141*, 5192-5200. h) Wilkins, C. J.; He, X.; Symons, H. E.; Harniman, R. L.; Faul, C. F. J.; Manners, I. *Chem. Eur. J.* **2018**, *24*, 15556-15565. i) Robinson, M. E.; Lunn, D. J.; Nazemi, A.; Whittell, G. R.; De Cola, L.; Manners, I. *Chem. Commun.* **2015**, *51*, 15921-15924. j) Aliprandi, A.; Mauro, M.; Cola, L. D. *Nat. Chem.* **2016**, *8*, 10-15. k) Kemper, B.; Zengerling, L.; Spitzer, D.; Otter, R.; Bauer, T.; Besenius, P. *J. Am. Chem. Soc.* **2018**, *140*, 534-537.

[10] a) Wagner, W.; Wehner, M.; Stepanenko, V.; Würthner, F. *J. Am. Chem. Soc.* **2019**, *141*, 12044-12054. b) Wagner, W.; Wehner, M.; Stepanenko, V.; Würthner, F. *CCS Chem.* **2019**, *1*, 598-613.

[11] Sarkar, A.; Sasmal, R.; Empereur-mot, C.; Bochicchio, D.; Kompella, S. V. K.; Sharma, K.; Dhiman, S.; Sundaram, B.; Agasti, S. S.; Pavan, G. M.; George, S. J. *J. Am. Chem. Soc.* **2020**, *16*, 7606-7617.

[12] a) Sakai, N.; Mareda, J.; Vauthey, E.; Matile, S. *Chem. Commun.* **2010**, *46*, 4225-4237. b) Würthner, F.; Ahmed, S.; Thalacker, C.; Debaerdemaeker, T. *Chem. Eur. J.* **2002**, *8*, 4742-4750. c) He, T.; Stolte, M.; Burschka, C.; Hansen, N. H.; Musiol, T.; Kälblein, D.; Pflaum, J.; Tao, X.; Brill, J.; Würthner, F. *Nat. Commun.* **2015**, *6*, 5954.

[13] a) Kulkarni, C.; Balasubramanian, S.; George, S. J. *ChemPhysChem* **2013**, *14*, 661-673. b) Kulkarni, C.; Bejagam, K. K.; Senanayak, P. S.; Narayan, K. S.; Balasubramanian, S.; George, S. J. *J. Am. Chem. Soc.* **2015**, *137*, 3924-3932.

[14] Zhao, D.; Moore, J. S. *Org. Bio. Chem.* **2003**, *1*, 3471-3491.

[15] Balamurugan, R.; Zhang, Y.-S.; Fitriyani, S.; Liu, J. H. *Soft Matter* **2016**, *12*, 5214-5223.

Chapter: 5

Tricomponent Supramolecular Block Copolymers via Sequential Seeded Polymerization

Chapter: 5

Tricomponent Supramolecular Block Copolymers via Sequential Seeded Polymerization

Abstract

The synthesis of supramolecular block copolymers is still a compelling challenge. Particularly sequential addition of three different self-assembling monomers leading to a tricomponent supramolecular block copolymer is a formidable challenge which requires three structurally similar, but different self-assembling monomers. Herein we have addressed this challenge and demonstrated an unprecedented three component supramolecular block copolymerization via sequential addition of three different structurally similar core-substituted naphthalene diimide monomers. Further presence of metastable states and kinetically controlled nucleation-elongation growth allowed the synthesis of three different sequences via sequential addition of the three different monomers. Fluorescent nature of core-substituted naphthalene diimide monomers have been further utilized to characterize the tricomponent supramolecular block copolymers via structured illumination microscopy (SIM).
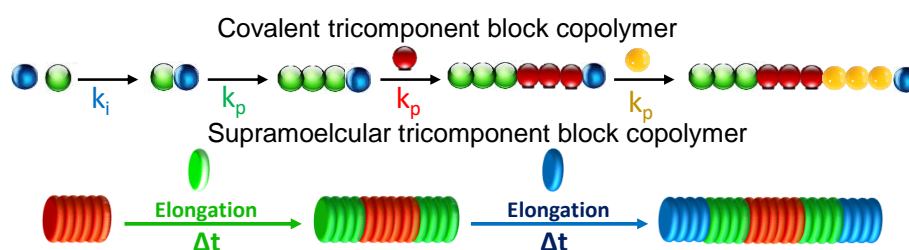
5.1. Introduction:

Supramolecular polymerization experiences a rapid development, which is fueled by the desire to produce complex adaptive and dynamic materials.[1] One of the intriguing challenges in this field is to make well-defined copolymers.[2] In contrast to the myriad of methods available for the synthesis of covalent block copolymers,[3] supramolecular block copolymer synthesis has started only recently. One of the pioneering development in this direction came from the group of Manners and coworkers, who has established living crystallization-driven self-assembly (CDSA) self-assembly of poly(ferrocenyldimethylsilane) (PFS)-core containing block copolymers.[4] The kinetically stable seeds allowed the synthesis of a plethora of supramolecular block copolymers of complex sequences, dimensions, and topology.[5] However, synthesis of supramolecular block copolymer from small molecules directed by specific supramolecular interactions is a significant challenge due to its dynamic nature. Recently Meijer and coworkers have reported block copolymerization between triarylamine based monomers having balanced homo- and hetero- free energy of interactions under thermodynamic control.[6]

In another example, Aida and coworkers have reported supramolecular copolymerization between nanotubular segments using multistep synthesis.[7] Takeuchi, Sugiyashu and coworkers reported coassembly between porphyrin monomers using solvent mixing protocol[8] which is analogous to the living crystallization driven self-assembly reported by Manners and coworkers. In this direction, most recently Würthner and coworkers reported seed induced living supramolecular polymerization[9,10] between core-substituted perylene diimides monomers[11]. Our group reported seeded coassembly with electronically different core-substituted naphthalene diimides which is analogous to the classical block copolymerization using living polymerization techniques (see Chapter 3).[12]

We envisage that synthesis of supramolecular block copolymers analogous to classical living polymerization techniques would render synthesis of supramolecular block copolymer of more complex topology and sequences as has been shown by Manners and coworkers. However, despite these encouraging developments, supramolecular copolymerization for the synthesis of complex sequences and topology still remains a grand challenge to be addressed. For example, controlled covalent living polymerization techniques could be utilized to make complex polymeric materials via sequential polymerization between there monomers leading to tricomponent block copolymers.[13] Such control in seeded supramolecular copolymerization is very challenging considering the rational design of monomers, because slight changes in monomer structures could interfere with the copolymerization process.[14] This scenario

encouraged us to explore the possibility of synthesis of tricomponent supramolecular block copolymers via sequential seeded assembly. In this Chapter, we demonstrate a sequential supramolecular copolymerization using kinetically controlled, seeded coassembly to synthesize tricomponent supramolecular block copolymer.

5.2. Molecular Design:
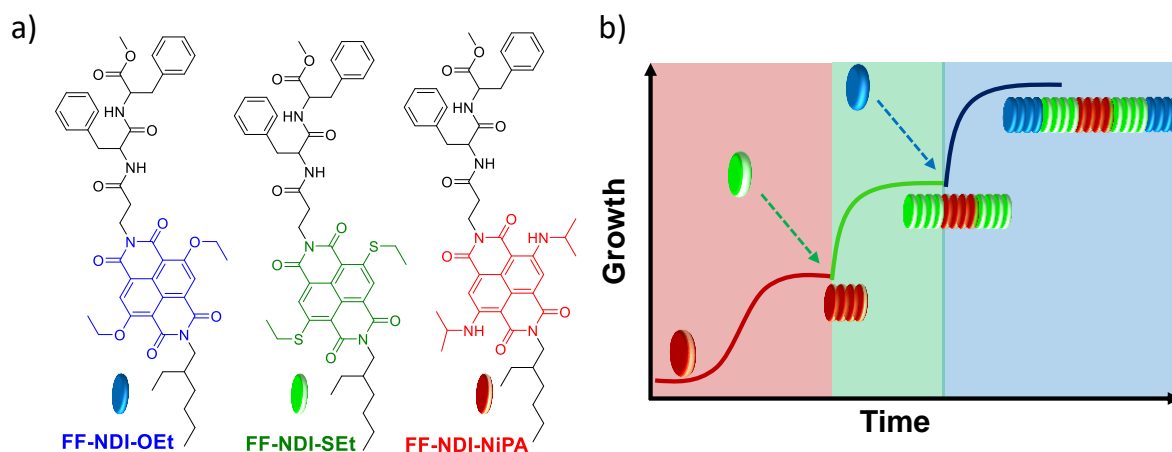
Figure 5.1. a) Molecular Structures of the monomers **FF-NDI-OEt**, **FF-NDI-SEt** and **FF-NDI-NiPA** used for synthesis of tricomponent supramolecular block copolymers. b) Schematic illustration of sequential addition of three monomers for synthesis of tricomponent block copolymer via seeded supramolecular polymerization.

To attempt this, we have chosen symmetrically disubstituted naphthalene diimide core as a self-assembling chromophore with ethoxy (**FF-NDI-OEt**), ethane thiol (**FF-NDI-SEt**) and isopropyl amine (**FF-NDI-NiPA**) core-substitution.[15] Different absorption and emission profiles (Figure 5.1a) of the chosen chromophores will enable orthogonal probing of the coassembly as well as characterization of the resultant tricomponent block copolymer using structured illumination microscopy (SIM).[16] Secondly, a tripeptide sequence containing the diphenylalanine motif was used as a self-assembling motif for hydrogen bonding driven cooperative nucleation-elongation assembly.[17] Molecules **FF-NDI-OEt**, **FF-NDI-SEt** and **FF-NDI-NiPA** were synthesized and characterized by ^{1}H, ^{13}C spectroscopy and mass spectrometry (see experimental section (Section 5.8, Scheme 5.1 to Scheme 5.6)).

5.3. Supramolecular Homopolymerization of the Monomers FF-NDI-OEt, FF-NDI-SEt and FF-NDI-NiPA:

The monomers **FF-NDI-OEt**, **FF-NDI-SEt** and **FF-NDI-NiPA** have distinct absorption (400 nm to 515 nm for **FF-NDI-OEt**, 470 nm to 580 nm for **FF-NDI-SEt** and 530 nm to 670 nm for **FF-NDI-NiPA**) and emission (455 nm to 580 nm for **FF-NDI-OEt**, 530 nm to 650 nm for **FF-NDI-SEt** and 610 nm to 720 nm for **FF-NDI-NiPA**) profiles in 1,1',2,2'-
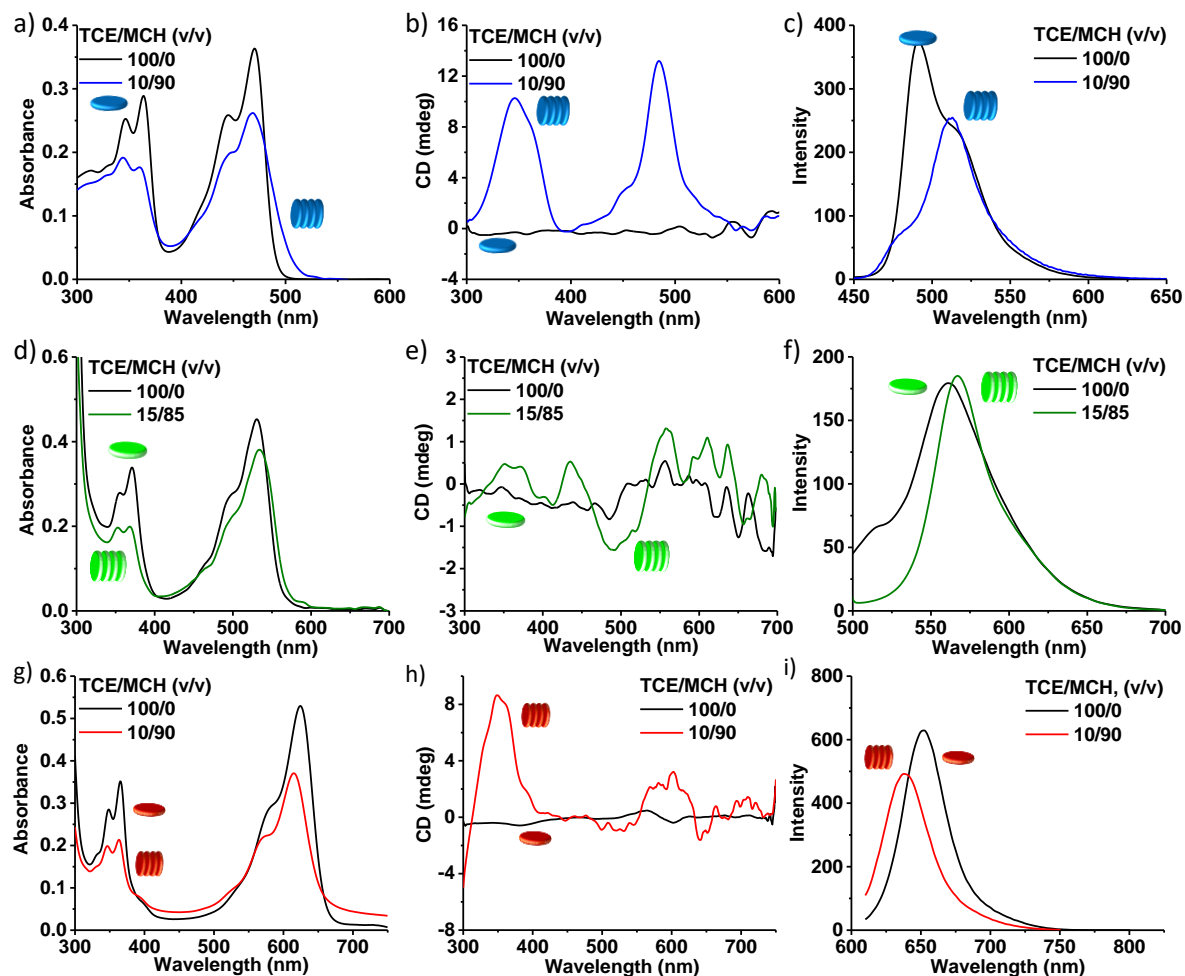
Figure 5.2. Absorption spectra of a) **FF-NDI-OEt**, d) **FF-NDI-SEt** and g) **FF-NDI-NiPA** in TCE and in TCE/MCH solvent mixture. CD spectra of b) **FF-NDI-OEt**, e) **FF-NDI-SEt** and h) **FF-NDI-NiPA** in TCE and in TCE/MCH solvent mixture. Emission spectra of c) **FF-NDI-OEt** (λ_{ex} = 430 nm), f) **FF-NDI-SEt** (λ_{ex}= 530 nm) and i) **FF-NDI-NiPA** (λ_{ex} = 590 nm) in TCE and in TCE/MCH solvent mixture. ([**FF-NDI-OEt**] = [**FF-NDI-SEt**] = [**FF-NDI-NiPA**] = 2.5×10^{-5} M, l = 10 mm).

tetrachloroethhane (TCE) solvent (Figure 5.2). Sharp absorption spectral features and absence of CD signal indicated monomeric nature of all these monomers in TCE. Supramolecular homopolymerization of **FF-NDI-OEt**, **FF-NDI-SEt**, and **FF-NDI-NiPA** monomers could be induced in TCE/methylcyclohexane (MCH) solvent mixture of varying composition ((TCE/MCH, 10/90 (v/v) to TCE/MCH, 5/95 (v/v) for **FF-NDI-OEt**), (TCE/MCH, 15/85 (v/v) to TCE/MCH, 5/95 (v/v) for **FF-NDI-SEt**), (TCE/MCH, 10/90 (v/v) to TCE/MCH, 5/95 (v/v) for **FF-NDI-NiPA**)). Absorption spectra of the self-assembled aggregates displayed broadening and reversal of intensities of vibronic transitions of π-π* absorption maxima (345 nm and 365 nm for **FF-NDI-OEt,** 355 nm and 370 nm for **FF-NDI-SEt,** and 349 nm and 365 nm for **FF-NDI-NiPA**) along with the broadening of n-π* absorption maxima (468 nm for

FF-NDI-OEt, 533 nm for **FF-NDI-SEt**, 615 nm for **FF-NDI-NiPA**) compared to the monomeric species in TCE (Figures 5.2a, 5.2d and 5.2g). Emission maxima revealed a bathochromic shift (490 nm to 515 nm for **FF-NDI-OEt**, 560 nm to 567 nm for **FF-NDI-SEt**, and 652 nm to 660 nm for **FF-NDI-NiPA**) on self-assembly (Figures 5.2c, 5.2f, 5.2i and 5.2j). The chiral diphenylalanine units arrange the chromophores in a helical manner, which is evident from the appearance of CD signal on self-assembly (346 nm and 484 nm for **FF-NDI-OEt** ($g_{CD} = 2.4 \times 10^{-3}$), 363 and 508 nm for **FF-NDI-SEt** ($g_{CD} = 3.24 \times 10^{-4}$), 350 nm and 600 nm for **FF-NDI-NiPA** ($g_{CD} = 1.15 \times 10^{-5}$) (Figures 5.2b, 5.2e, and 5.2h). Lifetime measurements revealed a completely different lifetime in case of the homopolymers than their monomeric state reiterating emissive nature of the homopolymers (Figure 5.3). Thus, detailed lifetime measurement along with the bathochromic shift in emission maxima assigns a slipped J-type organization of the chromophores. Emissive slipped J-type self-assembly of the homopolymer facilitated its visualization using structured illumination microscopy (SIM),
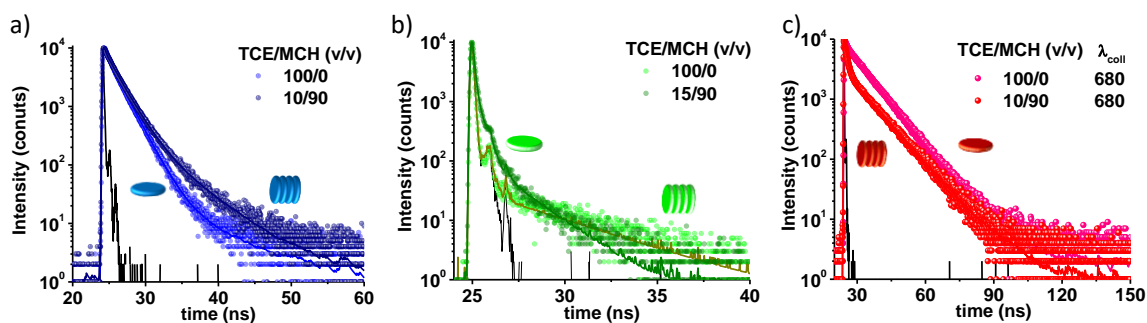
Figure 5.3. Lifetime decay profile of a) **FF-NDI-OEt** ($\lambda_{ex} = 442$ nm, $\lambda_{coll} = 510$ nm), b) **FF-NDI-SEt** ($\lambda_{ex} = 530$ nm, $\lambda_{coll} = 570$ nm) and c) **FF-NDI-NiPA** ($\lambda_{ex} = 634$ nm, $\lambda_{coll} = 680$ nm) in monomeric state in TCE and in homopolymeric state in TCE/MCH solvent mixture. ([**FF-NDI-OEt**] = [**FF-NDI-SEt**] = [**FF-NDI-NiPA**] = 2.5×10^{-5} M).

TCE/MCH (v/v)	λ_{coll} (nm)	t_1 (ns)	t_2 (ns)	t_3 (ns)
100	500	1.78 (86.76 %)	8.13 (1.70 %)	0.4 (11.54 %)
10	500	1.98 (82.08 %)	5.84 (10.81 %)	0.4 (9.73 %)

Table 5.1. Comparison of lifetime data ($\lambda_{ex} = 442$ nm) of homopolymeric **FF-NDI-OEt** in TCE/MCH, 10/90 (v/v) and monomeric **FF-NDI-OEt** in TCE. ([**FF-NDI-OEt**] = 2.5×10^{-5} M).

TCE/MCH (v/v)	λ_{coll} (nm)	t_1 (ns)	t_2 (ns)	t_3 (ns)
100	560	3.63 (93.17 %)		0.1 (6.83 %)
15	560	1.92 (5.18 %)	0.02 (36.05 %)	0.2 (58.77 %)

Table 5.2. Comparison of lifetime data (λ_{ex} = 532 nm) of homopolymeric **FF-NDI-SEt** in TCE/MCH, 15/85 (v/v) and monomeric **FF-NDI-SEt** in TCE. ([**FF-NDI-SEt**] = 2.5×10^{-5} M).

TCE/MCH (v/v)	λ_{coll} (nm)	t_1 (ns)	t_2 (ns)	t_3 (ns)
100	680	0.5 (3.13 %)		9.18 (96.87 %)
10	680	1.04 (5.18 %)	10.08 (57.19 %)	

Table 5.3. Comparison of lifetime data (λ_{ex} = 632 nm) of homopolymeric **FF-NDI-NiPA** in TCE/MCH, 10/90 (v/v) and monomeric **FF-NDI-NiPA** in TCE. ([**FF-NDI-NiPA**] = 2.5×10^{-5} M).
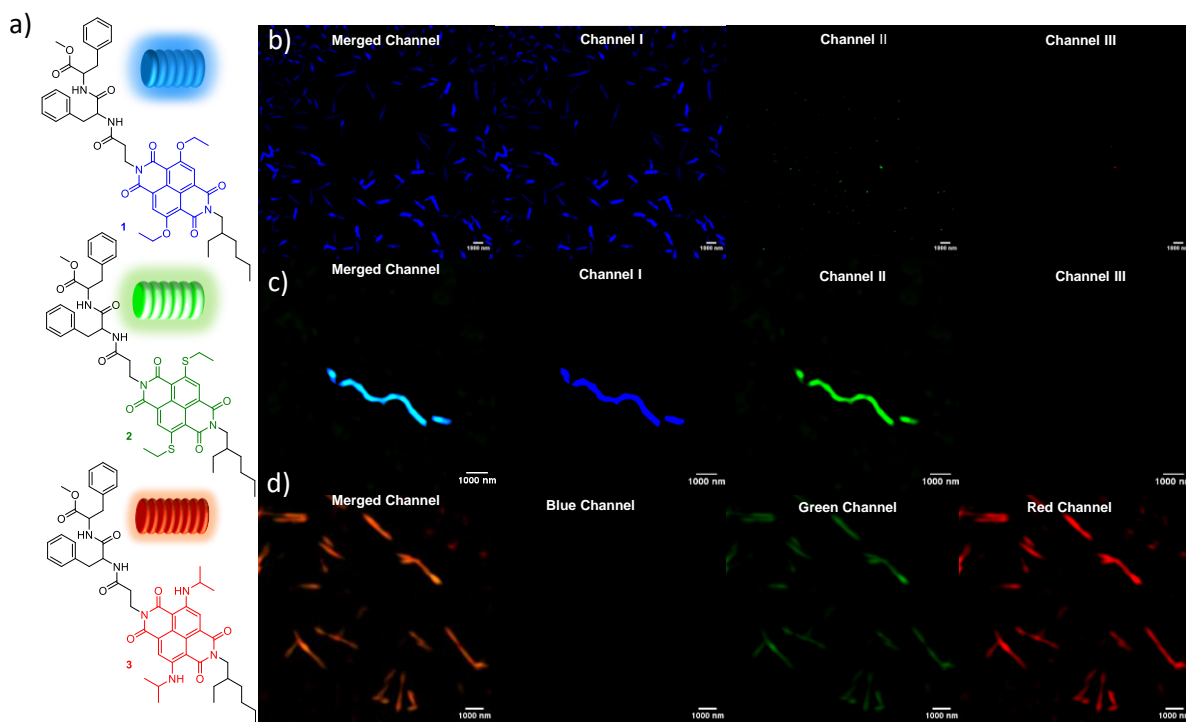
Figure 5.4. Selective excitation of **FF-NDI-OEt**, **FF-NDI-SEt** and **FF-NDI-NiPA** homopolymers for SIM imaging. a) Molecular structures of **FF-NDI-OEt**, **FF-NDI-SEt** and **FF-NDI-NiPA**. SIM images of b) self-assembled **FF-NDI-OEt** (TCE/MCH, 10/90 (v/v), [**FF-NDI-OEt**] = 2.5×10^{-5} M), c) self-assembled **FF-NDI-SEt** (TCE/MCH, 15/85 (v/v), [**FF-NDI-SEt**] = 2.5×10^{-5} M) and d) self-assembled **FF-NDI-NiPA** (TCE/MCH, 10/90 (v/v), [**FF-NDI-NiPA**] = 2.5×10^{-5} M) in channel I, channel II and channel III. (Channel I: λ_{ex} = 488 nm, λ_{coll} = 495-575; Channel II: λ_{ex} = 561 nm, λ_{coll} = 570-650; channel III: λ_{ex} = 642 nm, λ_{coll} = 655-800 nm).

which revealed the formation of one dimensional blue- (λ_{max} = 510 nm), green- (λ_{max} = 567 nm), and red-emitting (λ_{max} = 639 nm) supramolecular homopolymers for **FF-NDI-OEt**, **FF-NDI-SEt** and **FF-NDI-NiPA**, respectively (Figure 5.4). Distinct absorption and emission

spectra of stacked **FF-NDI-OEt**, **FF-NDI-SEt**, and **FF-NDI-NiPA** monomers (Figure 5.2) will enable the independent probing of monomers during the copolymerization process and the orthogonal visualization of the resultant supramolecular copolymers using SIM microscopy. For example, molecule **FF-NDI-OEt** gets excited at channel I and channel II, molecule **FF-NDI-SEt** gets excited only at channel II and III and molecule **FF-NDI-NiPA** gets excited exclusively at channel III, which will assist the visualization of supramolecular copolymers with different sequences (Figure 5.4).

5.4. Pathway Complexity of FF-NDI-OEt, FF-NDI-SEt and FF-NDI-NiPA:

Interestingly, addition of monomeric **FF-NDI-OEt**, **FF-NDI-NiPA** in TCE to MCH temporarily forms a metastable aggregate (TCE/MCH, 10/90 (v/v)) which after a lag time, transforms into thermodynamically equilibrated J-type homopolymeric state, which were characterized by absorption, emission, and CD spectra. Hence to investigate the pathway complexity of molecule **FF-NDI-OEt** and **FF-NDI-NiPA** we have investigated the transformation of metastable states of **FF-NDI-OEt** and **FF-NDI-NiPA** into thermodynamically stable J-aggregates by monitoring the absorbance and CD changes at 485 nm, and 360 nm for **FF-NDI-OEt**, and **FF-NDI-NiPA**, respectively. Probing of absorption and CD changes revealed, the transformation of metastable states to thermodynamically stable
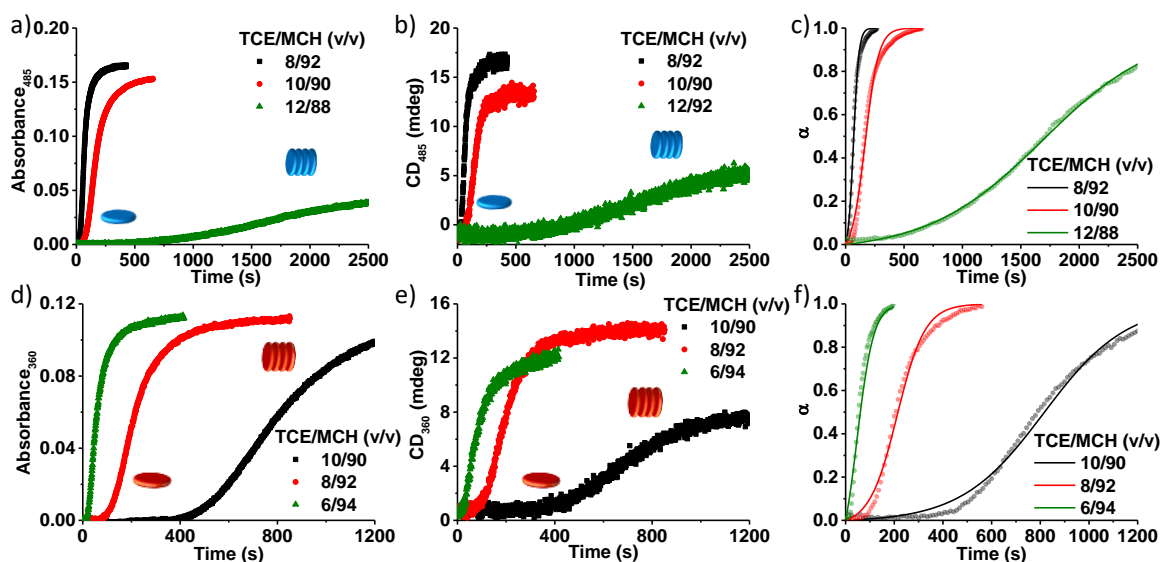
Figure 5.5. Time course of the supramolecular polymerization of metastable state into homopolymeric state of molecule **FF-NDI-OEt** and **FF-NDI-NiPA** monitored via a), d) Absorption, b), e) CD changes at 485 nm and 360 nm for **FF-NDI-OEt**, and **FF-NDI-NiPA**, respectively. c), f) Fitting of the kinetic data into Watzky-Finke model to extract the nucleation (k_{nu}) and elongation (k_e) rate constants. ([**FF-NDI-OEt**] = [**FF-NDI-NiPA**] = 2.5×10^{-5} M, l = 10 mm).

FF-NDI-OEt	TCE/MCH (v/v)	k_{nu} (s^{-1}) × 10^{-3}	k_e (M^{-1}s^{-1})	FF-NDI-NiPA	TCE/MCH (v/v)	k_{nu} (s^{-1}) × 10^{-3}	k_e (M^{-1}s^{-1})
	8	22	39		6	6	474
	10	9	328		8	0.4	343
	12	0.6	820		10	0.05	116

Table 5.4. Listed values of k_{nu} and k_e obtained using the kinetic data of Figure 5.5.

homopolymers after a lag time (80 seconds for **FF-NDI-OEt** and 476 seconds for **FF-NDI-NiPA**) and via non-linear sigmoidal transitions (Figure 5.5) which could be fitted using Watzky and Finke autocatalytic nucleation-elongation model (Table 5.4).[18]
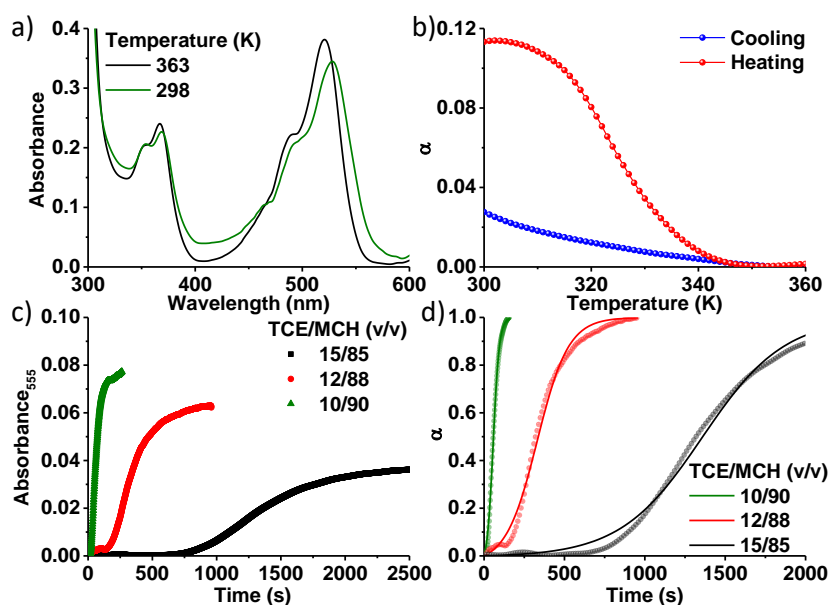
Figure 5.6. a) Temperature-dependent absorption spectra of molecule **FF-NDI-SEt** showing disassembly at 363 K. b) Temperature-dependent absorbance changes (cooling rate = heating rate = 1 K/min) monitored at 555 nm shows presence of hysteresis between heating and cooling curve suggesting self-assembly of molecule **FF-NDI-SEt** is under kinetic control ([**FF-NDI-SEt**] = 2.5×10^{-5} M, l = 10 mm, TCE/MCH, 15/85 (v/v)). c) Time course of the supramolecular polymerization of molecule **FF-NDI-SEt** after fast cooling from 363 K to 298 K (8 K/min cooling rate, monitored via absorption changes at 555 nm) showing formation of metastable state and its transformation into homopolymeric state. d) Fitting of time-dependent kinetic data of into Watzky-Finke nucleation-elongation model to extract the nucleation (k_{nu}) and elongation (k_e) rate constants. ([**FF-NDI-SEt**] = 1.5×10^{-5} M, l = 10 mm).

TCE/MCH (v/v)	k_{nu} (s^{-1}) $\times$ 10^{-3}	k_e (M^{-1}s^{-1})
10	20	750
12	2	199
15	0.19	78

Table 5.5. Listed values of k_{nu} and k_e obtained using the kinetic data of Figure 5.6d.

On the other hand, addition of monomeric **FF-NDI-SEt** in TCE to MCH (TCE/MCH, 10/90 (v/v), [**FF-NDI-SEt**] = 1.5×10^{-5} M) resulted in an instantaneous polymerization. However, when a monomeric solution at 363 K was cooled at 1K/min cooling rate to 298 K no polymerization was observed (Figure 5.6a). On heating the self-assembled solution (1 K/min heating rate) a large hysteresis (ΔT = 40 K) was observed between heating and cooling process (Figure 5.6b). This suggests the metastable state in case of **FF-NDI-SEt** can be accessed using fast cooling of a monomeric solution at high temperature. Indeed, a fast cooled solution (8 K/min cooling rate) of **FF-NDI-SEt** depicted formation of metastable state which then converts
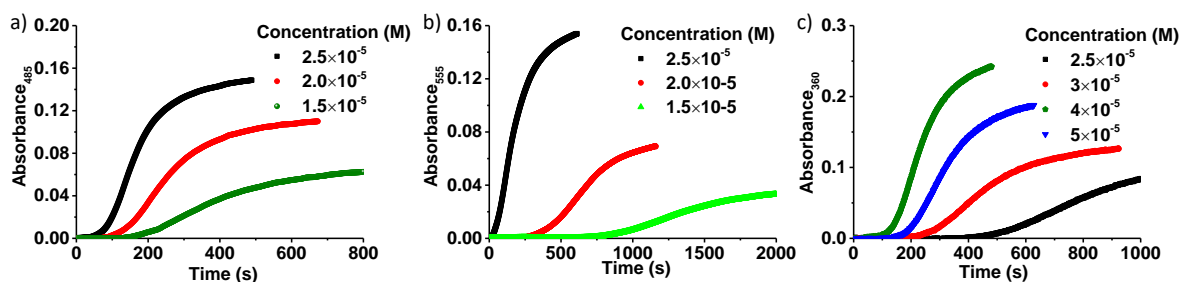
Figure 5.7. Concentration-dependent time course of supramolecular polymerization of metastable a) **FF-NDI-OEt** (10/90, TCE/MCH (v/v)), b) **FF-NDI-SEt** (TCE/MCH, 15/85 (v/v)) and c) **FF-NDI-NiPA** (TCE/MCH, 10/90 (v/v)) into thermodynamically stable homopolymeric state obtained by monitoring the absorption changes at 485 nm for **FF-NDI-OEt**, 555 nm for **FF-NDI-SEt** and 360 nm for **FF-NDI-NiPA**. (l = 10 mm).

into thermodynamically stable state via two-step non-linear sigmoidal transitions (Figure 5.6c) with a lag time of 20 seconds. Obtained kinetic data fits well with Whatzkey Finkey autocatalytic model, suggesting the transformation of metastable state to thermodynamically stable aggregated state takes place using nucleation-elongation assembly (Figure 5.6d, and Table 5.5). The observed pathway complexity and time-dependent nucleation-elongation growth mechanism is consistent with the usage of diphenylalanine self-assembling peptide moiety which is identified as one of the major components responsible for amyloid fibril formation for proteins via a nucleation-elongation mechanism.[19]

A decrease in lag time (t_{lag}) with an increase in concentration for monomers **FF-NDI-OEt**, **FF-NDI-SEt** and **FF-NDI-NiPA** assigned the metastable aggregates as an on-pathway aggregates *en route* transformation into the thermodynamically stable self-assembled state

(Figure 5.7). Molecule **FF-NDI-OEt**, **FF-NDI-SEt**, and **FF-NDI-NiPA** showed pathway complexity and kinetically controlled nucleation-elongation assembly in slightly different but overlapped solvent composition range (TCE/MCH, 6/94 (v/v) to TCE/MCH, 12/88 (v/v) for **FF-NDI-OEt**, TCE/MCH, 10/90 (v/v) to TCE/MCH, 15/85 (v/v) for molecule **FF-NDI-SEt**, and TCE/MCH, 6/94 (v/v) to TCE/MCH, 10/90 (v/v) for molecule **FF-NDI-NiPA**). Hence the solvent composition and concentration of molecule **FF-NDI-OEt**, **FF-NDI-SEt**, and **FF-NDI-NiPA** was appropriately chosen to move along the energy landscape and prior to the seeding studies.

5.5. Kinetically Controlled Two Component Supramolecular Block copolymers:
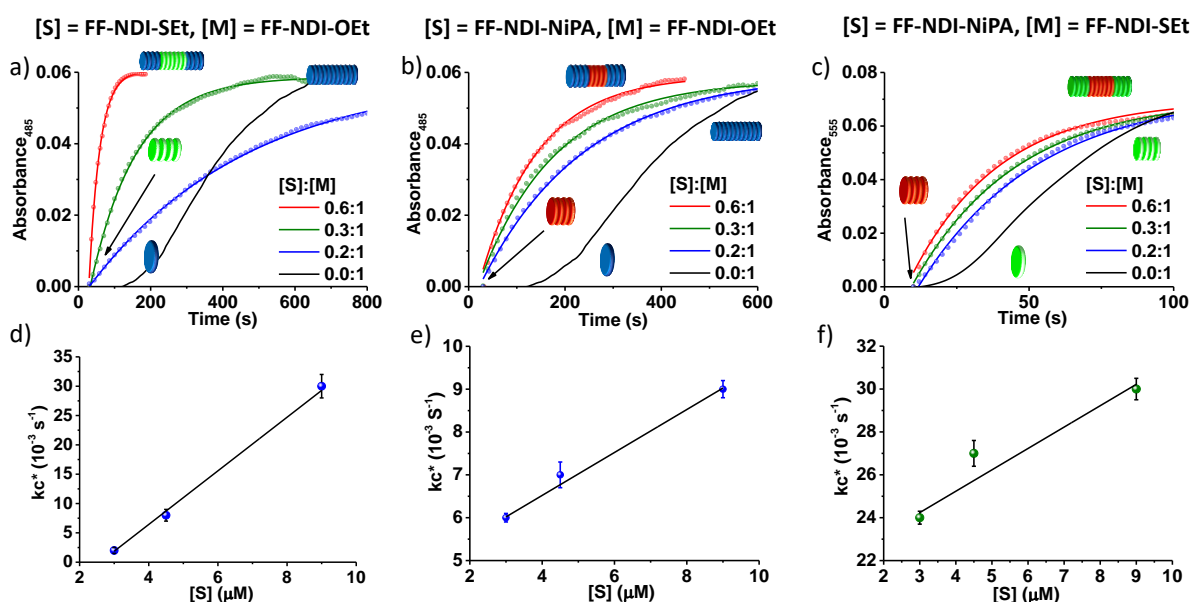
Figure 5.8. Time course of supramolecular polymerization of a) metastable **FF-NDI-OEt** initiated by addition of **FF-NDI-SEt$_{seed}$** under the condition of [**FF-NDI-diSEt**]:[**FF-NDI-OEt**] = 0.6:1, 0.3:1, 0.2:1 at constant [**FF-NDI-OEt**] = 1.5×10^{-5} M, b) metastable **FF-NDI-OEt** initiated by addition of **FF-NDI-NiPA$_{seed}$** under the condition of [**FF-NDI-NiPA**]:[**FF-NDI-OEt**] = 0.6:1, 0.3:1, 0.2:1 at constant [**FF-NDI-OEt**] = 1.5×10^{-5} M and c) metastable **FF-NDI-SEt** initiated by addition of **FF-NDI-NiPA$_{seed}$** under the condition of [**FF-NDI-NiPA**]:[**FF-NDI-SEt**] = 0.6:1, 0.3:1, 0.2:1 at constant [**FF-NDI-SEt**] = 1.5×10^{-5} M. Plots of kc* as a function of concentration of seed concentration corresponding to d) Figure 5.8a, e) Figure 5.8b, and f) Figure 5.8c shows a linear relationship which suggests the time course of the supramolecular polymerization could be controlled by changing the amount of seed added. (TCE/MCH, 10/90 (v/v)).

Synthesis of a tricomponent supramolecular block copolymer under kinetic control requires three molecules which can undergo seeded supramolecular polymerization with each other. Hence, we have first investigated the synthesis of two component supramolecular block copolymer between **FF-NDI-SEt$_{seed}$-FF-NDI-OEt$_{monomer}$**, **FF-NDI-NiPA$_{seed}$-FF-NDI-**

SEt_{monomer}, and **FF-NDI-NiPA**_{seed}-**FF-NDI-OEt**_{monomer} in same solvent composition (TCE/MCH, 10/90 (v/v)). Seed solutions of **FF-NDI-SEt** and **FF-NDI-NiPA** were prepared by sonicating respective kinetically grown self-assembled solutions (10^{-4} M) for 5 minutes as described in experimental section (TCE/MCH, 10/90, (v/v)). Seeds solution were added to the metastable states of the required monomer and the time progress of the growth was followed using absorbance changes (485 nm for **FF-NDI-OEt**, 555 nm for **FF-NDI-SEt**, and 360 nm for **FF-NDI-NiPA**). The addition of **FF-NDI-SEt**_{seed} within the lag phase of metastable state of **FF-NDI-OEt** ([**FF-NDI-SEt**]:[**FF-NDI-OEt**] = 0.6:1, [**FF-NDI-OEt**] = 1.5×10^{-5} M, TCE/MCH, 10/90 (v/v)) induces an instantaneous transformation of metastable **FF-NDI-OEt** into the thermodynamically stable aggregates with a much lower time ($t_{1/2}$ = 50 seconds for seeded assembly compared to $t_{1/2}$ = 386 seconds for unseeded assembly) and faster rate compared to the independent nucleation-elongation polymerization of **FF-NDI-OEt** (Figure 5.8a). An increase in **FF-NDI-SEt**_{seed} concentration leads to an accelerated transformation of metastable **FF-NDI-OEt**, into thermodynamically stable aggregated state of **FF-NDI-OEt** (Figure 5.8a). The kinetics of polymerization were analysed using the model proposed by Zhao and Moore where the experimental data was very well fitted with the equation to obtain the values of kc* (c* is the concentration of added seed termini and k is the polymerization rate constant).[18b] The value of kc* showed an increase with increase in seed concentration (Figure 5.8d). These features refer to the seeded supramolecular polymerization between **FF-NDI-OEt** and **FF-NDI-SEt**. Similar experimental results were obtained when **FF-NDI-NiPA** was used as a seed and **FF-NDI-OEt** and **FF-NDI-SEt** were used as monomers ((([**FF-NDI-NiPA**]:[**FF-NDI-OEt**] = 1:0.6, [**FF-NDI-OEt**] = 1.5×10^{-5} M, TCE/MCH, 10/90 (v/v)) and ([**FF-NDI-NiPA**]:[**FF-NDI-SEt**] = 1:0.6, [**FF-NDI-SEt**] = 1.5×10^{-5} M, TCE/MCH, 10/90 (v/v))) (Figures 5.8b, 5.8c, 5.8e and 5.8f). All these observations corroborate to the formation of two component supramolecular block copolymers between **FF-NDI-SEt**_{seed}-**FF-NDI-OEt**, **FF-NDI-NiPA**_{seed}-**FF-NDI-OEt** and **FF-NDI-NiPA**_{seed}-**FF-NDI-SEt,** respectively.

Absorption spectra of the resultant block copolymers shows that individual aggregation characteristics of the monomers are retained (Figures 5.9a, 5.9b and 5.9c). However, the CD spectra of the **FF-NDI-OEt**- **FF-NDI-SEt**_{seed}, **FF-NDI-NiPA**_{seed}- **FF-NDI-OEt** and **FF-NDI-NiPA**_{seed}- **FF-NDI-SEt** block structures showed shift in the CD maxima at the n-π* absorption band (Figures 5.9d, 5.9e and 5.9f). We attribute this CD spectral changes to the change in arrangement on the synthesis of block structure compared to its homopolymer.
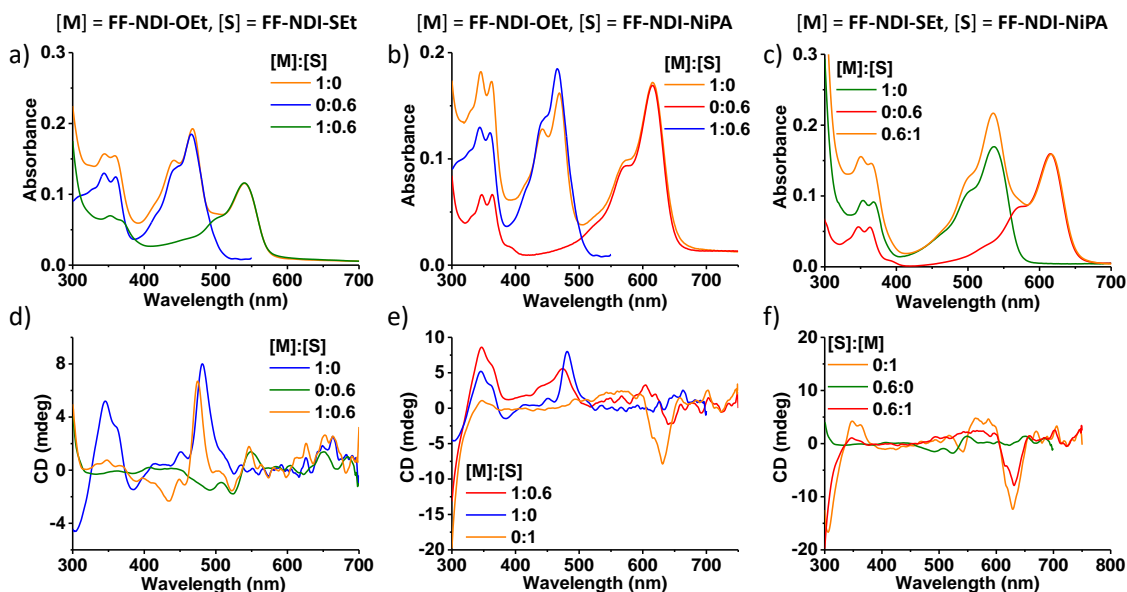
Figure 5.9. Comparison of absorption spectra of the two component block copolymers of a) **FF-NDI-OEt_monomer**-**FF-NDI-SEt_seed,** b) **FF-NDI-OEt_monomer**-**FF-NDI-NiPA_seed,** and c) **FF-NDI-SEt_monomer**-**FF-NDI-NiPA_seed** with corresponding individual homopolymer absorption spectra. Comparison of CD spectra of the two component block copolymer of d) **FF-NDI-OEt_monomer**-**FF-NDI-SEt_seed,** e) **FF-NDI-OEt_monomer**-**FF-NDI-NiPA_seed,** f) **FF-NDI-SEt_monomer**-**FF-NDI-NiPA_seed** with individual homopolymer CD spectra. ([**FF-NDI-OEt**] = [**FF-NDI-SEt**] = 1.5×10^{-5} M, TCE/MCH, 10/90 (v/v)).
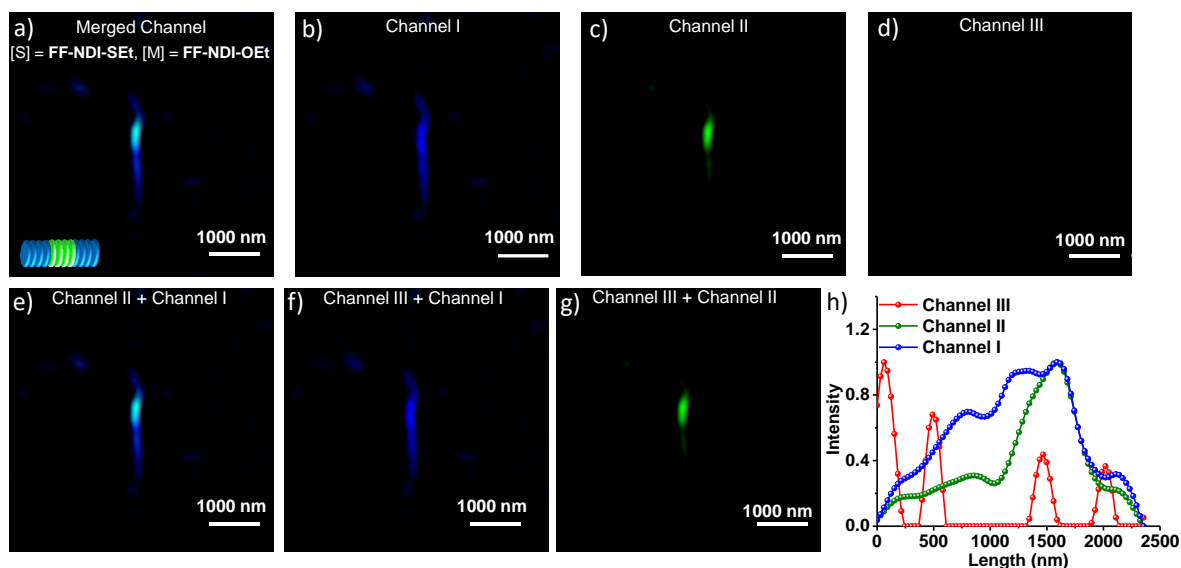
Figure 5.10. Visualization of supramolecular block copolymer between **FF-NDI-OEt_monomer** and **FF-NDI-SEt_seed** ([**FF-NDI-OEt**]:[**FF-NDI-SEt**] ratio of 1:0.6). SIM images of a) merged channel, b) channel I, c) channel II and d) channel III showing the formation of the supramolecular block copolymer. SIM image of the synthesized supramolecular block copolymer on e) channel II + channel I, f) channel I + channel III and g) channel III + channel II. h) Corresponding intensity profile of the supramolecular block copolymer in three channels. ([**FF-NDI-OEt**] = 1.5×10^{-5} M, TCE/MCH, 10/90 (v/v), Channel I: λ_{ex} = 488 nm, λ_{coll} = 495-575; Channel II: λ_{ex} = 561 nm, λ_{coll} = 570-650; channel III: λ_{ex} = 642 nm, λ_{coll} = 655-800 nm).
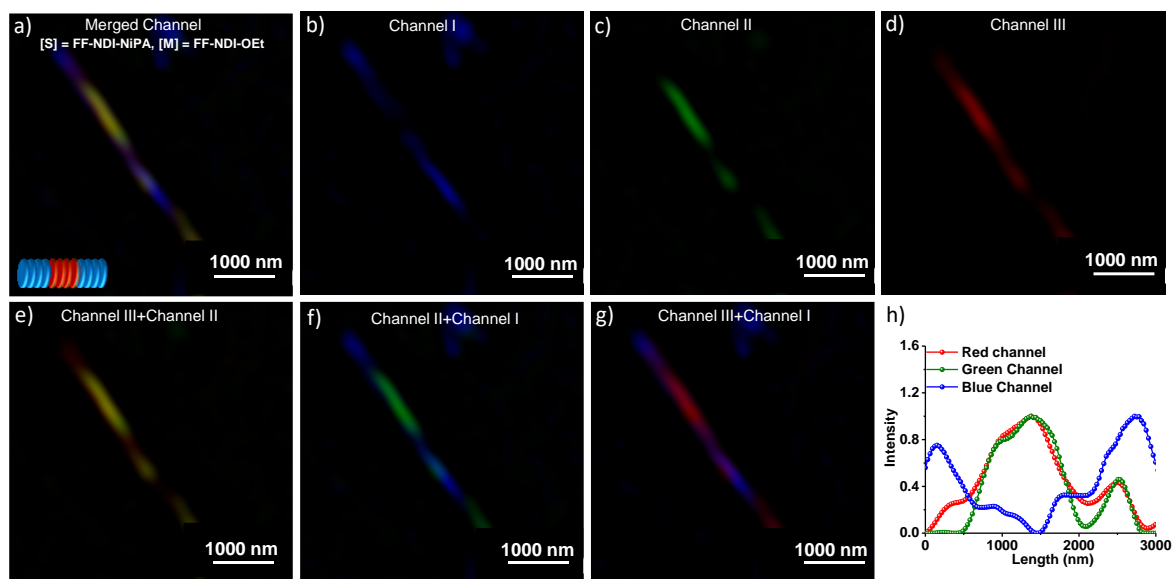
Figure 5.11. Visualization of supramolecular block copolymer between **FF-NDI-OEt_monomer** and **FF-NDI-NiPA_seed** ([M]:[S] ratio of 1:0.6). SIM images of a) merged channel, b) channel I, c) channel II, and d) channel III showing the formation of the supramolecular block copolymer. SIM image of the synthesized supramolecular block copolymer on e) merged channel II and channel II, f) merged channel I and channel II and g) merged channel III and channel I channel. h) Intensity profile of the supramolecular block copolymer in there channels ([**FF-NDI-OEt**] = 1.5×10^{-5} M, TCE/MCH, 10/90 (v/v)) (Channel I: λ_{ex} = 488 nm, λ_{coll} = 495-575; Channel II: λ_{ex} = 561 nm, λ_{coll} = 570-650; channel III: λ_{ex} = 642 nm, λ_{coll} = 655-800 nm).
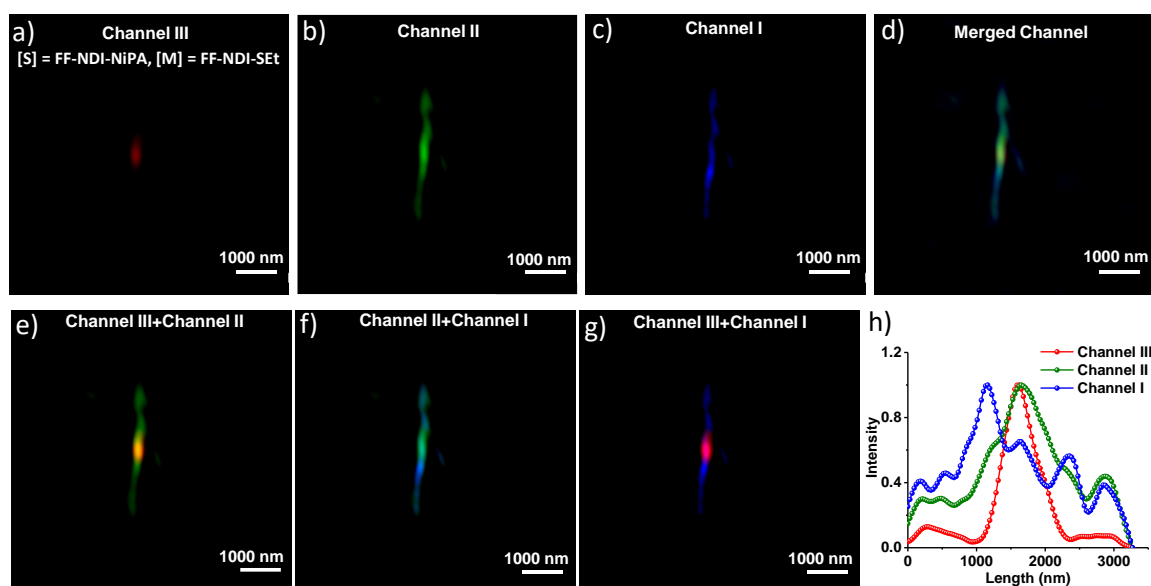
Figure 5.12. Visualization of supramolecular block copolymer between **FF-NDI-SEt_monomer** and **FF-NDI-NiPA_seed** ([**FF-NDI-SEt**]_monomer:[**FF-NDI-NiPA**]_seed ratio of 1:0.6). SIM images of a) channel III, b) channel II, c) channel I, and d) merged channel showing the formation of the supramolecular block copolymer. SIM image of the synthesized supramolecular block copolymer on e) merged channel II and channel III, f) merged channel I and channel II and g) merged channel III and channel I. h) Intensity profile of the block copolymer in there channels. ([**FF-NDI-OEt**] = [**FF-NDI-NiPA**] = 2.5×10^{-5} M, TCE/MCH, 10/90 (v/v), Channel I: λ_{ex} = 488 nm, λ_{coll} = 495-575; Channel II: λ_{ex} = 561 nm, λ_{coll} = 570-650; channel III: λ_{ex} = 642 nm, λ_{coll} = 655-800 nm).

175

We further visualized the coassembled polymers by merging the channel I, channel II and channel III in SIM images. The synthesized block copolymers of **FF-NDI-OEt**- **FF-NDI-SEt** shows connected segments of a green-emitting domain and blue-emitting domain due to differential excitation in channel I and channel II (Figure 5.10). Likewise, the two component block copolymers between **FF-NDI-NiPA**$_{seed}$- **FF-NDI-OEt** and **FF-NDI-NiPA**$_{seed}$- **FF-NDI-SEt** depicted connected segments of red- and blue-emitting domains (channel III and channel I) and connected segments of yellow and green-emitting domains (channel II and channel III) ,respectively (Figures 5.11 and 5.12).

5.6. Kinetically Controlled Tricomponent Block Copolymers:

Mutual seeded supramolecular polymerization between **FF-NDI-OEt**, **FF-NDI-SEt**, and **FF-NDI-NiPA** monomers encouraged us to explore the possibility of synthesis of tricomponent supramolecular block copolymers using the sequential addition of monomers. Hence, we have first synthesized supramolecular two component copolymer between **FF-NDI-NiPA**$_{seed}$ and **FF-NDI-SEt**$_{monomer}$ employing two component seeded supramolecular polymerization ([**FF-NDI-SEt**]:[**FF-NDI-NiPA**] = 1:0.6, [**FF-NDI-SEt**] = 1.5×10^{-5} M, TCE/MCH, 10/90 (v/v)) (Figures 5.13a and 5.13b). Next, to prepare the tricomponent block copolymer, we have added monomer **FF-NDI-OEt** in TCE into the two component block copolymer solution ([**FF-NDI-SEt**]:[**FF-NDI-NiPA**]:[**FF-NDI-OEt**] = 0.6:1:1, [**FF-NDI-SEt**] = 1.5×10^{-5} M, TCE/MCH, 10/90) and probed the time course of the polymerization using absorbance changes at 485 nm (Figures 5.13a and 5.13c). The addition of monomer **FF-NDI-OEt** into the two component block copolymer induces an instant transformation of metastable **FF-NDI-OEt** into the thermodynamically stable aggregates with a faster rate ($t_{1/2}$ = 36 seconds in presence of two component and $t_{1/2}$ = 354 seconds in absence of seed) and reduced time of polymerization compared to the independent nucleation-elongation polymerization of **FF-NDI-OEt**. This indicates that the incoming monomers of **FF-NDI-OEt** nucleate and grow at the active ends of two component copolymer leading to a tricomponent supramolecular block copolymer (**FF-NDI-NiPA:FF-NDI-SEt:FF-NDI-OEt**). Absorption spectra of the tricomponent copolymer resemble individual self-assembly characteristics, which implies the presence of long homopolymeric domains of molecule **FF-NDI-OEt**, **FF-NDI-SEt**, and **FF-NDI-NiPA** (Figure 5.14a). CD spectra of the coassembled block copolymer depicted substantial differences in the CD spectra of molecule **FF-NDI-SEt** and in π-π* absorption band (Figure 5.14b). We conjectured these changes take place due to the different packing of the copolymer compared to the pure homopolymers. Finally, the fluorescent nature of the core-substituted NDIs

facilitated visualization of the tricomponent block copolymer under SIM microscope (Figure 5.15). The tricomponent supramolecular block copolymer was visualized by merging channel I, channel II and channel III SIM images, which showed a spatial correlation of red-emitting fiber terminating with green-emitting fiber at the two sides followed by the presence of blue-emitting fiber at the end. The visualized tricomponent block copolymer corroborates well with the sequential assembly probed spectroscopically having molecule **FF-NDI-NiPA** as seed followed by sequential polymerization of green (**FF-NDI-SEt**) and blue monomer (**FF-NDI-OEt**).
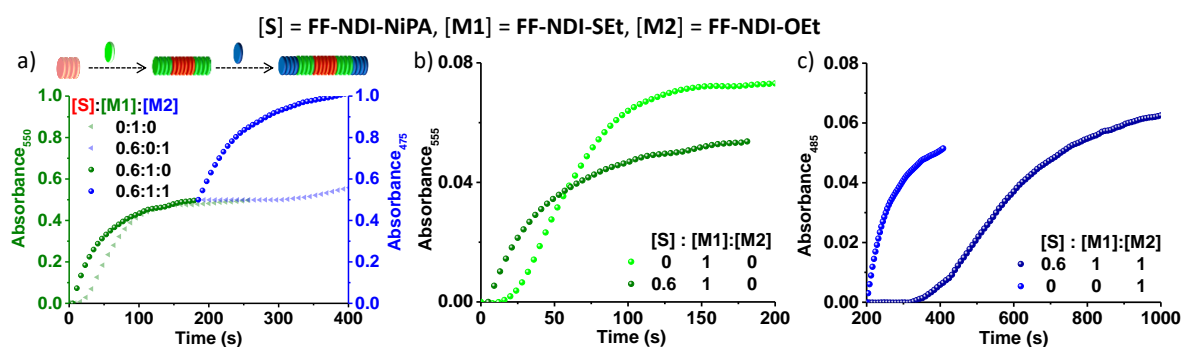
Figure 5.13. Time course of supramolecular polymerization on sequential addition of a) **FF-NDI-SEt**$_{monomer}$ and **FF-NDI-OEt**$_{monomer}$ on **FF-NDI-NiPA**$_{seed}$. Corresponding zoomed in plots of b) **FF-NDI-SEt**$_{monomer}$ addition onto **FF-NDI-NiPA**$_{seed}$ (obtained by following absorbance changes at 555 nm) and c) **FF-NDI-OEt**$_{monomer}$ addition onto **FF-NDI-NiPA**- **FF-NDI-SEt** two component block copolymer (obtained by absorbance changes at 485 nm). (TCE/MCH, 10/90 (v/v), [**FF-NDI-OEt**$_{monomer}$] = [**FF-NDI-SEt**$_{monomer}$] = 1.5×10^{-5} M).
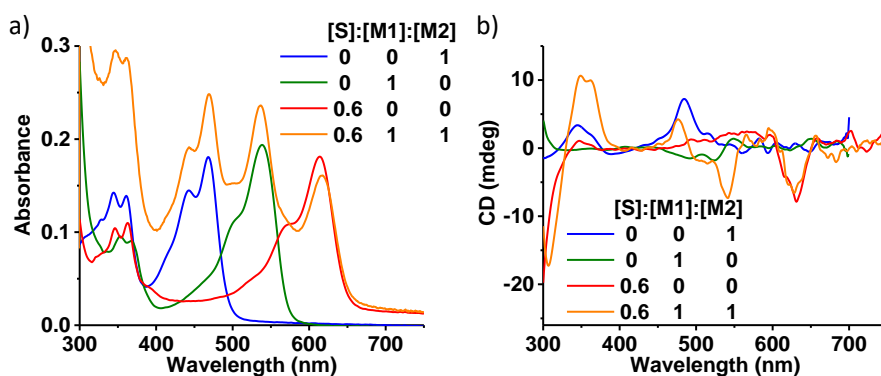
Figure 5.14. a) Absorption spectra of the tricomponent block copolymer and its comparison with individual homopolymer absorption spectra. b) CD spectra of the synthesized tricomponent block copolymer and its comparison with individual homopolymer CD spectra. (TCE/MCH, 10/90 (v/v), [**FF-NDI-OEt**$_{monomer}$] = [**FF-NDI-SEt**$_{monomer}$] = 1.5×10^{-5} M).
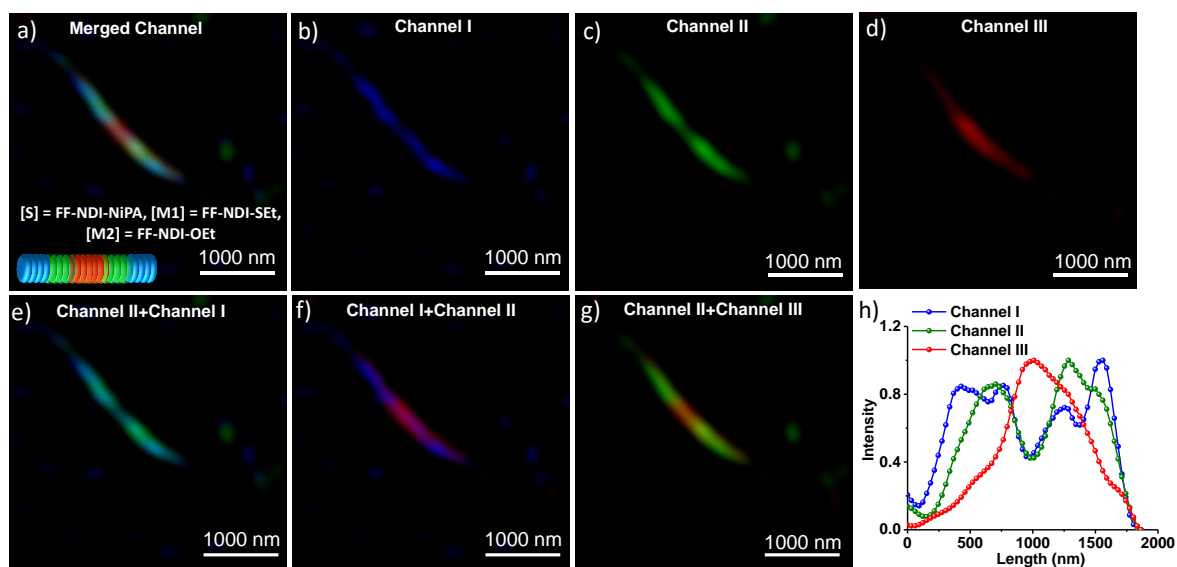
Figure 5.15. SIM microscopy image of the synthesized tricomponent block copolymer of **FF-NDI-NiPA$_{seed}$- FF-NDI-SEt- FF-NDI-OEt** in a) merged channel, b) channel I, c) channel II, d) channel III showing presence of connected segments of red-green- and blue-emitting domains respectively. Corresponding SIM images in e) channel II + channel I showing connected green and blue segments, f) channel II + channel I channel showing connected red and blue segments and g) channel III + channel II showing connected green and red segments. h) Corresponding intensity profile of the merged image in three channels. (TCE/MCH, 10/90 (v/v) [**FF-NDI-OEt$_{monomer}$**] = [**FF-NDI-SEt$_{monomer}$**] = 1.5×10^{-5} M, Channel I: λ_{ex} = 488 nm, λ_{coll} = 495-575; Channel II: λ_{ex} = 561 nm, λ_{coll} = 570-650; channel III: λ_{ex} = 642 nm, λ_{coll} = 655-800 nm).
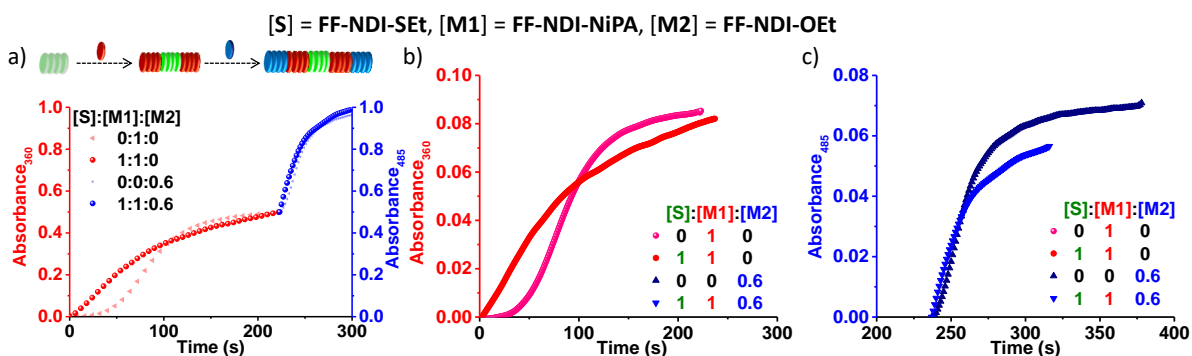
Figure 5.16. Time course of supramolecular polymerization on sequential addition of a) **FF-NDI-NiPA$_{monomer}$** and **FF-NDI-OEt$_{monomer}$** onto **FF-NDI-SEt$_{seed}$**. Corresponding zoomed in plot of b) **FF-NDI-NiPA$_{monomer}$** addition onto **FF-NDI-SEt$_{seed}$** (obtained by following the absorbance changes at 360 nm) and c) **FF-NDI-OEt$_{monomer}$** addition onto **FF-NDI-NiPA**-**FF-NDI-SEt** two component block copolymer (obtained by following the absorbance changes at 485 nm). (TCE/MCH, 6/94 (v/v), [**FF-NDI-NiPA$_{monomer}$**] = 2.5×10^{-5} M, [**FF-NDI-OEt$_{monomer}$**] = 1.5×10^{-5} M).
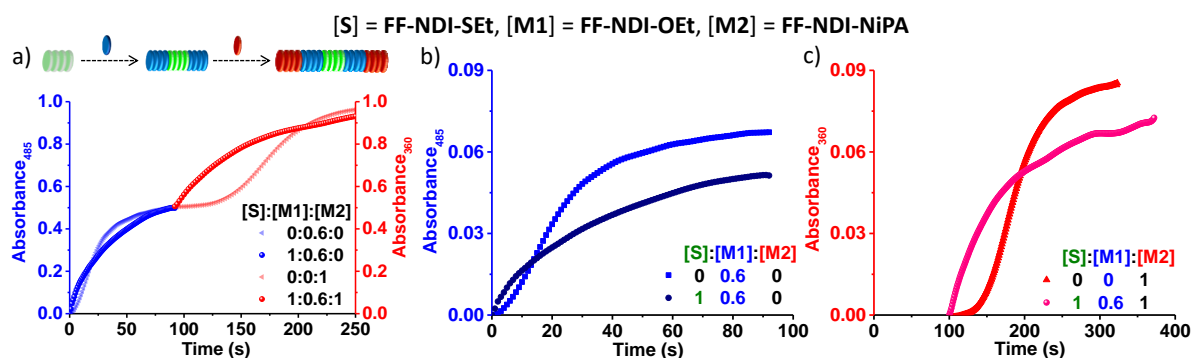
Figure 5.17. a) Time course of supramolecular polymerization on sequential addition of **FF-NDI-OEt**monomer and **FF-NDI-NiPA**monomer onto **FF-NDI-SEt**seed. Corresponding zoomed in plot of b) **FF-NDI-OEt**monomer addition onto **FF-NDI-SEt**seed (obtained by monitoring the absorbance changes at 485 nm) and c) **FF-NDI-NiPA**monomer addition onto **FF-NDI-SEt**-**FF-NDI-OEt** two component block copolymer (obtained by monitoring the absorbance changes at 360 nm). (TCE/MCH, 6/94 (v/v), [**FF-NDI-NiPA**monomer] = 2.5×10^{-5} M, [**FF-NDI-OEt**monomer] = 1.5×10^{-5} M).

The mutual seeding capability of the three monomers encouraged us to explore the possibility of synthesis of other tricomponent sequences. To do so, we have prepared supramolecular two component copolymer of **FF-NDI-SEt**seed- **FF-NDI-NiPA**monomer and **FF-NDI-SEt**seed- **FF-NDI-OEt**monomer. On addition of **FF-NDI-NiPA** and **FF-NDI-OEt** monomers on to the prepared seed of **FF-NDI-SEt** leads to a faster polymerization and without any lag phase, which was probed using absorbance changes at 360 and 485 nm, respectively (Figures 5.16a, 5.16b, 5.17a and 5.17b). Next, to synthesize tricomponent supramolecular block copolymer, we have introduced monomers of **FF-NDI-OEt** in **FF-NDI-SEt** - **FF-NDI-NiPA** two component copolymer and monomers of **FF-NDI-NiPA** in **FF-NDI-SEt** - **FF-NDI-OEt** two component copolymer seed (Figures 5.16c and 5.17c). The time progress of the polymerization was probed using absorbance changes at 485 nm for monomer **FF-NDI-OEt** and at 360 nm for monomer **FF-NDI-NiPA** respectively, which again depicted a characteristic of seed induced supramolecular polymerization (faster rate of polymerization without any lag phase). Absorption spectra of the tricomponent copolymer again retained self-assembly characteristics of the three molecules (Figures 5.18a and 5.19a). However, the CD spectra of the synthesized tricomponent block copolymers showed differences in component **FF-NDI-OEt** and **FF-NDI-NiPA** spectral region as observed during two component block copolymer formation (Figures 5.18b and 5.19b). The synthesize sequence of the tricomponent supramolecular block copolymer was visualized and characterized by merging channel I, channel II and channel III SIM images as a green-emitting fiber connected with red-emitting fiber at the two junction followed by blue-emitting fiber at the two termini for **FF-NDI-SEt**seed-

FF-NDI-NiPAmonomer- **FF-NDI-OEt**monomer sequence and cyan-emitting fiber terminating with blue-emitting fiber followed by red-emitting fiber at the two ends for **FF-NDI-SEt**seed- **FF-NDI-OEt**monomer- **FF-NDI-NiPA**monomer sequence (Figures 5.20 and 5.21).
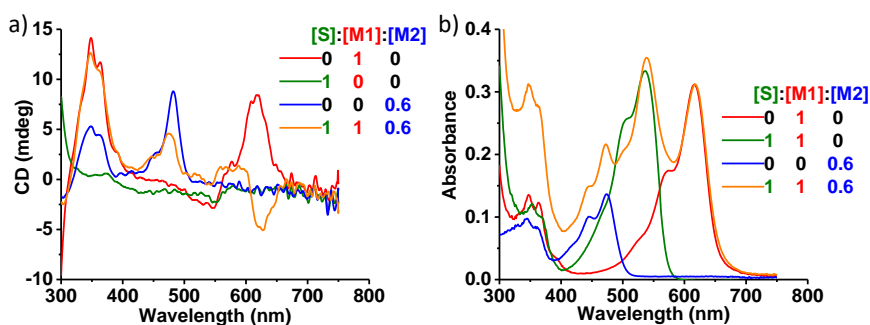
Figure 5.18. a) Absorption spectra of the tricomponent block copolymer of **FF-NDI-OEt**seed-**FF-NDI-NiPA**monomer-**FF-NDI-SEt**monomer and its comparison with individual homopolymers absorption spectra. b) CD spectra of the synthesized tricomponent block copolymer and its comparison with individual homopolymer CD spectra showing change in CD signal of n-π* absorption maxima of component **FF-NDI-NiPA** and **FF-NDI-OEt**. (TCE/MCH, 6/94 (v/v), [**FF-NDI-OEt**monomer] = 1.5×10^{-5} M, [**FF-NDI-NiPA**monomer] = 2.5×10^{-5} M).
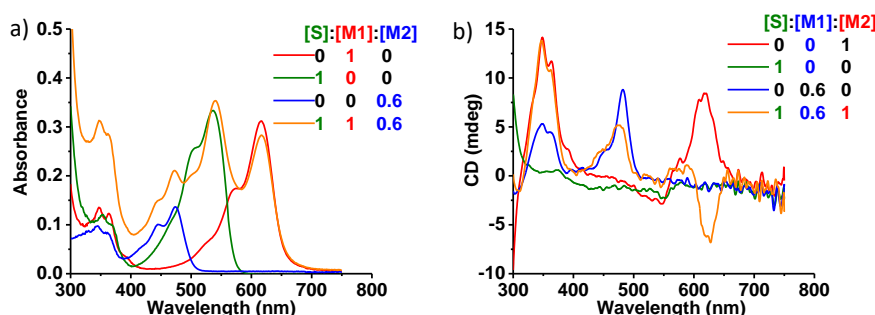
Figure 5.19. a) Absorption spectra of the tricomponent block copolymer of of **FF-NDI-SEt**seed- **FF-NDI-OEt** monomer- **FF-NDI-NiPA**monomer and its comparison with individual homopolymers absorption spectra. b) CD spectra of the synthesized tricomponent block copolymer and its comparison with individual homopolymer CD spectra showing change in CD signal of n-π* absorption maxima of component **FF-NDI-NiPA** and **FF-NDI-OEt**. (TCE/MCH, 6/94 (v/v), [**FF-NDI-OEt**monomer] = 1.5×10^{-5} M, [**FF-NDI-NiPA**monomer] = 2.5×10^{-5} M).
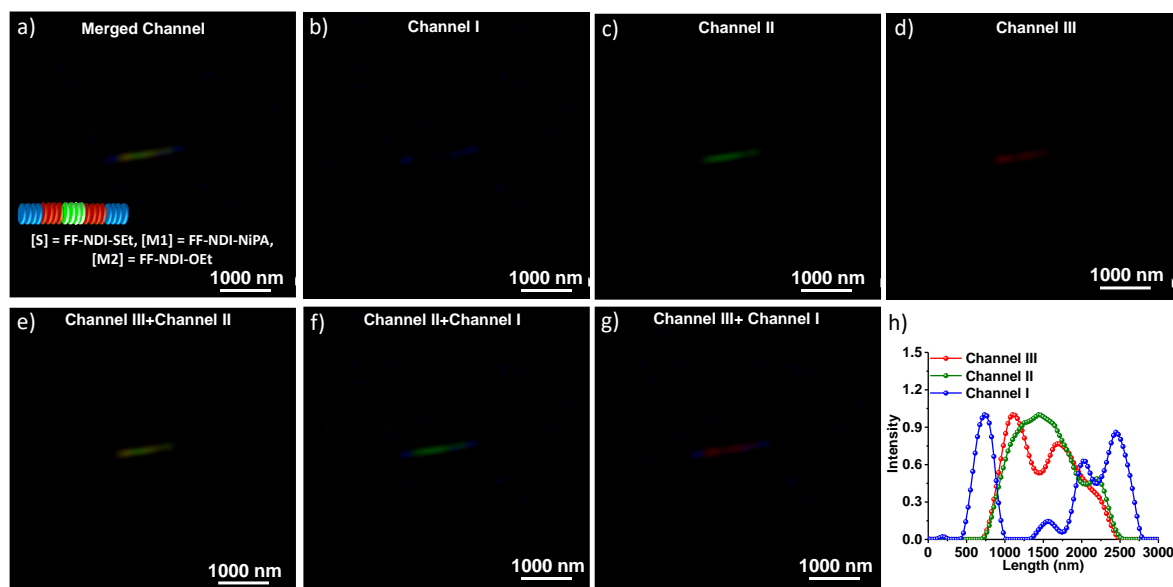
Figure 5.20. SIM microscopy image of the synthesized tricomponent block copolymer of **FF-NDI-NiPA**$_{seed}$- **FF-NDI-SEt- FF-NDI-OEt**, in a) merged channel, b) channel I, c) channel II, d) channel III showing presence of connected segments of green-red- and blue-emitting domains respectively. Corresponding SIM images in e) channel II + channel III, f) channel II + channel I and g) channel III + channel I. h) Corresponding intensity profile of the merged image. (TCE/MCH, 6/94 (v/v), [**FF-NDI-NiPA**$_{monomer}$] = [**FF-NDI-OEt**$_{monomer}$] = 1.5×10^{-5} M, Channel I: λ_{ex} = 488 nm, λ_{coll} = 495-575; Channel II: λ_{ex} = 561 nm, λ_{coll} = 570-650; channel III: λ_{ex} = 642 nm, λ_{coll} = 655-800 nm).

[S] = FF-NDI-SEt, [M1] = FF-NDI-OEt, [M2] = FF-NDI-NiPA
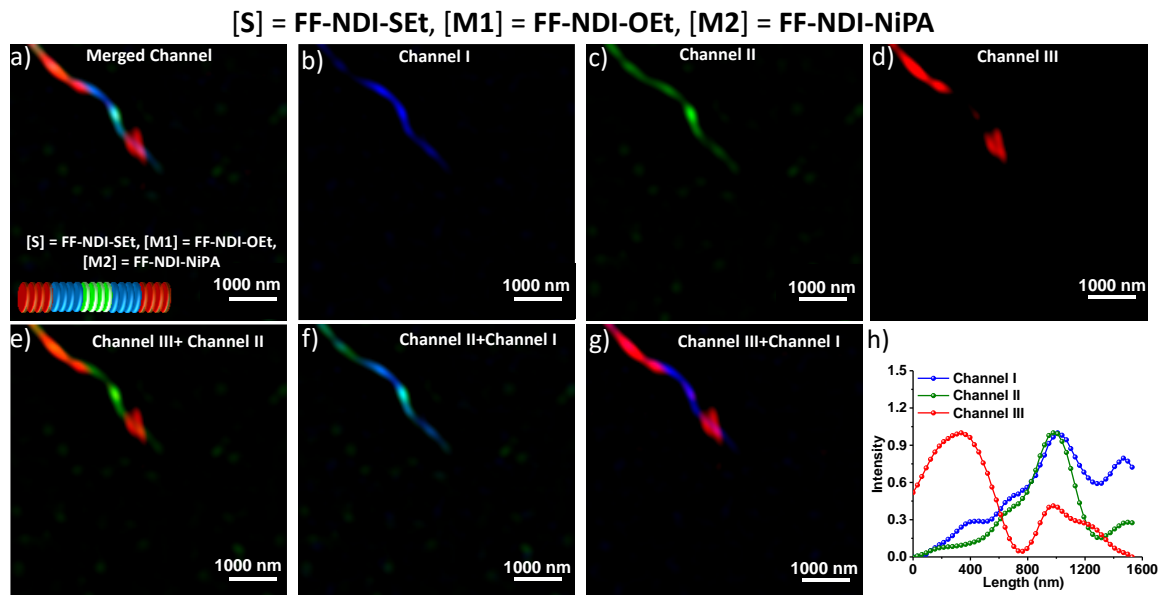
Figure 5.21. SIM microscopy image of the synthesized tricomponent block copolymer of **FF-NDI-SEt**$_{seed}$- **FF-NDI-OEt- FF-NDI-NiPA** in a) merged channel, b) channel I, c) channel II, d) channel III showing presence of connected segments of green-red- and blue-emitting domains respectively. Corresponding SIM images in e) channel II + channel III, f) channel II + channel I and g) channel III + channel I. h) Corresponding intensity profile collected from the merged channel. (TCE/MCH, 6/94 (v/v) [**FF-NDI-NiPA**$_{monomer}$] = 2.5×10^{-5} M, [**FF-NDI-OEt**$_{monomer}$] = 1.5×10^{-5} M, Channel I: λ_{ex} = 488 nm, λ_{coll} = 495-575; Channel II: λ_{ex} = 561 nm, λ_{coll} = 570-650; channel III: λ_{ex} = 642 nm, λ_{coll} = 655-800 nm).

5.7. Conclusion:

In conclusion, we have accomplished the synthesis of a tricomponent supramolecular block copolymer via sequential addition of distinct core-substituted naphthalene diimide π-conjugated monomers. We have utilized a self-assembling tripeptide motif containing diphenylalanine unit for hydrogen bonding driven cooperative supramolecular polymerization. All three monomers exhibited the presence of a metastable state *en route* thermodynamically stable supramolecular polymer. Hence, we could synthesize tricomponent supramolecular block copolymers via sequential addition of the three monomers via seeded supramolecular polymerization. By changing the sequence of addition of monomers, we were able to pursue the synthesis of three different sequences of the tricomponent supramolecular block copolymers. Further, the distinct optical properties of the core-substituted naphthalene diimide chromophores could be explored for the *in situ* spectroscopic probing of microstructure during sequential copolymerization of the three monomers. Further distinct blue, green, and red fluorescent of the three chromophores helped us to uniquely characterize the multicomponent structures by visualized under super-resolved structured illumination microscopy.

Synthesis of tricomponent supramolecular block copolymerization via sequential addition of monomer presented here is particularly exciting and mimic the block copolymer synthesis of covalent polymers using atom transfer radical polymerization, where sequential addition of monomers leads to more complex block copolymers. The strategy reported here certainly uplifts the synthesis of complex supramolecular block copolymer sequences. We plan to investigate the dispersity and length control of the block segments in near future, a feature which has been achieved in single component supramolecular polymers. Moving towards more complex structural systems, we plan to utilize stimuli-responsive (pH, redox, reaction driven) monomers for the synthesis of such complex sequences where we will be no longer dependent on the presence of pathway complexity and metastable state.

5.8. Experimental Section:

General Methods:

NMR Measurements: NMR spectra were recorded with a Bruker AVANCE 400 (400 MHz) and JEOL 600 MHZ NMR Fourier transform NMR spectrometer with chemical shifts reported in parts per million (ppm) with respect to TMS. Splitting patterns are designated as s, singlet; d, doublet; bs, broad singlet; m, multiplet; t, triplet; q, quartet; quin, quintet and br, broad.

Optical Measurements: Electronic absorption spectra were recorded on a Perkin Elmer Lambda 900 UV-Vis-NIR Spectrometer. Circular Dichroism (CD) spectra and temperature-

dependent CD spectra were recorded on a JASCO J-815 spectrometer where the sensitivity, time constant and scan rate were chosen appropriately. The temperature-dependent measurements were performed with a CDF-426S/15 Peltier-type temperature controller with a temperature range of 263-383 K and adjustable temperature slope. Emission spectra were recorded on Perkin Elmer LS 55 Luminescence Spectrometer. 10 mm x 10 mm or 10 mm x 2 mm quartz cuvettes were used for measurements at room temperature.

High-Resolution Mass Spectrometry (HRMS): High-Resolution Mass Spectra (HRMS) were recorded on an Agilent 6538 Ultra High Definition (UHD) Accurate-Mass Q-TOF-LC/MS system using electrospray ionization (ESI) and Atmospheric Pressure Chemical Ionization (APCI) modes.

Matrix-Assisted Laser Desorption Ionization (MALDI): MALDI was performed on a Bruker daltonics Autoflex Speed MALDI TOF System (GT0263G201) spectrometer using α-Cyano-4-hydroxy-cinnamic acid (CCA) as the matrix.

Fluorescent Lifetime Experiment: Time-resolved decay experiments were recorded on a Horiba Delta Flex time-correlated single-photon-counting (TCSPC) instrument. Nano-LEDs with a pulse repetition rate of 1 MHz was used as the light source. The instrument response function (IRF) was collected by using a scatterer (Ludox AS40 colloidal silica, Sigma-Aldrich). For the LED light source, the instrumental full width at half maximum including detector response was 0.2 ns. The excited state decay of the sample was collected by fixing the emission wavelength at a particular wavelength. The decay was fitted using IBH software (DAS6).

Structured Illumination Microscopy (SIM): Optical setup for imaging in Structured Illumination Microscopy (SIM) method: The fluorescence images of supramolecular polymers were acquired using an inverted Zeiss ELYRA PS1 microscope in structured illumination mode. Two lasers channel I - 488 nm (200 mW) (Green channel) and channel II - 561 nm (200 mW) (Red channel) have been used for respective excitation of 1 and 2 fluorophores. 10 % laser power from the objective top was used for structured illumination imaging. Imaging was performed using a Zeiss oil–immersion objective (Plan–apochromat 63x/1.40 Oil DIC M27, numerical aperture (NA) 1.40 oil). Fluorescence light was spectrally filtered with emission filters for channel I – MBS-488+EF BP 495-575/LP 750 for laser line 488 nm (blue channel) and for channel II – MBS-561+EF BP 570-650/LP 750 for laser line 561 nm (green channel) and for channel III – MBS-650+EF BP 655-800/LP 750 for laser line 650 nm (red channel) and imaged using a PCO edge sCMOS camera (quantum yield > 70 %). Structured illumination images were processed using structured illumination analysis package for Zen software (Zeiss).

Additional software have been used for colour adjustment (ImageJ). The channels were merged to investigate the spatial correlation between blue, green and red-emitting fibers.

5.9. Synthetic Schemes and Procedures:

The synthesis of **FF-NDI-OEt**, **FF-NDI-SEt** and **FF-NDI-NiPA** are shown in Scheme 5.1 to 5.6.

Materials: All chemicals were purchased from commercial suppliers and were used directly without any further purification.
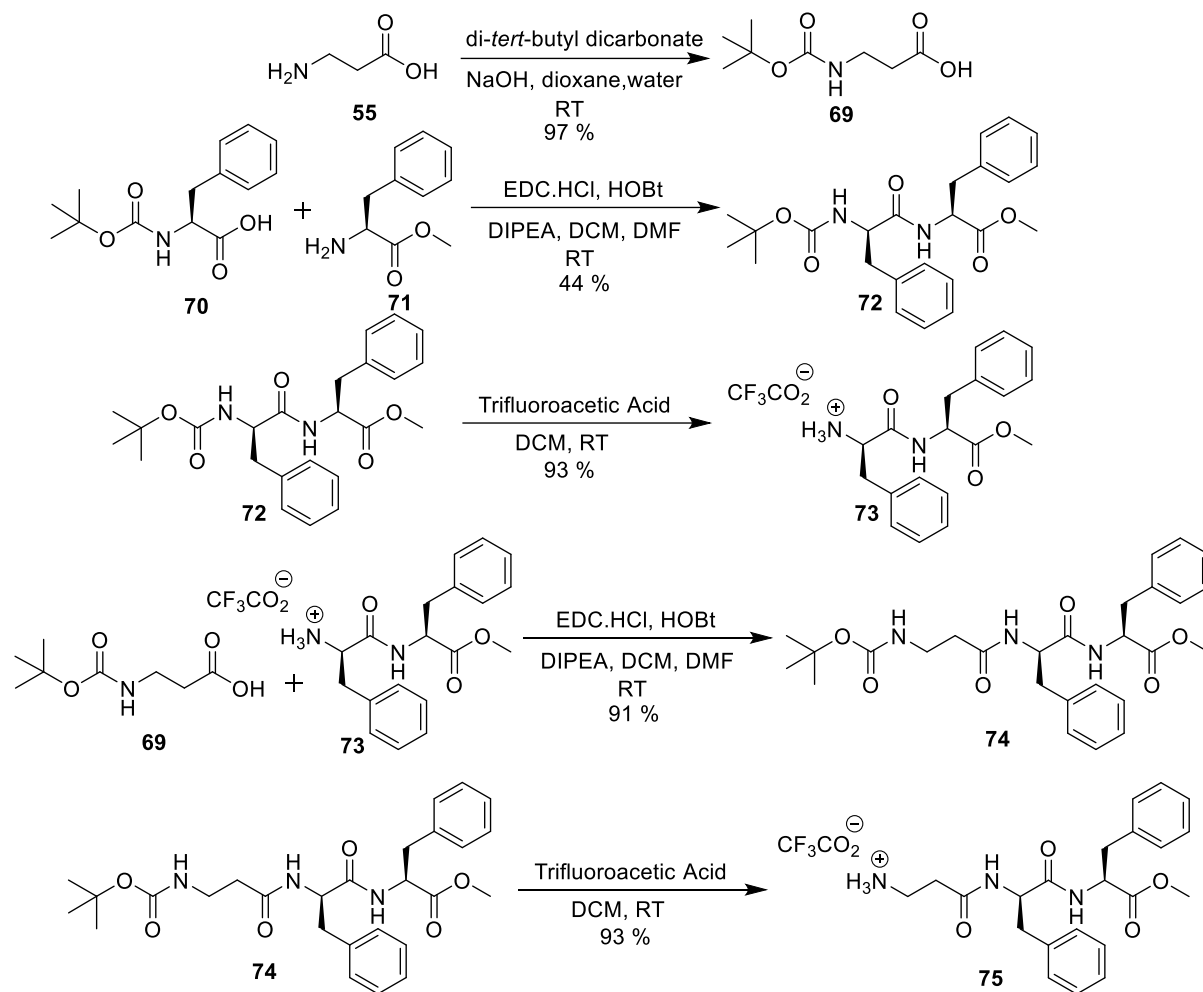
Scheme 5.1. Synthesis of molecules **69** to **75**.
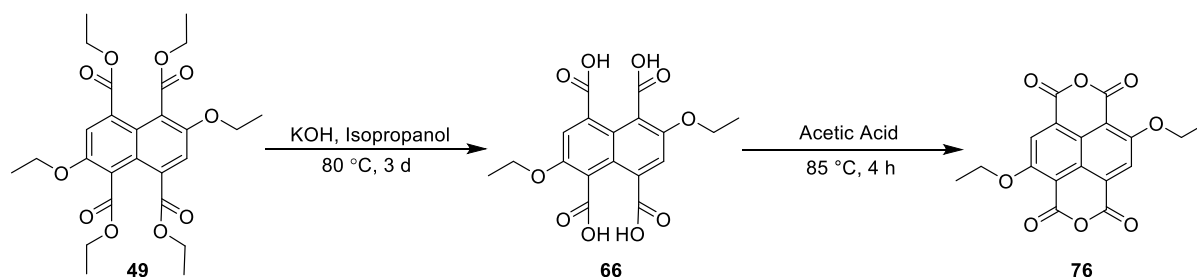
Scheme 5.2. Synthesis of molecules **76**.
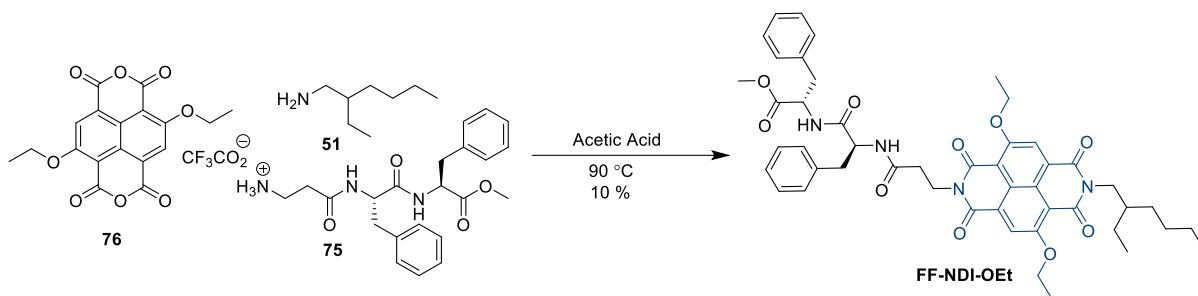
Scheme 5.3. Synthesis of molecules **FF-NDI-OEt.**
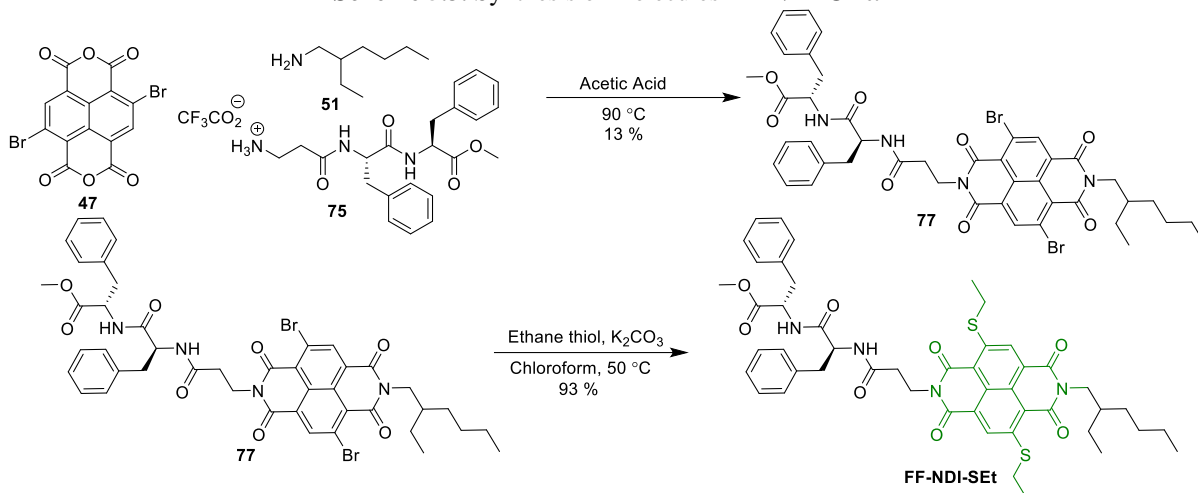
Scheme 5.4. Synthesis of molecules **FF-NDI-SEt**.
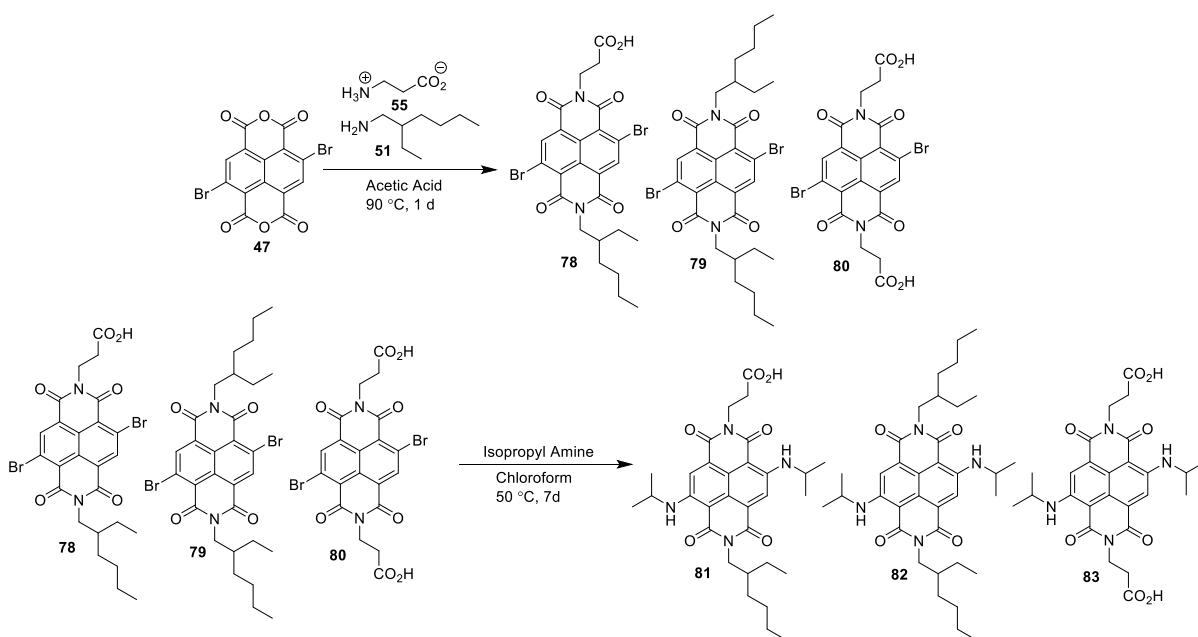
Scheme 5.5. Synthesis of molecule **81.**
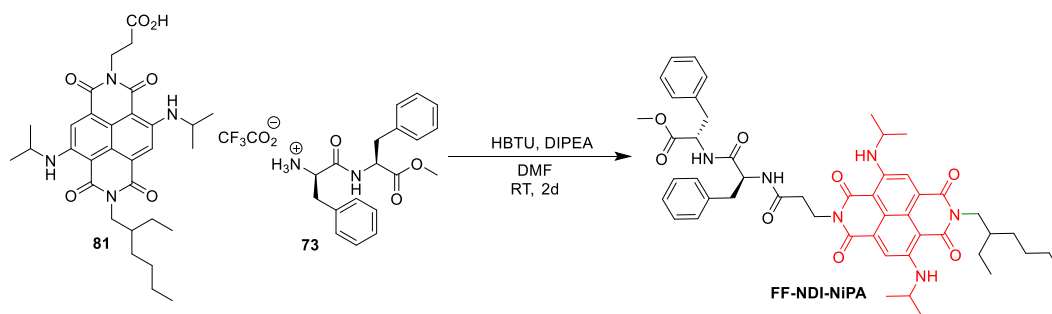
Scheme 5.6. Synthesis of molecules **FF-NDI-NiPA**.

Synthetic Procedures:

Molecule **47**, **49**, **69**, **70**, **73** was synthesized using earlier reported procedures.[12,20]

Synthesis of 74: 546 mg of **69** was taken in a round bottom flask (RB) and was dissolved in 20 mL of 3:1 mixture of DCM and DMF. The mixture was allowed to stir at 0 ˚C and in it 663 mg of EDC.HCl (1-Ethyl-3-(3-dimethylaminopropyl) carbodiimide), 430 mg of HOBT (Hydroxybenzotriazole) and 1.28 mL of DIPEA (N,N-Diisopropylethylamine) was added. It was allowed to stir at 0 ˚C for 1 hour. After 1 hour 1.4 g of **73** was added in it and the resultant mixture was allowed to stir at room temperature (RT) for 2 days. After 2 days the solvent was removed under reduced pressure and the residue was suspended in 30 mL of ethyl acetate and extracted subsequently with water, Na_2CO_3, 1 N HCl solution and finally with brine solution. The organic layer was collected and passed through Na_2SO_4 to remove remaining water. The organic layer was evaporated to get the crude product. The crude mixture was purified using a column chromatography with a gradient ranging from 20 % ethyl acetate in hexane to 50 % ethyl acetate in hexane to get 1.31 g of pure product as a white solid. Yield: 91 %. ^{1}H NMR (400 MHz, CDCl$_3$, ppm): δ = 7.12-7.26 (m, 10 H), 6.96 (dd, 2H, J = 2 Hz, 7.4 Hz), 6.121 (dd, 2H, J = 29.6 Hz, 6.8 Hz), 4.70 (q, 1H, J = 6.8 Hz), 4.55 (q, 1H, J = 7.2 Hz), 3.28 (q, 2H, J = 6 Hz), 3.05 (dd, 1H, J = 14 Hz, 5.6 Hz), 2.91-2.98 (m, 3H), 2.28 (t, 2H, J = 6.4 Hz), 1.38 (s, 9H); ^{13}C NMR (100 MHz, DMSO-d$_6$, ppm): δ = 171.68, 171.35, 170.06, 155.34, 137.81, 137.01, 129.10, 129.04, 128.23, 127.93, 126.54, 126.16, 77.55, 53.60, 53.34, 51.79, 37.44, 36.56, 35.47, 28.19.

Synthesis of 75: 1.3 g of **74** was taken in a 100 mL RB and was dissolved in 30 ml of dichloromethane (DCM) and placed in an ice bath at 0 ˚C. Then 9 mL of TFA was added drop wise to the solution. After 15 minutes the ice bath was removed and the reaction was allowed to stir at RT for 12 hours. After 12 hours a thin layer chromatography (TLC) was done to check completion of the reaction. After that the solvent was removed under reduced pressure and the product was obtained as a brown oil. 20 mL of cold diethyl ether was added to the brown liquid to obtain a white solid and the excess ether was decanted after that. The white solid was put

under high vaccum for 20 minutes to remove the remaining diethyl ether. The final product was obtained as 1.45 g off white sticky solid. Yield: 96 %. ^{1}H NMR (400 MHz, DMSO-d$_6$, ppm): δ = 8.57 (d, 1H, J = 7.6 Hz), 8.33 (d, 1H, J = 8.8 Hz), 7.64 (s, 3H), 7.30-7.18 (m, 10H), 4.59-4.54 (m, 1H), 4.45-4.51 (m, 1H), 3.58 (s, 3H), 2.81-3.07 (m, 5H), 2.65-2.71 (m, 1H), 2.31-2.45 (m, 2H); ^{13}C NMR (100 MHz, DMSO-d$_6$, ppm): δ = 171.69, 171.25, 169.08, 158.34, 157.99, 137.64, 137.04, 129.18, 129.14, 129.05, 128.25, 128.19, 127.97, 127.92, 126.56, 126.26, 53.67, 53.46, 51.94, 51.83, 37.62, 36.55, 35.24, 31.84.

Synthesis of 76: 200 mg of **49** was taken in a single neck RB and in it 60 mL of 1 M KOH in isopropanol was added and it was refluxed at 80 ˚C for 3 days. The color of the reaction changed from yellow to off white. After 3 days the excess isopropanol was evaporated. The resultant beige solution was suspended in 4 mL of warm water and 10 mL of methanol was added in it. The resultant white precipitate was filtered and washed with cold methanol to a white powder. The white powder was dissolved in 15 mL acetic acid and heated at 85 ˚C for four hours which resulted in a yellow colored solution. The reaction mixture was cooled to room temperature and excess water was added in it to precipitate out the product. The obtained precipitate was filtered and washed with cold methanol to remove excess of acetic acid and water and finally dried under vacuum to get 80 mg of **76** as a yellow solid. Obtained product was directly used for the next reaction without any further purification.

Synthesis of FF-NDI-OEt: In a single neck RB 80 mg of **76**, 87.05 mg of **51** and 344 mg of **75** was suspended in 20 mL of acetic acid and refluxed at 90 ˚C for 2 days. The progress of the reaction was monitored using NMR and thin layered chromatography. After 2 days excess water was added in it and the resultant precipitate was filtered washed with methanol to remove excess of water and acetic acid. The obtained precipitate was dissolved in chloroform was extracted using water and chloroform mixture. The organic layer was collected and evaporated to get the crude product. The crude product was purified using column chromatography using a gradient ranging from chloroform to 2 % methanol in chloroform to get 30 mg of pure product. Yield: 15 %. ^{1}H NMR: (600 MHz, CDCl$_3$, ppm): δ = 8.46 (s, 2H), 7.15-7.24 (m, 10H), 7.03 (d, 2H), 6.27 (dd, 2H), 4.64 (dd, 2H), 4.47 (t, 3H), 4.40 (m, 1H), 4.06-4.14 (m, 2H), 3.65 (s, 3H), 2.60-3.07 (m, 4H), 2.61 (m, 1H), 1.94 (m, 1H), 1.62 (m, 4H), 1.38 (m, 3H), 1.38 (m, 6H), 1.24 (m, 6H); ^{13}C NMR (150 MHz, CDCl$_3$, ppm): δ = 171.36, 170.38, 170.15, 162.91, 162.57, 161.48, 161.25, 160.32, 160.08, 136. 57, 135.73, 129.39, 129.26, 128.67, 127.22, 127.02, 119.73, 111.29, 110.59, 66.43, 66.37, 54.32, 53.51, 52.37, 44.60, 38.03, 37.90, 37.82, 30.77, 28.71, 24.09, 23.20, 14.88, 14.18, 10.725; MALDI-TOF (CCA matrix, negetive mode):

m/z calculated for $C_{48}H_{54}N_4O_{10}$: 846.38, found: 846.66 [M]$^{\cdot}$; HRMS (APCI, positive mode): m/z calculated for $C_{48}H_{54}N_4O_{10}$: 846.3840, found: 847.3837 [M+H]$^+$.

Synthesis of 77: 182 mg of **51** and 560 mg of **75** was dissolved in 30 mL of acetic acid and was added to 200 mg of **47** in a single neck RB. The resultant mixture was stirred at 90 ˚C. The progress of the reaction was monitored by proton NMR. After completion of the reaction it was cooled down to room temperature and water was added to it to precipitate out the product. The precipitate was filtered and washed with methanol to remove excess of water and acetic acid. The precipitate was dried under air to get the crude product. The crude product was purified using column chromatography using a gradient ranging from chloroform to 2 % methanol in chloroform to get 150 mg of pure product in 13 % yield. ^{1}H NMR (600 MHz, CDCl$_3$, ppm): δ = 8.98 (d, J = 6.8 Hz, 2H), 7.1-7.27 (m, 15H), 7.0 (bs, 2H), 6.14-6.27 (bs, 2H), 4.47-4.70 (bs, 4H), 4.15-4.22 (m, 2H), 3.67 (d, J = 8 Hz, 4H), 2.97-3.05 (m, 4H), 2.63 (d, J = 4 Hz, 2H), 1.25-1.39 (m, 14H), 0.88-0.95 (m, 8H); MALDI-TOF (CCA matrix, positive mode): m/z calculated for $C_{44}H_{44}Br_2N_4O_8$: 916.15, found: 939.24 [M+Na]$^+$.

Synthesis of FF-NDI-SEt: 150 mg of molecule **77**, 112 μl of ethane thiol and 226 mg of K$_2$CO$_3$ was taken in a single neck round bottom flask and in it 15 mL of chloroform was added. The reaction mixture was refluxed at 50 ˚C and the progress of the reaction was monitored by NMR and thin layered chromatography. After completion of the reaction (2 days) the excess chloroform and thiol was evaporated and the crude mixture was extracted using water and chloroform. The organic layer was collected and evaporated to dryness to get the crude mixture. The crude mixture was purified using column chromatography with a gradient ranging from chloroform to 2 % methanol in chloroform to get 130 mg of pure product as a red solid. Yield: 92 %. ^{1}H NMR (600 MHz, CDCl$_3$, ppm): δ = 8.60 (s, 2H), 7.22-7.26 (m, 10H), 7.01 (d, J = 8 Hz, 2H), 6.29-6.48 (m, 2H), 4.61-4.78 (m, 2H), 4.43-4.47 (m, 2H), 4.09-4.19 (m, 2H), 3.65 (s, 3H), 3.17-3.21 (m, 4H), 2.96-3.08 (m, 4H), 2.64-2.66 (m, 2H), 1.96 (m, 1H), 1.49-1.53 (m, 6H), 1.19-1.39 (m, 6H), 0.87-0.95 (m, 6H); ^{13}C NMR (150 MHz, CDCl$_3$, ppm): δ = 171.29, 170.37, 169.81, 163.68, 163.33, 162.60, 148.82, 148.45, 136.32, 135.43, 129.35, 129.16, 128.58, 128.38, 128.24, 127.14, 126.93, 125.06, 123.48, 118.78, 54.23, 53.43, 52.29, 44.82, 37.99, 37.77, 30.66, 28.58, 26.34, 23.98, 23.01, 14.07, 12.83, 10.59; MALDI-TOF (CCA matrix, positive mode): m/z calculated for $C_{48}H_{54}N_4O_8S_2$: 878.34, found: 917.37 [M+K]$^+$. HRMS (APCI, positive mode): m/z calculated for $C_{48}H_{54}N_4O_8S_2$: 878.3383, found: 879.3717 [M+H]$^+$.

Synthesis of 78: 1 g of molecule **47** was suspended in 90 mL of acetic acid in a round bottom flask and 0.910 g (7.04 mmol) of 2-ethylhexan-1-amine (**51**) and 0.627 g (7.04 mmol) of 3-ammoniopropanoate (**55**) was added in it. The reaction mixture was refluxed at 90 ˚C for 24 hours and after completion of the reaction excess water was added in it and the obtained precipitate was filtered and washed with methanol to remove excess of acetic acid and water. The obtained precipitate was dried under vacuum to get 762 mg of crude product as a mixture of **78**, **79**, **80** and was directly used for the next reaction without any further purification.

Synthesis of 81: 500 mg of the above crude mixture was taken in a round bottom flask and was suspended in 50 mL 1:1 mixture of chloroform and isopropyl amine and was refluxed at 60 ˚C for 14 days. After 14 days the excess chloroform and isopropyl amine was evaporated under reduced pressure and the crude mixture was extracted using brine and chloroform solution. The organic layer was collected and dried using sodium sulphate to remove excess of water and was evaporated to get the crude product. The crude product was purified using column chromatography using a gradient ranging from chloroform to 5 % methanol in chloroform to get 120 mg of the pure product. Combined yield of two-step is 9 %. ^{1}H NMR (400 MHz, CDCl$_3$, ppm): δ = 9.29 (q, J = 8 Hz, 2H), 8.12 (s, 2H), 4.50 (t, J = 4 Hz, 2H), 4.05-4.11 (m, 4H), 2.83 (t, J = 8 Hz, 2H), 1.98 (m, 1H), 1.25-1.37 (m, 24H), 0.88-0.93 (m, 6H); ^{13}C NMR (100 MHz, CDCl$_3$, ppm): δ = 165.45, 165.91, 163.39, 163.03, 148.51, 148.25, 126.08, 125.33, 121.24, 121.08, 118.71, 101.96, 101.21, 44.20, 44.17, 37.84, 35.76, 30.72, 29.69, 28.62, 24.07, 14.07, 10.70; MALDI-TOF (CCA matrix, negetive mode): m/z calculated for C$_{31}$H$_{40}$N$_4$O$_6$: 564.29, found: 564.39 [M]$^{\cdot -}$; HRMS (APCI, positive mode): m/z calculated for C$_{31}$H$_{40}$N$_4$O$_6$: 564.2948, found: 565.2988 [M+H]$^{+}$.

Synthesis of FF-NDI-NiPA: 50 mg of **81**, 47 mg of Hexafluorophosphate Benzotriazole Tetramethyl Uronium (HBTU), 17 mg of N,N-Diisopropylethylamine (DIPEA) was taken in a 25 mL two necked round bottom flask and 5 mL of dry DMF was added into it under nitrogen atmosphere. The reaction mixture was stirred for 30 minutes. After 30 minutes 46 mg of **73** dissolved in 5 mL of dry DMF was dropwise added into it. The reaction mixture was allowed to stir at room temperature for two days. After two days excess DMF was reduced under reduced pressure and the crude mixture was extracted using chloroform and brine solution. The organic layer was collected and evaporated to get the crude product which was further purified using column chromatography using a gradient ranging from chloroform to 2 % methanol in chloroform to get 32 mg of the pure product. Yield: 41 %. ^{1}H NMR (600 MHz, CDCl$_3$, ppm): δ = 9.30 (q , 2H, J = 4 Hz), 8.11(d, 2H, J = 4 Hz), 7.11-7.24 (m, 5H), 6.99 (d, 2H, J = 4 Hz), 6.47 (d, 1H, J = 4 Hz), 6.23 (d, 1H, J = 4 Hz), 4.70 (q, 1H, J = 8 Hz), 4.61 (q, 11H, J = 4 Hz),

4.40-4.42 (m, 2H), 3.65 (s, 3H), 2.92-3.06 (m, 4H), 2.58-2.65 (m, 2H), 2.0-2.04 (m, 1H), 1.91-1.95 (m, 1H), 1.2-1.39 (m, 25 H), 0.86-0.93 (m, 6H); ^{13}C NMR (150 MHz, CDCl$_3$, ppm): δ = 171.25, 170.32, 170.23, 166.50, 165.98, 163.43, 163.18, 148.53, 148.29, 136.50, 135.64, 129.28, 129.15, 128.56, 127.10, 126.90, 125.38, 118.73, 102.01, 101.24, 54.30, 53.41, 52.26, 44.13, 37.87, 36.51, 34.88, 32.12, 30.88, 29.61, 28.60, 26.38, 24.18, 23.10, 18.99, 14.07, 10.61; MALDI-TOF (CCA matrix, positive mode): m/z calculated for C$_{50}$H$_{60}$N$_6$O$_8$: 872.44, found: 873.20 [M+H]$^+$; HRMS (APCI, positive mode): m/z calculated for C$_{50}$H$_{60}$N$_6$O$_8$: 872.4473, found: 873.4539 [M+H]$^+$.

5.10. Experimental Procedure:

Protocol I: Preparation of spramolecular homopolymers of **FF-NDI-OEt**, **FF-NDI-SEt** and **FF-NDI-NiPA**: A stock solution of **FF-NDI-OEt**, **FF-NDI-SEt** and **FF-NDI-NiPA** (c = 5×10^{-5} M) was prepared in TCE. An appropriate volume of this stock is added to a TCE/MCH mixture to prepare the final self-assembling solution of appropriate concentration and solvent composition.

Protocol II: Preparation of two component copolymer between **FF-NDI-OEt** and **FF-NDI-SEt**: To prepare the two component copolymer between **FF-NDI-OEt** and **FF-NDI-SEt** a seed solution of 2 was prepared in TCE/MCH, 10/90 (v/v) and respective volume was injected into the lag phase of molecule **FF-NDI-OEt** to trigger a seeded supramolecular polymerization and formation of two component supramolecular copolymer.

Protocol III: Preparation of two component copolymer between **FF-NDI-OEt** and **FF-NDI-NiPA**: To prepare the two component copolymer between **FF-NDI-OEt** and **FF-NDI-NiPA** a seed solution of **FF-NDI-NiPA** was prepared in TCE/MCH, 10/90 (v/v) and respective volume was injected into the lag phase of molecule **FF-NDI-OEt** to trigger a seeded supramolecular polymerization and formation of two component supramolecular copolymer.

Protocol III: Preparation of two component copolymer between **FF-NDI-SEt** and **FF-NDI-NiPA**: To prepare the two component copolymer between **FF-NID-SEt** and **FF-NDI-NiPA** a seed solution of **FF-NDI-NiPA** was prepared in TCE/MCH, 10/90 (v/v) and respective volume was injected into the lag phase of molecule **FF-NDI-SEt** to trigger a seeded supramolecular polymerization and formation of two component supramolecular copolymer.

Protocol IV: Preparation of tricomponent block copolymer via sequential addition of **FF-NDI-NiPA**, **FF-NDI-SEt** and **FF-NDI-OEt**: A seed solution of molecule **FF-NDI-NiPA** was prepared in TCE/MCH, 10/90 (v/v) (c = 10^{-4} M). Subsequently the **FF-NDI-NiPA** seed solution was added to the lag phase of molecule **FF-NDI-SEt** to prepare two component block

copolymer between **FF-NDI-NiPA** and **FF-NDI-SEt** (TCE/MCH, 10/90 (v/v)). To prepare the tricomponent block copolymer monomer solution of **FF-NDI-OEt** in TCE was added into the two component copolymer of **FF-NDI-NiPA**$_{seed}$-**FF-NDI-OEt**$_{monomer}$ to prepare the tricomponent block copolymer between **FF-NDI-NiPA**$_{seed}$-**FF-NDI-SEt**$_{monomer}$-**FF-NDI-OEt**$_{monomer}$.

Protocol V: Preparation of tricomponent block copolymer via sequential addition of **FF-NDI-SEt**, **FF-NDI-NiPA** and **FF-NDI-OEt**: A seed solution of molecule **FF-NDI-SEt** was prepared in TCE/MCH, 6/94 (v/v) (c = 10^{-4} M). Subsequently the **FF-NDI-SEt** seed solution was added to the lag phase of molecule **FF-NDI-NiPA** to prepare two component block copolymer between **FF-NDI-SEt** and **FF-NDI-NiPA**. To prepare the tricomponent block copolymer monomer solution of **1** in TCE was added into the two component copolymer of **FF-NDI-NiPA**$_{seed}$-**FF-NDI-SEt**$_{monomer}$ to prepare the tricomponent block copolymer between **FF-NDI-NiPA**$_{seed}$-**FF-NDI-SEt**$_{monomer}$-**FF-NDI-OEt**$_{monomer}$.

5.11. References:

[1] a) Aida, T.; Meijer, E. W.; Stupp, S. I. *Science* **2012**, *335*, 813-817. b) Webber, M. J.; Appel, E. A.; Meijer, E. W.; Langer, R. *Nat. Matter.* **2016**, *15*, 13-26. c) Jain, A.; George, S. J. *Mater. Today*, **2015**, *18*, 206-214. d) Goor, O. J. G. M.; Hendrikse, S. I. S.; Dankers, P. Y. W.; Meijer, E. W. *Chem. Soc. Rev.* **2017**, *46*, 6621-6637. e) Merindol, R.; Walthers, A. *Chem. Soc. Rev.* **2017**, *46*, 5588-5619.

[2] a) Adelizzi, B.; Zee, N. V.; Windt, L. d.; Palmans, A. R. A.; Meijer, E. W. *J. Am. Chem. Soc.* **2019**, *141*, 6110-6121. b) Wehner, M.; Würthner, F. *Nat. Rev. Chem.* **2020**, *4*, 38-53. c) Lutz, J. F.; Lehn, J. M.; Meijer, E. W.; Matyjaszewski, K. *Nat. Rev. Matter.* **2016**, *1*, 1-14.

[3] a) Schacher, F. H.; Rupar, P. A.; Manners, I. *Angew. Chem., Int. Ed.* **2012**, *51*, 7898-7921. b) Davis, K. A.; Matyjaszewski, K. *Adv. Polym. Sci.* **2002**, *159*, 1-166. c) Gody, G.; Maschmeyer, T.; Zetterlund, P. B.; Perrier, S. *Nat. Commun.* **2013**, *4*, 2505. d) Gao, H.; Matyjaszewski, K. *Prog. Polym. Sci.* **2009**, *34*, 317-350.

[4] a) Wang, X.; Guerin, G.; Wang, H.; Wang, Y.; Manners, I.; Winnik, M. *Science* **2007**, *317*, 644-648. b) Gilroy, J. B.; Gädt, T.; Whittell, G. R.; Chabanne, L.; Mitchels, J. M.; Richardson, R. M.; Winnik, M. A.; Manners, I. *Nat. Chem.* **2010**, *2*, 566-570.

[5] a) Hudson, Z. M.; Lunn, D. J.; Winnik, M. A.; Manners, I. *Nat. Commun.* **2014**, *5*, 3372. b) Gädt, T.; Ieong, N. S.; Cambridge, G.; Winnik, M. A.; Manners, I. *Nat. Mater.* **2009**, *8*, 144-150. c) Hudson, Z. M.; Boott, C. E.; Robinson, M. E.; Rupar, P. A.; Winnik, M. A.; Manners, I. *Nat. Chem.* **2014**, *6*, 893-898. d) He, X.; Hsiao, M. S.; Boott, C. E.; Harniman, R. L.; Nazemi,

A.; Li, X.; Winnik, M. A.; Manners, I. *Nat. Mater.* **2017**, *16*, 481-488. d) Qiu, H.; Gao, Y.; Boott, C. E.; Gould, O. E. C.; Harniman, R. L.; Miles, M. J.; Webb, S. E. D.; Winnik, M. A.; Manners, I. *Science* **2016**, *352*, 697-701. e) Finnegan, J. R.; Lunn, D. J.; Gould, O. E. C.; Hudson, Z. M.; Whittell, G. R.; Winnik, M. A.; Manners, I. *J. Am. Chem. Soc.* **2014**, *136*, 13835-13844. f) Qiu, H.; Gao, Y.; An Du, V.; Harniman, R.; Winnik, M. A.; Manners, I. *J. Am. Chem. Soc.* **2015**, *137*, 2375-2385. g) Nazemi, A.; He, X.; MacFarlane, L. R.; Harniman, R. L.; Hsiao, M.-S.; Winnik, M. A.; Faul, C. F. J.; Manners, I. *J. Am. Chem. Soc.* **2017**, *139*, 4409-4417.

[6] a) Adelizzi, B.; Aloi, A.; Markvoort, A. J.; ten Eikelder, H. M. M.; Voets, I. K.; Palmans, A. R. A.; Meijer, E. W. *J. Am. Chem. Soc.* **2018**, *140*, 7168-7175.

[7] Zhang, W.; Jin, W.; Fukushima, T.; Saeki, A.; Seki, S.; Aida, T. *Science* **2011**, *334*, 340-343.

[8] Jung, S. H.; Bochicchio, D.; Pavan, G. M.; Takeuchi, M.; Sugiyasu, K. *J. Am. Chem. Soc.* **2018**, *140*, 10570-10577.

[9] a) Sorrenti, A.; Iglesias, J. L.; Markvoort, A. J.; de Greef, T. F. A.; Hermans, T. M. *Chem. Soc. Rev.* **2017**, *46*, 5476-5490. b) Korevaar, P. A.; de Greef, T. F. A.; Meijer, E. W. *Chem. Mater.* **2014**, *26*, 576−586. c) Korevaar, P. A.; George, S. J.; Markvoort, A. J.; Smulders, M. M.; Hilbers, P. A.; Schenning, A. P.; de Greef, T. F. A.; Meijer, E. W. *Nature* **2012**, *481*, 492-496. d) Matern, J.; Dorca, Y.; Sánchez, L.; Fernández, G. *Angew. Chem., Int. Ed.* **2019**, *58*, 16730-16740.

[10] a) Fukui, T.; Kawai, S.; Fujinuma, S.; Matsushita, Y.; Yasuda, T.; Sakurai, T.; Seki, S.; Takeuchi, M.; Sugiyasu, K. *Nat. Chem.* **2017**, *9*, 493-499. b) Ogi, S.; Sugiyasu, K.; Manna, S.; Samitsu, S.; Takeuchi, M. *Nat. Chem.* **2014**, *6*, 188-195. c) Ogi, S.; Stepanenko, V.; Sugiyasu, K.; Takeuchi, M.; Würthner, F. *J. Am. Chem. Soc.* **2015**, *137*, 3300-3307. d) Ogi, S.; Stepanenko, V.; Thein, J.; Würthner, F. *J. Am. Chem. Soc.* **2016**, *138*, 670-678. e) Endo, M.; Fukui, T.; Jung, S. H.; Yagai, S.; Takeuchi, M.; Sugiyasu, K. *J. Am. Chem. Soc.* **2016**, *138*, 14347-14353.

[11] Wagner, W.; Wehner, M.; Stepanenko, V.; Würthner, F. *J. Am. Chem. Soc.* **2019**, *141*, 12044-12054.

[12] Sarkar, A.; Sasmal, R.; Empereur-mot, C.; Bochicchio, D.; Kompella, S. V. K.; Sharma, K.; Dhiman, S.; Sundaram, B.; Agasti, S. S.; Pavan, G. M.; George, S. J. *J. Am. Chem. Soc.* **2020**, *142*, 7606-7617.

[13] a) Bates, F. S.; Hillmyer, M. A.; Lodge, T. P.; Bates, C. M.; Delaney, K. T.; Fredrickson, G. H. *Science* **2012**, *336*, 434-440. b) Onbulak, S.; Rzayev, J. *Polymer Chemistry* **2017**, *55*,

3868-3874. c) P. B.; Zetterlund, Thickett, S. C.; Perrier, S.; Bourgeat-Lami, E.; Lansalot, M. *Chem. Rev.* **2015**, *115*, 9745–9800.

[14] Wagner, W.; Wehner, M.; Stepanenko, V.; Würthner, F. *CCS Chem.* **2019**, *1*, 598-613.

[15] a) Sakai, N.; Mareda, J.; Vauthey, E.; Matile, S. *Chem. Commun.* **2010**, *46*, 4225-4237. b) Sarkar, A.; Dhiman, S.; Chalishazar, A.; George, S. J. *Angew. Chem., Int. Ed.* **2017**, *129*, 13955-13959.

[16] a) Kubota, R.; Nakamura, K.; Torigoe, S.; Hamachi, I. *ChemistryOpen* **2020**, *9*, 67-79. b) Pujals, S.; Feiner- Gracia, N.; Delcanale, P.; Voets, I.; Albertazzi, L. *Nat. Rev. Chem.* **2019**, *3*, 68-84.

[17] a) Narayan, B.; Bejagam, K. K.; Balasubramanian, S.; George, S. J. *Angew. Chem. Int. Ed.* **2015**, *54*, 13053-13057. b) Kulkarni, C.; Balasubramanian, S.; George, S. J. *Chem. Phys. Chem.* **2013**, *14*, 661-673.

[18] a) Oosawa, F.; Asakura, S. *Academic Press Inc., New York*, **1975**. b) Zhao, D.; Moore, J. S. *Org. Bio. Chem.* **2003**, *1*, 3471-3491.

[19] a) Arosio, P.; Knowles, T. P. J.; Linse, S. *Phys. Chem. Chem. Phys.,* **2015**, *17*, 7606-7618. b) Boyd-Kimball, D.; Abdul, H. M.; Reed, T.; Sultana, R.; Butterfield, D. A. *Chem. Res. Toxicol.* **2004**, *17*, 1743-1749

[20] Basak, S.; Singh, I.; Ferranco, A.; Syed, J.; Kraatz, H. B. *Angew. Chem., Int. Ed.* **2017**, *56*, 13288-13292.

Chapter: 6

Chirality Controlled Energy Transfer via Stereoselective Supramolecular Polymerization

Chapter: 6

Chirality controlled energy transfer via Stereoselective Supramolecular Polymerization

Abstract

Chirality driven self-sorting is envisaged to efficiently control functional properties in supramolecular materials. However, it faces challenges due to a lack of analytical methods to directly monitor the enantioselectivity of resulting supramolecular assemblies. In this context, we present two fluorescent core-substituted naphthalene diimide based donor and acceptor molecules with minimal structural mismatch and comprising of strong self-recognizing chiral motif, for solely chirality to determine the self-sorting process. As a consequence, stereoselective supramolecular polymerization with an unprecedented chirality control over energy transfer has been achieved. This chirality controlled energy transfer has been further exploited as an efficient probe to visualize microscopically the chirality driven self-sorting.
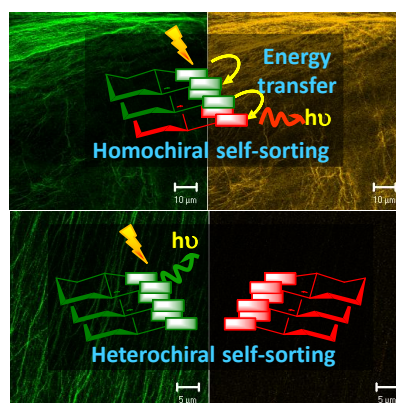
6.1. Introduction:

Supramolecular materials due to their adaptive and dynamic nature are promising candidates in designing new soft-materials with adaptive and responsive nature.[1] Multicomponent organic supramolecular assemblies have been utilized in the literature to construct artificial light-harvesting systems[2], where energy transfer from π-conjugated donor to π-conjugated acceptor has been exploited. There are several examples of multichromophoric light-harvesting arrays used not only for application towards artificial light harvesting,[3] but also in optoelectronics,[4] sensing[5], white light-emitting materials[6], as biological rulers[7] and for probing self-assembly dynamics.[8]

Control over energy transfer is a very efficient approach to tune optical outputs of a light-emitting device. It is well understood that the energy transfer properties can be controlled by the supramolecular organization of donor and acceptor molecules. In some very recent examples, control over donor and acceptor molecule has been attempted using pH changes,[9] wherein the changes in pH result in disassembly of donor and acceptor stacks and thus hinders the energy transfer process. We envisage that chirality controlled stereoselective assembly provides a unique opportunity to have a chirality control over excitonic energy transfer processes.[10] To achieve a supramolecular chirality control on energy transfer we have employed enantiomerically pure trans-1,2-diaminocyclohexane (trans-BAC) with two stereogenic centers as the self-assembling chiral group in our molecular design. The core to core hydrogen bonding between the amide groups is expected to provide enough energy difference between the homochiral and heterochiral supramolecular polymerization process. Tethering suitable donor and acceptor chromophores with spectral integral overlap with the trans-1,2-diaminocyclohexane unit would allow us to get control over the energy transfer process (Figure 6.1).

6.2. Molecular Design:

The two key requirements for an efficient chiral recognition driven energy transfer are: i) a minimum structural mismatch between the chromophores for chirality to control the self-sorting process and, ii) well-separated optical properties of donor (D) and acceptor (A). To fulfil the requirements, we chose core-substituted naphthalene diimide (NDI) derivatives as fluorescent chromophores.[11] For this, naphthalene diimides were appropriately core-substituted, with both side -OEt (ethoxy) as a green-emissive donor chromophore and with unsymmetrical core-substitution with -OEt and –iPA (N-isopropyl amine) groups for the red-emissive acceptor chromophore (Figure 6.1a). The donor was tethered in (S,S)-chiral BAC core
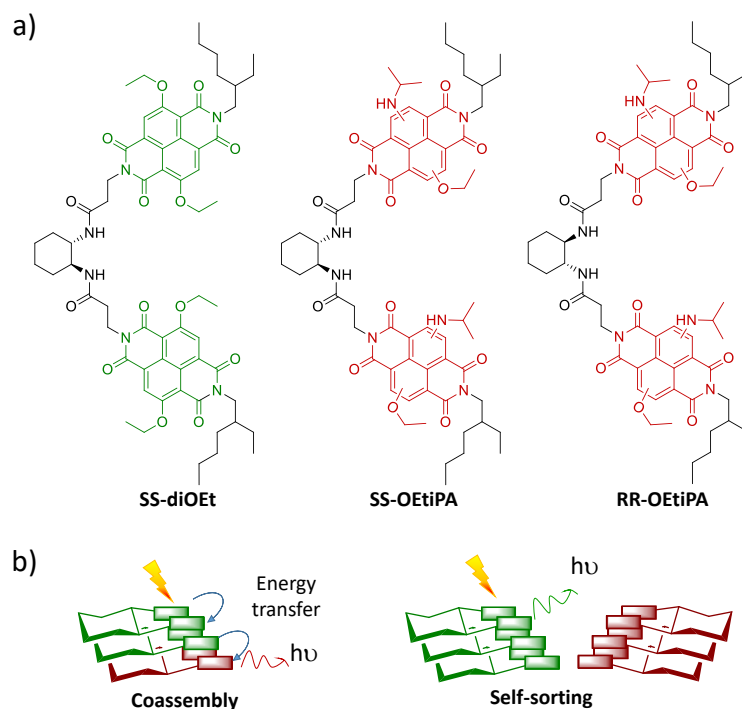
Figure 6.1. a) Molecular structures of donor **SS-diOEt** and acceptors **RR-/SS-OEtiPA**. b) Schematic representation of chirality controlled coassembly and self-sorting and resultant chirality controlled energy transfer process.

(**SS-diOEt**), whereas the acceptor NDI derivative was tethered in both (R,R) and (S,S)-chiral cores of BAC (**RR/SS-OEtiPA**) to investigate the chiral self-sorting process (Figure 6.1b). The donor was synthesized following reported procedure in Chapter 2 and acceptor NDI derivatives were synthesized and characterized by NMR and mass spectrometry (see experimental section for details).

6.3. Results and Discussion:

6.3.1. Self-assembly Studies:

Although, core-substituted naphthalene diimides (cNDIs) are well studied for their tunable optical and electron transfer properties,[13] their self-assembly has not been well investigated. Thus, we first investigated the self-assembly of the individual D and A molecules.

We have investigated the self-assembling properties of **SS-diOEt** in Chapter 2 which showed the formation of supramolecular fluorescent homopolymers in 25/75, TCE/MCH (v/v) solvent mixture. Here we have investigated the self-assembling properties of **SS-OEtiPA**. **SS-OEtiPA** exists in a molecularly dissolved state in polar solvents such as 1,1,2,2-tetrachloroethane (TCE) which is signified by sharp vibronic features at 347 nm and 367 nm
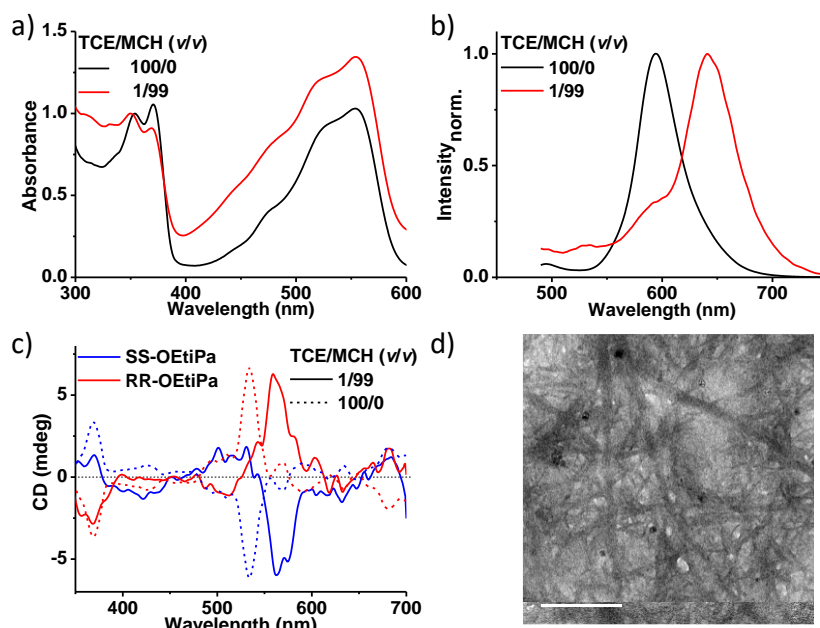
Figure 6.2. Self-assembly of **SS-OEtiPA**. a) Normalized absorption spectra and b) normalized emission spectra (430 nm for **SS-OEtiPA**), in TCE and in TCE/MCH, 1/99 (v/v). c) CD spectra in molecularly dissolved (TCE) and self-assembled states (TCE/MCH). c) also shows the mirror image CD spectra of both enantiomer **SS-OEtiPA** and **RR-OEtiPA** and d) TEM images showing 1D nanofibers in TCE/MCH, 1/99 (v/v) solutions respectively. ([**SS-OEtiPA**] = [**RR-OEtiPA**] = 2.5×10^{-5} M).

in the absorption spectrum (Figure 6.2a). Upon introducing non-polar solvents like methylcyclohexane (MCH), their self-assembly is induced which is depicted by the broadening of absorption spectra and reversal in the intensity of vibronic features of the π-π* band at 347 nm and 367 nm (Figure 6.2a). The assembled state (TCE/MCH, 1/99 (v/v)) **SS-OEtiPA** emission spectra show a new red shifted emission band from 591 nm to 641 nm on assembly
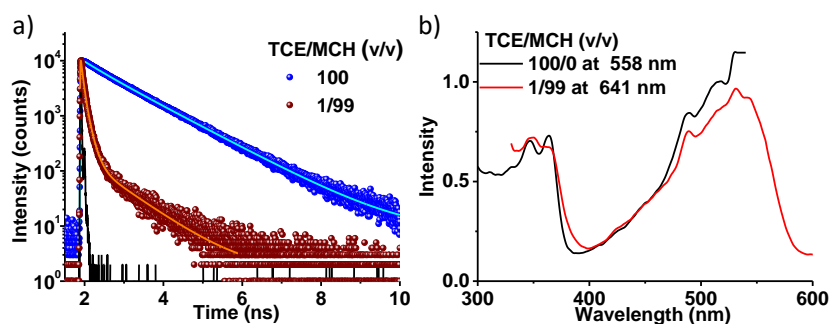
Figure 6.3. a) Lifetime decay profiles of **SS-OEtiPA** in monomeric and homopolymeric state (λ_{ex} = 442 nm, λ_{coll} = 590 nm for molecularly dissolved and 640 nm for homopolymeric state). b) Excitation spectra of **SS-OEtiPA** collected at 558 nm for molecularly dissolved state and 641 nm for self-assembled state. ([**SS-OEtiPA**] = 2.5×10^{-5} M).

TCE/MCH (v/v)	λ_{coll} (nm)	t_1 (ns)	t_2 (ns)	t_3 (ns)	$t_{average}$ (ns)
100/0	590	4.96 (7.36 %)	11.54 (92.64 %)		10.96
1/99	640	0.54 (43.28 %)	1.25 (43.78 %)	8.64 (12.95 %)	1.89

Table 6.1. Lifetime data of **SS-OEtiPA** in monomeric state in TCE and homopolymeric state in TCE/MCH, 1/99 (v/v). ([**SS-OEtiPA**] = 2.5×10^{-5} M, λ_{ex} = 442 nm).

(Figure 6.2b). The lifetime decay profile of the **SS-OEtiPA** assembly showed a sharp decay component (1.89 ns) in comparison to the monomeric state (10.96 ns) (Figure 6.3a, Table 6.1). Excitation spectra showed a red shift in the π-π* region corroborating to the formation of J-aggregates with an efficient excitonic migration in the stacks (Figure 6.3b). [3a, 12] CD spectra of **RR-** and **SS-OEtiPA** show mirror image bisignated CD signal in both molecularly dissolved and self-assembled state (Figure 6.2c), suggesting the presence of both intramolecular and intermolecular excitonic coupling, respectively.

The morphological investigations into D and A assemblies show that both of them form one dimensional (1D) fibers as visualized by Transmission Electron Microscopy (TEM) and Field Emission Scanning Electron Microscopy (FE-SEM) (Figure 6.2d, and 6.4). The fluorescent nature of these assemblies was further confirmed by confocal microscopy that shows green and red fluorescent 1D nanofibers of **SS-diOEt** and **SS-OEtiPA**, respectively (Figure 6.4b, and 6.4d).
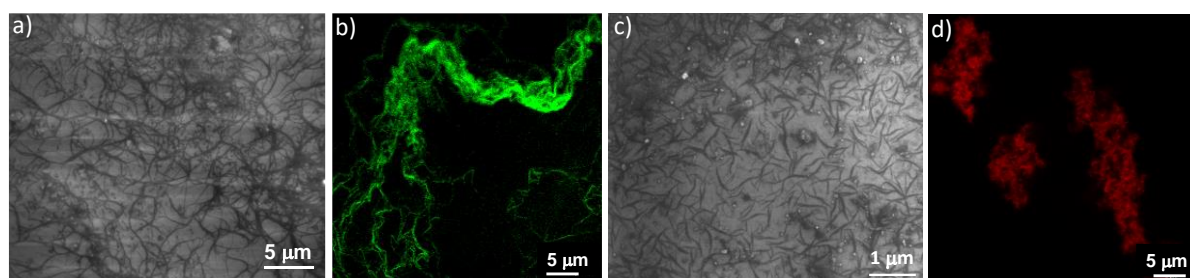
Figure 6.4. FESEM image of self-assembled solution of a) **SS-diOEt** and c) **SS-OEtiPA** and confocal microscopy images of self-assembled solution of b) **SS-diOEt** and d) **SS-OEtiPA** showing micrometer long fibers. ([**SS-diOEt**] = [**SS-OEtiPA**] = 2.5×10^{-5} M, TCE/MCH, 25/75 (v/v) for **SS-diOEt** and TCE/MCH, 1/99 (v/v) for **SS-OEtiPA**).

Spectroscopic investigations revealed sufficient spectral overlap of self-assembled **SS-diOEt** emission and **RR-/SS-OEtiPA** absorption spectra which is necessary to obtain an efficient energy transfer (Figure 6.5). Moreover, our previous study on BAC based D-A system suggests that due to strong hydrogen bonding between the chiral BAC motif, there is significant energy difference between homochiral and heterochiral stacks. Hence, we envisage to study the effect of chirality to determine the self-sorting behavior of present D and A system and to

use FRET as a probe to spectroscopically and microscopically discriminate between chirality driven self-sorted and coassembled D and A assemblies.
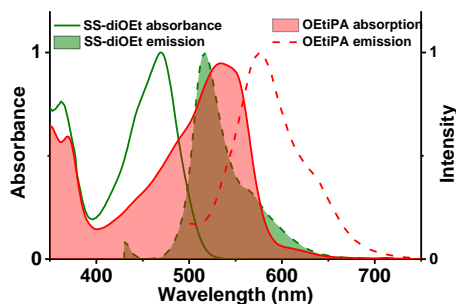
Figure 6.5. Normalized absorption and emission spectra of **SS-diOEt** (λ_{ex} = 415 nm) and **SS-OEtiPA** homopolymers (λ_{ex} = 430 nm). ([**SS-diOEt**] = [**SS-OEtiPA**] = 2.5×10^{-5} M, TCE/MCH, 25/75 (v/v) for **SS-diOEt** and 1/99 (v/v) TCE/MCH for **SS-OEtiPA**).

6.3.2. Energy Transfer Studies:
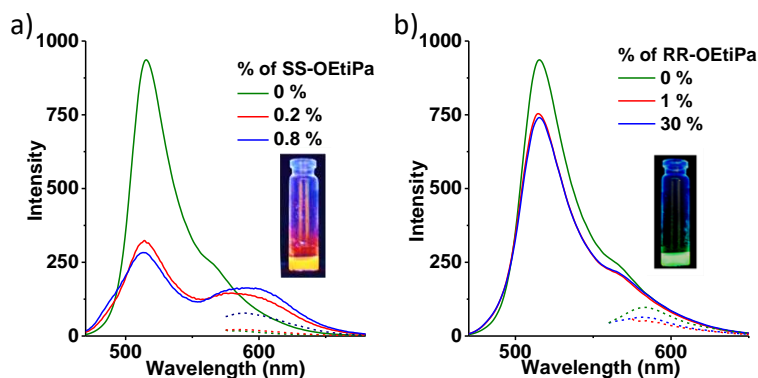
Figure 6.6. Chirality control on energy transfer. Emission spectra of a solution containing a) **SS-diOEt** and **SS-OEtiPA** and b) **SS-diOEt** and **RR-OEtiPA**. Note: Insets of a) and b) shows the corresponding photographs of the donor and acceptor mixture under UV-light (365 nm irradiation). ([**SS-diOEt**] = 2.5×10^{-5} M, TCE/MCH, 25/75 (v/v), λ_{ex} = 415 nm for donor excitation and λ_{ex} = 550 nm for acceptor excitation).

First, we investigated the spectroscopic properties of the homochiral mixture of D and A molecules. Upon excitation of the donor at 415 nm in a solution of **SS-diOEt** ([**SS-diOEt**] = 2.5×10^{-5} M, 25/75 (v/v) TCE/MCH) and 0.2 % **SS-OEtiPA** shows a significant quenching of donor fluorescence at 516 nm and build-up of acceptor emission at 591 nm (Figure 6.6a). An increase in acceptor percentage beyond 0.2 % does not result in further quenching of donor emission, suggesting saturation of energy transfer process with a mere 0.2 % of the acceptor. This indicates an efficient coassembly of D and A molecules and a very efficient energy transfer in these homochiral stacks, which is also confirmed by the excitation spectra (Figure 6.7a). The indirect excitation of the acceptor at 415 nm in the homochiral mixture showed emission at 591 nm corresponding to its monomeric emission, suggesting that the acceptors

are distributed in the stack as isolated molecules. Moreover, the direct excitation of the A at 550 nm shows a much lesser intensity than that by indirect excitation at 415 nm indicating an amplified emission via energy transfer (Figure 6.6a). We next investigated the D and A mixture of opposing chirality, **SS-diOEt**, and **RR-OEtiPA**, to see the effect of chirality on assembly characteristics. A solution of **SS-diOEt** ([**SS-diOEt**] = 2.5×10^{-5} M, TCE/MCH, 25/75 (v/v)) with up to 30 % **RR-OEtiPA**, on excitation at 415 nm, did not result in any significant quenching of donor emission suggesting the absence of energy transfer process, which also suggests a chirality driven self-sorting of D and A assemblies (Figure 6.6b). Excitation spectra also reiterated the chirality controlled energy transfer process which depicted higher intensity at donor absorbance (Figure 6.7a).

The energy transfer process was further validated by time-resolved fluorescence measurements. Homochiral, coassembled solutions of **SS-diOEt** and **SS-OEtiPA** show decrement in lifetime of donor and enhancement in lifetime of acceptor (Figures 6.7b, and 6.7c, Table 6.2, and 6.3) whereas chiral self-sorted assemblies of **SS-diOEt** and **RR-OEtiPA** do not
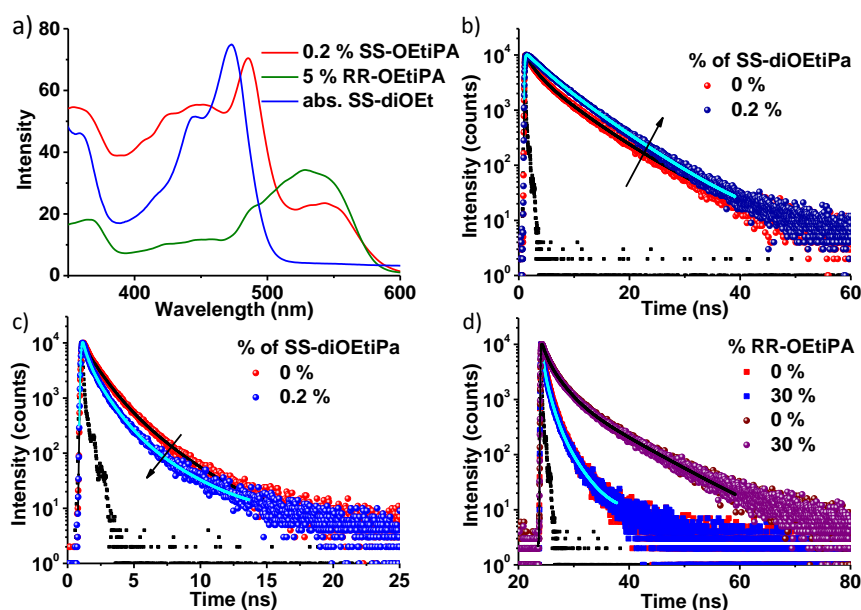
Figure 6.7. a) Comparison of absorption of donor (blue line) with excitation spectra of solution of **SS-diOEt** and 0.2 % **SS-OEtiPA** (red line) and **SS-diOEt** and 5 % **RR-OEtiPA** (green line) which reiterates the chirality driven energy transfer in **SS-diOEt** and **SS-OEtiPA** pair (λ_{ex} = 590 nm). b) Lifetime enhancement of acceptor (λ_{ex} = 442 nm, λ_{coll} = 596 nm) and c) lifetime decrement of donor in **SS-diOEt** and **SS-OEtiPA** coassembly (λ_{ex} = 442 nm, λ_{coll} = 515 nm). d) Lifetime decay profile of self-assembled solution of **SS-diOEt** and **RR-OEtiPA** showing no changes in lifetime of donor and acceptor confirming self-sorted stacks. (λ_{ex} = 442 nm, λ_{coll} = 515 nm for donor emission and λ_{coll} = 596 nm for acceptor emission, [**SS-diOEt**] = 2.5×10^{-5} M, TCE/MCH 25/75 (v/v)).

show any change in donor and acceptor lifetime, compared to the individual homochiral stacks of D and A molecules (Figures 6.7d, Table 6.4, and Table 6.5). The enantioselectivity of **SS-diOEt** towards **SS-OEtiPA** over **RR-OEtiPA** was calculated to be 98.6 % (Figure 6.8).

SS-OEtiPA %	t_1 (ns)	t_2 (ns)	t_3 (ns)	$t_{average}$ (ns)
0	0.97 (46.62 %)	2.33 (42.07 %)	0.19 (11.32 %)	1.44
0.2	0.95 (43.28 %)	0.18 (43.78 %)	3.20 (16.10 %)	1.06
0.3	0.98 (48.69 %)	3.56 (16.24 %)	0.18 (35.73 %)	1.10

Table 6.2. Comparison of donor lifetime with increasing percentage of acceptor in self-assembled solution of **SS-diOEt** and **SS-OEtiPA**. ([**SS-diOEt**] = 2.5×10^{-5} M, TCE/MCH, 25/75 (v/v), λ_{ex} = 442 nm, λ_{coll} = 516 nm).

SS-OEtiPA %	t_1 (ns)	t_2 (ns)	t_3 (ns)	$t_{average}$ (ns)
0	2.91 (35.59 %)	7.28 (56.62 %)	0.5 (7.79 %)	5.41
0.2	3.45 (38.63 %)	0.13 (-2.28 %)	6.66 (63.65 %)	5.50
0.3	3.24 (31.10 %)	3.56 (-3.45 %)	0.18 (72.35 %)	5.73

Table 6.3. Comparison of acceptor lifetime with increasing percentage of acceptor in self-assembled solution of **SS-diOEt** and **SS-OEtiPA**. ([**SS-diOEt**] = 2.5×10^{-5} M, TCE/MCH, 25/75 (v/v), λ_{ex} = 442 nm, λ_{coll} = 590 nm).

RR-OEtiPA %	t_1 (ns)	t_2 (ns)	t_3 (ns)	$t_{average}$ (ns)
0	0.97 (46.62 %)	2.33 (42.07 %)	0.19 (11.32 %)	1.44
1	0.94 (43.37 %)	2.22 (45.54 %)	0.19 (11.09 %)	1.42
30	1.10 (48.69 %)	2.62 (39.81 %)	0.2 (11.51 %)	1.51

Table 6.4. Comparison of donor lifetime with increasing percentage of acceptor in self-assembled solution of **SS-diOEt** and **RR-OEtiPA**. ([**SS-diOEt**] = 2.5×10^{-5} M, TCE/MCH, 25/75 (v/v), λ_{ex} = 442 nm, λ_{coll} = 516 nm).

RR-OEtiPA %	t_1 (ns)	t_2 (ns)	t_3 (ns)	$t_{average}$ (ns)
0	2.91 (35.59 %)	7.28 (56.62 %)	0.5 (7.79 %)	5.41
1	1.82 (43.08 %)	6.82 (49.31 %)	0.3 (7.61 %)	4.65
30	2.23 (48.69 %)	0.5 (39.81 %)	7.8 (41.07 %)	6.29

Table 6.5. Comparison of acceptor lifetime with increasing percentage of acceptor in self-assembled solution of **SS-diOEt** and **RR-OEtiPA**. ([**SS-diOEt**] = 2.5×10^{-5} M, TCE/MCH, 25/75 (v/v), λ_{ex} = 442 nm, λ_{coll} = 590 nm).
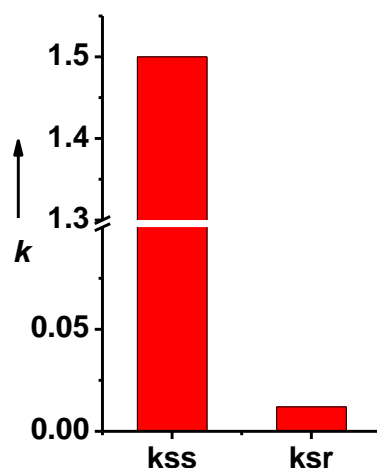
Figure 6.8. Graph for stereoselectivity showing 98.4 % enantioselectivity of **SS-diOEt** for **SS-OEtiPA** over **RR-OEtiPA**.

6.3.3. Visualization of Coassembly and Self-Sorting:
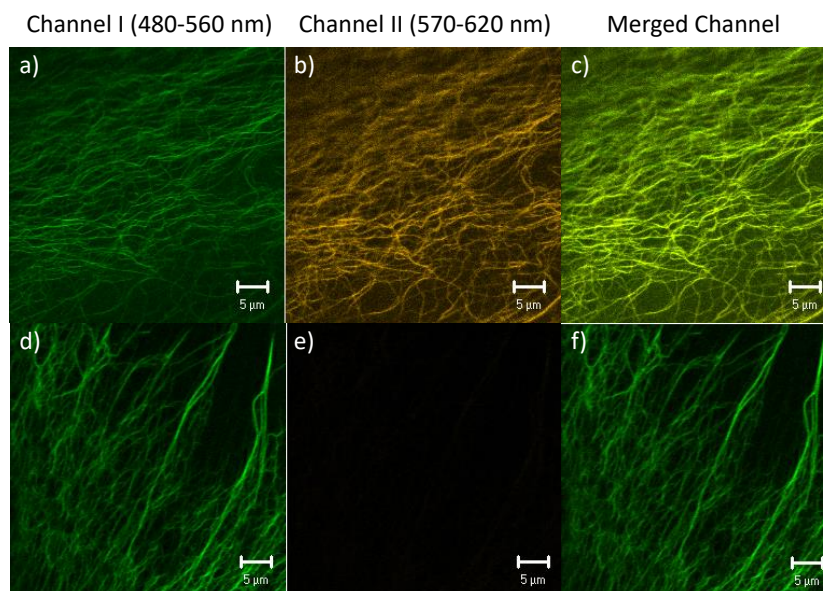
Figure 6.9. Top panel corresponds to solution of **SS-diOEt** and **SS-OEtiPA** whereas bottom panel corresponds to the solution of **SS-diOEt** and **RR-OEtiPA.** Confocal microscopy images collected by a), d) Channel I (480-560 nm), b), e) Channel II (570-620 nm) and c), f) Merged Channel I and II. a-c) Confocal microscopy images with 0.2 % **SS-OEtiPA.** a) Shows **SS-diOEt** green fluorescent fibers, b) shows energy transfer to incorporated **SS-OEtiPA** acceptor in donor stacks and c) merged image depicting spatial overlap of fibers emitting green and red emission confirming coassembly and energy transfer. d-f) Confocal microscopy images with 1 % **RR-OEtiPA**. d) Shows **SS-diOEt** green fluorescent fibers, e) shows absence of red-emitting species and absence of energy transfer and f) merged image depicting presence of solely **SS-diOEt** green-emitting fibers. ([**SS-diOEt**] = 2.5×10^{-5} M, TCE/MCH, 25/75 (v/v)).

Next, we visualized this chirality driven coassembled and self-sorted supramolecular polymers microscopically using energy transfer as a probe. The confocal images of various solutions

drop casted on glass slide were imaged. The donor was excited at 458 nm and the emission was collected in two channels, channel I for 480 to 560 nm and channel II for 570 to 610 nm emissions, corresponding to green- and orange/red emission respectively. The solution of **SS-diOEt** ([**SS-diOEt**] = 2.5×10^{-5} M, TCE/MCH, 25/75 (v/v)) and 0.2 mol % **SS-OEtiPA** showed fibers of green and orange emission, when viewed though channels I and II (Figures 6.9a and 6.9b). On merging them, we observe a perfect overlay of the two colours which confirms that the emission originates from the same fibers confirming coassembled fibers of D and A molecules, via stereoselective supramolecular polymerization (Figure 6.9d). A similar observation was concluded in fluorescence microscopic images (Figure 6.10).
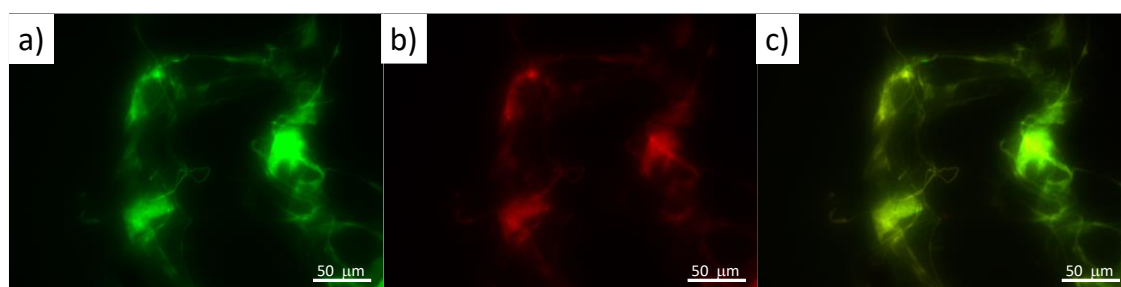
Figure 6.10. Visualization of coassembly of **SS-diOEt** and 0.2 % **SS-OEtiPA** using fluorescence microscopy. a) Excitation at the donor absorption using GFP (BP 470/40) filter and collection at donor emission showing green fluorescent fibers. b) Excitation at donor absorption using TX2 (BP 560/40) filter and collection at acceptor emission showing orange fluorescent fibers. c) Merged image showing no individual domain formation **SS-diOEt** and **SS-OEtiPA**. ([**SS-diOEt**] = 2.5×10^{-5} M, TCE/MCH, 25/75 (v/v)).

In contrast, the solution of **SS-diOEt** ([**SS-diOEt**] = 2.5×10^{-5} M, TCE/MCH, 25/75 (v/v)) and 1 mol % **RR-OEtiPA** showed only presence of green fibers on excitation of donor band at 458 nm (Figures 6.9d, 6.9e and 6.9f). No orange-/red-emissive species were obtained due to absence of any energy transfer process suggesting that no incorporation of A happened in the D stacks. To visually distinguish the chiral self-sorting process, a 1:1 solution of **SS-diOEt**:**RR-OEtiPA** ([**SS-diOEt**] = 2.5×10^{-5} M, TCE/MCH, 1/99 (v/v)) were seen under fluorescence microscope (Figure 6.11). Interestingly, distinguished regions of green and red emission were obtained, which show domain formation and hence we were able to successfully distinguish both donor and acceptor supramolecular fibers in the self-sorted assembly **SS-diOEt** and **RR-OEtiPA**.
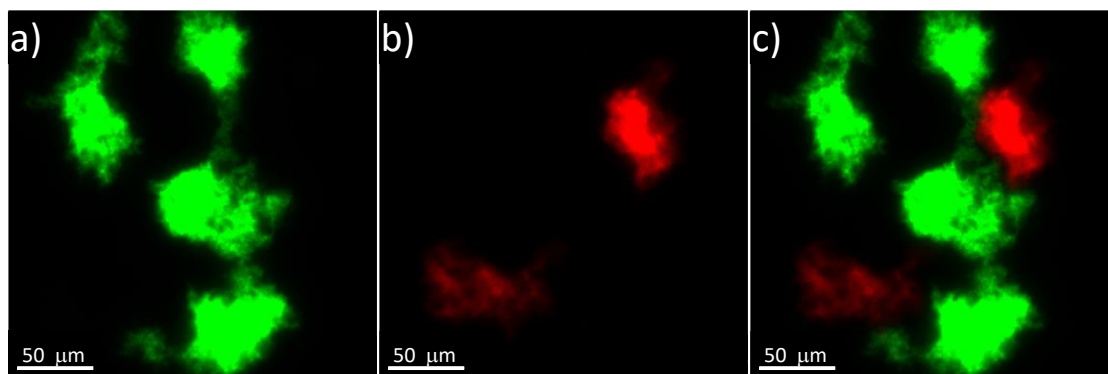
Figure 6.11. Visualization of self-sorted fibers of 1:1 mixture of **SS-diOEt** and **RR-OEtiPA**. Fluorescence microscopy images obtained by a) Excitation at the donor absorption using GFP (BP 470/40) filter and collection at donor emission showing green fluorescent domains, b) excitation at acceptor absorption using TX2 (BP 560/40) filter and collection at acceptor emission showing red fluorescent domains and c) merged image showing separate domains with no overlap of green and red domains. ([**SS-diOEt**] = 2.5×10^{-5} M, [**RR-OEtiPA**] = 2.5×10^{-5} M, TCE/MCH, 1/99 (v/v)).

6.4. Conclusion:

We have reported an unprecedented chirality driven energy transfer and self-sorting of fluorescent supramolecular fibers assembled from core-substituted NDI derivatives. We have shown a very efficient chiral recognition and resulting energy transfer with maximum efficiency with just 0.2 mol % acceptor in the coassembled solution. We have successfully distinguished the coassembly and self-sorting of the molecules spectroscopically and visually by our design strategy of structurally similar and chiral novel FRET pairs. We believe that, the present study will unveil the applications of chirality driven self-sorting process in opto-electronic materials and for the understanding of self-sorting events. It should also open the paths for the emerging kinetically controlled stereoselective supramolecular polymerization processes to be visualized.

6.5. Experimental Section:

General Methods:

NMR Measurements: NMR spectra were recorded with a Bruker AVANCE 400 (400 MHz) Fourier transform NMR spectrometer with chemical shifts reported in parts per million (ppm) with respect to TMS. Splitting patterns are designated as s, singlet; d, doublet; bs, broad singlet; m, multiplet; t, triplet; q, quartet; quin, quintet and br, broad.

Optical Measurements: Electronic absorption spectra were recorded on a Perkin Elmer Lambda 900 UV-Vis-NIR Spectrometer. Circular Dichroism (CD) spectra and temperature-dependent CD spectra were recorded on a JASCO J-815 spectrometer where the sensitivity, time constant and scan rate were chosen appropriately. The temperature-dependent

measurements were performed with a CDF-426S/15 Peltier-type temperature controller with a temperature range of 263-383 K and adjustable temperature slope. Emission spectra were recorded on Perkin Elmer LS 55 Luminescence Spectrometer. 10 mm x 10 mm or 10 mm x 2 mm quartz cuvettes were used for measurements at room temperature.

Transmission Electron Microscopy (TEM): TEM measurements were performed on a JEOL, JEM 3010 operated at 300 kV. Samples were prepared by placing a drop of the solution on carbon-coated copper grids followed by drying at room temperature. The images were recorded with an operating voltage of 300 kV.

Field Emission Scanning Electron Microscopy (FE-SEM): FE-SEM measurements were performed on a NOVA NANO SEM 600 (FEI) by drop casting the solutions on glass substrate followed by drying under high vacuum at room temperature and was operated with an accelerating voltage of 5 kV.

High-Resolution Mass Spectrometry (HRMS): High-Resolution Mass Spectra (HRMS) were recorded on an Agilent 6538 Ultra High Definition (UHD) Accurate-Mass Q-TOF-LC/MS system using electrospray ionization (ESI) and Atmospheric Pressure Chemical Ionization (APCI) modes.

Matrix-Assisted Laser Desorption Ionization (MALDI): MALDI was performed on a Bruker daltonics Autoflex Speed MALDI TOF System (GT0263G201) spectrometer using α-Cyano-4-hydroxy-cinnamic acid (CCA) as the matrix.

Confocal Microscopy: Confocal microscopy imaging was done at room temperature using a Zeiss LSM 510 META laser scanning confocal microscope with a laser excitation of λ_{ex} = 458 and 542 nm. The microscope objective of 63X (NA 1.4) and 100X (NA 0.5) were employed. Samples were prepared by dropping the solution on a glass slide and measurements were done in liquid state by following the standard procedure.

Optical Microscopy: Fluorescence images were taken using a LEIKA DMIL LED fluorescence microscope. Total magnification is 400x. Filter system used is TX2 (BP 560/40) and GFP (BP 470/40). Samples were prepared by dropping the solution on a glass slide and measurements were done in liquid state by following the standard procedure.

Fluorescent Lifetime Experiment: Time-resolved decay experiments were recorded on a Horiba Delta Flex time-correlated single-photon-counting (TCSPC) instrument. A 442-nm nano-LED with a pulse repetition rate of 1 MHz was used as the light source. The instrument response function (IRF) was collected by using a scatterer (Ludox AS40 colloidal silica, Sigma-Aldrich). For the 442-nm LED light source, the instrumental full width at half maximum including detector response was 0.2 ns. The excited state decay of the sample was collected by

fixing the emission wavelength at a particular wavelength. The decay was fitted using IBH software (DAS6).

Calculation of Stereoselectivity:

The equations used to calculate stereoselectivity are:

$$I = \frac{I_{591}}{I_{515}} \qquad \text{…………………………….. (1)}$$

$$k = \frac{(I_A - I_0)}{A} \qquad \text{…………………………….. (2)}$$

$$\% \text{ Stereoselecivity} = \frac{(k_{SS} - k_{SR})}{(k_{SS} + k_{SR})} \times 100 \qquad \text{…………………………….. (3)}$$

Where I is ratio of emission intensity at 591 nm and 515 nm corresponding to acceptor and donor respectively on excitation of donor at 415 nm. I_A and I_0 are I at acceptor mole percentage A % and 0 % respectively.

Using above equations to calculate stereoselectivity for **SS-diOEt** for **SS-OEtiPA** over **RR-OEtiPA**

$$k_{SS} = \frac{(I_{0.2A} - I_0)}{A} = \frac{(0.44 - 0.14)}{0.2} = 1.5$$

$$k_{SR} = \frac{(I_{1.0A} - I_0)}{A} = \frac{(0.15 - 0.14)}{1.0} = 0.01$$

$$\% \text{ Stereoselecivity} = \frac{(1.5 - 0.01)}{(1.5 + 0.01)} \times 100 = 98.6 \%$$

To calculate the stereoselectivity of the chirality controlled energy transfer we followed the relative change in emission intensity of **SS-diOEt** at 515 nm and **SS-OEtiPA** at 591 nm. Ideally, for **SS-diOEt** and **SS-OEtiPA** the I_{591}/I_{515} should increase linearly with increasing acceptor % before saturation. On the other hand, for **SS-diOEt** and **RR-OEtiPA** the I_{591}/I_{515} ratio should provide negligible variation due to absence of energy transfer in case of stereoselective supramolecular polymers. Subsequently the slopes (k) of the two curves can Be determined and using equation 3 the stereoselectivity can be calculated.[13] Since in our case the energy transfer got saturated with mere 0.2 % of acceptor, hence it was not possible to calculate the change in I_{591}/I_{515} with acceptor %. Hence, we have utilized the modified equation where I_A and I_0 were utilized to calculate the k and subsequently the stereoselectivity.

6.6. Synthetic Schemes and Procedures:

Synthetic Schemes

Scheme 6.1. Synthesis of molecules **RR-diOEt**.

Scheme 6.2. Synthesis of molecules **RR-OEtiPA**.

Scheme 6.3. Synthesis of molecules **SS-OEtiPA**.
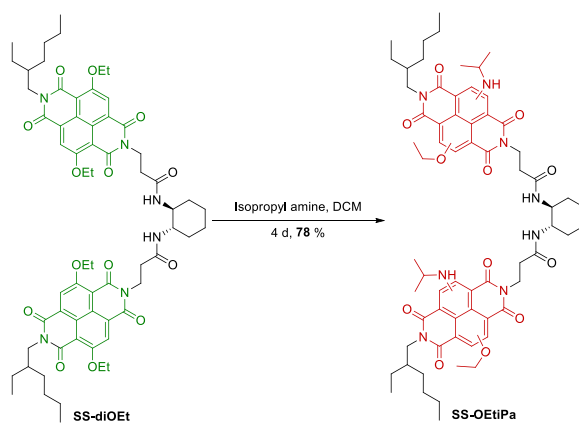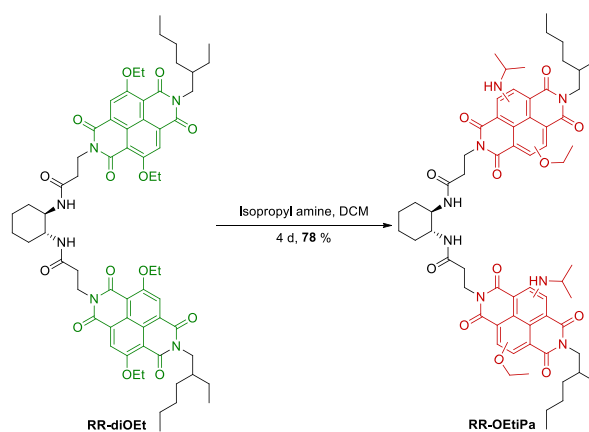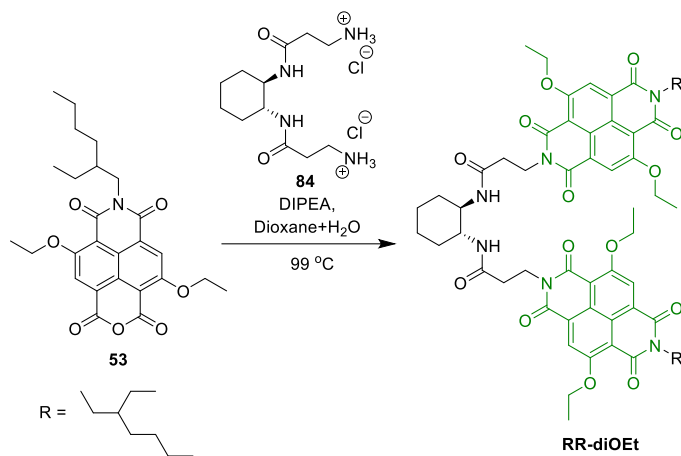
Synthetic Procedures:

SS-diOEt and molecule **53** was synthesized following reported procedure in Chapter 2. Molecule **84** was synthesized following earlier report.[10a]

Synthesis of RR-diOEt: 100 mg of compound **53** was taken in a single necked RB and in it 32 mg of **84** and 12 mg of DIPEA dissolved in 20 mL of dioxane and 20 mL of water was added and refluxed at 99 ˚C. The progress of the reaction was monitored by NMR and after completion of the reaction excess dioxane was evaporated and the reaction mixture was extracted using 1 (N) HCl and chloroform solution. The organic was collected and evaporated to dryness. The crude mixture was purified via column chromatography with a gradient ranging from chloroform to 1 % methanol in chloroform followed by using SX-3 bio beads in chloroform. The pure product was obtained as yellow powder in 64 % yield. ^{1}H NMR (400 MHz, CDCl$_3$, ppm): δ = 8.39 (d, 4H), 6.75 (d, 2H), 4.48 (m, 12H), 4.09 (t, 4H), 3.58 (m, 2H), 2.69 (t, 4H), 2.05-2.08 (m, 2H), 1.94-1.95 (m, 2H), 1.62-1.67 (m, 12 H), 1.19-1.39 (m, 22 H) 0.8-0.94 (m, 12 H); ^{13}C NMR (100 MHz, CDCl$_3$, ppm): δ = 179.14, 171.25, 162.68, 162.30, 161.29, 161.24, 161.10, 159.86, 127.34, 126.70, 126.63, 123.53, 123.47, 119.82, 119.43, 66.30, 66.17, 53.24, 44.47, 42.951, 37.71, 36.62, 30.66, 30.56, 29.72, 29.68, 29.34, 28.62, 23.17, 23.08, 14.85, 14.08, 10.62; HRMS (ESI, positive mode) m/z: calculated for C$_{64}$H$_{79}$N$_6$O$_{14}$: 1154.5576, found: 1156.5650 [M+H]$^+$; MALDI-TOF (CCA matrix, positive mode): m/z calculated for C$_{64}$H$_{78}$N$_6$O$_{14}$: 1154.5476, found: 1155.729 [M+H]$^+$.

Synthesis of RR-OEtiPA: RR-diOEt (18 mg, 0.015 mmol) was taken in a 50 mL round bottom flask and in it excess of isopropyl amine (IPA) in DCM was added and stirred at room temperature. The reaction was monitored by TLC. Reaction was stopped after the consumption of **RR-diOEt**. The crude product was obtained by vacuum evaporation of IPA and purified by column chromatography using 0 to 5 % chloroform to obtain pure product as red coloured powder in 78 % yield. ^{1}H NMR (400 MHz, CDCl$_3$, ppm): δ = 10.04-10.1 (m, 2H), 8.55-8.59 (m, 2H), 8.51-8.55 (m, 1.5H), 8.47-8.50 (m, 0.5H), 7.01-7.09 (m, 0.5H), 6.9-6.98 (m, 0.5 H), 6.75-6.84 (m, 1H), 4.68-4.82 (m, 8H), 4.38-4.48 (m, 6H), 3.91-4.01 (m, 2H), 2.95-3.05 (m, 4H), 2.35-2.44 (m, 2H), 2.22-2.30 (m, 2H), 2.02-2.09 (m, 2H), 1.91-1.98 (m, 12 H), 1.56-1.81 (26 H) 1.18-1.30 (m, 12 H); HRMS (APCI, positive mode): m/z calculated for C$_{66}$H$_{85}$N$_8$O$_{12}$: 1180.6209, found: 1181.6277 [M+H]$^+$, MALDI-TOF (CCA matrix, positive mode): m/z calculated for C$_{66}$H$_{84}$N$_8$O$_{12}$: 1180.62, found: 1181.49 [M+H]$^+$.

Note: **RR-OEtiPA** was obtained as mixture of isomers due to which peaks in NMR could not be resolved.

Synthesis of SS-OEtiPA: We have followed the similar synthetic procedure as that of **RR-OEtiPA**. We have used **SS-diOEt** instead of **RR-diOEt**. Yield: 74 %. ^{1}H NMR (400 MHz, CDCl3, ppm): δ = 10.04-10.10 (m, 2H), 8.55-8.59 (m, 2H), 8.51-8.55 (m, 1.5H), 8.47-8.50 (m, 0.5H), 7.01-7.09 (m, 0.5H), 6.9-6.98 (m, 0.5 H), 6.75- 6.84 (m, 1H), 4.68-4.82 (m, 8H), 4.38-4.48 (m, 6H), 3.91-4.01 (m, 2H), 2.95-3.05 (m, 4H), 2.35-2.44 (m, 2H), 2.22-2.30 (m, 2H), 2.02-2.09 (m, 2H), 1.91-1.98 (m, 12 H), 1.56-1.81 (m, 26 H) 1.18-1.30 (m, 12 H); HRMS (APCI, positive mode): m/z calculated for $C_{66}H_{85}N_8O_{12}$: 1181.6287, found: 1181.6273 $[M+H]^+$, MALDI-TOF (CCA matrix, positive mode): m/z calculated for $C_{66}H_{84}N_8O_{12}$: 1180.620, found: 1181.647 $[M+H]^+$.

Note: **SS-OEtiPA** was obtained as mixture of isomers due to which peaks in NMR could not be resolved.

6.7. Experimental Procedures:

Protocol of Sample Preparation: Spectroscopic grade solvents from commercial sources were used for performing all the studies at room temperature otherwise when mentioned. All solutions were prepared by injecting a monomeric solution of the compound in TCE to MCH. Stocks were prepared as 5×10^{-3} M in CHCl3. Respective volume were taken in a vial and CHCl3 was evaporated and the compound was re-dissolved in TCE and injected to MCH to adjust the final concentration to 2.5×10^{-5} M to get a self-assembled solution. All the solutions were annealed by slow heating and cooling to avoid any kinetic traps. Hence, all the observations are under thermodynamic conditions.

For coassembly studies stock concentration of the acceptor was prepared as 10^{-3} M and donor as 5×10^{-3} M. respective volumes of donor and acceptor solution were transferred in another vial and chloroform was evaporated and re-dissolved in TCE and injected to MCH at room temperature to adjust the final concentration to 2.5×10^{-5} M of donor.

6.8. References:

[1] a) Greef, T. F. A. D.; Smulders, M. M. J.; Wolffs, M.; Schenning, A. P. H. J.; Sijbesma, R. P.; Meijer, E. W. *Chem. Rev.* **2009,** *109,* 5687-5754. b) Aida, T.; Meijer, E. W.; Stupp, S. I. *Science* **2012**, *335*, 813-817.

[2] a) Jenkins, R. D.; Andrews, D. L. *J. Chem. Phys.* **2003**, *118*, 3470-3479. b) Kelley, R. F.; Shin, W. S.; Rybtchinski, B.; Sinks, L. E.; Wasielewski, M. R. *J. Am. Chem. Soc.* **2007**, *129*, 3173-3181. c) Peng, H. Q.; Niu, L.-Y.; Chen, Y.-Z.; Wu, L.-Z.; Tung, C.-H.; Yang, Q.-Z. *Chem. Rev.* **2015**, *115*, 7502-7542. d) Ahrens, M. J.; Sinks, L. E.; Rybtchinski, B.; Liu, W.;

Jones, B. A.; Giaimo, J. M.; Gusev, A. V.; Goshe, A. J.; Tiede, D. M.; Wasielewski, M. R. *J. Am. Chem. Soc.* **2004**, *126*, 8284-8294. e) Ziessel, R.; Ulrich, G.; Haefele, A.; Harriman, A. *J. Am. Chem. Soc.* **2013**, *135*, 11330-11344.

[3] a) Ajayaghosh, A.; Praveen, V. K.; Vijayakumar, C.; George, S. J. *Angew. Chem., Int. Ed.* **2007**, *46*, 6260-6265. b) Praveen, V. K.; Ranjith, C.; Bandini, E.; Ajayaghosh, A.; Armaroli, N. *Chem. Soc. Rev.* **2014**, *43*, 4222-4242. c) Zhang, X.; Chen, Z.-K.; Loh, K. P. *J. Am. Chem. Soc.* **2009**, *131*, 7210-7211. d) Bçsch, C. D.; Langenegger, S. M.; Häner, R. *Angew. Chem., Int. Ed.* **2016**, *55*, 9961-9964. e) Winiger, C. B.; Li, S.; Kumar, G. R.; Langenegger, S. M.; Häner, R. *Angew. Chem., Int. Ed.* **2014**, *53*, 13609-13613.

[4] Wong, K.-T.; Bassani D. M. *NPG Asia Mater.* **2014**, *6*, e116.

[5] a) Sun, X.; Wang, Y.; Lei, Y. *Chem. Soc. Rev.* **2015**, *44*, 8019-8061. b) Sandeep, A.; Praveen, V. K.; Kartha, K. K.; Karunakaranab, V.; Ajayaghosh, A. *Chem. Sci.* **2016**, *7*, 4460-4467.

[6] a) Giansante, C.; Schäfer, C.; Raffy, G.; Guerzo, A. D.; *J. Phys. Chem. C* **2012**, *116*, 21706-21716. b) Abbel, R.; Weegen, R. v. d.; Pisula, W.; Surin, M.; Leclère, P.; Lazzaroni, R.; Meijer, E. W.; Schenning, A. P. H. J. *Chem. Eur. J.* **2009**, *15*, 9737-9746. c) Vijayakumar, C.; Praveen, V. K.; Ajayaghosh, A. *Adv. Mater.* **2009**, *21*, 2059-2063. d) Praveen, V. K.; Ranjith, C.; Armaroli, N. *Angew. Chem., Int. Ed.* **2014**, *53*, 365-368.

[7] a) Sapsford, K. E.; Berti, L.; Medintz, I. L. *Angew. Chem., Int. Ed.* **2006**, *45*, 4562-4588. b) Peng, H. Q.; Niu, L. Y.; Chen, Y. Z.; Wu, L. Z.; Tung, C. H.; Yang, Q. Z. *Chem. Rev.* **2015**, *115*, 7502-7542.

[8] a) Schmid, S. A.; Abbel, R.; Schenning, A. P. H.; Meijer, E. W.; Sijbesma, R. P.; Herz, L. M. *J. Am. Chem. Soc.* **2009**, *131*, 17696-17704. b) Baker, M. B.; Albertazzi, L.; Voets, I. K.; Leenders, C. M. A.; palmans, A. R. A.; pavan, G. M.; Meijer, E. W. *Nat. Commun.* **2015**, *6*, 6324. c) Albertazzi, L.; Zwaag, D. v. d.; Leenders, C. M. A.; Fitzner, R.; Hofstad, R. W. v. d.; Meijer, E. W. *Science* **2014**, *344*, 491-495.

[9] a) Ardoña, H. A. M.; Tovar, J. D. *Chem. Sci.* **2015**, *6*, 1474-1484. b) León, C. F.; Oltra, S. D.; Galindo, F.; Miravet, J. F. *Chem. Mater.* **2016**, *28*, 7964-7972. c) Ardoña, H. A. M.; Draper, E. R.; Citossi, F.; Wallace, M.; Serpell, L. C.; Adams, D. J.; Tovar, J. D. *J. Am. Chem. Soc.* **2017**, *139*, 8685-8692.

[10] a) Narayan, B.; Bejagam, K. K.; Balasubramanian, S.; George, S. J. *Angew. Chem., Int. Ed.* **2015**, *54*, 13053-13057. b) Ishida, Y.; Aida, T. *J. Am. Chem. Soc.* **2002**, *124*, 14017-14019. c) Sato, K.; Itoh, Y.; Aida, T. *Chem. Sci.* **2014**, *5*, 136-140. c) Kang, J.; Miyajima, D.; Mori, T.; Inoue, Y.; Itoh, Y.; Aida, T. *Science* **2015**, *347*, 646-651.

[11] Sakai, N.; Mareda, J.; Vauthey, E.; Matile, S. *Chem. Commun.* **2010**, *46*, 4225-4237.

[12] a) Schmid, S. A.; Abbel, R.; Schenning, A. P. H. J.; Meijer, E. W.; Herz, L. M. *Philos. Trans. R. Soc*. London **2012**, *370*, 3787-3801.

[13] Nakashima, T.; Kimizuka, N. *Adv. Mater.* **2002**, *14*, 1113-1116

Chapter: 7

Charge-Transfer Resolution via Diastereoselective Supramolecular Polymerization

Chapter: 7

Charge-Transfer Resolution via Diastereoselective Supramolecular Polymerization

Abstract

The synthesis of diastereomeric supramolecular polymers is reported. The establishment of diastereomeric supramolecular polymer would require a two component supramolecular polymerization between chiral donors and acceptors. Herein we have investigated charge-transfer (CT) interaction driven supramolecular copolymerization between bischromophoric chiral donor and acceptor monomers. Strong electronic complementary nature of the two chiral monomers leads to the copolymer formation, and the chiral bias exerted by the cyclohexane diamine core leads to the unprecedented diastereoselective supramolecular polymerization process. The diastereoselectivity between two CT assemblies gets manifested in their microscopic, mechanistic and macroscopic properties. Molecular modelling studies provided more in-depth insights into the molecular level organization of the two CT assemblies and rationalized some of the spectroscopic and microscopic differences. The observed differences in macroscopic properties was further utilized to resolve the two CT assemblies using size exclusion chromatography.
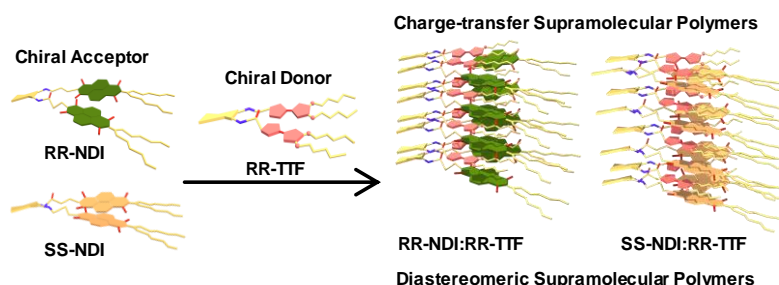
7.1. Introduction:

Self-recognizing chiral monomers led to the development of stereoselective or homochiral supramolecular polymers[1] and were recently extended to chain-growth living supramolecular systems.[2] Resultant enantiomeric assemblies are analogous to the stereoregular isotactic polymers constructed using an enantioselective catalyst.[3] Stereoselective copolymerization has also been shown to impart chirality control over the monomer sequence to modulate the functional properties such as energy transfer and charge-transfer interactions.[4] On the other hand, diastereoselective interactions during the supramolecular copolymerization of chiral monomers have not been reported yet, which has been extensively investigated in the crystal growth for the resolution of enantiomeric chiral monomers.[5] We envisage that the diastereomeric polymerization process would provide unprecedented opportunities for the sensing of chiral analytes shown in covalent polymers[6] or for the resolution of enantiomers like the classical crystallization process.[5]

In a classical experiment, Newman and coworkers have reported charge-transfer interaction driven diastereomeric complexes between the enantiomers of helically shaped hexahelicenes and electron-deficient fluorene derivatives (Scheme 7.1a).[7] They have also pursued separation of hexahelicene derivatives using differential crystallization of the two diastereomeric CT complexes. Later Wynberg and coworkers have shown opposite chiroptical signals for the corresponding CT band confirming diastereoselectivity controlled CT complexation (Scheme 7.1a).[8] We envisage that diastereomeric charge-transfer interactions between chiral donor and acceptor chromophores are essential for a diastereoselective supramolecular copolymerization. However, previous examples of alternate supramolecular copolymers involving chiral donor and acceptor monomers devoid of any diastereomeric interactions as one of these factors (chirality against CT interaction) always overruled the other. For example, in charge-transfer driven foldameric assemblies, the strong CT interactions dominated the chirality and consequently led to an optically inactive CT band.[9] On the other hand, strong chiral motifs only result in homochiral CT assemblies and heterochiral D and A monomers always narcissistically self-sort to form homochiral supramolecular polymers via chiral self-recognition process.[4a] Hence the synergy between chirality and charge-transfer interaction remains a compelling challenge to be addressed to achieve diastereomeric charge-transfer supramolecular polymeric systems. In this Chapter, we report for the first time a diastereoselective supramolecular polymerization in charge-transfer alternatively stacked copolymers of donor-acceptor monomers. The resultant charge-transfer
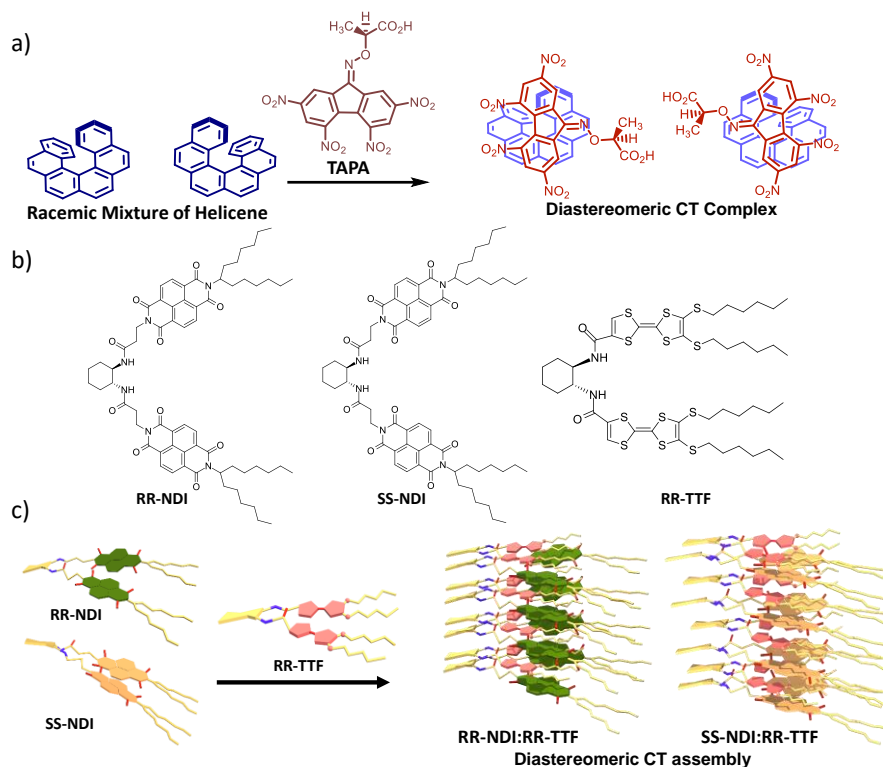
Scheme 7.1. a) Schematic representation of optical resolution of racemic mixture of helicene through diastereomeric charge-transfer complexation with optically active **TAPA** (2-(2,4,5,7-Tetranitro-9-fluorenylideneaminooxy) propionic acid), carried out by Newman and coworkers. b) Molecular structures of enantiomeric naphthalene diimide (NDI) acceptors (**RR-NDI**, **SS-NDI**) and tetrathiafulvalene (TTF) donor (**RR-TTF**) used in the present study. c) Schematic representation of the possible supramolecular structures of diastereomeric CT assembly, formed by charge-transfer complexation between **RR-TTF** and **RR-/SS-NDI**.

alternatively, stacked copolymers assemblies showed a significant difference in the chiroptical properties, polymerization mechanism, and morphology, which validated their diastereomeric relationship. We have further exploited the differential properties of the two resultant diastereomeric assemblies to implement a diastereomeric resolution of the enantiomeric naphthalene acceptor chromophores.[10]

We have recently demonstrated the stereoselective supramolecular polymerization of naphthalene diimide (NDIs) acceptor chromophores tethered to strongly self-recognizing chiral trans-(1,2-bis(amido)cyclohexane) (trans-BAC) groups resulting in the self-assembled conglomerates of enantiomeric NDIs in resolution.[4a] We have a further auto-resolution of segregated and mixed donor-acceptor stacks through stereoselective supramolecular polymerization in solution. Upon introduction of chiral dialkoxy naphthalene (DAN), donors led to the auto-resolution of the NDI stacks with the chirality opposite to the donor and mixed CT stacks with the acceptor with the same chirality.[4a] However, this chirality driven self-sorting strategy may be subjective to the strength of the donor-acceptor pair.[9,11] A more potent

donor with a better CT overlap with NDI may bind to both the components of a supramolecular conglomerate of the acceptor, resulting in diastereomeric stacks.

7.2. Molecular Design:

To realize the concept of diastereomeric supramolecular copolymerization, we have employed tetrathiafulvalene (TTF)[12] and NDI as the donor and acceptor monomers, since they are known to form strong CT complexes. We have employed enantiomerically pure trans-BAC with two stereogenic centers as the self-assembling chiral group in our molecular design to promote a stereo-bias during the copolymerization process. Scheme 7.1b shows the molecular structures of the bis chromophoric molecules **RR-NDI**, **SS-NDI** (acceptor), and **RR-TTF** (donor), used in the present study. We envisage that strong chiral bias and CT interactions, which are known to be sensitive to the molecular organization of D and A molecules would facilitate diastereoselectivity during the CT driven supramolecular copolymerization process. (Scheme 7.1c, *vide infra*).

SS- and **RR-NDI** were synthesized according to our previous report[4a], whereas we have synthesized the bischromophoric **RR-TTF** by the amide coupling of the corresponding TTF acid precursor with (1R, 2R)-(+)-1,2 cyclohexane diamine (see experimental section) and all the molecules were completely characterized using NMR and mass spectrometry.

7.3. Results and Discussion:

7.3.1. Self-assembly Studies:

We have previously reported the cooperative helical supramolecular polymerization of both **RR-** and **SS-NDI** molecules in TCE/MCH solvent mixtures, and they exhibited mirror-imaged bisignated CD spectra characteristic of the enantiomeric supramolecular homopolymers. **RR-TTF** existed in the monomeric state in 1,1,2,2 tetrachloroethane (TCE). However, a 10^{-4} M solution of **RR-TTF** in TCE/MCH, 1/99 (v/v), showed characteristic spectroscopic features of helically assembled TTF monomers. Although the changes in UV/Vis absorption is minimal, a bisignated CD signal with zero-crossing at the absorption maximum (293 nm) confirmed the
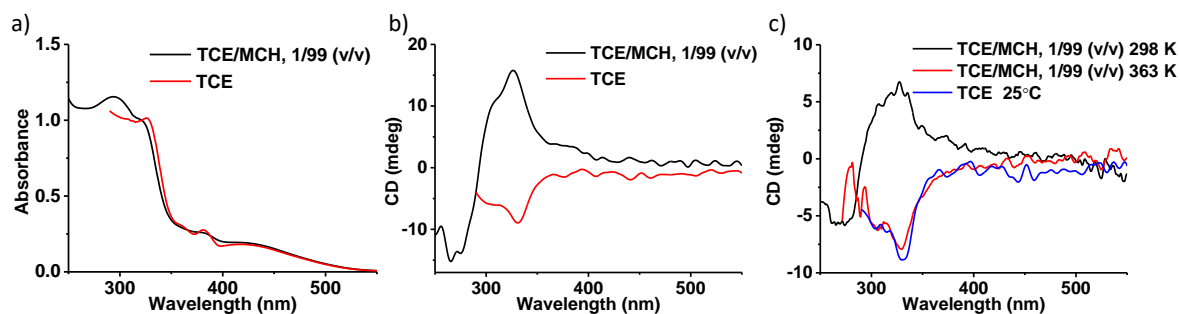
Figure 7.1. a) Absorption spectra and b) CD spectra of monomeric **RR-TTF** in TCE and self-assembled **RR-TTF** in TCE/MCH, 1/99 (v/v) ([**RR-TTF**] = 10^{-4} M). b) Temperature-dependent CD spectra of **RR-TTF** in self-assembled state (TCE/MCH, 1/99 (v/v), [**RR-TTF**] = 10^{-4} M).
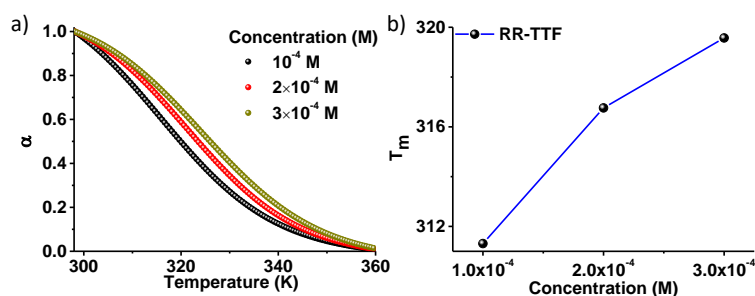
Figure 7.2. Mechanistic investigation of **RR-TTF** self-assembly. a) Temperature-dependent degree of aggregation (α) obtained by monitoring the CD changes at 375 nm (TCE/MCH, 1/99 (v/v), [**RR-TTF**] = 10^{-4} M, dT/dt = 1 Kmin^{-1}, l = 2 mm) for self-assembled solution of **RR-TTF** at different concentration showing an isodesmic mechanism of polymerization. b) Plot of T_m (melting temperature) against different concentrations of **RR-TTF**, showing increasing trend.

Concentration (M)	ΔH_e (kJ/mol)	ΔS_e (kJ/molK)	ΔH_{nuc} (kJ/mol)	T_e (K)
1×10^{-4} M	-90.33±0.33	-0.21±0.001	0	311.31±0.35
2.0×10^{-4} M	-96.66±0.36	-0.23±0.001	0	316.76.83±0.11
3.0×10^{-5} M	-96.76±0.45	-0.23±0.001	0	319.57±0.128

Table 7.1. Thermodynamic parameters (ΔH_e = enthalpy of elongation, ΔS_e = entropy of elongation, ΔH_{nuc} = enthalpy of nucleation) obtained by fitting the temperature-dependent degree of aggregation of **RR-TTF** with an isodesmic polymerization model.

the presence of excitonically coupled, helically stacked TTF chromophores (Figures 7.1a and 7.1b). Thus, supramolecular polymerization of **RR-TTF** monomers was performed under thermodynamic conditions by cooling the **RR-TTF** from its monomeric state at high temperature (363 K) (Figure 7.1c) to 298 K with a slow temperature gradient of 1 K/min. Probing the self-assembly process using the changes in CD intensity at 375 nm showed a sigmoidal growth which could be well fitted to an isodesmic model with a melting temperature (T_m) of 311 K, which showed a gradual increase with increase in concentration (Figure 7.2, and Table 7.1).

To investigate the charge-transfer interaction driven diastereomeric assembly, we have performed two component supramolecular copolymerization of **RR-** / **SS-NDI** acceptors with **RR-TTF** donor under thermodynamic conditions. Injecting a monomeric mixture of **RR-NDI-RR-TTF** (1:3) and **SS-NDI**:**RR-TTF** (1:1.5) in TCE into MCH (TCE/MCH, 1/99 (v/v)) yielded a green colored solution, characteristic of NDI-TTF CT complexation.[4a,12c] The respective mixture of **RR-NDI** or **SS-NDI** and **RR-TTF** in TCE/MCH, 99/1 (v/v) solvent mixture were heated to 363 K and slowly cooled with a temperature gradient –dT/dt = 1K/min to synthesize the supramolecular copolymers under thermodynamic conditions devoid of any kinetic traps. The formation of charge-transfer copolymers was also evident from the reversal of the intensity of the vibronic peaks characteristic of the transformation from NDI homopolymers to an alternate donor-acceptor arrangement (Figures 7.3a and 7.3b). Both **RR-NDI**:**RR-TTF** and **SS-NDI**:**RR-TTF** supramolecular copolymers showed CT absorption but with remarkably different absorption maxima of 706 nm and 800 nm, respectively (Figure 7.3c). This strikingly different charge-transfer absorption maxima for the two assemblies conjecture towards a different molecular organization, unlike the previously reported NDI-DAN systems, where the strong self-recognizing chiral monomers lead to an exclusive
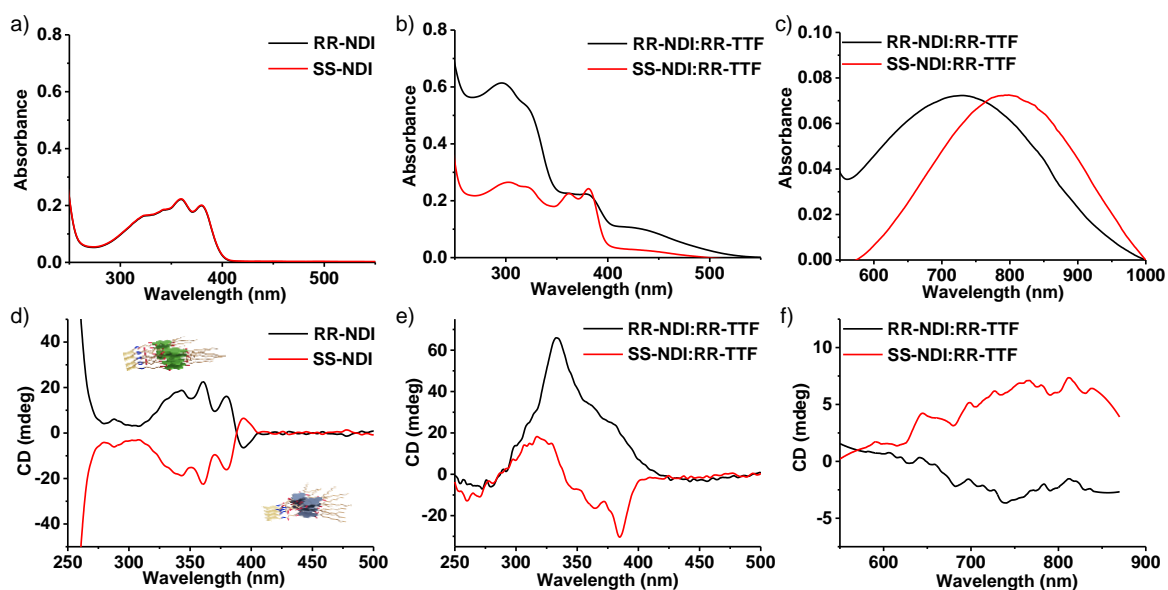
Figure 7.3. Absorption spectra of self-assembled solution of a) **RR-NDI** and **SS-NDI** and of b) **RR-NDI**:**RR-TTF** (1:3) and **SS-NDI**:**RR-TTF** (1:1.5) (l = 2 mm) CT copolymers. c) Respective CT absorption band of **RR-NDI**:**RR-TTF** (1:3) and **SS-NDI**:**RR-TTF** (1:1.5) CT copolymers. CD spectra of self-assembled solution of d) **RR-NDI** and **SS-NDI** and of e) **RR-NDI**:**RR-TTF** (1:3) and **SS-NDI**:**RR-TTF** (1:1.5) CT copolymers (l = 2 mm). f) CD spectra showing optically activity of the CT band and opposite CD signal for **RR-NDI**:**RR-TTF** (1:3) and **SS-NDI**:**RR-TTF** (1:1.5) CT copolymers (l = 10 mm, TCE/MCH, 1/99 (v/v), [**RR-NDI**] = [**SS-NDI**] = 10^{-4} M).
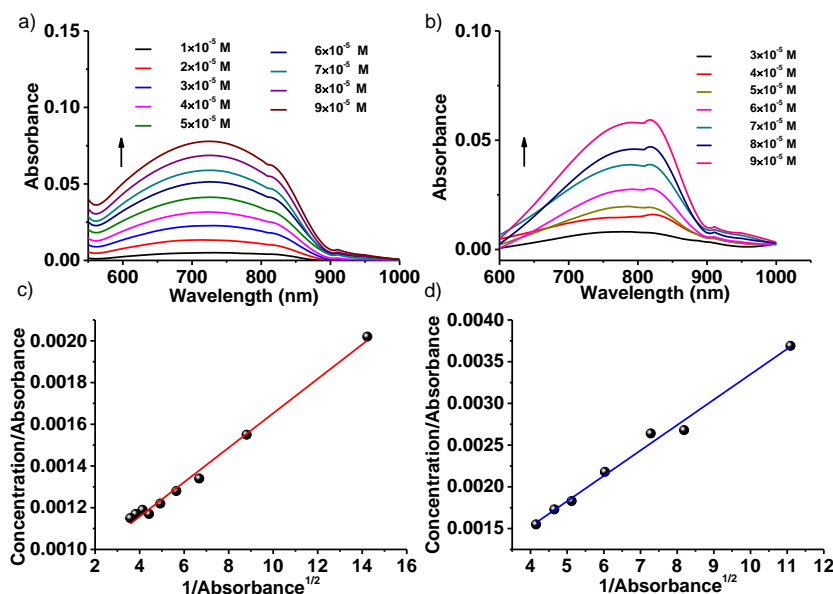
Figure 7.4. Association constant calculation of two charge-transfer copolymers. Concentration-dependent absorption spectra of CT band for a) **RR-NDI**:**RR-TTF** (1:3) and b) **SS-NDI**:**RR-TTF** (1:1.5) CT copolymers (TCE/MCH, 1/99 (v/v), [**RR-NDI**] = [**SS-NDI**] = 10^{-4} M, l = 10 mm). Plot of Concentration/Absorbance against 1/Absorbance$^{1/2}$ for c) **RR-NDI**:**RR-TTF** (1:3) and for d) **SS-NDI**:**RR-TTF** (1:1.5) CT copolymers.

	Binding Constant (M^{-1})
RR-NDI:**RR-TTF** (1:3)	2.7×10^4
SS-NDI:**RR-TTF** (1:1.5)	3.3×10^3

Table 7.2. Association constants of **RR-NDI**:**RR-TTF** (1:3) and **SS-NDI**:**RR-TTF** (1:1.5) charge-transfer copolymers.
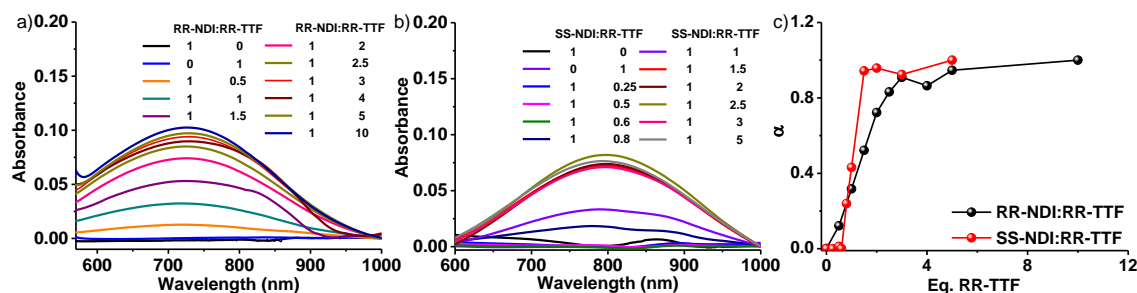
Figure 7.5. Absorption spectra of the CT band (TCE/MCH, 1/99 (v/v), [**RR-NDI**] = [**SS-NDI**] = 10^{-4} M, l = 10 mm) of a solution containing a) **RR-NDI** and b) **SS-NDI** with different equivalent of **RR-TTF**. c) Plot of absorbance changes of the charge-transfer band of **RR-NDI** (726 nm) and **SS-NDI** (800 nm) against different equivalent of **RR-TTF** showing formation of the charge-transfer assembly. (TCE/MCH, 1/99 (v/v), [**RR-NDI**] = [**SS-NDI**] = 10^{-4} M, l = 10 mm).

homochiral supramolecular polymerization. Circular dichroism (CD) spectra of the supramolecular CT copolymers showed opposite but not mirror image CD signals at the π-π* absorption maxima at 380 nm and 360 nm (Figures 7.3d, and 7.3e). Unlike the enantiomeric NDI derivatives synthesized CT assemblies of **RR-NDI**:**RR-TTF** and **SS-NDI**:**RR-TTF**

depicted CD maxima at 334 and 380 nm. An intriguing observation is the occurrence of an optically active CT band, which is opposite and unequal in magnitude, corroborating with the reverse and different CD signals at NDI region, which is indicative of diastereomeric interactions (Figure 7.3e). Optically active CT bands are rare in literature for supramolecular assemblies.[11] Moreover, this is a unique example where CD active CT bands unambiguously pertain to the diastereomeric stacks in the solution phase. We envisage that a combination of strong electronic complementary of the two monomers and chiral bias of the cyclohexane diamine core leads to this unprecedented diastereoselective supramolecular polymerization process. Diastereomeric relationship between the two CT assembly gets manifested in their differential stability, which showed a higher association constant for **RR-NDI**:**RR-TTF** CT assembly (2.7×10^4 M^{-1}) in comparison to **SS-NDI**:**RR-TTF** (3.3×10^3 M^{-1}) CT assembly (Figure 7.4 and Table 7.2).[13] Interestingly the titration experiments of **RR-TTF** with the enantiomeric NDI acceptors reflected their difference in association constant, (Figure 7.5) where more than 0.6 equivalent of **RR-TTF** was required for **SS-NDI**:**RR-TTF** CT assembly to drive the equilibrium towards a CT complexed state. Below 0.6 equivalent stereoselective supramolecular polymerization takes over the CT complex state of **SS-NDI**:**RR-TTF** assembly. In contrast to that, higher association constant of **RR-NDI**:**RR-TTF** pair induced CT assembly even with 0.2 equivalent of **RR-TTF**, which eventually gets saturated with 3 equivalent of **RR-TTF**.

7.3.2. Mechanistic Investigations:

We have further investigated the mechanistic aspects of this diastereoselective supramolecular polymerization process under thermodynamic conditions by probing spectroscopic changes during the assembly process. In an attempt to do so, the diastereomeric CT assemblies were heated to 363 K to access the monomeric state (Figures 7.6a, 7.6b and 7.6c). Subsequently, we have probed the self-assembly following the temperature-dependent CD changes (375 nm) for **RR-NDI**:**RR-TTF** and for **SS-NDI**:**RR-TTF** with a cooling rate of 1 K/min. Temperature-dependent degree of aggregation (α) for **RR-NDI**:**RR-TTF** followed a sigmoidal transition that could be fitted to an isodesmic mechanism of self-assembly to yield a T$_m$ of 319 K (Figures 7.6e and 7.6f). On the other hand, the temperature-dependent degree of aggregation for **SS-NDI**:**RR:TTF** (1:1.5) followed a two-step nucleation-elongation process which was fitted using cooperative nucleation-elongation assembly with a T$_e$ (elongation temperature) of 325 K. On comparing with the cooperative curve for the formation of **SS-NDI** stacks or the

isodesmic mechanism for the formation of **RR-TTF** stacks (Figures 7.6e and 7.6f) we have found the T_m and T_e vary by 3 K and 19 K respectively (Table 7.3, and 7.4). To prove that we
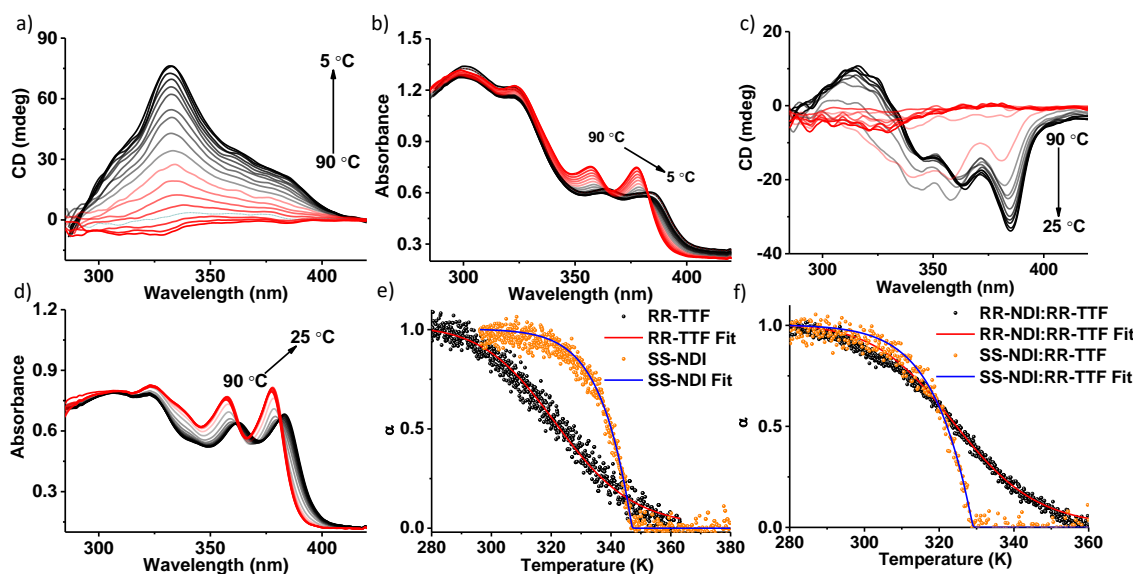
Figure 7.6. Mechanistic investigations of formation of diastereomeric charge-transfer assemblies. Temperature-dependent a) CD and b) absorption spectra of **RR-NDI**:**RR-TTF** (1:3) CT copolymer. Temperature-dependent c) CD and d) absorption spectra of **SS-NDI**:**RR-TTF** (1:1.5) CT copolymer. e) Plot of CD spectral changes (375 nm) with temperature for self-assembled **SS-NDI** and **RR-TTF**, demonstrating sigmoidal cooling curve for **RR-TTF** assembly and non-sigmoidal cooling curve for **SS-NDI** assembly. f) Plot of CD spectral changes (375 nm) with temperature for **RR-NDI**:**RR-TTF** (1:3) and **SS-NDI**:**RR-TTF** (1:1.5) charge-transfer copolymers showing sigmoidal cooling curve for **RR-NDI**:**RR-TTF** CT copolymers and non-sigmoidal cooling curve for **SS-NDI**:**RR-TTF** CT copolymers. (TCE/MCH, 1/99 (v/v), [**RR-NDI**] = [**SS-NDI**] = 10^{-4} M, dT/dt =1 Kmin^{-1}, l = 2 mm).

Concentration (M)	**RR-NDI**:**RR-TTF**	ΔH_e (KJ/mol)	ΔS_e (KJ/molK)	ΔH_{nuc} (KJ/mol)	Cooperativity Factor	T_m (K)
10^{-4}	0:3	-75.21±0.99	-0.16±0.002	0.00±0.00	1	316±0.26
10^{-4}	1:0	-45.26±0.24	-0.05±0.001	-29.41±0.63	0.99	345±0.06
10^{-4}	1:3	-88.41±0.61	-0.20±0.001	0.00±0.00	1	319±0.11

Table 7.3. Thermodynamic parameters obtained from fitting of cooling curves of **RR-NDI**:**RR-TTF** at different **RR-TTF** equivalent in TCE/MCH, 1/99 (v/v).

Concentration (M)	**SS-NDI**:**RR-TTF**	ΔH_e (KJ/mol)	ΔS_e (KJ/molK)	ΔH_{nuc} (KJ/mol)	Cooperativity Factor	T_m (K)
10^{-4}	0:3	-75.21±0.99	-0.16±0.002	0.00±0.00	1	316±0.26
10^{-4}	1:0	-45.43±0.54	-0.05±0.002	-27.31±0.66	0.99	344.91±0.08
10^{-4}	1:1.5	-107.4±0.20	-0.23±0.006	-13.88±0.56	0.99	325.72±0.18

Table 7.4. Thermodynamic parameters obtained from fitting of cooling curves of **SS-NDI**:**RR-TTF** at different **RR-TTF** equivalent in TCE/MCH, 1/99 (v/v).
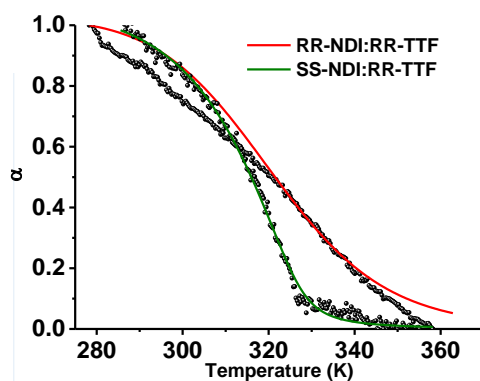
Figure 7.7. Mechanistic investigations of formation of diastereomeric charge-transfer assembly. Plot of absorption spectral changes with temperature for coassembled solution of **RR-NDI**:**RR-TTF** (1:3) and **SS-NDI**:**RR-TTF** (1:1.5), monitored at charge-transfer band showing sigmoidal cooling curve for **RR-NDI**:**RR-TTF** and non-sigmoidal cooling curve for **SS-NDI**:**RR-TTF**. (TCE/MCH, 1/99 (v/v), [**RR-NDI**] = [**SS-NDI**] = 10^{-4} M, dT/dt = 1 Kmin^{-1}, l = 10 mm).

are not monitoring individual TTF or NDI growth during mechanistic investigations, we probed the temperature-dependent absorbance changes at the respective CT Band (726 nm for **RR-NDI**:**RR-TTF** and 800 nm for **SS-NDI**:**RR-TTF**) which follows the same trend as that of that of obtained by monitoring the CD spectral changes (Figure 7.7).

7.3.3. Morphological Investigations:

Morphological investigation revealed effect of diastereomeric interactions on macroscopic scale as well. Transmission electron microscopy (TEM) of a 10^{-4} M solution of **RR-NDI**:**RR-TTF** (1:3) in TCE/MCH, 1/99 (v/v) revealed the formation of large sheets with widths ranging from 5 μm to 20 μm (Figures 7.8a and 7.8b), whereas TEM images of 10^{-4} M solutions of **SS-NDI**:**RR-TTF** (1:1.5) in TCE/MCH, 1/99 (v/v) showed the formation of bundles of long one dimensional (1D) fibers (Figure 7.9a). Tapping mode Atomic Force Microscopy (AFM) images showed the presence of multiple layers in the sheets (Figure 7.8c) for **RR-NDI**:**RR-TTF** CT nanostructures with heights of 3.4 nm and long 1D supramolecular polymer for **SS-NDI**:**RR-TTF** CT nanostructures with hight of 3.10 nm (Figure 7.9b). Dynamic light scattering (DLS) measurements also confirmed the differences in sizes of the two diastereomeric assemblies in which the average hydrodynamic diameter of the **SS-NDI**:**RR-TTF** assemblies was found to be around 100±34 nm while that of **RR-NDI**:**RR-TTF** was around 1000±134 nm (Figure 7. 9c).

226
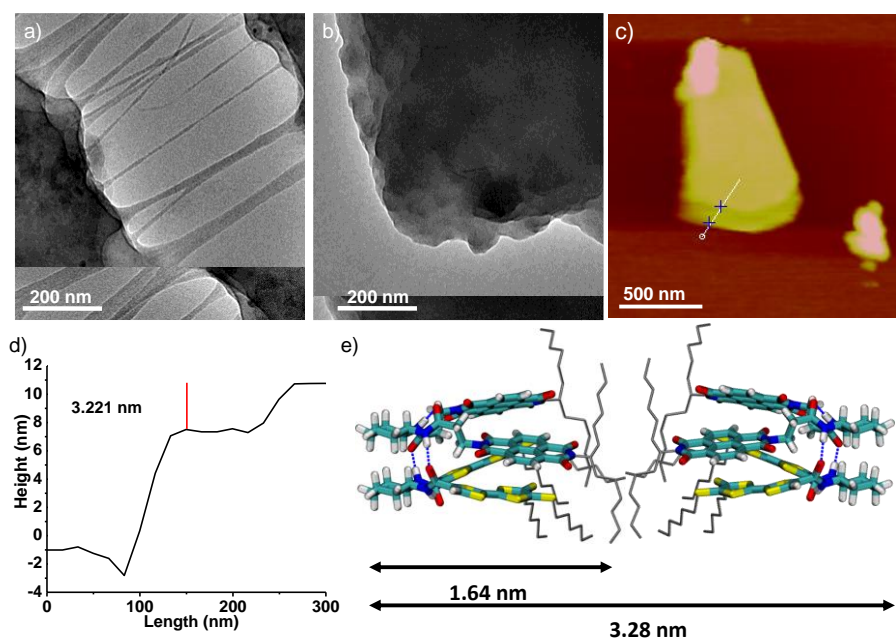
Figure 7.8. a), b) TEM (sample was stained with uranyl acetate for TEM) showing the sheet structure of **RR-NDI**:**RR-TTF** (1:3) CT copolymers. c) AFM image of **RR-NDI**:**RR-TTF** (1:3) CT copolymers. d) Height analysis of the sheet structures showing the sheets are having thickness of 3.22 nm, which correlates well with the e) Schematic representation and distance of two **RR-NDI**:**RR-TTF** CT complex interacting via alkyl alkyl interaction to result in a sheet structure.
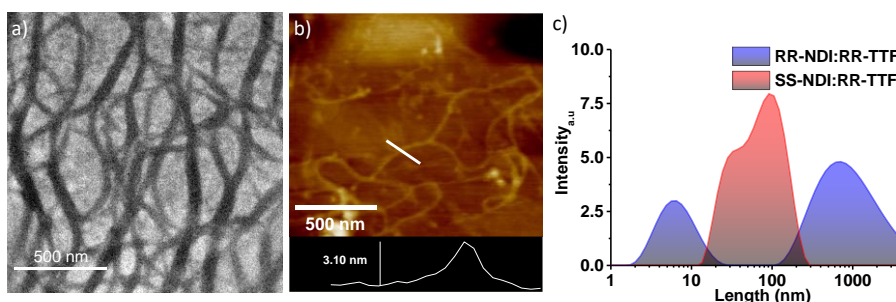
Figure 7.9. a) TEM and b) AFM images of **SS-NDI**:**RR-TTF** (1:1.5) CT copolymer, showing 1D supramolecular polymers. c) DLS data for self-assembled solution of **RR-NDI**:**RR-TTF** (1:3) and **SS-NDI**:**RR-TTF** (1:1.5), showing larger size of aggregates for **RR-NDI**:**RR-TTF** (TCE/MCH, 1/99 (v/v), [**RR-NDI**] = 10^{-4} M , l = 10 mm).

7.3.4. Computational Investigations:

To shed light on the molecular level origin of different spectroscopic and microscopic properties of the two diastereomeric assembly, we have performed molecular modelling studies both on a dimer and oligomer of the CT assemblies. Molecular dynamics simulations performed on dimers of both the CT assemblies shows, whereas in the case of **RR-NDI**:**RR-TTF** CT pair the two chromophores are nicely packed using intermolecular hydrogen bonding

of two amide groups and CT complexation, (Figures 7.10a and 7.10c) for the **SS-NDI**:**RR-TTF** CT pair the packing is distorted containing only one intermolecularly hydrogen-bonded
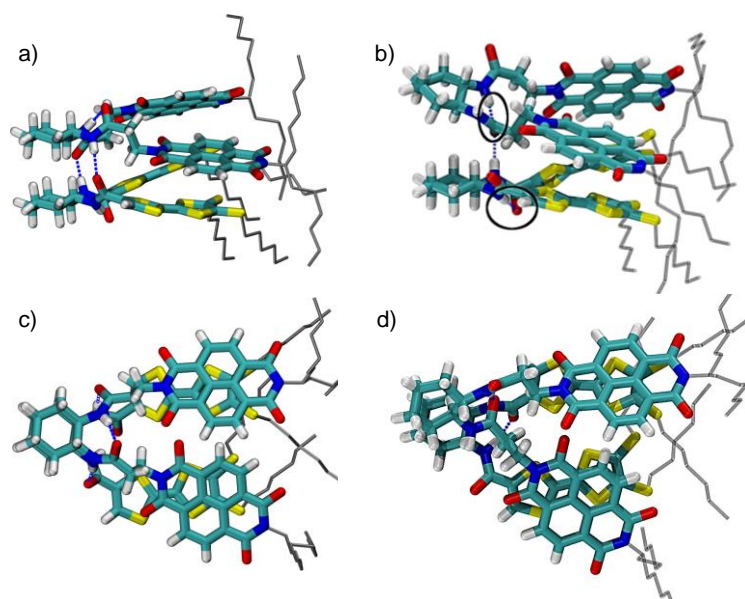
Figure 7.10. Organization of side view of a) **RR-NDI**:**RR-TTF** and b) **SS-NDI**:**RR-TTF** pair and top view of c) **RR-NDI**:**RR-TTF** and d) **SS-NDI**:**RR-TTF** pair depicting distorted nature of arrangement in case of **SS-NDI**:**RR-TTF** CT pair. The blue dotted lines represent the intermolecular hydrogen bonding between the donor and acceptor.

amide group between the dimer (Figures 7.10b and 7.10c). Due to such difference in packing, the homochiral dimer has seen to be 16 kcal/mol more stable than the heterodimer which could be correlated with the calculated association constant difference between the two CT assembly (2.7×10^4 M^{-1} and 3.3×10^3 M^{-1}). The difference of packing in dimer level is further gets manifested in the extended self-assembled molecular organization of the two CT assemblies. For the **RR-NDI**:**RR-TTF** CT assembly, it forms extended assembly by using both hydrogen bonding and CT interaction between donor and acceptor (Figures 7.11a and 7.11b). In contrast to that, the extended self-assembled structure of **SS-NDI**:**RR-TTF** CT interactions are still present, but the number of such pairs is less when compared to an oligomer of **RR-NDI**:**RR-TTF** pair (Figures 7.11b and 7.11c). For **SS-NDI**:**RR-TTF** CT nanostructures organization of the cyclohexane chromophores are not in π- π fashion and the π- π distance is more (3-7 A˚ for **RR-NDI**:**RR-TTF** and 3-15 A˚ for **SS-NDI**:**RR-TTF**), and the distribution is wider compared to homo one (Figure 7.12). Also, the patterns of hydrogen bonding are different in the two cases. Thus, the two diastereomeric CT assemblies are having a different arrangement of the
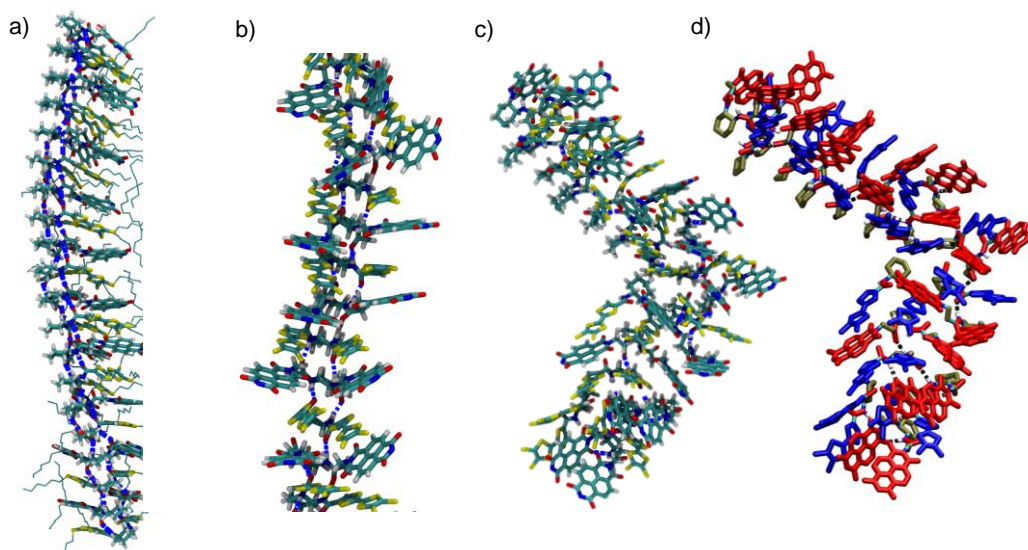
Figure 7.11. Organization of a) **RR-NDI**:**RR-TTF** and c) **SS-NDI**:**RR-TTF** self-assembled stacks representing organized packing with continuous hydrogen bonding in case of **RR-NDI**:**RR-TTF** CT assembly, where as in case of **SS-NDI**:**RR-TTF** assembly the CT interaction is not continuous throughout the stacks and thus results in distorted arrangement of the stacks. b) and d) represents zoomed in view of **RR-NDI**:**RR-TTF** and **SS-NDI**:**RR-TTF** stacks, respectively.
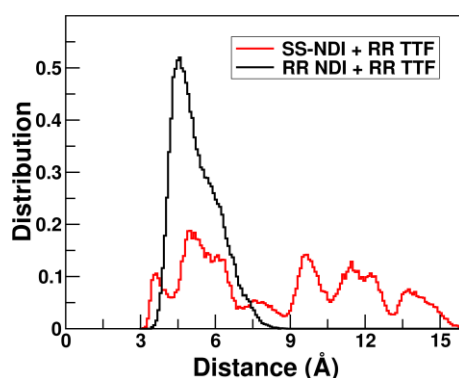
Figure 7.12. Distribution of π-π stacking distance of **RR-NDI**:**RR-TTF** and **SS-NDI**:**RR-TTF** CT copolymers.

donor and acceptor, which results in the differences in spectroscopic properties as mentioned earlier. The distorted structure of the **SS-NDI**:**RR-TTF** is unable to form a continuous network of hydrogen bonds, thus results in the formation of short fibers, contrary to that the well-ordered arrangement of **RR-NDI**:**RR-TTF** oligomers gives rise to higher ordered assembly and morphology. Also, in the case of **SS-NDI**:**RR-TTF** CT oligomers due to the discreteness of the CT pairs, the growth is mainly governed by the hydrogen bonding and thus follows a cooperative pathway of growing. Since the **RR-NDI**:**RR-TTF** oligomers contain a continuous network of hydrogen bonding as well as CT interaction, these two forces might not act cooperatively, giving rise to an isodesmic pathway of growth for **RR-NDI**:**RR-TTF** CT oligomers.

7.3.5. Diastereomeric Resolution using Diastereomeric CT Assemblies:
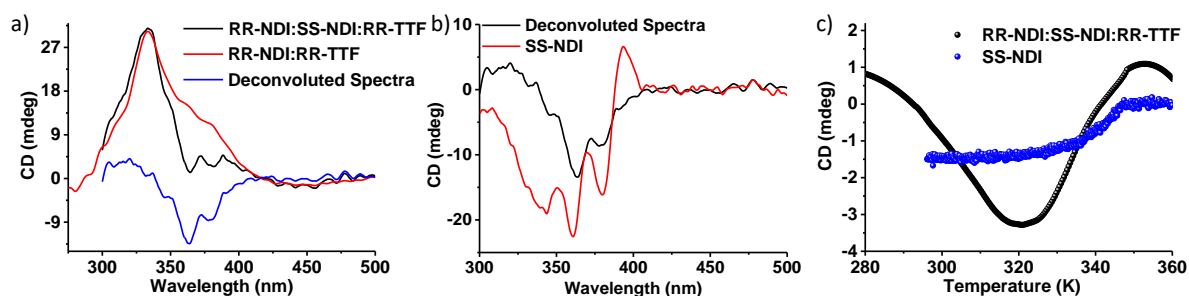
Figure 7.13. a) CD spectrum of tricomponent solution of **RR-NDI**, **SS-NDI** and **RR-TTF** (1:1:1.5). b) Comparison of deconvoluted CD spectrum (obtained by subtracting **RR-NDI:RR-TTF** (1:1.5) CD spectrum from the tricomponent CD spectrum) with self-assembled **SS-NDI** CD spectrum. c) Plot of CD changes at 375 nm with temperature for tricomponent solution of **RR-NDI**, **SS-NDI** and **RR-TTF** (1:1:1.5) showing presence of **RR-NDI:RR-TTF** charge-transfer assembly and **SS-NDI** assembly. (TCE/MCH, 1/99 (v/v), [**RR-NDI**] = [**SS-NDI**] = 10^{-4} M, dT/dt = 1 Kmin^{-1}, l = 2 mm).

After successfully synthesizing the CT nanostructures individually, we sought to looking into the formation of diastereomeric CT assemblies in a tricomponent mixture (**RR-NDI**, **SS-NDI**, **RR-TTF**). An equimolar mixture of **RR-**/**SS-NDI** (c = 10^{-4} M) with 1.5 equivalents of **RR-TTF** indicated the formation of **SS-NDI** assemblies along with the formation of **RR-NDI:RR-TTF** stacks which were analysed using the different and opposite CD signal of **RR-NDI:RR-TTF** CT assembly and **SS-NDI** homopolymer. Subtraction of previously shown **RR-NDI:RR-TTF** (1:1.5) CD signal from the tricomponent mixture implied presence of **SS-NDI** homo assembly, which has the similar CD signal as that of pure **SS-NDI** assembly of same concentration (Figures 7.13a and 7.13b). More over temperature-dependent self-assembly obtained via monitoring the CD changes at 375 nm showed the presence of two transitions (Figure 7.13c). The initial transition resembles a two-step nucleation-elongation assembly with a T_e of 348 K which matched well with the T_e of pure **SS-NDI** homopolymers (345 K) of same concentration. Thus, we infer existence of 100 % **RR-NDI:RR-TTF** CT assemblies along with 100 % **SS-NDI** homopolymer with lower equivalents of donor. To drive the tricomponent mixture towards diastereomeric CT assemblies thus we have utilized 5 equivalents of donor to ensure the complete complexation of both enantiomeric acceptors. Subtracted CD spectra of **RR-NDI:RR-TTF** (1:3) from the tricomponent CD spectra of **RR-NDI,SS-NDI** and **RR-TTF** (1:1:5) implied presence of **SS-NDI:RR-TTF** CT nanostructure along with **RR-NDI:RR-TTF** CT nanostructures (Figures 7.14a and 7.14b). The subtracted CD spectra matched well and has the similar CD intensity (-35 mdeg at 385 nm) as that of individual CD spectra of **SS-NDI:RR-**
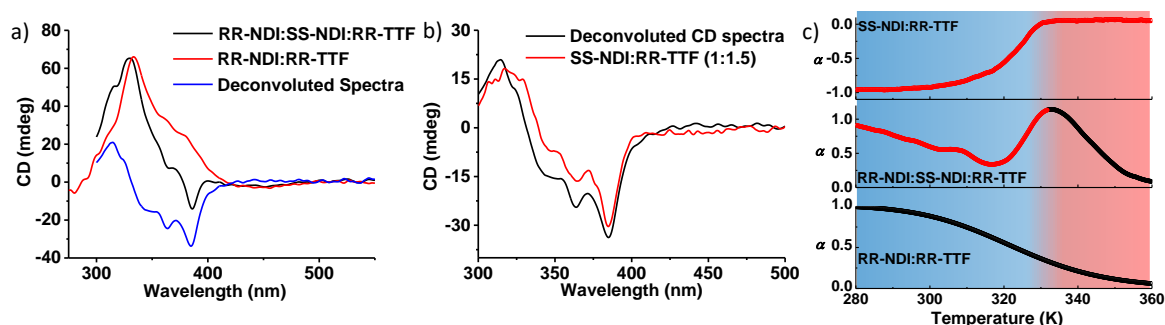
Figure 7.14. a) CD spectrum of tricomponent mixture of **RR-NDI**, **SS-NDI**, **RR-TTF** (1:1:5) and deconvoluted CD spectrum obtained by subtracting **RR-NDI**:**RR-TTF** (1:3) CD spectrum, from **RR-NDI**:**SS-NDI**:**RR-TTF** (1:1:1.5) CD spectrum, showing identical CD spectra as that of **SS-NDI**:**RR-TTF** CT assembly. b) Comparison of deconvoluted CD spectrum of the tricomponent mixture with **SS-NDI**:**RR-TTF** (1:1.5) CD spectrum. c) Cooling curve of the tricomponent mixture obtained by monitoring the CD changes at 375 nm of **RR-NDI**, **SS-NDI**, **RR-TTF** (1:1:5) depicting an initial isodesmic growth followed by a cooperative growth which matches well with temperature-dependent growth of individual CT assembly of **RR-NDI**:**RR-TTF** (1:3) and **SS-NDI**:**RR-TTF** (1:1.5), suggesting presence of both individual **RR-NDI**:**RR-TTF** and **SS-NDI**:**RR-TTF** CT assembly in solution. (TCE/MCH, 1/99 (v/v), [**RR-NDI**] = [**SS-NDI**] = 10^{-4} M, l = 10 mm).

TTF (-30 mdeg at 385 nm) CT assemblies. Moreover, temperature-dependent self-assembly recorded for the tricomponent mixture following CD changes at 375 nm (1 K/min cooling rate) showed presence of two transition thus confirming presence of two species (Figure 7.14c). Since, **RR-NDI**:**RR-TTF** CT assembly follows a isodesmic mechanism of polymerization hence we observe an initial sigmoidal growth followed by a transition at around 328 K, which was ascribed due to the cooperative nucleation-elongation growth of **SS-NDI**:**RR-TTF** (T_e = 325 K) CT nanostructures. The transition temperature coincides well with individual CT assemblies. Hence both CD spectral analysis and temperature-dependent degree of aggregation conforms presence of independent diastereomeric stacks of **RR-NDI**:**RR-TTF** CT assembly and **SS-NDI**:**RR-TTF** CT assembly.

The presence of independent diastereomeric stacks encouraged us to look into the possibility of separation of the CT nanostructures using their differential properties. Since the two CT assemblies are having significant differences in size, we thought of utilizing size exclusion chromatography to resolve the diastereomeric stacks. To avoid any effect of dilution, we have coupled a spin filtration column filled with polystyrene size-exclusion bead with a pore size of 50-100 nm (Figure 7.15a). We anticipated **RR-NDI**:**RR-TTF** CT assemblies by virtue of larger size will get eluted from the column, whereas small size **SS-NDI**:**RR-TTF** CT assemblies will remain in the pores of polystyrene beads.

After equilibration of the column with TCE/MCH solvent mixture (TCE/MCH, 1/99 (v/v)) self-assembled solution of a tricomponent mixture containing the diastereomeric stacks in solution was added on top of the spin filtration column and centrifuged to take out the added
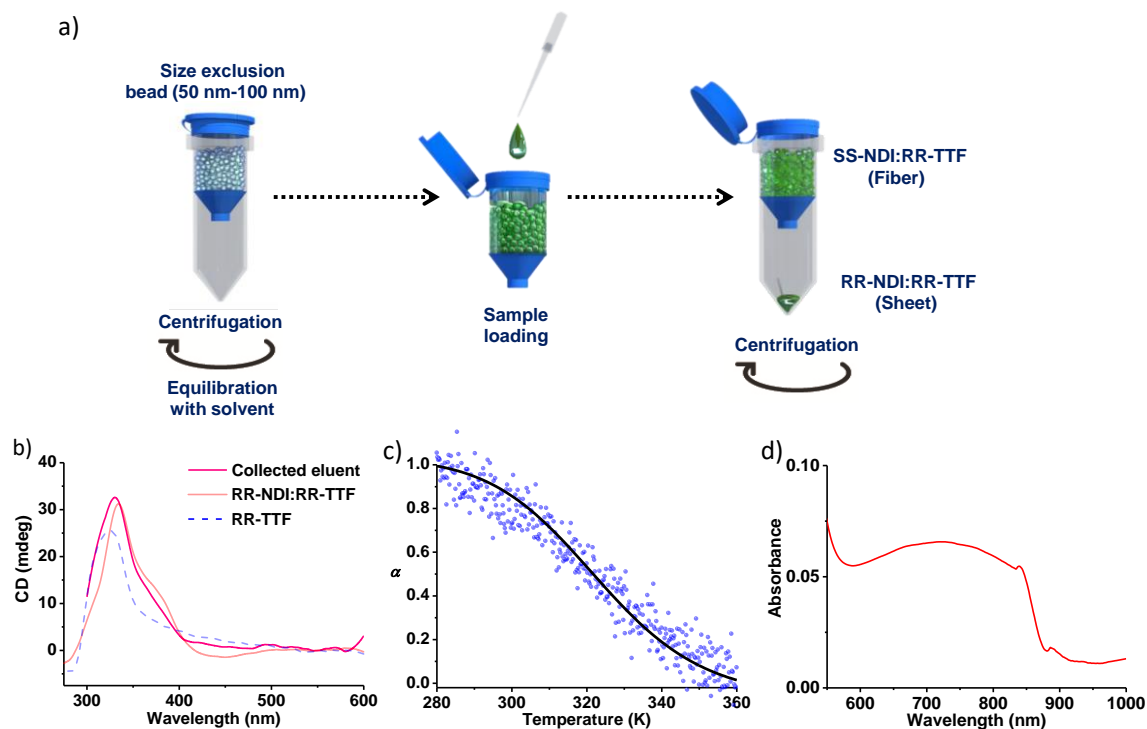
Figure 7.15. a) Schematic representation of diastereomeric resolution and separation of two CT nanostructures using size exclusion spin filtration chromatography. b) CD spectra and c) plot of CD spectral changes with temperature for the collected eluent after spin filtration column, demonstrating presence of **RR-NDI:RR-TTF** CT copolymer only. d) Absorption spectra of the charge-transfer band of the collected eluent showing presence of **RR-NDI:RR-TTF** CT copolymer. (TCE/MCH, 1/99 (v/v), $[\text{RR-NDI}] = [\text{SS-NDI}] = 10^{-4}$ M, dT/dt = 1 Kmin^{-1}, l = 2 mm).
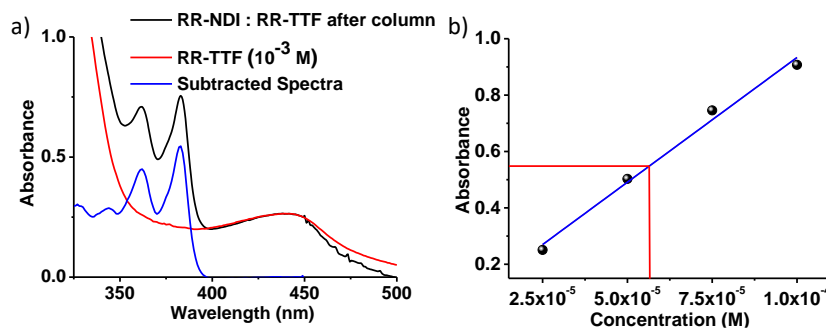
Figure 7.16. a) Deconvolution of collected eluent absorption spectrum by subtraction of **RR-TTF** absorption spectrum to get exclusive absorption spectrum of **RR-NDI**. b) Calibration curve of **RR-NDI** (375 nm) against concentration and concentration calculation of the recovered **RR-NDI** using the absorption spectrum of Figure 7.16a. (TCE/MCH, 1/99 (v/v), $[\text{RR-NDI}] = 10^{-4}$ M, l = 2 mm).
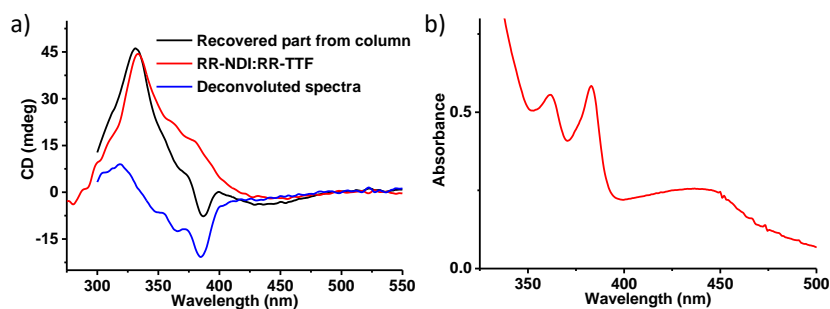
Figure 7.17. a) CD and b) absorption spectra of the recovered part from the column, showing presence of **SS-NDI:RR-TTF** CT copolymers. (TCE/MCH, 1/99 (v/v), l = 2 mm).

solvent (Figure 7.15a). Spectroscopic characterization of the eluent collected from the column chromatography unambiguously assigned the presence of **RR-NDI**:**RR-TTF** stacks exclusively. The CD spectrum matched well with that of the two-component **RR-NDI**:**RR-TTF** (Figure 7.15b). Moreover, the cooling curve of the eluent monitored at 375 nm showed isodesmic mechanism of self-assembly with T_m at 316 K, similar to that of **RR-NDI**:**RR-TTF** mixture (T_m = 319 K) (Figure 7.15c). The absorption spectrum shows a CT band at 726 nm pertaining to **RR-NDI**:**RR-TTF** mixture (Figure 7.15d). Further, we have subtracted the **RR-TTF** absorbance from collected eluent to decipher the absorbance of collected **RR-NDI** monomers, which was utilized to find out the concentration of resolved **RR-NDI**-monomer (c = 5.65×10^{-5}) using a concentration-dependent calibration curve for **RR-NDI** (Figure 7.16). Moreover, deconvoluted CD spectra obtained by subtracting the **RR-NDI**:**RR-TTF** mixture from the CD spectra of the recovered tricomponent mixture showed features of **SS-NDI:RR-TTF** CT copolymers (Figure 7.17).

7.4. Conclusion:

In conclusion, we have demonstrated a diastereomeric resolution of kinetically labile supramolecular stacks in solution. By exploiting the differences in the spectroscopic properties and morphological features, we could achieve resolution of helical supramolecular assemblies. The spectroscopic and mechanistic investigations enabled unambiguous assignment of the stacks. By a clever exploitation of the strength of associations of the two diastereomeric stacks, we could achieve either stereoselective polymerization (with lower donor equivalents) or a diastereomeric resolution from the same pool of donor-acceptor mixture.

7.5 Experimental section:

General Methods:

NMR Measurements: NMR spectra were recorded with a Bruker AVANCE 400 (400 MHz) Fourier transform NMR spectrometer with chemical shifts reported in parts per million (ppm) with respect to TMS. Splitting patterns are designated as s, singlet; d, doublet; bs, broad singlet; m, multiplet; t, triplet; q, quartet; quin, quintet and br, broad.

Optical Measurements: Electronic absorption spectra were recorded on a Perkin Elmer Lambda 900 UV-Vis-NIR Spectrometer. Circular Dichroism (CD) spectra and temperature-dependent CD spectra were recorded on a JASCO J-815 spectrometer where the sensitivity, time constant and scan rate were chosen appropriately. The temperature-dependent measurements were performed with a CDF-426S/15 Peltier-type temperature controller with a temperature range of 263-383 K and adjustable temperature slope.

Transmission Electron Microscopy (TEM): TEM measurements were performed on a JEOL, JEM 3010 operated at 300 kV. Samples were prepared by placing a drop of the solution on carbon-coated copper grids followed by drying at room temperature. The images were recorded with an operating voltage of 300 kV.

Field Emission Scanning Electron Microscopy (FE-SEM): FE-SEM measurements were performed on a NOVA NANO SEM 600 (FEI) by drop casting the solutions on glass substrate followed by drying under high vacuum at room temperature and was operated with an accelerating voltage of 5 kV.

High-Resolution Mass Spectrometry (HRMS): High-Resolution Mass Spectra (HRMS) were recorded on an Agilent 6538 Ultra High Definition (UHD) Accurate-Mass Q-TOF-LC/MS system using electrospray ionization (ESI) and Atmospheric Pressure Chemical Ionization (APCI) modes.

Matrix-Assisted Laser Desorption Ionization (MALDI): MALDI was performed on a Bruker daltonics Autoflex Speed MALDI TOF System (GT0263G201) spectrometer using α-Cyano-4-hydroxy-cinnamic acid (CCA) as the matrix.

Fitting of Cooling Curves: Cooperative fits were performed using MATLAB R2008b software. Though the codes pertain to one component systems, we have extrapolated them to two component systems, and the thermodynamic parameters thus obtained are well within accepted limits.

Separation Procedure of two CT Nanostructure: The separation was performed by using a spin filtration column bought from Thermo Fisher scientific (catalog no 89883). Size exclusion

beads of styrene-divinylbenzene were bought from sigma Aldrich (CAS Number 9003-70-7. Centrifugation was done on centrifuge 5424/5424 R of Eppendorf. The spin filtration column was filled with the size exclusion bead and equilibrated with 1 % TCE in MCH solution followed by centrifugation at 4000 RCF to take out the excess of solvent. The equilibrated column was loaded with 100 µl of the tricomponent mixture and centrifuged at 1000 RCF for 1 minute. The eluent was collected in an Eppendorf tube was further loaded into another fresh equilibrated column and again centrifuged at 1000 RCF. The eluent thus collected was used for UV and CD measurement.

7.6. Synthetic Schemes and Procedures:

Synthetic schemes for synthesis of **RR-TTF** is shown in Scheme 7.2 and Scheme 7.3. **RR-NDI**, **SS-NDI** was synthesized following previous reports.[14]

Synthetic Schemes:
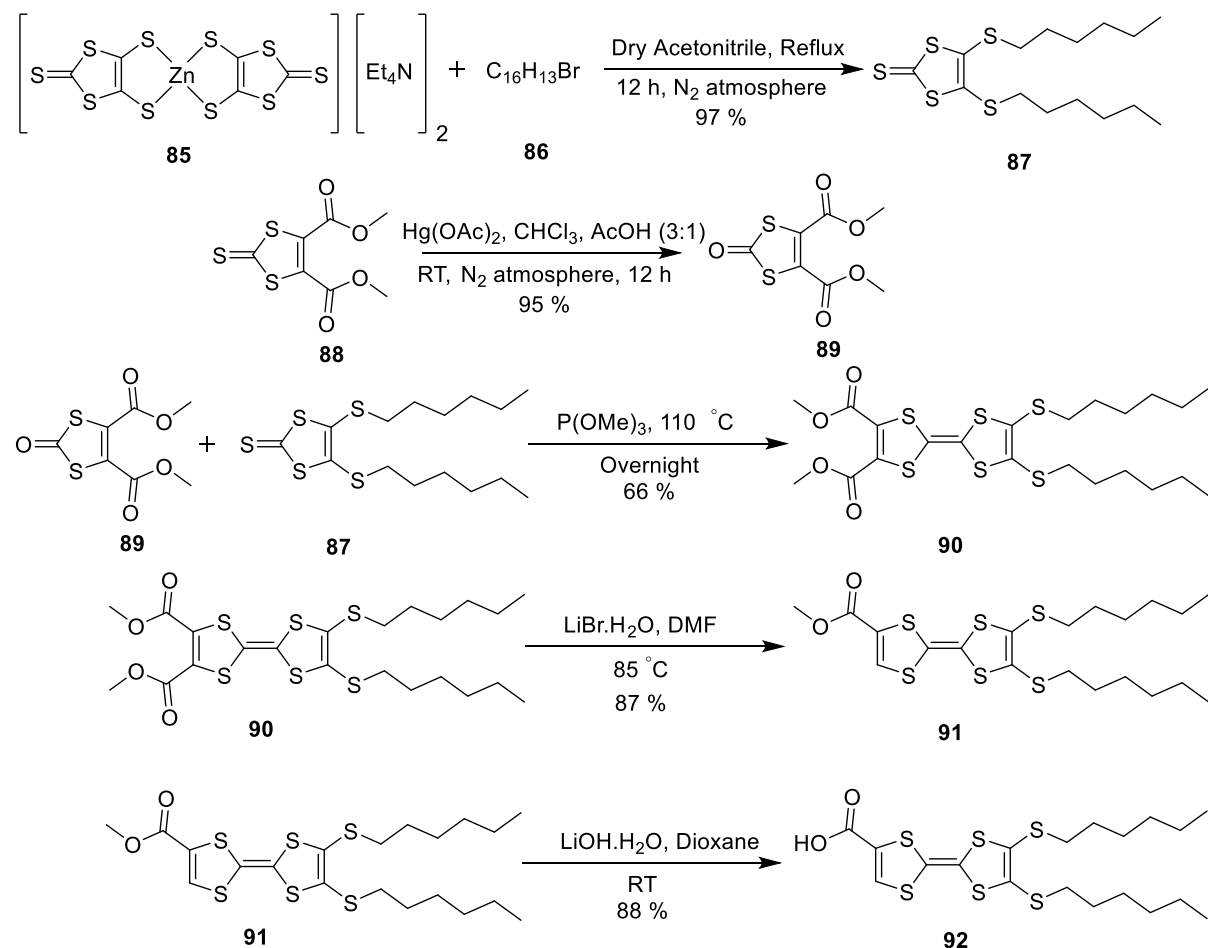
Scheme 7.2. Synthesis of molecule **92**.
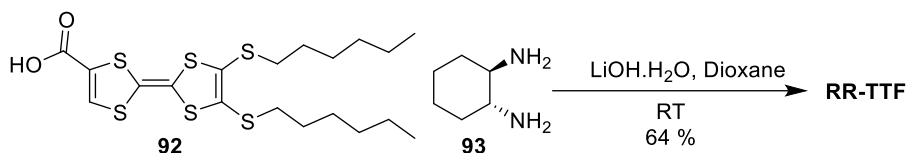
Scheme 7.3. Synthesis of molecules **RR-TTF**.

Synthetic Procedure:

Molecules **85** and **89** were synthesized following previously reported procedures.

Synthesis of 87: Molecule **85** (4 g, 5.57 mmol) and **86** (3.65 g, 22.28 mmol) were mixed under nitrogen in dry acetonitrile (100 ml). The solution was stirred overnight, changing color from red to brown. The solvent was then evaporated and concentrated. It was purified by column chromatography with elution with 10 % chloroform in hexane to obtain a brown liquid. R_f (Hexane) = 0.82. Yield: 97.53 %; ^{1}H NMR (400 MHz, CDCl$_3$, ppm): δ = 2.87 (t, J = 8 Hz, 4H), 1.66 (quin, J = 8 Hz, 4H), 1.42 (quin, J = 8 Hz, 4H), 1.27-1.35 (m, 8H), 0.89 (t, J = 8 Hz, 6H); ^{13}C NMR (100 MHz, CDCl$_3$, ppm): 211.64, 136.49, 36.91, 31.36, 29.75, 28.30, 22.61, 14.09; HRMS (ESI, positive mode): m/z calculated for C$_{15}$H$_{26}$S$_6$: 366.0638, found for **87**: 367.0714 [M+H]$^+$.

Synthesis of 90: **87** (2.43 g, 10.36 mmol) and **89** (1.90 g, 5.18 mmol) were mixed under nitrogen atmosphere in freshly distilled Trimethyl Phosphite (50 ml) and the mixture was heated at 110 °C for 10 hours. The solvent was evaporated under reduced pressure and then toluene was added (20 ml) and evaporated. The product was filtered on a silica column with DCM to remove remaining phosphite and then purified by column chromatography with elution with a gradient elution ranging from 5 % ethyl acetate in hexane to 15 % ethyl acetate in hexane, followed by size exclusion chromatography (biobeads , S-X1, CHCl$_3$) to get a brown liquid. R_f (Chloroform) = 0.83. Yield: 66.25 %; ^{1}H NMR (400 MHz, CDCl$_3$, ppm): δ = 3.84 (s, 6H), 2.80 (t, J = 7.2 Hz, 4H), 1.62 (quin, J = 6.8 Hz, 4H), 1.40 (quin, J = 6.8 Hz, 4H), 1.29-1.34 (m, 8H), 0.90 (t, J = 6.8 Hz, 6H); ^{13}C NMR: (100 MHz, CDCl$_3$, ppm): δ = 160.20, 132.28, 128.27, 113.31, 107.87, 53.60, 36.70, 31.57, 29.99, 28.46, 22.80, 14.28; HRMS (ESI, positive mode): m/z calculated for C$_{22}$H$_{32}$O$_4$S$_6$: 552.0625, found for **90**: 553.0695 [M+H]$^+$.

Synthesis of 91: **90** (1 g, 1.80 mmol) and LiBr (2.83 g) were mixed in DMF. The solution was stirred at 85.8 °C. The reaction was monitored by TLC. After completion of the reaction, DMF was evaporated and it was extracted with ethyl acetate and brine solution. The organic layer was collected and then purified by column chromatography by elution with a gradient ranging from 80 % hexane in chloroform to pure chloroform to obtain an orange liquid. R_f (Chloroform) = 0.69. Yield: 72.13 %; ^{1}H NMR (400 MHz, CDCl$_3$, ppm): δ = 7.34 (s, 1H), 3.81 (s, 3H), 2.79-

2.83 (m, 4H), 1.62 (quin, J = 7.2 Hz, 4H), 1.36-1.44 (m, 4H), 1.28-1.30 (m, 8H), 0.8-0.89 (m, 6H); ^{13}C NMR (100 MHz, CDCl$_3$, ppm): δ = 160.13, 132.30, 128.71, 128.46, 127.75, 112.22, 110.43, 53.07, 36.70, 30.09, 30.05, 28.54, 22.87, 14.35; HRMS (ESI, positive mode): m/z calculated for C$_{20}$H$_{30}$O$_2$S$_6$: 494.0570, found for **91**: 494.0567 [M]$^{+}$.

Synthesis of 92: LiOH (0.469 g, 17.7 mmol) solution in water was added dropwise to a stirring solution of **7** (0.750 g, 1.51 mmol) in THF. After stirring for 12 hours the mixture was diluted with 30 ml of diethyl ether and 30 ml of 0.5 M HCl and shaken vigorously. The resulting dark orange layer was separated and dried over sodium sulphate and evaporated to dryness. It was purified by column chromatography by elution with a gradient ranging from 40 % hexane in chloroform to 20 % methanol in chloroform to get a brown solid. R$_f$ (Methanol/Chloroform 1:10) = 0.16 Yield: 97.94 %. ^{1}H NMR (400 MHz, CDCl$_3$, ppm): δ = 7.26 (s, 1H), 4.65 (m, 4H), 2.56 (m, 4H), 1.2-1.5 (m, 12H), 0.8-0.99 (m, 6H); ^{13}C NMR: (100 MHz, CDCl$_3$, ppm): δ = 158.39, 132.47, 128.52, 128.67, 127.72, 112.28, 110.46, 36.53, 31.42, 30.11, 28.48, 22.86, 14.28; HRMS (ESI, positive mode): m/z calculated for C$_{19}$H$_{28}$O$_2$S$_6$: 480.0414, found for **92**: 480.0409 [M]$^{.+}$.

Synthesis of RR-TTF: In a 25 ml 2-necked RB, 250 mg (0.520 mmol) of **92** was taken in 2 ml of dry DMF. 174 mg (0.458 mmol) of HBTU was then added to the solution to activate the acid, followed by the addition of 81 mg (0.625 mmol) of N, N-Diisopropylethylamine (DIPEA). 28 mg (0.208 mmol) of **93** was dissolved in dry DMF in a separate RB and then injected into the reaction mixture. The reaction mixture was stirred at room temperature overnight. The completion of the reaction was checked by thin layer chromatography. The reaction mixture was cooled and then extracted with a saturated K$_2$CO$_3$ solution / diisopropyl ether solvent mixture. The organic layer was further extracted with brine / diisopropyl ether solvent mixture. The organic layer thus obtained was then collected, dried over Na$_2$SO$_4$, concentrated and dried in a rotary evaporator. The resulting crude product was then purified using column chromatography (silica gel) by elution with chloroform to obtain a sticky orange solid R$_f$ (Chloroform) = 0.29. Yield: 64 %. ^{1}H NMR (400 MHz, CDCl$_3$, ppm): δ = 7.01 (s, 2H), 6.28 (d, J = 7.6 Hz, 2H), 3.69-3.72 (m, 2H), 2.78-2.83 (m, 8H), 2.09-2.11 (m, 2H), 1.79 (br, 2H), 1.60-1.79 (m, 8H), 1.25-1.43 (m, 28H), 0.88 (t, J = 6 Hz, 12H); ^{13}C NMR (100 MHz, CDCl$_3$, ppm): δ = 160.41, 132.10, 128.51, 127.81, 126.33, 111.51, 110.57, 54.96, 36.66, 36.63, 32.25, 31.57, 29.98, 29.94, 28.47, 24.84, 22.80, 22.79; HRMS (ESI, positive mode): m/z calculated for C$_{44}$H$_{66}$N$_2$O$_2$S$_{12}$: 1038.1773, found for **RR-TTF**: 1038.1768 [M]$^{+}$.

7.7. Experimental Procedures:

Protocol of Sample Preparation: Spectroscopic grade solvents from commercial sources were used for performing all the studies at room temperature otherwise when mentioned. All solutions were prepared by injecting a monomeric solution of the compound in TCE to MCH. Stocks were prepared as 5×10^{-3} M in CHCl$_3$. Respective volume was taken in a vial and CHCl$_3$ was evaporated and the compound was re-dissolved in TCE and injected to MCH to adjust the final concentration to 2.5×10^{-5} M to get a self-assembled solution. All the solutions were annealed by slow heating and cooling to avoid any kinetic traps. Hence, all the observations are under thermodynamic conditions.

For co-assembly studies stock concentration of the acceptor was prepared as 10^{-3} M and donor as 5×10^{-3} M. respective volumes of donor and acceptor solution were transferred in another vial and chloroform was evaporated and re-dissolved in TCE and injected to MCH at room temperature to adjust the final concentration to 2.5×10^{-5} M of donor.

7.8. References:

[1] a) Ishida, Y.; Aida, T. *J. Am. Chem. Soc.* **2002**, *124*, 14017-14019. b) Sato, K.; Itoh, Y.; Aida, T. *Chem. Sci.* **2014**, *5*, 136-140.

[2] Kang, J.; Miyajima, D.; Mori, T.; Inoue, Y.; Itoh, Y.; Aida, T. *Science*, **2015**, *347*, 646-651.

[3] Odian, G. G. Principle of Polymerization, Third Ed.; Wiley, Ed.; 1991.

[4] a) Narayan, B.; Bejagam, K. K.; Balasubramanian, S.; George, S. J. *Angew. Chem. Int. Ed.* **2015**, *54*, 13053-13057. b) Sarkar, A.; Dhiman, S.; Chalishazar, A.; George, S. J. *Angew Chem. Int. Ed.* **2017**, *129*, 13955-13959.

[5] a) Springuel, G.; Leyssens, T. *Cryst. Growth Des.* **2012**, *12*, 3374-3378.

[6] a) Yashima, E.; Maeda, K. *Macromolecules*, **2008**, *41*, 3-12. b) Yashima, E.; Maeda, Y.; Okamoto, Y. *J. Am. Chem. Soc.* **1998**, *120*, 8895-8896. c) Morino, K.; Maeda, K.; Yashima, E. *Macromolecules*, **2003**, *36*, 1480-1486. d) Yashima, E.; Maeda, K.; Sato, O. *J. Am. Chem. Soc.* **2001**, *123*, 8159-8160. e) Maeda, K.; Mochizuki, H.; Watanabe, M.; Yashima, E. *J. Am. Chem. Soc.* **2006**, *128*, 7639-7650.

[7] a) Newman, M. S.; Lutz, W. B.; Lednicer, D. *J. Am. Chem. Soc.* **1955**, *77*, 3420-3421. b) Newman, M. S.; Lednicer, D. *J. Am. Chem. Soc.* **1956**, *78*, 4765-4770. c) Newman, M. S.; Lutz, W. B. *J. Am. Chem. Soc.* **1956**, *78*, 2469-2473. d) Newman, M. S.; Darlak, R. S.; Tsai, L. *J. Am. Chem. Soc.* **1967**, *89*, 6191-6193.

[8] a) Wynberg, H.; Groen, M. B. *J. Chem. Soc. Chem. Commun. D.* **1969**, 964-965. b) Groen, M. B.; Stulen, G.; Visser, G. J.; Wynberg, H. *J. Am. Chem. Soc.* **1970**, *92*, 7218-7219.

[9] a) Nguyen, J. Q.; Iverson, B. L. *J. Am. Chem. Soc.* **1999**, *121*, 2639-2640. b) Nalluri, S. K.; Berdugo, M.; Javid, C.; Frederix, N.; Pim, W. J. M.; Ulijn, R. V. *Angew. Chem., Int. Ed.* **2014**, *53*, 5882-5887. c) Peebels, C.; Piland, R.; Iverson, B. L. *Chem. Eur. J.* **2013**, *19*, 11598-11602. d) Babu, P.; Sangeetha, N. M.; Vijaykumar, P.; Maitra, U.; Rissanen, K.; Raju, A. R. *Chem. Eur. J.* **2003**, *9*, 1922-1932. e) Kumar, M.; Rao, K. V.; George, S. J. *Phys. Chem. Chem. Phys.* **2014**, *16*, 1300-1313. f) Lockey, R. S.; Iverson, B. L. *Nature* **1995**, *375*, 303-305.

[10] S. J. George, R. de Bruijn, Ž. Tomović, B. V. Averbeke, D. Beljonne, R. Lazzaroni, A. P. H. J. Schenning, E. W. Meijer, *J. Am. Chem. Soc.* **2012**, *134*, 17789-17796.

[11] a) Kumar, M.; Ushie, O. A.; George, S. J. *Chem. Eur. J.* **2014**, *20*, 5141-5148. b) Bhattacharjee, S.; Bhattacharya, S. *Chem. Asian J.* **2015**, *10*, 572-580. c) Mori, T.; Inoue, Y. *Angew. Chem., Int. Ed.* **2005**, *44*, 2582-2585. d) krishnan, S. B.; Gopidas, K. R. *Chem. Eur. J.* **2017**, *23*, 9600-9606.

[12] a) Nielsen, M. B.; Lomholt, C.; Becher, J. *Chem. Soc. Rev.* **2000**, *29*, 153-164. b) Canevet, D.; Salle, M.; Zhang, G.; Zhang, D.; Zhu, D. *Chem. Commun.* **2009**, 2245-2269.

[13] Das, A.; Ghosh, S. *Angew. Chem. Int. Ed.* **2014**, 53, 2038-2034.

[13] a) Pop, F.; Melan, C.; Danila, I.; Linares, M.; Beljonne, D.; Amabilino, D. B.; Avarvari, N. *Chem. Eur. J.* **2014**, *20*, 17443-1745. b) Colquhoun, H. M.; Goodings, E. P.; Maud, J. M.; Stoddart, J. F.; Wolstenholme, J. B.; Williams, J. D. *J. Chem. Soc. Perkin Trans.* **1985**, *2*, 607.

Chapter: 8

Impact of NDI Core-Substitution on the pH-Responsive Nature of Peptide-Tethered Luminescent Supramolecular Polymers

Chapter: 8

Impact of NDI Core-Substitution on the pH-Responsive Nature of Peptide-Tethered Luminescent Supramolecular Polymers

Abstract

The pH-responsive nature of two self-assembled core-substituted naphthalene diimide (cNDI)-peptide amphiphile conjugates is reported. The diethoxy-substituted NDI showed a pH-dependent assembly behaviour as expected, but surprisingly the isopropylamino- and ethoxy-substituted NDI based supramolecular polymer was stable towards acidification of the aqueous medium. These finding highlights how subtle changes in the molecular design of π-stacked chromophore-peptide conjugates have a drastic impact on their equilibrium structure and ultimately functional properties.
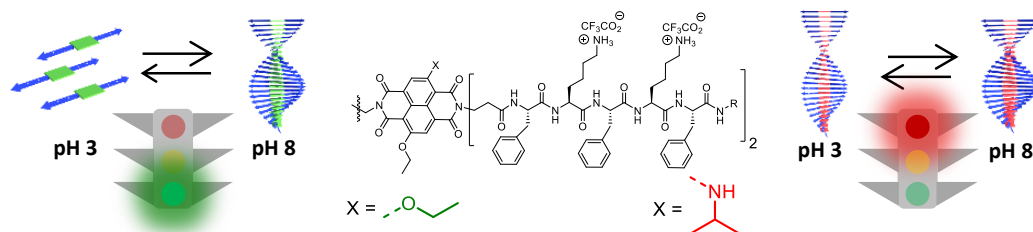
8.1. Introduction:

Self-assembly of peptide-chromophore conjugate amphiphiles has been investigated for the design of functional supramolecular materials, in order to combine the stimuli-responsive nature of self-assembled oligopeptide domain with the tunable optical properties of organic chromophores. Highly directional hydrogen bonding interactions between peptide segments as the structure-directing motif provide access to ordered supramolecular polymers.[1] Furthermore, the side-chains of the amino acid sequences are able to embed tunable stimulus-responsive features into the peptide-chromophoric assemblies. For example, peptide-naphthalene diimide based self-assembled nanotubes were shown to act as receptors for C_{60} and C_{70} fullerenes.[2] Parquette synthesized n-type chromophore-peptide conjugates for electron transfer and optoelectronic devices.[3] Ulijn and coworkers used enzyme-responsive peptide sequences to have structural, and spatiotemporal control over chromophore nanostructures using bio-catalytic reactions.[4] A controlled pH decrease coupled to pH-responsive peptide-chromophore molecules was designed by Adams and Smith to achieve programmable self-sorted photoconductive gels.[5] On the other hand, a collaborative effort the Stupp and Meijer labs showed that tethered chromophores can be used to probe the exchange kinetics of peptide amphiphiles.[6] In the present work, we synthesize peptide-naphthalene diimide conjugate amphiphiles, using the organic chromophore as a functional probe, but also as a rigid π-stacking segment. The latter therefore allows us to modulate the self-assembly and stimuli-responsive nature of the peptide sequences in order to control and direct the one dimensional (1D) supramolecular polymerization of the peptide-NDI amphiphiles in water.

Earlier from our group, we have reported the self-assembly of charged dendritic peptide sequences containing alternating phenylalanine (hydrophobic)-lysine (hydrophilic) sequences into 1D supramolecular polymers, on screening the charges via varying the pH or by the use of charge complementary comonomers.[7] However, the stimuli-responsive self-assembly of these peptide amphiphiles is highly dependent on the delicate balance between the attractive interactions of the hydrophobic segments and the charge repulsion between the side chains.[8] We envisage that appending charged, pH-responsive peptide domains with fluorescent π-conjugated chromophores would allow the spectroscopic and microscopic probing of the self-assembly process and would also provide additional structural insights into the role of additional π-π stacking and hydrophobic interactions in modulating the pH-responsive nature of these assemblies.

8.2. Molecular Design:
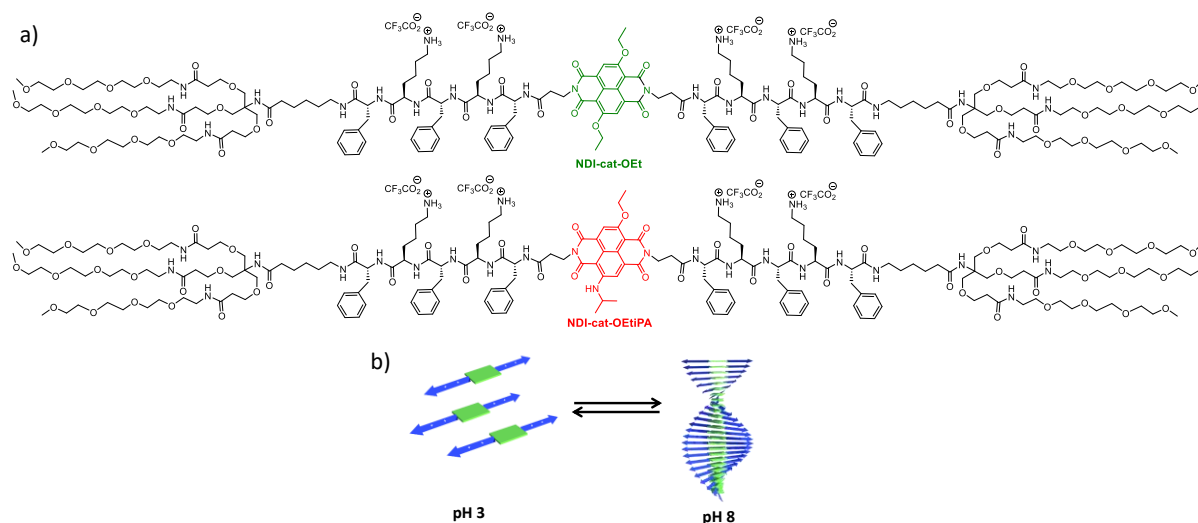
Figure 8.1. a) Molecular structures of **NDI-cat-OEt** and **NDI-cat-OEtiPA**. b) Schematic illustration of pH-responsive self-assembly of cNDI-peptide amphiphiles.

With this objective, in this chapter we have tethered ß-sheet forming peptide segments, with alternating phenylalanine (hydrophobic) and lysine (hydrophilic) amino acid sequences, to ethoxy substituted cNDI (**NDI-cat-OEt**) and ethoxy- and isopropyl amine-substituted cNDI (**NDI-cat-OEtiPA**) through the imide position of the NDIs (Figure 8.1a). **NDI-cat-OEt** and **NDI-cat-OEtiPA** were synthesized by coupling the pentapeptide sequence, end-functionalized with solubilizing dendritic tetraethylene glycol chains, with either of the substituted cNDI based dicarboxylic acids. The final amphiphiles and all intermediate compounds were characterized via NMR and mass spectrometry (see experimental section for details). We have recently reported fluorescent supramolecular polymers of cNDI chromophores with J-type molecular organization in organic solvents,[9] and were expecting to use the luminescent chromophores as an efficient probe to study supramolecular assembly characteristics in the water when conjugated with ß-sheet forming peptides.

8.3. Self-assembly Studies of NDI-cat-OEt:
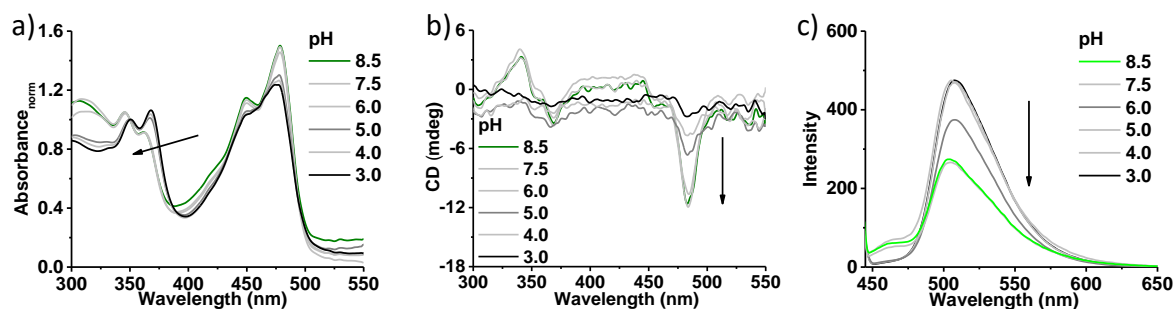
Figure 8.2. pH-dependent a) absorption, b) CD and c) emission spectra (λ_{ex} = 430 nm) of **NDI-cat-OEt**, which shows a change in the ratio of intensity between π-π^* vibronic bands, appearance of CD signal and quenching of emission (λ_{ex} = 430 nm) on increasing the pH of the solution. These spectral features refer to the self-assembled structures at pH 8.5 and monomeric or molecular dissolved species at pH 3 due to charge repulsion between lysine moieties. ([**NDI-cat-OEt**] = 5×10^{-5} M, l = 10 mm).

To investigate the pH-responsive self-assembling behavior of **NDI-cat-OEt** and **NDI-cat-OEtiPA** in water using spectroscopic techniques, we first dissolved the charged amphiphiles in acidic pH (pH 3.0 and 3.98 respectively) and performed a pH titration by gradually adding base (Tris-HCl buffer). The self-assembly of both peptide-cNDI amphiphilic conjugates could be spectroscopically probed using specific changes in cNDI spectral features which are characteristic for intermolecular interactions.[10]

The absorption spectrum of a 5×10^{-5} M solution of **NDI-cat-OEt** in pH 3 citric acid buffer displayed sharp π-π^* transition with vibronic features (λ_{max} = 350 nm and 368 nm) and a n-π^* transition with a maximum at λ = 480 nm (Figure 8.2a). The higher absorbance of the 368 nm vibronic peak in comparison to the one at 350 nm, along with the sharp spectral features are indicative of the molecularly dissolved nature of **NDI-cat-OEt** in acidic solution due to charge repulsion between protonated lysine moieties. The monomeric nature of **NDI-cat-OEt** in acidic pH is further supported by the absence of induced circular dichroism (ICD) in the spectral range of cNDI electronic transitions (Figure 8.2b). Increasing the pH of the solution of **NDI-cat-OEt**, by the addition of Tris-HCl buffer showed distinct spectroscopic changes in the cNDI absorption range characteristic of cNDI self-assembly. The self-assembled **NDI-cat-OEt** at basic pH 8.5 displayed a reversed ratio of the intensities of the π-π^* vibronic transitions at λ = 350 nm and 368 nm along with a decrease and broadening of the absorbance (Figure 8.2a). The self-assembled **NDI-cat-OEt** further displayed the appearance of an induced circular dichroism and negative band at λ = 480 nm, as well as a bisignated CD signal at the π-π^* absorption maximum, indicating helically π-π stacked cNDI chromophores (Figure 8.2b).[11] Additionally, the presence of a negative CD band at λ = 215 nm is indicative of the formation

of ß-sheets in the peptide dendron domains of the self-assembling motifs (Figure 8.3a). Furthermore, titration studies using a gradual increase in the pH value revealed that self-assembly of **NDI-cat-OEt** starts at pH 6 (Figure 8.2), which is much lower than the pH change expected purely from the pK_a of isolated lysine side chains ($pK_a = 10.6$). This indicates due to the increased hydrophobicity of the amphiphiles containing hydrophobic cNDI core and aromatic side chains of the phenylalanine groups can initiate supramolecular polymerization much before complete neutralization of charges on lysine moieties. These results are consistent with our earlier reports of pH responsive self-assembly of weakly acidic and basic dendritic peptide amphiphiles.[7]

Next, we probed the changes in the luminescent properties upon varying the pH, to get an insight into the emission of the **NDI-cat-OEt** assembly. Excitation of the n-π* band ($\lambda_{ex} = 430$ nm) of **NDI-cat-OEt** monomers in acidic pH, showed a broad emission with an emission maximum at $\lambda_{em} = 510$ nm, characteristic of cNDI chromophores (Figure 8.2c). After gradually increasing the pH of the solution we observed quenching of the emission, which is indicative of π-stacking between the cNDI chromophores during supramolecular polymerization (Figure 8.2c). Normalized emission spectra of the monomeric (pH = 3) and self-assembled (pH = 8.5) **NDI-cat-OEt** did not show significant differences apart from a slight broadening of the emission in the self-assembled state (Figure 8.3b). However, the excitation spectrum collected at $\lambda = 510$ nm for the self-assembled state is broadened in comparison to the monomer excitation spectrum, supporting the emissive nature of the self-assembled chromophores (Figure 8.3c). This was corroborated by the time-resolved fluorescence lifetime decay profile of the self-assembled chromophores collected at $\lambda = 510$ nm, which showed a shorter average lifetime of 1.76 ns compared to monomer lifetime of 13.03 ns (Figures 8.3d and Table 8.1).
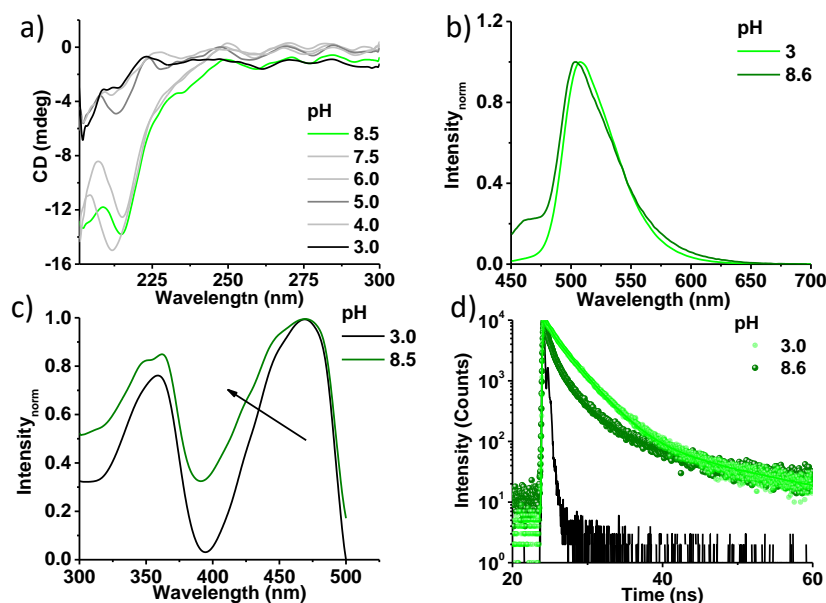
Figure 8.3. a) pH-dependent CD spectra of **NDI-cat-OEt** from 200-300 nm showing β-sheet formation at pH = 8.5. b) Normalized emission spectra (λ_{ex} = 430 nm) of monomeric (pH = 3) and self-assembled (pH = 8.6) **NDI-cat-OEt** showing a slight broadening in self-assembled state. c) Excitation spectra (λ_{coll} = 510 nm) collected for monomeric and self-assembled state of **NDI-cat-OEt** showing slight broadening and blue shift for self-assembled state in comparison to monomeric state. d) Time-resolved lifetime decay profile (λ_{ex} = 442 nm) shows a quenched and different lifetime for self-assembled **NDI-cat-OEt**, compared to monomers, confirming the emissive nature of the aggregates. ([**NDI-cat-OEt**] = 5×10^{-5} M, l = 10 mm).

pH	λ_{coll} (nm)	t_1 (ns)	t_2 (ns)	t_3 (ns)	$t_{average}$ (ns)
8.6	505	1.5 (37.27 %)	4.74 (24.50 %)	0.25 (30.49 %)	1.76
3.0	505	0.29 (12.10 %)	2.79 (79.76 %)	13.5 (8.15 %)	13.03

Table 8.1. Lifetime data of **NDI-cat-OEt** in self-assembled state (pH = 8.6) and monomeric state (pH = 3.0). ([**NDI-cat-OEt**] = 5×10^{-5} M, λ_{ex} = 442 nm).

The fluorescent nature of these chromophore-peptide stacks was utilized to visualize the assemblies using fluorescence microscopy (*vide infra*). Transmission electron microscopy of the negatively stained (uranyl acetate) **NDI-cat-OEt** assemblies at pH 8 showed a dense network of micrometer long fibers (Figure 8.4a), which provides further evidence for the one-dimensional supramolecular polymerization process. The fluorescent **NDI-cat-OEt** assemblies facilitated its visualization as green 1D structures in a solution using the SIM (structured illumination microscopy) technique (Figure 8.4b). Morphological investigations of **NDI-cat-OEt** (Figures 8.4c and 8.4d) at lower pH, did not show any ordered supramolecular structures. The morphological investigations agree with findings from spectroscopic
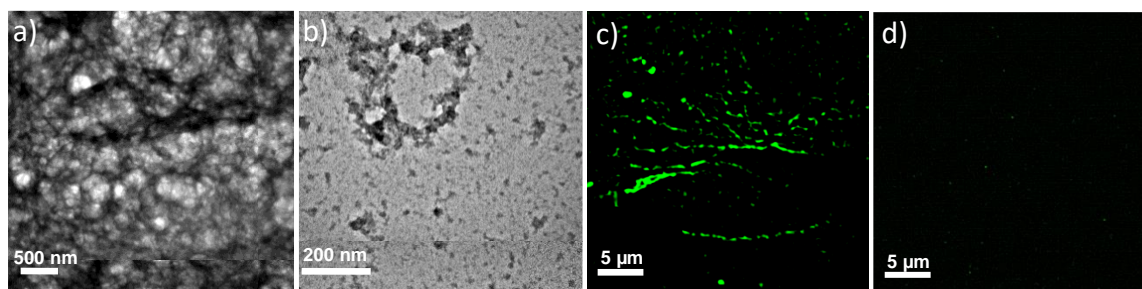
Figure 8.4. TEM images of **NDI-cat-OEt** at a) pH 8 (10 mM Tris-HCl buffer) and at b) pH 3 (0.15 M citric acid buffer, 9:1 Ca/Na₃C) shows the presence of 1D supramolecular polymers and absence of elongated self-assembled structures, respectively. SIM microscopy images (λ_{ex} = 488 nm) depicts c) long fibre like green fluorescent supramolecular polymers at pH 8 and d) absence of any fluorescent self-assembled structures at pH 3. ([**NDI-cat-OEt**] = 5×10^{-5} M, l = 10 mm).

signatures, suggesting hydrogen bonding, hydrophobic desolvation and π-π stacking driven 1D self-assembly at pH 8. On the other hand, acidic pH leads to protonation of lysine moieties to trigger charge repulsion between self-assembling monomers and the formation of a molecular dissolved or monomeric state.

To investigate the pH-responsive disassembly and reversibility of the self-assembly process of **NDI-cat-OEt**, we added citric acid buffer to acidify the basic solution of self-assembled **NDI-cat-OEt**. Upon acidification, the spectral signatures resemble that of a monomeric state (Figure 8.5) (the ratio between π-π* vibronic transitions reverses, the induced CD signal disappears and the intensity of the photoluminescence increases).
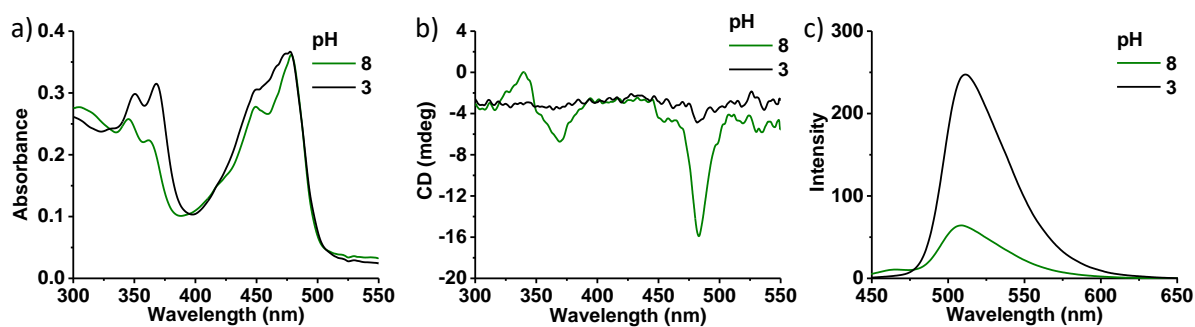
Figure 8.5. pH-induced disassembly of **NDI-cat-OEt** supramolecular polymers. a) Absorption spectra, b) CD spectra and c) emission spectra (λ_{ex} = 430 nm). ([**NDI-cat-OEt**] = 5×10^{-5} M, l = 10 mm).

8.4. Self-assembly Studies of NDI-cat-OEtiPA:

In contrast to the pH-responsive supramolecular polymerization of **NDI-cat-OEt**, we were surprised to realize that **NDI-cat-OEtiPA** remains self-assembled at both acidic and basic pH (Figure 8.6). Absorption spectra of a 2.5×10^{-5} M solution of **NDI-cat-OEtiPA** at pH 8.9 and pH 3.9 both gave rise to π-π^* vibronic transitions around $\lambda = 350$ nm and 368 nm, characteristic of π- stacked cNDI chromophores (Figure 8.6a). Furthermore, the presence of an induced circular dichroism signal with a positive band at $\lambda = 578$ nm (n-π^* transitions) and a bisignated CD signal at the π-π^* transition (Figure 8.6b), characteristic of helically stacked chromophores.[11] This confirms the self-assembled nature of the **NDI-cat-OEtiPA** amphiphiles at both pH values. Further, negatively stained TEM images of **NDI-cat-OEtiPA** at both acidic pH = 3.9 and basic pH = 8.5 show the presence of high aspect ratio 1D supramolecular polymers (Figures 8.6d, and 8.6e). SIM microscopy images of **NDI-cat-OEtiPA** reveal the presence of red-emitting supramolecular polymers at pH 8 and pH 3 (Figures 8.6f and 8.6g).
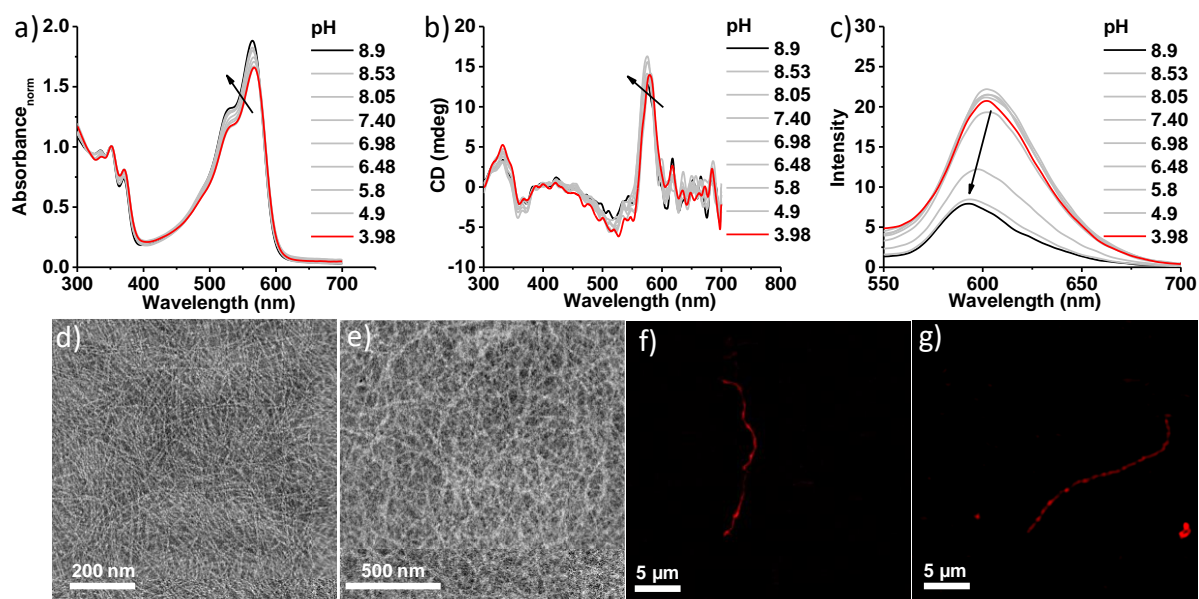
Figure 8.6. pH-dependent a) normalized absorption spectra and b) CD spectra of **NDI-cat-OEtiPA**, showing a reversed ratio of intensity between π-π^* vibronic bands and the presence of an induced CD signal at both high and low pH values. This is indicative of a pH-insensitive self-assembly of **NDI-cat-OEtiPA**. c) Corresponding emission spectra ($\lambda_{ex} = 530$ nm) shows a red shift and increased emission upon decreasing the pH. TEM images of **NDI-cat-OEtiPA** show the presence of supramolecular polymers at both d) pH 8 (10 mM Tris-HCl buffer) and at e) pH 3 (0.15 M citric acid buffer, 9:1 Ca/Na$_3$C). SIM microscopy images ($\lambda_{ex} = 561$ nm) also show fibre-like red fluorescent supramolecular polymers at both f) pH 8 and at g) pH 3. ([**NDI-cat-OEtiPA**] = 2.5×10^{-5} M, 0.15 M citric acid buffer, 9:1 Ca/Na$_3$C for pH = 3, 10 mM Tris-HCl buffer for pH 9, l = 10 mm).

However, careful observation of the absorption spectra reveals a slight shift of the n-π^* absorption maximum ($\lambda = 566$ nm at pH 3.9 and $\lambda = 564$ nm at pH 8.9) along with a decrease

in the absorbance and corresponding change in the CD maximum (λ = 580 nm at pH 3.9 and λ = 575 nm at pH 8.9) on going from pH 3.9 to pH 8.9 (Figures 8.6a and 8.6b). These slight changes indicate that although the **NDI-cat-OEtiPA** molecules are self-assembled at both pH values of interest, there are likely changes in the molecular organization within stacks due to the pH-induced variation in electrostatic interactions between the charged peptide segments. This is also indicated by the changes in the photoluminescent, which showed a significant quenching of the emission upon increasing the pH from 3.9 to 8.9 (Figure 8.6c). We attribute the decrease in fluorescence to the stronger π-π-stacking between the cNDI cores, upon the neutralization of the charges in the peptide segments, thus minimizing the electrostatic repulsion between the molecules. This is further reflected in the time-resolved fluorescence
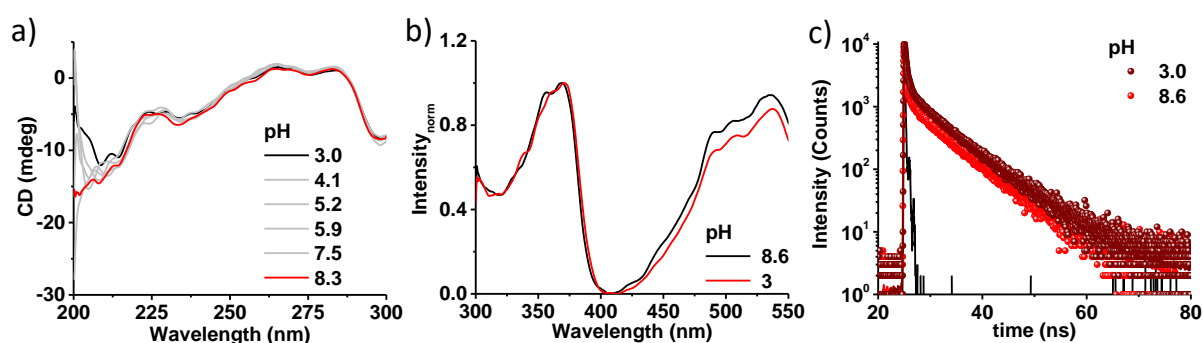
Figure 8.7. a) pH-dependent CD spectra of **NDI-cat-OEtiPA** from 200-300 nm showing a β-sheet conformation of the peptide indicating its self-assembly (l = 2 mm). b) Excitation spectra (λ_{coll} = 580 nm) measured at low (pH = 3) and high pH (pH = 8.6) matches with each other which shows the emission in both the pH is coming from same species. c) Time-resolved lifetime decay profile showing a sharp decay due to self-assembled π-π stacked NDI chromophores, which increases on going from a low pH (pH = 3) to high pH (pH = 8.6). ([**NDI-cat-OEt**] = 2.5×10^{-5} M).

pH	λ_{coll}	t_1 (ns)	t_2 (ns)	t_3 (ns)
8.6	580	0.9 (10.57 %)	6.79 (61.81 %)	0.1 (27.61 %)
3.0	505	0.7 (12.10 %)	6.66 (66.66 %)	0.12 (15.61 %)

Table 8.2. Lifetime data of **NDI-cat-OEtiPA** at pH = 8.6 and at pH = 3.0. ([**NDI-cat-OEtiPA**] = 2.5×10^{-5} M, λ_{ex} = 532 nm).

measurements (Figure 8.7c) revealing an increased contribution of the shorter lifetime component of 0.1 ns at pH 8.6 (27 %) compared to the 0.12 ns contribution at pH 3.0 (15 %), which could be due to an enhanced exciton migration in the closely packed stacks at pH 8.6.[12] These observations indicate that **NDI-cat-OEtiPA** stacks are not responsive to the changes in the pH, suggesting a very delicate balance between interactions in the hydrophobic domains

and the charge repulsion which are required for a pH-responsive assembly in this classes of cNDI-peptide amphiphile conjugates. A change in the substitution of the NDI core, from ethoxy to aminopropyl altered the hydrophobic to hydrophilic balance in the molecular design, and the electrostatic repulsion between the charged lysine moieties no longer overruled the strong hydrophobic desolvation, hydrogen bonding and π- π stacking between chromophores. This is in agreement with the calculated logP (partition coefficient) values online calculation service at www.molinspiration.com which gives a higher logP value for **NDI-an-OEtIpa** core (2.46) than that of **NDI-an-OEt** core (1.69) (Figure 8.8).[13] This suggests an increased hydrophobicity for **NDI-an-OEtIpa** than that of **NDI-an-OEt**.

NDI-an-OEt core   **NDI-an-OEtiPA** core

Molecule	logP value
NDI-an-OEt core	1.69
NDI-an-OEtiPA core	2.46
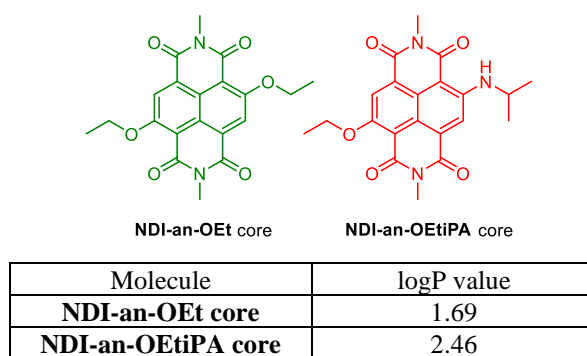
Figure 8.8. Calculated log P values using online calculation service at www.molinspiration.com suggests higher hydrophobicity in case of **NDI-an-OEtIpa** than that of **NDI-an-OEt.**

8.5. Conclusion:

In conclusion, we have investigated the stimuli-responsive nature using two different self-assembled π-conjugated cNDIs, tethered with the same dendritic-peptide amphiphiles in aqueous solution. The charged dendritic-peptide segments were previously shown to exhibit pH-responsive behavior during self-assembly. However, the pH-responsive behavior is dependent on the balance between attractive hydrophobic, π-π stacking and hydrogen bonding interactions versus the repulsive interaction embedded in the side chains of lysine amino acids in the peptide segment. In this study, we have shown that incorporating the π-conjugated segments of cNDI cores has a significant impact on the delicate balance between the attractive and repulsive interactions that modulate the pH-responsive behavior of alternating oligopeptide sequences of phenyl alanine and basic lysine. The diethoxy-substituted cNDI derivatives show a pH-responsive assembly behavior, as expected, but surprisingly the unsymmetrical isopropylamino- and ethoxy-substituted cNDI based supramolecular polymer was stable towards protonation of the lysine side chains after lowering the pH. Thus, subtle changes after introducing a slightly larger isopropyl substituent and the more electron-rich nature of the NDI, shifts the balance between attractive (π-π stacking, hydrogen bonding, dispersive interactions)

and repulsive Coulomb interactions. This renders the supramolecular polymerization process insensitive towards pH. Finally, the fluorescent nature of the π-stacked cNDI chromophores helped the spectroscopic probing and microscopic visualization of the supramolecular polymerization process for both cNDI conjugates. The pH-responsive nature of the peptide segments, along with the tunable optical properties of the core-substituted NDI chromophores provide attractive molecular designs, which will be investigated in the future for spatio-temporal resolution and multicomponent functional materials.

8.6. Experimental Section:

General Methods:

Materials: All chemicals were purchased from commercial sources and were used as such without any further purification. Spectroscopic grade solvents were used for all spectroscopic measurements.

NMR Measurements: NMR spectra were obtained with JEOL (600 MHz) Fourier transform NMR spectrometer at the Jawaharlal Nehru Centre for Advanced Scientific Research (JNCASR) and on a Bruker Avance II 400 (400 MHz) at the Institute of Organic Chemistry of the Johannes Gutenberg-University Mainz with chemical shifts reported in parts per million (ppm) with respect to TMS. Splitting patterns are designated as s (singlet), d (doublet), m (multiplet), t (triplet), q (quartet), dd (doublet of doublet) and dt (doublet of triplet).

Mass Spectrometry: MALDI was performed on a Bruker Daltonics Autoflex Speed MALDI TOF System (GT0263G201) Spectrometer using trans-2-[3-(4-*tert*-Butylphenyl)-2-methyl-2-propenylidene] malononitrile (DCTB) and α-Cyano-4-hydroxycinnamic acid (CCA) as matrix. ESI measurements were executed on an Agilent 6545QTOF-MS device at the Johannes Gutenberg-University Mainz.

Spectroscopic Measurements: Electronic absorption spectra were recorded on a Perkin Elmer Lambda 900 UV-Vis-NIR Spectrometer and emission spectra were recorded on Perkin Elmer LS 55 Luminescence Spectrometer. UV-Vis and emission spectra were recorded in 10 mm path length cuvettes. Circular Dichroism measurements were performed on a Jasco J-815 spectrometer and were recorded using 10 mm and 2 mm path length cuvettes. The sensitivity, time constant and scan rate were chosen appropriately.

Fluorescence Lifetime Measurements: Time-resolved decay experiments were recorded on a Horiba Delta Flex Time-Correlated Single Photon Counting (TCSPC) instrument. A 442 nm and 532 nm nano-LED with a pulse repetition rate of 1 MHz were used as light source. The instrument response function (IRF) was collected by using a scatterer (Ludox AS40 colloidal

silica, Sigma Aldrich). For the 442 nm and 532 nm LED light source the instrumental full width at half maximum including detector response was 0.2 ns. The excited state decay of the sample was collected by fixing the emission wavelength. The decay was fitted to appropriate best fit multiexponential decay using IBH software (DAS6).

Transmission Electron Microscopy (TEM): TEM measurements were performed on a JEOL (JEM 3010) operated at 300 kV. Samples were prepared by placing a drop of the solution on carbon coated copper grids followed by drying at room temperature in desiccator (samples were negatively stained with uranyl acetate).

Optical Setup for Imaging in Structured Illumination Microscopy (SIM) method: The fluorescence images of supramolecular polymers were acquired using an inverted Zeiss ELYRA PS1 microscope in structured illumination mode. 488 nm (200 mW) were used for the excitation of **NDI-cat-OEt** and 561 nm (200 mW) for **NDI-cat-OEtiPA**. 5% laser power from the objective top was used for structured illumination imaging. Imaging was performed using a Zeiss oil–immersion objective (Plan–apochromat 63x/1.40 Oil DIC M27, numerical aperture (NA) 1.40 oil). Fluorescence light was spectrally filtered with emission filters for channel I - MBS–488+EF BP 495–575/LP 750 for laser line 488 nm and for channel II - MBS– 561+EF BP 570–650/LP 750 for laser line 561 nm and imaged using a PCO edge sCMOS camera (quantum yield > 70%). Structured illumination images were processed using structured illumination analysis package for Zen software (Zeiss). Additional software was used for colour adjustment (ImageJ).

8.7. Synthetic Schemes and Procedures:

Synthetic Schemes:

The synthetic route for the core-substituted NDI derivatives **NDI-cat-OEt** and **NDI-cat-OEtiPA** are shown in Scheme 8.1 to Scheme 8.4. Peptide **89** was synthesized in Institute of Organic Chemistry of the Johannes Gutenberg-University Mainz by Prof. Pol Besenius Group.
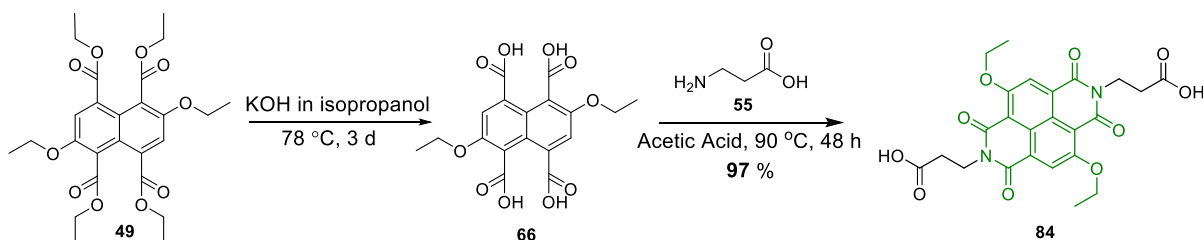
Scheme 8.1. Synthetic route to the molecule **84**.
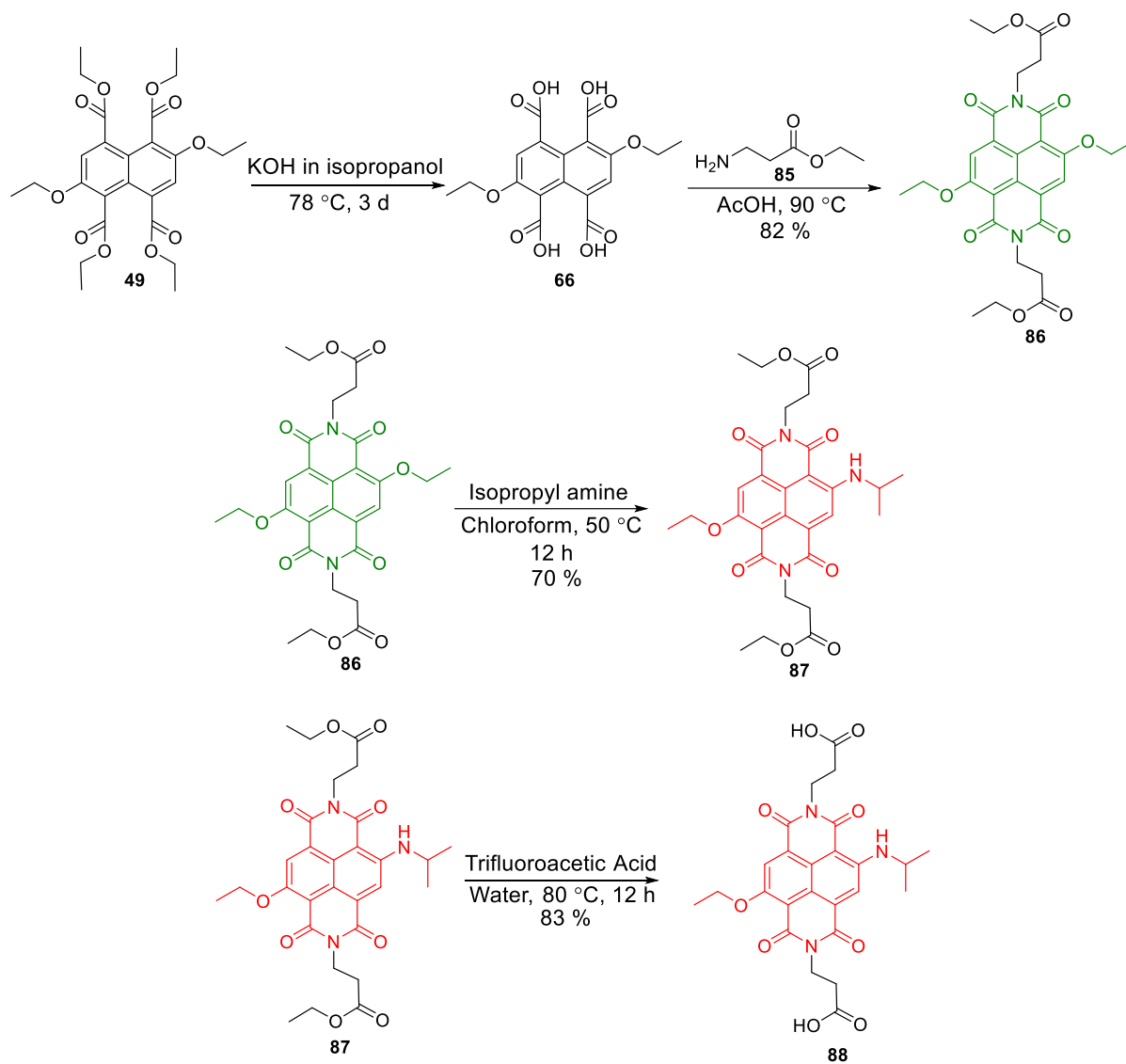
Scheme 8.2. Synthetic route to the molecule **88**.
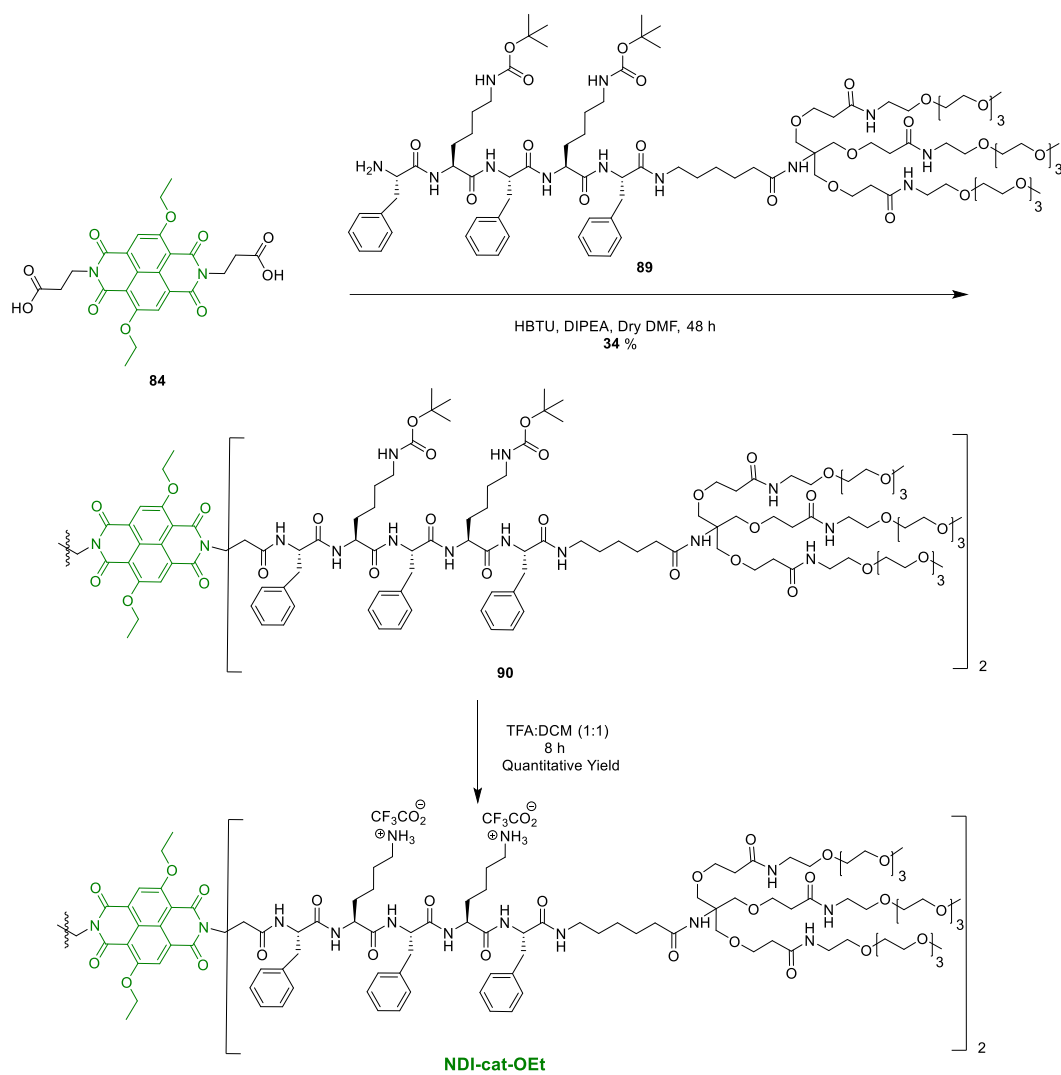
Scheme 8.3. Synthetic route to **NDI-cat-OEt**.
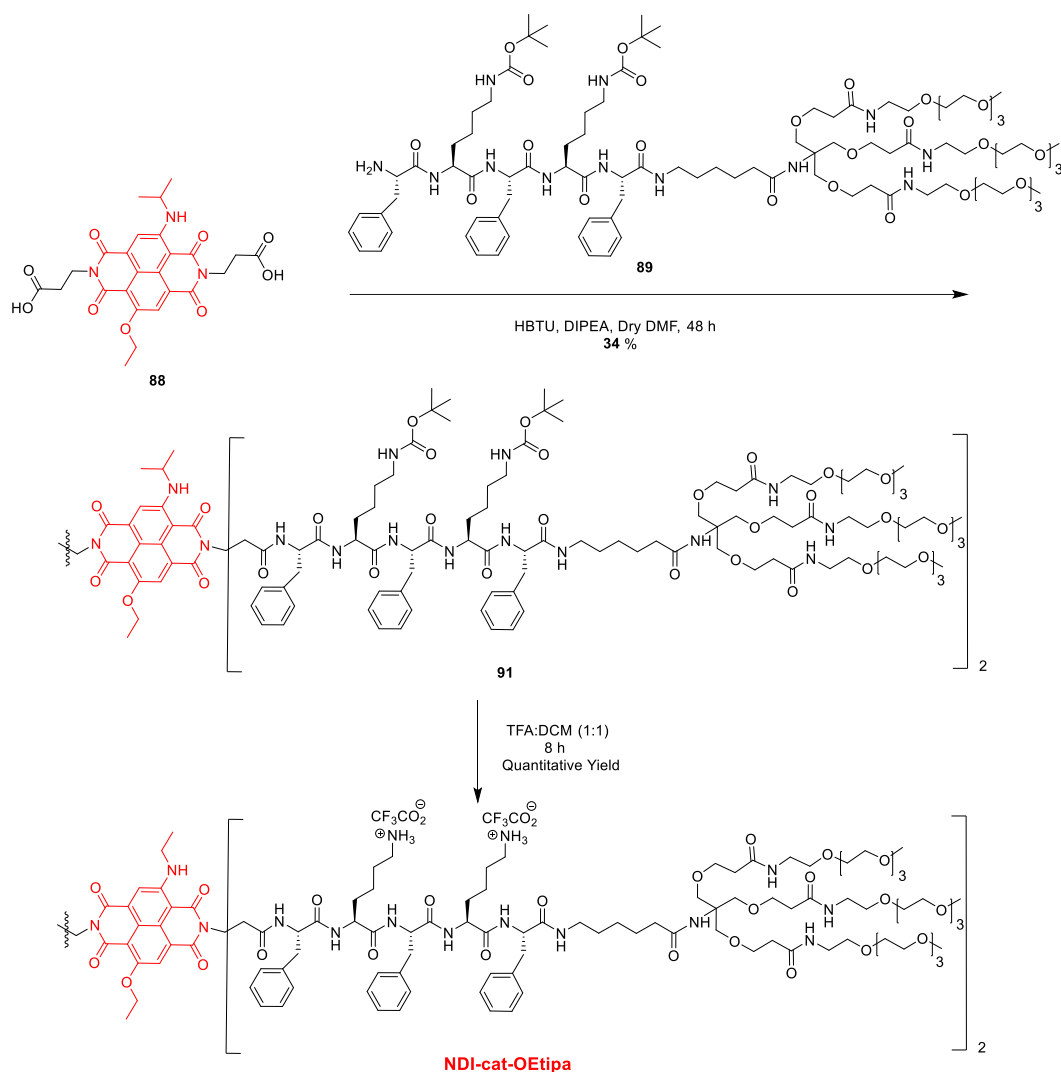
Scheme 8.4. Synthetic route to **NDI-an-OEtiPA**.

Synthetic Procedures:

Synthesis of 84: 125 mg of **49** was taken in a round bottom flask and 30 mL of 1 N KOH in isopropanol was added. The reaction was refluxed at 80 °C for 3 d. The color of the reaction slowly changed from yellow to colorless. After 3 days the solvent was evaporated and the crude mixture obtained was used as such for the subsequent synthetic step. The crude mixture was suspended in 20 mL of acetic acid and 66 mg of 3-aminopropionic acid (**55**) was added to it and refluxed at 90 °C. The progress of the reaction was monitored by ^{1}H-NMR spectroscopy. After completion of the reaction (2 days), it was cooled down to room temperature and excess water was added to it. The precipitate was filtered and washed with methanol to remove water and acetic acid. The precipitate was dried under ambient conditions and 120 mg of pure product was obtained as a yellow powder. Combined yield of step 1 and 2 is 97 %. ^{1}H NMR (400 MHz, DMSO-d$_6$, ppm): δ = 8.24 (s, 2H, H^{Ar}), 4.45 (q, J = 6.9 Hz, 4H, OCH_2^{NDI}), 4.21 (t, J = 7.9 Hz,

4H, NCH_2^{NDI}), 2.58 (t, J = 7.8 Hz, 4H, NCH$_2$CH_2), 1.51 (t, J = 6.9 Hz, 6H, CH_3); ^{13}C NMR (100 MHz, DMSO-d$_6$, ppm): δ = 172.39, 161.19, 159.51, 158.85, 125.96, 122.17, 118.55, 109.27, 65.64, 35.99, 31.96, 14.53; MALDI-TOF (CCA matrix, positive mode): m/z calculated for: $[C_{24}H_{22}N_2O_{10}Na]^+$: 521.12, found: $[M]^{\cdot}$ = 521.23.

Synthesis of 86: 1.8 g of **49** was taken in a single necked round bottom flask and 120 ml of 1 N KOH in isopropanol was added. The reaction was refluxed at 80 °C for 3 days. The color of the reaction gradually changed from yellow to colorless. The solvent was evaporated to get the crude mixture. 0.9 g of ethyl 3-aminopropanoate (**85**) and 90 mL acetic acid were added to the resultant crude mixture and refluxed at 90 °C. The progress of the reaction was monitored by thin layer chromatography and NMR. After completion of the reaction (2 days), the reaction mixture was cooled down to room temperature and water was added to precipitate the crude product. The obtained precipitate was filtered and washed with methanol to remove the remaining water and acetic acid. The crude mixture was purified using column chromatography with a solvent gradient ranging from 100 % chloroform to 5 % methanol in chloroform to get 1.67 g of pure product as a yellow solid in 82 % yield. ^{1}H NMR (400 MHz, CDCl$_3$, ppm): δ = 8.46 (s, 2H, H^{Ar}), 4.53-4.47 (m, 8H, CH_2CH$_3$, NCH_2), 4.15 (q, 4H, J = 7.1 Hz, CH_2CH$_3$), 2.76 (t, 4H, J = 7.5 Hz, NCH$_2$CH_2), 1.66 (t, 6H, J = 7.0 H, CH_3^{OEt}), 1.23 (t, 6H, J = 7.1 Hz, CH_3^{COOEt}); ^{13}C NMR (100 MHz, CDCl$_3$, ppm): δ = 171.40, 162.42, 161.11, 160.30, 127.33, 123.82, 119.95, 110.99, 66.53, 60.86, 36.61, 32.76, 29.85, 14.92, 14.30; MALDI-TOF (CCA matrix, positive mode): m/z calculated for $[C_{28}H_{31}N_2O_{10}]^+$: 555.20, found: $[M]^{\cdot}$ = 555.66.

Synthesis of 87: 350 mg of **86** was taken in a 100 mL single necked round bottom flask and 10 mL of isopropyl amine and 20 mL of chloroform were added to it and stirred at 50 °C for 12 h. The progress of the reaction was monitored by thin layer chromatography. After completion (12 hours) of the reaction, the excess amine and chloroform was removed under reduced pressure to get the crude product. The crude mixture was purified using column chromatography with a gradient ranging from 100 % chloroform to 2 % methanol in chloroform to get 250 mg of pure product as a red solid in 70 % yield. ^{1}H NMR (400 MHz, CDCl$_3$, ppm): δ = 9.76 (d, 1H, J = 7.7 Hz, NH), 8.31 (s, 1H, H^{Ar}), 8.25 (s, 1H, H^{Ar}), 4.52-4.42 (m, 6H, CH_2CH$_3$, NCH_2), 4.18–4.12 (m, 5H, CH_2CH$_3$, NHCH(CH$_3$)$_2$), 2.76 (t, 4H, J = 7.5 Hz, NCH$_2$CH), 1.63 (t, 3H, J = 6.9 Hz, CH_3^{OEt}), 1.41 (d, 6H, J = 6.4 Hz, CH_3^{iPr}), 1.27–1.22 (m, 6H, CH_3^{COOEt}); ^{13}C NMR (101 MHz, CDCl$_3$, ppm): δ = 171.39, 171.34, 165.89, 162.76, 162.67, 161.45, 158.09, 150.11, 127.43, 125.13, 124.33, 121.43, 120.96, 118.24, 112.22, 99.88, 66.12,

60.87, 60.82, 44.66, 36.54, 36.32, 32.88, 32.79, 29.85, 23.34, 14.95, 14.30; MALDI-TOF (CCA matrix, positive mode): m/z calculated for $[C_{28}H_{34}N_3O_9]^+$: 568.23, found: $[M]^{\dot{+}}$ = 568.11.

Synthesis of 88: 30 ml of TFA and 10 mL of water were added to 180 mg of **87** and stirred at 80 °C for 12 h. The progress of the reaction was monitored by thin layer chromatography. After completion of the reaction (12 hours), water and TFA were removed under reduced pressure to get the crude product. The crude product was washed with methanol to remove the excess water and TFA and dried under reduced pressure to get 132 mg of the pure product as a red solid in 83 % yield. ^1H NMR (400 MHz, DMSO-d_6, ppm): δ = 12.42 (s, 2H, COOH), 9.47 (d, 1H, J = 7.4 Hz, NH), 7.76 (s, 1H, H^{Ar}), 7.75 (s, 1H, H^{Ar}), 4.25–3.96 (m, 7H, CH_2CH₃, NCH_2, NHCH(CH₃)₂), 2.56 (t, 3H, J = 7.9 Hz, NCH₂CH_2), 1.50 (t, 3H, J = 6.9 Hz, CH_3O^{Et}), 1.38 (d, J = 6.3 Hz, 6H, C$H_3{}^{iPr}$); ^{13}C NMR (δ ppm, 100 MHz, DMSO-d_6, 298 K): = 172.39, 172.35, 164.66, 161.32, 161.10, 159.53, 156.59, 148.60, 126.20, 123.49, 122.42, 119.83, 119.07, 116.48, 110.36, 98.16, 65.08, 43.98, 35.88, 31.89, 22.68, 14.57. MALDI-TOF (CCA matrix, positive mode): m/z calculated for $[C_{25}H_{26}N_3O_9]^+$: 512.17, found: $[M]^{\dot{+}}$ = 512.49.

Synthesis of 90: In a round bottom flask, 48 mg of HBTU, 11 mg of **84** and 11.2 mg DIPEA were suspended in 5 mL of DMF and stirred at room temperature for 30 min. After 30 min, 100 mg of **89** dissolved in 5 mL of DMF were added dropwise to the reaction mixture. The progress of the reaction was monitored by thin layer chromatography. After 3 d, DMF was removed under reduced pressure and the crude mixture was purified using size exclusion chromatography (SX-1 biobeads, chloroform) to get 42 mg of the pure product as a yellow sticky solid in 40 % yield. ^1H NMR (600 MHz, CD₃OD, ppm): δ = 8.42 (s, 2H, CH^{NDI}), 7.33-7.06 (m, 30H, CH^{Phe}), 4.55-4.05 (m, 18H, α-CH, OC$H_2{}^{NDI}$, NC$H_2{}^{NDI}$), 3.70-3.50 (m, 108H, CH_2OC$H_2{}^{Tris}$, C$H_2{}^{OEG}$), 3.38-3.24 (m, 30H, C$H_3{}^{OEG}$, NCH₂CH_2O), 3.17-2.67 (m, 28H, NHC$H_2{}^{Ahx}$, C$H_2{}^{Phe}$, ε-C$H_2{}^{Lys}$, CH_2N^{NDI}), 2.43 (t, 12H, J = 6.0 Hz, CH_2CH₂CO^{Tris}), 2.16 (t, J = 7.5 Hz, 4H, CH_2CO^{Ahx}), 1.78-1.18 (m, 78H, C$H_2{}^{Ahx}$, C$H_2{}^{Lys}$, C$H_3{}^{Boc}$, C$H_3{}^{OEt}$); MALDI-TOF (DCTB matrix, linear positive mode): m/z calculated for $[C_{214}H_{334}N_{26}O_{64}Na]^+$: 4318.13, found: $[M+H]^+$ = 4319.57.

Synthesis of NDI-cat-OEt: 40 mg of **89** was dissolved in a 25 mL round bottom flask in 8 mL of a mixture of 1:1 TFA:DCM and stirred at room temperature for 4 h. The solvent was evaporated under reduced pressure to get 40 mg of **NDI-cat-OEt** as a yellow solid in quantitative yields. ^1H NMR (600 MHz, DMSO-d_6, ppm): δ = 8.35 (s, 2H, CH^{NDI}), 8.28-8.11 (m, 4H, N$H^{Phe/Lys}$,), 7.98-7.80 (m, 14H, CONH^{Ahx}, N$H^{Phe/Lys}$, CONH^{OEG}), 7.75-7.60 (m, 12H, CH_2NH_3), 7.28-7.09 (m, 30H, CH^{Phe}), 6.99 (s, 2H, NHC$_q$), 4.60-4.41 (m, 10H, α-CH,

OCH_2^{NDI}), 4.25-4.05 (m, 8H, α-CH, NCH_2^{NDI}), 3.57-3.37 (m, 108H, CH_2OCH_2^{Tris}, CH_2^{OEG}), 3.23 (s, 18H, CH_3^{OEG}), 3.21-3.17 (m, 12H, NCH_2CH_2O), 3.09-2.67 (m, 28H, CH_2^{Phe}, NHCH_2^{Ahx}, ε-CH_2^{Lys}, CH_2N^{NDI}), 2.29 (t, 12H, J = 6.5 Hz, CH_2CH_2CO^{Tris}), 2.04 (t, 4H, J = 7.5 Hz, CH_2CO^{Ahx}), 1.64-1.09 (m, 42H, CH_2^{Ahx}, CH_2^{Lys}, CH_3^{OEt}); MALDI-TOF (DCTB matrix, linear positive mode) m/z calculated for [C$_{194}$H$_{303}$N$_{26}$O$_{56}$]$^+$: 3893.17, found: [M+H]$^+$ = 3894.93.

Synthesis of 91: 88 (21.35 mg, 0.042 mmol, 1.0 eq.) and HBTU (63.70 mg, 0.168 mmol, 4.0 eq.) were suspended in 8 ml DMF (peptide grade). DIPEA (22.00 µL, 0.126 mmol, 3.0 eq.) was added and the reaction was stirred at room temperature under inert atmosphere for 2 h. Compound **89** (200.00 mg, 0.104 mmol, 2.5 eq.), dissolved in 2 ml DMF (peptide grade), was added and the solution was stirred at room temperature for 2 d. Volatiles were removed under reduced pressure and the residue was purified *via* size exclusion chromatography to get 83.50 mg of pure purple product in 46 % yield. (SX-1 Bio-Beads™-Chloroform). ^{1}H NMR (600 MHz, DMSO-d$_6$, ppm): δ = 9.70 (d, 1H, J = 6.8 Hz, NH^{iPr}), 8.25-8.21 (m, 2H, N$H^{Phe/Lys}$), 8.20 (s, 1H, CH^{NDI}), 8.12 (s, 1H, CH^{NDI}), 8.09-8.03 (m, 2H, N$H^{Phe/Lys}$), 8.02-7.96 (m, 2H, CONH^{Ahx}), 7.94-7.85 (m, 10H, N$H^{Phe/Lys}$, CONH^{OEG}), 7.85-7.80 (m, 2H, N$H^{Phe/Lys}$), 7.25-7.10 (m, 30H, CH^{Phe}), 7.00-6.96 (m, 2H, NHC$_q$), 6.72 (t, 4H, J = 5.3 Hz, CH_2NH^{Boc}), 4.57-4.48 (m, 4H, α-CH), 4.46-4.40 (m, 2H, α-CH), 4.39-4.32 (m, 2H, α-CH), 4.21-4.06 (m, 9H, α-CH, NCH_2^{NDI}, NCH^{iPr},CH_2^{OEt}), 3.58-3.37 (m, 108H, CH_2OCH_2^{Tris}, CH_2^{OEG}), 3.23 (s, 18H, CH_3^{OEG}), 3.21-3.17 (m, 12H, NCH_2CH_2O), 3.08-2.66 (m, 28H, NHCH_2^{Ahx}, CH_2^{Phe}, CH_2NH^{Lys}, CH_2N^{NDI}), 2.29 (t, 12H, J = 6.5 Hz, CH_2CH_2CO^{Tris}), 2.03 (t, J = 7.6 Hz, 4H, CH_2CO^{Ahx}), 1.62-1.05 (m, 81H, CH_2^{Ahx}, CH_2^{Lys}, CH_3^{Boc}, CH_3^{iPr}, CH_3^{OEt}); MALDI-TOF (CCA matrix, positive mode): m/z calculated for [C$_{215}$H$_{337}$N$_{27}$O$_{63}$Na]$^+$: 4328.39, found: [M]$^{\dot{+}}$ = 4328.94.

Synthesis of NDI-an-OEtiPA: Compound **91** (80 mg, 0.018 mmol, 1.0 eq.) was dissolved in 10 ml of a 1:1 mixture of TFA and DCM. The solution was stirred at room temperature for 3 h. Solvents were removed under reduced pressure and remaining TFA was co-distilled with toluene. The product was dried *in vacuo* to get 80 mg of the pure purple product in quantitative yields. ^{1}H NMR (600 MHz, DMSO-d$_6$, ppm): δ = 9.71 (d, 1H, J = 7.3 Hz, NH^{iPr}), 8.29-8.10 (m, 6H, N$H^{Phe/Lys}$, CH^{NDI}), 7.98-7.80 (m, 14H, CONH^{Ahx}, N$H^{Phe/Lys}$, CONH^{OEG}), 7.75-7.60 (m, 12H, CH_2NH_3), 7.25-7.10 (m, 30H, CH^{Phe}), 6.99 (s, 2H, NHC$_q$), 4.60-4.42 (m, 6H, α-CH), 4.40-4.34 (m, 2H, α-CH), 4.30-4.05 (m, 9H, α-CH, NCH_2^{NDI}, NCH^{iPr},CH_2^{OEt}), 3.57-3.37 (m, 108H, CH_2OCH_2^{Tris}, CH_2^{OEG}), 3.23 (s, 18H, CH_3^{OEG}), 3.21-3.17 (m, 12H, NCH_2CH_2O), 3.10-2.66 (m, 28H, CH_2^{Phe}, CONHCH_2^{Ahx}, ε-CH_2^{Lys}, CH_2N^{NDI}), 2.29 (t, 12H,

$J = 6.5$ Hz, CH$_2$CH_2CO^{Tris}), 2.04 (t, 4H, $J = 7.5$ Hz, CH_2CO^{Ahx}), 1.64-1.00 (m, 45H, C$H_2{}^{Ahx}$, C$H_2{}^{Lys}$, C$H_3{}^{iPr}$, C$H_3{}^{OEt}$); MALDI-TOF (DCTB matrix, linear positive mode): m/z calculated for [C$_{195}$H$_{306}$N$_{27}$O$_{55}$]$^+$: 3906.20, found: [M+H]$^+$ = 3907.21.

8.8. Experimental Procedures:

NDI-cat-OEt and **NDI-cat-OEtiPA** stock solutions (5×10^{-3} M) were prepared in pH 7 water and the required volume was added to the desired pH solution to adjust the final concentration. Citric acid/sodium citrate buffer (Ca/Na$_3$C) was used as a source of acidic pH and Tris-HCl was used as source of basic pH. TEM Samples were prepared by placing a drop of the solution on carbon coated copper grids followed by drying at room temperature in desiccator (samples were negatively stained with uranyl acetate).

8.9. References:

[1] a) Aida, T.; Meijer, E. W.; Stupp, S. I. *Science*, **2012**, *335*, 813-817. b) Hendricks, M. P.; Sato, K.; Palmer, L. C.; Stupp, S. I. *Acc. Chem. Res.* **2017**, *50*, 2440-2448. c) Sato, K.; Hendricks, M. P.; Palmer, L. C.; Stupp, S. I. *Chem. Soc. Rev.* **2018**, *47*, 7539-7551. d) Ulijn, R. V.; Smith, A. M. *Chem. Soc. Rev.* **2008**, *37*, 664-675. e) Pashuck, E. T.; Cui, H.; Stupp. S. I. *J. Am. Chem. Soc.* **2010**, *132*, 6041-6046. e) Behanna, H. A.; Donners, J. J. J. M.; Gordon, A. C.; Stupp, S. I. *J. Am. Chem. Soc.* **2005**, *127*, 1193-1200. f) Cornelissen, J. J. L. M. Donners, J. J. J. M.; de Gelder, R.; Graswinckel, W. S.; Metselaar, G. A.; Rowan, A. E.; Sommerdijk, N. A. J. M.; Nolte, R. J. M. *Science* **2001**, *293*, 676-680. g) Matmour, R.; De Cat, I.; George, S. J.; Adriaens, W.; Leclère, P.; Bomans, P. H. H.; Sommerdijk, N. A. J. M.; Gielen, J. C.; Christianen, P. C. M.; Heldens, J. T.; van Hest, J. C. M.; Löwik, D. W. P. M.; Feyter, S. D.; Meijer, E. W.; Schenning, A. P. H. J. *J. Am. Chem. Soc.* **2008**, *130*, 14576-14583.

[2] a) Pantos, G. D.; Wietor, J. L.; Sanders, J. K. M. *Angew. Chem., Int. Ed.* **2007**, *46*, 2238-2240. b) Wietor, J.-L.; Pantos, G. D.; Sanders, J. K. M. *Angew. Chem., Int. Ed.* **2008**, *47*, 2689-2692.

[3] a) Shao, H.; Gao, M.; Kim, S. H.; Jaroniec, C. P.; Parquette, J. R. *Chem. Eur. J.* **2011**, *17*, 12882-12885. b) Shao, H.; Seifert, J.; Romano, N. C.; Gao, M.; Helmus, J. J.; Jaroniec, C. P.; Modarelli, D. A.; Parquette, J. R. *Angew. Chem., Int. Ed.* **2010**, *49*, 7688-7691. c) Shao, H.; Nguyen, T.; Romano, N. C.; Modarelli, D. A.; Parquette, J. R. *J. Am. Chem. Soc.* **2009**, *131*, 16374-16376. d) Shao, H.; Parquette, J. R. *Chem. Commun.* **2010**, *46*, 4285-4287; e) Tu, S.; Kim, S. H.; Joseph, J.; Modarelli, D. A.; Parquette, J. R. *J. Am. Chem. Soc.* **2011**, *133*, 19125-19130.

[4] a) Nalluri, S. K. M.; Berdugo, C.; Javid, N.; Frederix, P. W. J. M.; Ulijn, R. V. *Angew. Chem., Int. Ed.* **2014**, *53*, 5882-5887. b) Kumar, M.; Ing, N. L.; Narang, V.; Wijerathne, N. K.; Hochbaum, A. I.; Ulijn, R. V. *Nat. Chem.* **2018**, *10*, 696-703.

[5] a) Cross, E. R.; Sproules, S.; Schweins, R.; Draper, E. R.; Adams, D. J. *J. Am. Chem. Soc.* **2018**, *140*, 8667-8670. b) Ardoña, H. Ann M.; Tovar, J. D. *Chem. Sci.* **2015**, *6*, 1474-1484. c) Ardoña, H. Ann M.; Draper, E. R.; Citossi, F.; Wallace, M.; Serpell, L. C.; Adams, D. J.; Tovar, J. D. *J. Am. Chem. Soc.* **2017**, *139*, 8685-8692.

[6] a) da Silva, R. M. P.; Zwaag, D. v. d.; Albertazzi, L.; Lee, S. S.; Meijer, E. W.; Stupp, S. I. *Nat. Commun.* **2016**, *7*, 11561. b) Matmour, R.; De Cat, I.; George, S. J.; Adriaens, W.; Leclère, P.; Bomans, P. H. H.; Sommerdijk, N. A. J. M.; Gielen, J. C.; Christianen, P. C. M.; Heldens, J. T.; van Hest, J. C. M.; Löwik, D. W. P. M.; Feyter, S. D.; Meijer, E. W.; Schenning, A. P. H. J. *J. Am. Chem. Soc.* **2008**, *130*, 14576-14583.

[7] a) Frisch, H.; Patrick, J.; Unsleber, Lüdeker, D.; Peterlechner, M.; Brunklaus, G.; Waller, M.; Besenius, P. *Angew. Chem., Int. Ed.* **2013**, *52*, 10097-10101. b) Frisch, H.; Nie, Y.; Raunser, S.; Besenius, P. *Chem. Eur. J.* **2015**, *21*, 3304-3309. c) Ahlers, P.; Frisch, H.; Besenius, P. *Polym. Chem.* **2015**, *6*, 7245-7250. d) Spitzer, D.; Lucas Rodrigues, L.; Straßburger, D.; Mezger, M.; Besenius, P. *Angew. Chem., Int. Ed.* **2017**, *56*, 15461-15465. e) van Buel, R.; Spitzer, D.; Berač, C. M.; van der Schoot, P.; Besenius, P.; Jabbari-Farouji, S. *J. Chem. Phys.* **2019**, *151*, 014902. f) Berac, C. M.; Zengerling, L.; Straßburger, D.; Otter, R.; Urschbach, M.; Besenius, P. *Macromol. Rapid Commun.* **2019**, 1900476.

[8] a) Krieg, E.; Bastings, M. M. C.; Besenius, P.; Rybtchinski, B. *Chem. Rev.* **2016**, *116*, 2414-2477. b) Chakraborty, S.; Berac, C. M.; Kemper, B.; Besenius, P.; Speck, T. *Macromolecules* **2019**, *52*, 7661-7667.

[9] Sarkar, A.; Dhiman, S.; Chalishazar, A.; George, S. J. *Angew. Chem., Int. Ed.* **2017**, *56*, 13767-13771.

[10] a) Sakai, N.; Mareda, J.; Vauthey, E.; Matile, S. *Chem. Commun.* **2010**, *46*, 4225-4237. b) Würthner, F.; Ahmed, S.; Thalacker, C.; Debaerdemaeker, T. *Chem. Eur. J.* **2002**, *8*, 4742-4750.

[11] a) George, S. J.; Tomović, Ž.; Schenning, A. P. H. J.; Meijer, E. W. *Chem. Commun.* **2011**, *47*, 3451-3453. b) Cat, I. D.; Guo, Z.; George, S. J.; Meijer, E. W.; Schenning, A. P. H. J.; Feyter, S. D. *J. Am. Chem. Soc.* **2012**, *134*, 3171-3177.

[12] Schmid, S. A.; Abbel, R.; Schenning. A. P. H. J.; Meijer, E. W.; Herz, L. M. *Philos. Trans. R. Soc. London* **2012**, *370*, 3787-3801.

[13] Garrey, C. J.; Schreiber, S. L. *Nat. Rev. Drug discov.* **2018**, *17*, 333-352.

Chapter: 9

Charge-Regulated, Cooperative Disassembly of a Chemically Fuelled Transient Supramolecular Polymer

Chapter: 9

Charge-Regulated, Cooperative Disassembly of a Chemically Fuelled Transient Supramolecular Polymer

Abstract

Synthetic dissipative supramolecular polymers has enabled the synthesis of complex adaptive and programmable materials and should bridge the gap between passive to living and thinking materials. However, an examination of man-made dissipative systems shows that energy is dissipated in a very different way compared to natural dissipative systems. Biological molecules typically employ chemical energy stored in a kinetically stable, high energy state which acts via a ratcheting growth mechanism. On the other hand, most of the synthetic dissipative systems, due to their dynamic nature readily equilibrates with the solvent and thus fails to store the energy. Herein, we report a cooperative charge-regulated disassembly of core-substituted naphthalene diimide (cNDI) derivative, which is extended with an alternating phenylalanine and glutamic acid peptide sequence and dendritic tetraethylene glycols. Detailed spectroscopic and zeta potential measurement shows a steady build-up of negative charges on the stable non-dynamic supramolecular polymers which pushes the system to a high energy state before undergoing a highly cooperative disassembly. By coupling the pH-dependent charge-regulated disassembly to a urease catalyzed conversion of urea into ammonia, we have demonstrated a pH-driven transient supramolecular polymer with temporal assembly characteristics. The kinetic experiments under dissipative condition are indicative of a highly cooperative disassembly regulated by the formation of a charged high-energy metastable state. The fluorescent nature of the cNDI further enabled visualization of the active cooperative disassembly process using time-dependent super-resolved structured illumination microscopy (SIM).
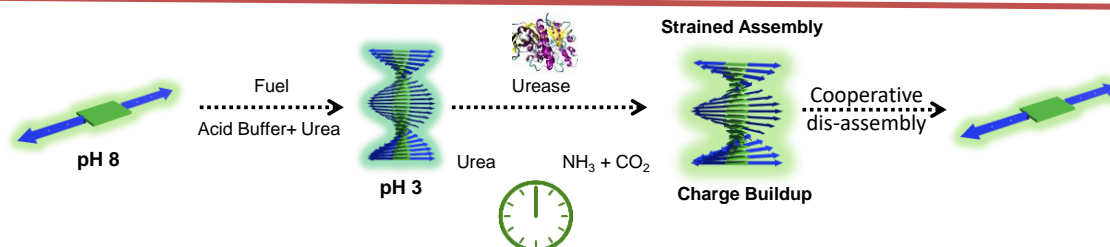
9.1. Introduction:

Nature elegantly maintains complex adaptive and dynamic behaviours by virtue of competing transient activation and deactivation processes. A fascinating example is out-of-equilibrium self-assembly of tubulin dimer to form micro-tubules, fuelled by guanosine triphosphates (GTP) which mediates important biological functions such as cell motility.[1] Thus temporal control over the supramolecular polymerization process has attracted much attention recently to construct transient materials.[2] Design of supramolecular dissipative systems can lead to emerging materials with programmable and adaptive functions and has been achieved recently by coupling fuel-driven, temporal reaction profiles to self-assembled systems.[3] Thus in recent years, chemical reaction,[4] redox,[5] enzyme,[6] pH,[7] and light fuelled[8] self-assembled materials with temporal assembly characteristics have been reported. Such temporal regulation of self-assembling behaviour has delivered new emergent functions such as transient signalling, catalysis, or self-erasing inks.[9] However, most of the synthetically designed self-assembled systems by virtue of its highly dynamic nature readily equilibrates when the fuel gets converted into waste and thus fails to store energy in the dissipative structure.[10] In contrast natural microtubules assemble through a ratcheting growth mechanism, where they disassemble in a catastrophic manner following the build-up of strain.[11] It has been demonstrated that the strain builds up in these disassembly events can be used to generate work. Thus, unlike the highly dynamic dissipative systems, a stable non-dynamic system involving strong non-covalent interactions would be able to accumulate the energy (a high energy metastable state) before disassembly. Particularly kinetic studies on supramolecular polymers has established non-dynamic systems as a tool box for pathway complexity and determine whether the equilibrium state can be reached in the first place.[12] This will be particularly prominent during self-assembly of strongly hydrophobic groups with π-conjugated molecules having extended π-surface, resulting in a high kinetic barrier and slow exchange dynamics.[13] Hence generation of temporally stable high energy states to facilitate a catastrophic disassembly and storing of energy in the dissipative structure requires fine tuning of the molecular structure with attractive/repulsive interactions and monomer exchange dynamics. Recently Katsonis and co-workers have demonstrated strain mediated disassembly of a supramolecular tubule that incorporates photo switchable building blocks.[14] Unlike highly dynamic dissipative supramolecular systems, slow dynamics allows a build-up of strain in these artificial supramolecular tubules, which leads to a catastrophic disassembly.

In this Chapter, a new mechanism for the generation of temporally stable high energy metastable states via pH-driven charge-regulated transient supramolecular polymerization and cooperative disassembly of a peptide-appended, core-substituted naphthalene diimide (cNDI) bolaamphiphile is demonstrated. Non-dynamic nature of the self-assembled supramolecular polymers allows build-up of negative charges in the self-assembled stacks during transient pH changes[7] thus pushing the system to a high energy state. Build-up of negative charges eventually induces a highly cooperative disassembly of the supramolecular polymers. The process is similar to the recently designed pH-driven conformational switches in natural proteins where protonation of large number of histidine units results in both steric and electrostatic repulsion across the subunit interfaces, thereby triggering a highly cooperative conformational changes.[15] Furthermore, optical properties of the π-conjugated monomers, which are very sensitive to the intermolecular interactions, has been used as an efficient spectroscopic probe to monitor the temporal changes in the self-assembly as well as to visualize the cooperative disassembly event via time-dependent super-resolved structural illumination microscopy (SIM) imaging.[16] Spectroscopic probing of the cNDI core provided mechanistic insights into the highly cooperative disassembly process.

9.2. Molecular Design:
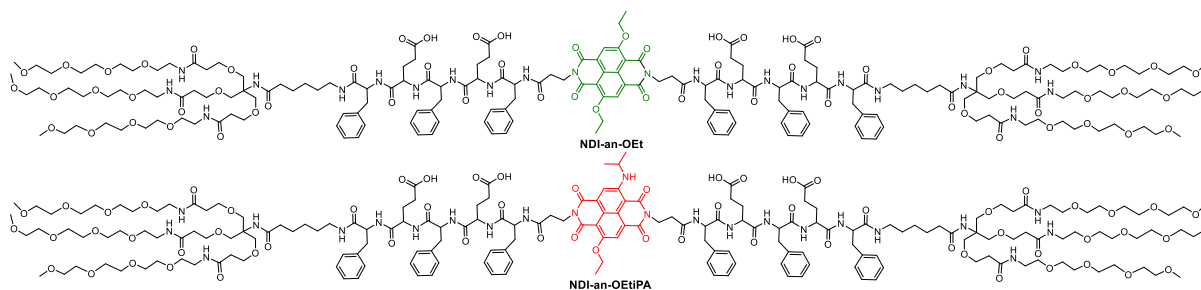
Figure 9.1. Molecular structures of **NDI-an-OEt** and **NDI-an-OEtiPA** used in this Chapter for pH-dependent steady state and active disassembly.

The molecular design of the peptide amphiphiles is shown in Figure 9.1. We have employed ethoxy-substituted (OEt) cNDI and unsymmetrical ethoxy and isopropyl amine (OEtiPA) molecule as the fluorescent chromophore which exhibits green and red emission, respectively in solution and aggregated states.[17,18] In order to modulate the pH-dependent self-assembly, we have appended β-sheet-forming peptide, with alternating phenyl-alanine (hydrophobic) and glutamic acid (hydrophilic) amino acid sequences to the imide positions of cNDI (Figure 9.1), a motif extensively investigated by Besenius and co-workers for the design of charge-regulated responsive peptide assemblies.[19] The resultant **NDI-an-OEt** and **NDI-an-OEtiPA** peptide bola amphiphiles are expected to undergo 1-D self-assembly via cooperative H-bonding,

hydrophobic and π-stacking interactions. Further the strong π-stacking interaction between cNDI cores and large number of hydrophobic phenylalanine units will render a highly stable non-dynamic stacks.[20] Further, we envisage that the carboxylic acid groups of the glutamic acid moieties would regulate the pH-responsive nature of the resulting stacks, as the charge repulsion between the carboxylate groups at higher pH values leads to the disassembly of the stacks. The pH-responsive behaviour of the stacks can be probed spectroscopically through the optical properties of the cNDI derivative, which are highly sensitive to inter-chromophore interactions.[21] **NDI-an-OEt** and **NDI-an-OEtiPA** were synthesized by coupling the peptide sequence, end-functionalized with solubilizing dendritic tetraethylene glycol chains, with the corresponding cNDI core and was characterized via NMR and mass spectrometry (see experimental section for details).

9.3. pH-Dependent, Charge-Regulated Steady State Disassembly of NDI-an-OEt and NDI-an-OEtiPA:
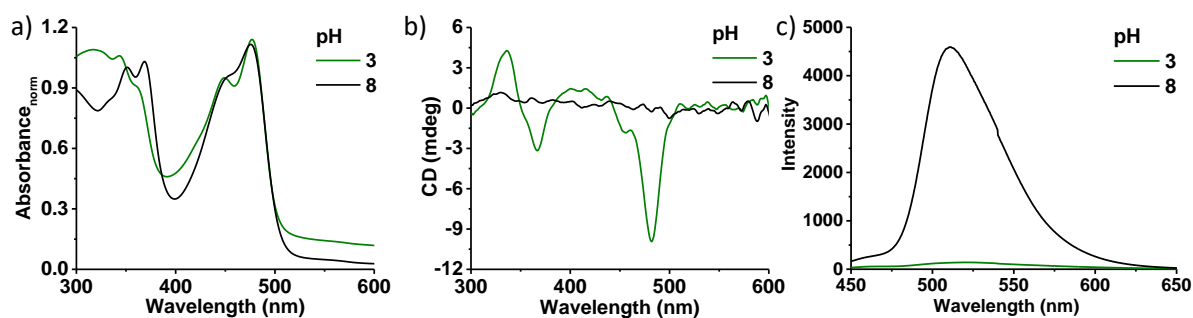
Figure 9.2. a) Absorption, b) CD, and c) emission spectra (λ_{ex} = 430 nm) of **NDI-an-OEt** at pH 3 and pH 8. ([**NDI-an-OEt**] = 5×10^{-5} M, 0.15 M citric acid buffer, 9:1 Ca/Na$_3$C for pH = 3, 0.1 mM Tris-HCl buffer for pH 8).

First, we investigated the steady-state pH-dependent self-assembly of **NDI-an-OEt** using spectroscopic techniques. The absorption spectrum of a 5×10^{-5} M solution of **NDI-an-OEt** in pH 8 Tris-HCl buffer showed sharp π-π* (λ_{max} = 370 and 350 nm) and n-π* (λ_{max} = 475 nm) transitions characteristic of monomeric cNDI (Figure 9.2a).[17,18] This is further observed from the absence of induced circular dichroism (ICD) signals at the NDI electronic transitions (Figure 9.2b). The monomeric nature at pH 8 can be attributed to the electrostatic repulsion between the anionic carboxylate groups of the glutamic acid (pK$_a$ = 4.3) sequences that prevent the stacking of the monomers, in agreement with the previous reports on similar peptide-appended derivatives.[19] Lowering the pH to 3 by addition of citric acid buffer, resulted in the stacking of **NDI-an-OEt** molecules as evident form the reversal of intensity ratios of the vibronic bands at 370 and 350 nm of the π-π* absorption (1.04 at pH = 8 to 0.84 in pH = 3)
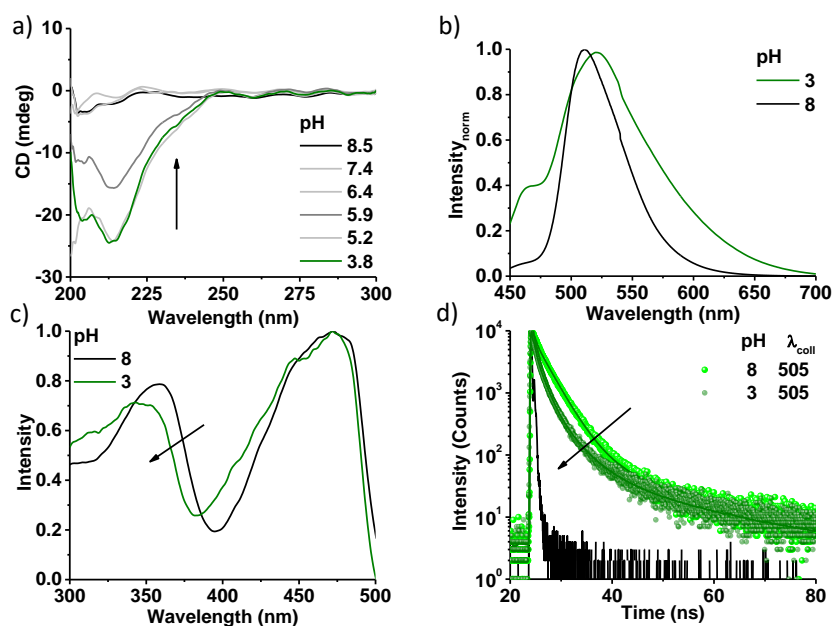
Figure 9.3. a) CD spectra of **NDI-an-OEt** in the 200 to 300 nm region showing β-sheet formation on self-assembly. b) Normalized emission spectra (λ_{ex} = 430 nm) of **NDI-an-OEt** at pH= 8 and pH= 3 showing brodening and red shift of emission on self-assembly at pH 3. c) Excitation spectra collected at 510 nm shows different features for self-assembled state at pH 3 than that of disassembled state at pH 8. d) Lifetime decay profile (λ_{ex} = 442 nm) also follows a quenching of lifetime in self-assembled state at pH 3 in comparison to monomeric state at pH 8. These features refers to the emissive nature of the self-assembled state. ([**NDI-an-OEt**] = 5×10^{-5} M, 0.15 M citric acid buffer, 9:1 Ca/Na$_3$C for pH = 3, 0.1 mM Tris-HCl buffer for pH = 8).

pH	λ_{coll}/nm	t_1/ns	t_2/ns	t_3/ns	t_3/ns
8	505	0.31 (13.16 %)	2.82 (78.93 %)	11.72 (7.91 %)	
3	505	1.54 (45.79 %)	4.02 (23.07 %)	17.5 (7.05 %)	0.27 (24.11 %)

Table 9.1. Lifetime data (λ_{ex} = 442 nm) for self-assembled **NDI-an-OEt** at pH 3 and monomeric **NDI-an-OEt** at pH 8.

along with the appearance of scattering in the 500-600 nm region (Figure 9.2a). Furthermore, induced circular dichroism (ICD)at the n-π* and π-π* adsorption region, with a bisignation at the π-π* absorption maximum confirms the interchromophore π-π stacking of the **NDI-an-OEt** molecules (Figure 9.2b). In addition, CD signal in the 200-300 nm region showed a characteristic spectrum for the β-sheet formation by the peptide segments. This induces chirality into achiral cNDI chromophores to form a helical organization (Figure 9.3a).

Next, we monitored the changes in the emission of the fluorescent cNDI molecule upon pH-induced self-assembly, which is important to visualize the assemblies under SIM. On self-assembling at pH = 3, **NDI-an-OEt** displayed a decreased intensity compared to the monomeric state (Figure 9.2c). The normalized emission spectra showed a broadening of emission the spectrum and bathochromic shift in the emission maximum compared to the

monomeric state (520 nm for pH = 3 and 505 nm for pH = 8) (Figure 9.3b). The excitation spectrum collected at 510 nm for self-assembled state resembles the absorption of self-assembled **NDI-an-OEt**, and is different from the excitation spectrum collected for monomeric state elucidating the emissive nature of these aggregates (Figure 9.3c). The time-resolved fluorescence decay profile at pH 3 further confirms the emissive nature of the **NDI-an-OEt** stacks, which showed a decrease in lifetime (4.02 ns) different from the monomers (at pH 8) (Figure 9.3d and Table 9.1).
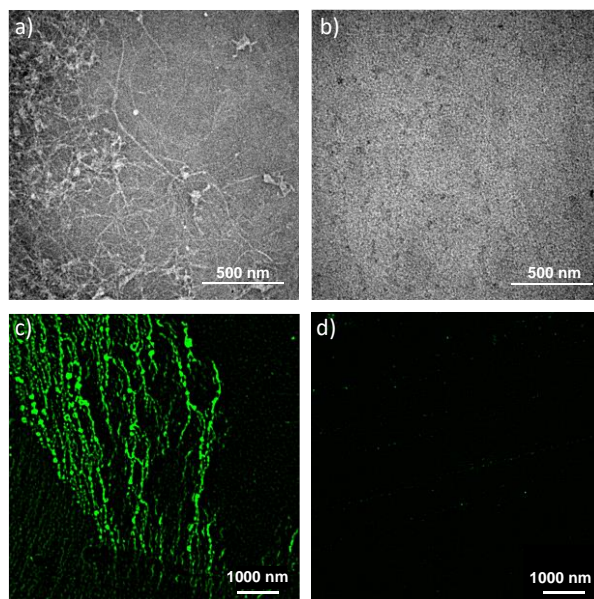
Figure 9.4. a), c) TEM and SIM images (λ_{ex} = 488 nm, λ_{coll} = 495-575 nm) of **NDI-an-OEt** at pH 3 and b), d) at pH 8 depicting presence of long 1D supramolecular polymer at pH 3 and absence of any self-assembled structures at pH 8. ([**NDI-an-OEt**] = 5×10^{-5} M, 0.15 M citric acid buffer, 9:1 Ca/Na$_3$C for pH = 3, 0.1 mM Tris-HCl buffer for pH = 8, TEM samples were prepared by placing a drop of the solution on carbon coated copper grids followed by drying at room temperature in desiccator).

This self-assembly of **NDI-an-OEt** at pH 3 was visualized as one-dimensional micrometer long supramolecular fibers in negatively stained transmission electron microscopy (TEM) (Figure 9.4a). As **NDI-an-OEt** assembly is emissive in the aggregated state, the self-assembly was seen as one-dimensional green-emissive fibers under structured illumination microscopy (SIM) (Figure 9.4c). The monomeric state of **NDI-an-OEt** at pH 8 was confirmed by TEM and SIM imaging (Figures 9.4b and 9.4d) as no structures could be visulaized.

Next, we have investigated the disassembly of the self-assembled **NDI-an-OEt** by the gradual addition of Tris-HCl buffer to increase the pH of the solution from pH 3 to pH 8, important to couple it to a temporality-controlled pH changes for a transient assembly. The extent of disassembly as a function of pH was probed using spectroscopic tools (Figure 9.5).
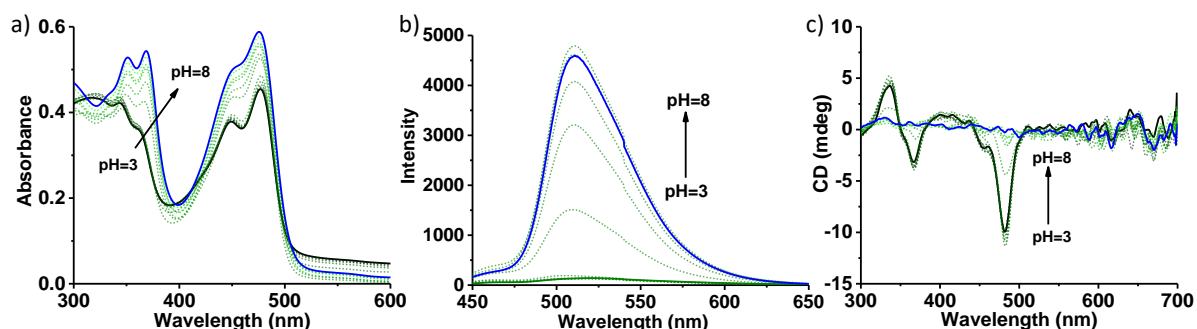
Figure 9.5. Passive pH-dependent disassembly of **NDI-an-OEt**. pH-dependent a) absorption, b) emission (λ_{ex} = 430 nm) and c) CD spectra showing disassembly upon increase in pH. ([**NDI-an-OEt**] = 5×10^{-5} M, 0.15 M citric acid buffer, 9:1 Ca/Na$_3$C for pH = 3, 0.1 mM Tris-HCl buffer for pH = 8).
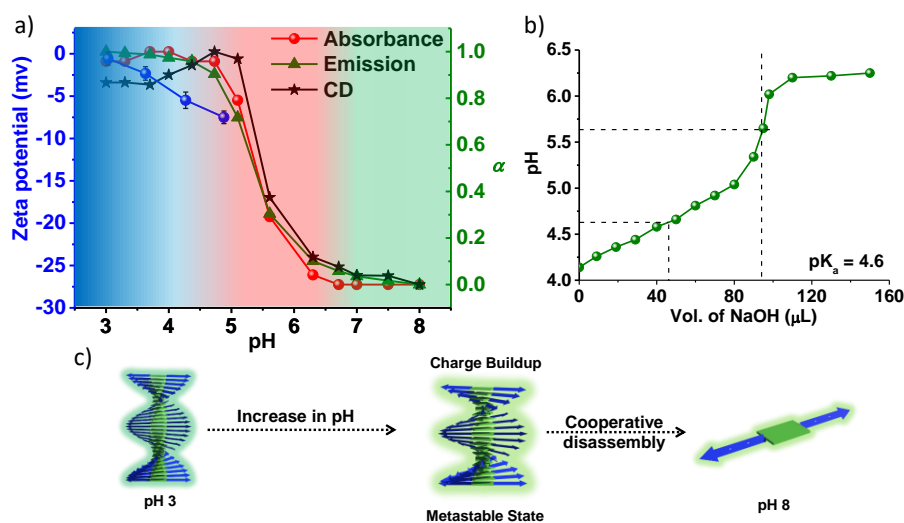
Figure 9.6. a) pH-dependent disassembly profiles probed by monitoring the absorbance (λ = 369 nm), fluorescence intensity (λ = 505 nm) and CD intensity (λ = 480 nm) as a function of the degree of aggregation (α) and pH-dependent zeta potential measurement on **NDI-an-OEt** stacks. b) pH titration experiment of a **NDI-an-OEt** solution to calculte its pK$_a$. c) Schematic illustration of deprotonation and charge buildup in **NDI-an-OEt** stacks and cooperative disassembly of the high energy metastable state. ([**NDI-an-OEt**] = 5×10^{-5} M, 0.15 M citric acid buffer, 9:1 Ca/Na$_3$C for pH = 3, 0.1 mM Tris-HCl buffer for pH = 8).

The plot revealed a sharp transition from aggregate to the monomers above pH 5.2, suggesting a highly cooperative disassembly process (Figure 9.6). Interestingly, the disassembly initiates at pH 5.2, which is higher than the pK$_a$ (4.3) of the side chain carboxylic acid in isolated glutamic acid motifs. We hypothesize such an increase in disassembly pH compared to the pK$_a$ of isolated glutamic acid could be due to hydrophobicity driven shift in pK$_a$ or due to build-up of charges in the non-dynamic highly stable **NDI-an-OEt** stacks in aqueous medium which leads to a charge-mediated highly cooperative disassembly. To get more insight into the process, we have measured the zeta potential and DLS of the stacks with a gradual increase in pH of the solution (Figure 9.6a). Steady-state zeta potential measurements revealed a steady

build-up of negative zeta potential up to pH 5.4 (-11.93 mV), above which an increase in pH failed to produce any response from the instrument. A pH-titration experiment on **NDI- an-OEt** homopolymers revealed a pK_a of 4.6, which ruled out the hydrophobicity driven shift in pK_a of the side chain carboxylic acids (Figure 9.6b). These features are likely due to the accumulation of negative charges on the non-dynamic **NDI-an-OEt** stacks. The sudden disassembly afterward resulted in monomeric anionic **NDI-an-OEt** monomers, which did not produce any zeta potential response.
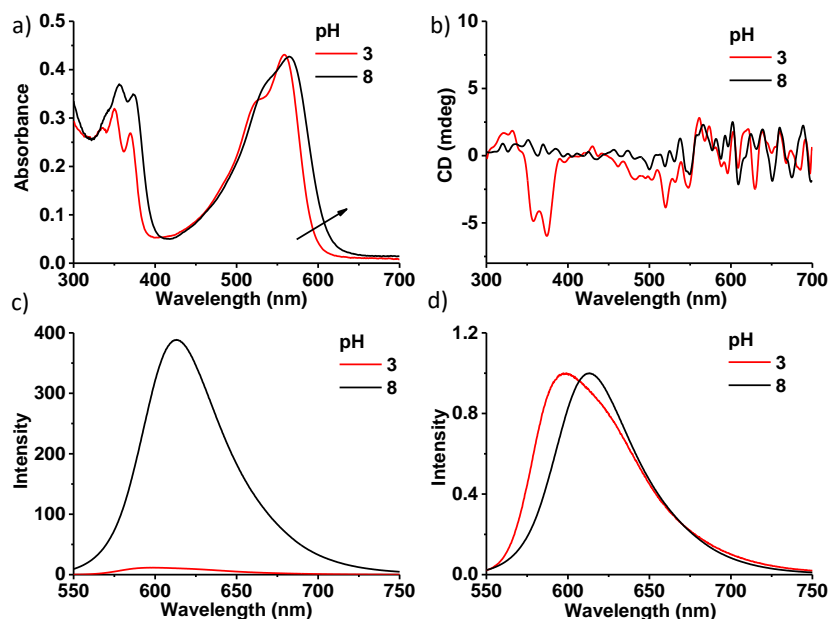
Figure 9.7. a) Absorption, b) CD, c) emission (λ_{ex}= 530 nm), d) normalized emission (λ_{ex} = 530 nm) spectra of **NDI-an-OEtiPA** at pH 8 and pH 3. ([**NDI-an-OEtiPA**] = 5×10^{-5} M, 0.15 M citric acid buffer, 9:1 Ca/Na$_3$C for pH = 3, 10 mM Tris-HCl buffer for pH 8).

The build-up of charges on the stacks will be dependent on the dynamics and stability of the stacks; hence we speculate increase in hydrophobicity of the molecule will provide a less dynamic system, thus allowing more charges to accumulate on the stacks. We have previously observed substitution of one of the ethoxy groups with isopropyl amine group leads to two order of increase in hydrophobicity (log p of the ethoxy-substituted core is 1.69 and ethoxy and isopropyl amine-substituted core is 2.46, p = partition coefficient). This motivated us to explore the pH-dependent disassembly and zeta potential of **NDI-an-OEtiPA** stacks and compare it with **NDI-an-OEt** disassembly.[18b] **NDI-an-OEtiPA** exhibited a pH-responsive self-assembly which was evident from its spectroscopic signatures (change in ratio between vibronic transitions of π-π^* absorption band, quenching and shift in emission and appearance of CD signal) (Figure 9.7).
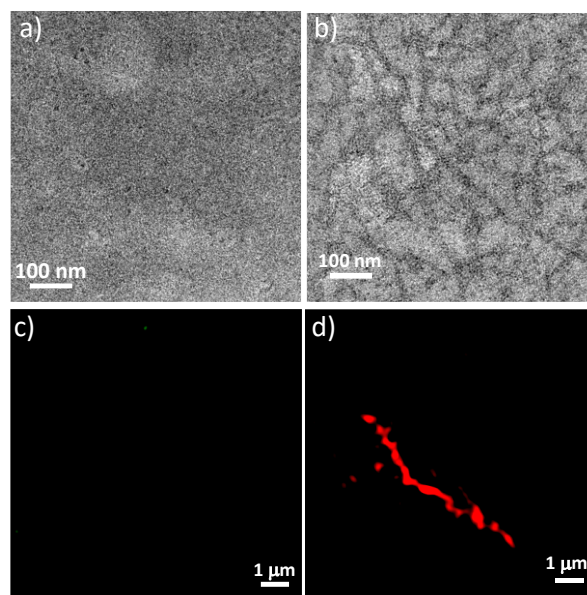
Figure 9.8. a) TEM and c) SIM images of **NDI-an-OEt** at pH 8 and b) TEM, and d) SIM images at pH 3 depicting presence of long 1D supramolecular polymer at pH 3 and absence of any self-assembled structures at pH 8 ([**NDI-an-OEtiPA**] = 5×10^{-5} M, 0.15 M citric acid buffer, 9:1 Ca/Na$_3$C for pH = 3, 0.1 mM Tris-HCl buffer for pH = 8, TEM samples were prepared by placing a drop of the solution on carbon coated copper grids followed by drying at room temperature in desiccator).

The pH-responsive self-assembly was also reflected in the morphological investigations which showed presence of 1D fibers at pH 3 in SIM and TEM images, and absence of self-assembled structures at pH 8 (Figure 9.8). The extent of disassembly against pH shows **NDI-an-OEtiPA** shows a cooperative disassembly event with disassembly starting at pH 6.21 much higher than the dis-assembling pH of **NDI-an-OEt** (pH = 5.2) and the pK$_a$ of isolated glutamic acid (pK$_a$ = 4.3) (Figure 9.9a).
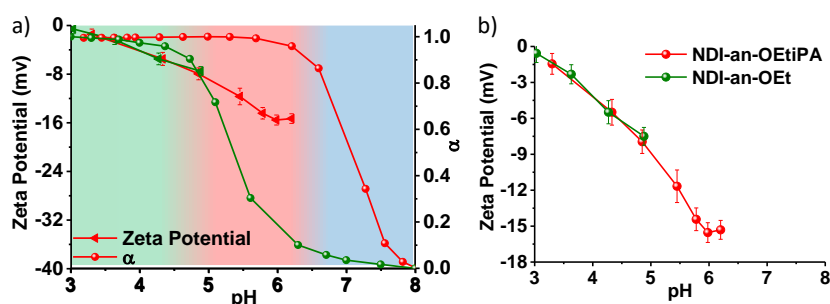
Figure 9.9. a) pH-dependent disassembly profiles probed by monitoring the fluorescence intensity (λ = 505 nm for **NDI-an-OEt** and λ = 610 for **NDI-an-OEtiPA**) as a function of the degree of aggregation (α) and pH-dependent zeta potential measurement on **NDI-an-OEt** and **NDI-an-OEtiPA** stacks. b) Combined zeta potential plots against pH measured on the **NDI-an-OEt** and **NDI-an-OEtiPA** stacks. ([**NDI-an-OEt**] = [**NDI-an-OEtiPA**] = 5×10^{-5} M, 0.15 M citric acid buffer, 9:1 Ca/Na$_3$C for pH = 3, 0.1 mM Tris-HCl buffer as a source of basic pH).

Again, to get insight into the build-up of negative charges and the disassembly process, we have measured the zeta potential with a steady-state increase in pH (Figures 9.9a and 9.9b). The plot of zeta potential against pH depicted a steady increase in negative zeta potential - 16.52 mV) up to pH 6.2 after, which the disassembly event takes over, and the instrument did not show any response. The negative zeta potential indicates the accumulation of negative charges on the **NDI-an-OEtiPA** stacks. Interestingly, the observed negative zeta potential value is much higher for **NDI-an-OEtiPA**, which is in line with a higher stabilized stack of **NDI-an-OEtiPA**, which can accumulate more number of negative charges before disassembly.

9.4. Chemically-Fuelled, Charge-Regulated Disassembly of NDI-an-OEt and NDI-an-OEtiPA Transient Supramolecular Polymers:
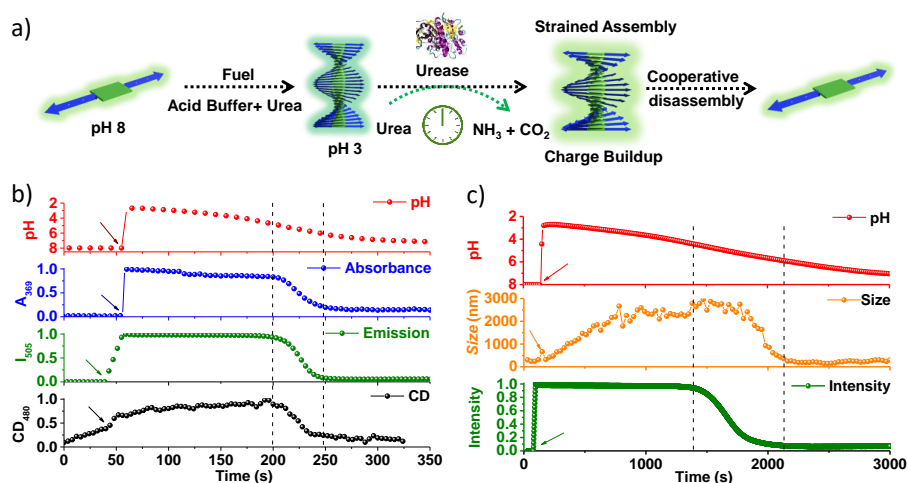
Figure 9.10. a) Schematic illustration of charge-mediated active transient self-assembly of **NDI-an-OEt** which shows increase in pH leads to accumulation of charges on the stacks (metastable state) followed by a cooperative disassembly event. b) pH-responsive temporally programmed transient self-assembly of **NDI-an-OEt** monitored through time-dependent absorbance (369 nm), emission intensity (λ_{ex} = 430 nm , 505 nm) and CD intensity (480 nm) changes along with the temporal pH profiles ([**NDI-an-OEt**] = 5×10^{-5} M, 50 units/mL urease, 100 mM urea). c) Time-depnedent changes in size of **NDI-an-OEt** ([**NDI-an-OEt**] = 5×10^{-5} M) self-assembly monitored via DLS along with the pH profile and changes in the emission intensity with 10 Units/ml of urease and 100 mM urea.

The pH-responsive charge-mediated steady state disassembling behaviour of the **NDI-an-OEt** supramolecular polymer further prompted us to explore its active, transient self-assembly by coupling to a temporally controlled pH profile (Figure 9.10a). We hypothesize coupling it to a temporally controlled pH change would store charges in the stacks, which will subsequently lead to a cooperative disassembly. This would be similar to the stain-mediated transient disassembly observed in microtubules where microtubule disassembles following a slow build-

up of strain. Since **NDI-an-OEt** remains in its monomeric state at higher pH (> 6) and self-assembles at lower pH (< 4.4) (*vide supra*), we require a self-regulating pH profile in the acidic regime to achieve temporal self-assembly. Hence, we have used citric acid buffer as a fast promoter to trigger the pH change from basic to acidic range, and urease catalysed conversion of urea into ammonia as a temporal deactivator.[6e] Thus, the addition of urea containing acidic buffer to basic **NDI-an-OEt** solution (pH 8) containing 100 mM urea, resulted in an instantaneous decrease in the pH to 3, followed by a slow temporal increase in pH back to 7.5 within 200 seconds, characteristic of autocatalytic feedback-driven activity of urease on urea (Figure 9.10b). This temporal pH cycle can affect the **NDI-an-OEt** self-assembly which was probed by time-dependent changes in absorbance (λ = 369 nm), fluorescence (λ_{em} = 505 nm) and CD (λ = 480 nm) intensity which are sensitive to the assembly induced changes in the inter-chromophore interactions (Figure 9.10b). As expected, **NDI-an-OEt** self-assembles instantaneously on the addition of the buffer, followed by a highly cooperative disassembly thus rendering, pH-responsive transient nanostructures (Figure 9.10b). In order to confirm the pH-induced temporal self-assembly, we have performed time-dependent scattering under dissipative conditions. Thus, the addition of acid promoter results in an immediate increase in size due to the assembly formation, which depletes to smaller size assemblies with time, in line with the temporal changes in pH and fluorescence intensity (10 units/mL of urease, Figure 9.10c).
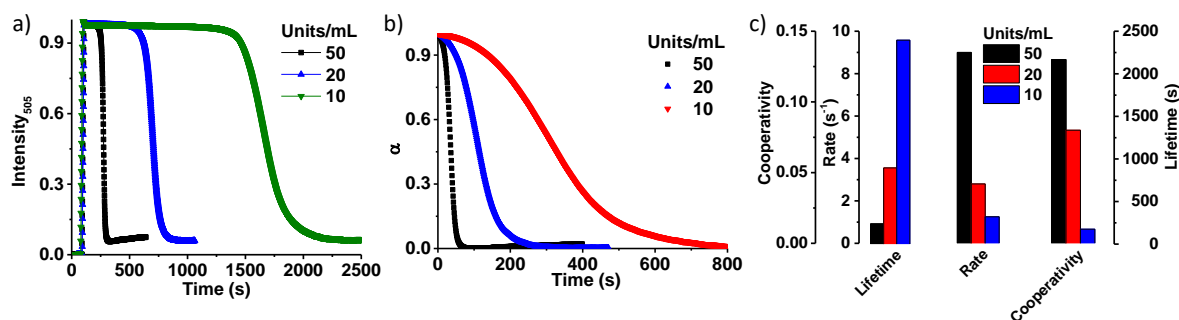
Figure 9.11. a) Emission changes (λ_{ex} = 430 nm) of temporally controlled self-assembly of **NDI-an-OEt** with varying enzyme concentration ([**NDI-an-OEt**] = 5×10⁻⁵ M, 100 mM urea). b) The decay region extracted from Figure 9.8a by cropping the initial unchanged transient state against varying enzyme concentration. f) Bar diagram for comparison of lifetime of the transient assembly, decay rate and cooperativity calculated from Figure 11a against different enzyme concentration.

Since the rate of generation of dormant deactivator to decrease the pH depends on the urease enzyme concentration, the lifetime of the transient **NDI-an-OEt** self-assembly could be modulated from 220 s to 2200 s by varying the enzyme concentration from 50 units/mL to 10 units/mL (Figure 9.11a). Interestingly, spectroscopic properties in the disassembling regime

follow a non-linear change suggesting a highly cooperative disassembly rather than a gradual depolymerization process. Further, the cooperative disassembly kinetics with varying enzyme concentrations suggest that the rate of depolymerization decreases from 0.009 s^{-1} to 0.001 s^{-1} with a decrease in enzyme concentration from 50 units/mL to 10 units/mL (Figures 9.11b and 9.11c). Further the disassembly profile was fitted with cooperative disassembly model to calculate the cooperativity which showed a decreased cooperativity with decrease in enzyme concentration (Figure 9.11c). Again, in line
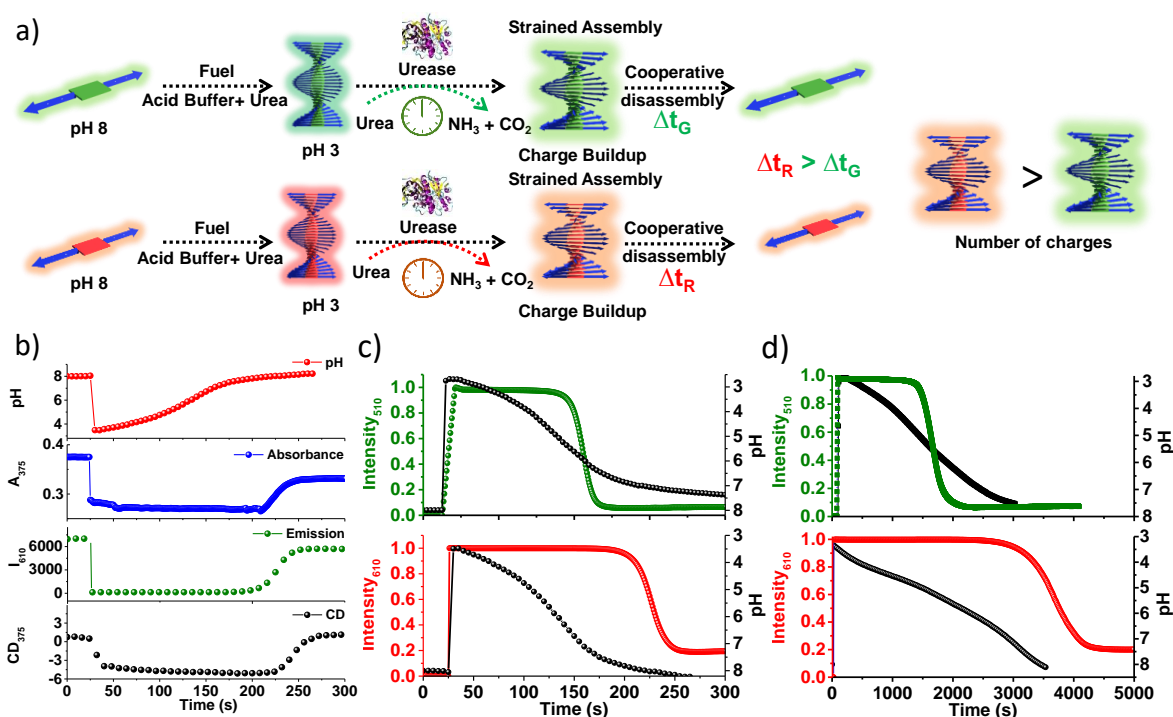
Figure 9.12. a) Schematic illustration of charge-mediated active transient self-assembly of **NDI-an-OEtiPA** and its comparison with **NDI-an-OEt** transient self-assembly showing higher stabilization and accumulation of more charges in metastable state of **NDI-an-OEtiPA** disassembly. b) pH-responsive temporally programmed transient self-assembly of **NDI-an-OEtiPA** monitored through time-dependent absorbance (375 nm), emission intensity (λ_{ex} = 530 nm , 610 nm) and CD intensity (375 nm) changes along with the temporal pH profiles ([**NDI-an-OEtiPA**] = [**NDI-an-OEtiPA**] = 5×10^{-5} M, 50 units/mL urease, 100 mM urea). Comparison of emission changes of temporally controlled self-assembly of **NDI-an-OEt** (green curve) and **NDI-anOEtipa** (Red curve) for c) 50 units/mL urease, 100 mM urea and d) 10 units/mL urease, 100 mM urea. ([**NDI-an-OEt**] = [**NDI-an-OEtiPA**] = 5×10^{-5} M).

with the steady state disassembly process, a faster change in pH at high enzyme concentration leads to more rapid accumulation of charges over the whole **NDI-an-OEt** stack, thus leading to a more cooperative disassembly event. Whereas a slow change in pH at lower enzyme concentration governs a steady build-up charges, thus allowing the system to equilibrate, hence it dis-assembles with lower cooperativity and rate.

On coupling the slow temporal increase in pH to the pH-responsive disassembly of more hydrophobic **NDI-an-OEtiPA**, **NDI-an-OEtiPA** stacks remain stabilized for a longer time and up to a higher pH (even if the pH changes reaches the plateau) than **NDI-an-OEt** stacks followed by a cooperative disassembly (Figure 9.12). The increased hydrophobicity of **NDI-an-OEtiPA** forms a more stabilized and more non-dynamic stacks of **NDI-an-OEtiPA**, which can accumulate more charges during transient pH changes (*vide supra*), thus remains stabilized up to a longer time and higher pH (Figures 9.12c and 9.12d).

9.5. Visualization of the Cooperative Disassembly of Transient NDI-an-OEt and NDI-anOEtiPA Supramolecular Polymers:

The long fluorescent one dimensional fibers further facilitated the real-time probing of the active disassembly mechanism under SIM microscope. Hence, we have investigated the active dynamics of the **NDI-an-OEt** and **NDI-anOEtiPA** fibers with 50 Units/mL enzyme concentration under SIM microscope using time-lapsed images of the fiber in every 10 seconds. The visualization of transient disassembly of **NDI-an-OEt** and **NDI-an-OEtiPA** under SIM microscope corroborate well with the solution state spectroscopic measurements. Instead of a gradual and slow disassembly, the fiber remains unchanged upto 140±20 seconds for **NDI-an-OEt** and 180±10 seconds for **NDI-an-OEtiPA**, which followed a rapid disassembly within 20±10 seconds for **NDI-an-OEt** (Figure 9.13a) and within 10 seconds for **NDI-an-OEtiPA** (Figure 9.13b). Furthermore, the time-dependent intensity changes at three different locations depicted the two fibers disassembled concomitantly throughout its length instead of a gradual disassembly from one position of the fiber (Figure 9.13c). However, the time-dependent intensity profile collected from the fiber plotted against time was found to be less cooperative than the time-dependent intensity changes obtained from solution state ensemble spectroscopic measurements. Also, the plotted time-dependent intensity changes revealed an initial decrease followed by a sharp decrease in intensity (Figure 9.13c). We hypothesize the initial changes in the intensity of the fiber is due to the bleaching of the chromophores on exposure to high-intensity laser during the imaging process. Hence, we have performed time-dependent intensity changes of the fiber in the absence of transient pH changes via continuous irradiation of laser to evaluate the effect of laser on fiber stability. We found indeed in the absence of transient pH changes the intensity decreases gradually with the number of captured frame and time and the plotted time-dependent intensity changes are similar in magnitude (50 % decrease) to the
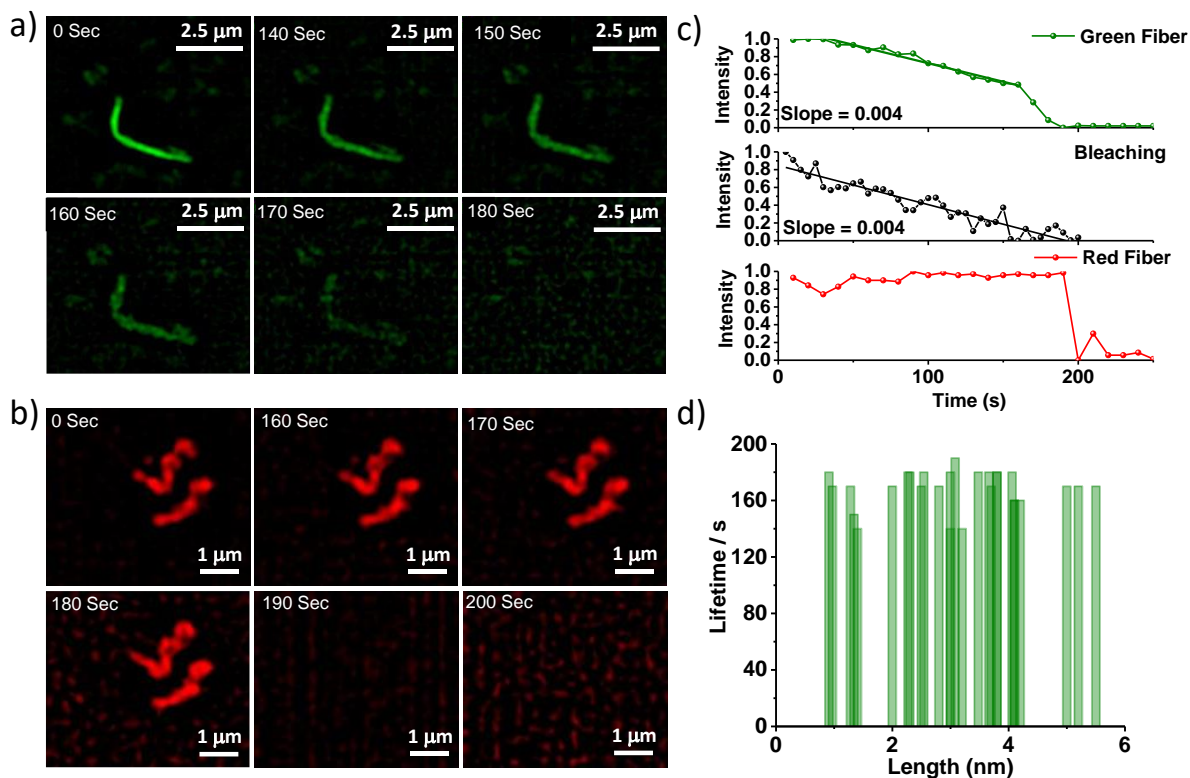
Figure 9.13. Time-lapsed SIM micrographs images of a) **NDI-an-diOEt** (λ_{ex} = 488 nm, λ_{coll} = 495-575 nm) and b) **NDI-an-OEtiPA** (λ_{ex} = 561 nm, λ_{coll} = 570-650 nm) under temporally controlled pH changes showing an intial 140 seconds of stable transient state follwed by a rapid disassembly of the fiber within 20 seconds for **NDI-an-OEt** and initial 180 seconds of stable transient state followed by rapid disassembly within 10 seconds for **NDI-an-OEtiPA**. c) Top pannel: plot of time-dependent intensity changes from three different position of the fibers, extracted using the time lapsed SIM micrograph images for **NDI-an-OEt** fiber. Middle panel: plot of time-dependent intensity changes of a steady state self-assembled **NDI-an-OEt** fiber under continuous irradiation. Bottom panel: plot of time-dependent intensity changes from three different position of the fibers, extracted using the time lapsed SIM micrograph images for **NDI-an-OEtiPA** fiber. d) Histogram of lifetime of the **NDI-an-OEt** fibers of different length showing the disassembly process is length independent. ([**NDI-an-OEt**] = [**NDI-an-OEtiPA**] = 5×10^{-5} M, 100 mM urea, 50 units/mL urease).

initial decrease we observe in case of active self-assembly. This explains the less cooperativity of the time-dependent intensity changes obtained from microscopic studies. We have further visualized the active disassembly process for 27 other fibers which demonstrated the disassembly kinetics is independent of fiber length and all the fibers have same disassembly profile (remains unchanged upto 140±20 seconds, that followed a rapid disassembly within 20±10 seconds) (Figure 9.13d). We envisage the homogeneous increase in pH of the solution leads to a uniform accumulation of charges in the fibers thus the disassembly kinetics is independent of fiber length and the whole fiber disassembles all together. We believe that the process is similar to natural systems such as microtubules where the build-up of non-

assembling GDP-bound monomers in the tubular assembly of GTP-bound monomers or occurs to a critical point after which a disassembly follows.

9.6. Conclusion:

In summary, we have demonstrated a complex, multistep transient one-dimensional supramolecular polymerization of strongly hydrophobic self-assembling moieties in aqueous environments. The molecular design is based on an ethoxy-substituted and unsymmetrical ethoxy- and amine-substituted naphthalene diimide derivatives, extended with alternating phenylalanine and glutamic acid oligopeptide sequence and peripheral dendritic tetra-ethylene glycols (**NDI-an-OEt** and **NDI-an-OEtiPA**). The carboxylic acid side groups endowed pH-responsive self-assembling properties to the molecule. The characteristic optical properties of cNDI derivative, facilitated the spectroscopic and microscopic probing of the steady-state and active disassembly events. We have observed the self-assembly of **NDI-an-OEt** and **NDI-an-OEtiPA** is dominated by hydrophobic effects, thus resulting in high kinetic barriers and slow monomer exchange dynamics. The steady-state pH-dependent disassembly properties probed by spectroscopic techniques revealed a highly cooperative disassembly event. Detailed Zeta potential measurement revealed a charge build-up within the stacked **NDI-an-OEt** and **NDI-an-OEtiPA** with increase in pH assisted by non-dynamic **stacks**, which after a certain threshold disassembles cooperatively. The increased hydrophobicity and more stabilized stacks of **NDI-an-OEtiPA** unravelled a higher charge accumulation and greater stabilization of the metastable state.

Further, by coupling the pH-dependent steady state cooperative disassembly with urea catalyzed conversion of urea into ammonia for temporally regulated pH changes, we were able to demonstrate a chemically fuelled transient supramolecular polymerization reminiscent of stain induced microtubule disassembly. Extensive spectroscopic probing of the active disassembly pathways displayed an initial unchanged and stabilized **NDI-an-OEt** and **NDI-an-OEtiPA** stacks followed by a highly cooperative disassembly. The enzyme concentration-dependent profiles suggest that the rate of depolymerization decreases, and the lifetime of the transient polymer increases with a decrease in the enzyme concentration. Finally, the fluorescent 1D stacks of **NDI-an-OEt** and **NDI-an-OEtiPA** enabled the visualization of the active disassembly event in SIM microscope, which depicted an initial unchanged period followed by a sudden disassembly process. Further investigations revealed fiber disassembles simultaneously from the different positions rather than a gradual disassembly starting from a specific position and the process is independent of the polymer length. The transient

supramolecular polymer coupled to a chemically fuelled temporally regulated pH changes accumulates charges before a highly cooperative disassembly which is analogous to the strain-driven disassembly of microtubules.

9.7. Experimental Section:

General Methods:

Materials: All chemicals were purchased from commercial sources and were used as such without any further purification. Spectroscopic grade solvents were used for all spectroscopic measurements.

NMR Measurements: NMR spectra were obtained with JEOL (600 MHz) Fourier transform NMR spectrometer at the Jawaharlal Nehru Centre for Advanced Scientific Research (JNCASR) with chemical shifts reported in parts per million (ppm) with respect to TMS. Splitting patterns are designated as s, singlet; d, doublet; bs, broad singlet; m, multiplet; t, triplet.

Mass Spectrometry: MALDI was performed on a Bruker Daltonics Autoflex Speed MALDI TOF System (GT0263G201) Spectrometer using trans-2-[3-(4-*tert*-Butylphenyl)-2-methyl-2-propenylidene] malononitrile (DCTB) and α-Cyano-4-hydroxycinnamic acid (CCA) as matrix.

Spectroscopic Measurements: Electronic absorption spectra were recorded on a Perkin Elmer Lambda 900 UV-Vis-NIR Spectrometer and emission spectra were recorded on Perkin Elmer LS 55 Luminescence Spectrometer. UV-Vis and emission spectra were recorded in 10 mm path length cuvettes. Circular Dichroism measurements were performed on a Jasco J-815 spectrometer and were recorded using 10 mm and 5 mm path length cuvettes. The sensitivity, time constant and scan rate were chosen appropriately.

Fluorescence lifetime measurements: Time-resolved decay experiments were recorded on an Horiba Delta Flex Time-Correlated Single Photon Counting (TCSPC) instrument. A 442 nm and 532 nm nano-LED with a pulse repetition rate of 1 MHz were used as light source. The instrument response function (IRF) was collected by using a scatterer (Ludox AS40 colloidal silica, Sigma Aldrich). For the 442 nm and 532 nm LED light source the instrumental full width at half maximum including detector response was 0.2 ns. The excited state decay of the sample was collected by fixing the emission wavelength. The decay was fitted to appropriate best fit multiexponential decay using IBH software (DAS6).

Transmission Electron Microscopy (TEM): TEM measurements were performed on a JEOL (JEM 3010) operated at 300 kV. Samples were prepared by placing a drop of the solution on

carbon coated copper grids followed by drying at room temperature in desiccator (samples were negatively stained with uranyl acetate).

Optical Setup for Imaging in Structured Illumination Microscopy (SIM) method: The fluorescence images of supramolecular polymers were acquired using an inverted Zeiss ELYRA PS1 microscope in structured illumination mode. 488 nm (200 mW) were used for the excitation of **NDI-cat-OEt** and 561 nm (200 mW) for **NDI-cat-OEtIpa**. 5% laser power from the objective top was used for structured illumination imaging. Imaging was performed using a Zeiss oil–immersion objective (Plan–apochromat 63x/1.40 Oil DIC M27, numerical aperture (NA) 1.40 oil). Fluorescence light was spectrally filtered with emission filters for channel I - MBS–488+EF BP 495–575/LP 750 for laser line 488 nm and for channel II - MBS– 561+EF BP 570–650/LP 750 for laser line 561 nm and imaged using a PCO edge sCMOS camera (quantum yield > 70%). Structured illumination images were processed using structured illumination analysis package for Zen software (Zeiss). Additional software was used for colour adjustment (ImageJ).

Calculation of Cooperativity:

To calculate the cooperativity of Figure 9.11 the following modified equation was utilized[15]

$$\alpha = \frac{100}{1+e^{-k(t-t_0)}}$$

Where, α = degree of aggregation, k = cooperativity parameter, t_0 is the transition time (midpoint of time dependent disassembly curve). This equation was inserted in "OriginPro" software and subsequently the graphs in Figure 9.11 were fitted to calculate the cooperativity.

9.8. Synthetic Schemes and Procedures:

Synthetic Schemes:

The synthetic route for the core-substituted NDI derivatives **NDI-an-OEt** Scheme 9.1 and Scheme 9.2. Compound **84**, and **88** were synthesized following reported procedures in Chapter 8. Compound **92** was synthesized following earlier reported procedure.[19]
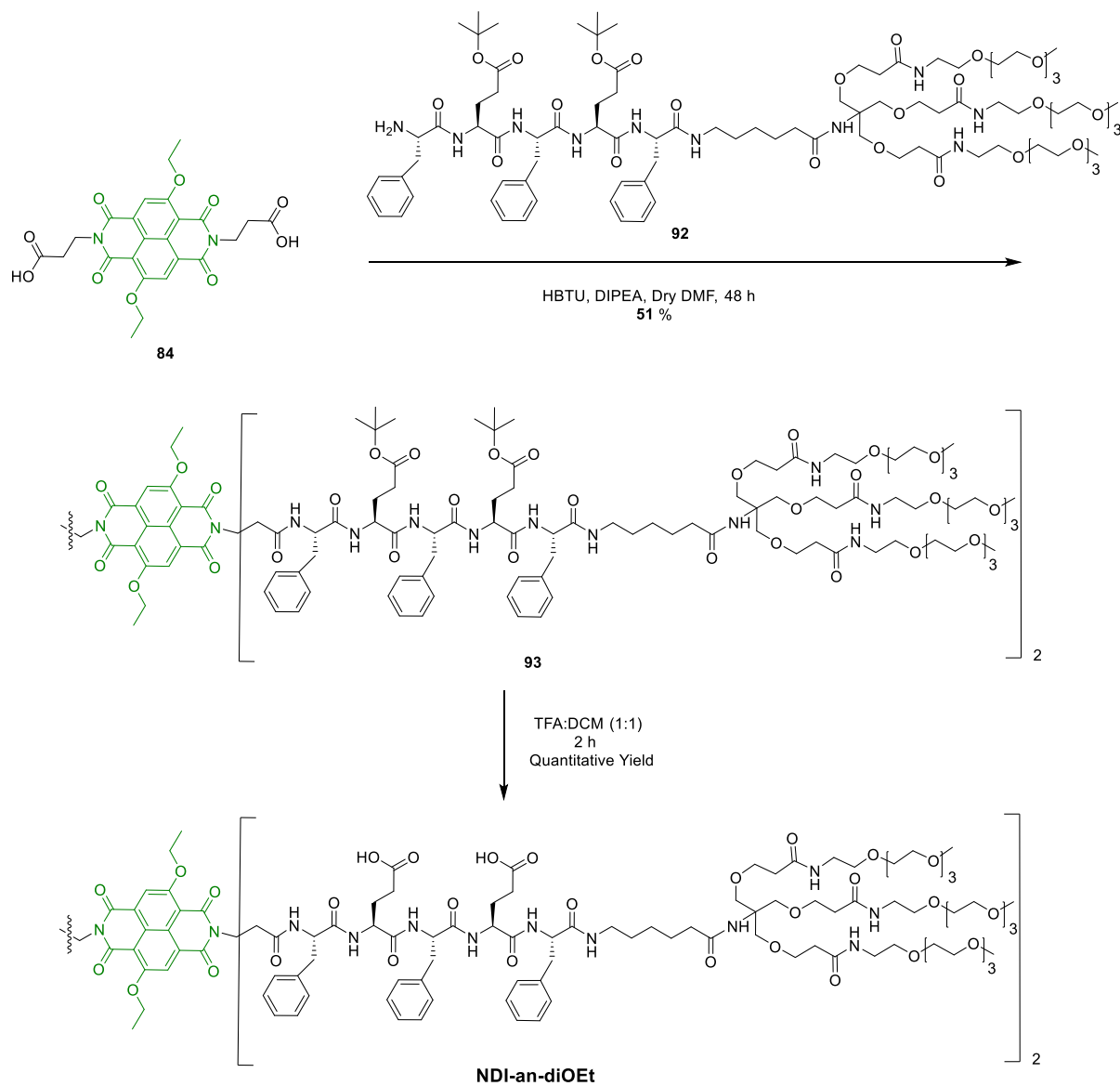
Scheme 9.1. Synthetic Route to **NDI-an-OEt**.
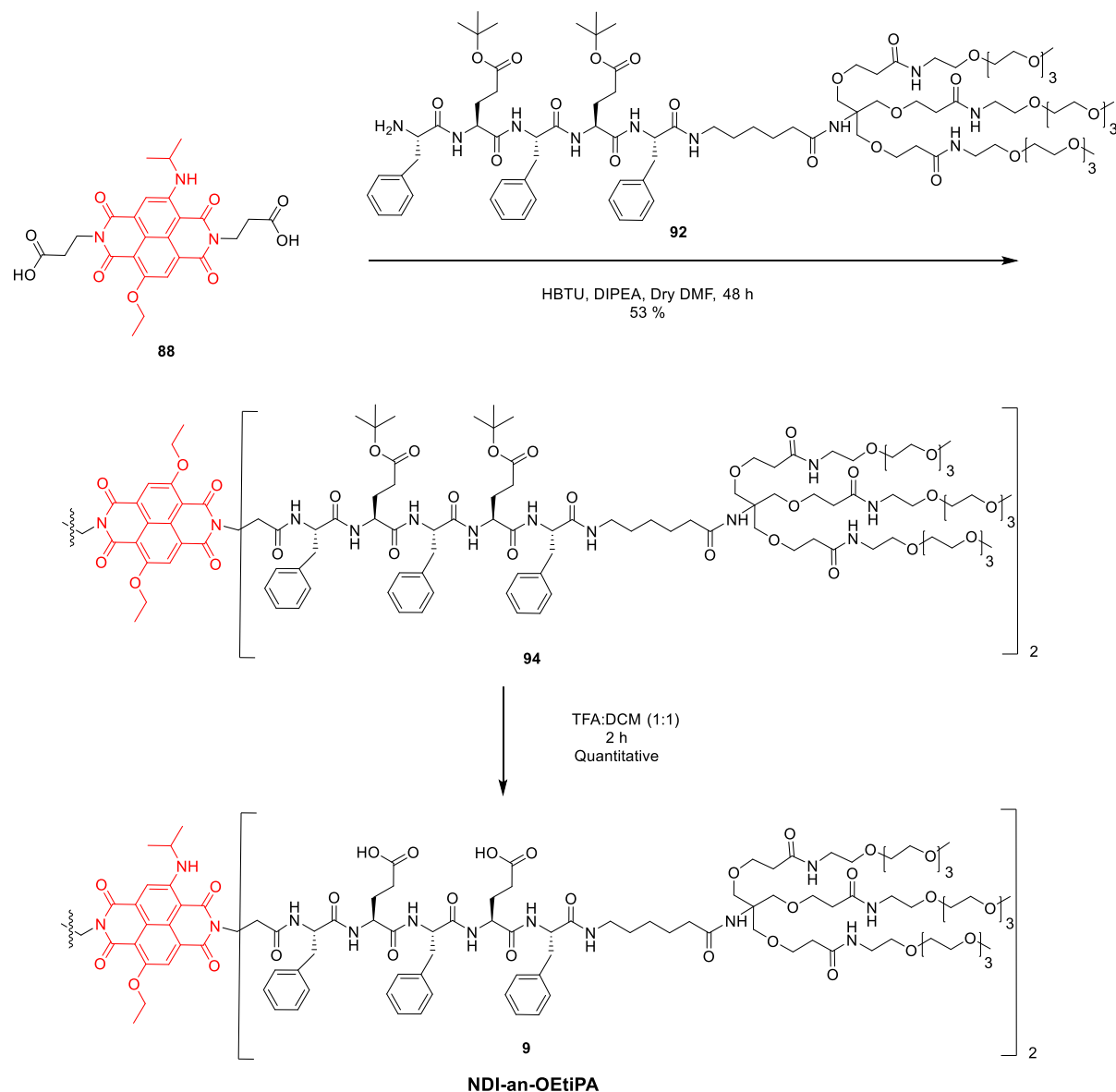
Scheme 9.2. Synthetic Route to **NDI-an-OEtiPA**.

Synthetic Procedures:

Synthesis of molecule 93: In a round bottom flask 10.4 mg of (2-(1H-benzotriazol-1-yl)-1,1,3,3-tetramethyluronium hexafluorophosphate (HBTU), 5.67 mg of **84** and 2.94 mg of N,N-Diisopropylethylamine (DIPEA) was suspended in 5 mL of DMF and stirred at room temperature for 30 minutes. After 30 minutes, 50 mg of **92** dissolved in 1 mL of DMF was added dropwise to the reaction mixture. The progress of the reaction was monitored by TLC. After 3 days excess DMF was removed under reduced pressure and the crude mixture was purified using size exclusion chromatography (SX-1 biobeads, chloroform) to get 24 mg of the pure product as a sticky solid. Yield: 51 %. ^{1}H NMR (600 MHz, CDCl$_3$, ppm): δ = 8.40 (s, 2H), 8.30-8.34 (bs, 2H), 7.45 (bs, 2H), 7.36 (bs, 2H), 7.10-7.19 (m, 10H), 6.83 (m, 4H), 6.34 (bs, 2H), 4.59 (t, 2H), 4.45 (m, 4H), 4.37 (m, 4H), 3.96 (bs, 4H), 2.71-3.67 (m, 219H), 2.41 (m,

25H), 1.88-2.14 (m, 15H), 1.23-1.61 (m, 82H), 0.82 (m, 3H); MALDI-TOF (DCTB matrix, linear positive mode): m/z calculated for $C_{206}H_{314}N_{22}O_{64}$: 4122.2059, found: 4145.990 $[M+Na]^+$.

Synthesis of NDI-an-OEt: 40 mg of **93** was taken in a 25 mL round bottom flask and 8 mL of 1:1 TFA:DCM mixture was added dropwise to it and stirred at room temperature for 4 hours. After 4 hours the solvent was evaporated under reduced pressure to get 34 mg of **NDI-an-OEt** as a pure product. Yield: 97 %. ^{1}H NMR (600 MHz, DMSO-d_6, ppm): δ = 12.09 (bs, 2H), 8.34 (s, 2H), 8.21 (d, 2H), 8.13 (d, 4H), 7.87-7.94 (m, 15H), 7.01-7.22 (m, 30H), 6.97 (m, 2H), 4.43-4.50 (m, 8H), 4.11-4.22 (m, 8H), 3.55 (m, 89H), 2.29 (t, 14H), 2.15-2.21 (m, 9H) 2.02-2.04 (m, 4H), 1.69-1.75 (m, 4H), 1.47 (t, 6H), 1.37-1.42 (m, 4H), 1.27-1.30 (m, 4H), 1.21-1.23 (s, 2H), 1.08-1.17 (m, 4H); MALDI-TOF (DCTB matrix, linear positive mode): m/z calculated for $C_{206}H_{314}N_{22}O_{64}$: 3897.955, found: 3894.346 $[M]^+$; HRMS (ESI, positive mode): m/z calculated for $C_{206}H_{314}N_{22}O_{64}$: 3897.9555, found: 1949.9887 $[M+2H]^{2+}$, 975.4995 $[M+4H]^{4+}$.

Synthesis of molecule 94: In a round bottom flask 51 mg of (2-(1H-benzotriazol-1-yl)-1,1,3,3-tetramethyluronium hexafluorophosphate (HBTU), 17 mg of **84** and 17.5 μL of N,N-Diisopropylethylamine (DIPEA) was suspended in 5 mL of DMF and stirred at room temperature for 30 minutes. After 30 minutes, 152 mg of **2** dissolved in 2 mL of DMF was added dropwise to the reaction mixture. The progress of the reaction was monitored by TLC. After 3 days excess DMF was removed under reduced pressure and the crude mixture was purified using size exclusion chromatography (SX-1 biobeads, chloroform) to get 72.7 mg of the pure product as a red sticky solid. Yield: 53 %. ^{1}H NMR (600 MHz, DMSO-d_6, ppm): δ = 9.68 (s, 1H), 8.03-8.29 (d, 10H), 7.78-7.95 (m, 15H), 7.08-7.25 (m, 30H), 6.92-7.07 (m, 2H), 4.47-4.58 (m, 4H), 4.41-4.47 (m, 2H), 4.30-4.35 (m, 2H), 4.07-4.25 (bs, 8H), 3.48-3.54 (M, 80H), 3.36-3.41 (M, 26H), 3.16-3.21 (m, 20H), 2.87-3.05 (m, 12H), 2.80-2.64 (m, 8H), 2.29-2.27 (t, 16H), 2.07-2.17 (m, 8H), 2.01-2.03 (m, 4H), 1.75-1.84 (m, 4H), 1.71-1.66 (m, 2H), 1.47-1.10 (m, 46H); MALDI-TOF (DCTB matrix, linear positive mode): m/z calculated for $C_{207}H_{317}N_{23}O_{63}$: 4135.2376, found: 4158.766 $[M+Na]^+$.

Synthesis of NDI-an-OEtiPA: 70 mg of **94** was taken in a 25 mL round bottom flask and 8 mL of 1:1 TFA:DCM mixture was added dropwise to it and stirred at room temperature for 4 hours. After 4 hours the solvent was evaporated under reduced pressure and it was codistilled with toluene to remove excess of TFA to get 68 mg of **NDI-an-OEtiPA** as a pure product. Yield: quantitative. ^{1}H NMR (600 MHz, DMSO-d_6, ppm): 11.9-12.2 (br, 3H), 9.68 (d, 1H), 8.03-8.28 (m, 10H), 7.76-7.98 (m, 16H), 7.04-7.29 (m, 30H), 6.97 (m, 2H), 4.44-4.50 (m, 4H),

4.43-4.39 (m, 2H), 4.30-4.35 (m, 2H), 4.20-4.27 (m, 10H), 3.48-3.56 (m, 80H), 3.36-3.41 (m, 30H), 3.16-3.21 (m, 14H), 2.88-3.09 (m, 10H), 2.64-2.81 (m, 8H), 2.37-2.45 (m, 2H), 2.11-2.27 (m, 10H), 1.97-2.03 (m, 4H), 1.82-1.90 (m, 4H), 1.64-1.75 (m, 5H), 1.01-1.45 (m, 40H); MALDI-TOF (DCTB matrix, linear positive mode): m/z calculated for $C_{191}H_{285}N_{23}O_{63}$: 3910.9872, found: 3912.3464 $[M]^+$.

9.9. Experimental procedures:

A stock of concentration of **NDI-an-OEt** and **NDI-an-OEtiPA** (5×10^{-3} M) was prepared in pH 8 Tris-HCl water and the required volume was added to the desired pH solution to adjust the final concentration. Citric acid/sodium citrate buffer was used as a source of acidic pH and Tris-HCl was used as source of basic pH. Urease and urea solution were prepared in pH 7 water solution.

9.10. References:

[1] a) Korn, E. D. *Physiol. Rev.* **1982**, *62*, 672-737. b) Mitchison, T.; Kirschner, M. *Nature* **1984**, *312*, 237-242.

[2] a) Grzybowski, B. A.; Fitzner, K.; Paczesny, J.; Granick. S. *Chem. Soc. Rev.* **2017**, *46*, 5647-5678. b) Zwaag, D. v. d.; de Greef, T. F. A.; Meijer, E. W. *Angew. Chem., Int. Ed.* **2015**, *54*, 334-336. c) Sorrenti, A.; Leira-Iglesias, J.; Markvoort, A. J.; de Greef, T. F.; Hermans, T. M. *Chem. Soc. Rev.* **2017**, *46*, 5476-5490. d) Dhiman, S.; George, S. J. *Bull. Chem. Soc. Jpn.* **2018**, *91*, 687-699. e) Dhiman, S.; Sarkar, A.; George, S. J. *RSC Adv.* **2018**, *8*, 18913-18925. f) Mukhopadhyay, R. D.; Ajayaghosh, A. *Science*, **2015**, *349*, 241-242. g) Mishra, A.; Dhiman, S.; George, S. J. *Angew. Chem., Int. Ed.* **2020**, doi.org/10.1002/anie.202006614

[3] a) van Rossum, S. A. P.; Tena-Solsona, M.; van Esch, J. H.; Eelkema, R.; Boekhoven, J. *Chem. Soc. Rev.* **2017**, *46*, 5519-5535. b) Merindol, R.; Walther, A. *Chem. Soc. Rev.* **2017**, *46*, 5588-5619. c) Ashkenasy, G.; Hermans, T. M.; Otto, S.; Taylor, A. F. *Chem. Soc. Rev.* **2017**, *46*, 2543-2554. d) Huck, W. T. S. *Nat. Nanotech.* **2016**, *11*, 585-592.

[4] a) Boekhoven, J.; Brizard, A. M.; Kowlgi, K. N. K.; Koper, G. J. M.; Eelkema, R.; van Esch, J. H. *Angew. Chem., Int. Ed.* **2010**, *49*, 4825-4828. b) Boekhoven, J.; Poolman, J. M.; Maity, C.; Li, F.; van der Mee, L.; Minkenberg, C. B.; Mendes, E.; van Esch, J. H.; Eelkema, R. *Nat. Chem.* **2013**, *5*, 433-437. c) Boekhoven, J.; Hendriksen, W. E.; Koper, J. M.; Eelkema, R.; van Esch, J. H. *Science* **2015**, *349*, 1075-1079. d) Jain, A.; Dhiman, S.; Dhayani, A.; Vemula, P. K.; George, S. J. *Nat. Commun.* **2019**, *10*, 1-9. e) Grötsch, R. K.; Wanzke, C.; Speckbacher, M.; Ang, A.; Rieger, B.; Boekhoven, J. *J. Am. Chem. Soc.* **2019**, *141*, 9872-9878.

f) Singh, N.; Lainer, B.; Formon, G. J. M.; Piccoli, S. D.; Hermans, T. M. *J. Am. Chem. Soc.* **2020**, *142*, 4083-4087.

[5] a) Wojciechowski, J. P.; Martin, A. D.; Thordarson, P. *J. Am. Chem. Soc.* **2018**, *140*, 2869-2874. b) Jalani, K.; Dhiman, S.; Jain, A.; George, S. J. *Chem. Sci.* **2017**, *8*, 6030-6036. c) Spitzer, D.; Rodrigues, L. L.; Straßburger, D.; Mezger, M.; Besenius, P. *Angew. Chem., Int. Ed.* **2017**, *56*, 15461-15465. d) Leira-Iglesias, J.; Tassoni, A.; Adachi, T.; Stich, M.; Hermans, T. M. *Nat. Nanotech.* **2018**, *13*, 1021-1027.

[6] a) Debnath, S.; Roy, S.; Ulijn, R. V. *J. Am. Chem. Soc.* **2013**, *135*, 16789-16792. b) Pappas, C. G.; Sasselli, I. R.; Ulijn, R. V. *Angew. Chem., Int. Ed.* **2015**, *54*, 8119-8123. c) Sahoo, J. K.; Pappas, C. G.; Sasselli, I. R.; Abul-Haija, Y. M.; Ulijn, R. V. *Angew. Chem., Int. Ed.* **2017**, *56*, 6828-6832. d) Kumar, M.; Ing, N. L.; Narang, V.; Wijerathne, N. K.; Hochbaum, A. I.; Ulijn. R. V. *Nat. Chem.* **2018**, *10*, 696-703. e) Dhiman, S.; Jain, A.; George, S. J. *Angew. Chem., Int. Ed.* **2017**, *56*, 1329-1333. f) Dhiman, S.; Jain, A.; Kumar, M.; George, S. J. *J. Am. Chem. Soc.* **2017**, *139*, 16568-16575. g) Maiti, S.; Fortunati, I.; Ferrante, C.; Scrimin, P.; Prins, L. J. *Nat. Chem.* **2016**, *8*, 725-731. h) Mishra, A.; Korlepara, D. B.; Kumar, M.; Jain, A.; Jonnalagadda, N.; Bejagam, K. K.; Balasubramanian, S.; George, S. J. *Nat. Commun.* **2018**, *9*, 1295.

[7] a) Heuser, T.; Weyandt, E.; Walther, A. *Angew. Chem., Int. Ed.* **2015**, *54*, 13258-13262. b) Angulo-Pachln, C. A.; Miravet, J. F. *Chem. Commun.* **2016**, *52*, 5398-5401. c) Che, H.; Cao, S.; van Hest, J. C. M. *J. Am. Chem. Soc.* **2018**, *140*, 5356-5359. d) Heuser, T.; Merindol, R.; Loescher, S.; Klaus, A.; Walther, A. *Adv. Mater.* **2017**, *29*, 1606842. e) Heuser, T.; Steppert, A.; Lopez, C. M.; Zhu, B.; Walther, A. *Nano Lett.* **2015**, *15*, 2213-2219. f) Panzarasa, G.; Torzynski, A. L.; Sai, T.; Mannschott, K. S.; Dufresne, E. R. *Soft Matter,* **2020**, *16*, 591-594.

[8] a) Kundu, P. K.; Samanta, D.; Leizrowice, R.; Margulis, B.; Zhao, H.; Börner, M.; Udayabhaskararao, T.; Manna, D.; Klajn, R. *Nat. Chem.* **2015**, *7*, 646-652. b) Klajn, R.; Wesson, P. J.; Bishop, K. J. M.; Grzybowski, B. A. *Angew. Chem., Int. Ed.* **2009**, *48*, 7035-7039. c) Klajn, R.; Stoddart, J. F.; Grzybowski, B. A. *Chem. Soc. Rev.* **2010**, *39*, 2203-2237.

[9] a) della Sala, F.; Maiti, S.; Bonanni, A.; Scrimin, P.; Prins, L. J. *Angew. Chem., Int. Ed.* **2018**, *130*, 1611-1615. b) Pezzato, C.; Prins, L. J. *Nat. Comm.* **2015**, *6*, 7790. c) Rieß, B.; Boekhoven, J. *ChemNanoMat* **2018**, *4*, 710-719. d) Tena-SolsonA, M.; Rieß, B.; Grötsch, R. K.; Löhrer, F. C.; Wanzke, C.; Käsdorf, B.; Bausch, A. R.; Müller-Buschbaum, P.; Lieleg, O.; Boekhoven, J. *Nat. Commun.* **2017**, *8*, 15895. e) Dhiman, S.; Jalani, K.; George, S. J. *ACS Appl. Mater. Interfaces* **2020**, *12*, 5259-5264.

[10] Ragazzon, G.; Prins, L. J. *Nat. Nanotech.* **2018**, *13*, 882-889.

[11] Grishchuk, E. L.; Molodtsov, M. I.; Ataullakhanov, F. I.; McIntosh, J. R. *Nature* **2005**, *438*, 383-388.

[12] a) Korevaar, P. A.; George, S. J.; Markvoort, A. J.; Smulders, M. M. J.; Hilbers, P. A. J.; Schenning, A. P. H. J.; De Greef, T. F. A.; Meijer, E. W. *Nature*, **2012**, *481*, 492-496. b) Korevaar, P. A.; de Gree, T. F. A.; Meijer, E. W. *Chem. Mater.* **2014**, *26*, 576-586. c) Ogi, S.; Sugiyasu, K.; Manna, S.; Samitsu, S.; Takeuchi, M. *Nat. Chem.* **2014**, *6*, 188-195.

[13] a) Leira-Iglesias, J.; Sorrenti, A.; Sato, A.; Dunne, P. A.; Hermans, T. M. *Chem. Commun.* **2016**, *52*, 9009-9012. b) Tidhar, Y.; Weissman, H.; Wolf, S. G.; Gulino, A.; Rybtchinski, B. *Chem. Eur. J.* **2011**, *17*, 6068-6075. c) Görl, D.; Zhang, X.; Würthner, F. *Angew. Chem., Int. Ed.* **2012**, *51*, 6328-6348. d) Tantakitti, F.; Boekhoven, J.; Wang, X.; Kazantsev, R. V.; Yu, T.; Li, J.; Zhuang, E.; Zandi, R.; Ortony, J. H.; Newcomb, C. J.; Palmer, L. C.; Shekhawat, G. S.; de la Cruz, M. O.; Schatz, G. C.; Stupp, S. I. *Nat. Matter.* **2016**, *15*, 469-476.

[14] a) Fredy, J. W.; Mendez-Ardoy, A.; Kwangmettatam, S.; Bochicchio, D.; Matt, B.; Stuart, M. C. A.; Huskens, J.; Katsonis, N.; Pavan, G. M.; Kudernac, T. *Proc. Natl. Acad. Sci. U. S. A.* **2017**, *114*, 11850-11855. b) Bochicchio, D.; Kwangmettatam, S.; Kudernac, T.; Pavan, G. M. *ACS Nano* **2019**, *13*, 4322-4334.

[15] Boyken, S. E.; Benhaim, M. A.; Busch, F.; Jia, M.; Bick, M. J.; Choi, H.; Klima, J. C.; Chen, Z.; Walkey, C.; Mileant, A.; Sahasrabuddhe, A.; Wei, K. Y.; Hodge, E. A.; Byron, S.; Quijano-Rubio, A.; Sankaran, B.; King, N. P.; Lippincott-Schwartz, J.; Wysocki, V. H.; Lee, K. K.; Baker, D. *Science* **2019**, *364*, 658-664.

[16] a) Adelizzi, B.; Aloi, A.; Van Zee, N. J.; Palmans, A. R. A.; Meijer, E. W.; Voets, I. K. *ACS Nano* **2018**, *12*, 4431-4439. b) Kubota, R.; Nakamura, K.; Torigoe, S.; Hamachi, I. *ChemistryOpen* **2020**, *9*, 67-79. c) Albertazzi, L.; Zwaag, D. v. d.; Leenders, C. M. A.; Fitzner, R.; van der Hofstad, R. W.; Meijer, E. W. *Science* **2014**, *344*, 491-495.

[17] a) Sakai, N.; Mareda, J.; Vauthey, E.; Matile, S. *Chem. Commun.* **2010**, *46*, 4225-4237. b) Würthner, F.; Ahmed, S.; Thalacker, C.; Debaerdemaeker, T. *Chem. Eur. J.* **2002**, *8*, 4742-4750.

[18] a) Sarkar, A.; Dhiman, S.; Chalishazar, A.; George, S. J. *Angew. Chem., Int. Ed.* **2017**, *56*, 13767-13771. b) Sarkar, A.; Kölsch, J. C.; Berač, C. M.; Venugopal, A.; Sasmal, R.; Otter, R.; Besenius, P.; George, S. J. *ChemistryOpen* **2020**, *9*, 346-350.

[19] a) Frisch, H.; Unsleber, J. P.; Lüdeker, D.; Peterlechner, M.; Brunklaus, G.; Waller, M.; Besenius, P. *Angew. Chem., Int. Ed.* **2013**, *52*, 10097-10101. b) Frisch, H.; Nie, Y.; Raunser, S.; Besenius, P. *Chem. Eur. J.* **2015**, *21*, 3304-3309. c) Ahlers, P.; Frisch, H.; Besenius, P. *Polym. Chem.* **2015**, *6*, 7245-7250. d) Frisch, H.; Nie, Y.; Raunser, S.; Besenius, P. *Chem. Eur. J.* **2015**, *21*, 3304-3309.

[20] a) Sarkar, A.; Sasmal, R.; Empereur-mot, C.; Bochicchio, D.; Kompella, S. V. K.; Sharma, K.; Dhiman, S.; Sundaram, B.; Agasti, S. S.; Pavan, G. M.; George, S. J. *J. Am. Chem. Soc.* **2020**, *142*, 7606-7617.

[21] a) Kumar, M.; Brocorens, P.; Tonnelé, C.; Beljonne, D.; Surin, M.; George, S. J. *Nat. Commun.* **2014**, *6*, 5793. b) Kulkarni, C.; George, S. J. *Chem. Eur. J.* **2014**, *20*, 4537-4541.

<u>Curriculum Vitae</u>

Aritra Sarkar was born on November 10, 1992 in Berhampore, Murshidabad, West Bengal. He finished his B. Sc. in chemistry from Krishnath College under Kalyani University, Berhampore, in 2013. Subsequently he moved to Indian Institute of Technology Guwahati-Guwahati, Assam in 2013 to pursue his M. Sc. in Chemical Science. After finishing his M. Sc. he joined Jawaharlal Nehru Centre for Advanced Scientific Research as a Ph. D. student under Prof. Subi J. George in 2015. His research work at Supramolecular Chemistry Laboratory focused on molecular self-assembly and multicomponent supramolecular polymerization.

List of Publication

From Thesis

1. Sarkar, A.; Dhiman, S.; Chalishazar, A.; George, S. J. Visualization of Stereoselective Supramolecular Polymers by Chirality-Controlled Energy Transfer, *Angew. Chem., Int. Ed.* **2017**, *56*, 13767-13771.

2. Sarkar, A.; Kölsch, J. C.; Berač, C. M.; Venugopal, A.; Sasmal, R.; Otter, R.; Besenius, P.; George, S. J. Impact of NDI-Core Substitution on the pH -Responsive Nature of Peptide-Tethered Luminescent Supramolecular Polymers, *ChemistryOpen* **2020**, *9*, 346-350.

3. Sarkar, A.; Sasmal, R.; Empereur-mot, C.; Bochicchio, D.; Kompella, S. V. K.; Sharma, K.; Dhiman, S.; Sundaram, B.; Agasti, S. S.; Pavan, G. M.; George, S. J. Self-Sorted, Random, and Block Supramolecular Copolymers via Sequence Controlled, Multicomponent Self-Assembly, *J. Am. Chem. Soc.* **2020**, *142*, 7606-7617.

4. Sarkar, A.; Behera, T.; Sasmal, R.; Capelli, R.; Empereur-mot, C.; Mahato, J.; Agasti, S. S.; Pavan, G. M.; Chowdhury, A.; George, S. J. Cooperative Supramolecular Block Copolymerization for the Synthesis of Functional Axial Organic Heterostructures, *J. Am. Chem. Soc.* **2020**, *142*, 11528-11539.

Other Publications

1. Dhiman, S.; Sarkar, A.; George, S. J. Bioinspired temporal supramolecular polymerization, *RSC Adv.,* **2018**, *8*, 18913.

2. Kaur, M.; Singh, N. K.; Sarkar, A.; George, S. J.; Rao, C. N. R. Supramolecular Hybrids of MoS2 and Graphene Nanosheets with Organic Chromophores for Optoelectronic Applications, *ACS Appl. Nano Mater.* **2018**, *1*, 5101-5107.

3. Kaur, M.; Singh, N. K.; Gupta, U.; Sarkar, A.; George, S. J.; Rao, C. N. R. Supramolecularly Bonded Layered Heterostructures Exhibiting HER Activity, *Chem. Asian J.* **2019**, *14*, 1523-1529.

4. Sarkar, S.; Sarkar, A.; George, S. J. Stereoselective Seed-Induced Living Supramolecular Polymerization, *Angew. Chem., Int. Ed.* **2020**, doi.org/10.1002/anie.202006248